6-21-2016 12:00 AM

X-ray Populations in The Local Group: Insights with Hubble & Chandra

Neven Vulic, *The University of Western Ontario*

Supervisor: Dr. Pauline Barmby, *The University of Western Ontario*
Joint Supervisor: Dr. Sarah C. Gallagher, *The University of Western Ontario*
A thesis submitted in partial fulfillment of the requirements for the Doctor of Philosophy degree in Astronomy

Abstract

X-ray observations provide a unique perspective on the most energetic processes in the Universe. In particular, X-ray binaries are used to probe the compact object population and study relationships with galactic properties, such as star formation and mass distribution. Low-mass X-ray binaries (LMXBs) found in globular clusters have been shown to depend on the mass, radius, and metallicity of the cluster. This thesis focuses on the impact environmental parameters have on X-ray sources and the underlying physical explanations for them.

I studied the X-ray binary population in M31 using 1 Ms of *Chandra* ACIS data and 6-filter photometry from the Panchromatic *Hubble* Andromeda Treasury Survey. From a sample of 83 star clusters we found the brightest and most compact star clusters preferentially hosted an X-ray source. An investigation of 1566 H II regions found that neither radius nor Hα luminosity was a predictor of an H II region hosting an X-ray source. To study the faintest X-ray sources a stacking analysis of star clusters and H II regions was completed. Non-detections throughout resulted in upper limits of $\approx 10^{32}$ erg s^{-1}.

Following-up this work, the most sensitive *Chandra* X-ray point source catalogue of M31 was compiled. We detected 795 X-ray sources in an area of ≈ 0.6 deg^2, to a limiting unabsorbed $0.5 - 8.0$ keV luminosity of $\sim 10^{34}$ erg s^{-1}. Cross-correlating our catalogue with previous surveys we found 259 previously undetected sources in our catalogue. We found the completeness-corrected X-ray luminosity functions flatten at $\approx 1.3 \times 10^{37}$ erg s^{-1}, and the distribution is flatter in the bulge than the disk, consistent with previous work. This indicates a lack of bright high-mass X-ray binaries in the disk and an aging population of LMXBs in the bulge.

I also investigated the origin of the relationship between globular cluster metallicity and LMXB formation by studying the number density of red giant branch (RGB) stars. We determined the number of RGB stars for 109 Galactic globular clusters using *Hubble* data. Spearman and Kendall Rank tests between the RGB star density and metallicity [Fe/H] confirmed the data could not have been drawn from a random distribution. This result is inherently depen-

dent on the half-light radius, which affects LMXB formation, and thus does not independently probe the RGB star density.

Keywords: galaxies: individual: Milky Way, M31, NGC 224 — galaxies: H II regions — star clusters — X-rays: binaries — X-rays: galaxies — Galaxy: globular clusters: general — stars: color-magnitude diagrams

Co-Authorship Statement

The work presented in this thesis has greatly benefited from the advice of my supervisors, Dr. Pauline Barmby and Dr. Sarah C. Gallagher. Although I performed all the analysis and wrote the manuscripts, their guidance and feedback improved the quality of this work. Chapter 2: Vulic, N., Gallagher, S. C., and Barmby, P., *Faint X-ray Binaries and Their Optical Counterparts in M31* has been published in The Astrophysical Journal, Volume 790, Issue 2, 2014. Chapter 3: Vulic, N., Gallagher, S. C., and Barmby, P., *X-rays Beware: The Deepest Chandra Catalogue of Point Sources in M31*, has been published in The Monthly Notices of The Royal Astronomical Society, DOI: 10.1093/mnras/stw1523. Chapter 4 will be submitted to the Monthly Notices of the Royal Astronomical Society in 2016.

Acknowlegements

I would first and foremost like to thank both my supervisors, Prof. Pauline Barmby and Prof. Sarah C. Gallagher, for their endless support. I was very fortunate to have them both as supervisors. Not only have I improved as a researcher, teacher, and colleague, but as a person. Their emphasis on the important aspects of scientific research and critical thinking has been invaluable to my development. Being co-supervised from the start of my tenure at Western has been an amazing experience that I will never forget. Gallarmby #1! To my advisory committee, Prof. Jan Cami and Prof. Martin Houde, for their guidance both within and outside of our meetings. The grad club proves to be a great place for disseminating 'advice'. To my thesis committee, I thoroughly enjoyed and have benefitted from our conversations. To the entire department faculty in both physics and astronomy, whom I have interacted with at some level throughout my tenure in a number of different instances/circumstances, it has been a pleasure. The staff, Jodi, Jackie, Clara, Brian, Keri, Phin, Peter, Shailesh, and Henry, thank you for all your help. My fellow graduate students, of which I have seen a few generations come and go, great times knowing you and hopefully our paths cross again. I would also like to thank the anonymous referees and the following people who have provided feedback that made this work possible: B. F. Williams, L. C. Johnson, P. S. Broos, L. K. Townsley, A. Georgakakis, S. Fabbro, M. Hahn, and D. M. Nataf. To both my friends and extended family, thanks for being there for me. Lastly, my family. Mom, Dad, Kat, thank you so much for everything, I love you. Natasa, bebo, volim te.

Contents

Abstract i

Co-Authorship Statement iii

Acknowlegements iv

Contents v

List of Tables ix

List of Figures xi

List of Appendices xiii

List of Abbreviations xiv

1 Introduction 1

1.1 Sources of X-ray Emission 2

1.2 Star Clusters in the Milky Way and Nearby Galaxies 4

1.2.1 The Star Cluster Initial Mass Function and Disruptive Processes 6

1.2.2 Formation of Binaries in Star Clusters 8

1.2.3 Metallicity Trends in Star Clusters 10

1.2.3.1 Globular Clusters 10

1.2.3.2 Open Clusters 11

1.2.4 Stellar Evolution and Colour-Magnitude Diagrams 11

1.3 X-ray Binaries . . . 14
1.3.1 Low-Mass X-ray Binaries . . . 14
1.3.1.1 Accretion and Variability . . . 15
1.3.1.2 LMXB Formation and Evolution in GCs . . . 20
1.3.2 High-Mass X-ray Binaries . . . 23
1.3.2.1 Accretion and Variability . . . 24
1.3.2.2 Formation and Evolution . . . 26
1.3.2.3 Ejections . . . 27
1.3.3 Ultraluminous X-ray Sources . . . 28
1.3.4 X-ray Colour Analysis . . . 29
1.4 X-ray Point Source Populations of Galaxies . . . 31
1.4.1 The Milky Way . . . 32
1.4.2 Extragalactic Studies . . . 34
1.4.2.1 LMXB Evolution . . . 35
1.4.2.2 X-ray Luminosity Function and Star Formation Rate . . . 37
1.4.3 X-ray Binary Simulations . . . 39
1.5 Outstanding Questions . . . 40
Bibliography . . . 42

2 X-Rays Beware: The Deepest Chandra Catalogue of Point Sources in M31 54
2.1 Executive Summary . . . 54
2.2 Introduction . . . 55
2.3 Observations and Data Reduction . . . 59
2.3.1 Observations and Preliminary Reduction . . . 59
2.3.2 Image Registration . . . 65
2.3.3 Merging . . . 67
2.3.4 Source Catalogue Creation . . . 68
2.4 X-ray Source Catalogue Properties . . . 71

2.4.1 Source Catalogue . . . 71
2.4.2 Cross-Correlation With Existing Catalogues . . . 73
2.4.3 Sensitivity Curve . . . 77
2.4.4 The log$N$-log$S$ Relation and X-ray Luminosity Functions . . . 80
2.5 Summary . . . 86
Bibliography . . . 87

3 Faint X-Ray Binaries and Their Optical Counterparts in M31 91
3.1 Executive Summary . . . 91
3.2 Introduction . . . 92
3.3 Observations . . . 96
3.3.1 X-ray Data . . . 96
3.3.1.1 Data Reduction . . . 100
3.3.1.2 X-Ray Point Source Detection . . . 101
3.3.2 Optical Data . . . 103
3.4 Data Analysis . . . 105
3.4.1 Matching Results . . . 105
3.4.2 X-ray Properties of Matched Star Clusters & H II Regions . . . 109
3.4.3 Optical Properties of Matched Star Clusters and H II Regions . . . 111
3.5 X-Ray Stacking . . . 117
3.6 Discussion . . . 123
3.6.1 Star Clusters . . . 123
3.6.2 H II Regions . . . 125
3.6.3 *Chandra* Coverage of M31 . . . 126
3.7 Summary . . . 127
Bibliography . . . 128

4 Milky Way Globular Clusters and LMXBs: Red Giant Influence 135

4.1 Executive Summary . . . 135
4.2 Introduction . . . 136
4.3 Data . . . 138
4.4 Isochrone Fitting . . . 139
4.5 Red Giant Branch Star Numbers . . . 142
4.6 Normalizations . . . 144
4.6.1 Globular Cluster Luminosity and Foreground Contamination . . . 144
4.6.2 Globular Cluster Mass . . . 146
4.6.3 Globular Cluster Volume . . . 151
4.7 Impact of RGB Stars on Globular Cluster LMXBs . . . 158
4.8 Improvements and Future Work . . . 161
4.9 Summary . . . 162
Bibliography . . . 163

5 Conclusions & Future Work **168**

A Complete M31 Source List **174**

B Complete Additional M31 Source Properties **193**

C Complete Catalogue Cross-Matches **214**

D Colour-Magnitude Diagrams For ACS Globular Clusters **234**

E Colour-Magnitude Diagrams For WFPC2 Globular Clusters **242**

Curriculum Vitae **249**

List of Tables

2.1 Summary of Previous M31 X-ray Surveys 57
2.2 Summary of Previous *Chandra* M31 X-ray Catalogues 59
2.3 M31 Point Source Catalogue ACIS-S Observations 61
2.4 M31 Point Source Catalogue ACIS-I Observations 62
2.5 M31 Point Source Catalogue Completeness Limits 72
2.6 M31 X-ray Point Source List 72
2.7 Additional M31 X-ray Source Properties 72
2.8 M31 X-ray Point Source Catalogue Matching Results 77
2.9 M31 X-ray Point Source Catalogue Cross-Matches 77

3.1 ACIS-S Observations 97
3.1 ACIS-S Observations 98
3.2 ACIS-I Observations 98
3.3 X-ray Sources Detected in Merged ACIS Observations 103
3.4 Star Cluster & X-ray Point Source Matches 108
3.5 GC-LMXB Fraction Comparisons 109
3.6 H II Region & X-ray Point Source Matches 110
3.7 Matching Analysis Summary 111
3.8 Logistic Regression Results for Star Clusters and H II regions 114
3.9 Stacked Image Properties 122

4.1 Globular Cluster Isochrone Fitting Parameters 140
4.2 Milky Way Globular Cluster Parameters and RGB Values 156

A.1 Complete M31 Source List 175

B.1 Complete Additional M31 Source Properties 194

C.1 Complete Catalogue Cross-Matches 215

List of Figures

1.1 *Chandra* image of spiral galaxy M83 5

1.2 Colour-magnitude diagram of stars in M15 13

1.3 Geometry of an X-ray binary 17

1.4 X-ray colour-colour diagram classification 31

1.5 X-ray luminosity functions and star formation rate 38

2.1 M31 *Chandra* X-ray point source catalogue fields 60

2.2 Histogram of M31 X-ray point source net counts and source flux 73

2.3 Deprojected radial distribution of M31 X-ray point sources 74

2.4 *Chandra* and *XMM-Newton* X-ray catalogue offset and flux comparison 76

2.5 M31 X-ray catalogue sensitivity curves 79

2.6 M31 uncorrected and completeness-corrected X-ray luminosity functions compared with CDF-S 82

2.7 M31 X-ray luminosity functions compared to optically-identified sources . . . 83

2.8 M31 disk and bulge X-ray luminosity functions 84

3.1 M31 *Chandra* and *HST* footprints and source locations 96

3.2 F475W band M31 star cluster images with multiple X-ray sources 106

3.3 X-ray colour-colour diagram of M31 sources 112

3.4 Optical colour-colour diagram of 83 M31 star clusters 116

3.5 Colour-magnitude diagram of 83 M31 star clusters 117

3.6 F475W magnitude vs. effective radius and $L_{\mathrm{H}\alpha}$ vs. radius for M31 star clusters and H II regions 118

3.7 X-ray luminosity of M31 star clusters vs. F475W magnitude and effective radius 119
3.8 Stacked *Chandra* images of M31 star clusters and H II regions 120
3.9 Upper limits for M31 star cluster and H II region stacking 123

4.1 Colour-magnitude diagram of NGC 7099 143
4.2 RGB number vs. metallicity 147
4.3 RGB star number vs. globular cluster mass 148
4.4 RGB star number per $M_{\odot}$ vs. metallicity 150
4.5 RGB star number density per $M_{\odot}$ vs. metallicity 153
4.6 RGB star number density vs. metallicity 155

D.1 Colour-magnitude diagram for ACS GCs (1-6) 235
D.2 Colour-magnitude diagram for ACS GCs (7-12) 236
D.3 Colour-magnitude diagram for ACS GCs (13-18) 237
D.4 Colour-magnitude diagram for ACS GCs (19-24) 238
D.5 Colour-magnitude diagram for ACS GCs (25-30) 239
D.6 Colour-magnitude diagram for ACS GCs (31-34) 240

E.1 Colour-magnitude diagram for WFPC2 GCs (1-6) 243
E.2 Colour-magnitude diagram for WFPC2 GCs (7-12) 244
E.3 Colour-magnitude diagram for WFPC2 GCs (13-18) 245
E.4 Colour-magnitude diagram for WFPC2 GCs (19-24) 246
E.5 Colour-magnitude diagram for WFPC2 GCs (25-27) 247

List of Appendices

Appendix A Complete M31 Source List 174
Appendix B Complete Additional M31 Source Properties 193
Appendix C Complete Catalogue Cross-Matches 214
Appendix D Colour-Magnitude Diagrams For ACS Globular Clusters 234
Appendix E Colour-Magnitude Diagrams For WFPC2 Globular Clusters 242

List of Abbreviations

Abbreviation	Definition
2MASS	Two Micron All-Sky Survey
ACIS	Advanced CCD Imaging Spectrometer
ACS	advanced camera for surveys
AE	ACIS extract
AGN	active galactic nuclei
ASCA	Advanced Satellite for Cosmology and Astrophysics
BH	black hole
CALDB	Chandra calibration database
CCD	charge-coupled device
CDF-S	Chandra deep-field south survey
CFHT	Canada-France-Hawaii Telescope
CIAO	Chandra interactive analysis of observations
CIMF	cluster initial mass function
CTI	charge transfer inefficiency
CV	cataclysmic variables
Decl.	declination
GC	globular cluster
Gyr	gigayear
H II	singly ionized Hydrogen (H+)
HMXB	high-mass X-ray binary

HRC	high resolution camera
HST	Hubble Space Telescope
IMXB	intermediate-mass X-ray binary
KS	Kolmogorov-Smirnov
ks	kilosecond (10^3 s)
LMXB	low-mass X-ray binary
MS	main sequence
Ms	megasecond (10^6 s)
MSP	milli-second pulsar
Myr	megayear
NED	NASA/IPAC extragalactic database
NIR	near-infrared
NS	neutron star
NuSTAR	Nuclear Spectroscopic Telescope Array
OB	spectral types of high-mass stars
ObsID	observation identification
PHAT	Panchromatic Hubble Andromeda Treasury Survey
pc	parsec
pns	probability of no source
PSF	point spread function
qLMXB	quiescent low-mass X-ray binary
R.A.	right ascension

RGB	red giant branch
ROSAT	Röntgensatellit
RXTE	Rossi X-ray Timing Explorer
SNR	supernova remnant
SFR	star formation rate
TARA	tools for ACIS review and analysis
TOPCAT	tool for operations on catalogues and tables
UCXB	ultracompact X-ray binary
ULX	ultraluminous X-ray source
UV	ultraviolet
WD	white dwarf
WFPC2	wide-field planetary camera 2
XLF	X-ray luminosity function
XMM	X-ray Multi-Mirror Mission
XRB	X-ray binary

Chapter 1

Introduction

After the detection of X-rays from the Sun by a sounding rocket in 1949 (Friedman et al., 1951), the first celestial X-ray source (Scorpius X-1) was discovered from another sounding rocket in 1962 by Giacconi et al. (1962). This discovery led to the construction of the first orbiting X-ray satellite in 1970, *Uhuru*, which studied variable accreting binary X-ray sources and compiled the first X-ray point source catalogue. This was followed by the launch of the first imaging X-ray telescope, the *Einstein Observatory*, in 1978, which revealed coronal X-ray emission from stars and X-ray jets from galaxies among other results (Bradt et al., 1992). Results from *Einstein* raised many important questions concerning the nature of (non-nuclear) ultra-luminous X-ray sources (ULXs) and emission from starburst galaxies. Other important missions that followed included *Röntgensatellit* (*ROSAT*), the *Advanced Satellite for Cosmology & Astrophysics*, the *Rossi X-ray Timing Explorer* (*RXTE*), the *Chandra X-Ray Observatory*, and the *X-ray Multi-Mirror Mission* (*XMM-Newton*). The subarcsecond resolution of *Chandra* revolutionized the field by allowing astronomers to perform more detailed population studies of Galactic and extragalactic X-ray sources by probing smaller scales (e.g., *ROSAT's* angular resolution was $5''$) and having a better sensitivity to fainter X-ray sources.

1.1 Sources of X-ray Emission

The dominant mechanisms for X-ray emission in the Universe are blackbody, thermal, and synchrotron radiation. Additionally, if high-energy electrons are present then inverse Compton scattering must be considered. Blackbody radiation has a spectrum defined by continuum emission with a peak at an energy that depends only on the temperature T. For objects with $T \gtrsim 10^6$ K most of the energy is emitted as X-rays. In a hot ionized gas, electrons that are deflected by positive ions emit radiation, termed free-free emission or bremsstrahlung ('braking radiation'). If the electrons and positive ions are in thermal equilibrium then the electrons have speeds modelled by the Maxwell-Boltzmann distribution, and the gas emits thermal bremsstrahlung. The thermal bremsstrahlung spectrum can contain line emission from elements heavier than hydrogen that are not completely ionized. When an electron collides with an ion it excites a bound electron to a higher state, which is unstable. The ion decays to its ground state and emits an X-ray photon with a characteristic energy (based on the spacing of the energy levels). If the energy of the incident electron (or photon) is larger than the threshold (binding) energy, a core electron is knocked out and a cascade of electrons produces X-ray emission. These processes are dependent on the density and temperature of the ambient plasma. Radiation from a gas is therefore a combination of thermal bremsstrahlung and line (spectral line emission) radiation, where X-rays are emitted at gas temperatures $\gtrsim 10^6$ K. Synchrotron radiation (also magnetic bremsstrahlung) is produced when relativistic free electrons are deflected by a magnetic field, changing their velocity vector and thus accelerating them. The spectrum of electrons is generally assumed to be a power law and consequently so is that of synchrotron radiation, having intensity $I(E) = AE^{\Gamma}$, with A a constant and Γ the spectral (or photon) index (Seward & Charles, 2010). Another source of nonthermal emission is inverse Compton scattering, where an ultra-relativistic electron collides with and transfers energy to a photon, again exhibiting a power law spectrum.

There are various sources of X-ray emission in galaxies, where X-ray binaries (XRBs) comprise most of the resolved point sources we observe. They consist of a compact object,

such as a neutron star (NS) or black hole (BH), that accretes matter generally from a main sequence (MS) or red giant star. Active XRBs have luminosities[1] of $\sim 10^{34-38}$ erg s^{-1} while those in quiescence are $\sim 10^{30-34}$ erg s^{-1} (Heinke et al., 2005). Most of the emission is from the accretion disk as a blackbody component along with thermal and nonthermal emission from a hot corona. A subclass of XRBs are ULXs, which have $L_X > 10^{39}$ erg s^{-1} as a result of super-Eddington accretion (details to follow). Yet another subclass are cataclysmic variables (CVs), similar to an XRB except that the compact object in this case is a white dwarf, with $L_X \sim 10^{30-34}$ erg s^{-1} (Sazonov et al., 2006). Supernova remnants (SNRs), the result of a supernova explosion whose shock wave heats gas to X-ray temperatures ($\sim 10^6$ K), emit at $L_X \sim 10^{35-37}$ erg s^{-1} (Stiele et al., 2011). Most stars emit X-rays (Schmitt, 2000) but only hot (temperature $> 10^4$ K) OB stars[2] reach significant luminosities of 10^{30-33} erg s^{-1} (Stiele et al., 2011). Nevertheless, OB stars are still too faint to be individually detected outside the Galaxy. Moreover, an OB association or H II region (a cloud of hydrogen gas ionized by massive stars) may produce diffuse X-ray emission. This occurs as a result of supernovae and OB star winds that collide with the interstellar medium, which can heat the interstellar medium and produce thermal X-ray emission. In H II regions spectra are required to determine whether an XRB and/or SNR is present due to diffuse emission. Normal stars on the lower MS emit X-rays from their coronae as a consequence of their rotation, which slows as they age. Yet when these stars are in close binaries known as active binaries they are tidally locked and thus rotate at high rates, producing X-ray emission in the $\sim 10^{31}$ erg s^{-1} range (Heinke, 2010). Active binaries actually constitute the majority of faint X-ray sources in globular clusters (GCs). Planetary nebulae, which are shells of ionized gas consisting of stellar material that was ejected by low-intermediate mass stars at the end of their lives, have $L_X \sim 10^{30-32}$ erg s^{-1} (Ruiz et al., 2013), again too low to currently be of significance in extragalactic X-ray studies. A rare class of objects known as magnetars, of which only 21 have been confirmed (all in the Milky Way), are strongly

[1] X-ray luminosities will be in the $0.3 - 8$ keV range unless otherwise stated

[2] Stars are classified by a single letter based on their spectral types as OBAFGKM and ordered by decreasing surface temperature (also equivalent to decreasing mass)

magnetized isolated neutron stars that emit X-rays by spontaneous decay of their magnetic fields. Their X-ray luminosities are $\sim 10^{30-35}$ erg s^{-1}, making extragalactic detection difficult. A caveat to observing X-ray point sources in galaxies is the population can be contaminated by background active galactic nuclei.

The X-ray sources mentioned above are not ubiquitous in all galaxies, although XRBs are the most common. Elliptical galaxies, often referred to as 'red and dead' due to the absence of young stars and gas for star formation, consequently do not host SNRs or OB stars, and so contain almost exclusively (detectable) low-mass X-ray binaries (LMXBs). Many spiral galaxies undergo star formation episodes and have sufficient cold gas to sustain them for extended periods of time, meaning their X-ray population also consists of SNRs and high-mass X-ray binaries (HMXBs). Figure 1.1 shows an X-ray image of spiral galaxy M83 taken with *Chandra*. Certain X-ray sources form preferentially in specific environments. For example, in the Milky Way, LMXB formation is approximately two orders of magnitude more efficient in GCs (Peacock et al., 2010) than in the field of the Galaxy. Conversely, HMXBs are associated with star-forming regions (OB associations, H II regions, and infrared-bright dusty regions) as opposed to old star clusters (e.g. Ranalli et al., 2003; Persic & Rephaeli, 2007; Shtykovskiy & Gilfanov, 2007; Swartz et al., 2011). Before outlining the properties of XRB subclasses and their relation to galactic environments, a review of star clusters is necessary to understand their role in hosting X-ray sources.

1.2 Star Clusters in the Milky Way and Nearby Galaxies

A star cluster is an approximately compact, spherical collection of hundreds to millions of gravitationally bound stars found throughout galaxies. Long-lived star clusters must be stable against tidal disruption by the host galaxy and nearby interstellar clouds as well as have dissolution timescales $> 10^8$ yrs (Lada, 2010). The stars generally all formed at about the same time and out of similar material, meaning they can be modelled as a simple stellar population. To un-

Figure 1.1: *Chandra* image of spiral galaxy M83. The ∼ 800 ks exposure is 9.5′ a side and shows photons with energies of 0.35 − 1.1 keV, 1.1 − 2.6 keV, and 2.6 − 8 keV in red, green, and blue, respectively. The diffuse soft X-ray emission tracing out the spiral arms is prominent, as are the numerous X-ray point sources throughout the galaxy, comprised of SNRs, HMXBs, and LMXBs. (Credit: NASA/CXC/STScI/Long et al. 2014)

derstand how stars form and evolve we must study star clusters since most stars (70 – 90%) are thought to form in clusters (Lada & Lada, 2003). Star clusters are divided into two categories based on their properties: GCs, which orbit the centres of galaxies and consist of hundreds of thousands to millions of old stars that are tightly-bound, and open clusters, which contain

up to thousands of young stars and are weakly bound, thus more susceptible to disruption. Clusters can be destroyed (stars are stripped from the cluster) over time via interactions with giant molecular clouds or tidal forces from the gravitational field of the host galaxy, where the stars then become part of the stellar field population. Internal processes such as relaxation can also cause dissolution. Star clusters are important tracers of the stellar population and the star formation history of galaxies. However, questions remain on how star formation is triggered and how the stellar mass distribution in clusters is established.

Star cluster formation occurs in giant molecular clouds of cool ($\sim$10 K) H_2 gas. After collapse and fragmentation, where turbulence, magnetic fields, and shocks can all influence star formation efficiency, generally $\lesssim 10\%$ of the original mass of the molecular cloud is converted into stars (Evans et al., 2009). Studying star cluster formation is difficult because GCs are no longer formed in the Galaxy and open clusters are born in molecular clouds such that they are embedded in molecular gas and dust. We are thus limited to the use of infrared imaging to observe open cluster formation and must rely on simulations to reproduce the observations of GCs. GCs are thought to form from massive open clusters that do not evaporate or possibly the merger of multiple clusters (Griffen et al., 2010).

1.2.1 The Star Cluster Initial Mass Function and Disruptive Processes

Once formed, an important property of star clusters is the cluster initial mass function (CIMF), defined in equation 1.1. The power-law index $\alpha = -2$ was determined for observations of the Antennae galaxies (NGC 4038/9) (Zhang & Fall, 1999) while similar values have been obtained for other galaxies such as M51, the Small and Large Magellanic Clouds, and the Milky Way (Elmegreen & Efremov, 1997; Bik et al., 2003; de Grijs et al., 2003; Hunter et al., 2003). These surveys each covered varying mass ranges but overall probed $\sim 10^{3-6}$ $M_\odot$ clusters.

$$dN(M_{cl})/dM \propto M_{cl}^{-\alpha} \tag{1.1}$$

The nature of star clusters with masses $> 10^4\ M_\odot$, which have been observed to be common in merging and starburst galaxies, is pertinent to investigating the high-mass end of the CIMF. Whether the CIMF is truncated at large masses, preventing the formation of massive clusters, is still an open question. This is a consequence of the steep decline that has been proposed for the high-mass end of the CIMF (Lada, 2010). In the Milky Way, the CIMF prediction for the low-mass end is similar to scaled local observations, but the predicted CIMFs for high-mass clusters are not. Within a distance of 1 kpc there should exist ≈10 super star clusters, which are massive young clusters that are thought to be the progenitors of GCs. The recent determination of Westerlund 1 as a super star cluster with a mass $\sim 10^5\ M_\odot$ (Clark et al., 2005) is the first and only identification. It is unlikely that this population is yet unobserved and hints at a cutoff of the CIMF at $\sim 10^5\ M_\odot$, although a survey of the disk to larger distances is required (Larsen, 2009b). The same results were found for other spiral galaxies but starbursts do contain clusters with masses upwards of $\sim 10^7\ M_\odot$(Larsen, 2009a). The truncation of the CIMF is consistent with the upper limit of the giant molecular cloud mass function when scaling by formation efficiency, although this is a simple argument that does not account for multiple clumps within the same cloud. Whitmore et al. (2007) showed that, after applying a normalization to the CIMF of a galaxy based on its star formation rate (SFR), that there was no evidence for truncation of the CIMF at the high-mass end in the Antennae galaxies. The CIMF of GCs has the same power-law slope of $\alpha = -2$ for masses $> 10^5\ M_\odot$ but is flat below this value (McLaughlin & Pudritz, 1996). Massive open clusters are great analogs of GCs in terms of mass and (in some cases) metallicity (all elements heavier than hydrogen and helium), therefore providing us with a rare environment in which to study the evolution of the young to intermediate-age stellar population.

Star clusters undergo dynamical evolution that can disrupt the cluster on varying timescales. First, cluster 'infant mortality' occurs within $\lesssim 10 - 30$ Myr whereby the intracluster gas is removed via supernova explosions or stellar winds. Since up to ∼90% of the cluster mass is in the form of gas based on the star formation efficiency, to maintain virial equilibrium the

cluster expands and disassembles (de Grijs, 2010). This mechanism may remove anywhere from 50 – 90% of young clusters from a given population (Goodwin & Bastian, 2006). Mass loss as a result of stellar evolution (supernovae and stellar winds) may also disrupt the cluster. Mass segregation occurs via stellar encounters that result in dynamical relaxation, meaning stars lose all information of their initial state. This can cause high-mass stars to be ejected from the cluster core via binary interactions while low-mass stars in the halo can be lost due to diffusion (de Grijs & Parmentier, 2007). This process can quickly lead to the evaporation of the cluster as the tidal radius (where stars are still gravitationally bound to the cluster) shrinks further and more low-mass stars become unbound. Additionally, many tidal and gravitational effects take place as a result of interactions with other high-mass objects and the spiral arms. Also, clusters experience shocks from the bulge or disk and dynamical friction along their orbits. For a cluster of initial mass M, a typical disruption timescale is $t_{dis} \approx 1.3$ Gyr $(M/10^4\ M_\odot)^{0.62}$ (Lamers et al., 2005; de Grijs & Parmentier, 2007), meaning a cluster of mass $10^5\ M_\odot$ would disrupt in 5 Gyrs while those of $10^6\ M_\odot$ survive for > 20 Gyrs. Cluster disruption timescales are also dependent on stellar binarity, galactocentric distance, orbital velocity, and the stellar initial mass function, but all these contribute to second order when compared with mass (de Grijs & Parmentier, 2007).

1.2.2 Formation of Binaries in Star Clusters

Most stars are thought to form in binaries or higher order systems, as reproducing the observed binary fraction dynamically is unreasonable. However, this is only true for high-mass stars that can have binary fractions of 50 – 100%, whereas the value for low-mass stars such as M dwarfs ($\lesssim 0.5\ M_\odot$) is closer to 30% (Lada, 2006; Kalirai & Richer, 2010). Since anywhere from 70 – 90% of stars are M dwarfs most stars are not in binaries. Most studies of binarity have been limited to nearby solar-metallicity populations (de Grijs, 2010), therefore extrapolating to extragalactic systems is not trivial. Star clusters specifically are thought to dynamically disrupt low-mass binaries after birth due to their typically wide separations (Goodwin, 2010).

Dynamical evolution of binaries within clusters depends on whether the binding energy (of the binary) per unit mass is large or small compared to the velocity dispersion of the star cluster ('hard' and 'soft' binaries respectively). Most soft binaries are destroyed by an encounter because they are weakly bound whereas hard binaries become harder with time and are less likely to be disrupted.

The stellar encounter rate Γ (to be mentioned in detail later) is also important when comparing binaries in clusters to those in the field, because the stellar densities of the surrounding environments vary drastically. Specifically, even a hard binary in a cluster will be rapidly disrupted compared to a soft binary in the field. Especially in the cores of star clusters, dynamical formation of binaries occurs by two or three-body interactions (Katz, 1975; Clark, 1975) or tidal capture (Fabian et al., 1975). For two-body interactions, single stars interact and form a binary, where in the case of evolved stars they can lose their envelopes from the transfer of orbital energy (shrinking the orbit to form a binary). In a three-body or exchange encounter, a single star replaces a member of a binary system. Tidal capture results when two isolated stars interact and each raises tides on the other, dissipating orbital energy via heat and forming a binary. In the case where a compact object is involved, the larger the radius of the companion star, the more likely it is to be captured, biasing this method towards red giant stars with larger envelopes (also known as red giant collisions). In fact, red giants are more likely to be involved in stellar encounters because of their large cross-sections for collisions. Exchange encounters would seem to be the more prevalent method simply because a star or compact object just needs to interact somewhere near a wide binary to eject a member, and replace it. However, wide binaries are thought to be extremely rare at the ages of GCs (Verbunt & Hut, 1987) and therefore tidal capture is the favoured process for binary formation in GCs. Stellar encounters can also result in the ejection of single stars or binaries into the field. The field population of binaries is a combination of both dynamically processed binaries from clusters, primordial binaries from isolated (diffuse/small-scale) star formation, and clustered star formation (Goodwin, 2010). de Grijs (2010) points out that cluster metallicity might influence the initial population of binaries

by altering the opacity limit for fragmentation during star formation as a result of increased cooling.

1.2.3 Metallicity Trends in Star Clusters

An important property of the evolution of a stellar population is the heavy element abundance or metallicity. The ratio of the abundance of iron to that of hydrogen, [Fe/H], is often used as a proxy for metallicity with the Sun's value being the zeropoint. Fe is a good proxy because the increase in metallicity is driven by stellar evolution. This results from supernovae depositing enriched gas back into the interstellar and intracluster media for future star formation. Metallicity can be determined spectroscopically but also photometrically by using a colour index that probes blue and red colours such as $(B-I)$. Young clusters often suffer from the age-metallicity degeneracy because the B colour is sensitive to the MS turnoff (age) and the I colour to giant branch stars (metallicity) (Worthey, 1994; Puzia et al., 2002; Wolf et al., 2007). However, broadband photometry reflects the heavy element abundance for GCs older than about 5 Gyr very well (Harris, 2010), allowing the use of a colour-metallicity relation, which has been determined spectroscopically for GCs in several galaxies.

1.2.3.1 Globular Clusters

GCs in our Galaxy are older than 10 Gyr (GCs are generally $>$ 1 Gyr old) and are located mainly in the bulge and the halo. None have yet been identified in the disk, where $\sim 90\%$ of the stellar mass resides (Larsen, 2009b). Since galaxy haloes and bulges are metal-poor (compared to the disk population) as a consequence so are the GCs that reside in them. In the Milky Way there are 157 GCs currently identified (Harris, 1996)[2010 edition] that show a bimodal colour/metallicity distribution: metal-poor (blue) clusters have [Fe/H] ≈ -1.5 and metal-rich (red) clusters have [Fe/H] ≈ -0.5 (Zinn, 1985). The reason that red GCs are metal-rich is because heavy elements preferentially absorb blue light emitted by stars. The metal-poor GCs have larger galactocentric radii up to 100 kpc and reside in the halo while metal-rich GCs

represent the bulge population and have radii up to 20 kpc (van Loon, 2010). The bimodal GC distribution has also been well established in other galaxies such as M31 (Barmby et al., 2000); regardless of galaxy type the mean metallicities of blue and red GCs are similar (Harris, 2010). Aside from the bulge/halo division, the nature of bimodality in GCs is still puzzling. A mass relation was hinted at by Harris et al. (2006) for blue GCs in brightest cluster galaxies, where the metallicity increases with cluster mass. Intuitively, one would expect that higher-mass GCs retain metals better than their lower-mass counterparts via self-enrichment. As of yet no trend has been found among red GCs.

1.2.3.2 Open Clusters

While the number of open clusters is not well constrained past a few kiloparsecs due interstellar extinction, Dias et al. (2002)[2012 edition] report $\approx$ 2100 in our Galaxy. Open clusters are generally metal-rich (compared with GCs) with [Fe/H] equivalent to the solar value, reflecting the metallicity of the giant molecular clouds in which they formed. They are found in spiral arms and galaxy disks and largely confined to the galactic plane, with age ranges from 1 Myr to 1 Gyr. A metallicity gradient exists in the Milky Way and other spiral galaxies where metal-poor open clusters are found at larger radial distances (Maciel & Costa, 2010; Cheng et al., 2012). Specifically, there is a steep gradient out to $\sim$10 kpc after which the metallicity gradient flattens. No age dependence is observed among open cluster metallicities. These results are relevant to the X-ray populations of galaxies, especially XRBs, which are strongly influenced by metallicity.

1.2.4 Stellar Evolution and Colour-Magnitude Diagrams

Stellar evolution is important to the understanding of both star cluster populations and XRB systems. A Hertzsprung-Russell diagram plots the luminosities of stars against their effective temperatures, allowing us to track their evolution. A colour-magnitude diagram (CMD), also known as the observational Hertzsprung-Russell diagram, plots the magnitude (equivalent to

luminosity) of a star as a function of its colour (equivalent to effective temperature). A CMD allows one to locate different stellar populations and assess the properties of a star cluster, such as its age. Figure 1.2 shows a CMD of a 12 Gyr old GC, M15, with parts of the diagram labelled to indicate various stellar populations. Because the age and metallicity of all stars in a GC are expected to be identical, the mass (usually) differentiates regions of a CMD. However, multiple stellar populations have been identified in GCs in our Galaxy (e.g. Bedin et al., 2004; Milone et al., 2015; Piotto et al., 2015), which complicates analysis and challenges formation and evolution scenarios. These appear as separate main sequences and/or giant branches in GC CMDs, having a combination of different ages and/or metallicities.

A star lives most of its life on the main sequence, where it converts hydrogen into helium in its core. The mass of a star determines both the amount of hydrogen that can be burned and the rate at which it is consumed. High-mass stars of mass $> 10M_{\odot}$ live only $\sim$ 10 Myr on the main sequence, while for the Sun this stage of nuclear burning lasts 10 Gyr, which explains why $80\% - 90\%$ of stars in the solar neighbourhood are main sequence stars. In Milky Way GCs, which are all $\gtrsim$ 10 Gyr old, stars with similar mass to our Sun are just evolving off the main sequence to the subgiant branch. As the core contracts, the hydrogen shell burning causes an increase in the star's luminosity, but a decrease in its effective temperature. On the CMD, the subgiant branch moves up and to the right. At the base of the red giant branch (RGB), a convective zone near the surface begins to develop and moves closer towards the interior of the star. As this happens the star's luminosity increases and it moves up the RGB. The RGB bump is a feature of CMDs on the RGB first predicted by Iben (1968) and Thomas (1967) and later observed by King et al. (1985). It occurs due to a change in the luminosity of RGB stars. During the first ascent of the RGB, as the convective envelope of an RGB star moves inward it is eventually halted by the outward advance of the hydrogen-burning shell. As the convective envelope is pushed outwards, a chemical discontinuity is left behind. As the hydrogen-burning shell crosses this discontinuity the luminosity of the star temporarily drops (Sweigart et al., 1990). This results in an RGB star having the same luminosity on three separate occasions.

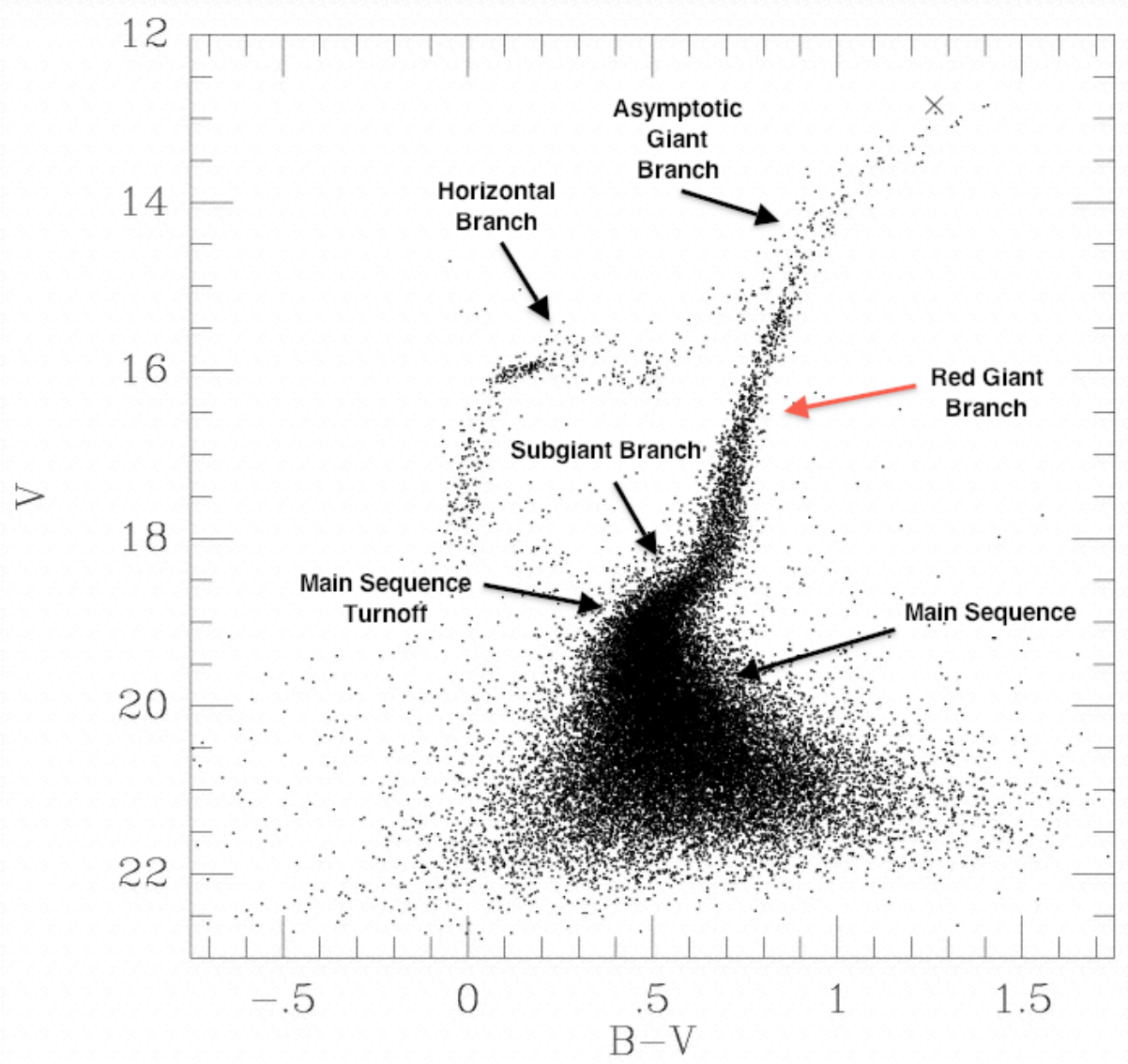

Figure 1.2: The Colour-magnitude diagram (CMD) of M15. The $V-$band magnitude is related to the star's luminosity, and increases moving up the y-axis. The $(B-V)$ colour is related to the star's effective temperature, which increases to the left. (Credit: This figure was modified from van der Marel et al. (2002), who created it from photometry using the WFPC2 instrument on *HST*)

The horizontal branch is where stable helium core burning (and some hydrogen shell burning) takes place, called the 'second main sequence'. This stage and the RGB are short-lived compared to the main sequence. As the energy output rises the effective temperature increases and the star moves left on the CMD. Core contraction and expansion of the star's envelope move the star back to the right as effective temperature decreases. The onset of helium-shell

burning outside the core eventually results in the star moving up the asymptotic giant branch, which approaches the RGB asymptotically from the left, and can be thought of as the analogue of RGB shell burning.

1.3 X-ray Binaries

As previously mentioned, an XRB is a binary system where the primary, either a NS or BH, accretes matter from a secondary star, which is either a MS or red giant star. Matter falling onto the accretor releases gravitational potential energy as X-rays, although this is a small contribution when compared with emission from the accretion disk. XRBs are divided into different categories based on the mass of the donor star: low-mass (LMXB), intermediate-mass (IMXB), and high-mass (HMXB). IMXBs have companions with masses between those of LMXBs and HMXBs and are very rare. Accretion for IMXBs is thought to be suppressed due to weak stellar winds for larger donors and Roche lobe overflow that is halted due to super-Eddington accretion from smaller donors. There are other divisions made, which depend on system properties/states, that define X-ray bursters, X-ray pulsars, millisecond pulsars (MSPs), and microquasars. Being transient sources approximately $\sim 90\%$ of XRBs are in quiescence while the rest are in an outburst state. Since XRBs contain at least one compact object, which are the endpoints of stellar evolution, they are interesting topics of study because they shed light on star formation as well as galaxy evolution.

1.3.1 Low-Mass X-ray Binaries

Of the various types of XRBs, LMXBs in elliptical galaxies are by far the most popular topic of study. Since elliptical galaxies typically have very little gas and dust compared to spiral galaxies, they are unable to form young stars. Therefore the XRB population must be comprised of LMXBs almost exclusively. Their relation with cluster populations, specifically GCs in ellipticals, has been well-documented and will be explained shortly.

In LMXB systems, neutron stars have masses $\lesssim 2.5M_\odot$ (Lattimer, 2012, largest well-measured mass is $\sim 2M_\odot$) and black holes have masses $\gtrsim 5M_\odot$ (Wiktorowicz et al., 2014). The donor stars are usually spectral type G-M with masses $\lesssim 1.5$ $M_\odot$ (Hynes, 2010). The systems with A or F-type companions have been classified as IMXBs since the donor has a slightly larger mass. As a result of both members being low-mass, LMXBs typically have periods of minutes to days and lifetimes $\sim 10^{8-9}$ years. The donor star is extremely difficult to observe directly because it is faint and cool compared to the accretion disk. One method to identify such low-mass systems would be to look for eclipses in the infrared (D'Avanzo et al., 2011; Naylor et al., 1991). Since eclipses are more frequent in close binaries and low-mass stars are brightest in the infrared (Hynes, 2010), observations of LMXB light curves can reveal the companion star.

1.3.1.1 Accretion and Variability

LMXBs accrete matter by Roche lobe overflow (a star's Roche lobe defines the region within which matter is gravitationally bound to the star). This process occurs when the donor star has evolved to fill its Roche lobe, allowing matter to escape via perturbations and be accreted onto the compact object. A system in this state is known as a semi-detached binary. The donor star becomes distorted due to its proximity with the compact object and transfers matter through the inner Lagrangian point L_1, where the Roche surfaces of each object intersect. For stars that are smaller than their Roche Lobes, we have a detached binary where mass transfer is unlikely except through strong stellar winds. In the rare case that each star fills its Roche lobe, a contact binary is formed where the stars may evolve within a common envelope. As a result of mass transfer in semi-detached binaries, the masses of the primary (M_1) and secondary (M_2), period, and orbital separation a will change. Assuming conservative mass transfer (binary mass and angular momentum remain constant), the binary separation shrinks for mass transfer from the more massive star and widens when mass is transferred from the less massive star (Frank et al., 2002). The size of the Roche lobe is affected by the mass ratio $q = M_2/M_1$ and the

orbital separation. For a mass ratio $q > \frac{5}{6}$ mass transfer is unstable and violent. However, most binaries have $q \lesssim \frac{5}{6}$, which causes the Roche lobe of the secondary to expand under conservative mass transfer. Therefore the secondary must either expand or the binary must lose angular momentum in order for mass transfer to continue. These two mechanisms successfully predict the average observed accretion rates in binary systems of $\sim 10^{-11} - 10^{-8}\ M_\odot\ \mathrm{yr}^{-1}$ (Frank et al., 2002).

Once matter has been transferred an accretion disk forms around the compact object due to the angular momentum of the infalling material. Figure 1.3 shows a schematic of an X-ray binary system, depicting the accretion disk and other regions of emission. The α-disk model (Shakura & Sunyaev, 1973) used assumes the disk is in a steady state, is optically thick, thus emitting as a blackbody, and that the flow of matter is confined to the orbital plane of the binary restricting pressure and temperature gradients vertically (thin-disk approximation). The material moves orthogonally to the line of centres (between the cores of each star) as it emerges from L_1 since the orbital speed is so rapid. The matter assumes a circular orbit R_{circ} around the primary that is generally $2-3$ times smaller than the Roche lobe radius. Furthermore, because $R_{circ} \lesssim R_\odot$ for typical LMXBs and compact objects have radii $\lesssim 0.01 R_\odot$ (typical white dwarf (WD) radius), an accretion disk must form. Conversely, for accreting MS stars material may be deposited directly since their radii are $\sim R_\odot$ (Frank et al., 2002), and thus an accretion disk cannot form. Since the accretion disk is subject to differential rotation, material at differing radii move at different angular velocities. This causes viscous stresses that transport angular momentum perpendicular to the motion of gas. Viscous forces along with other dissipative processes such as collisions of gas elements and shocks all convert orbital energy of the gas into internal (heat) energy. Since some of this energy is radiated the orbiting material sinks deeper into the potential of the accretor, losing angular momentum. Internal torques have the effect of transferring angular momentum outwards in order to allow gas to lose angular momentum and fall in. This, however, results in the original ring of matter at R_{circ} spreading to both larger and smaller radii.

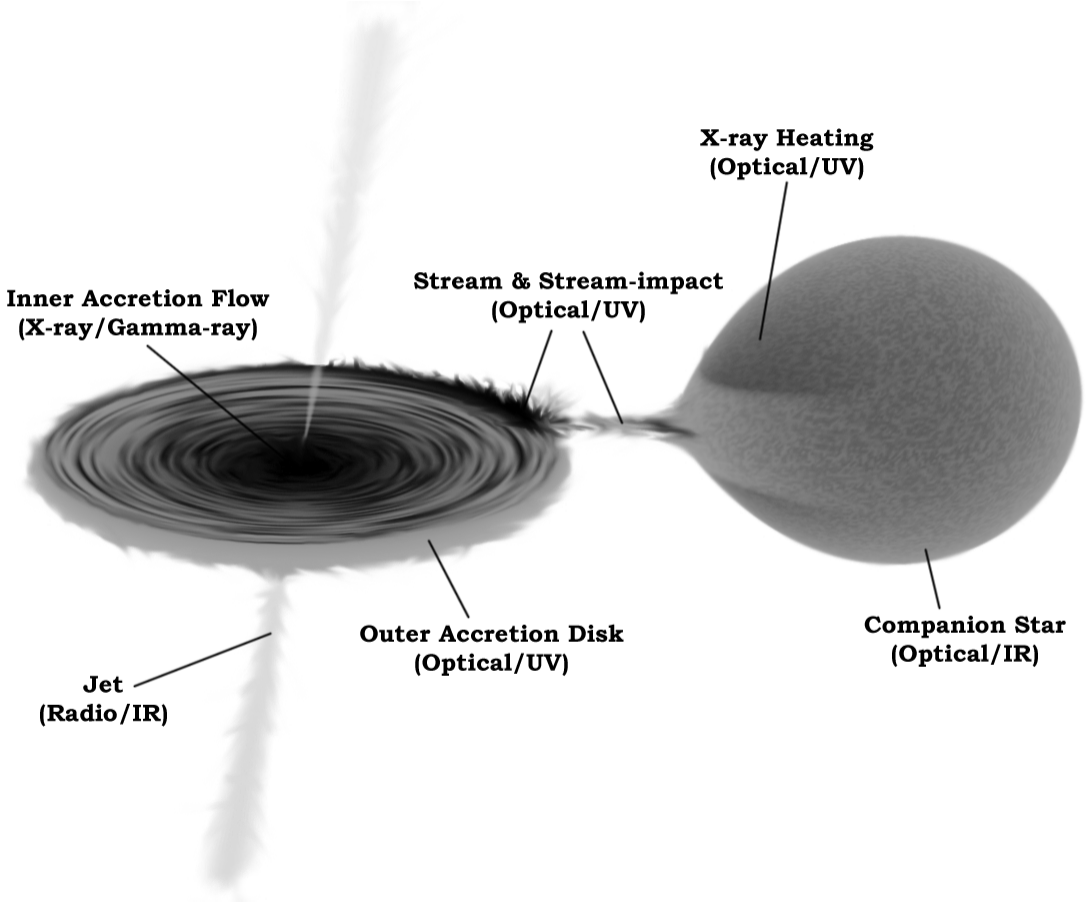

Figure 1.3: Geometry of an X-ray binary system (not to scale) accreting mass via Roche Lobe overflow, showing regions of emission. The colour scale is inverted with the darkest shades indicating bright areas. (Credit: Figure 1.1 from Hynes 2010)

As matter orbits closer to the surface of a compact object its angular velocity decreases to match that of the star. This region is known as the boundary layer, in which there exists a point where the change in angular momentum of the gas is zero, meaning that viscous forces vanish. In the absence of viscosity as a channel to transport angular momentum, the star gains angular momentum from the accreting matter and is spun up as a result. The remaining energy is released in the boundary layer as radiation. The total disk luminosity in a steady state is $L_{disk} = \frac{1}{2}L_{acc}$, such that half the energy is released by radiation and the other half is gravitational potential energy of the infalling matter. Therefore the disk emission is just as important as radiation that will be emitted from the boundary layer. However, the gravitational potential energy that is released as radiation from the surface of a NS or WD (BHs have no surface and

thus accreting matter is thought to increase their mass) is only a fraction of that emitted by the accretion disk for typical LMXBs. For rapidly rotating stars that have angular velocities similar to that of the accreting matter (the case for most observed LMXBs), viscous forces in the boundary layer act outwards and matter is no longer accreted onto the surface. Therefore X-rays are emitted primarily from the inner part of the accretion disk where viscous forces raise gas temperatures above $\sim 10^6$ K. Additional heating can occur via X-rays emitted from the surface, but as we have seen this is not typical of most LMXBs. In some cases, such as the AM Herculis system (a magnetic CV), the compact object has a strong enough magnetic field to suppress the formation of an accretion disk, funnelling matter directly onto the surface (Frank et al., 2002).

Based on what is known from accretion theory we can determine the energy output and maximum accretion rate for accretion onto a compact object. The amount of gravitational potential energy released by a mass m of accreted matter onto an object of mass M and radius R is:

$$E_{acc} = \frac{GMm}{R} \tag{1.2}$$

For accretion onto a NS this is ~ 20 times more energy than would be released for a mass m as a result of nuclear fusion (Frank et al., 2002). The luminosity of the system is dependent on the mass accretion rate $\dot{M}$ (typically $\sim 1.5 \times 10^{-10}\, M_\odot\ \mathrm{yr}^{-1}$ for WDs and NSs), which is in turn governed by the outward momentum from radiation via scattering and absorption of accreting matter. When the force from radiation pushing electron-proton pairs outwards balances that of gravity that draws them inwards, we obtain the limiting luminosity, called the Eddington luminosity, for a star of mass M:

$$L_{Edd} \cong 1.3 \times 10^{38} \frac{M}{M_\odot}\ \mathrm{erg\ s}^{-1} \tag{1.3}$$

The continuum spectrum that we observe is expressed through the temperature of emitted

radiation as $T_{rad} = h\bar{\nu}/k$ where $\bar{\nu}$ is the typical photon frequency. The blackbody temperature $T_b = (L_{acc}/4\pi R^2\sigma)^{1/4}$ derives from the Stefan-Boltzmann law while the thermal temperature $T_{th} = GMm_p/3kR$ assumes all gravitational potential energy of the accreted material is completely converted into thermal energy ($3kT$ for an electron-proton pair). We have $T_b \lesssim T_{rad} \lesssim T_{th}$ since the system cannot radiate below the blackbody temperature while the maximum corresponds to the thermal energy defined above. T_{rad} is similar to T_b for optically thick disks and to T_{th} for optically thin ones. Assuming generic values for NSs and WDs we find that their expected energy ranges are 1 keV $\lesssim h\bar{\nu} \lesssim$ 50 MeV and 6 eV $\lesssim h\bar{\nu} \lesssim$ 100 keV respectively (Frank et al., 2002). This confirms that for NS-LMXBs most of their energy is emitted in the X-ray regime (and partly γ-ray) while CVs range from the ultraviolet to X-ray depending on their accretion state.

XRB variability can be the result of geometric or kinematic processes. In low-inclination ($< 60°$) binaries (where 90° is face-on) we are able to observe the entire disk and the compact object. For inclinations of 60° to 80° the accretor is visible but its lightcurve may undergo dips when the line of sight to it passes near the edge of the accretion disk. A bulge around the edge of the disk occurs as a result of the impact of the accretion stream from the donor. It is this non-uniformly thickened outer edge that causes variations in the X-ray emission from the source, producing dips in the light curve (White & Swank, 1982; Frank et al., 1987). Dips can also result from gas clouds larger than the source that cross the line of sight. Eclipses are possible if the donor blocks the compact object from view during its orbit. For the highest inclination systems the compact object is not visible, but we do see scattered X-rays from a wind or accretion disk corona. As X-rays from the compact object heat gas in the disk, the accretion disk corona is formed above and below it as gas settles in these regions. In the case where the central source is blocked from our line of sight, we see this weaker extended emission from the accretion disk corona. The above-mentioned types of variability have been crucial in uncovering details of disk structure in LMXBs and understanding the kinematics of these systems.

1.3.1.2 LMXB Formation and Evolution in GCs

The luminous X-ray sources in the Galaxy are preferentially found in GCs (Heinke, 2010). The population of stars is predominantly low-mass since all high-mass stars have evolved and left remnants, specifically NSs and BHs, which are the compact objects needed for LMXB formation. Given enough time, WDs form as low-mass stars reach the final stage of their evolution. We would expect LMXB formation to be biased towards GCs because they are the densest collections of stars, which promotes dynamical interactions in forming binaries.

The formation of LMXBs in GCs takes place largely by tidal capture as outlined in section 1.2.2. The stellar encounter rate $\Gamma \propto \int \rho^2/\sigma$ describes the frequency of stellar encounters in a GC, where ρ is the density and σ the velocity dispersion of the GC. Instead of integrating over the cluster volume, a King model (King, 1962, 1966) is used where the density is constant in the core and then rapidly falls off outside of it. Therefore Γ is approximated by only considering its value in the core using a constant density, $\Gamma \propto \rho_c^2 r_c^3/\sigma$, with r_c the physical core radius. The King profile has $\sigma \propto \rho_c^{1/2} r_c$, such that $\Gamma \propto \rho_c^{3/2} r_c^2$ (Verbunt & Hut, 1987). Bahramian et al. (2013) recently calculated Γ for 124 Galactic GCs based on observational data and used simulations to produce the first results with uncertainties. They found strong correlations between Γ and the population of both MSPs and γ-ray fluxes (from MSPs, in agreement with Abdo et al. 2010). Γ scales with the number of XRBs observed in clusters, where Pooley et al. (2003) estimated that ~ 100 LMXBs should reside in GCs in the Galaxy, yet only 14 have been identified for $L_X > 10^{36}$ erg s^{-1} (Liu et al., 2007). In the Milky Way the number of identified LMXBs per unit stellar mass is two orders of magnitude higher in GCs compared to the field (Pooley et al., 2003). A similar trend has been observed in elliptical galaxies (Sarazin et al., 2003; Jordán et al., 2004; Kim et al., 2006; Sivakoff et al., 2007; Kundu et al., 2007; Humphrey & Buote, 2008; Kim et al., 2009). However, detailed studies of GC-LMXBs in spiral galaxies are lacking and thus leave us without a comparison sample for ellipticals.

GCs also house some exotic and interesting LMXB systems, one of which is an ultra-compact X-ray binary (UCXB). The short orbital periods ($<$ 80 min Heinke et al. 2013) of

these binaries require the donor star to be of very low-mass (on the order of hundredths of $M_\odot$) and therefore degenerate (a WD or Helium star), making this system ultra-compact. UCXBs are thought to be the result of common envelope (CE) evolution of binaries (Paczynski, 1976). A CE occurs when a binary orbit becomes unstable as a result of either tidal forces or, more likely, rapid mass transfer. The accretor is unable to accommodate such a large mass transfer and thus forms a CE that both stars orbit within. The orbital energy and angular momentum of the binary is transferred to the CE either resulting in a stellar merger or ejecting the envelope and leaving the system with a much smaller orbital separation. Due to the short-lived nature of the CE phase only indirect evidence has been provided, mainly observations of close binaries for which CE evolution is the only explanation. Recently Ivanova et al. (2013) claimed to have accurately modelled the outburst and merger of V1309 Sco with a CE event. Various models of CE evolution can account for LMXBs, CVs, and merger scenarios such as gamma-ray bursts and type Ia supernovae, but the physics is still not well understood (Zuo & Li, 2014).

Chandra has identified many low-luminosity ($L_X = 10^{30-34}$ erg s^{-1}) sources in Galactic GCs (Heinke et al., 2005) such as MSPs and CVs, which can be confirmed with optical observations. Unfortunately WD-LMXBs are generally too faint to be seen because the compact object does not impart as much gravitational energy to infalling matter as a NS or BH would. MSPs have $L_X \sim (1-4) \times 10^{30}$ erg s^{-1}and are believed to be the final stage of NS-LMXB evolution whereby the NS stops accreting appreciable amounts of material and turns on as a radio pulsar. These rapidly-spinning NSs have periods on the order of ms and are generally < 10 ms. With 22 discovered MSPs in GC 47 Tucanae (Lorimer et al., 2003) and possibly twice as many undetected (Heinke et al., 2005), GCs are a hotspot for the study of evolved LMXBs. *Chandra* has been pivotal in resolving X-ray emission into point sources, such as the X-ray source in the M15 GC core that was later discovered to be two LMXBs (White & Angelini, 2001; Hannikainen et al., 2005). The fact that multiple LMXBs at different evolutionary stages can reside in GCs motivates the study of these systems.

Paolillo et al. (2011) have identified two of the main observational problems that currently

limit our ability to understand important external dynamical factors that dictate LMXB formation in GCs. First, observations of GC-LMXBs with *HST* and *Chandra* have been confined to the central parts of nearby elliptical galaxies. This restricted field of view overlooks the presence of GCs at large distances from the core. It also prevents us from determining how varying GC orbits influence LMXB formation. Therefore, blue metal-poor GCs would be largely excluded from any analysis since mostly red metal-rich GCs are found close to the galactic centre. As a result of the GC metallicity distribution and the limited field of view, the sizes of GCs would also be skewed to those that are brightest and found in galaxy centres. Coincidentally, one of the more detailed studies of the GC-LMXB connection of a rich GC population was completed by Paolillo et al. via wide-field, high spatial resolution observations with *HST* and *Chandra* in the nearby massive elliptical galaxy NGC 1399. Their results were similar to previous groups, where LMXBs were found to favour GCs that are massive, compact, red, and bright. They also found the highest fraction of GC-LMXBs of all early-type galaxies, which was dependent on galactocentric distance. They calculated the cumulative X-ray luminosity function (XLF) of LMXBs in both the field and in GCs (more to follow in Section 1.4). The XLF is a measure of the number of sources per luminosity interval while the cumulative XLF measures the number of sources brighter than a given luminosity L. Investigating the shape of the XLF in relation to fundamental parameters such as galactocentric distance allows us to obtain insight into the metallicity effect (Peacock et al., 2010) and by extension the formation and evolution of these systems. It also forms the observational basis for X-ray population synthesis models.

Nevertheless, not all ellipticals can be surveyed in such a way or even contain the rich GC population of NGC 1399. Fortunately, spiral galaxies generally have an equal distribution of red and blue GCs and are smaller than their elliptical counterparts, enabling wide-field studies. It is well-known that GCs in elliptical galaxies have a bimodal colour and therefore metallicity distribution. However, GCs in spiral galaxies other than the Milky Way and M31 have not been studied to the same extent. Still, the appearance of bimodality in spiral galaxies is evident

(Harris et al., 2006; Cantiello & Blakeslee, 2007). Chandar et al. (2004) found that ∼40% of GCs in M81 are metal-rich, consistent with GCs in M31 and the Milky Way. Knowing that there are similarities between the metallicities of GCs in elliptical and spiral galaxies makes the comparison of LMXB properties between the two more meaningful. In this way one can determine the impact the host galaxy might have on the formation of GC-LMXBs.

The dynamical formation processes for LMXBs are still being debated. One possibility is that all LMXBs in galaxies were formed in GCs and later expelled into the field (Humphrey & Buote, 2008). Another view is that LMXBs can be formed in significant numbers in the field, especially through dynamical interactions near the galactic core, such as the inner bulge of M31 (Voss & Gilfanov, 2007), where a larger volume compensates for lower stellar density. Even though *Chandra* has been very successful at identifying faint sources ($L_X = 10^{30-34}$ erg s^{-1}), this has been limited to nearby galaxies ($\lesssim 1$ Mpc) and the less-obstructed fields of ellipticals. Finding faint sources in spiral galaxies is even more complicated due to diffuse X-ray emission that smears out regions of the spiral arms. Zezas et al. (2007) studied X-ray sources in the Antennae galaxies (∼19 Mpc) and with 7 co-added individual *Chandra* observations totalling 411 ks were able to probe luminosities down to $\sim 10^{37}$ erg s^{-1}. M31 is the only nearby galaxy where *Chandra* can observe sources below $L_X \sim 10^{35}$ erg s^{-1} (Zhang et al., 2011). Recent evidence of a different XLF for GC-LMXBs and those in the field (Voss et al., 2009, among others) was confirmed by Zhang et al. (2011), who combined the populations of several different nearby spiral and elliptical galaxies. These results elicit more important questions regarding the low-luminosity end ($\lesssim 10^{37}$ erg s^{-1}) of GC-LMXB systems.

1.3.2 High-Mass X-ray Binaries

Unlike LMXBs, HMXBs are found in areas of active star formation, such as spiral or irregular galaxies, and as such are generally found in galactic disks. These galaxies allow the formation of massive O or B-type stars (generally > 10 M$_\odot$), which, when found in HMXB systems, are much easier to observe directly ($L_{opt} > L_X$) compared with their low-mass counterparts.

Because the donor star is large, HMXBs have longer periods, typically days to months or possibly years. HMXB lifetimes are $\sim 10^{6-7}$ years. In contrast to LMXBs, HMXBs do not form preferentially in star clusters. Instead, an association exists between HMXBs and star-forming regions, where Shtykovskiy & Gilfanov (2007) found a low-significance ($\lesssim 2\sigma$) constraint on the (wider) distribution of HMXBs relative to bright H II regions. A study of three starburst galaxies by Kaaret et al. (2004) suggest that bright HMXBs are located near young clusters of stars. In the Milky Way, Bodaghee et al. (2012) found clustering between a sample of 79 HMXBs and 458 OB associations with an average offset of 0.4 ± 0.2 kpc, consistent with natal kicks for NSs and BHs. Spiral galaxies with large SFRs have many young open clusters that can be similar in mass to GCs. In these extreme environments, coupled with the weak gravitational attraction to the cluster core, stars and compact objects can be easily ejected from open clusters. Before going into any detail, it is important to understand how HMXB properties are different from those of LMXBs in terms of accretion and evolution.

1.3.2.1 Accretion and Variability

HMXBs accrete matter from the strong stellar wind of their high-mass companion star. This wind is driven by ultraviolet photons that impart momentum to material around the star as they are absorbed and scattered. OB-type stars can have mass loss rates of $\sim 10^{-6}-10^{-5}\ M_\odot\ \mathrm{yr}^{-1}$. As the compact object moves through the wind, any material with kinetic energy smaller than the gravitational potential energy from the compact object in that area will be accreted. This mechanism is known as Bondi-Hoyle accretion and contributes a large part of the X-ray luminosity. Because only a fraction ($10^{-4} - 10^{-3}$) of the total mass lost from the companion is captured by an area on the accretor, this type of accretion is very inefficient compared to Roche lobe overflow, where almost all the mass lost from the companion is accreted by the primary. It is only because of the high mass loss rates of massive stars that we are able to observe HMXBs, where they have similar luminosities to those of LMXBs. Some NS-HMXBs like Cen X-3 do not accrete enough matter from the donor wind to explain their X-ray luminosity (Seward & Charles,

2010). The remaining fraction is a result of the process described in LMXBs whereby the donor star evolves to fill its Roche lobe, transferring material onto the compact object via the L_1 point. However, unlike LMXBs that have old NSs with decayed magnetic fields, HMXBs are young systems with newly-formed NSs and therefore strong magnetic fields (strength frozen-in at the time of formation). This results in the motion of matter from the accretion disk being dictated by the magnetosphere of the NS, funnelling material to the poles. X-rays are produced in a beam since accreting material from each side of the pole (along the field lines) shadows the remaining emission. The pulsar nature results from the misaligned axes of the NS spin and its magnetic poles. Going back to the mechanism for XBs in LMXBs, bursts should also occur in HMXBs when enough material is accreted above the poles. However, this is not the case because accretion rates are so high that unstable helium burning cannot take place. In addition, the strong magnetic fields of NSs in HMXBs do not collapse to allow clumps of matter to fall onto the surface, suppressing type II burst activity. These processes divide NSs between the burst behaviour in LMXBs and X-ray pulsars in HMXBs.

X-ray pulsars were originally discovered by the *Uhuru* satellite in the early 1970s with the eclipsing binary sources Cen X-3, Vela X-1, and 4U1700-37. The spin period of a pulsar undergoes two modulations mentioned earlier, one due to the accretion of matter increasing the spin rate of the NS and the other due to orbital motion around the donor. As the NS rotates, pulses of X-rays are emitted from infalling matter near its magnetic poles. The observations of double-lined spectroscopic X-ray pulsars were crucial in determining NS masses. Measuring the radial velocity of the donor in the optical and the accretor in the X-ray is possible by inspecting the Doppler shift in absorption lines in the spectra of each object. From the velocities determined at different times, orbital parameters, and subsequently the masses, can be calculated using Kepler's third law. The most accurate determination of NS masses has come from double-NS binaries (Lattimer & Prakash, 2005) and defined the common 1.4 $M_\odot$ NS mass. Aside from advancing the study of X-ray pulsars, the upper limit for NS mass (currently $\approx 2.5 M_\odot$) is an important parameter that constrains the equation of state, giving us clues to how stars behave

at extreme values of pressure, density, and temperature (Lattimer & Prakash, 2010; Lattimer, 2011).

The HMXBs outlined thus far are those with the common OB-type companions. Another class of these systems are those with a B*e* star companion. B*e* stars are B-type stars that are rapidly rotating and have hydrogen emission lines in their spectra. As a result of rapid rotation near breakup speed, B*e* stars expel material from around their equator, forming a disk. This material can also contribute to the accretion stream and produce an increase in the X-ray luminosity of the primary. The luminosity is modulated by the orbital period in systems with eccentric orbits, leading to periods of quiescence. An overwhelmingly large fraction ($\sim$ 70%) of HMXBs were thought to have had B*e* companions as opposed to OB supergiants (Hayasaki & Okazaki, 2005), but recent observations have discovered more supergiant companions (Chaty, 2012; Coleiro et al., 2013). Lutovinov et al. (2013) even suggest that most Galactic HMXBs have supergiant companions. Properties of B*e* stars, such as the formation and dissipation of the equatorial disk, mass-ejection mechanisms, and rotation rates can be determined in B*e*-XRBs. In addition to the properties of the neutron star (nearly all B*e*-XRBs are pulsar systems where the companion is a neutron star) that can be discerned, the interaction of the system reveals details of the accretion process and impact on the disk of the B*e* star (Reig, 2011). This includes disk truncation and mass transfer, which are different from the mechanisms and evolution present in isolated B*e* stars. Consequently, observations of B*e*-HMXBs continue to advance our understanding of X-ray transients and the properties of B*e* stars.

1.3.2.2 Formation and Evolution

HMXB formation is thought to occur from a binary system with stars of different masses (Seward & Charles, 2010). The evolutionary scenario for HMXBs is not immediately obvious as one would expect that the massive star in the system would evolve before the compact object. Currently, the best scenario involves a binary star system as the starting point, in which the compact object would have been the more massive of the pair. As it evolves faster to the

supergiant phase, matter would be deposited onto the companion increasing its mass. Following the supergiant phase and supernova explosion, the newly formed compact object would eventually begin accreting matter from its supergiant companion. These HMXB systems are all progenitors of double NS or BH binaries after the companion undergoes a supernova, as opposed to those which undergo inspiral before the companion explodes. The first supernova in the system is the stage where many binaries are separated due to mass loss and asymmetry in the explosion. This causes the period to become longer and the orbit highly eccentric. An important note to make is that the HMXB phase is short-lived, lasting Myrs and varying as a function of the mass of the original stars.

1.3.2.3 Ejections

The mass of each binary member plays an important role in the evolution of HMXBs, specifically regarding the separation and ejection of a member from the host cluster. With the weak gravitational attraction in open clusters, the binary system is loosely bound and the escape velocity is low compared to GCs. This is exacerbated by natal kicks imparted to a NS or BH due to asymmetry in the supernova explosion. Belczynski et al. (2006) state that the velocities imparted to newly formed BHs can be in the range of $100 - 500$ km s^{-1}. Using the StarTrack population synthesis code they found that a significant fraction (40%) of single or binary BHs are ejected from clusters that have escape speeds of $V_{esc} \lesssim 100$ km s^{-1}. Different groups (Kalogera, 2006; Kalogera et al., 2007; Sepinsky et al., 2005) have used the StarTrack code to show that $\simeq 70\%$ of binaries born within young cluster potentials are ejected anywhere from $30 - 100$ pc as a result of supernova (natal) kicks for cluster ages of 15 Myr or older. The fact that few bright ($\sim 10^{36}$ erg s^{-1}) XRBs are discovered near young clusters is in line with observations of nearby starburst galaxies where ejections of $\gtrsim 200$ pc (Rangelov et al., 2011; Kaaret et al., 2004) have been found. Kaaret et al. (2004) explain that even in the absence of natal kicks to a NS or BH, the symmetric ejection of matter from a supernova explosion can result in an ejection. As ejected matter moves with the orbital velocity (~ 50 km s^{-1}) at the

time of the explosion, momentum conservation requires that the compact object move in the opposite direction therefore disrupting the orbit and possibly resulting in ejection. Dynamical interactions with stars or other binaries in the cluster can also result in ejections.

1.3.3 Ultraluminous X-ray Sources

Ultraluminous X-ray sources were first identified in galaxies by the *Einstein Observatory* as off-nuclear sources with $L_X \gtrsim 10^{39}$ erg s^{-1}. Therefore they could not be powered by accretion onto supermassive BHs located in galaxy centres ($M_{BH} \gtrsim 10^6\ M_\odot$). They are predominantly found in starburst or star-forming galaxies. A proposed explanation for these sources includes accretion onto intermediate mass BHs ($10^{2-5}\ M_\odot$). However, it is now widely accepted that most ULXs with $L_X < 10^{41}$ erg s^{-1} are stellar mass BHs ($20\ M_\odot \lesssim M_{BH} \lesssim 100\ M_\odot$) accreting at super-Eddington luminosities in young HMXB systems (Gladstone et al., 2009; Prestwich et al., 2013; Sutton et al., 2013). The slightly larger BH masses coupled with super-Eddington accretion can explain the observed luminosities. Servillat et al. (2012) found that ULXs were coincident with molecular clouds in the spiral arms of star-forming galaxies using *Herschel* infrared observations. The large stellar mass loss rates of OB stars and identification of these optical counterparts in some ULXs (Liu et al., 2002; Jonker et al., 2012) lends credence to the HMXB scenario. Gladstone et al. (2013) investigated the optical counterparts of ULXs in nearby galaxies and found that a high-mass companion was ruled out for only 1 of the 20 systems included in the study. Relativistic beaming from jets is an unlikely explanation for ULXs due to the number of unbeamed sources that would be required in galaxies (King, 2004). Further evidence against intermediate-mass BH primaries stems from the break in the X-ray luminosity function at $\sim 10^{40}$ erg s^{-1} for star-forming galaxies (Mineo et al., 2012), where these ULXs are expected to be detected. Also, spectral fits to *XMM-Newton* data discounting sub-Eddington accretion (Gladstone et al., 2009) indicates these sources are stellar mass compact objects accreting above the Eddington limit.

The subclasses of ULXs are split based on luminosity into standard ($\sim 10^{39-40}$ erg s^{-1}),

extreme ($\sim 10^{40-41}$ erg s^{-1}), and hyperluminous ($\gtrsim 10^{41}$ erg s^{-1}) X-ray sources (Gladstone, 2013). Both the extreme and hyperluminous classes only have 2 confirmed sources respectively. Hyperluminous X-ray sources in particular cannot be explained using the standard scenario, and thus are thought to be either the stripped nuclei of dwarf galaxies (Bellovary et al., 2010), produced via interactions involving supermassive BHs (Jonker et al., 2010, 2012), or intermediate-mass BHs. In addition, many ULX candidates are actually background galaxies, explaining the elevated emission (Heida et al., 2013). A study from Prestwich et al. (2013) has shown that ULXs favour formation in metal-poor galaxies by 2.3σ over metal-rich galaxies. Possible explanations include both the frequency of ULXs and BH masses being higher in metal-poor galaxies (Mapelli et al., 2010). No ULXs have been identified in the Milky Way but recently an M31 ULX was identified as an LMXB (Middleton et al., 2012)[along with another candidate from Barnard et al. 2013]. However, this source is of low luminosity and transient, whereas most ULXs are persistent.

1.3.4 X-ray Colour Analysis

Once an X-ray source has been identified, naturally one wants to discover the nature of the source. XRBs can be classified, albeit loosely, based on their X-ray colours. This alternative to spectral fitting and/or using multiwavelength data is essentially photometry at X-ray wavelengths[3]. When working with *Chandra* data generally soft and hard colours are used, defined as $(M-S)/F$ and $(H-M)/F$ respectively, where S, M, H, and F correspond to source counts in the $0.3-1$ keV (soft), $1-2$ keV (medium), $2-8$ keV (hard), and $0.3-8$ keV (full) energy bands respectively. X-ray colours are also known as hardness ratios. X-ray colour-colour diagrams are used when classifying point sources, because specific sources will reside in a particular region of the plot and follow a track based on their spectral evolution. A downside of

[3]Effective area represents the geometric collecting area of the X-ray telescope (face-on) multiplied by the reflectivity, vignetting, and quantum efficiency. It is a strong function of energy and decreases with off-axis angle (known as vignetting). Because X-ray instruments all have different effective areas as a function of energy, photon counts vary and are not universal (Grimm et al., 2009).

using colours is that a source with few counts will have large uncertainties, and thus its classification becomes further complicated. The classification scheme proposed by Prestwich et al. (2003) based on X-ray colours from *Chandra* data represents the definitions mentioned above. The study compares X-ray point sources in elliptical galaxies or the bulges of spiral galaxies to those from late-type galaxies. Using the locations (in the diagram) of identified sources in conjunction with various power law spectra having different absorption and photon index, they establish which region of space in the diagram corresponds to a certain source type (Figure 1.4).

Distinguishing sources is difficult due to overlap between different source type regions, absorption moving sources into incorrect classification regions, and the spectral state of the source. Specifically, BH-HMXBs have softer spectra than NS-HMXBs and so will be found closer to or in the thermal SNR regime. While identifying individual sources solely based on their X-ray colours is far from conclusive, it allows one to determine general trends of the population as a whole. Subsequent studies have altered the definitions from those indicated by Prestwich et al. (2003), where Kilgard et al. (2005) specifically included a region for background sources (mostly active galactic nuclei). In addition, when dealing with X-ray point sources that reside in star clusters we can roughly determine the age of the source. This is done using the optical colours of the star cluster to determine age via a stellar evolutionary track in an optical colour-colour plot. The same technique has been used albeit with resolved stellar optical photometry near HMXBs to identify HMXB ages (Williams et al., 2013). Coincident with the X-ray data this allows one to determine if the source is young (HMXB or SNR) or old (LMXB). While X-ray colours are useful to an extent, in order to convincingly classify an X-ray source a combination of spectral analysis, variability, galactic position, and identification of a possible optical/infrared counterpart must be attained.

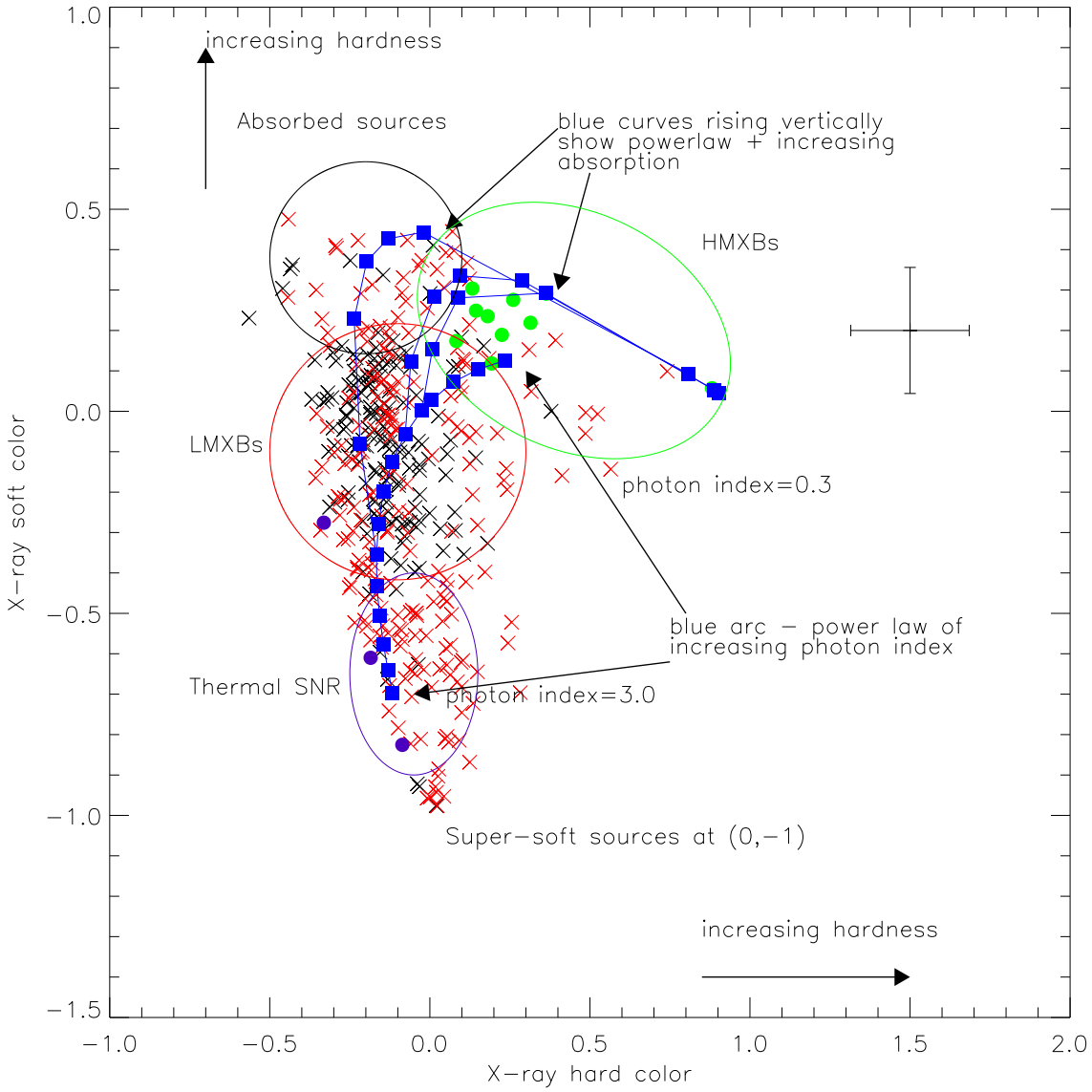

Figure 1.4: X-ray colour classification scheme of Prestwich et al. (2003) based on *Chandra* data. The regions where certain sources dominate are indicated. Blue squares and curves show the effects of various values of the photon index Γ and absorption for a simple power-law spectral model $I(E) = AE^{\Gamma}$. Red crosses are for sources observed in late-type galaxies and black crosses are those for early-type galaxies. Green and blue circles represent known NS-HMXBs and thermal SNRs respectively. (Credit: Figure 4 from Prestwich et al. 2003)

1.4 X-ray Point Source Populations of Galaxies

Before the launch of the *Chandra X-Ray Observatory* in 1999, the study of X-ray sources was limited to the Local Group due to the low angular resolution and/or sensitivity of previous

missions. Much progress has been made investigating XRB populations in the last decade as a result of *Chandra's* subarcsecond resolution. However, studies of XRBs in other galaxies are largely limited to luminous objects with the exception of M31 and the Magellanic Clouds where *Chandra* can observe sources below $L_x \sim 10^{35}$ erg s^{-1} (Zhang et al., 2011). Therefore we have only probed the low-luminosity population of X-ray sources in our Galaxy and nearby satellite galaxies such as the Magellanic Clouds. Studies of the X-ray source population of the Milky Way is hindered by absorption and scattering of X-rays by the gas and dust in the Galactic plane, obstructing our view of sources with soft spectra in particular (energies < 2 keV). Also, uncertainties in the distances to point sources vary by a factor of 2 and thus their luminosities are highly uncertain (Seward & Charles, 2010).

1.4.1 The Milky Way

There are about ~ 400 confirmed XRBs in the Milky Way, with about ~ 200 LMXBs (Liu et al., 2007) and > 200 HMXBs (Liu et al., 2006; Bird et al., 2010; Coleiro & Chaty, 2013). As expected the HMXB population coincides with tangential points of the spiral arms and is concentrated in the Galactic plane (scale height $\simeq 85$ pc; Lutovinov et al. 2013). LMXB locations are consistent with the Galactic Centre/bulge, with their concentration in Galactic longitude rapidly declining outside this region (Grimm, 2003). LMXBs have a much larger vertical distribution than HMXBs and thus require a combination of an exponential with a scale height of ≈ 410 pc and a power law for sources at $z > 1.5 - 2$ kpc above the disk. The XLF of HMXBs (see Section 1.4.2.2) and LMXBs in the Milky Way is consistent with those of other galaxies, giving slopes of $\alpha \approx -1.6$ and $\alpha \approx -1.3$ respectively (Grimm, 2003).

There have been numerous pointed observations and surveys of X-ray sources in different environments in the Milky Way. Muno et al. (2009) completed an analysis of 2 Ms of *Chandra* data on a $2^\circ \times 0.8^\circ$ field (central 150 pc) around the Galactic Centre. With a sensitivity limit of 4×10^{32} erg s^{-1} (90% confidence), they identified 9017 sources, where only 76 are detected below 2 keV (the component of soft X-ray emission < 2 keV from many sources was absorbed,

so the detection of soft sources is incomplete). This biases the source emission towards hard X-rays. The luminosity range studied was 10^{31-34} erg s^{-1} for 0.5 − 8.0 keV, where a power law with $\Gamma = 1.5$, $N_H = 10^{22}$ cm^{-2}, and $D = 8$ kpc was assumed. This survey is up to two orders of magnitude fainter than that possible in the Local Group of galaxies (Trudolyubov & Priedhorsky, 2004; Kilgard et al., 2005). Sources below $L_X < 10^{33}$ erg s^{-1}, which comprise $\approx$ 90% of the catalogue, are thought to be CVs while the remaining sources are accreting NSs, BHs, and isolated pulsars. The old stellar population observed in the infrared matches the spatial distribution of X-ray point sources, confirming they are mostly CVs. This study of low-luminosity Galactic X-ray sources is complemented by Sazonov et al. (2006) who used the *RXTE* slew survey and *ROSAT* all-sky survey to probe sources down to $\sim 10^{27.5}$ erg s^{-1}. These deep observations were able to resolve most of the diffuse emission in the Galactic centre, known as the Galactic ridge emission, into many faint point sources. Together active binaries and CVs had an estimated L_X (2 − 10 keV) $\sim 2 \times 10^{38}$ erg s^{-1}, which is only 3% of the total expected LMXB emission for the Milky Way, but still accounts for most of the ridge emission (Revnivtsev et al., 2006). Studying galaxy-wide populations, Boroson et al. (2011) found that the luminosity of LMXBs was 10 times that of the combined active binary and CV luminosity in a sample of 30 early-type galaxies. The active binary and CV luminosity was estimated using a scaling relation based on results from M31 and M32 and thus subject to large uncertainty. The population of undetected LMXBs was quantified (number of sources) by an extrapolation of the XLF and spectral fitting of unresolved X-ray emission.

Low-luminosity sources have been catalogued in Milky Way GCs as well, namely active binaries, CVs, MSPs, and quiescent LMXBs. Quiescent LMXBs have been identified in many Galactic GCs such as Terzan 5 (12 candidates from Heinke et al. 2006 and 1 confirmed by Wijnands et al. 2005) and 47 Tucanae (3 candidates from Heinke et al. 2005). Heinke (2010) predicts that $\sim$ 200 quiescent LMXBs reside in Galactic GCs. Investigating XRBs in GCs allows one to constrain the mass and radius of NSs much better than using the field population of XRBs because GC distances are more accurate (Heinke, 2010). For instance, Ratti et al.

(2012) found that the BH-LMXB source XTE J1752 − 223 had $L_X \sim 10^{31}$ erg s^{-1} (distance of 8 kpc) in what they assume is a quiescent state based on consistent flux levels in their observations. However, this may have been a plateau after which the source flux decreased. The distance determined for this field LMXB varies from $3.5 \lesssim d \lesssim 8$ kpc, which leads to large uncertainties when calculating NS properties such as the mass and radius. Therefore accurate distance measurements of GC-LMXBs are crucial when studying NS parameters.

1.4.2 Extragalactic Studies

Stellar X-ray sources, specifically bright XRBs, can be studied out to distances of $\sim 30 - 40$ Mpc with *Chandra* (beyond this the sensitivity limit is too large and therefore requires prohibitively long integration times). As such most results only sample the high-luminosity end of the XLF ($\gtrsim 10^{37}$ erg s^{-1}), leaving the low-luminosity end with a flatter slope and ultimately biased by incompleteness. M31's X-ray population has been studied in detail by *ROSAT* (Supper et al., 1997, 2001) and *XMM-Newton* (Stiele et al., 2011). The two deep *ROSAT* surveys reported 560 total sources while the *XMM-Newton* data is much deeper, cataloguing 1897 sources. Each survey was galaxy-wide and therefore allowed the detailed study of a Milky Way analogue below the luminosity of bright XRBs. Interestingly, no HMXBs have been confirmed yet in M31, stressing the importance of multiwavelength observations in classifying X-ray sources. Further motivation stems from the 65% of sources in the *XMM-Newton* survey that have no classification. The LMXB population has been extensively studied in M31, particularly in the bulge, where numerous *Chandra* observations exist. Zhang et al. (2011) found a different XLF for LMXBs in the bulge and those in GCs, with a break at $\approx 10^{37}$ erg s^{-1} for the XLF of GC-LMXBs. Similar breaks are found for the XLF in the inner and outer bulge and disk regions, although the break moves to lower luminosities as radial distance decreases. Fabbiano (2006b) stressed the need for a comparison of the low-luminosity XLFs in early-type galaxies with those for M31. Kim et al. (2009) addressed this issue by observing 3 old elliptical galaxies and confirming the low-luminosity break in GC-LMXBs compared to

the field sources. Unfortunately the 90% completeness limits are similar to the values for low-luminosity breaks in the GC XLFs. Thus a deeper sample of data that includes more galaxies is necessary to confirm these results.

1.4.2.1 LMXB Evolution

LMXBs dominate the total luminosity of elliptical galaxies in the 0.3 − 8 keV band, whereas in NGC 1316 the integrated LMXB emission (including undetected LMXBs) is upwards of $\sim 4 \cdot 10^{40}$ erg s^{-1} (Fabbiano, 2006a). The spectra of LMXBs are remarkably consistent throughout early-type galaxies with a power law fit having a photon index $\Gamma \sim 1.56 \pm 0.02$. Higher luminosity sources are better fit with a softer spectrum of $\Gamma \sim 2$. The number of LMXBs is known to scale with the stellar mass in a galaxy (Gilfanov et al., 2004; Lehmer et al., 2010; Boroson et al., 2011; Zhang et al., 2012b). Zhang et al. (2012a) completed a study of 20 massive nearby early-type galaxies using *Chandra* with over 2000 point sources. They found that N_x ($> 5 \times 10^{37}$ erg s^{-1})/10^{10} $M_\odot$= 5.4, consistent with the studies mentioned above. In addition, older galaxies ($t > 6$ Gyr) tended to host more LMXBs than their younger counterparts, with an LMXB frequency for $L_X > 5 \times 10^{37}$ erg s^{-1} of 6.27 ± 0.26 and 4.18 ± 0.27 per 10^{10} $M_\odot$ respectively. They attribute this to the intrinsic evolution of the LMXB population of a galaxy over time, further exacerbated by the presence of more GCs in galaxies with older stellar populations. The evolution of the XLF (for $\log(L_X) > 37.5$) with age showed that younger galaxies have more bright sources and fewer fainter sources (a flatter slope) than older galaxies.

The consensus within the community is that LMXBs are preferentially found in massive, compact, high-metallicity (redder) GCs that are luminous. The reasons for GC compactness and luminosity as a direct link to the detection of LMXBs is clear from the processes mentioned earlier. Dense clusters promote dynamical interactions triggering binary formation while a larger number of stars would make the GC optically brighter. The metallicity relation, however, is not as well-understood. In a study of early-type Virgo cluster galaxies, Sivakoff et al. (2007) found that red GCs are 3.15 ± 0.54 times more likely to host LMXBs than are blue

GCs. Several explanations have been put forth to describe the metallicity relation. Ivanova & Kalogera (2006) posited a process involving magnetic braking in MS stars that would result in the suppression of LMXB formation in metal-poor GCs. Metal-poor MS stars of approximately solar mass lack outer convection zones and subsequently magnetic braking is inhibited, not allowing the orbit to shrink and possibly form a binary. Maccarone et al. (2004) have suggested that irradiation-induced stellar winds (originating from the donor star reprocessing X-ray luminosity from the accretion disk) are stronger in low-metallicity stars because emission line cooling is not efficient, speeding up the evolutionary process of LMXBs. This would cause a decrease in the number of observed LMXBs in GCs. Agar & Barmby (2013) conducted a survey of M31 GC-LMXBs and interestingly found the probability that a GC hosts an LMXB had no dependence on metallicity. However, the GC sample had a small galactocentric distance and high average metallicity, possibly biasing the results. The LMXB metallicity relation is clearly still in its infancy and requires more investigation, especially concerning the nature of this dependence in spiral galaxies.

Ivanova et al. (2012) suggests that the metallicity dependence of GC-LMXBs is due to the differences in the number densities and average masses of red giants in both blue and red GCs. GC-LMXBs have 3 sub-populations based on the evolutionary state of the companion star: those with MS, red giant, and WD donors. Ivanova et al. (2008) showed that most GC-LMXBs should be accreting NSs. They would be formed mainly through a distinct class of core-collapse supernovae or accretion-induced collapse of a WD. NSs and BHs that are produced via core-collapse supernovae generally all have large enough natal kick velocities (mean velocity $\sim$ 400 km s^{-1}) due to asymmetric explosion to be ejected from the cluster. The most efficient formation channel for GC-LMXBs is a NS with a MS donor. This occurs through binary exchange interaction with a NS or the accretion-induced collapse of an existing WD-MS binary. However, the accretion rates from MS stars are not substantial enough to give X-ray luminosities above $> 10^{37}$ erg s^{-1}, and thus the sources are transient and have low outburst L_X (Fragos et al., 2008; Revnivtsev et al., 2011), meaning that bright LMXBs must consist of red

giant donors with higher mass loss rates. Ivanova et al. (2012) found that red giants are on average larger and more numerous in metal-rich clusters, leading to the observed trend that ~ 3 times as many bright LMXBs are found in red clusters. Nonetheless, a population synthesis study incorporating the effects of red giant stars on metallicity is still required.

In a survey of early-type Virgo cluster galaxies with *Chandra* and *HST*, Sivakoff et al. (2007) did not find any dependence on the galactocentric distance to the association of an X-ray source with a GC. At all radii there is a strong dependence of the GC luminosity, compactness, and colour. However, a deeper survey of NGC 4278 (Fabbiano et al., 2010) found a significant radial effect on the luminosity of X-ray sources in GCs, showing a preference for more luminous sources at smaller radii. The sample consisted of only 7 sources and therefore cannot be considered statistically significant. Similar work considering XRBs in a quiescent state has not been studied to the extent of bright XRBs as a result of observational limits.

1.4.2.2 X-ray Luminosity Function and Star Formation Rate

The correlation between HMXBs and the SFR in spiral galaxies was investigated by Grimm et al. (2003) when they inspected the luminosity function of HMXBs. The much smaller Small Magellanic Cloud had as many identified HMXBs as the Milky Way due to the recent star-formation episode triggered within the past 100 Myr. Even though most galaxies followed a similar curve that declined with increasing luminosity, their values were shifted with respect to each other. By scaling each galaxy with its corresponding SFR, the XLFs overlapped along a single curve to support the correlation of HMXBs as a SFR indicator (Figure 1.5).

The differential XLF from Grimm et al. (2003) in equation 1.4 has a power-law slope of α and a normalization constant β, with $L_{38} = L/10^{38}$ erg s^{-1}.

$$\frac{dN}{dL_{38}} = \beta \cdot \mathrm{SFR}\, L_{38}^{\alpha} \tag{1.4}$$

The universal XLF of HMXBs in numerous nearby spiral galaxies determined by Grimm et al.

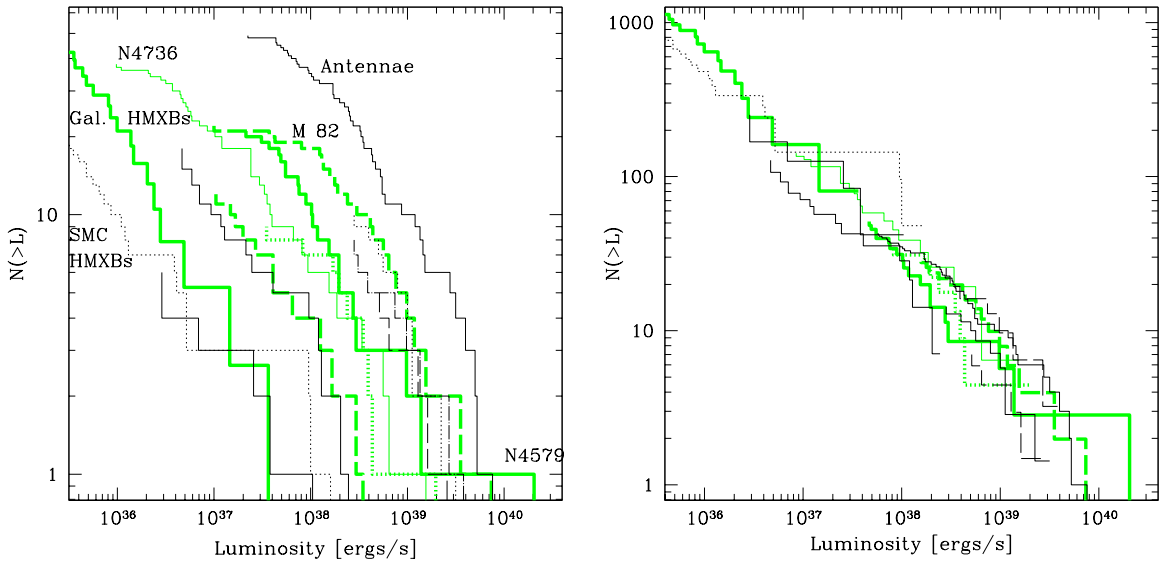

Figure 1.5: Figure 1 from Grimm et al. (2003) showing X-ray luminosity functions of X-ray sources from late-type and starburst galaxies obtained with *Chandra* data. On the left the observed XLFs for various galaxies are shown. On the right the XLF of each galaxy has been scaled by the ratio of its star formation rate to that of the Antennae. Even though the SFRs of the sample varied by factors ~ 50 the scaled XLFs reside in a narrow region of the $N(>L) - L$ plane.

(2003) was recently updated by Mineo et al. (2012). They found the same results for a universal XLF that was well-fit by a power law with a slope of $\alpha \sim -1.6$, $\beta = 3.3$, and a cutoff at $L_X \sim 10^{40}$ erg s^{-1}. The normalizations are proportional to the SFR of the host galaxy. Bulge sources of galaxies with inclination i $\lesssim 65°$ were excluded to remove contributions from LMXBs that may have skewed their results. The crucial conclusion was that the collective X-ray luminosity of HMXBs (with LMXBs possibly included in the sample) is proportional to the SFR via the relation $L^{XRB}_{0.5-8\ keV}$ (erg s^{-1}) = 2.61×10^{39} SFR (M$_\odot$ yr^{-1}). The scatter in the L_X-SFR relation (0.4 dex) is due to the XLF normalization and the number and luminosity of the brightest sources. A key driver in the population of HMXBs and ultimately how it influences the XLF is metallicity. Higher-metallicity donor stars will have stronger winds, which subsequently leads to higher (wind) accretion rates and X-ray luminosity of the accretion flow (Linden et al., 2010). However, star formation at low-metallicity does not allow for significant cooling, resulting in the birth of more massive stars and therefore a higher number of compact

objects in binaries. Shtykovskiy & Gilfanov (2005) state that the effects of metallicity variations on XRB populations are poorly understood and require more investigation. Specifically, more detailed analyses of the HMXB-XLF in star-forming galaxies will help to further our understanding of the role of metallicity in relation to XRBs.

1.4.3 X-ray Binary Simulations

XRBs can only be identified in galaxies within a few tens of Mpc. Due to the limitations of observations, especially the significant amount of observing time required for distant galaxies, population synthesis models are the only way to investigate the evolution of XRBs through cosmic time. One example of such models is the advanced stellar population synthesis code StarTrack developed by Belczynski et al. (2008). The code incorporates single and binary star populations, orbital evolution as influenced by tides, magnetic braking, mass loss via stellar winds and mass transfer phases, and gravitational radiation. The formation and evolution of compact objects (WDs, NSs, BHs) is carefully modelled since these are necessary requirements for studying XRBs.

Most intriguing has been the recent work by Fragos et al. (2013b) that modelled XRB evolution across cosmic time. Using StarTrack in tandem with cosmological simulations they can account for the star formation history and metallicity evolution of the Universe. Local observations of the XRB population were used to constrain model parameters. The authors found that their results were in excellent agreement with observations in the nearby Universe. They showed that the X-ray luminosity density from XRBs is currently dominated by LMXBs and only at $z \gtrsim 2.5$ do HMXBs become dominant. Also, the peak of HMXB luminosity density at $z \sim 3.9$ occurs ~ 0.5 Gyr before the peak of SFR density. This can be explained due to the X-ray luminosity of XRBs per unit stellar mass or SFR being much higher for low-metallicity populations because OB stars do not lose as much mass from their winds. Subsequently, more numerous and more massive BHs are formed and hence more luminous XRBs (BH-HMXBs are more luminous than their NS-HMXB counterparts).

An unanswered question involves the role that XRBs might play in galaxy formation and evolution as a result of feedback processes. While most studies of feedback have focused on active galactic nuclei and O stars, Fragos et al. (2013a) suggests that the X-ray emission from HMXBs dominates that from active galactic nuclei for $z \gtrsim 6-8$. However, current population synthesis only models the XRBs formed from primordial isolated binaries and hence the field population. As we have seen XRBs are found in significant numbers in star clusters, specifically GCs, where dynamically formed binaries are crucial to the formation of LMXBs (up to half of bright LMXBs reside in GCs; Humphrey & Buote 2008). StarTrack has been used with a stellar dynamics code to study dynamical interactions in a handful of Galactic GCs by Ivanova et al. (2010), but this is limited to binary fractions and formation.

1.5 Outstanding Questions

XRB populations are important probes of star formation and the physics of binary evolution. Due to the association of XRBs with star clusters and star forming regions, they are intricately linked to how galaxies evolve and allow us to explore the formation of stellar populations. An example is the high-mass end of the stellar initial mass function, which can be investigated because XRB primaries are the endpoints of massive star evolution. However, the faint-end of the XLF, where the majority of sources exist, has yet to be studied in detail beyond the Milky Way.

Low-luminosity X-ray sources represent the next step in understanding XRBs and other transient systems. With current X-ray telescopes such as *Chandra*, only nearby (large) galaxies such as M31 represent realistic targets for examining X-ray sources below luminosities of $\sim 10^{36}$ erg s^{-1}. The increase in wide-field surveys across the electromagnetic spectrum, such as the Panchromatic Hubble Andromeda Treasury Survey (*HST*; Dalcanton et al. 2012), Next Generation Virgo Cluster Survey (*Canada-France-Hawaii Telescope*; Ferrarese et al. 2012), and the all-sky survey by the *Fermi*-Large Area Telescope (Atwood et al., 2009), enables the

detailed study of XRBs. Multiwavelength observations are crucial in understanding X-ray sources, specifically their classification. Radio and γ-ray observations are used in detecting pulsars while XRB counterparts can be identified and star cluster catalogues constructed with optical/infrared observations. These types of observations are particularly useful when studying LMXBs and MSPs, especially in GCs. The evolutionary link between LMXBs and MSPs is still not well understood and requires more investigation. Recently, the first binary MSP was identified that was seen to shift between an accretion-powered X-ray state and a rotation-powered radio state (Papitto et al., 2014)[similar work by Patruno et al. (2013)]. This type of behaviour is evidence for an LMXB evolving into a MSP. Monitoring this population for variability can reveal information on accretion disk physics and the evolution of XRBs. Thus an emphasis must be put on exploring XRBs in a quiescent state.

There are still unanswered questions regarding the association of XRBs with different galaxy environments. We have stated that HMXBs are found at large separations (0.4 ± 0.2 kpc) from star-forming regions with low significance. This suggests that HMXBs are ejected from their parent environments at birth. Both the spatial and luminosity distributions of HMXBs below 10^{36} erg s^{-1} have not been studied outside our Galaxy, where the focus has mostly been on ULXs in starburst galaxies. In addition, the impact of star cluster metallicity on HMXBs is not well understood. However, unlike HMXBs, LMXBs are preferentially found in metal-rich GCs. The prevalence of LMXBs in metal-rich GCs by a factor of ~ 3 compared to metal-poor GCs is astounding for a number of reasons. The effect is independent over the entire range of bright ($> 10^{36}$ erg s^{-1}) LMXB luminosity, the GC age, stellar encounter rate, and selection effects. A plausible explanation for this wide-ranging phenomenon is still needed (Kim et al., 2013).

Future efforts should therefore comprise studies of quiescent emission in XRB transients both inside and outside the Milky Way, along with detailed studies of the GC-LMXB metallicity effect. Multiwavelength observations are paramount to advance our understanding of XRBs and X-ray point sources in general. Detailed theoretical modelling of binary evolution in star

clusters and galaxies is complex and requires observations to provide input constraints and a comparison sample. Tzanavaris et al. (2013) cite deeper *Chandra* observations as critical for comparing models to sources with fainter luminosities. XRBs also provide information on the dynamics and evolution of star clusters. Ultimately, the link between XRBs and star clusters is invaluable to studying and achieving a better understanding of both populations.

This thesis focuses on the nature of low-luminosity X-ray sources and the connection between XRBs and star clusters. Using optical and X-ray data from *HST* and *Chandra*, respectively, in our Galaxy and M31, we can probe the faintest sources at both wavelengths and study connections between star cluster and X-ray properties. Our goals are to discover the faintest extragalactic XRBs in star clusters and explore the GC-LMXB metallicity effect. In Chapter 2, we focus on the star cluster and star-forming environments of M31, and probe the relationships between their parameters and X-ray sources at the faintest X-ray luminosities. Chapter 3 presents a detailed X-ray point source catalogue of M31, which is the deepest for any large galaxy outside the Milky Way. In Chapter 4 we study the GC population of our Galaxy to explain the dependence of LMXB formation on metallicity. Chapter 5 summarizes our important conclusions and discusses necessary follow-up as well as other areas of relevant work.

Bibliography

Abdo, A. A., Ackermann, M., Ajello, M., et al. 2010, A&A, 524, A75

Agar, J. R. R., & Barmby, P. 2013, AJ, 146, 135

Atwood, W. B., Abdo, A. A., Ackermann, M., et al. 2009, ApJ, 697, 1071

Bahramian, A., Heinke, C. O., Sivakoff, G. R., & Gladstone, J. C. 2013, ApJ, 766, 136

Barmby, P., Huchra, J. P., Brodie, J. P., et al. 2000, AJ, 119, 727

Barnard, R., Garcia, M., & Murray, S. S. 2013, ApJ, 772, 126

Bedin, L. R., Piotto, G., Anderson, J., et al. 2004, ApJ, 605, L125

Belczynski, K., Kalogera, V., Rasio, F. A., et al. 2008, ApJS, 174, 223

Belczynski, K., Sadowski, A., Rasio, F. A., & Bulik, T. 2006, ApJ, 650, 303

Bellovary, J. M., Governato, F., Quinn, T. R., et al. 2010, ApJ, 721, L148

Bik, A., Lamers, H. J. G. L. M., Bastian, N., Panagia, N., & Romaniello, M. 2003, A&A, 397, 473

Bird, A. J., Bazzano, A., Bassani, L., et al. 2010, ApJS, 186, 1

Bodaghee, A., Tomsick, J. A., Rodriguez, J., & James, J. B. 2012, ApJ, 744, 108

Boroson, B., Kim, D.-W., & Fabbiano, G. 2011, ApJ, 729, 12

Bradt, H. V. D., Ohashi, T., & Pounds, K. A. 1992, ARA&A, 30, 391

Cantiello, M., & Blakeslee, J. P. 2007, ApJ, 669, 982

Chandar, R., Whitmore, B., & Lee, M. G. 2004, ApJ, 611, 220

Chaty, S. 2012, in Proceedings of "An INTEGRAL view of the high-energy sky (the first 10 years)" - 9th INTEGRAL Workshop and celebration of the 10th anniversary of the launch (INTEGRAL 2012). 15-19 October 2012. Bibliotheque Nationale de France, Paris, France., 13

Cheng, J. Y., Rockosi, C. M., Morrison, H. L., et al. 2012, ApJ, 746, 149

Clark, G. W. 1975, ApJ, 199, L143

Clark, J. S., Negueruela, I., Crowther, P. A., & Goodwin, S. P. 2005, A&A, 434, 949

Coleiro, A., & Chaty, S. 2013, ApJ, 764, 185

Coleiro, A., Chaty, S., Zurita Heras, J. A., Rahoui, F., & Tomsick, J. A. 2013, A&A, 560, A108

Dalcanton, J. J., Williams, B. F., Lang, D., et al. 2012, ApJS, 200, 18

D'Avanzo, P., Campana, S., Muñoz-Darias, T., et al. 2011, A&A, 534, A92

de Grijs, R. 2010, Royal Society of London Philosophical Transactions Series A, 368, 693

de Grijs, R., Anders, P., Bastian, N., et al. 2003, MNRAS, 343, 1285

de Grijs, R., & Parmentier, G. 2007, Chinese J. Astron. Astrophys., 7, 155

Dias, W. S., Alessi, B. S., Moitinho, A., & Lépine, J. R. D. 2002, A&A, 389, 871

Elmegreen, B. G., & Efremov, Y. N. 1997, ApJ, 480, 235

Evans, II, N. J., Dunham, M. M., Jørgensen, J. K., et al. 2009, ApJS, 181, 321

Fabbiano, G. 2006a, ARA&A, 44, 323

—. 2006b, Advances in Space Research, 38, 2937

Fabbiano, G., Brassington, N. J., Lentati, L., et al. 2010, ApJ, 725, 1824

Fabian, A. C., Pringle, J. E., & Rees, M. J. 1975, MNRAS, 172, 15P

Ferrarese, L., Côté, P., Cuillandre, J.-C., et al. 2012, ApJS, 200, 4

Fragos, T., Lehmer, B. D., Naoz, S., Zezas, A., & Basu-Zych, A. 2013a, ApJ, 776, L31

Fragos, T., Kalogera, V., Belczynski, K., et al. 2008, ApJ, 683, 346

Fragos, T., Lehmer, B., Tremmel, M., et al. 2013b, ApJ, 764, 41

Frank, J., King, A., & Raine, D. J. 2002, Accretion Power in Astrophysics: Third Edition (Cambridge: Cambridge Univ. Press)

Frank, J., King, A. R., & Lasota, J.-P. 1987, A&A, 178, 137

Friedman, H., Lichtman, S. W., & Byram, E. T. 1951, Physical Review, 83, 1025

Giacconi, R., Gursky, H., Paolini, F. R., & Rossi, B. B. 1962, Physical Review Letters, 9, 439

Gilfanov, M., Grimm, H.-J., & Sunyaev, R. 2004, MNRAS, 347, L57

Gladstone, J. C. 2013, Mem. Soc. Astron. Italiana, 84, 629

Gladstone, J. C., Copperwheat, C., Heinke, C. O., et al. 2013, ApJS, 206, 14

Gladstone, J. C., Roberts, T. P., & Done, C. 2009, MNRAS, 397, 1836

Goodwin, S. P. 2010, Royal Society of London Philosophical Transactions Series A, 368, 851

Goodwin, S. P., & Bastian, N. 2006, MNRAS, 373, 752

Griffen, B. F., Drinkwater, M. J., Thomas, P. A., Helly, J. C., & Pimbblet, K. A. 2010, MNRAS, 405, 375

Grimm, H.-J. 2003, PhD thesis, Ludwig-Maximilians-Universitat, Munchen

Grimm, H.-J., Gilfanov, M., & Sunyaev, R. 2003, MNRAS, 339, 793

Grimm, H.-J., McDowell, J., Fabbiano, G., & Elvis, M. 2009, ApJ, 690, 128

Hannikainen, D. C., Charles, P. A., van Zyl, L., et al. 2005, MNRAS, 357, 325

Harris, W. E. 1996, AJ, 112, 1487

—. 2010, Royal Society of London Philosophical Transactions Series A, 368, 889

Harris, W. E., Whitmore, B. C., Karakla, D., et al. 2006, ApJ, 636, 90

Hayasaki, K., & Okazaki, A. T. 2005, MNRAS, 360, L15

Heida, M., Jonker, P. G., Torres, M. A. P., et al. 2013, MNRAS, 433, 681

Heinke, C. O. 2010, in American Institute of Physics Conference Series, Vol. 1314, American Institute of Physics Conference Series, ed. V. Kalogera & M. van der Sluys, 135–142

Heinke, C. O., Grindlay, J. E., Edmonds, P. D., et al. 2005, in American Institute of Physics Conference Series, Vol. 797, Interacting Binaries: Accretion, Evolution, and Outcomes, ed. L. Burderi, L. A. Antonelli, F. D'Antona, T. di Salvo, G. L. Israel, L. Piersanti, A. Tornambè, & O. Straniero, 40–45

Heinke, C. O., Ivanova, N., Engel, M. C., et al. 2013, ApJ, 768, 184

Heinke, C. O., Wijnands, R., Cohn, H. N., et al. 2006, ApJ, 651, 1098

Humphrey, P. J., & Buote, D. A. 2008, ApJ, 689, 983

Hunter, D. A., Elmegreen, B. G., Dupuy, T. J., & Mortonson, M. 2003, AJ, 126, 1836

Hynes, R. I. 2010, ArXiv e-prints, 1010.5770

Iben, I. 1968, Nature, 220, 143

Ivanova, N., Chaichenets, S., Fregeau, J., et al. 2010, ApJ, 717, 948

Ivanova, N., Heinke, C. O., Rasio, F. A., Belczynski, K., & Fregeau, J. M. 2008, MNRAS, 386, 553

Ivanova, N., Justham, S., Avendano Nandez, J. L., & Lombardi, J. C. 2013, Science, 339, 433

Ivanova, N., & Kalogera, V. 2006, ApJ, 636, 985

Ivanova, N., Fragos, T., Kim, D.-W., et al. 2012, ApJ, 760, L24

Jonker, P. G., Torres, M. A. P., Fabian, A. C., et al. 2010, MNRAS, 407, 645

Jonker, P. G., Heida, M., Torres, M. A. P., et al. 2012, ApJ, 758, 28

Jordán, A., Côté, P., Ferrarese, L., et al. 2004, ApJ, 613, 279

Kaaret, P., Alonso-Herrero, A., Gallagher, J. S., et al. 2004, MNRAS, 348, L28

Kalirai, J. S., & Richer, H. B. 2010, Royal Society of London Philosophical Transactions Series A, 368, 755

Kalogera, V. 2006, Ap&SS, 304, 257

Kalogera, V., Sepinsky, J., & Belczynski, K. 2007, in Astronomical Society of the Pacific Conference Series, Vol. 367, Massive Stars in Interactive Binaries, ed. N. St.-Louis & A. F. J. Moffat, 623

Katz, J. I. 1975, Nature, 253, 698

Kilgard, R. E., Cowan, J. J., Garcia, M. R., et al. 2005, ApJS, 159, 214

Kim, D.-W., Fabbiano, G., Ivanova, N., et al. 2013, ApJ, 764, 98

Kim, D.-W., Fabbiano, G., Brassington, N. J., et al. 2009, ApJ, 703, 829

Kim, E., Kim, D.-W., Fabbiano, G., et al. 2006, ApJ, 647, 276

King, A. R. 2004, MNRAS, 347, L18

King, C. R., Da Costa, G. S., & Demarque, P. 1985, ApJ, 299, 674

King, I. 1962, AJ, 67, 471

King, I. R. 1966, AJ, 71, 64

Kundu, A., Maccarone, T. J., & Zepf, S. E. 2007, ApJ, 662, 525

Lada, C. J. 2006, ApJ, 640, L63

—. 2010, Royal Society of London Philosophical Transactions Series A, 368, 713

Lada, C. J., & Lada, E. A. 2003, ARA&A, 41, 57

Lamers, H. J. G. L. M., Gieles, M., Bastian, N., et al. 2005, A&A, 441, 117

Larsen, S. S. 2009a, A&A, 494, 539

—. 2009b, Young Massive Clusters - Formation Efficiencies and (Initial) Mass Functions, ed. T. Richtler & S. Larsen (Springer Berlin Heidelberg), 95

Lattimer, J. M. 2011, Ap&SS, 336, 67

—. 2012, Annual Review of Nuclear and Particle Science, 62, 485

Lattimer, J. M., & Prakash, M. 2005, Physical Review Letters, 94, 111101

—. 2010, ArXiv e-prints, arXiv:1012.3208

Lehmer, B. D., Alexander, D. M., Bauer, F. E., et al. 2010, ApJ, 724, 559

Linden, T., Kalogera, V., Sepinsky, J. F., et al. 2010, ApJ, 725, 1984

Liu, J.-F., Bregman, J. N., & Seitzer, P. 2002, ApJ, 580, L31

Liu, Q. Z., van Paradijs, J., & van den Heuvel, E. P. J. 2006, A&A, 455, 1165

—. 2007, A&A, 469, 807

Long, K. S., Kuntz, K. D., Blair, W. P., et al. 2014, ApJS, 212, 21

Lorimer, D. R., Camilo, F., Freire, P., et al. 2003, in Astronomical Society of the Pacific Conference Series, Vol. 302, Radio Pulsars, ed. M. Bailes, D. J. Nice, & S. E. Thorsett, 363

Lutovinov, A. A., Revnivtsev, M. G., Tsygankov, S. S., & Krivonos, R. A. 2013, MNRAS, 431, 327

Maccarone, T. J., Kundu, A., & Zepf, S. E. 2004, ApJ, 606, 430

Maciel, W. J., & Costa, R. D. D. 2010, in IAU Symposium, Vol. 265, IAU Symposium, ed. K. Cunha, M. Spite, & B. Barbuy, 317–324

Mapelli, M., Ripamonti, E., Zampieri, L., Colpi, M., & Bressan, A. 2010, MNRAS, 408, 234

McLaughlin, D. E., & Pudritz, R. E. 1996, ApJ, 457, 578

Middleton, M. J., Sutton, A. D., Roberts, T. P., Jackson, F. E., & Done, C. 2012, MNRAS, 420, 2969

Milone, A. P., Marino, A. F., Piotto, G., et al. 2015, MNRAS, 447, 927

Mineo, S., Gilfanov, M., & Sunyaev, R. 2012, MNRAS, 419, 2095

Muno, M. P., Bauer, F. E., Baganoff, F. K., et al. 2009, ApJS, 181, 110

Naylor, T., Charles, P. A., & Longmore, A. J. 1991, MNRAS, 252, 203

Paczynski, B. 1976, in IAU Symposium, Vol. 73, Structure and Evolution of Close Binary Systems, ed. P. Eggleton, S. Mitton, & J. Whelan, 75

Paolillo, M., Puzia, T. H., Goudfrooij, P., et al. 2011, ApJ, 736, 90

Papitto, A., Ferrigno, C., Bozzo, E., & Rea, N. 2014, in European Physical Journal Web of Conferences, Vol. 64, European Physical Journal Web of Conferences, 1004

Patruno, A., Archibald, A. M., Hessels, J. W. T., et al. 2013, ArXiv e-prints, arXiv:1310.7549

Peacock, M. B., Maccarone, T. J., Kundu, A., & Zepf, S. E. 2010, MNRAS, 407, 2611

Persic, M., & Rephaeli, Y. 2007, A&A, 463, 481

Piotto, G., Milone, A. P., Bedin, L. R., et al. 2015, AJ, 149, 91

Pooley, D., Lewin, W. H. G., Anderson, S. F., et al. 2003, ApJ, 591, L131

Prestwich, A. H., Irwin, J. A., Kilgard, R. E., et al. 2003, ApJ, 595, 719

Prestwich, A. H., Tsantaki, M., Zezas, A., et al. 2013, ApJ, 769, 92

Puzia, T. H., Zepf, S. E., Kissler-Patig, M., et al. 2002, A&A, 391, 453

Ranalli, P., Comastri, A., & Setti, G. 2003, A&A, 399, 39

Rangelov, B., Prestwich, A. H., & Chandar, R. 2011, ApJ, 741, 86

Ratti, E. M., Jonker, P. G., Miller-Jones, J. C. A., et al. 2012, MNRAS, 423, 2656

Reig, P. 2011, Ap&SS, 332, 1

Revnivtsev, M., Postnov, K., Kuranov, A., & Ritter, H. 2011, A&A, 526, A94

Revnivtsev, M., Sazonov, S., Gilfanov, M., Churazov, E., & Sunyaev, R. 2006, A&A, 452, 169

Ruiz, N., Chu, Y.-H., Gruendl, R. A., et al. 2013, ApJ, 767, 35

Sarazin, C. L., Kundu, A., Irwin, J. A., et al. 2003, ApJ, 595, 743

Sazonov, S., Revnivtsev, M., Gilfanov, M., Churazov, E., & Sunyaev, R. 2006, A&A, 450, 117

Schmitt, J. H. M. M. 2000, in Reviews in Modern Astronomy, Vol. 13, Reviews in Modern Astronomy, ed. R. E. Schielicke, 115

Sepinsky, J., Kalogera, V., & Belczynski, K. 2005, ApJ, 621, L37

Servillat, M., Coleiro, A., & Chaty, S. 2012, in Proceedings of "An INTEGRAL view of the high-energy sky (the first 10 years)" - 9th INTEGRAL Workshop and celebration of the 10th anniversary of the launch (INTEGRAL 2012). 15-19 October 2012. Bibliotheque Nationale de France, Paris, France., 101

Seward, D. F., & Charles, A. P. 2010, Exploring the X-ray Universe, 2nd edn. (Cambridge: Cambridge Univ. Press)

Shakura, N. I., & Sunyaev, R. A. 1973, A&A, 24, 337

Shtykovskiy, P., & Gilfanov, M. 2005, MNRAS, 362, 879

Shtykovskiy, P. E., & Gilfanov, M. R. 2007, Astronomy Letters, 33, 299

Sivakoff, G. R., Jordán, A., Sarazin, C. L., et al. 2007, ApJ, 660, 1246

Stiele, H., Pietsch, W., Haberl, F., et al. 2011, A&A, 534, A55

Supper, R., Hasinger, G., Lewin, W. H. G., et al. 2001, A&A, 373, 63

Supper, R., Hasinger, G., Pietsch, W., et al. 1997, A&A, 317, 328

Sutton, A. D., Roberts, T. P., & Middleton, M. J. 2013, ArXiv e-prints, arXiv:1307.8044

Swartz, D. A., Soria, R., Tennant, A. F., & Yukita, M. 2011, ApJ, 741, 49

Sweigart, A. V., Greggio, L., & Renzini, A. 1990, ApJ, 364, 527

Thomas, H.-C. 1967, ZAp, 67, 420

Trudolyubov, S., & Priedhorsky, W. 2004, ApJ, 616, 821

Tzanavaris, P., Fragos, T., Tremmel, M., et al. 2013, ApJ, 774, 136

van der Marel, R. P., Gerssen, J., Guhathakurta, P., Peterson, R. C., & Gebhardt, K. 2002, AJ, 124, 3255

van Loon, J. T. 2010, Royal Society of London Philosophical Transactions Series A, 368, 801

Verbunt, F., & Hut, P. 1987, in IAU Symposium, Vol. 125, The Origin and Evolution of Neutron Stars, ed. D. J. Helfand & J.-H. Huang, 187

Voss, R., & Gilfanov, M. 2007, MNRAS, 380, 1685

Voss, R., Gilfanov, M., Sivakoff, G. R., et al. 2009, ApJ, 701, 471

White, N. E., & Angelini, L. 2001, ApJ, 561, L101

White, N. E., & Swank, J. H. 1982, ApJ, 253, L61

Whitmore, B. C., Chandar, R., & Fall, S. M. 2007, AJ, 133, 1067

Wijnands, R., Heinke, C. O., Pooley, D., et al. 2005, ApJ, 618, 883

Wiktorowicz, G., Belczynski, K., & Maccarone, T. 2014, in Binary Systems, their Evolution and Environments, 37

Williams, B. F., Binder, B. A., Dalcanton, J. J., Eracleous, M., & Dolphin, A. 2013, ApJ, 772, 12

Wolf, M. J., Drory, N., Gebhardt, K., & Hill, G. J. 2007, ApJ, 655, 179

Worthey, G. 1994, ApJS, 95, 107

Zezas, A., Fabbiano, G., Baldi, A., et al. 2007, ApJ, 661, 135

Zhang, Q., & Fall, S. M. 1999, ApJ, 527, L81

Zhang, Z., Gilfanov, M., & Bogdan, A. 2012a, ArXiv e-prints, arXiv:1202.2331

Zhang, Z., Gilfanov, M., & Bogdán, Á. 2012b, A&A, 546, A36

Zhang, Z., Gilfanov, M., Voss, R., et al. 2011, A&A, 533, A33

Zinn, R. 1985, ApJ, 293, 424

Zuo, Z.-Y., & Li, X.-D. 2014, ApJ, 797, 45

Chapter 2

X-Rays Beware: The Deepest Chandra Catalogue of Point Sources in M31

2.1 Executive Summary

This study represents the most sensitive *Chandra* X-ray point source catalogue of M31. Using 133 publicly available *Chandra* ACIS-I/S observations totalling $\sim$ 1 Ms, we detected 795 X-ray sources in the bulge, northeast, and southwest fields of M31, covering an area of ≈ 0.6 deg^2, to a limiting unabsorbed $0.5-8.0$ keV luminosity of $\sim 10^{34}$ erg s^{-1}. In the inner bulge, where exposure is approximately constant, X-ray fluxes represent average values because they were determined from many observations over a long period of time. Similarly, our catalogue is more complete in the bulge fields since monitoring allowed more transient sources to be detected. The catalogue was cross-correlated with a previous *XMM-Newton* catalogue of M31's D_{25} isophote consisting of 1948 X-ray sources, with only 979 within the field of view of our survey. We found 387 (49%) of our *Chandra* sources (352 or 44% unique sources) matched to within 5″ of 352 *XMM-Newton* sources. Combining this result with matching done to previous *Chandra* X-ray sources we detected 259 new sources in our catalogue. We created X-ray luminosity functions (XLFs) in the soft ($0.5-2.0$ keV) and hard ($2.0-8.0$ keV) bands that are

the most sensitive for any large galaxy based on our detection limits. Completeness-corrected XLFs show a break around $\approx 1.3 \times 10^{37}$ erg s^{-1}, consistent with previous work. As in past surveys, we find the bulge XLFs are flatter than the disk, indicating a lack of bright high-mass X-ray binaries in the disk and an aging population of low-mass X-ray binaries in the bulge.

2.2 Introduction

M31 is the nearest large spiral galaxy to our own, and as such allows for the best possible spatial resolution and sensitivity of any Milky Way-sized galaxy. The X-ray population of spiral galaxies can include X-ray binaries (XRBs), both low-mass (LMXBs) and high-mass (HMXBs), supernova remnants, supersoft sources, and massive stars. There is also contamination from background active galactic nuclei (AGN) or galaxies/galaxy clusters and Galactic foreground stars. Unlike the Milky Way, which is difficult to observe in X-rays due to absorption and the fact we are in the disc, M31 has moderate Galactic foreground absorption ($N_{\rm H} = 7 \times 10^{20}$ cm^{-2} Dickey & Lockman 1990) and can provide a galaxy-wide survey of the X-ray population, specifically XRBs. With an increased sample size, it is possible to study large-scale properties like the radial distribution across a range of L_X. The goal of this paper is to create the deepest *Chandra* X-ray catalogue of regions with archival observations in M31. Specifically, the bulge has > 1 Ms of data largely from monitoring programs that have not been fully exploited.

The X-ray point source population of M31 was first studied by (Trinchieri & Fabbiano, 1991) using ≈ 300 ks of *Einstein* imaging observations. They detected 108 sources of which 16 showed variability. They did not find a significant difference between the luminosity distribution of the bulge and disc population. Primini et al. (1993) completed a survey of the central ∼34′ of M31 using the *ROSAT* High-Resolution Imager (HRI). They found 18 variable sources within 7.5′ of the nucleus and 3 probable transients. Also, > 75% of the unresolved X-ray emission in the bulge was either thought to be diffuse of from a new class of X-ray sources.

This work was followed-up by deeper *ROSAT* observations (Supper et al., 1997, 2001) detecting 560 sources down to 5×10^{35} erg s^{-1} in the ~ 10.7 deg^2 view. They associated 55 sources with foreground stars, 33 with globular clusters, 16 with supernova remnants, and 10 with radio sources and galaxies, leaving 80% of sources without an optical/radio identification. They confirmed the previous result from *Einstein* that the total luminosity is distributed evenly between the bulge and disc. A comparison with the *Einstein* results revealed 11 variable sources and 7 transients, while comparison with the first *ROSAT* Position Sensitive Proportional Counter (PSPC) survey found 34 variable sources and 8 transients. The *ROSAT* surveys also revealed the presence of supersoft sources (a class of white dwarf X-ray binary) in M31 (Supper et al., 1997; Kahabka, 1999). Trudolyubov & Priedhorsky (2004) used *XMM-Newton* and *Chandra* to detect 43 X-ray sources coincident with globular cluster candidates, finding 31 of the brightest had spectral properties similar to Galactic LMXBs. X-ray monitoring of optical novae in the centre of M31 with *ROSAT*, *XMM-Newton*, and *Chandra* (Pietsch et al., 2005, 2007) showed them to be primarily supersoft sources. Shaw Greening et al. (2009) completed an *XMM-Newton* spectral survey of 5 fields along the major axis of M31 (excluding the bulge) and detected 335 X-ray sources, which were correlated with earlier X-ray surveys and radio, optical, and infrared catalogues. They classified 18 sources as HMXB candidates by spectral fitting with a power law model with a photon index of $0.8 - 1.2$, indicating they were magnetically accreting neutron stars. Peacock et al. (2010b) used the 2XMMi catalogue of X-ray point sources along with supplemental *Chandra* and *ROSAT* observations to identify 45 globular cluster LMXBs. This study covered 80% of the known globular clusters in M31 (Peacock et al., 2010a) and confirmed trends whereby high metallicity, luminosity, and stellar collision rate correlated positively with the likelihood of a cluster hosting an LMXB. Henze et al. (2014) completed monitoring observations with *XMM-Newton* and *Chandra* of the bulge of M31 and detected 17 new X-ray counterparts of optical novae, with 24 detected in total.

The most comprehensive X-ray population survey of M31 to date was completed by Stiele et al. (2011) using the *XMM-Newton* European Photon Imaging Camera. They detected 1897

Table 2.1: Summary of Previous M31 X-ray Surveys

Observatory	Detected Sources	L_X (erg s^{-1})	Region	References
Einstein	108	$5 \times 10^{36} - 10^{38}$ (0.2 – 4.0 keV)	14 *Einstein* imaging observations ($\sim$ 4 deg^2)	Trinchieri & Fabbiano (1991)
ROSAT (HRI)	86	$\gtrsim 1.8 \times 10^{36}$ (0.2 – 4.0 keV)	central $\sim$34′ ($\sim$ 0.3 deg^2)	Primini et al. (1993)
ROSAT (PSPC)	560	$5 \times 10^{35} - 5.5 \times 10^{38}$ (0.1 – 2.4 keV)	whole Galaxy (> D_{25} ellipse, 10.7 deg^2)	Supper et al. (1997, 2001)
XMM-Newton/*Chandra*	43	$\sim 10^{35} - 10^{39}$ (0.3 – 10.0 keV)	bulge & major axis (1.7 deg^2)	Trudolyubov & Priedhorsky (2004)
XMM-Newton	335	$\sim 10^{34} - 10^{39}$ (0.3 – 10.0 keV)	5 fields along major axis (1 deg^2)	Shaw Greening et al. (2009)
XMM-Newton/*Chandra*	45	$\sim 10^{35} - 7 \times 10^{38}$ (0.2 – 12.0 keV)	whole Galaxy (> D_{25} ellipse, 4 deg^2)	Peacock et al. (2010b)
XMM-Newton	1897[1]	$4.4 \times 10^{34} - 2.7 \times 10^{38}$ (0.2 – 4.5 keV)	whole Galaxy (> D_{25} ellipse, 4 deg^2)	Stiele et al. (2011)
XMM-Newton/*Chandra*	24	$\sim 10^{35} - 9 \times 10^{37}$ (0.2 – 2.0 keV)	centre ($\sim$ 0.2 deg^2)	Henze et al. (2014)

Luminosities have all been corrected to a distance of 776 kpc used in this paper. *Chandra* surveys are summarized in Table 2.2. See Stiele et al. (2011) for a more comprehensive list.

[1] The *XMM-Newton* LP total catalogue includes 1948 X-ray sources.

sources to a limiting luminosity of 4.4×10^{34} erg s^{-1}, including 914 new X-ray sources. Their source classification/identification was based on several methods: X-ray hardness ratios, spatial extent of the sources, long-term X-ray variability, and cross-correlation with X-ray, optical, infrared, and radio catalogues. Confirmed identifications included 25 supernova remnants, 46 LMXBs, 40 foreground stars, and 15 AGN/galaxies. There were many candidates for each of these classes as well, including 2 HMXBs and 30 supersoft sources. Nevertheless, 65% of their sources had no classification. We summarize a few of the major X-ray surveys of M31 in Table 2.1 (for a more detailed list please see Stiele et al. (2011)).

Chandra has not observed all of M31 as previous observatories have, but instead mostly monitored the supermassive black hole in the nucleus, with the majority of exposures each being 5 ks. Various groups have used a handful of observations to survey the bulge and create a catalogue of sources with either the Advanced CCD Imaging Spectrometer (ACIS-I/S) or the High-Resolution Camera (HRC-I/S). Kong et al. (2002) compiled the first *Chandra* catalogue of M31 within the bulge, finding 204 sources above $\gtrsim 2 \times 10^{35}$ erg s^{-1}. Their most important result was finding different X-ray luminosity functions (XLFs) when different regions (inner/outer bulge and disc) were considered separately. The inner bulge showed a break at 10^{36} erg s^{-1} and this break shifted to higher luminosities when moving outwards from the inner bulge to the disc. In addition, the slopes became steeper, indicating non-uniform star formation history. Kaaret (2002) used the HRC-I to detect 142 sources, which when compared to

ROSAT observations revealed 50% of the sources $> 5\times10^{36}$ erg s^{-1} to be variable. No evidence was found for X-ray pulsars, leading to the conclusion that most sources should be LMXBs. Di Stefano et al. (2002) used 3 disc fields in M31 to analyse globular cluster LMXBs while Di Stefano et al. (2004) used these fields with a nuclear pointing to study supersoft/quasi-soft sources. Williams et al. (2004) used HRC-I to study the disc and bulge of M31 with snapshot images, finding variability in 25% of 166 detected sources. Voss & Gilfanov (2007) combined 26 ACIS observations to investigate the X-ray population in the bulge, finding 263 X-ray sources (64 new) down to 10^{35} erg s^{-1}. They clearly demonstrated the power of merging observations to obtain deeper exposures and detect the faintest sources, decreasing the (completeness-corrected) XLF limit by a factor of 3. Hofmann et al. (2013) used 64 HRC-I observations totalling 1 Ms to detect 318 X-ray sources. They studied the long-term variability of sources by producing light curves and found 28 new sources, along with classifying 115 as candidate XRBs. A further 14 globular cluster XRB candidates, several new nova candidates, and a new supersoft X-ray source outburst were discovered. Recently, the ~12 yrs of monitoring observations of the nucleus have been utilized in a number of studies to investigate variability and detect transients (Barnard et al., 2012a,b, 2013). Specifically, Barnard et al. (2014) used 174 *Chandra* ACIS and HRC observations to detect 528 X-ray sources in the bulge down to 10^{35} erg s^{-1}. By studying source variability, they identified 250 XRBs (200 new) with X-ray data alone, a factor of 4 increase. At the time of writing, a large *Chandra* program (350 ks) has been accepted to survey a part of the star-forming disc of M31 (PI: B. Williams). Aside from being able to confirm the first HMXBs in M31, it will completely characterize a large part of the X-ray source population using optical photometry and spectroscopy.

This paper aims to study the properties of M31 X-ray point sources down to the lowest luminosities for any large galaxy. Specifically, we will report general source catalogue characteristics (e.g. flux and radial distributions), cross-correlate our catalogue with previous *XMM-Newton* and *Chandra* surveys, and study the XLF. In addition, high-resolution *Hubble Space Telescope* data from the Panchromatic Hubble Andromeda Treasury (PHAT) Survey (Dalcan-

Table 2.2: Summary of Previous *Chandra* M31 X-ray Catalogues

Instrument	Detected Sources	L_X (erg s^{-1})	Region	References
ACIS -I	204	$\gtrsim 2 \times 10^{35}$ (0.3 – 7.0 keV)	central $\sim 17' \times 17'$ (0.08 deg^2)	Kong et al. (2002)
HRC-I	142	$2 \times 10^{35} - 2 \times 10^{38}$ (0.1 – 10.0 keV)	central $\sim 30' \times 30'$ (0.25 deg^2)	Kaaret (2002)
ACIS -I/S & HRC-I	28	$5 \times 10^{35} - 3 \times 10^{38}$ (0.3 – 7.0 keV)	3 disc fields (0.7 deg^2)	Di Stefano et al. (2002)
ACIS -S3	33	$\sim 10^{35} - 10^{38}$ (0.1 – 7.0 keV)	3 disc fields and nucleus (0.7 deg^2)	Di Stefano et al. (2004)
HRC-I	166	$\sim 10^{36} - 5 \times 10^{38}$ (0.1 – 10.0 keV)	disc & bulge (0.9 deg^2)	Williams et al. (2004)
ACIS -I/S	263	$5 \times 10^{33} - 2 \times 10^{38}$ (0.5 – 8.0 keV)	12′ radius from core (0.126 deg^2)	Voss & Gilfanov (2007)
HRC-I	318	N/A (0.1 – 10.0 keV)	30′ radius from core (0.8 deg^2)	Hofmann et al. (2013)
ACIS -I/S & HRC-I	528	$5 \times 10^{34} - 5 \times 10^{38}$ (0.3 – 10.0 keV)	20′ radius from core (0.35 deg^2)	Barnard et al. (2014)

Luminosities have all been corrected to a distance of 776 kpc used in this paper.

ton et al., 2012) allows optical counterpart identifications for X-ray sources, especially AGN. We adopt a distance to M31 of 776 ± 18 kpc as in Dalcanton et al. (2012), which corresponds to a linear scale of 3.8 pc arcsecond^{-1}.

2.3 Observations and Data Reduction

2.3.1 Observations and Preliminary Reduction

We used 133 publicly available *Chandra* ACIS observations of M31, composed of 29 ACIS-S and 104 ACIS-I observations, summarized in Tables 2.3 and 2.4 respectively. Data reduction was performed using the *Chandra* Interactive Analysis of Observations (*CIAO*) tools package version 4.5 (Fruscione et al., 2006) and the *Chandra* Calibration database (*CALDB*) version 4.5.5 (Graessle et al., 2006). Before astrometric alignment could be completed we had to create source lists for each of the 133 ACIS observations in order to match them to a reference list. Starting from the level-1 events file, we created a bad pixel file using `acis_run_hotpix` and eliminated cosmic ray afterglows with only a few events using `acis_detect_afterglow`. We then processed the level-1 events file with `acis_process_events` using the default parameters to update charge transfer inefficiency (CTI), time-dependent gain, and pulse height. The VFAINT option was set for certain observations as appropriate. We removed the pixel randomization option by setting `pix_adj` to "none" to maintain the native position of each photon. Each events file was then filtered using the standard (ASCA) grades $(0, 2-4, 6)$, status bits (0),

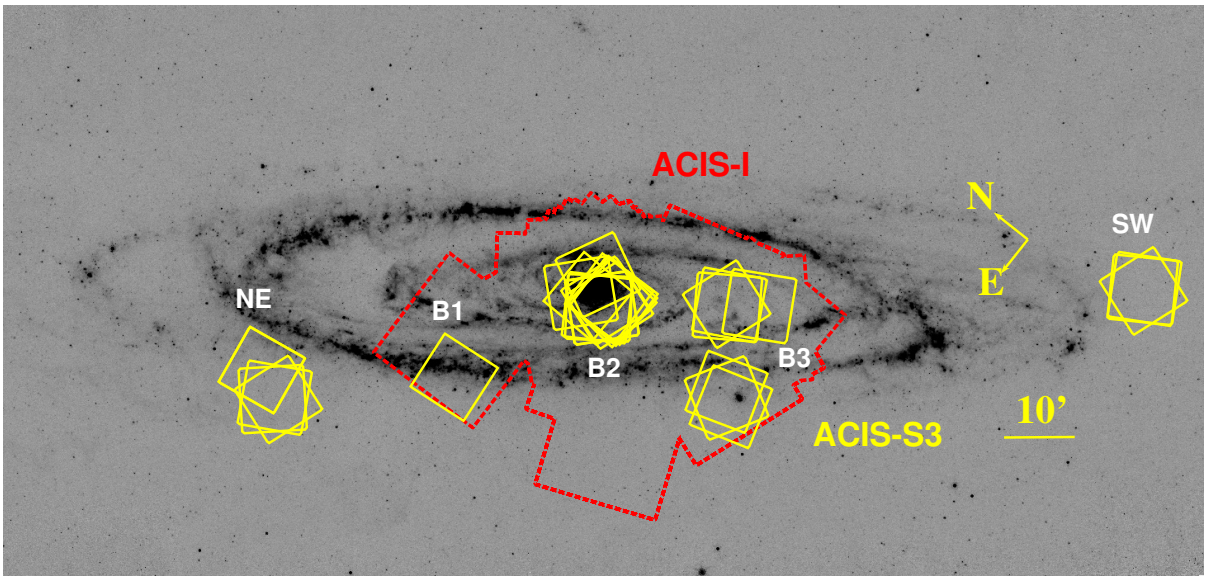

Figure 2.1: The field of view of the ACIS-I (red dashed outline) merged observations and ACIS-S3 chips (yellow) for each observation used in our analysis overlaid on a Spitzer 24 μm image of M31 (Gordon et al., 2006). Far left is the northeast region (NE), the bulge region is approximated by the red dashed outline (includes the ACIS-S observations within it), and the southwest region is far right (SW). The bulge region is additionally labelled into 3 separate regions based on the distribution of ACIS-S observations, bulge 1 (B1), bulge 2 (B2), and bulge 3 (B3). B3 includes the observations overlapping M32 as well as the fields just above it.

good time intervals, and CCD chips (I0-I3 for ACIS-I and S3 for ACIS-S). We only used data from the S3 chip from ACIS-S observations due to the degradation of the point spread function (PSF) at large off-axis angles. We then created exposure maps and exposure-corrected images using `fluximage` with a binsize of 1 in the soft (0.3 – 2 keV), hard (2 – 8 keV), and full (0.3 – 8 keV) energy bands. Source lists in each energy band were created with `wavdetect` using the $\sqrt{2}$ series from 1 to 8 for the *scales* parameter and corresponding exposure maps to reduce false positives. Default settings were used for all other parameters. We did not remove background flares from our level-2 events files because the background for point sources is addressed in the sensitivity calculation (Section 2.4.3). Flaring was negligible for > 99% of our observations.

Table 2.3: ACIS-S Observations

ObsID	Date	R.A. (J2000)	Decl. (J2000)	Distance (′)	Livetime (ks)	Datamode	CCDs	Roll Angle (°)	Region	δx (Pixels)	δy (Pixels)	Rotation (°)	Scale Factor	Matched Sources	Catalogue
309	2000-06-01	10.68800	41.27877	0.6	5110	FAINT	235678	87.5	B2	-0.16364	-0.26018	-0.03257	0.99909	4	CFHT
310	2000-07-02	10.68311	41.27876	0.6	5263	FAINT	235678	108.7	B2	0.36313	-0.19187	0.10652	1.00187	8	CFHT
313	2000-09-21	10.65816	40.87837	23.5	5980	FAINT	235678	162.9	B3	0.48271	-0.96208	0.03642	1.00353	3	2MASS
314	2000-10-21	10.64900	40.86757	24.1	5190	FAINT	235678	209.4	B3	0.49169	-1.32084	0.05563	1.00032	6	X-ray
2052	2000-11-01	11.53802	41.65947	45.0	13878	FAINT	235678	226.9	NE	-0.00785	-0.60853	0.08427	1.00164	4	CFHT
2046	2000-11-05	9.62713	40.26241	77.2	14767	FAINT	235678	237.6	SW	1.25572	-0.05402	-0.10691	0.99895	8	X-ray
2049	2000-11-05	10.44879	40.98187	20.2	14572	FAINT	235678	236.1	B3	-0.42443	0.56398	-0.23159	1.00028	5	2MASS
1580	2000-11-17	10.66379	40.85630	24.8	5407	FAINT	235678	251.5	B3	0.42793	-0.92874	0.19477	1.00102	4	2MASS
1854	2001-01-13	10.67349	41.25548	0.9	4697	FAINT	235678	295.6	B2	-0.65829	-0.27766	0.09229	1.00050	5	CFHT
2047	2001-03-06	9.69689	40.27309	74.7	14591	FAINT	235678	330.4	SW	2.11548	-1.17785	-0.01302	0.99931	7	X-ray
2053	2001-03-08	11.61538	41.66618	48.2	13363	FAINT	235678	330.5	NE	0.25278	-1.17593	-0.09831	0.99927	4	CFHT
2050	2001-03-08	10.51841	40.99440	18.1	13046	FAINT	235678	331.7	B3	-1.22735	-0.54781	0.06256	1.00063	4	2MASS
2048	2001-07-03	9.64190	40.33115	73.5	13779	FAINT	235678	109.6	SW	-0.25110	-0.31239	-0.10373	0.99851	4	Nomad
2051	2001-07-03	10.45902	41.05868	16.2	13583	FAINT	235678	109.0	B3	0.50294	-0.03155	-0.18985	0.99596	5	2MASS
2054	2001-07-03	11.54972	41.71649	47.3	14531	FAINT	235678	108.3	NE	-0.59834	-0.00160	-0.19307	0.99860	4	CFHT
1575	2001-10-05	10.66840	41.27894	1.0	39093	FAINT	235678	180.4	B2	0.21776	-0.65811	0.06315	1.00038	10	CFHT
2900	2002-11-29	11.16410	41.35916	22.3	5331	FAINT	136789	263.7	B1	0.00674	-1.04238	-0.15971	1.00138	4	SDSS
4541	2004-11-25	11.51934	41.70871	45.9	25631	FAINT	235678	260.0	NE	0.00551	-0.98102	-0.00539	0.99743	7	SDSS
6167	2004-11-26	11.51931	41.70871	45.9	24230	FAINT	235678	260.0	NE	0.76975	-0.25521	-0.04166	1.00155	7	SDSS
4536	2005-03-07	10.46483	40.93912	22.1	56181	FAINT	235678	330.4	B3	0.24710	-2.32722	-0.09497	1.00424	3	X-ray
14197	2011-09-01	10.68124	41.26788	0.2	37465	FAINT	235678	143.6	B2	-0.18277	-0.08271	0.01628	0.99981	7	CFHT
14198	2011-09-06	10.68135	41.26769	0.2	39875	FAINT	235678	147.7	B2	-0.22336	0.35097	-0.00697	1.00107	9	CFHT
13825	2012-06-01	10.68170	41.27070	0.2	39791	FAINT	23567	87.7	B2	-0.09198	0.00991	0.03199	1.00160	8	CFHT
13826	2012-06-06	10.68155	41.27051	0.2	36681	FAINT	235678	91.9	B2	-0.32372	-0.29423	0.03545	1.00100	9	CFHT
13827	2012-06-12	10.68139	41.27031	0.2	41481	FAINT	235678	96.2	B2	0.12455	1.22787	-0.10924	1.00182	8	CFHT
13828	2012-07-01	10.68111	41.26974	0.2	39881	FAINT	235678	107.9	B2	-0.06387	-0.33627	0.02094	1.00162	8	CFHT
14195	2012-08-14	10.68103	41.26846	0.2	27891	FAINT	235678	132.2	B2	0.49410	0.38553	-0.00897	1.00107	10	CFHT
15267	2012-08-16	10.68105	41.26846	0.2	11103	FAINT	235678	132.2	B2	0.41818	-0.28493	0.01966	0.99979	8	CFHT
14196	2012-10-28	10.68565	41.26598	0.2	42851	FAINT	23567	221.7	B2	-0.02078	-0.09118	0.05369	1.00091	10	CFHT

The R.A. and Decl. represent the pointing of the optical axis, the RA_PNT and DEC_PNT keywords from the level-2 events files. Distance represents the distance in arcminutes of the observation's pointing (RA_PNT and DEC_PNT) from the centre of M31 (J004244.33+411607.50). Livetime is the total amount of time that CCDs actually observe a source, which excludes the dead time (e.g. time it takes to transfer charge from the image region to the frame store region). CCDs indicates the CCD chips that were on during the observation, where for ACIS-S we only used chip 7 (S3) for analysis. Region defines one of the 5 ACIS-S regions in Figure 2.1: northeast (NE), bulge left (B1), bulge centre (B2), bulge right (B3), and southwest (SW). The last 6 columns summarize the results from matching each ObsID to a reference astrometric catalogue (see Section 2.3.2 for details) using the *CIAO* tool `wcs_match`.

Table 2.4: ACIS-I Observations

ObsID	Date	R.A. (J2000)	Decl. (J2000)	Distance ($'$)	Livetime (ks)	Datamode	CCDs	Roll Angle ($^\circ$)	δx (Pixels)	δy (Pixels)	Rotation ($^\circ$)	Scale Factor	Matched Sources	Catalogue
303	1999-10-13	10.67806	41.26989	0.3	11839	FAINT	012367	193.0	-0.18797	0.16872	0.02523	0.99995	15	CFHT
305	1999-12-11	10.68273	41.26395	0.3	4131	FAINT	01236	274.0	-0.26412	0.36347	0.02543	0.99911	12	CFHT
306	1999-12-27	10.68409	41.26370	0.3	4134	FAINT	01236	285.4	-0.00194	-0.34534	0.03549	1.00060	12	CFHT
307	2000-01-29	10.68116	41.25783	0.7	4118	FAINT	01236	304.3	-0.14524	-0.12621	0.02251	0.99985	15	CFHT
308	2000-02-16	10.68763	41.25244	1.0	4015	FAINT	012356	315.0	-0.02836	-0.76721	-0.03976	1.00036	13	CFHT
311	2000-07-29	10.68737	41.28525	1.0	4899	FAINT	012367	122.7	-0.13431	-0.67450	0.04802	1.00043	16	CFHT
312	2000-08-27	10.68037	41.28501	1.0	4668	FAINT	012367	140.6	-0.16983	0.31778	-0.04185	1.00034	13	CFHT
1581	2000-12-13	10.68382	41.25888	0.6	4406	FAINT	235678	276.0	-0.45828	-1.28464	0.09892	0.99917	10	CFHT
1582	2001-02-18	10.69296	41.26084	0.6	4307	FAINT	235678	317.2	-0.78685	-0.53480	0.08891	0.99944	8	CFHT
1583	2001-06-10	10.69713	41.28246	1.0	4908	FAINT	012356	94.9	-0.50360	0.02511	0.01140	0.99987	13	CFHT
1584	2001-07-03	10.66362	40.92284	20.8	4905	FAINT	012356	108.9	-0.05211	0.00191	0.14256	1.00122	5	2MASS
1577	2001-08-31	10.78014	41.32134	5.3	4918	FAINT	012367	143.0	0.36987	0.45146	0.00790	0.99990	17	CFHT
1576	2001-10-05	10.62845	40.96574	18.4	4892	FAINT	012367	181.2	0.05064	0.73209	-0.03749	0.99969	6	SDSS
1585	2001-11-19	10.75553	41.27497	3.2	4886	FAINT	012367	254.0	0.41805	-0.67229	-0.02047	1.00076	15	CFHT
2895	2001-12-07	10.77235	41.29267	4.2	5055	FAINT	012367	271.7	0.01760	-0.37528	0.01302	0.99955	12	CFHT
2897	2002-01-08	10.79083	41.31215	5.4	4905	FAINT	012367	292.4	-0.16044	-0.66610	-0.04185	0.99963	15	CFHT
2896	2002-02-06	10.77472	41.27972	4.1	4905	FAINT	012367	309.5	-0.15638	-0.09599	-0.00221	1.00057	16	CFHT
2898	2002-06-02	10.79337	41.32117	5.8	4902	FAINT	012367	88.6	-0.03274	0.24621	0.01292	0.99998	10	CFHT
2901	2002-07-08	10.53524	40.93252	21.3	4627	FAINT	012367	111.9	0.42453	0.19072	-0.11024	0.99938	5	SDSS
4360	2002-08-11	10.68315	41.27364	0.3	4908	FAINT	012367	130.0	0.04342	-0.22668	0.04692	1.00062	15	CFHT
2899	2002-08-23	10.47542	40.95079	21.3	4905	FAINT	012367	137.4	-0.20195	0.66568	-0.11795	1.00029	5	2MASS
2894	2002-10-14	10.63939	40.95643	18.9	4659	FAINT	012367	196.0	-0.69152	0.48268	0.10681	1.00541	5	SDSS
2902	2002-12-06	10.47560	40.94230	21.7	4700	FAINT	012367	270.6	0.30385	-1.60939	-0.03482	1.00054	5	2MASS
4678	2003-11-09	10.67435	41.25902	0.7	3897	FAINT	012367	239.5	0.38197	0.20299	0.01075	0.99960	12	CFHT
4679	2003-11-26	10.68017	41.25681	0.7	3823	FAINT	012367	261.4	0.22436	-1.00081	-0.03694	1.00023	15	CFHT
4680	2003-12-27	10.68713	41.25622	0.8	4201	FAINT	012367	285.1	0.48351	-0.52435	-0.06144	0.99969	14	CFHT
4681	2004-01-31	10.69271	41.25761	0.8	4588	FAINT	012367	305.6	0.11161	-0.32357	0.00695	0.99925	14	CFHT
4682	2004-05-23	10.69035	41.28109	0.8	3974	FAINT	012367	80.0	-0.72828	0.18097	-0.02200	0.99988	16	CFHT
4719	2004-07-17	10.67908	41.28108	0.8	5401	FAINT	012367	116.8	-0.07209	0.57077	-0.00202	1.00086	18	CFHT
4720	2004-09-02	10.68136	41.27297	0.3	4649	FAINT	012367	144.8	0.48472	-0.11297	0.00632	1.00026	14	CFHT
4721	2004-10-04	10.66766	41.27061	0.8	4662	FAINT	012367	180.5	0.26892	0.18019	-0.04184	0.99997	15	CFHT
4722	2004-10-31	10.67124	41.26128	0.8	3900	FAINT	012367	226.0	0.84482	-0.24614	-0.03245	1.00074	14	CFHT
4723	2004-12-05	10.70594	41.27487	1.0	4108	FAINT	012367	269.8	0.42644	-0.38791	-0.03446	1.00017	15	CFHT
7136	2006-01-06	10.68904	41.25669	0.7	3996	VFAINT	012367	291.7	-0.17839	-0.78181	0.01757	0.99950	12	CFHT
7137	2006-05-26	10.68974	41.28120	0.8	3958	VFAINT	012367	81.8	-0.38001	0.02828	-0.04487	0.99910	14	CFHT
7138	2006-06-09	10.68639	41.28173	0.8	4297	VFAINT	012367	93.9	-0.67241	0.02672	-0.00053	1.00068	14	CFHT
7139	2006-07-31	10.67776	41.28059	0.8	3993	VFAINT	012367	123.5	0.06284	0.27645	0.02426	1.00077	15	CFHT
7140	2006-09-24	10.66931	41.27371	0.8	4182	VFAINT	012367	166.0	-0.14144	-0.43678	0.00150	0.99986	13	CFHT
7064	2006-12-04	10.68236	41.25921	0.6	24073	VFAINT	012367	269.0	-0.06875	-0.19312	0.07135	0.99978	15	CFHT
8183	2007-01-14	10.68552	41.26435	0.3	3971	VFAINT	012367	296.1	0.10751	-0.41637	0.02249	1.00002	13	CFHT
8184	2007-02-14	10.68740	41.26454	0.3	4646	VFAINT	012367	313.8	0.34149	-0.79722	0.00335	1.00007	12	CFHT
8185	2007-03-10	10.69569	41.26756	0.5	3971	VFAINT	012367	332.6	0.31739	-0.65844	-0.00948	1.00058	13	CFHT
7067	2007-06-02	11.05451	41.43989	19.6	8121	VFAINT	012367	88.0	-0.81062	-1.22614	-0.05564	0.99899	9	SDSS

ObsID	Date	R.A.	Decl.	Distance	Livetime	Datamode	CCDs	Roll Angle	δx	δy	Rotation	Scale Factor	Matched Sources	Catalogue
7068	2007-06-02	10.68775	41.27877	0.6	7699	VFAINT	012367	88.5	-0.47939	-0.15489	0.01308	1.00042	14	CFHT
8191	2007-06-18	10.68003	41.27608	0.5	3964	VFAINT	012367	99.6	-0.28039	-0.27341	0.00140	1.00052	15	CFHT
8192	2007-07-05	10.67864	41.27540	0.5	4079	VFAINT	012367	109.8	-0.31076	-0.56861	0.01216	0.99986	15	CFHT
8193	2007-07-31	10.67661	41.27398	0.5	4710	VFAINT	012367	123.4	-0.27693	0.25171	-0.00170	1.00011	11	CFHT
8194	2007-08-28	10.67494	41.27198	0.5	4038	VFAINT	012367	140.5	-0.67721	-0.30881	0.03039	0.99919	16	CFHT
8195	2007-09-26	10.67416	41.26813	0.5	3971	VFAINT	012367	168.0	0.27897	0.79859	0.02101	1.00071	15	CFHT
8186	2007-11-03	10.68074	41.26147	0.5	5055	VFAINT	012367	229.9	0.01452	-0.12753	0.00188	0.99906	14	CFHT
8187	2007-11-27	10.68674	41.26097	0.5	3843	VFAINT	012367	261.5	0.21790	-0.04676	0.00418	1.00026	13	CFHT
9520	2007-12-29	10.69095	41.26234	0.5	3967	VFAINT	012367	286.6	-0.33855	-0.35814	0.02606	1.00000	15	CFHT
9522	2008-07-15	10.67764	41.27492	0.5	4054	VFAINT	012367	115.6	-0.18323	-0.27477	0.01229	1.00045	15	CFHT
9523	2008-09-01	10.67481	41.27168	0.5	4159	VFAINT	012367	143.8	0.07670	0.58406	-0.03829	1.00110	11	CFHT
9521	2008-11-27	10.68689	41.26097	0.5	3971	VFAINT	012367	262.9	-0.10196	-0.08820	0.04509	1.00049	13	CFHT
10551	2009-01-09	10.69205	41.26274	0.5	3971	VFAINT	012367	293.7	0.49079	-0.22179	-0.03383	0.99980	13	CFHT
10552	2009-02-07	10.69356	41.26405	0.5	3967	VFAINT	012367	305.2	0.34094	-0.29859	0.00876	0.99934	15	CFHT
10553	2009-03-11	10.69564	41.26787	0.5	4374	VFAINT	012367	334.4	0.23873	-0.76979	-0.00412	1.00030	14	CFHT
10554	2009-05-29	10.68273	41.27687	0.5	4041	VFAINT	012367	84.7	-0.56556	0.07285	0.00426	1.00103	13	CFHT
10555	2009-07-03	10.67865	41.27546	0.5	4067	VFAINT	012367	108.9	-0.02769	0.13497	-0.03107	1.00107	15	CFHT
11256	2009-09-17	11.01530	41.01168	21.5	20310	VFAINT	012367	157.4	-0.54140	1.12794	-0.03195	1.00079	11	2MASS
10715	2009-09-18	10.67420	41.26954	0.5	3971	VFAINT	012367	158.7	0.02450	0.27329	-0.02508	1.00097	14	CFHT
11252	2009-09-19	10.85959	41.12999	11.5	59305	VFAINT	012367	159.8	0.40544	0.16412	-0.00072	0.99981	15	SDSS
10716	2009-09-25	10.67432	41.26833	0.5	4185	VFAINT	012367	166.8	0.13559	0.66831	-0.00862	0.99995	15	CFHT
10717	2009-10-22	10.67710	41.26358	0.5	4854	VFAINT	012367	205.2	0.36644	0.17879	-0.05317	0.99947	14	CFHT
11275	2009-11-11	10.68321	41.26092	0.5	4601	VFAINT	012367	243.0	0.54003	0.26701	0.01006	1.00053	14	CFHT
10718	2009-11-19	10.49746	41.08611	13.8	4201	VFAINT	012367	254.4	0.43349	0.34527	-0.05374	0.99860	10	2MASS
11276	2009-12-08	10.68868	41.26143	0.5	3967	VFAINT	012367	272.5	0.24870	-0.47094	-0.00522	1.00019	14	CFHT
10719	2009-12-27	10.69083	41.26230	0.5	4108	VFAINT	012367	285.7	-0.08609	-0.42409	-0.04862	0.99925	15	CFHT
11277	2010-01-01	10.69067	41.26210	0.5	4614	VFAINT	012367	283.9	0.30779	-0.30216	-0.00430	0.99981	10	CFHT
11278	2010-02-04	10.69378	41.26431	0.5	3974	VFAINT	012367	307.9	-0.06177	-0.12961	-0.01722	0.99978	15	CFHT
11279	2010-03-05	10.69539	41.26694	0.5	4217	VFAINT	012367	328.6	0.31962	-0.69587	0.00493	0.99906	13	CFHT
11838	2010-05-27	10.68307	41.27688	0.5	3974	VFAINT	012367	83.1	-0.46033	-0.27450	0.02231	1.00031	14	CFHT
11839	2010-06-23	10.67964	41.27597	0.5	3977	VFAINT	012367	103.1	0.14325	0.64976	-0.03658	0.99975	14	CFHT
11840	2010-07-20	10.67727	41.27462	0.5	3977	VFAINT	012367	118.1	0.07491	0.27887	-0.06298	1.00017	17	CFHT
11841	2010-08-24	10.67529	41.27231	0.5	3977	VFAINT	012367	137.8	-0.42007	0.36477	-0.03208	1.00009	12	CFHT
11842	2010-09-25	10.67422	41.26849	0.5	3977	VFAINT	012367	166.3	0.65928	0.06021	-0.04522	1.00082	14	CFHT
12160	2010-10-19	10.67699	41.26365	0.5	3977	VFAINT	012367	204.4	0.32090	0.14500	-0.00119	0.99918	13	CFHT
12161	2010-11-16	10.68436	41.26084	0.5	3977	VFAINT	012367	249.8	0.41203	-0.45001	0.03996	1.00048	14	CFHT
12162	2010-12-12	10.68905	41.26150	0.5	3977	VFAINT	012367	275.1	0.81924	-0.36948	-0.04017	0.99998	14	CFHT
12163	2011-01-13	10.69237	41.26305	0.5	3977	VFAINT	012367	295.1	-0.42920	-1.36273	0.01307	1.00008	12	CFHT
12164	2011-02-16	10.69499	41.26594	0.5	3977	VFAINT	012367	320.2	-0.07968	-0.28806	-0.01727	0.99898	13	CFHT
12970	2011-05-27	10.68323	41.27705	0.5	3980	VFAINT	012367	82.7	-0.51350	-1.11785	-0.00247	1.00046	12	CFHT
12971	2011-06-30	10.67889	41.27572	0.5	3980	VFAINT	012367	107.0	0.09747	-0.18439	-0.01104	1.00029	15	CFHT
12972	2011-07-25	10.67697	41.27440	0.5	3980	VFAINT	012367	120.3	0.09864	0.05232	-0.03337	1.00020	14	CFHT
12973	2011-08-25	10.67517	41.27224	0.5	3948	VFAINT	012367	138.3	-0.20888	0.41130	-0.00126	1.00071	14	CFHT
12974	2011-09-28	10.67774	41.26745	0.3	3980	VFAINT	012367	170.8	-0.82263	1.01165	0.01951	0.99986	13	CFHT
13833	2011-10-31	10.68240	41.26348	0.3	3961	FAINT	01237	224.9	0.83320	0.68904	0.00380	1.00045	15	CFHT
13834	2011-11-24	10.68628	41.26085	0.5	3913	FAINT	012367	259.0	0.78463	0.46586	-0.01648	1.00029	15	CFHT

ObsID	Date	R.A.	Decl.	Distance	Livetime	Datamode	CCDs	Roll Angle	δx	δy	Rotation	Scale Factor	Matched Sources	Catalogue
13835	2011-12-19	10.69011	41.26183	0.5	3910	FAINT	012367	280.2	0.20214	-0.43945	-0.00500	0.99960	12	CFHT
13836	2012-01-16	10.69261	41.26329	0.5	3910	FAINT	012367	297.1	0.97548	-0.28084	0.02845	1.00032	16	CFHT
13837	2012-02-19	10.69464	41.26549	0.5	3913	FAINT	012367	317.3	0.51683	-0.30897	-0.05184	0.99886	14	CFHT
13298	2012-05-26	10.68313	41.27691	0.5	3910	FAINT	012367	83.1	-0.97454	-0.05975	-0.01830	1.00027	12	CFHT
13299	2012-06-21	10.67966	41.27592	0.5	3916	FAINT	012367	102.4	-0.40194	0.12213	0.04446	0.99999	13	CFHT
13300	2012-07-20	10.67725	41.27467	0.5	3913	FAINT	012367	118.1	-0.11729	0.33603	-0.04938	1.00019	15	CFHT
13301	2012-08-19	10.67548	41.27276	0.5	3769	FAINT	012367	134.7	0.63460	0.29579	-0.00960	1.00032	16	CFHT
13302	2012-09-12	10.67443	41.27028	0.5	3913	FAINT	012367	153.5	0.22866	0.07022	0.01487	0.99955	15	CFHT
14927	2012-12-09	10.68876	41.26139	0.5	3913	FAINT	012367	273.0	0.35798	-0.90453	0.01258	0.99993	15	CFHT
14928	2012-12-31	10.69127	41.26235	0.5	3913	FAINT	012367	288.0	0.22543	-0.75450	-0.00883	0.99940	13	CFHT
14929	2013-01-21	10.69308	41.26350	0.5	3910	FAINT	012367	300.2	-0.43826	-1.25006	-0.01289	0.99999	15	CFHT
14930	2013-02-18	10.69467	41.26542	0.5	3913	FAINT	012367	316.9	-0.37481	-0.85622	-0.01640	1.00028	15	CFHT
14931	2013-03-12	10.69573	41.26854	0.5	3913	FAINT	012367	339.2	-1.19938	-0.68429	-0.00579	0.99929	15	CFHT

The R.A. and Decl. represent the pointing of the optical axis, the RA_PNT and DEC_PNT keywords from the level-2 events files. Distance represents the distance in arcminutes of the observation's pointing (RA_PNT and DEC_PNT) from the centre of M31 (J004244.33+411607.50). Livetime is the total amount of time that CCDs actually observe a source, which excludes the dead time (e.g. time it takes to transfer charge from the image region to the frame store region). CCDs indicates the CCD chips that were on during the observation, where for ACIS-I we used chips 0123 (I0-I3) for analysis. Also, ObsID's 1581/82 only had 2 active CCDs. The last 6 columns summarize the results from matching each ObsID to a reference astrometric catalogue (see Section 2.3.2 for details) using the *CIAO* tool `wcs_match`.

2.3.2 Image Registration

While *Chandra* has absolute astrometry of $\approx 0.6''$ (90 per cent uncertainty circle, within $3'$ of the aimpoint)[1], creating an X-ray point source catalogue requires more precision. Therefore we performed alignment to a ground-based standard for every ACIS observation to improve astrometry to the extent possible. We began by using a wide-field image that covers the PHAT-fields (Williams et al., 2014) obtained with the *Canada-France-Hawaii Telescope* (*CFHT*) MegaPrime/MegaCam in the *i* (MP9701) filter. The astrometry in this image had already been corrected to match the Two Micron All Sky Survey (2MASS, Skrutskie et al. 2006) reference system, which is accurate to $< 0.2''$. We used this image because the PHAT data was aligned to it, therefore making optical counterpart identification more precise. We used the `daofind` tool in the `IRAF\DAOPHOT` package (Stetson, 1987) to compile a source list from the *CFHT* image. We only chose sources in the *CFHT* image that were point (circular) sources, which represented background galaxies/LMXBs. For the `datapars` settings we changed the *fwhmpsf* parameter to 2 based on an analysis of numerous point sources in the image. The *sigma* (the standard deviation of the mode of the background), *datamin*, and *datamax* parameters were all calculated from the image; the *readnoise* was set to 5. For `centerpars` the *calgorithm* was set to centroid, while the `fitskypars` parameter *salgorithm* was set to median and *annulus* and *dannulus* were both set to 8 ($4\times$ *fwhmpsf*). The `photpars` parameter *zmag* was set to 25.72, the zero point of the magnitude scale for the *i* filter on the *CFHT* MegaPrime/MegaCam[2]. The `findpars` settings were left to their defaults. We ran the `phot` procedure with the above settings to determine precise centroids for our output source list.

We used the *CIAO* tool `wcs_match` to match and then align the X-ray source list (from the full energy band) for an observation to the reference source list created using `IRAF\DAOPHOT` from the *CFHT* image. We set the search radius to $2''$ and use the WCS from the input (X-ray) source list since the program requires WCS parameters to specify a tangent point for

[1] `http://cxc.harvard.edu/cal/ASPECT/celmon/`

[2] `http://www.cfht.hawaii.edu/Instruments/Imaging/MegaPrime/generalinformation.html`

the transform calculations. To eliminate matches with large positional errors from the final transformation calculation, we disabled the *residlim* parameter (set to 0), set the *residtype* parameter to 0, and set the *residfac* parameter to 25. If any residual-to-source pair position error ratio exceeds the value of *residfac* it is omitted from the transformation calculation, where the *residtype* parameter setting ensures this is completed for each individual source-pair as opposed to averaging all source-pairs. The program then created a transformation matrix with x and y offsets (R.A. and decl.) as well as a rotation and scale parameter. This matrix was then used with `wcs_update` to correct the astrometry of the aspect solution file for each individual observation. Since we reprocessed each observation from the level-1 events file, which specifies events in chip coordinates, only the aspect solution file needed to be corrected since it provides the appropriate WCS for `acis_process_events` to convert from chip coordinates to sky coordinates. A complication arose during matching that stems from the exposure mode for many of our observations. The majority of observations were completed in interleaved mode (known as alternating exposure mode), which is carried out by alternating short and long frame times. Two separate event files are produced, one representing events with long frame times and another the short frame times. This is advantageous when observing sources that may be piled-up, such as those in the nucleus of M31. The event files with short frame times all have small livetime exposures and therefore it was difficult to find matching sources for alignment. Since the event files with long frame times always had much larger livetime exposures, they provided more precise astrometric alignment because more sources were detected. Therefore we used the same transformation matrix from the long frame time event file to correct the astrometry for the short frame time event file.

However, 10 ACIS-I and 13 ACIS-S observations were either outside of the PHAT-field or did not have at least three source-pair matches to *CFHT* image sources. For these observations we first attempted to introduce more matches by using a source list of galaxies from the Sloan Digital Sky Survey (SDSS) Data Release 10. We obtained the source list through the CasJobs

batch query service[3] because it has no limit on the number of rows output. In the cases where the SDSS match failed, we introduced stars found in the SDSS, whose positions are not necessarily as precise because they may be subject to large proper motions (foreground stars). The proper motions of matched stars that were available were found to be negligible (< 5 mas yr^{-1}). Lastly, we introduced a source list of galaxies from the Two Micron All Sky Survey (2MASS) All-Sky Point Source Catalogue. Since 2MASS publishes an error ellipse, we used $\sqrt{a \times b}$ to determine the error for R.A. and Decl., where a and b are the semi-major and semi-minor axes. The remaining ACIS-I observations were all aligned with the inclusion of the 2MASS point sources. However, 5 ACIS-S observations (314, 4536, 2046, 2047, and 2048) still had < 3 reliable matches. We then included stars from the Naval Observatory Merged Astrometric Dataset (Zacharias et al., 2005), which also mostly appeared in the SDSS catalogue. This helped us align observation 2048, where we were careful to check that the proper motions of the matched stars were negligible. For the last 4 observations we merged the `wavdetect` X-ray source lists from the soft, hard, and full energy bands and repeated the matching procedure above with no success. Since many of our observations overlap one another, we used the astrometric alignments calculated to update the `wavdetect` X-ray source lists from observations that overlapped the 4 that were still unaligned. This method was still unsuccessful for observation 4536, and so it maintains its original astrometry. The details of astrometric alignment are summarized in Tables 2.3 and 2.4.

2.3.3 Merging

We needed to create merged images of each M31 region (northeast, bulge, southwest) in order to detect the faintest sources. After correcting the astrometry in each individual observation by updating the aspect solution file, we repeated the same preliminary reduction process for events files outlined in Section 2.3.1 with one minor change: we enabled the energy-dependent subpixel event repositioning algorithm in `acis_process_events` to improve the spatial reso-

[3] `http://skyserver.sdss3.org/casjobs/`

lution of point sources on-axis. This algorithm is useful to later distinguish nearby X-ray point sources since most of the observations are centred on the nucleus of M31, and point sources are denser in this region of the galaxy. We then reprojected the cleaned event files for all 29 ACIS-S and 104 ACIS-I observations using `reproject_obs`. Reprojections were made to the tangent points of the longest observations within the given region. We then created exposure maps and exposure-corrected images (photons cm^{-2} s^{-1} $pixel^{-1}$) for each observation with the `flux_obs` tool, which combined them to create an exposure-corrected image of the 104 ACIS-I observations in the bulge and 5 exposure-corrected images of the various 29 ACIS-S observations based on their overlapping fields (northeast and southwest regions, and 3 regions in the bulge: nucleus and left and right of the nucleus; see Figure 2.1). The right bulge field has 2 ACIS-S regions that we combined due to their proximity. We used a binsize of 1 to maintain the native resolution and weighted spectrum files (corresponding to the soft, hard, and full energy bands) to calculate instrument maps.

We created a total of 18 images throughout the soft, hard, and full energy bands, 3 ACIS-I and 15 ACIS-S, with each representing the regions in Figure 2.1. The plate scale of the *Chandra* images is 0.5 arcsecond $pixel^{-1}$, corresponding to 1.9 pc $pixel^{-1}$ at the distance of 776 kpc for M31 adopted at the end of Section 2.2. *Chandra* ACIS has spatial resolution that ranges from 1″ on-axis to 4″ at 4′ off-axis for 1.5 keV X-rays at 90 per cent encircled energy fraction[4]. The ACIS-I images of the bulge were each $\approx$ 150 MB and had dimensions of 5824 pixels by 6145 pixels. Executing `flux_obs` and `wavdetect` to create this image and detect sources required a large amount of memory (e.g. $\sim$ 25 GB for ACIS-I image creation) and storage space (> 1 TB for all data and ancillary files).

2.3.4 Source Catalogue Creation

Source detection was accomplished using `wavdetect` in order to create a preliminary list of source positions. Starting from our merged exposure-corrected images (one ACIS-I region

[4] `http://cxc.harvard.edu/proposer/POG/`

and five ACIS-S regions) in the soft, hard, and full bands, we used the $\sqrt{2}$ series from 1 to 8 for the *scales* parameter, corresponding exposure maps to reduce false positives, and the inverse of the number of pixels in an image for the *sigthresh* parameter as recommended by the *Chandra* X-ray Center. Since our merged images are larger than the standard 1024×1024 pixels for most images, the *sigthresh* parameter needed to be modified to reduce the number of false sources detected. It was set to 3×10^{-8} for the ACIS-I image and ~few$\times 10^{-6}$ for the five ACIS-S images. The *expthresh* parameter was changed from its default value of 0.1 to 0.001 for all 6 merged images. Pixels with a relative exposure (pixel exposure value over maximum value of exposure in the map) less than *expthresh* are not analysed, and adopting the default value would exclude the analysis of many of the low-exposure regions in our merged images. All other `wavdetect` parameters were left at their default values. The source lists we obtained were then combined into a master source list using the `match_xy` tool from the Tools for ACIS Review and Analysis (TARA) package[5], resulting in a candidate list of 1068 sources. In addition, to ensure all possible sources were detected `reproject_image` was used to merge the 3 ACIS-S bulge region counts images with the ACIS-I counts image. Running `wavdetect` on each energy range for this master bulge region image and combining the source lists following the same procedure as above we recovered 331 additional sources (unique from the original 1068). Therefore we had a total of 1399 `wavdetect` sources.

To obtain source properties from our preliminary list of source positions we used *ACIS Extract* (*AE*; Broos et al., 2010), which performed source extraction and characterization. AE analyses the level-2 event files of each observation individually before merging and determining source properties. In order to create a reliable catalogue, we followed the methods outlined in the validation procedure[6] used by the authors of AE. This multi-step process (summarized in Figure 1 of Broos et al. 2010) involved many iterations of extracting, pruning, and repositioning sources in the candidate catalogue. We pruned sources using the *AE* parameter *pns* (‘*prob_no_source*’ or the p-value for no-source hypothesis), which calculates the Poisson prob-

[5] `http://www2.astro.psu.edu/xray/docs/TARA/`

[6] `http://www2.astro.psu.edu/xray/docs/TARA/ae_users_guide/procedures/`

ability of a detection not being a source by taking the uncertainty of the local background into account. Using the *pns* value removes the bias inherent in using the traditional 3σ source significance criterion, where sources with low count rates would have been left out.

Before pruning any source we visually inspected it in any of the observations it appeared to be sure that it was insignificant. In some cases 2 neighbouring sources were both selected for pruning, but it was often found that either one would survive if the other was removed. The most advantageous aspect of the validation procedure was the ability to review each source and select the most likely position based on the properties of an individual source. Specifically, the repositioning stage displays the original catalogue position and also calculates 3 other position estimates: the mean data, correlation, and maximum-likelihood reconstruction positions. The catalogue and/or centroid positions were used most often, but for sources with large off-axis angles ($\gtrsim 5'$) the correlation position was used, whereas for crowded sources with overlapping PSFs the maximum-likelihood reconstruction position was used (see §7.1 of Broos et al. 2010 for a detailed description of source positions). *AE* also produces smoothed residual images for each observation, which are the smoothed residuals remaining after the point source models are subtracted from the observation data. The residual image is scaled to emphasize only bright residuals, which are possible sources that may have been missed by `wavdetect` or were accidentally pruned. Inspecting the observed events and point source model for a bright residual reveals whether it is an artefact or likely point source. We found 43 sources using the residual images that were added to our source list. After catalogue positions were validated, the one-pass photometry procedure (follows the validation procedure, see footnote 6) completed the final extraction for all 795 sources in our final M31 catalogue; output source properties are summarized in Tables 2.6–2.7. To be included in the final catalogue a source was required to have a *pns* value $\leq 1 \times 10^{-2}$ (default in *AE*) in any of the energy bands (full, soft, or hard). We chose this value since it was used for the *Chandra* Carina Complex Project (Broos et al., 2011) to balance sensitivity with source detection significance. In the full band, all 795 (100%) of our sources had a *pns* value $\leq 1 \times 10^{-2}$.

2.4 X-ray Source Catalogue Properties

2.4.1 Source Catalogue

Our final M31 catalogue consists of 795 X-ray point sources. Their properties are summarized in Tables 2.6−2.7. The detailed FITS tables from *AE*, which include ∼ 100 other source photometric properties used in *AE* (e.g. background region metrics) in 16 energy bands (see Section 7.8 of the *AE* manual for these bands), are available on the journal website. Of the 795 sources, 42 are in the northeast portion of M31, 728 are in the bulge, and 25 are in the southwest. The luminosities in Table 2.7 were calculated using conversion factors of 3.94, 1.34, and 2.43 in units of $10^{41}\left(\frac{d}{776\,\mathrm{kpc}}\right)^2$ erg cm^2 photons^{-1} for the full, soft, and hard bands (to convert from photon flux in photons cm^{-2} s^{-1}). Photon fluxes were estimated by *AE* (*flux2* parameter) based on the number of net source counts (*net_cts*), the exposure time, and the mean ancillary response function (*MEAN_ARF*) in the given energy band. This flux estimate suffers from a systematic error (compared to the true incident flux) because the *MEAN_ARF* is the correct effective area normalization based on an incident spectrum that is flat. To obtain a more accurate flux estimate, one should sum the flux values over narrow energy bands. We converted this photon flux into an energy flux assuming an absorbed power-law spectrum with $\Gamma = 1.7$ and $N_H = 6.66 \times 10^{20}$ cm^{-2} (details in Section 2.4.3). In Figure 2.2, we show histograms of the net counts (left panel) and source flux (right panel) for all our sources. The left panel shows sources with < 200 counts, while the inset shows a log distribution of all sources, clearly indicating the majority of sources have < 100 counts. The 191 sources that have $\gtrsim$ 200 counts are suitable for spectral modelling. The source flux histogram shows a peak in the flux distribution near our 90% detection limit of $\approx 5 \times 10^{-15}$ erg s^{-1} cm^{-2} (3×10^{35} erg s^{-1}). The X-ray point source population of M31 is comprised of LMXBs and HMXBs, supernova remnants, and background AGNs. To determine the makeup of our population of point sources we created XLFs and used various catalogues from previous studies.

Table 2.5: Completeness Limits

Completeness	Full [0.5 − 8.0 keV]	Soft [0.5 − 2.0 keV]	Hard [2.0 − 8.0 keV]
50%	0.66	0.20	0.33
70%	1.37	0.45	0.69
90%	4.05	1.58	1.98
95%	6.73	2.68	3.29

Completeness limits in various energy bands calculated from our sensitivity curves. Values show unabsorbed luminosities in units of 10^{35} erg s^{-1}.

Table 2.6: M31 Source List

Source No.	CXOU J	R.A. (J2000) (°)	Decl. (J2000) (°)	Distance (′)	PosErr (″)	θ (′)	No. of Obs	Detector	Region	Tot Exp (ks)	Tot Exp. Map Value (s cm^2)	R_{src} (sky pixel)	SNR	E_{median} (keV)	Match
(1)	(2)	(3)	(4)	(5)	(6)	(7)	(8)	(9)	(10)	(11)	(12)	(13)	(14)	(15)	(16)
1	004542.90+414312.6	11.428779	41.720189	43.03	0.2	4.1	2	ACIS-S	NE	49	1.14E+07	4.5	6.5	2.1	
2	004551.05+414452.4	11.462750	41.747912	45.26	0.3	3.5	2	ACIS-S	NE	49	1.64E+07	3.5	2.7	2.7	
3	004551.30+414220.7	11.463769	41.705754	43.74	0.2	2.8	3	ACIS-S	NE	64	2.20E+07	2.8	2.4	2.3	AGN
4	004552.93+414441.8	11.470551	41.744965	45.42	0.2	3.1	2	ACIS-S	NE	49	1.68E+07	3.0	2.8	2.0	
5	004555.72+414551.8	11.482172	41.764389	46.56	0.3	3.7	2	ACIS-S	NE	49	1.67E+07	4.0	2.5	2.5	
6	004556.82+414440.8	11.486787	41.744673	45.98	0.2	2.6	2	ACIS-S	NE	49	1.72E+07	2.5	2.5	2.7	
7	004556.99+414831.7	11.487497	41.808829	48.48	0.2	6.2	2	ACIS-S	NE	49	1.60E+07	9.3	9.6	2.4	AGN
8	004559.07+414113.0	11.496132	41.686945	44.27	0.2	2.6	5	ACIS-S	NE	91	3.38E+07	3.0	5.3	2.9	
9	004602.43+414515.7	11.510137	41.754377	47.16	0.2	3.1	3	ACIS-S	NE	63	1.84E+07	3.3	5.7	2.1	
10	004602.70+413856.7	11.511251	41.649095	43.61	0.3	3.4	3	ACIS-S	NE	41	1.62E+07	4.1	3.6	1.4	

Notes. Column 2: source ID, which contains the source coordinates (J2000.0). Column 5: distance in arcminutes of the source from the centre of M31 (J004244.33+411607.50). Column 6: positional uncertainty $\sqrt{\sigma_x^2 + \sigma_y^2}$, where the single-axis position errors σ_x and σ_y are estimated from the standard deviations of the PSF in the extraction region and the number of counts extracted. Column 7: average off-axis angle for merged observations. Column 8: number of observations extracted. Column 9: source detected in ACIS-I, ACIS-S, or Both. Column 10: for a source detected in ACIS-S or Both, indicates which region from Figure 2.1 it belongs to. Columns 11 & 12: total values for merged observations. Column 13: average radius of the source extraction region (1 sky pixel = 0.492″). Column 14: photometric significance (net counts / upper error on net counts) (0.3 − 8.0 keV). Column 15: background-corrected median photon energy (0.3 − 8.0 keV). Column 16: cross-match results from Section 2.4.4: active galactic nuclei (AGN) or low-mass X-ray binary (LMXB).
(This table is available in its entirety in Appendix A.)

Table 2.7: Additional M31 Source Properties

Source No.	*pns* (0.5 − 8.0 keV)	*pns* (0.5 − 2.0 keV)	*pns* (2.0 − 8.0 keV)	*net_cts* (0.5 − 8.0 keV)	*net_cts* (0.5 − 2.0 keV)	*net_cts* (2.0 − 8.0 keV)	*luminosity* (0.5 − 8.0 keV)	*luminosity* (0.5 − 2.0 keV)	*luminosity* (2.0 − 8.0 keV)
(1)	(2)	(3)	(4)	(5)	(6)	(7)	(8)	(9)	(10)
1	0.00E+00	1.40E-45	1.37E-23	$55.65^{+8.60}_{-7.53}$	$33.52^{+6.90}_{-5.80}$	$22.13^{+5.87}_{-4.76}$	2.22E+36	2.86E+35	6.36E+35
2	7.48E-12	6.96E-09	6.96E-05	$13.01^{+4.84}_{-3.69}$	$7.65^{+3.96}_{-2.76}$	$5.35^{+3.60}_{-2.38}$	3.87E+35	4.56E+34	1.19E+35
3	2.17E-09	1.18E-08	5.55E-03	$10.96^{+4.57}_{-3.41}$	$7.63^{+3.96}_{-2.76}$	$3.33^{+3.18}_{-1.91}$	2.45E+35	3.43E+34	5.55E+34
4	4.98E-14	1.50E-10	1.19E-05	$13.32^{+4.84}_{-3.69}$	$7.79^{+3.96}_{-2.76}$	$5.53^{+3.60}_{-2.38}$	3.93E+35	4.57E+34	1.22E+35
5	2.19E-09	1.08E-06	2.45E-04	$11.71^{+4.71}_{-3.56}$	$6.53^{+3.78}_{-2.58}$	$5.18^{+3.60}_{-2.38}$	3.50E+35	3.85E+34	1.17E+35
6	1.04E-13	2.88E-08	5.85E-07	$11.56^{+4.57}_{-3.41}$	$5.84^{+3.60}_{-2.37}$	$5.72^{+3.60}_{-2.37}$	3.36E+35	3.36E+34	1.25E+35
7	0.00E+00	2.01E-41	0.00E+00	$117.40^{+12.23}_{-11.18}$	$50.47^{+8.34}_{-7.26}$	$66.93^{+9.55}_{-8.48}$	3.68E+36	3.12E+35	1.58E+36
8	1.88E-39	1.19E-12	2.21E-28	$40.21^{+7.54}_{-6.45}$	$12.37^{+4.71}_{-3.56}$	$27.84^{+6.46}_{-5.35}$	6.21E+35	3.74E+34	3.25E+35
9	0.00E+00	6.44E-38	1.24E-16	$44.71^{+7.84}_{-6.76}$	$28.51^{+6.45}_{-5.35}$	$16.20^{+5.21}_{-4.08}$	1.22E+36	1.52E+35	3.34E+35
10	3.91E-18	8.90E-20	5.38E-03	$21.35^{+5.88}_{-4.76}$	$17.42^{+5.33}_{-4.20}$	$3.93^{+3.40}_{-2.16}$	7.29E+35	1.14E+35	1.03E+35

Notes. Columns (2)-(4) represent the *pns* values discussed in Section 2.3.4. Columns (5)-(7) are net counts with 90% uncertainty limits. Blank values correspond to undetermined uncertainties. Columns (8)-(10) give unabsorbed luminosities (derived from the *flux2* parameter in *AE*) in units of erg s^{-1}. Conversion factors were 3.94, 1.34, and 2.43 in units of $10^{41}\left(\frac{d}{776\,\mathrm{kpc}}\right)^2$ erg cm^2 photons^{-1} for the full, soft, and hard bands (to convert from photon flux in photons cm^{-2} s^{-1}). The conversion factors account for foreground absorption using an absorbed power-law spectrum with $\Gamma = 1.7$ and $N_H = 6.66 \times 10^{20}$ cm^{-2}. For some sources the soft or hard band had < 0 counts, and so uncertainties could not be determined and are represented as -99.99. By extension, some fluxes in the soft or hard band were < 0 and so luminosities appear as -9.99. Each source has a *pns* value $< 1 \times 10^{-2}$ in at least one energy band.
(This table is available in its entirety in Appendix B.)

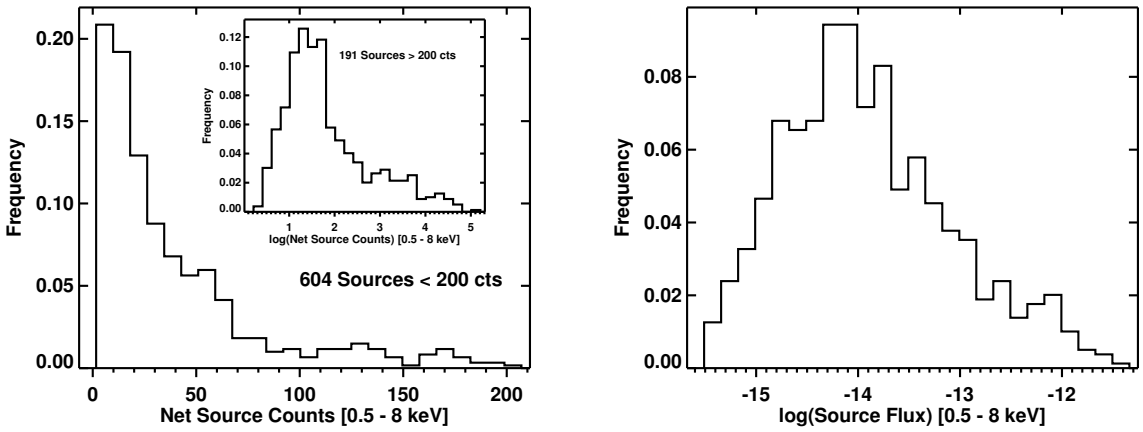

Figure 2.2: Histograms of the net source counts (left panel) and source flux (right panel) in the full energy band. The left panel shows sources with < 200 counts while the inset shows a histogram of all 795 sources. While the majority of sources have < 200 counts, the 191 sources (mostly in the nucleus) with $\gtrsim$200 counts are candidates for spectral modeling. In the right panel, the peak in the distribution is near our 90% detection limit of $\approx 5 \times 10^{-15}$ erg s^{-1} cm^{-2} (3×10^{35} erg s^{-1}).

2.4.2 Cross-Correlation With Existing Catalogues

Of the many previous studies in M31 summarized in Tables 2.1 - 2.2, not all actually publish a traditional X-ray catalogue. Approximately half the studies were focused on only one specific X-ray population. Our first comparisons are to the *XMM-Newton* catalogue (Stiele et al., 2011) because it is complete throughout M31 to a limiting luminosity of $\sim 10^{35}$ erg s^{-1}. Of the 1948 X-ray sources identified, only 979 appear within the field of view of our *Chandra* data. Figure 2.3 shows the deprojected radial distribution of X-ray sources in our catalogue (black) compared to those from the *XMM-Newton* survey (blue). Because our survey has sporadic coverage, only the nuclear region, where the exposure is significant, do we see a greater source density. Also, the subarcsecond resolution of *Chandra* allowed us to separate closely-spaced sources that *XMM-Newton* was unable to resolve due to its 5″ PSF.

We also matched our catalogue to the *XMM-Newton* catalogue using a matching radius of 5″, equivalent to *XMM-Newton*'s source positional uncertainty. We found that 352 *XMM-Newton* sources matched to 387 (49%) of our *Chandra* sources, where the 352 unique *Chandra*

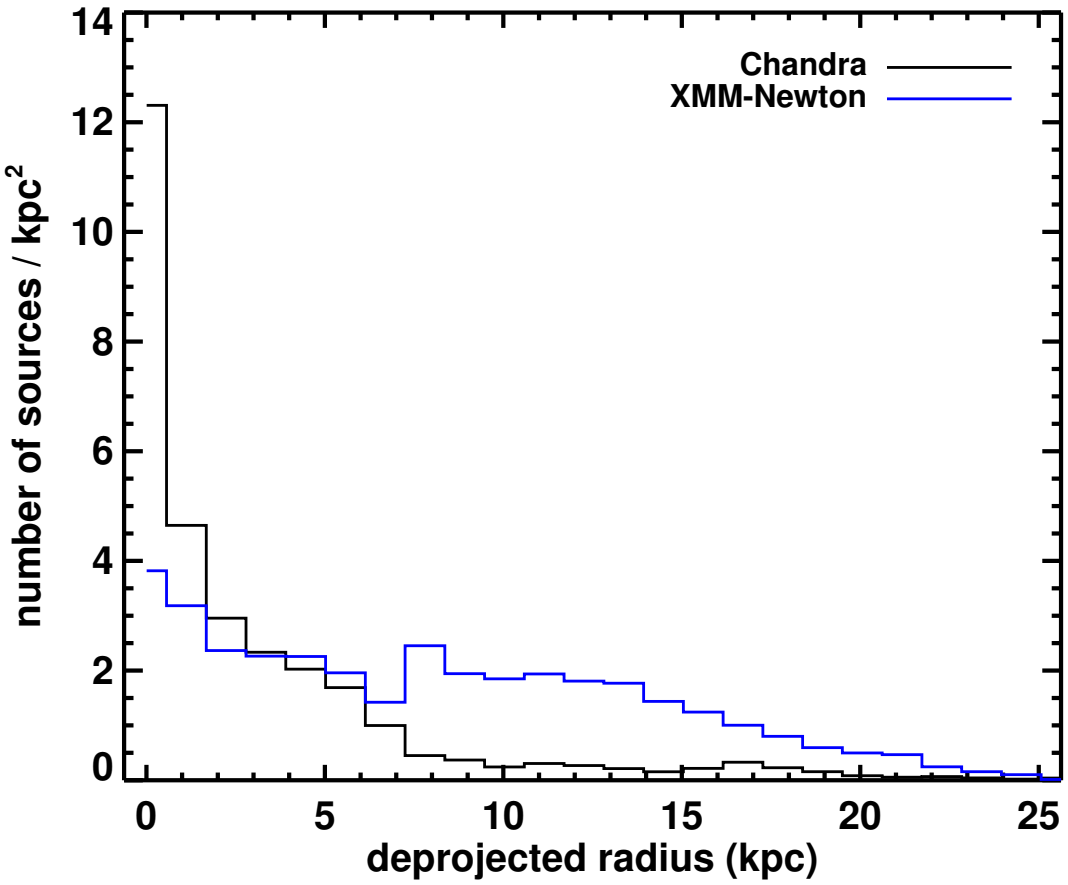

Figure 2.3: Deprojected radial source distribution of X-ray point sources in our catalogue (black) compared with those from the *XMM-Newton* survey (blue). Our *Chandra* sources drop off considerably around a few kpc because the coverage of our survey is sparse (see Figure 2.1). However, the deeper observations of the nucleus combined with the sub-arcsecond resolution of *Chandra* results in a $\sim$ 3-fold increase in the number of sources within the central kpc.

sources (closest matches) made up 44 per cent of our catalogue. Because the *XMM-Newton* PSF is much larger than *Chandra's*, multiple *Chandra* sources were matched to within 5″ of an *XMM-Newton* source. The median offset between matches was 1.08″. In Figure 2.4 we show the positional offset between the matches (left panel) and compare the average fluxes from both surveys (right panel). *Chandra* fluxes appeared systematically brighter, possibly a result of the *AE* flux estimate uncertainty mentioned in Section 2.4.1. In addition, since *Chandra* sources were observed more frequently over a longer time period, there is an increased probability that a source was detected in a brighter state (compared to *XMM-Newton*) that would dominate other flux measurements. To address the sources in the *XMM-Newton* catalogue that were not matched to our catalogue, we compiled a list of all the original input sources throughout all three fields (1399) and included an additional $\sim$ 5000 sources from a low-significance `wavdetect` run. Matching this list to the *XMM-Newton* catalogue within 5″ we find that 895 (91%) of *XMM-Newton* sources were matched. Therefore many sources can be identified as candidates in the *Chandra* observations but not 'detected' due to a low significance (e.g., shallow exposure, transience).

Our catalogue was also matched to within 1″ of previous *Chandra* catalogues of various X-ray sources. From the *Chandra* surveys in Table 2.2, a total of 1436 sources (some authors omitted sources from their catalogue if they were not new) were cross-matched with those from our catalogue. Among the past *Chandra* catalogues there is some redundancy as groups do not always exclude previously detected sources from their catalogue. Using this matching radius we find only 347 of our sources that matched to previously detected *Chandra* sources, with a median offset of 0.27″. 448 of our catalogue sources were detected for the first time from *Chandra* observations. When combining the unique matches from both *XMM-Newton* and previous *Chandra* surveys we find that 536 matched from our catalogue of 795 sources, meaning 259 of our X-ray sources were detected for the first time. These new sources have a factor of 2 smaller exposure times, a factor of three fewer counts and photon fluxes, a factor of six fewer observations per source, and *pns* values that are twelve orders of magnitude less

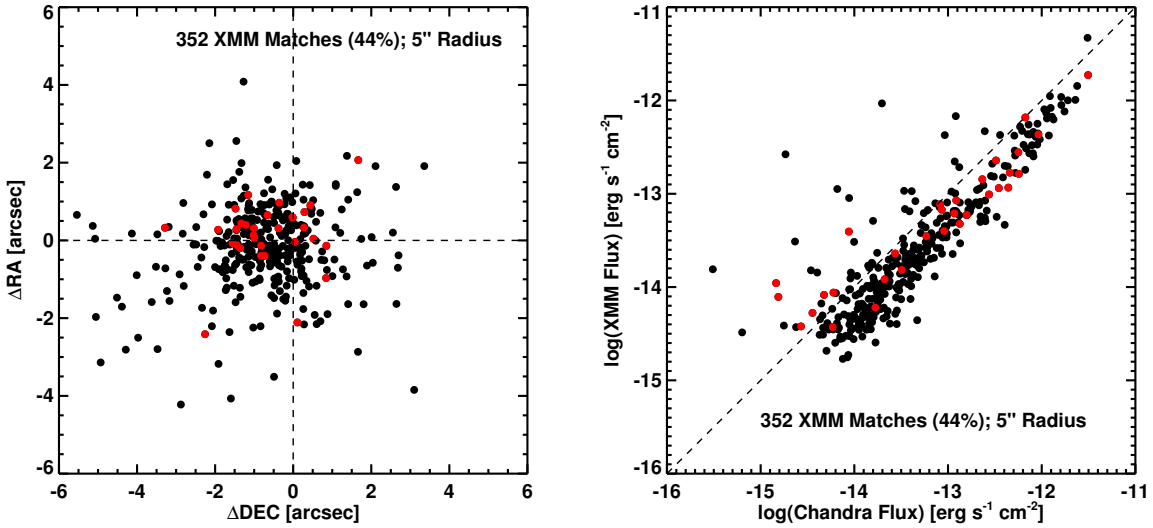

Figure 2.4: A comparison of the 352 (44 %) unique *Chandra* X-ray sources (a total of 387 (49%) were matched) detected in this work that were the closest matches to those from the *XMM-Newton* catalogue within 5″ (approximately the positional uncertainty associated with *XMM-Newton* sources). The left panel shows the approximate positional offset between the matches while the right panel compares the fluxes. The red circles represent *XMM-Newton* sources that were matched to multiple *Chandra* sources, where the values plotted came from the closest-matched source. *XMM-Newton* fluxes (0.2 – 4.5 keV) have been corrected to the *Chandra* energy range (0.5 – 8.0 keV) assuming the spectral model from Section 2.4.3. *Chandra* fluxes are generally brighter because many *Chandra* sources were observed multiple times over a longer time period, thus increasing the probability they would be detected in a bright state.

Table 2.8: Matching Results

	XMM-Newton	Previous *Chandra*	Total Matched	New sources
This work (795)	387 (352 unique)	347	536	259

A 5″ radius was used for matching to *XMM-Newton*, while a 1″ radius was used when matching to previous *Chandra* catalogues. 387 of our catalogue sources were matched to 352 *XMM-Newton* sources.

Table 2.9: Catalogue Cross-Matches

Source	CXOU J	*XMM-Newton* Match		*Chandra* Match		LMXB Match			AGN Match			
No.		ID	Classification	Catalogue	ID	Peacock et al.; GC	Stiele et al.; Field	Stiele et al.; GC	PHAT	SDSS DR12	NED	SIMBAD
(1)	(2)	(3)	(4)	(5)	(6)	(7)	(8)	(9)	(10)	(11)	(12)	(13)
1	004542.90+414312.6	1685	<hard>	-	-	-	-	-	-	-	-	-
2	004551.05+414452.4	-	-	-	-	-	-	-	-	-	-	-
3	004551.30+414220.7	-	-	-	-	-	-	-	3900	-	-	-
4	004552.93+414441.8	-	-	-	-	-	-	-	-	-	-	-
5	004555.72+414551.8	-	-	-	-	-	-	-	-	-	-	-
6	004556.82+414440.8	-	-	-	-	-	-	-	-	-	-	-
7	004556.99+414831.7	1716	<hard>	-	-	-	-	-	1938	-	-	-
8	004559.07+414113.0	-	-	-	-	-	-	-	-	-	-	-
9	004602.43+414515.7	1732	<SNR>	-	-	-	-	-	-	-	-	-
10	004602.70+413856.7	-	-	-	-	-	-	-	-	-	-	-

Notes. This table summarizes the details of the cross-match between our catalogue and various others. Columns (1) and (2) represent our catalogue. Columns (3) and (4) are the *XMM-Newton* catalogue identification number and classification. Column (5) is the *Chandra* catalogue matched to: BA (Barnard et al., 2014), DS02 (Di Stefano et al., 2002), DS04 (Di Stefano et al., 2004), HO (Hofmann et al., 2013), KA (Kaaret, 2002), KO (Kong et al., 2002), VO (Voss & Gilfanov, 2007), WI (Williams et al., 2004). Column (6) is the catalogue source identification value taken from each respective paper. Columns (7)-(9) represent matches to LMXBs from Peacock et al. (2010b) globular clusters (GC), and Stiele et al. (2011) field and globular clusters (GC), with the corresponding names or identification number. Columns (10)-(13) show the results of AGN matching to various catalogues. For PHAT, we used the Andromeda project identification number from Johnson et al. (2015). See Section 2.4.4 for more details on matching.
(This table is available in its entirety in Appendix C.)

significant, when compared to median values of the whole catalogue (e.g. $pns \approx 10^{-17}$). When compared to only the matched sources, these differences are exacerbated even more so. Matching results are shown in Table 2.8. The cross-match information between our catalogue and previous *XMM-Newton* and *Chandra* catalogues, including their identification numbers/values (where available), is shown in Table 2.9.

2.4.3 Sensitivity Curve

In order to create corrected XLFs (log$N$-log$S$) we had to evaluate the sensitivity of each point in the survey field, which gives the energy flux at which a source would be detected. Complications arise when attempting to compute sensitivity for overlapping observations/regions, which are prevalent in our survey field. In addition, the *CIAO* tools are not designed for this

type of analysis and also do not accommodate combining ACIS-I/S observations. Therefore we take a statistical approach and follow the method of Georgakakis et al. (2008) to determine the sensitivity throughout the survey field. The source extraction process in *AE* estimates the Poisson probability that the observed counts in the detection cell arise completely from random fluctuations of the background. The three parameters that define this process are the size and shape of the detection cell and the Poisson probability threshold P_{thresh} (*AE* value *pns*). The size and shape of the detection cell are defined by *AE* for each source based on the count distribution, source crowding, off-axis angle. By setting P_{thresh} to 1×10^{-2} for our analysis, which is the *AE* default value, we set the minimum number of photons required in a detection cell to be considered a source.

With the parameters of the source extraction process in hand, two additional data products are needed to proceed: an exposure map and a background map. The exposure map is the total exposure at any point in the field. We created 3 exposure maps from our existing data products for 3 separate regions of the M31 field: the northeast, bulge, and southwest. In the bulge, we merged the ACIS-I/S exposure maps using the *CIAO* tool `reproject_image` to reproject the maps to a common tangent plane and merge them. The background maps were required to be identical in size to the exposure maps and so we generated 3 maps for each of the regions as for the exposure maps.

The background map is an estimate of the source-free background across the different regions in the survey. We started by using the merged counts images in each region (created in the same manner as the merged exposure maps). We removed the counts in the vicinity of detected sources using an aperture 1.5 times larger than the 90 per cent enclosed PSF radius (obtained from *AE*). These pixel values were replaced by the background values calculated by *AE* for each source. We now had an image in units of counts where we have removed the contribution from all detected sources. However, the background map should have units of counts pixel^{-1} so that every pixel in the survey field has a background value associated with it. This was required for us to estimate the sensitivity at each pixel. Such an image is created by using

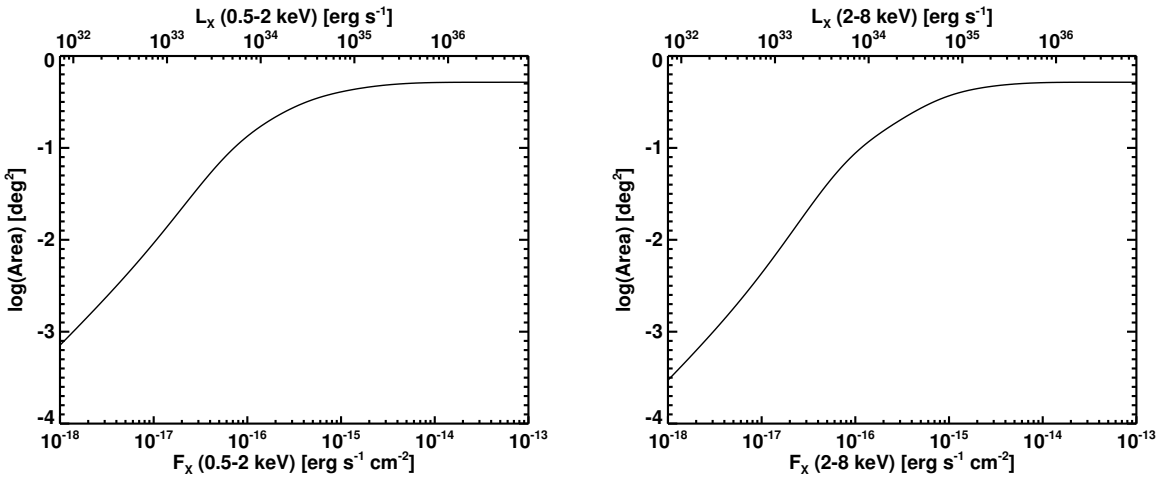

Figure 2.5: Sensitivity curves in the soft and hard energy bands for the complete *Chandra* survey area in M31. Sensitivity for the various overlapping observations and different fields was calculated using the method of Georgakakis et al. (2008). Unabsorbed fluxes and luminosities are shown assuming an absorbed power-law spectrum with $\Gamma = 1.7$ and $N_H = 6.66 \times 10^{20}$ cm^{-2} (see Section 2.4.3 for more details).

the *CIAO* tool `dmimgpm`, which calculates a modified Poissonian mean for each pixel using a box of width 64″ as the sampling region around that pixel.

Using the background map values we estimated the minimum number of counts required in each pixel for a detection (above our threshold P_{thresh}) with the inverse survival function (Python version 2.7.8; scipy.stats.poisson module version 0.14.0). We then estimated the mean expected number of counts ($T = S + B$) that would be produced at each pixel for a range of fluxes. B is the background value of the pixel and S is the mean expected source contribution (equation (5) of Georgakakis et al. 2008). Finally, we estimated the probability that a given flux would produce the mean expected number of counts above the minimum counts required for a detection in each pixel using the survival function (python scipy.stats.poisson module). To correct our log$N$-log$S$ relations to represent the number of sources at a given flux per deg^{-2} we created an area curve. This was accomplished by summing the probabilities for each pixel at a given flux to obtain the total area, which when done for the various flux values in the soft and hard energy bands gave the area curves shown in Figure 2.5.

As in Stiele et al. (2011), we assumed an absorbed power-law spectrum with $\Gamma = 1.7$ and

chose $N_H = 6.66 \times 10^{20}$ cm^{-2} (Dickey & Lockman, 1990), which was the weighted average for a 1 degree radius cone around the M31 nucleus. This model matches what we expect from XRBs and background AGN in M31. As Tüllmann et al. (2011) point out, the model fails for extremely hard (soft) sources by overestimating (underestimating) the flux, but does not bias the log$N$-log$S$ relation to systematically higher or lower fluxes. In addition, most of the previous M31 surveys have used the same Γ value and a similar Galactic foreground absorption, therefore making comparisons more accurate.

2.4.4 The log$N$-log$S$ Relation and X-ray Luminosity Functions

The log$N$-log$S$ relation is calculated by determining the cumulative number of sources $N(> S)$ above a given flux S (in erg s^{-1} cm^{-2}) that are found in a survey with a total geometric area A:

$$N(> S) = \sum_{S_i > S} \frac{1}{A(S_i)} \tag{2.1}$$

The value $N(> S)$ has units of sources deg^{-2} and is weighted by the survey area over which a source with flux S could have been detected. We constructed log$N$-log$S$ distributions for the soft (0.5 − 2.0 keV) and hard (2.0 − 8.0 keV) bands using all 795 sources in our catalogue with calculated fluxes in the given band. These XLFs are shown in Figure 2.6. We show both the uncorrected (grey) and completeness-corrected (black) data, which indicates the level of completeness of our survey in each band at the turnover of the grey curve, similar to the values in Table 2.5. We calculated 1σ uncertainties for our XLFs using Poisson statistics (Gehrels, 1986). We have only accounted for foreground (Galactic) extinction in computing our fluxes and therefore any internal extinction in M31 would push our curves right towards brighter fluxes. We also plot the expected contribution from AGN using the distribution of AGN from the 4 Ms *Chandra* Deep-Field South (CDF-S) survey (Lehmer et al., 2012). The curve is shown in red with corresponding uncertainties. As expected, the hard-band XLF shows a significant contribution from expected AGN across the entire flux range. Near the 95 per cent

completeness limit of 3.29×10^{35} erg s^{-1}, the AGN contribution overtakes the corrected curve, possibly a result of cosmic variance from the CDF-S survey.

In Figure 2.7 we plot the AGN-subtracted completeness-corrected curve (blue) to represent the X-ray sources that belong to M31. We matched our detected X-ray sources in each band to a catalogue of LMXBs in M31 to within 1″. The catalogue consisted of 26 confirmed globular cluster X-ray sources and 10 confirmed field LMXBs from Stiele et al. (2011), along with 45 confirmed LMXBs from Peacock et al. (2010b). The XLF of known LMXBs is shown in gold. We cannot produce an XLF curve for HMXBs because none have been confirmed in M31. We also used several catalogues of background galaxies/AGN to match to our X-ray point sources within 1″. These catalogues include the 2270 background galaxies from the PHAT survey (Johnson et al., 2015), 1870 background quasars identified with the LAMOST survey (Huo et al., 2010, 2013, 2015), and radial searches of 2 degrees around the M31 centre in NED, SIMBAD, and SDSS DR12. The known AGN are represented by the purple curve in Figure 2.6. In Table 2.6 we have indicated if one of our catalogue sources was matched to an AGN or LMXB. We have also added the detailed cross-match information with the various AGN/LMXB catalogue identifications (where available) to Table 2.9. In both energy bands, the brightest sources have a significant contribution from LMXBs, whereas the known AGN are only identified for fainter fluxes. Similarly, the break in the XLFs is observed at $\approx 1.3 \times 10^{37}$ erg s^{-1}. Stiele et al. (2011) found that $\sim$ 65 per cent of sources in M31 have no confirmed optical counterparts, which is reflected in the lack of known LMXB/AGN sources. The gap in the AGN-subtracted completeness-corrected curve (blue) in the hard band is likely due to cosmic variance biasing the results from the CDF-S (our 95% completeness limit is also located in this region).

In addition to our XLFs for all our sources, we also divided our sample to study the bulge and disk fields in M31. In Figure 2.8, we show the soft and hard band XLFs for these regions. Courteau et al. (2011) found that the M31 bulge light dominates for $R_{min} \lesssim 1.2$kpc, which represents the projected minor axis radius. The disk dominates in the range 1.2 kpc $< R_{min} <$

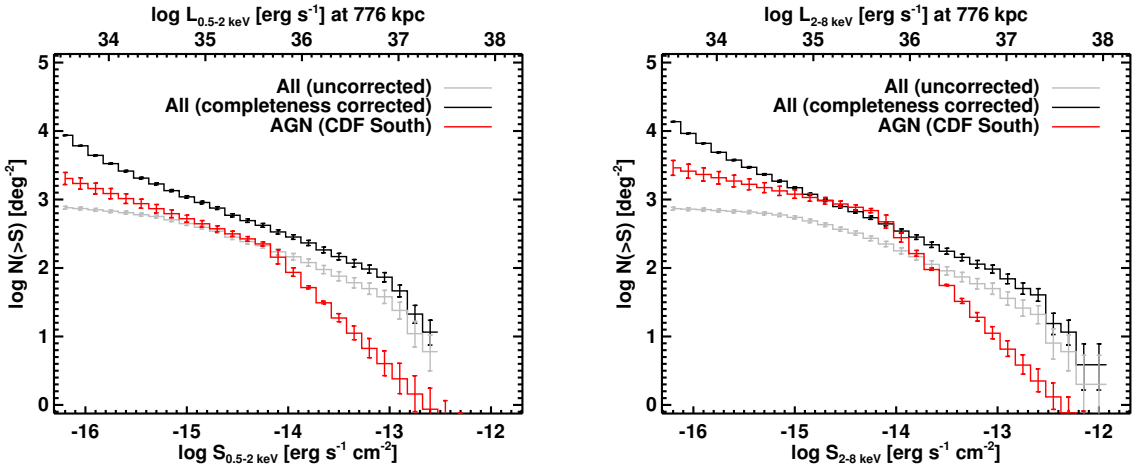

Figure 2.6: Cumulative number counts for the soft and hard energy bands. Both uncorrected (grey) and completeness-corrected curves (black) are plotted using all X-ray point sources with calculated fluxes in the given energy band from our catalogue. All uncertainties are 1σ (Gehrels, 1986). The AGN number counts from the 4 Ms *Chandra* Deep-Field South survey (Lehmer et al., 2012) are shown in red with their corresponding uncertainties. The red curve overtakes the black curve around the 95% completeness limit in the hard band, indicating that the majority of sources near this flux are AGN. The flattening observed begins at $\approx 1.3 \times 10^{37}$ erg s^{-1} and is consistent with previous results from M31 (Kong et al., 2002).

9 kpc, and the halo beyond that. We include the disk+halo curve in our XLF ($R_{min} > 1.2$ kpc) because there is no change in the XLF when excluding the halo sources as defined in Courteau et al. (2011). In the soft band, the bulge has a larger number of brighter sources (although this may be biased due to the incompleteness of disk data), which is unexpected for an older stellar population. In the hard band, the disk+halo harbours the brightest sources but again the bulge has a larger cumulative number of bright sources above the break at $\approx 1.3 \times 10^{37}$ erg s^{-1}. The flatter bulge XLFs in both bands are consistent with previous results from M31 (e.g. Kong et al., 2002; Williams et al., 2004). The M31 XLF is different from other galaxies (e.g. Colbert et al., 2004; Binder et al., 2012) in that the older stellar population in the bulge has a flatter slope than the younger stellar population in the disk. The lack of bright sources and steeper XLF in the disk indicates that star formation in the disk is low, and thus any HMXBs would be faint (likely a reason none have yet been confirmed). Using *XMM-Newton*, Trudolyubov et al. (2002) analysed the bulge and two northeast fields and found the disk and bulge XLFs to

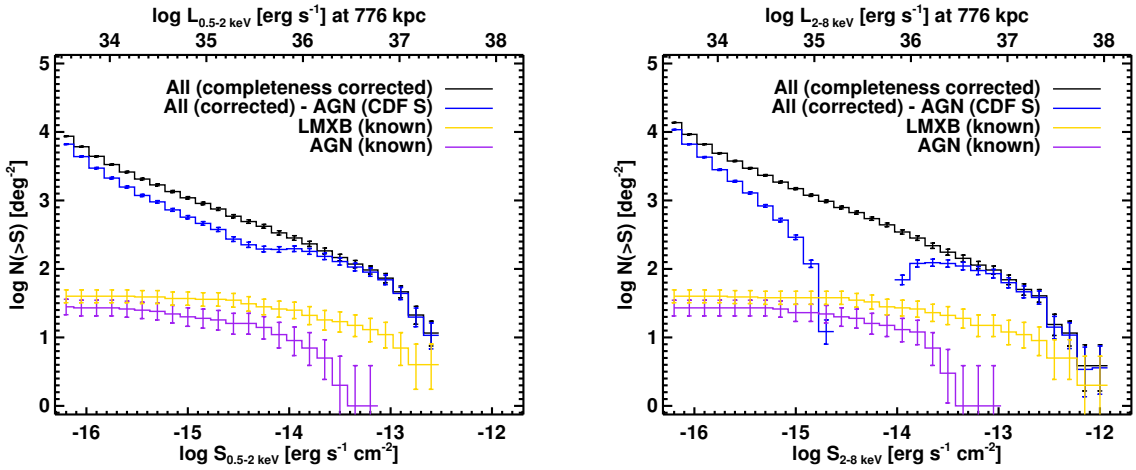

Figure 2.7: Cumulative number counts for the soft and hard energy bands. The completeness-corrected curve (black) is plotted using all 795 X-ray point sources from our catalogue. Known LMXBs have been matched to within 1″ of our point sources and their XLF is shown in gold. We also used various observational catalogues of known AGN and background galaxies to match within 1″ of our point sources, with their XLF shown in purple. The blue curve shows our completeness-corrected curve after subtracting the contribution from AGN CDF-S (red curve from Figure 2.6). All uncertainties are 1σ (Gehrels, 1986). As Stiele et al. (2011) pointed out, many sources in M31 have no confirmed optical counterparts; this is reflected in the lack of known sources. Additionally, the gap in the blue curve in the hard band is likely due to cosmic variance biasing the results from the CDF-S (our 95% completeness limit is also located in this region).

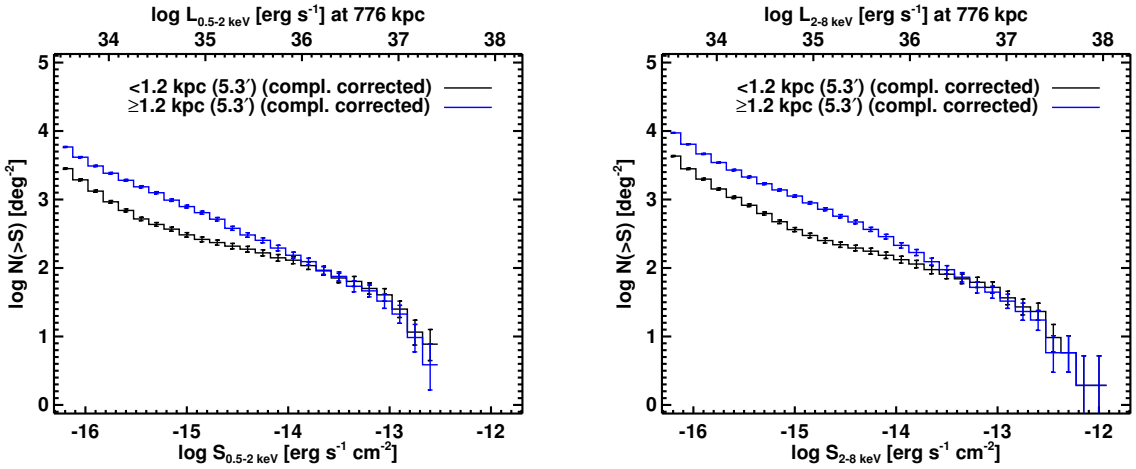

Figure 2.8: Cumulative number counts for the soft and hard energy bands in the bulge (black) and disk+halo (blue) fields of M31. The completeness-corrected curves have uncertainties of 1σ (Gehrels, 1986). The bulge and disk+halo populations were separated using projected radii based on the results of Courteau et al. (2011). In the soft band, the bulge has a larger number of brighter sources (although this may be biased due to the incompleteness of disk data), which is unexpected for an older stellar population. However, both curves are similar within uncertainties near the bright-end. In the hard band the disk+halo harbours the brightest sources but again the bulge has a larger cumulative number of bright sources above the break at $\approx 1.3 \times 10^{37}$ erg s^{-1}. The flatter bulge XLFs in both bands are consistent with previous studies.

have a similar slope, but using a 15′ radius for the bulge. They did find that disk sources are all fainter than 2×10^{37} erg s^{-1}, while bulge sources were brighter.

XLF's have been produced for the M31 X-ray population in a number of different *Chandra* surveys. Kong et al. (2002) found 204 sources in the bulge to a detection limit of 10^{35} erg s^{-1} (no mention of a completeness limit), whereas we have about a factor of ~ 1.5 more at the same limit in the full band (uncorrected). However, they do not correct for completeness so a direct comparison is difficult, particularly since the total areas vary. Kong et al. (2002) also found that the flattening of the XLF below 10^{36} erg s^{-1} in the inner bulge (2′ by 2′) was intrinsic and not due to the incompleteness of their survey. The same flattening is seen in our XLFs albeit at a higher flux, beginning at $\approx 1.3 \times 10^{37}$ erg s^{-1}, after correcting for completeness. The discrepancy arises from the different definition for bulge, where ours was much larger (5.3′ radius). Kong et al. (2003) extended their own work to three disc fields in M31, and when combining this with their data from the bulge they recovered ~ 200 sources at a completeness

limit of 10^{36} erg s^{-1}. We have 315 sources (uncorrected XLF) at this level, but it is again difficult to compare values since their XLF is not completeness-corrected. They also found that the bulge (central 17′ square) XLF was flatter than the disk fields they surveyed. The sources in the bulge were more luminous than the outer disk fields only when removing globular cluster X-ray sources from disk fields. Williams et al. (2004) detected 85 sources above 4×10^{36} erg s^{-1}, while we detected twice as many above the same limit. They also found that the disk XLF was steeper than the bulge with a power law slope comparable to typical elliptical galaxies. We detected a larger number of sources due to variations in sensitivity, coverage (M31 X-ray source density varies with radius), and source extraction parameters. While these factors all contributed to some degree, the transient nature of X-ray sources, specifically binary systems, is the primary reason for such a discrepancy. This was demonstrated by the matching results from Section 2.4.2, where 627 and 408 *XMM-Newton* and *Chandra* sources respectively were unmatched in the same field of view. Sensitivity is a factor, however, since *XMM-Newton* and *Chandra* surveys did not have equal exposure throughout, and *Chandra* is generally more sensitive.

Our XLFs are the deepest in terms of luminosity produced for any large galaxy based on our detection limits. The AGN contribution from the CDF South dominates the hard band XLF as expected, whereas a larger proportion of sources in the soft band are representative of M31 X-ray sources (e.g. LMXBs, supernova remnants). Based on the distribution of AGN from the CDF-S, the M31 contribution observed from various catalogues is incomplete below 5×10^{-13} erg s^{-1} cm^{-2} in the hard band. The PHAT survey has identified many AGN by-eye using crowd-sourcing and criteria that led to a minimal number of misclassifications (Section 3 of Johnson et al. 2015). However, the field of view of these AGN did not overlap well with the *Chandra* data in this catalogue. As in the Milky Way, M31 has only a handful of very bright X-ray sources (mostly in globular clusters), and none above $\approx 10^{38}$ erg s^{-1}. Due to M31's low star formation rate, very few bright HMXBs would be expected, and to date only ~ 20 candidates have been identified.

2.5 Summary

We have used 133 publicly available *Chandra* ACIS-I/S observations totalling $\sim$ 1 Ms to create the deepest X-ray point source catalogue of M31. We detected 795 X-ray sources within our field of view (0.6 deg^2) to a limiting unabsorbed 0.5 – 8.0 keV luminosity of $\sim 10^{34}$ erg s^{-1}. Our 90% (0.3 – 8.0 keV) completeness limit is 4×10^{35} erg s^{-1}. We detected 728, 42, and 25 sources in the bulge, northeast, and southwest fields of M31 respectively. In the bulge fields, X-ray fluxes are closer to average values because they are calculated from many observations over a long period of time. Similarly, our catalogue is more complete in the bulge fields since monitoring allows more transient sources to be detected. Cross-correlating our catalogue with a previous *XMM-Newton* catalogue of 1948 X-ray sources, with only 979 within the field of view of our survey area, we found 387 (49%) of our *Chandra* sources (352 or 44% were unique sources) matched to within 5″ of 352 *XMM-Newton* sources with a median offset of 1.08″. Similarly, we matched our catalogue to a master list of 1436 previously published *Chandra* sources in M31 and found 347 of our sources within 1″. Collating the matching results from all catalogues we found 259 new sources in our catalogue. We also created XLFs in the soft and hard bands that are the deepest for any large galaxy based on our detection limits. Using published catalogues of AGN and LMXBs we determined the contribution to the XLF from these populations. The observationally identified AGN in M31 are incomplete below $\sim 10^{-13}$ erg s^{-1} cm^{-2} (hard band) based on data from the *Chandra* Deep Field South. The completeness-corrected XLFs show a break at $\approx 1.3 \times 10^{37}$ erg s^{-1}, which is consistent with previous work in M31. We found that the bulge XLFs are flatter compared to the disk, consistent with other studies. This indicates a lack of bright high-mass X-ray binaries in the disk due to a low star formation rate and an aging population of low-mass X-ray binaries in the bulge. This catalogue is more robust and complete than the latest *Chandra* source catalogue release due to the stringent processing and requirements we have placed on source detection. In addition, we have published a much more detailed set of source characteristics using *ACIS Extract*.

Impending *Chandra* and *NuSTAR* X-ray surveys in M31 will cover new regions of the galaxy (e.g. PHAT field) that have only been observed by *XMM-Newton*. This will result in high spatial resolution $0.3 - 30$ keV data that will be crucial for classifying and characterising the X-ray source population.

Bibliography

Barnard, R., Galache, J. L., Garcia, M. R., et al. 2012a, ApJ, 756, 32

Barnard, R., Garcia, M., & Murray, S. S. 2012b, ApJ, 757, 40

Barnard, R., Garcia, M. R., & Murray, S. S. 2013, ApJ, 770, 148

Barnard, R., Garcia, M. R., Primini, F., et al. 2014, ApJ, 780, 83

Binder, B., Williams, B. F., Eracleous, M., et al. 2012, ApJ, 758, 15

Broos, P. S., Townsley, L. K., Feigelson, E. D., et al. 2010, ApJ, 714, 1582

—. 2011, ApJS, 194, 2

Colbert, E. J. M., Heckman, T. M., Ptak, A. F., Strickland, D. K., & Weaver, K. A. 2004, ApJ, 602, 231

Courteau, S., Widrow, L. M., McDonald, M., et al. 2011, ApJ, 739, 20

Dalcanton, J. J., Williams, B. F., Lang, D., et al. 2012, ApJS, 200, 18

Di Stefano, R., Kong, A. K. H., Garcia, M. R., et al. 2002, ApJ, 570, 618

Di Stefano, R., Kong, A. K. H., Greiner, J., et al. 2004, ApJ, 610, 247

Dickey, J. M., & Lockman, F. J. 1990, ARA&A, 28, 215

Fruscione, A., McDowell, J. C., Allen, G. E., et al. 2006, in Society of Photo-Optical Instrumentation Engineers (SPIE) Conference Series, Vol. 6270, CIAO: Chandra's data analysis system

Gehrels, N. 1986, ApJ, 303, 336

Georgakakis, A., Nandra, K., Laird, E. S., Aird, J., & Trichas, M. 2008, MNRAS, 388, 1205

Gordon, K. D., Bailin, J., Engelbracht, C. W., et al. 2006, ApJ, 638, L87

Graessle, D. E., Evans, I. N., Glotfelty, K., et al. 2006, in Society of Photo-Optical Instrumentation Engineers (SPIE) Conference Series, Vol. 6270, The Chandra X-ray Observatory calibration database (CalDB): building, planning, and improving

Henze, M., Pietsch, W., Haberl, F., et al. 2014, A&A, 563, A2

Hofmann, F., Pietsch, W., Henze, M., et al. 2013, A&A, 555, A65

Huo, Z.-Y., Liu, X.-W., Yuan, H.-B., et al. 2010, Research in Astronomy and Astrophysics, 10, 612

Huo, Z.-Y., Liu, X.-W., Xiang, M.-S., et al. 2013, AJ, 145, 159

—. 2015, Research in Astronomy and Astrophysics, 15, 1438

Johnson, L. C., Seth, A. C., Dalcanton, J. J., et al. 2015, ApJ, 802, 127

Kaaret, P. 2002, ApJ, 578, 114

Kahabka, P. 1999, A&A, 344, 459

Kong, A. K. H., DiStefano, R., Garcia, M. R., & Greiner, J. 2003, ApJ, 585, 298

Kong, A. K. H., Garcia, M. R., Primini, F. A., et al. 2002, ApJ, 577, 738

Lehmer, B. D., Xue, Y. Q., Brandt, W. N., et al. 2012, ApJ, 752, 46

Peacock, M. B., Maccarone, T. J., Knigge, C., et al. 2010a, VizieR Online Data Catalog, 740, 20803

Peacock, M. B., Maccarone, T. J., Kundu, A., & Zepf, S. E. 2010b, MNRAS, 407, 2611

Pietsch, W., Fliri, J., Freyberg, M. J., et al. 2005, A&A, 442, 879

Pietsch, W., Haberl, F., Sala, G., et al. 2007, A&A, 465, 375

Primini, F. A., Forman, W., & Jones, C. 1993, ApJ, 410, 615

Shaw Greening, L., Barnard, R., Kolb, U., Tonkin, C., & Osborne, J. P. 2009, A&A, 495, 733

Skrutskie, M. F., Cutri, R. M., Stiening, R., et al. 2006, AJ, 131, 1163

Stetson, P. B. 1987, PASP, 99, 191

Stiele, H., Pietsch, W., Haberl, F., et al. 2011, A&A, 534, A55

Supper, R., Hasinger, G., Lewin, W. H. G., et al. 2001, A&A, 373, 63

Supper, R., Hasinger, G., Pietsch, W., et al. 1997, A&A, 317, 328

Trinchieri, G., & Fabbiano, G. 1991, ApJ, 382, 82

Trudolyubov, S., & Priedhorsky, W. 2004, ApJ, 616, 821

Trudolyubov, S. P., Borozdin, K. N., Priedhorsky, W. C., Mason, K. O., & Cordova, F. A. 2002, ApJ, 571, L17

Tüllmann, R., Gaetz, T. J., Plucinsky, P. P., et al. 2011, ApJS, 193, 31

Voss, R., & Gilfanov, M. 2007, A&A, 468, 49

Williams, B. F., Garcia, M. R., Kong, A. K. H., et al. 2004, ApJ, 609, 735

Williams, B. F., Lang, D., Dalcanton, J. J., et al. 2014, ApJS, 215, 9

Zacharias, N., Monet, D. G., Levine, S. E., et al. 2005, VizieR Online Data Catalog, 1297, 0

Chapter 3

Faint X-Ray Binaries and Their Optical Counterparts in M31

3.1 Executive Summary

X-ray binaries (XRBs) are probes of both star formation and stellar mass, but more importantly remain one of the only direct tracers of the compact object population. To investigate the XRB population in M31, we utilized all 121 publicly available observations of M31 totalling over 1 Ms from *Chandra's* ACIS instrument. We studied 83 star clusters in the bulge using the year 1 star cluster catalogue from the Panchromatic Hubble Andromeda Treasury Survey. We found 15 unique star clusters that matched to 17 X-ray point sources within 1″ (3.8 pc). This population is composed predominantly of globular cluster low-mass XRBs, with one previously unidentified star cluster X-ray source. Star clusters that were brighter and more compact preferentially hosted an X-ray source. Specifically, logistic regression showed that the F475W magnitude was the most important predictor followed by the effective radius, while color (F475W−F814W) was not statistically significant. We also completed a matching analysis of 1566 H II regions and found 10 unique matches to 9 X-ray point sources within 3″ (11 pc). The H II regions hosting X-ray point sources were on average more compact than

unmatched H II regions, but logistic regression concluded that neither the radius nor Hα luminosity was a significant predictor. Four matches have no previous classification and thus are high-mass XRB candidates. A stacking analysis of both star clusters and H II regions resulted in non-detections, giving typical upper limits of $\approx 10^{32}$ erg s^{-1}, which probes the quiescent XRB regime.

3.2 Introduction

Compact objects are the end-states of the evolution of massive stars and as such are signposts of the star formation history of a galaxy. X-ray binaries (XRBs) consist of a compact object, either a neutron star or black hole, which accretes matter from a companion star. Active XRBs have luminosities of $\sim 10^{35-41}$ erg s^{-1} (those $>10^{39}$ erg s^{-1} are classified as ultra-luminous X-ray sources) while those in quiescence are $\lesssim 10^{34}$ erg s^{-1}. XRBs are classified into two main categories based on the mass of the companion star: low-mass (LMXB) and high-mass (HMXB) (Fabbiano, 2006). LMXBs accrete matter via Roche lobe overflow while HMXBs transfer mass predominantly by Bondi-Hoyle (wind) accretion (Bondi & Hoyle, 1944; Iben et al., 1995). LMXB formation is more efficient in globular clusters (GCs) than in the field of a galaxy due to the higher stellar densities in GCs (Katz, 1975; Clark, 1975; Fabian et al., 1975; Pooley et al., 2003). In the Milky Way, LMXB formation is approximately two orders of magnitude more efficient in GCs (Katz, 1975; Clark, 1975). Conversely, HMXBs are associated with star-forming regions (OB associations, H II regions, and infrared-bright dusty regions) as opposed to star clusters (Ranalli et al., 2003; Grimm et al., 2003; Swartz et al., 2004; Persic & Rephaeli, 2007; Shtykovskiy & Gilfanov, 2007; Lehmer et al., 2010; Walton et al., 2011; Swartz et al., 2011; Mineo et al., 2012a). Due to their evolutionary timescales, LMXBs trace the stellar mass of a galaxy (Gilfanov, 2004; Kim & Fabbiano, 2004; Zhang et al., 2011) while HMXBs probe the star formation rate (Grimm et al., 2003; Mineo et al., 2012a) within the past $\sim$100 Myr (Shtykovskiy & Gilfanov, 2007).

The Milky Way's XRBs have been studied extensively in the Galactic Center, star clusters, and the field (e.g. Grimm et al., 2002; Revnivtsev et al., 2008; Muno et al., 2009; Bodaghee et al., 2012; Lutovinov et al., 2013; Nebot Gómez-Morán et al., 2013). Faint X-ray sources (quiescent XRBs, cataclysmic variables, millisecond pulsars, etc.) in the Milky Way have been studied to 10^{30} erg s^{-1} and lower (Heinke et al., 2003; Sazonov et al., 2006; Heinke et al., 2006) as a result of *Chandra's* subarcsecond resolution and optical counterpart identifications with the *Hubble Space Telescope* (*HST*). Due to dust obscuration, we can only probe X-ray sources in the plane of the disk out to ≈8 kpc from the Solar System. This hinders our ability to obtain a complete sample of the Galaxy's XRB population. Fortunately, M31 provides a convenient nearby analogue that allows us to perform an analysis of the faint X-ray population in a large galaxy.

M31's XRB population has been studied numerous times over the past decades with various X-ray telescopes (*X-ray Multi-Mirror Mission* (*XMM-Newton*), *Röntgensatellit* (*ROSAT*), *Einstein*). However, only the spatial resolution of *Chandra* allows us to study low-luminosity X-ray sources by separating them from the diffuse emission in the disk and crowding in the bulge. The LMXBs in M31 have been extensively studied by various groups (Trudolyubov & Priedhorsky, 2004; Voss & Gilfanov, 2007a,b; Peacock et al., 2010b; Zhang et al., 2011; Barnard et al., 2012b,a, 2013) that report on X-ray luminosity functions, spatial distributions, variability, and spectral analysis. Peacock et al. (2010b) used *XMM-Newton* to study 80% of the 416 confirmed GCs in M31 (Peacock et al., 2010a). They found 41 GCs associated with X-ray sources along with an additional 4 GCs identified with *Chandra* and *ROSAT*, for a total of 11% of GCs with X-ray sources. M31's GCs with LMXBs were found to be brighter, redder (metal-rich), and more compact than GCs without LMXBs, in agreement with other extragalactic XRB studies (Sivakoff et al., 2007; Paolillo et al., 2011; Mineo et al., 2014). Voss & Gilfanov (2007b) predicted a large number of faint transient sources in the bulge of M31, similar to the numerous faint X-ray sources (accreting millisecond pulsars) found in the Galactic Center (Muno et al., 2009).

A recent study by Stiele et al. (2011) with *XMM-Newton* covered all of M31 for the first time and reported on the X-ray source population compared to all previous studies. The survey catalogued 1897 point sources (914 new) and reached a limit of $\sim 10^{35}$ erg s^{-1} in the 0.2 – 4.5 keV energy band. Sources were classified/identified by X-ray hardness ratios, spatial extent and distribution, cross-correlations in other wavelengths, and variability (using *Chandra* and *ROSAT* observations). They found 10 field LMXBs and 26 field LMXB candidates by analyzing long-term X-ray source variability. In addition, another 36 LMXBs were associated with GCs and 17 LMXB candidates were associated with GC candidates. No HMXBs were identified - in fact none have been confirmed in M31 to date - although 2 new candidates were proposed in addition to the 18 candidates from Shaw Greening et al. (2009). The comprehensive X-ray population analysis by Stiele et al. (2011) has classified hundreds of sources and shed light on their long-term variability and spatial/flux distributions. However, they pointed out that ∼65% of their point sources are classified as "hard", meaning that they have no optical identification and their X-ray colors are ambiguous: they could be XRBs, supernova remnants, or background active galaxies.

Barnard et al. (2014) have attempted to address the issue of unclassified X-ray point sources by identifying them using X-ray data alone. They used structure functions, which estimate the mean intensity deviation of data over a time interval. By determining structure functions for each source they constrained its variability and were able to differentiate XRBs from active galactic nuclei. They found 220 X-ray sources above $\gtrsim 10^{35}$ erg s^{-1} with significantly more variability than expected in the structure function for active galactic nuclei. Based on their analysis they classified these sources as XRBs, with an additional 30 XRB sources for a total of 250 probable XRBs (200 new) out of their sample of 528 X-ray sources in the central 20′ of M31. Low-luminosity XRBs are more variable than luminous XRBs and thus are well-suited to this classification technique given sufficient signal-to-noise data.

One of the most powerful methods to confidently classify an X-ray source is identifying an optical counterpart. However, in crowded and extragalactic fields this generally requires the

exquisite spatial resolution of *HST*. The ability to observe a large fraction of identified X-ray sources is limited since *HST* has both high demand and a small field of view. The Panchromatic *Hubble* Andromeda Treasury (PHAT) survey is a multicycle *HST* program to map one-third of M31's disk and provide an unprecedented catalogue of star clusters and stars (Dalcanton et al., 2012). While it does not cover all of M31, it provides the best possible resource for determining optical counterparts to X-ray sources on such a large scale. M31's bulge has been monitored extensively with *Chandra*, whose 0.5″ point spread function (PSF) is superior to the 6″ provided by *XMM-Newton*.

To probe low-luminosity X-ray sources in M31 below the level achieved by Stiele et al. (2011), we will use the stacking method developed by Brandt et al. (2001c,a) and Hornschemeier et al. (2001). By stacking star cluster positions obtained from the PHAT survey and H II region positions (see Section 3.3.2) in a *Chandra* X-ray image of M31, we can determine, on average, if these objects host faint point sources. Young star clusters and H II regions will probe the HMXB population while GCs will probe the LMXBs. Our study is not focused on the field population of XRBs. Stacking analyses enable us to study the effect that metallicity has on faint X-ray sources by separating metal-rich and metal-poor classes of GCs. Stacking is a unique way to investigate whether HMXBs in M31 exist but are below our current detection limits. By pushing extragalactic XRB luminosities into the quiescent regime ($<10^{34}$ erg s^{-1}), we can reveal undetected populations that will help constrain binary evolution models (e.g. Hurley et al., 2002; Kiel & Hurley, 2006; Belczynski et al., 2008; Lipunov et al., 2009; Bhadkamkar & Ghosh, 2012, 2013; Siess et al., 2013; Bhadkamkar & Ghosh, 2014).

We adopt a distance to M31 of 776 ± 18 kpc as in Johnson et al. (2012, hereafter J12), which corresponds to a linear scale of 3.8 pc arcsecond^{-1}. In Section 3.3, we describe the optical and X-ray observations and reduction procedure for the X-ray data. In Section 3.4, we report results from matching star clusters and H II regions to X-ray point sources. In Section 3.5, we present results from an X-ray stacking analysis of star clusters and H II regions. In Sections 3.6 and 3.7 we discuss our results and summarize our main conclusions.

3.3 Observations

3.3.1 X-ray Data

Chandra has observed M31 numerous times, but the small field of view (compared to *XMM-Newton*) of *Chandra's* Advanced CCD Imaging Spectrometer (ACIS) instrument ($8' \times 8'$ for ACIS-S and $16' \times 16'$ for ACIS-I) combined with the proximity of M31 require many pointings to cover an appreciable area of the galaxy. We used 121 publicly available ACIS-S and ACIS-I observations in M31 for our matching and stacking analyses of star clusters and H II regions, having a total exposure time over 1 Ms. Due to the degradation of the PSF at large off-axis angles, we only use data from the S3 chip from the ACIS-S observations. The observations are listed in Tables 3.1 and 3.2 and their fields of view shown in Figure 3.1.

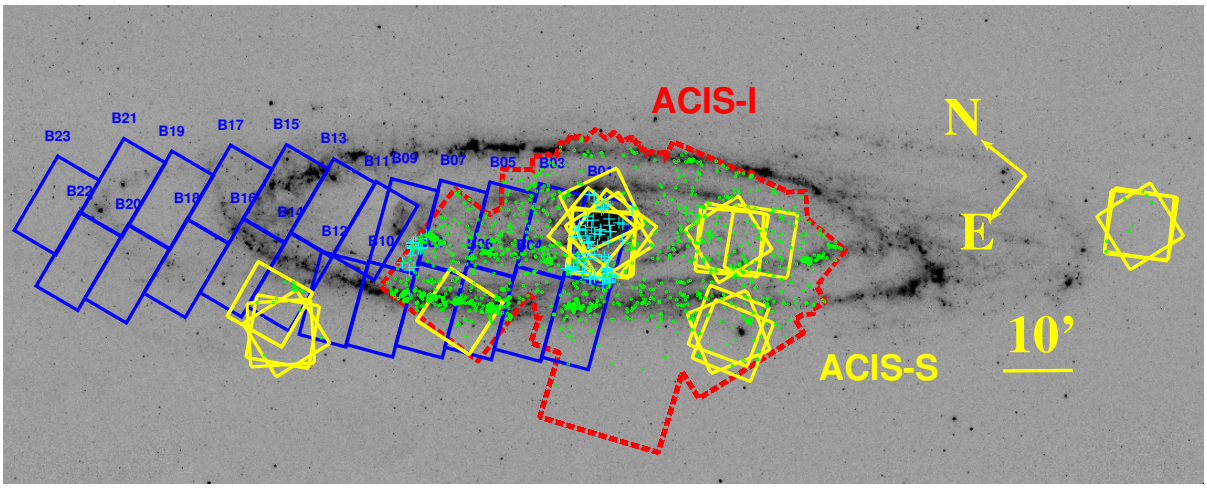

Figure 3.1: The field of view of the ACIS-I (dashed outline, red in the online version) merged observations and ACIS-S3 chips (yellow in the online version) for each observation used in our analysis overlaid on a Spitzer 24 μm image of M31 (Gordon et al., 2006). The PHAT footprint is included with each rectangular brick (blue in the online version) labelled to show the overlap with *Chandra* data. The year 1 PHAT star cluster catalogue only includes bricks 1, 9, 15, 21, and parts of 17 and 23. Crosses (cyan in the online version) and circles (green in the online version) represent star clusters and H II regions, respectively, within the field of view of *Chandra* data (see Section 3.3.2 for more details). Most *Chandra* observations were part of an ongoing monitoring program of the supermassive black hole, while off-center ACIS-S pointings studied supersoft X-ray sources.

Table 3.1. ACIS-S Observations

ObsID[a]	Date	R.A. (J2000)	Decl. (J2000)	Livetime (s)	Datamode	CCDs	Roll Angle (degrees)
309	2000-06-01	10.688	41.27877	5129	FAINT	235678	87.5
310	2000-07-02	10.68311	41.27876	5284	FAINT	235678	108.7
313	2000-09-21	10.65816	40.87837	6002	FAINT	235678	162.9
314	2000-10-21	10.649	40.86757	5212	FAINT	235678	209.4
2052	2000-11-01	11.53802	41.65947	13890	FAINT	235678	226.9
2046	2000-11-05	9.62713	40.26241	14780	FAINT	235678	237.6
2049	2000-11-05	10.44879	40.98187	14580	FAINT	235678	236.1
1580	2000-11-17	10.66379	40.8563	5415	FAINT	235678	251.5
1854	2001-01-13	10.67349	41.25548	4706	FAINT	235678	295.6
2047	2001-03-06	9.69689	40.27309	14600	FAINT	235678	330.4
2053	2001-03-08	11.61538	41.66618	13380	FAINT	235678	330.5
2050	2001-03-08	10.51841	40.9944	13060	FAINT	235678	331.7
2048	2001-07-03	9.6419	40.33115	13790	FAINT	235678	109.6
2051	2001-07-03	10.45902	41.05868	13600	FAINT	235678	109.0
2054	2001-07-03	11.54972	41.71649	14550	FAINT	235678	108.3
1575	2001-10-05	10.6684	41.27894	39100	FAINT	235678	180.4
2900	2002-11-29	11.1641	41.35916	5349	FAINT	136789	263.7
4541	2004-11-25	11.51934	41.70871	25660	FAINT	235678	260.0
6167	2004-11-26	11.51931	41.70871	24260	FAINT	235678	260.0
4536	2005-03-07	10.46483	40.93912	56200	FAINT	235678	330.4

Table 3.1 (cont'd)

ObsID[a]	Date	R.A. (J2000)	Decl. (J2000)	Livetime (s)	Datamode	CCDs	Roll Angle (degrees)
14197*	2011-09-01	10.68124	41.26788	38870	FAINT	235678	143.6
14198*	2011-09-06	10.68135	41.26769	41380	FAINT	235678	147.7
13825*	2012-06-01	10.6817	41.2707	41330	FAINT	23567	87.7
13826*	2012-06-06	10.68155	41.27051	38060	FAINT	235678	91.9
13827*	2012-06-12	10.68139	41.27031	43040	FAINT	235678	96.2
13828*	2012-07-01	10.68111	41.26974	41380	FAINT	235678	107.9

Note. — Positions represent the aimpoint.

[a]An asterisk indicates an interleaved observation.

Table 3.2: ACIS-I Observations

ObsID[a]	Date	R.A. (J2000)	Decl. (J2000)	Livetime (s)	Datamode	CCDs	Roll Angle degrees
303	1999-10-13	10.67806	41.26989	11890	FAINT	012367	193.0
305	1999-12-11	10.68273	41.26395	4185	FAINT	01236	274.0
306	1999-12-27	10.68409	41.2637	4189	FAINT	01236	285.4
307	2000-01-29	10.68116	41.25783	4174	FAINT	01236	304.3
308	2000-02-16	10.68763	41.25244	4073	FAINT	012356	315.0
311	2000-07-29	10.68737	41.28525	4957	FAINT	012367	122.7
312	2000-08-27	10.68037	41.28501	4728	FAINT	012367	140.6
1581	2000-12-13	10.68382	41.25888	4446	FAINT	235678	276.0
1582	2001-02-18	10.69296	41.26084	4348	FAINT	235678	317.2
1583	2001-06-10	10.69713	41.28246	4951	FAINT	012356	94.9
1584	2001-07-03	10.66362	40.92284	4949	FAINT	012356	108.9
1577	2001-08-31	10.78014	41.32134	4957	FAINT	012367	143.0
1576	2001-10-05	10.62845	40.96574	4931	FAINT	012367	181.2
1585	2001-11-19	10.75553	41.27497	4930	FAINT	012367	254.0
2895	2001-12-07	10.77235	41.29267	5102	FAINT	012367	271.7
2897	2002-01-08	10.79083	41.31215	4954	FAINT	012367	292.4
2896	2002-02-06	10.77472	41.27972	4953	FAINT	012367	309.5
2898	2002-06-02	10.79337	41.32117	4951	FAINT	012367	88.6
2901	2002-07-08	10.53524	40.93252	4678	FAINT	012367	111.9
4360	2002-08-11	10.68315	41.27364	4969	FAINT	012367	130.0
2899	2002-08-23	10.47542	40.95079	4956	FAINT	012367	137.4
2894	2002-10-14	10.63939	40.95643	4704	FAINT	012367	196.0

ObsID[a]	Date	R.A.	Decl.	Livetime	Datamode	CCDs	Roll Angle
2902	2002-12-06	10.4756	40.9423	4753	FAINT	012367	270.6
4678*	2003-11-09	10.67435	41.25902	4105	FAINT	012367	239.5
4679*	2003-11-26	10.68017	41.25681	4029	FAINT	012367	261.4
4680*	2003-12-27	10.68713	41.25622	4422	FAINT	012367	285.1
4681*	2004-01-31	10.69271	41.25761	4825	FAINT	012367	305.6
4682*	2004-05-23	10.69035	41.28109	4188	FAINT	012367	80.0
4719*	2004-07-17	10.67908	41.28108	5670	FAINT	012367	116.8
4720*	2004-09-02	10.68136	41.27297	4891	FAINT	012367	144.8
4721*	2004-10-04	10.66766	41.27061	4905	FAINT	012367	180.5
4722*	2004-10-31	10.67124	41.26128	4116	FAINT	012367	226.0
4723*	2004-12-05	10.70594	41.27487	4333	FAINT	012367	269.8
7136*	2006-01-06	10.68904	41.25669	4196	VFAINT	012367	291.7
7137*	2006-05-26	10.68974	41.2812	4157	VFAINT	012367	81.8
7138*	2006-06-09	10.68639	41.28173	4508	VFAINT	012367	93.9
7139*	2006-07-31	10.67776	41.28059	4196	VFAINT	012367	123.5
7140*	2006-09-24	10.66931	41.27371	4391	VFAINT	012367	166.0
7064*	2006-12-04	10.68236	41.25921	25050	VFAINT	012367	269.0
8183*	2007-01-14	10.68552	41.26435	4199	VFAINT	012367	296.1
8184*	2007-02-14	10.6874	41.26454	4900	VFAINT	012367	313.8
8185*	2007-03-10	10.69569	41.26756	4201	VFAINT	012367	332.6
7067*	2007-06-02	11.05451	41.43989	8498	VFAINT	012367	88.0
7068*	2007-06-02	10.68775	41.27877	8061	VFAINT	012367	88.5
8191*	2007-06-18	10.68003	41.27608	4198	VFAINT	012367	99.6
8192*	2007-07-05	10.67864	41.2754	4318	VFAINT	012367	109.8
8193*	2007-07-31	10.67661	41.27398	4973	VFAINT	012367	123.4
8194*	2007-08-28	10.67494	41.27198	4277	VFAINT	012367	140.5
8195*	2007-09-26	10.67416	41.26813	4208	VFAINT	012367	168.0
8186*	2007-11-03	10.68074	41.26147	5328	VFAINT	012367	229.9
8187*	2007-11-27	10.68674	41.26097	4070	VFAINT	012367	261.5
9520*	2007-12-29	10.69095	41.26234	4206	VFAINT	012367	286.6
9529*	2008-05-31	10.68243	41.2768	4948	VFAINT	012367	87.0
9522*	2008-07-15	10.67764	41.27492	4297	VFAINT	012367	115.6
9523*	2008-09-01	10.67481	41.27168	4408	VFAINT	012367	143.8
9524*	2008-10-13	10.67577	41.2647	5249	VFAINT	012367	194.1
9521*	2008-11-27	10.68689	41.26097	4210	VFAINT	012367	262.9
10551*	2009-01-09	10.69205	41.26274	4120	VFAINT	012367	293.7
10552*	2009-02-07	10.69356	41.26405	4118	VFAINT	012367	305.2
10553*	2009-03-11	10.69564	41.26787	4540	VFAINT	012367	334.4
10554*	2009-05-29	10.68273	41.27687	4196	VFAINT	012367	84.7
10555*	2009-07-03	10.67865	41.27546	4224	VFAINT	012367	108.9
11256	2009-09-17	11.0153	41.01168	20320	VFAINT	012367	157.4
10715*	2009-09-18	10.6742	41.26954	4125	VFAINT	012367	158.7
11252	2009-09-19	10.85959	41.12999	59320	VFAINT	012367	159.8
10716*	2009-09-25	10.67432	41.26833	4348	VFAINT	012367	166.8

ObsID[a]	Date	R.A.	Decl.	Livetime	Datamode	CCDs	Roll Angle
10717*	2009-10-22	10.6771	41.26358	5043	VFAINT	012367	205.2
11275*	2009-11-11	10.68321	41.26092	4786	VFAINT	012367	243.0
10718*	2009-11-19	10.49746	41.08611	4367	VFAINT	012367	254.4
11276*	2009-12-08	10.68868	41.26143	4130	VFAINT	012367	272.5
10719*	2009-12-27	10.69083	41.2623	4272	VFAINT	012367	285.7
11277*	2010-01-01	10.69067	41.2621	4801	VFAINT	012367	283.9
11278*	2010-02-04	10.69378	41.26431	4138	VFAINT	012367	307.9
11279*	2010-03-05	10.69539	41.26694	4391	VFAINT	012367	328.6
11838*	2010-05-27	10.68307	41.27688	4140	VFAINT	012367	83.1
11839*	2010-06-23	10.67964	41.27597	4144	VFAINT	012367	103.1
11840*	2010-07-20	10.67727	41.27462	4145	VFAINT	012367	118.1
11841*	2010-08-24	10.67529	41.27231	4146	VFAINT	012367	137.8
11842*	2010-09-25	10.67422	41.26849	4148	VFAINT	012367	166.3
12160*	2010-10-19	10.67699	41.26365	4148	VFAINT	012367	204.4
12161*	2010-11-16	10.68436	41.26084	4150	VFAINT	012367	249.8
12162*	2010-12-12	10.68905	41.2615	4151	VFAINT	012367	275.1
12163*	2011-01-13	10.69237	41.26305	4151	VFAINT	012367	295.1
12164*	2011-02-16	10.69499	41.26594	4152	VFAINT	012367	320.2
12970*	2011-05-27	10.68323	41.27705	4157	VFAINT	012367	82.7
12971*	2011-06-30	10.67889	41.27572	4158	VFAINT	012367	107.0
12972*	2011-07-25	10.67697	41.2744	4159	VFAINT	012367	120.3
12973*	2011-08-25	10.67517	41.27224	4127	VFAINT	012367	138.3
12974*	2011-09-28	10.67774	41.26745	4161	VFAINT	012367	170.8
13833*	2011-10-31	10.6824	41.26348	4148	FAINT	01237	224.9
13834*	2011-11-24	10.68628	41.26085	4094	FAINT	012367	259.0
13835*	2011-12-19	10.69011	41.26183	4092	FAINT	012367	280.2
13836*	2012-01-16	10.69261	41.26329	4093	FAINT	012367	297.1
13837*	2012-02-19	10.69464	41.26549	4097	FAINT	012367	317.3
13298*	2012-05-26	10.68313	41.27691	4089	FAINT	012367	83.1

Note. — Positions represent the aimpoint.
[a]An asterisk indicates an interleaved observation.

3.3.1.1 Data Reduction

Each observation was reprocessed with the *Chandra* Interactive Analysis of Observations (*CIAO*) tools package version 4.5 (Fruscione et al., 2006) and the *Chandra* Calibration database (*CALDB*) version 4.5.5 (Graessle et al., 2006). We started with the level-1 events file and produced a bad pixel file that identified observation-specific bad pixels, hot pixels, bright bias pixels, and afterglow events using `acis_run_hotpix`. Since we are studying faint sources,

we ran `acis_detect_afterglow` to eliminate cosmic ray afterglows with only a few events. The level-1 events file was updated and filtered using the standard (ASCA) grades $(0, 2-4, 6)$, status bits (0), good time intervals, charge transfer inefficiency (CTI), time-dependent gain, and pulse height with `acis_process_events`. We used the energy-dependent subpixel event repositioning algorithm to improve astrometry and, where necessary, set the VFAINT option in `acis_process_events`.

We then created merged event files for all 26 ACIS-S observations and all 95 ACIS-I observations with `reproject_obs` to obtain fully-reduced images in the soft, hard, and full-bands corresponding to energy ranges of $0.3-2$ keV, $2-8$ keV, and $0.3-8$ keV respectively. We produced exposure-corrected images (in units of photons cm^{-2} s^{-1} pixel^{-1}) with the `flux_obs` tool using a binsize of 1 to maintain the native resolution. Weighted spectrum files (corresponding to the soft, hard, and full energy bands) were used to calculate instrument maps. The merged ACIS-S and ACIS-I images have dimensions[1] of $1.7^\circ \times 1.7^\circ$ and $0.8^\circ \times 0.85^\circ$ and correspond to exposures of ~548 ks and ~ 510 ks respectively[2]. The plate scale of the *Chandra* images is 0.5 arcsecond pixel^{-1}, corresponding to 1.9 pc pixel^{-1}. *Chandra's* absolute astrometry is ~0.6″ at the 90% confidence level (Broos et al., 2010) and has spatial resolution that ranges from 1″ on-axis to 4″ at 4′ off-axis for 1.5 keV at 90% encircled energy fraction for ACIS[3].

3.3.1.2 X-Ray Point Source Detection

Given that we have produced deep images of M31's bulge, there may be new point sources that have not been previously identified. We used `wavdetect` on the full, hard, and soft-band images with scales[4] of 1, 2, 4, 8, and 16 as recommended by the Chandra X-ray Center to have a wide range of source sizes[5]. This ensures that the variation of the PSF at different off-

[1] Since *Chandra* ACIS-S observations are sparse (Figure 3.1) large parts of the image are devoid of data.

[2] These exposure times are not consistent across the fields of view since merging results in overlap of varying exposures from each observation.

[3] `http://cxc.harvard.edu/proposer/POG/`

[4] Using the $\sqrt{2}$ series from 1 to 8 we detected an additional 60 X-ray sources. However, this does not change the results of our matching analysis (see Section 3.4.1).

[5] `http://cxc.harvard.edu/ciao/ahelp/wavdetect.html#plist.scales`

axis angles is accounted for. Exposure maps were also input to reduce false positives. The sigthresh parameter, which determines how many false detections are allowed, should not be larger than the inverse of the number of pixels in the image being analyzed. Therefore it was set to 3×10^{-8} for the ACIS-I merged image and 7×10^{-9} for the ACIS-S merged image. These numbers are small since the ACIS-I merged image (0.68 deg^2) covers an area larger than the bulge and the ACIS-S merged image (2.89 deg^2) covers the majority of the galaxy even though only the nucleus and various pointings have data (see Figure 3.1 and Section 3.3.1.1). In any case, setting the sigthresh parameter to the default value of 10^{-6} did not change the number of X-ray sources matched to star clusters or H II regions. We obtained source lists for the full, hard, and soft-band merged ACIS-I and ACIS-S images. From the six source lists we collated our results into a master source list with the `match_xy` tool from the Tools for ACIS Review and Analysis (TARA) package[6]. We found a total of 1033 independent X-ray point sources across all 3 bands (a source was not necessarily detected in more than one band) for the ACIS-I merged observations and ACIS-S merged observations. We report the number of sources detected in each energy band for both ACIS-I and ACIS-S in Table 3.3. While the `match_xy` tool filtered X-ray sources based on their positional uncertainties from `wavdetect` (e.g. retains only one source position if detected in all 3 energy bands), `match_xy` does not consolidate pairs of extremely close `wavdetect` sources detected only in one band. We performed an internal match of our 1033 sources to remove sources within 0.5″ of another source. This found a further 112 matches that we removed to obtain 921 effective X-ray sources.

We input our list of sources to the ACIS Extract package (Broos et al., 2010) along with exposure maps (calculated using weighted spectrum files) so that each observation could be individually analyzed. ACIS Extract then merged all observations (ACIS-I and ACIS-S) and produced the relevant source properties and statistics, such as X-ray luminosity. ACIS Extract aligns each observation to a published astrometric catalogue[7] and thus gives precision of ∼0.1″

[6] `http://www2.astro.psu.edu/xray/docs/TARA/`

[7] Naval Observatory Merged Astrometric Dataset (Zacharias et al., 2004) or 2MASS Point Source Catalog (Skrutskie et al., 2006)

Table 3.3. X-ray Sources Detected in Merged ACIS Observations

Detector	Full	Hard	Soft	Total	Total Effective Sources
ACIS-I	435	344	388	1167	921
ACIS-S	353	217	334	904	

Note. — Total Effective Sources (ACIS-I & ACIS-S) refers to the number of actual X-ray sources detected after filtering those that appear in multiple energy bands and on both detectors. An internal match to within 0.5″ filtered out sources with separations closer than the pixel scale.

for most point sources. We required ACIS Extract's PROB_NO_SOURCE statistic for each X-ray source to be > 99.9%, except where by-eye inspection of the images showed source crowding that biased this statistic to lower values (i.e. 5 sources included that were not > 99.9%). The majority of our sources (∼75%) are located in the bulge, where the *Chandra* observations are deeper compared with the rest of the galaxy. We only processed (through ACIS Extract) the 26 X-ray sources that matched to star clusters and H II regions (see Section 3.4.1 for details). The luminosity range of these 26 X-ray sources was 8.5×10^{33} erg s^{-1} to 7.8×10^{37} erg s^{-1}. There is no meaningful, single value for the completeness limit since the exposure time varies significantly across the usable field of view. The deepest exposure of any 1 pixel reaches ∼ 500 ks in both the merged ACIS-I and merged ACIS-S images; this occurs in the nucleus and corresponds to a sensitivity limit of $\approx 10^{33}$ erg s^{-1}. The complete X-ray point source catalogue will follow in a subsequent paper (Vulic et al., in prep.).

3.3.2 Optical Data

We use the star cluster catalogue compiled by J12 from the PHAT survey. The survey operates using the Advanced Camera for Surveys (filters F475W and F814W) as well as the Wide Field Camera 3 (filters F275W, F336W, F110W, and F160W) on the *HST*. The observational tech-

nique used by the survey is detailed in Dalcanton et al. (2012) and comprises 23 areas known as "bricks", with each one consisting of 18 different fields of view. The survey produces photometry with a signal-to-noise ratio of 4 at $m_{F275W} = 25.1$, $m_{F336W} = 24.9$, $m_{F475W} = 27.9$, $m_{F814W} = 27.1$, $m_{F110W} = 25.5$, and $m_{F160W} = 24.6$ for single pointings in the uncrowded outer disk. The PHAT year 1 star cluster catalogue was compiled from bricks 1, 9, 15, 21, and parts of 17 and 23. Due to the limited *Chandra* data we only utilize brick 1 and a small part of brick 9 (proposal 12058, PI: Julianne Dalcanton). Even though Figure 3.1 shows numerous PHAT bricks coincident with *Chandra* data, the only bricks with published star cluster catalogues that overlap are 1 and 9. There are 83 star clusters[8] in the field of view of the *Chandra* observations that we use for our matching and stacking analyses (indicated by crosses in Figure 3.1). J12 have corrected the absolute astrometry to agree with the 2MASS reference system within ~60 mas. The PSF (full width at half maximum) for F475W is $\approx 0.10'' - 0.13''$ (Ubeda & et al., 2012).

In addition, we use the new catalogue of H II regions in M31 compiled by Azimlu et al. (2011). M31's entire disk is covered out to ~24 kpc from the center based on observations with the Mayall 4 m telescope as part of the Nearby Galaxies Survey (Massey et al., 2006). A total of 3691 H II regions down to $L_{H\alpha} = 10^{34}$ erg s^{-1} are identified in the 2.2 deg^2 mosaic, with 1566 in the field of view of the *Chandra* data (indicated by circles in Figure 3.1). The average PSF (full width at half maximum) of the survey was 1″, which is generally better than *Chandra's* range of $1'' - 4''$ but not as good as the $\approx 0.10'' - 0.13''$ for F475W from the PHAT survey. The astrometric calibration of the H II region catalogue is good to 0.1″, better than *Chandra's* 0.6″ but not as precise as the 60 mas for PHAT.

[8] A PHAT year 1 'possible cluster' catalogue exists that we have not used.

3.4 Data Analysis

3.4.1 Matching Results

Prior to stacking star clusters and H II regions we must exclude those with identified X-ray point sources. Stacking probes faint X-ray point sources by co-adding star clusters (or H II regions) that are undetected in X-rays. In this way one hopes to detect a signal in the source aperture (centered on the position of the star cluster or H II region) above the background (see Section 3.5 for more details). Therefore, including a star cluster (or H II region) with a detected X-ray point source in the complete stack of all undetected star clusters (or H II regions) would defeat the purpose of detecting a faint X-ray source in the stack. Figure 3.1 shows where the star clusters and H II regions we analyzed are located in M31. The 83 star clusters in the field of view of *Chandra* data are located mainly in the bulge (PHAT brick 1), while a handful are in the disk (PHAT brick 9); the 1566 H II regions are spread throughout the disk. Here we summarize our matching results, beginning with star clusters.

We used TOPCAT (Taylor, 2005) to complete a matching analysis with the 83 star clusters and 921 X-ray point sources. A total of 15 star clusters were matched to 17 unique X-ray point sources within 1″. The matching results are shown in Table 3.4. Two star clusters (PHAT IDs 594 and 1374) each had two X-ray point source matches. Figure 3.2 shows these star clusters in the F475W band image from PHAT. The clusters are plausible double XRB hosts since the X-ray sources are separated by >0.5″. Even though we used a 1″ matching radius, only 2 star clusters (PHAT IDs 1403 and 1415) had a separation >0.5″ from their matched X-ray point source. No additional clusters were matched when increasing the matching radius to >10″. Only one star cluster (PHAT ID 1374) has not previously been associated with an X-ray source. In addition, one star cluster (PHAT ID 1375) that was previously identified as a GC candidate X-ray source by (Voss & Gilfanov, 2007a) was not associated with an X-ray source in our analysis. Upon further inspection of our ACIS-I image it seemed that `wavdetect` did not identify what was likely an X-ray source.

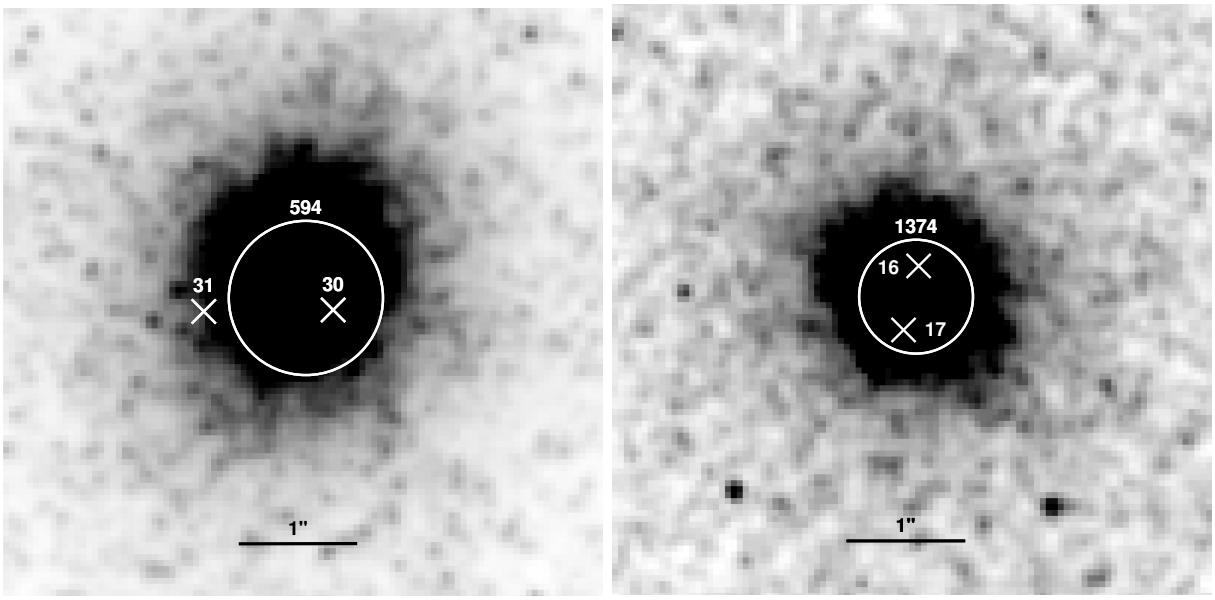

Figure 3.2: Images from the F475W band of the PHAT survey showing star clusters with double X-ray point source matches, where each panel is 5″ on a side. White circles represent star clusters (with the radius equal to the effective radius of the star cluster) while an "×" represents the position of an X-ray source. The numbers correspond to the PHAT and AE identification numbers respectively from Table 3.4.

To address the chance coincidence probability of our matches we created 25 source lists from our original X-ray catalogue that offset each source by ± 5−10″ (Antoniou et al., 2009; Zezas et al., 2002). A false-match rate of ∼2% was recovered (≤1 false match). We also used the cumulative number counts of Brandt et al. (2001b) to estimate the expected background sources in the 83 star cluster regions of radius 1″ each. In equation 3.1, S is the flux in erg s^{-1} cm^{-2} and N is the number of background sources per deg^2 above that flux, where we used the faintest X-ray point source from our matches ($\approx 1.4 \times 10^{-16}$ erg s^{-1} cm^{-2}). This gave $N(> 1.4 \times 10^{-16}$ erg s^{-1} cm$^{-2}) = (9.4 \times 10^{-4})^{+5.4\times10^{-4}}_{-1.3\times10^{-3}}$ expected background sources, indicating that our matches are likely authentic. We also completed cone searches in the NASA/IPAC Extragalactic Database (NED) within 30″ around each of the 17 X-ray point sources that were matched to star clusters and found no background galaxies.

$$N(> S) = 3970 \left(\frac{S}{1 \times 10^{-16}} \right)^{-0.67\pm0.14} \text{deg}^{-2} \quad (3.1)$$

Our results show that ∼18% (15/83) of star clusters were matched to an X-ray point source within 1″. In a survey of eight Fornax and Virgo elliptical galaxies (limiting luminosities typically few $\times 10^{37}$ erg s^{-1}) Kim et al. (2013) found that 408 of 5904 (∼7%) GCs are associated with an X-ray source within 0.5″. Similarly, a survey of 11 Virgo Cluster early-type galaxies (limiting luminosities typically few $\times 10^{37}$ erg s^{-1}) by Sivakoff et al. (2007) found that 270 of 6488 (∼4%) GCs were associated with an X-ray source within 1″. Our analysis was restricted to the bulge/central region of M31 and thus the concentration of X-ray point sources is larger than throughout the rest of the galaxy (as Muno et al. 2009 found for the Milky Way). Since LMXBs trace stellar mass (Gilfanov, 2004), and stellar mass density is larger in the bulge, we would therefore expect to have a higher percentage of matches (LMXBs) compared to the value for the entire galaxy. Additionally, our luminosity limit is a factor of 10^3 fainter than previous surveys and therefore increases our percentage of matches. To more directly compare different galaxies, we compare the fraction (and number) of GCs with an LMXB versus those without above a given luminosity limit from our survey with those of Sivakoff et al. (2007) and Kim et al. (2013) in Table 3.5. We compared our results to individual galaxies from these two surveys since most galaxies they studied had varying limiting L_X (i.e. their complete sample is not completeness-corrected). The fractions are comparable (e.g. 6% for our work and 6.5% for Sivakoff et al. 2007) at low-L_X limits ($L_X > 5 \times 10^{37}$ erg s^{-1}). For $L_X > 2.6 \times 10^{37}$ erg s^{-1} a fraction of 3.6% found in our study is much lower than the 8.3% of Kim et al. (2013). In general, we and Sivakoff et al. (2007) find a difference in the fraction that is lower by a factor of $2-4$ than Kim et al. (2013) for $L_X > 2.6 \times 10^{37}$ erg s^{-1}, which could be attributed to small-number statistics. When analyzing the same galaxies as Sivakoff et al. (2007), Kim et al. (2013) found more GC-LMXBs as a result of deeper X-ray observations over an extended period of time, which also allowed for the identification of previously quiescent sources that went into outburst.

Of the 1566 H II regions in the field of view, we found 10 that matched to 9 unique X-ray point sources within 3″ (∼11.2 pc, their average radius). The results are shown in Table 3.6.

Table 3.4. Star Cluster & X-ray Point Source Matches

Star Cluster Positions[a]			Results from ACIS Extract								Group Data[b]			Previous Classification	
PHAT ID	RA (J2000)	Dec	AE ID	RA (J2000)	Dec	PErr[c] (″)	Prob[d]	OAA[e] (′)	PSF %	$\log(L_X)$[f] (erg s^{-1})	ID	Size	Sep (″)	Class[g]	Ref.[h]
594	10.856666	41.260284	30	10.856581	41.260256	0.00	1.00[i]	4.3	0.4	33.32	1	2	0.25	GC	HO
594	10.856666	41.260284	31	10.856984	41.260252	0.00	1.00[i]	4.3	0.4	33.37	1	2	0.87	GC	HO
1374	10.711676	41.285381	16	10.711668	41.285453	0.15	0.11[j]	1.6	0.39	34.24	2	2	0.26	···	···
1374	10.711676	41.285381	17	10.711715	41.285303	0.25	0.70[j]	1.6	0.39	27.88[k]	2	2	0.30	···	···
612	10.749429	41.268238	21	10.749429	41.268268	0.01	0.00	3.5	0.9	37.61	···	···	0.11	GC/BH?	ZH/BA
616	10.766111	41.301309	24	10.766068	41.301343	0.01	0.00	2.0	0.39	37.42	···	···	0.17	GC/BH?	ZH/BA
642	10.794234	41.247575	27	10.794231	41.2476	0.02	0.00	3.1	0.39	37.82	···	···	0.09	GC/BH?	ZH/BA
663	10.762226	41.25627	23	10.7622	41.256281	0.01	0.00	3.2	0.4	37.37	···	···	0.08	GC/BH?	VO/BA
682	10.814255	41.190284	28	10.814253	41.190228	0.13	0.00	7.0	0.9	35.98	···	···	0.20	GC	VO
1377	10.731713	41.309748	19	10.731691	41.309742	0.02	0.00	3.1	0.39	36.39	···	···	0.06	fgStar/GC	VO/KO
1381	10.692025	41.293409	13	10.692013	41.293426	0.03	0.00	1.5	0.39	35.91	···	···	0.07	GC	KO
1386	10.63027	41.327441	6	10.630254	41.327479	0.01	0.00	4.2	0.4	37.24	···	···	0.14	GC	VO
1395	10.672678	41.256623	10	10.672652	41.256609	0.01	0.00	1.0	0.39	36.51	···	···	0.09	GC	VO
1401	10.638559	41.295108	7	10.638544	41.295104	0.02	0.00	2.6	0.9	36.31	···	···	0.04	GC	HO
1403	10.623894	41.2993	4	10.624093	41.299152	0.39	0.00	3.5	0.9	34.79	···	···	0.76	GC	ZH
1415	10.68207	41.211915	11	10.681932	41.211796	0.28	0.07	3.7	0.9	33.82	···	···	0.57	GC	HO
1444	10.58984	41.238797	3	10.589851	41.238801	0.20	0.00	4.2	0.4	35.85	···	···	0.03	IRsrc	KA

[a] Taken from the catalogue of J12.

[b] Group ID identifies star clusters that were matched to multiple X-ray point sources (Group Size).

[c] Source positional uncertainty.

[d] Probability source does not exist.

[e] Average off-axis angle.

[f] In the 0.3 − 8 keV band.

[g] BH = Black Hole, GC = globular cluster, fgStar = foreground star, IRsrc = infrared source, ? indicates a candidate.

[h] BA (Barnard et al., 2013), HO (Hofmann et al., 2013), KA (Kaaret, 2002), KO (Kong et al., 2002), VO (Voss & Gilfanov, 2007a), ZH (Zhang et al., 2011).

[i] X-ray sources located at the edge of ACIS-S image and thus only contribute to the background, resulting in a large probability.

[j] Suffer from crowding and thus have unreasonably high values.

[k] Source has a large A_V from best-fit XSPEC (Arnaud, 1996) model and thus the luminosity is unreliable.

Table 3.5. GC-LMXB Fraction Comparisons

Study	Galaxies	Percentage of GCs with an LMXB				
		$\gtrsim 0.05$	$\gtrsim 0.09$	$\gtrsim 0.14$ (10^{38} erg s^{-1})	$\gtrsim 0.26$	$\gtrsim 0.3$
This work	M31	6% (5)	6% (5)	6% (5)	3.6% (3)	2.4% (2)
Kim et al. (2013)[a]	NGC 4365, NGC 4649	···	···	···	8.3% (209)	···
	NGC 4472	···	···	···	···	9.2% (70)
Sivakoff et al. (2007)[b]	NGC 4374, NGC 4697	6.5% (52)	···	···	···	···
	NGC 4365, NGC 4406	···	3.8% (49)	···	···	···
	NGC 4486, NGC 4552	···	···	3.8% (80)	···	···
	NGC 4526	···	···	···	···	2.9% (7)

Note. — Values shown in brackets represent the number of GC-LMXBs. Since the comparison studies do not publish values above a given L_X for the entire sample we can only compare individual galaxies.

[a]Sample of Virgo and Fornax cluster early-type galaxies; uses $L_{X,min}$ (0.3 − 10 keV) as limiting luminosity.

[b]Sample of Virgo cluster early-type galaxies; uses $L_{X,min}$ (0.3 − 8 keV) at 50% detection probability as limiting luminosity.

The false-match rate for H II regions was ∼35%, which is higher due to the increased matching radius and their larger physical size compared to star clusters. For each of the 9 X-ray point sources that were matched to H II regions, we completed NED cone searches using a radius of 30″. Only one source (AE ID 38, 2.3″ from an H II region; see Table 3.6) had any nearby entries in NED. These were a nova at a distance of 0.4″, an H II region at a distance of 3.2″, and a background galaxy at a distance of 7″. We summarize our matching results and state completeness limits in Table 3.7.

3.4.2 X-ray Properties of Matched Star Clusters & H II Regions

An X-ray color-color plot of the X-ray point sources matched to star clusters and H II regions is shown in Figure 3.3, with the X-ray color classification scheme of Kilgard et al. (2005) overlaid. Soft and hard colors are defined by the soft (S, 0.3 − 1 keV), medium (M, 1 − 2 keV), hard (H, 2 − 8 keV), and total (T, 0.3 − 8 keV) band energies as $(M - S)/T$ and $(H - M)/T$ respectively. X-ray photometry was completed separately for each observation for each X-ray point source. The photometry results for each observation were then merged for each X-ray

Table 3.6. H II Region & X-ray Point Source Matches

H II Region Data[a]					Results from ACIS Extract								Group Data[b]			Previous Classification	
HII ID	RA (J2000)	Dec	Radius (pc)	$\log(L_{H\alpha})$ (erg s^{-1})	AE ID	RA (J2000)	Dec	PErr[c] ($''$)	Prob[d]	OAA[e] ($'$)	PSF %	$\log(L_X)$[f] (erg s^{-1})	ID	Size	Sep ($''$)	Class[g]	Ref.[h]
2165	10.8667	41.3092	10.99	36.87	33	10.866947	41.309129	0.14	0.00	7.8	0.5	35.94	1	2	0.7	SNR	WI/ST
2164	10.8667	41.3091	10.43	36.94	33	10.866947	41.309129	0.14	0.00	7.8	0.5	35.94	1	2	0.7	SNR	WI/ST
1686	10.6429	40.9527	13.33	35.31	8	10.643727	40.95233	0.46	0.00	4.2	0.9	35.87	···	···	2.6	GC	PE/ZH/ST
1798	10.7046	41.4017	7.83	36.72	14	10.704479	41.402351	0.28	0.00	7.9	0.9	35.53	···	···	2.4	SNR	ST
1805	10.7083	40.8914	8.62	34.44	15	10.707519	40.891337	0.59	0.00	3.7	0.9	34.86	···	···	2.1	···	···
1831	10.7233	41.4307	9.48	36.91	18	10.722953	41.430795	0.31	0.00	9.3	0.9	35.99	···	···	1.0	SNR	ST/VO
2080	10.8287	41.338	7.83	35.64	29	10.828635	41.338083	0.25	0.00	7.2	0.9	35.61	···	···	0.3	SSS?	HO/ST
2241	10.885	41.3499	7.83	35.11	34	10.884631	41.349752	1.09	0.23	8.6	0.9	35.02	···	···	1.1	···	···
2471	10.9721	41.2017	10.43	36.03	36	10.972348	41.200971	0.62	0.00	6.9	0.9	35.44	···	···	2.7	···	···
3005	11.1367	41.4225	7.83	37.52	38	11.13587	41.422606	0.76	0.00	3.9	0.9	35.11	···	···	2.3	···	···

[a]Taken from the catalogue of Azimlu et al. (2011).

[b]Group ID identifies an H II region matched to multiple X-ray point sources (Group Size).

[c]Source positional uncertainty.

[d]Probability source does not exist.

[e]Average off-axis angle.

[f]In the $0.3 - 8$ keV band.

[g]SNR = supernova remnant, GC = globular cluster, SSS = supersoft X-ray source, ? indicates a candidate.

[h]WI (Williams et al., 2004), ST (Stiele et al., 2011), PE (Peacock et al., 2010b), ZH (Zhang et al., 2011), VO (Voss & Gilfanov, 2007a), HO (Hofmann et al., 2013).

Table 3.7. Matching Analysis Summary

Type	Completeness Limit	Matched	Matched X-ray Sources
PHAT Star Clusters	$M_{F475W} = -4.0$ & $M_{F814W} = -5.0$	15	17
H II Regions	$L_{H\alpha} = 10^{34}$ erg s^{-1}	10	9

Note. — The H II region catalogue (Azimlu et al., 2011) reports a limiting luminosity but not a completeness limit; the star cluster catalogue (J12) is 80% complete to the indicated magnitudes. X-ray sources have a limiting luminosity of 8.5×10^{33} erg s^{-1}.

point source in each of the energy bands to determine colors. Due to the variation in the spectral states of XRBs, the same source can end up in different areas of the diagram. Also, only flux measurements account for the changing effective area of *Chandra*, whereas counts do not. Since the observations we used were spread over 13 years, using counts introduces another source of uncertainty. Absorption also moves X-ray sources into different regions of the diagram and thus can result in misclassifications. Most of the sources are clustered between the XRB and background source regions. However, given the low false match rate for star clusters and previous confirmations as GC sources it is likely that these are mostly XRBs. The X-ray source with AE ID #3 has a luminosity typical of bright XRBs and was previously classified to match within 0.1″ of an infrared source by Kaaret (2002). The remaining X-ray sources were already identified as GCs by various studies (see Table 3.4 for refs.) with many that are likely black hole XRBs (Barnard et al., 2013).

3.4.3 Optical Properties of Matched Star Clusters and H II Regions

A color-color diagram of the 83 star clusters (J12) in the *Chandra* coverage region is shown in Figure 3.4. A theoretical evolutionary track from the simple stellar population models of Marigo et al. (2008) with $Z = 0.02$ is overlaid after applying a total reddening (external and internal) of $E(B - V) = 0.13$ (Caldwell et al., 2011). The 15 star clusters correspond to the 17 X-ray point sources they were matched to from Figure 3.3 (results in Table 3.4). In Figure 3.4

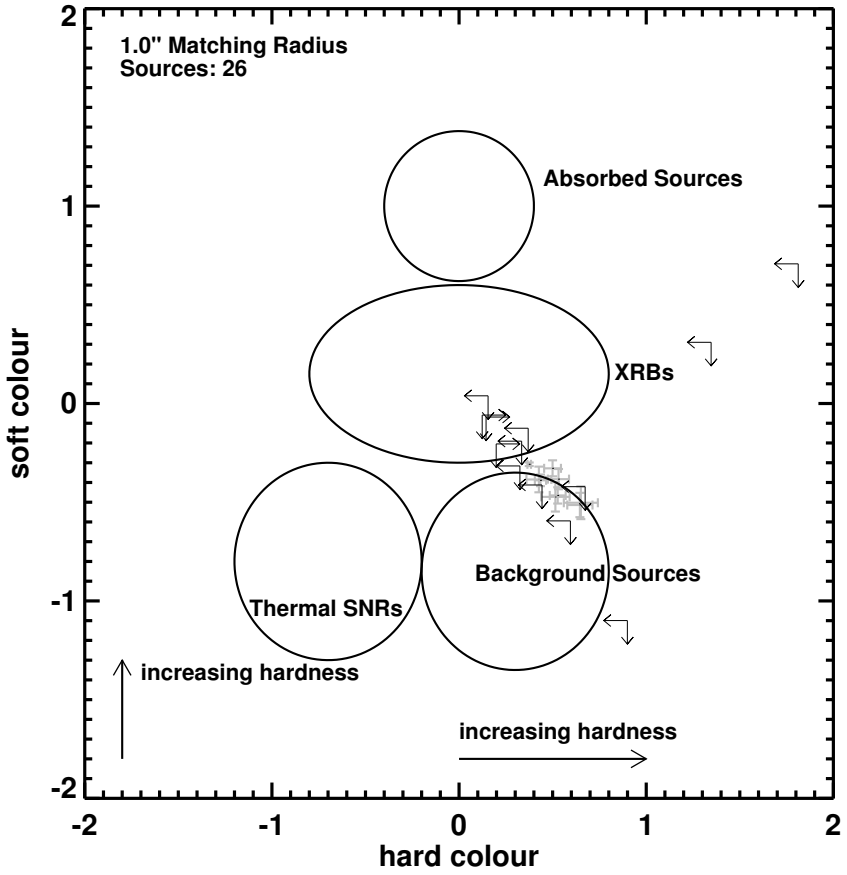

Figure 3.3: X-ray color-color diagram of the 26 X-ray point sources in M31 that were matched to star clusters or H II regions. The X-ray color classification scheme of Kilgard et al. (2005) is overlaid. Sources that were not detected in one or more energy bands ($< 3\sigma$) are plotted as upper or lower limits in one or both axes. Misclassification can result from the variation of XRBs spectral states over time. Also, since counts do not incorporate the change in effective area of *Chandra* over time, additional uncertainty is introduced because observations are spread over 13 years. Most sources are found in the region of color space between XRBs and background sources, where previous classifications from Table 3.4 confirm the majority of those matched to star clusters as GC-LMXBs.

most star clusters are ≥1 Gyr old as expected for an old bulge population.

To determine whether our matches correspond to brighter and redder star clusters, we created the color-magnitude diagram shown in Figure 3.5. It is evident that the matches are all brighter and redder than star clusters without a detected X-ray point source. This is in agreement with the studies of GC-LMXBs in both elliptical and spiral galaxies mentioned earlier (Sivakoff et al., 2007; Peacock et al., 2010b; Paolillo et al., 2011; Mineo et al., 2014). The

average F475W magnitude of matched star clusters was 17 ± 0.6 compared to 20.7 ± 0.6 for unmatched clusters, while the average effective radius of matched clusters was 1.6 ± 0.1 pc compared to 2 ± 0.1 pc for unmatched clusters[9]. This confirms the trend that more luminous, compact star clusters preferentially host an X-ray source. Further evidence is shown in the left panel of Figure 3.6, where it is clear that our matches are all above the 80% completeness limit (m_{F475W} = 20.47) mentioned in Table 3.7. Figure 3.7 shows the X-ray luminosity of point sources that were matched to star clusters plotted against the F475W magnitude and effective radius $R_{\rm eff}$. The histograms show that our sample (dark portion) has preferentially more bright clusters than the complete year 1 sample (black outline - mostly disk clusters), while no significant variations in $R_{\rm eff}$ between the samples is seen. Specifically, the F475W magnitudes of our sample are skewed towards the bright end compared to the complete sample. We performed a Kolmogorov-Smirnov (KS) test on the two distributions, namely our sample and the complete year 1 sample of star clusters, for both the F475W magnitude and $R_{\rm eff}$. We found that the probability that the two distributions are drawn from the same sample is 3.7×10^{-14} for the F475W magnitude and 0.09 for $R_{\rm eff}$, confirming that the F475W magnitudes of the two distributions are different.

To assess the statistical significance of our results we used the **R** statistical software (R Development Core Team, 2008) to complete a logistic regression on our data. This allows us to assess the impact that a parameter has on the probability of a star cluster hosting an X-ray source. The generalized linear model (*glm*) in **R** is best-suited for this and has the form shown in equation 3.2, where p_i is the probability of success averaged over i trials (outcome of 1 or 0, i.e. matched or not) and the β_m's are the regression coefficients of the variables $x_{m,i}$ that we model.

$$ln\left(\frac{p_i}{1-p_i}\right) = \beta_0 + \beta_1 x_{1,i} + \cdots + \beta_m x_{m,i} \tag{3.2}$$

For star clusters we modelled 3 variables, specifically the effective radius $R_{\rm eff}$, F475W magni-

[9]Uncertainties were not published for $R_{\rm eff}$ so we computed the standard error of the mean.

Table 3.8. Logistic Regression Results for Star Clusters and H II regions

Variable	Coefficient β	Standard Error	$z-$Value	Pr($>|z|$)
Star Clusters				
$R_{\rm eff}$	−20.7241	9.0953	−2.279	0.02269
F475W	−2.9285	1.0582	−2.767	0.00565
F475W − F814W	0.5696	2.2257	0.256	0.79802
H II regions				
Radius	-0.9283	2.7518	-0.337	0.736
Hα Luminosity	13.9974	36.3963	0.385	0.701

Note. — Results for a model fit to equation 3.2. The z-statistic in column 4 tells us how many standard error units the sample mean is from the population mean while the p-value in the last column gives us the probability that the null hypothesis is true. A variable in the model is significant for a p-value Pr($>|z|$) < 0.05.

tude, and color (F475W−F814W). We only included the 83 star clusters that were in the field of view of the *Chandra* data, since only these star clusters could possibly have been matched to an identified X-ray point source. The results of the logistic regression are shown in Table 3.8.

Since a variable in the model is generally significant for a p-value Pr($>|z|$) < 0.05 (i.e. null hypothesis is rejected), only $R_{\rm eff}$ and the F475W magnitude are statistically significant. From Table 3.8 the coefficient gives the *ln* odds increase of a match for a unit increase in the respective variable. Therefore, a unit increase in $R_{\rm eff}$ results in a decrease of $\approx$ 21 in the *ln* odds. However, because each variable has a different range of values, a unit increase does not have a 1:1 correspondence across variables. Therefore the smallest p-value indicates which variable is most important to the outcome. From this we see that the F475W magnitude is more significant when determining if a star cluster hosts a bright X-ray source, followed by the effective radius. However, star cluster color was not important, at odds with the surveys of GC-LMXBs in spiral and elliptical galaxies mentioned above. These surveys studied entire

galaxy populations, meaning that even if GC catalogues were incomplete their numbers were not radically biased towards metal-poor or metal-rich. Our result could be a consequence of our sample since it was restricted mostly to bulge clusters, which are metal-rich (see Figure 3.5). Indeed, a KS test between the F475W−F814W color of star clusters in our sample and the complete year 1 PHAT clusters gives a probability of 1.7×10^{-13} that the two distributions are drawn from the same sample. This confirms that bulge clusters are more metal-rich than those in the disk. Complete surveys of M31's GCs by Peacock et al. (2010b) and Agar & Barmby (2013) showed that metal-rich star clusters were more likely to host an X-ray source, indicating our result is biased by our sample.

The 10 H II regions matched to X-ray sources have average radii and Hα luminosities of $R = 9.4 \pm 0.6$ pc and $L_{\mathrm{H}\alpha} = 1.4 \pm 0.2 \times 10^{36}$ erg s^{-1} compared to averages of $R = 11.2 \pm 0.2$ pc and $L_{\mathrm{H}\alpha} = 1.2 \pm 3.2 \times 10^{36}$ erg s^{-1} for unmatched H II regions[10]. While H II regions that were matched to X-ray point sources seem to favour those that are more compact, we cannot claim a trend exists with Hα luminosity due to the large errors associated with their average values. The right panel of Figure 3.6 shows the distribution of H II region luminosity and radius, with matches crowding the compact end. However, H II regions have a much wider range of radii than globular clusters and generally are not well approximated by circular apertures (Azimlu et al., 2011). These differences complicate comparisons between the populations. The limiting $L_{\mathrm{H}\alpha}$ for H II regions from Table 3.7 applies across the entire R_{eff} range; those with larger radii naturally have a larger luminosity and are not biased by incompleteness.

As for star clusters we also completed logistic regression on the 1566 H II regions that were in the field of view of the *Chandra* data. We modelled the radius and Hα luminosity of H II regions to assess their impact on the probability of hosting an X-ray source, with the results shown in Table 3.8. From the p-values of both variables we can see that neither is significant in determining the presence of an X-ray source as both are $\gg 0.05$. In the right panel of Figure 3.6 it would seem that at least the most compact H II regions were more likely to host an X-ray

[10]Uncertainties were not published for radii and Hα luminosities so we computed the standard error of the mean.

source. However, based on the distribution of the population, specifically that most H II regions have small radii, this impression is not supported by our statistical analysis.

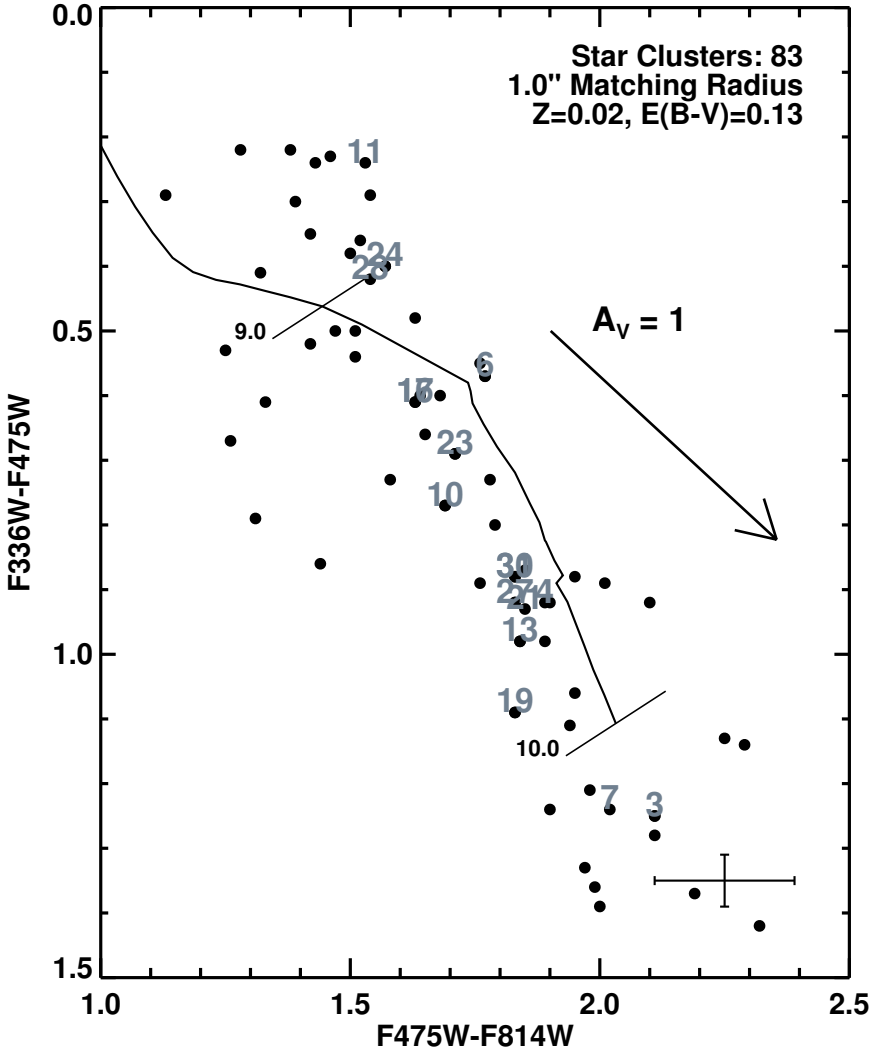

Figure 3.4: Optical color-color diagram of the 83 star clusters in M31 from the catalogue of J12 that are within the field of view of the *Chandra* X-ray image. A theoretical evolutionary track from the simple stellar population model of Marigo et al. (2008) with $Z = 0.02$ is included with a total reddening (external and internal) of $E(B - V) = 0.13$ applied (Caldwell et al., 2011). Bars on the track represent log(age) in years. Numbers labelling individual data points indicate the AE IDs of the 17 unique X-ray point sources that matched to 15 star clusters (Table 3.4). The foreground reddening vector is of length $A_V = 1$ mag.

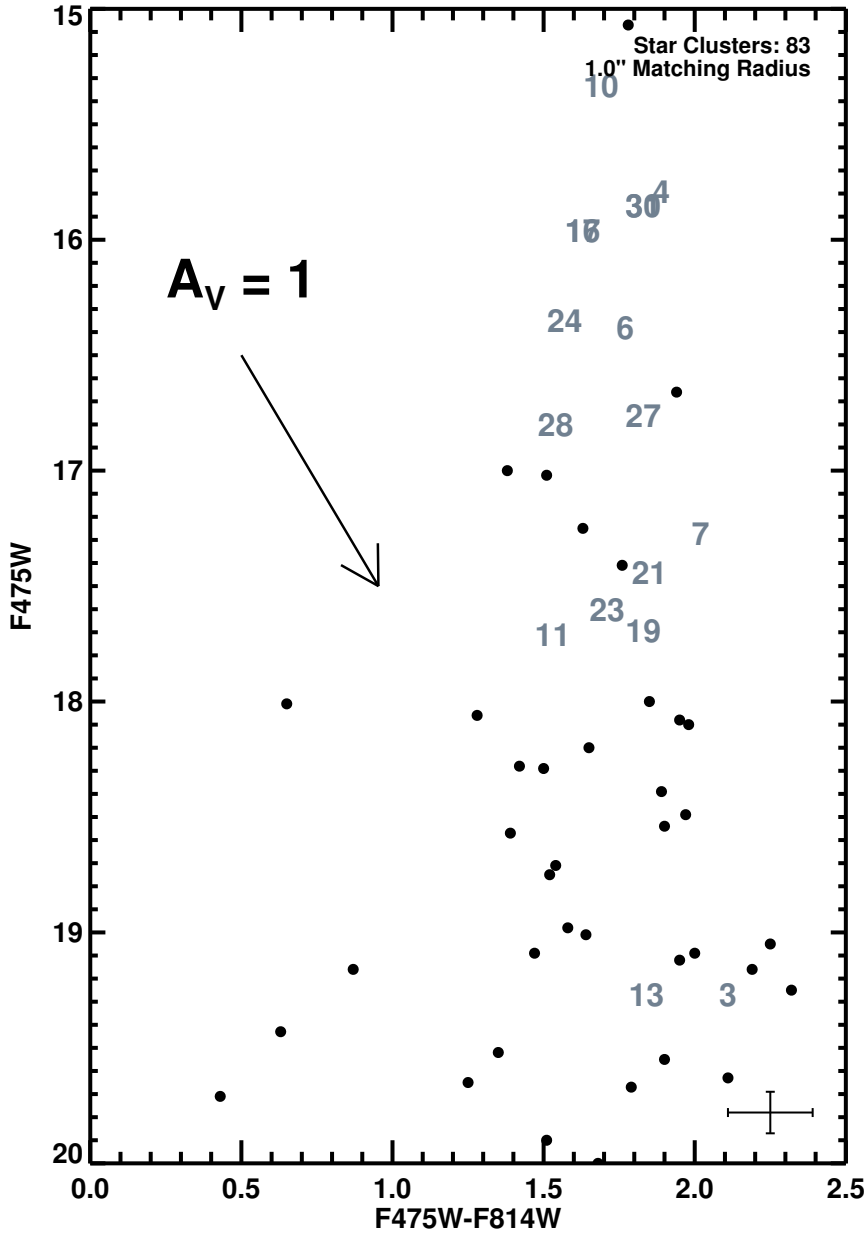

Figure 3.5: Color-magnitude diagram of the 83 star clusters from the catalogue of J12 in the field of view of the *Chandra* data in M31. Numbers labelling individual data points indicate the AE IDs of the 17 unique X-ray point sources that matched to 15 star clusters (Table 3.4). The foreground reddening vector is of length $A_V = 1$ mag. Most of the matched star clusters are brighter and redder than the remaining sample, as expected for clusters that host X-ray sources.

3.5 X-Ray Stacking

To study the faint population of X-ray sources we performed a stacking analysis of the 68 unmatched star clusters and 1556 unmatched H II regions in M31. Using the techniques of

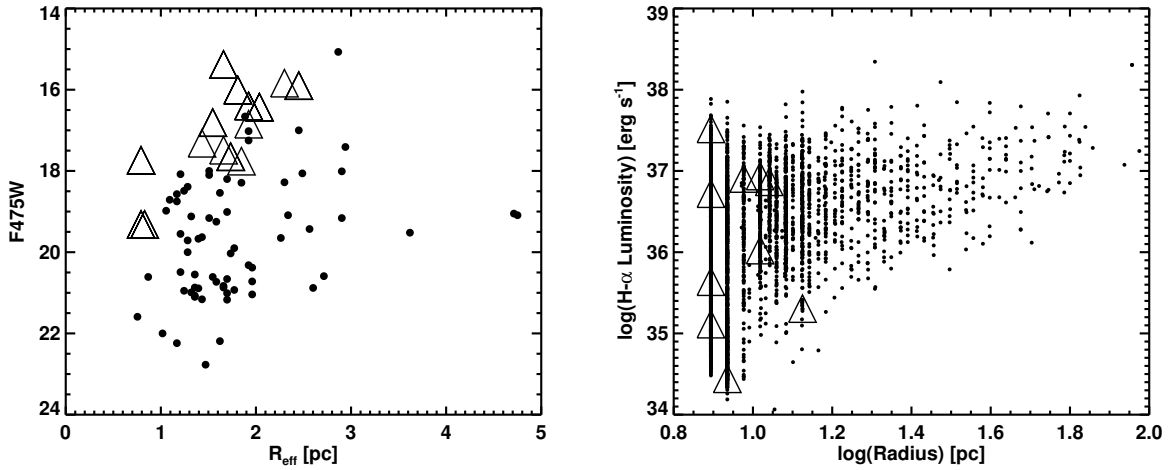

Figure 3.6: F475W magnitude vs. effective radius $R_{\rm eff}$ for the 83 star clusters in M31 (J12) that are within the field of view of the *Chandra* data (left) and $L_{\rm H\alpha}$ vs. radius for the 1566 H II regions in the field of view of the *Chandra* data (right). Triangles indicate the matches to X-ray point sources from Tables 3.4 and 3.6. X-ray sources are preferentially found in luminous, compact star clusters. The apparent preference for compact H II regions to host X-ray sources is a artifact of their distribution (much larger number of compact H II regions). A statistical analysis (see Section 3.4.3) showed that neither the radius nor Hα luminosity was a predictor of whether an H II region would host an X-ray source.

Brandt et al. (2001c,a) and Hornschemeier et al. (2001) we stacked 31 by 31 (45 by 45) pixel regions centered on star cluster (H II region) positions in X-ray images of M31.

Star cluster (H II region) positions closer than 16 (23) pixels to the edge of an X-ray image were excluded since each image in the stack has to be complete (i.e. cannot have null data in any pixels). This left a total of 54 star clusters and 1386 H II regions in each sample. Since there are only a handful of star clusters and they are all older than 1 Gyr we do not subdivide the population by color. However, because brighter and smaller clusters preferentially host X-ray sources we do filter[11] by $R_{\rm eff}$ and F475W magnitude (see Table 3.9) to take advantage of these trends. We followed a similar method for H II regions. There are two peaks in the luminosity function for H II regions in M31, at 10^{35} erg s^{-1} and 4×10^{36} erg s^{-1} for B stars and O stars respectively (Azimlu et al., 2011). These values were used to separate the population by luminosity when stacking. We stacked star clusters and H II regions in the full (0.3 – 8 keV),

[11] We chose our filter cutoffs based on the histograms for radius and magnitude.

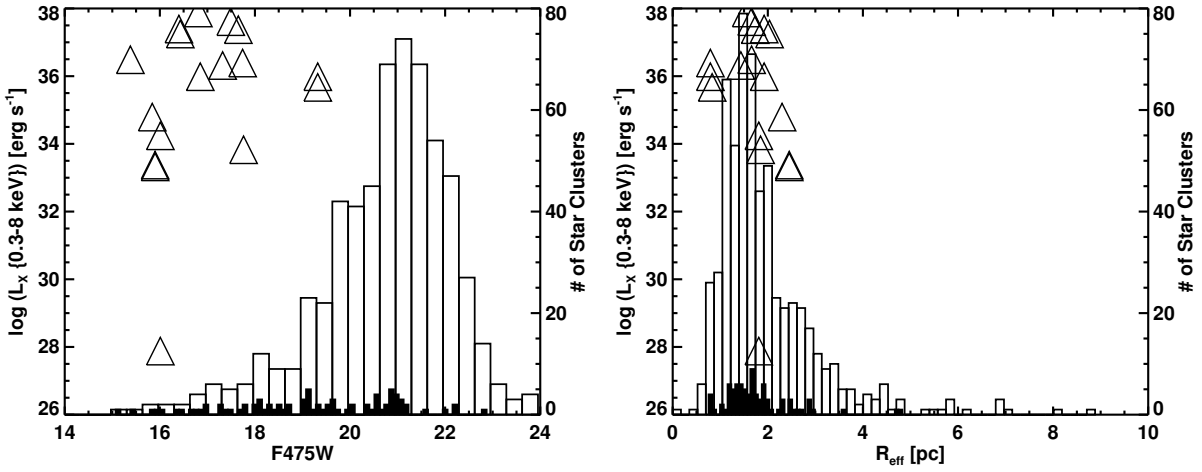

Figure 3.7: The X-ray luminosity of star cluster matches compared with the F475W magnitude (left) and effective radius $R_{\rm eff}$ (right) of star clusters. The X-ray luminosity is that of the X-ray point source matched to the star cluster and was determined by ACIS Extract (see Section 3.3.1.2). The 83 star clusters in the field of view of the *Chandra* data are shown in the filled black histogram while the entire year 1 PHAT survey star cluster sample is represented by the larger unfilled histogram. Triangles indicate the matches to X-ray point sources from Tables 3.4 and 3.6. Our sample has preferentially more bright clusters than the complete year 1 sample while the distributions of effective radius in the two samples appear consistent. A KS test confirmed these conclusions (see Section 3.4.3).

hard (2 − 8 keV), and soft (0.3 − 2 keV) energy bands. Sample stacked images of star clusters and H II regions are shown in Figure 3.8.

The net counts in the source aperture $C_n = C_s - C_b \times A_s/A_b$, where C and A represent the counts and area respectively for the source (s) and background (b) regions. The source region for star clusters in a stacked image is 1″ (2 pixels) in radius, which corresponds to the radius used to match star clusters to X-ray point sources. Keeping the source aperture radius consistent with the matching radius ensures that we do not include any X-ray sources outside of the original matching radius in our stacked images. The background region is defined to be outside the 90% encircled energy radius of the source aperture, which for star clusters that are 4′ off-axis from the *Chandra* aimpoint is 10 pixels[12]. H II regions are more extended and also randomly distributed throughout the ACIS field of view compared to star clusters.

[12]Most star clusters are found in the bulge and thus are within ∼4′ of the aimpoint for ACIS observations (centered on the supermassive black hole).

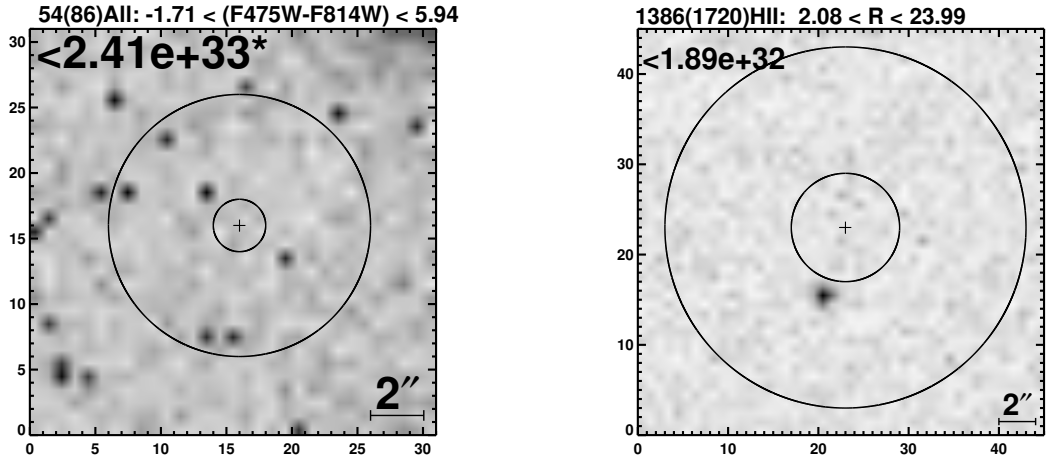

Figure 3.8: Stacked *Chandra* images (0.3 – 8 keV) of all 54 unique star clusters (left) and 1386 unique H II regions (right) in M31 (total number from ACIS-I and ACIS-S in brackets). Star cluster color range (H II region radius in pc) is also indicated. Pixels are 0.492″ with 31 (45) per side. North is up and east is to the left. The source aperture is 4 (12) pixels in diameter while the background was calculated outside the larger aperture of diameter 10 (20) pixels. The value in the top left corner indicates the 1.3σ upper limit per star cluster (H II region) in the stack on the source luminosity in erg s^{-1} (asterisk denotes a negative luminosity in the source aperture). The grayscale represents the brightest pixel (darkest) relative to the dimmest pixel (lightest). All stacked images of star clusters and H II regions across all energy bands resulted in non-detections.

Average off-axis angles for H II regions are not much larger than 8′ and so we use a 20 pixel diameter for the background region (corresponding to 90% encircled energy radius for sources 8′ off-axis). A negative source aperture luminosity results when the background-subtracted source aperture counts are <0. This means that the background has a larger average value per pixel than the source aperture. We use Poisson statistics (method of Gehrels 1986) to calculate our uncertainties. We computed the 3σ-clipped mean μ (C_b/A_b) in the background, where pixels with counts $> \mu + 3\sigma$ were excluded. Upper and lower limits for both the source and background regions were calculated using equations (9) and (14) from Gehrels (1986), using $S = 1.282$ (number of Gaussian σ) and confidence level parameters $\beta = 0.01$ and $\gamma = -4.0$. Uncertainties in the net counts C_n were calculated by normalizing background values to those of the source aperture. Luminosities for stacked images were computed from

fluxes[13] (photons cm^{-2} s^{-1}) using a power-law spectrum with Γ=1.7 for each energy band and assuming a distance of 776 kpc. Uncertainties for luminosities were determined by multiplying the ratio of luminosity to counts in the source aperture by the uncertainties in counts. We use a larger size for our stacked images of H II regions (45 pixels) than star clusters (31 pixels) since H II regions have larger average radii. A caveat to our method is that our merged X-ray images of M31 have an inconsistent PSF at any point in the complete ACIS-I or ACIS-S image. This is a result of observations overlapping at different off-axis angles. This compounds the problem of stacking since we already introduce the same type of effect by stacking objects at various off-axis angles. All stacking completed on star clusters and H II regions resulted in non-detections. The results are displayed in Table 3.9 and shown graphically in Figure 3.9. Correcting for foreground absorption (assuming a Galactic $N_{\rm H}$ value of 6.6×10^{20} cm^{-2} (Dickey & Lockman, 1990) and a power-law spectrum of $\Gamma \sim 1.7$) would increase all our luminosities by $\sim 14\%$.

[13]See section 3.3.1.1 for details on exposure-corrected images.

Table 3.9. Stacked Image Properties

Filter	Unique Number	Total Number[a]	FULL			HARD			SOFT		
			Upper Limit[b]	Sky[c]	Sky Sigma[d]	Upper Limit[b]	Sky[c]	Sky Sigma[d]	Upper Limit[b]	Sky[c]	Sky Sigma[d]
			(10^{32} erg s^{-1})			(10^{32} erg s^{-1})			(10^{32} erg s^{-1})		
H II regions											
None	1386	1720	1.889	2.18	0.018	2.389	1.122	0.012	1.421	0.892	0.011
R <17 pc	711	865	1.116	2.257	0.023	0.117	1.123	0.015	13.02	0.854	0.013
$L_{H\alpha} > 4 \times 10^{36}$ erg s^{-1}	476	617	3.186	2.032	0.041	6.678	0.983	0.025	3.435	0.674	0.021
R >34 pc	83	106	113.128	1.794	0.08	35.079	0.175	0.011	379.804	0.064	0.005
$L_{H\alpha} > 10^{35}$ erg s^{-1}	1231	1515	1.3	2.16	0.02	2.087	1.104	0.013	1.121	0.872	0.012
$L_{H\alpha} > 4 \times 10^{36}$ erg s^{-1} & R <17 pc	132	172	105.83	1.442	0.061	63.978	0.131	0.007	28.521	0.04	0.003
Star Clusters											
None	54	86	24.058	4.641	0.054	0.632	1.573	0.03	0.187	3.054	0.045
R_{eff} >0.4 pc	33	51	2.302	4.42	0.069	0.74	1.473	0.038	0.553	2.871	0.057
F475W >20.5	21	28	1.678	3.073	0.09	1.157	1.283	0.05	1.158	1.651	0.073
R_{eff} <0.4 pc	21	35	0.711	4.952	0.089	2.156	1.693	0.05	0.07	3.276	0.074
F475W <19	15	25	1.044	6.528	0.113	3.587	1.685	0.055	0.818	4.723	0.097
R_{eff} <0.4 pc & F475W <19	4	7	3.315	7.475	0.222	2.827	1.565	0.091	2.413	5.602	0.197

Note. — A foreground absorption term (assuming Galactic $N_H \approx 6.6 \times 10^{20}$ cm^{-2} (Dickey & Lockman, 1990) and a power-law spectrum of $\Gamma \sim 1.7$) would increase all our luminosities by $\sim 14\%$.

[a]From ACIS-I and ACIS-S data.

[b]On source aperture (radius of 1″ and 3″ for star clusters and H II regions respectively) luminosity.

[c]The background aperture (outside a radius of 5″ and 10″ for star clusters and H II regions respectively) luminosity per pixel.

[d]Uncertainty in the background per pixel, determined by averaging the upper and lower limits calculated using equations (9) and (14) of Gehrels (1986).

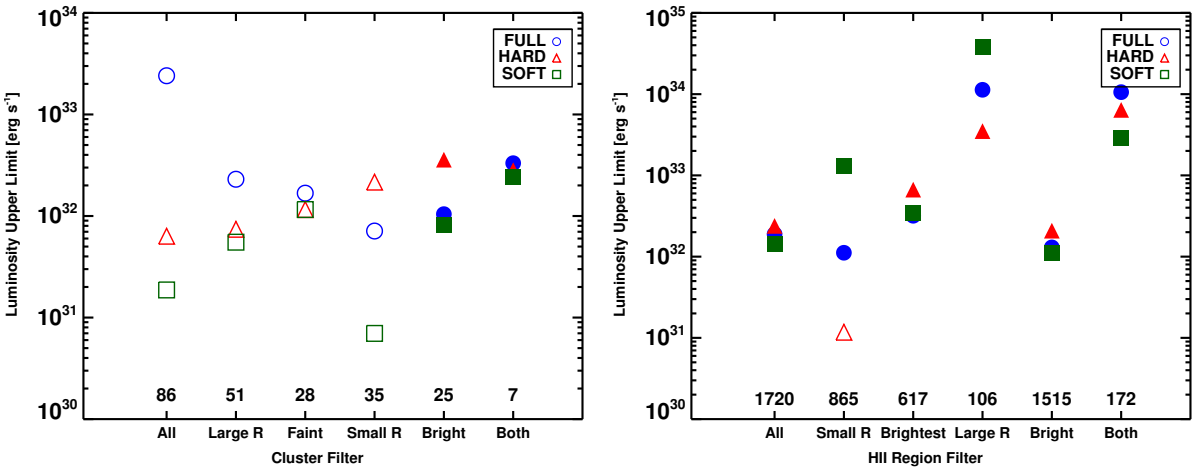

Figure 3.9: Upper limits in erg s^{-1} for a specific filter type in the full band (circles), hard band (triangles), and soft band (squares) for star clusters (left) and H II regions (right). Values above the x-axis indicate the total number of stacked objects (see Table 3.9 for the filter ranges). Filled shapes represent positive source luminosities while empty shapes are negative source luminosities (background-subtracted source aperture counts <0). When stacking star clusters with the 'bright' and 'both' (bright and small) filters we see that the source aperture luminosity becomes positive (average pixel value is larger than the background). This can be attributed to the higher probability of brighter and (in combination) more compact clusters hosting X-ray sources. Star cluster upper limits are approximately two orders of magnitude fainter than those found for M51 (Vulic et al., 2013).

3.6 Discussion

3.6.1 Star Clusters

Since we analyzed the bulge of M31, which is comprised of an old stellar population and thus globular clusters, it is not surprising that our X-ray point sources are predominantly GC-LMXBs (Table 3.4). When comparing the averages of star cluster colour, magnitude, and effective radius our results showed that redder, brighter, and compact star clusters were more likely to host X-ray sources. However, a logistic regression analysis showed that the F475W magnitude is the most significant predictor followed by the effective radius. The F475W−F814W color (an indicator of metallicity in old stellar populations) was not a significant predictor of

whether a cluster hosted an X-ray source. A statistical analysis using logistic regression is a more robust method than comparing averages and as such accurately represents trends in the data. Peacock et al. (2010b) found different trends when using *XMM-Newton* observations of M31 to identify 45 GC-LMXBs, namely that the stellar collision rate (proportional to stellar density and core radius), luminosity, and metallicity are all significant. However, Agar & Barmby (2013) came to similar conclusions to ours when using *HST* data to derive structural parameters for 29 GC-LMXBs, and complementing the sample with published values for a total of 41 GC-LMXBs and 65 non-LMXB GCs. They found the probability of a GC hosting an X-ray source increased with increasing collision rate and proximity to the galaxy center. Metallicity was not as important a predictor but an increasing cluster mass at fixed collision rate decreased the probability of hosting an X-ray source (although the authors stress this may be a sample selection effect). The latter result does not agree with our positive trend between GC magnitude (which scales with mass) and a GC's probability of hosting an LMXB. This discrepancy could be due to our limited sample of bulge GCs that do not have as wide a range in metallicity as GCs at larger galactocentric distances.

Studies of the GC-LMXB connection in spiral galaxies are limited. Rangelov et al. (2012) studied XRBs in the Antennae galaxies and found that massive young star clusters are more likely to host an X-ray source than less massive young clusters. When studying 32 GC-LMXBs in the spiral galaxy M104 with *Chandra*, Di Stefano et al. (2003) found that metal-rich GCs were more likely to host an X-ray source. Bellazzini et al. (1995) found similar trends in the Milky Way. Peacock et al. (2010b) does mention that the observed trends in M31 are weaker than those found for elliptical galaxies, which further stresses the need to analyze the updated star cluster data from PHAT with *Chandra*, along with surveys of other spiral galaxies.

Our stacking results gave upper limits of $\approx 10^{32}$ erg s^{-1} across all bands for different stacks. When stacking star clusters that were brightest (F475W magnitude), most compact (smallest $R_{\rm eff}$), and a combination of the two, we found that the detection significance[14] increased across

[14]aperture luminosity / aperture upper limit

all bands, although not to a statistically significant level. Due to the proximity of M31 the upper limits are approximately two orders of magnitude smaller than for star clusters in M51 (Vulic et al., 2013). Studies of globular clusters in the Milky Way have found a plethora of faint X-ray sources that include quiescent XRBs (typically $L_X \sim 10^{33}$ erg s^{-1}) (Heinke et al., 2005, 2006, 2009, 2010; Bahramian et al., 2014). In GC 47 Tucanae, five classified quiescent LMXBs had a mean $L_X(0.5-2.5\,\mathrm{keV}) \approx 10^{32}$ erg s^{-1} (Heinke et al., 2005). Therefore, assuming M31's GCs are similar to those in the Milky Way, we should be probing this population with our stacking analysis. Given that a single GC may only have a handful of faint LMXBs, even our stacked sample of 4 of the brightest and smallest GCs fails to provide a detection. At this point it seems that stacking star clusters to identify faint XRBs is proving difficult, at least in spiral galaxies/crowded fields. With the higher concentration of X-ray sources in galaxy bulges source crowding is a problem. Along with diffuse emission in spiral disks, this complicates stacking analyses. Specifically, the background level of each image in a stack is larger making it more difficult to detect faint sources in the aperture. Ultimately a detailed, deep survey of a large sample of GCs in an early-type galaxy would be most promising for obtaining a stacking detection.

3.6.2 H II Regions

H II regions emit thermal X-rays at $kT \sim 0.2 - 0.3$ and $0.6 - 0.7$ keV due to shocks from OB star winds and supernovae/supernova remnants (Strickland et al., 2000; Grimes et al., 2005; Tüllmann et al., 2009; Mineo et al., 2012b; Li & Wang, 2013). The lifetimes of H II regions (a few Myr) are long enough that HMXBs can form, providing another possible source of X-ray emission. Therefore we would expect X-ray emission in H II regions to come from various sources, with bright HMXBs and supernova remnants (if present) dominating. Tüllmann et al. (2009) found an HMXB in the giant H II region IC131 in M33, while Ducci et al. (2013) found 2 HMXB candidates in H II regions in M83. Berghea et al. (2013) studied ultraluminous X-ray sources in nearby galaxies and concluded that 18 of 27 were located inside OB associations or

star forming regions. However, most HMXBs are not found in H II regions or OB associations. In the Milky Way, Bodaghee et al. (2012) found clustering between 79 HMXBs and 458 OB associations (7σ for distances < 1 kpc). The average offset of 0.4 ± 0.2 kpc between HMXBs and OB associations was consistent with compact object natal kicks of 100 ± 50 km s^{-1}. The average kinematical age (time from supernova to HMXB phase) was ∼4 Myr. A follow up to this work by Coleiro & Chaty (2013) found the upper limit on kinematical age to be ∼3 Myr. Therefore unless natal kicks are small HMXBs could be located ≈ 6.5′ (400 pc) from H II regions in M31. Based on these results one would expect most X-ray emission from H II regions to be thermal rather than from XRBs.

From Table 3.6 most of the previous classifications for H II regions hosting X-ray point sources in M31 have been supernova remnants as opposed to HMXBs. However, these are only supernova remnant candidates that have been found using optical line ratios (Hα/S II). In addition, our X-ray color-color plot (Figure 3.3) shows that none of the X-ray point sources appear in the supernova remnant regime. When comparing the average radii of matched and unmatched H II regions those that were more compact were the most likely hosts of X-ray sources. Nevertheless, a logistic regression analysis showed that both the luminosity and radius of an H II region were not significant predictors of it hosting an X-ray source. The four H II region matches that are previously unidentified can be classified as HMXB candidates and require further analysis to determine their nature. As with star clusters our stacking results of H II regions gave upper limits of ≈ 10^{32} erg s^{-1} across all bands for most stacks. We saw the most improvement in detection significance (soft band) when filtering by the smallest radii (< 8.5 pc) and $L_{H\alpha} > 4 \times 10^{36}$ erg s^{-1}, although not to a statistically significant level.

3.6.3 *Chandra* Coverage of M31

While most of the *Chandra* observations have been restricted to the central region of M31, an extension of the data to the disk is necessary to probe both young star clusters and the numerous H II regions. The resolution of X-ray data that does cover most of M31 (i.e. *XMM-Newton* and

ROSAT) is not sufficient to distinguish individual X-ray point sources in crowded regions or reliably associate them with clusters. More specifically, with the exquisite resolution of *HST* observations such as the PHAT survey only *Chandra* will allow for robust identification of X-ray counterparts.

Figure 3.1 is truly striking. While *Chandra* ACIS-I data does cover a large portion of the first 8 bricks of the PHAT survey, the remaining bricks and almost the entire northeast quadrant of M31 are unobserved. In M31, *Chandra* has been used mostly for a long-term monitoring program of the supermassive black hole in the nucleus. Other observations throughout the galaxy were used to study supersoft X-ray sources. Due to the degradation of the PSF at large off-axis angles, data outside of the ACIS-S3 chip has poor resolution and therefore is not useful even for stacking. Further motivation lies in the absence of a confirmed HMXB in M31, which can be addressed by using both the H II region and star cluster catalogues available to identify candidates. Investigating the spiral arm regions that the PHAT survey has observed with (future) complementary *Chandra* data would be invaluable to furthering our understanding of the XRB population in M31.

3.7 Summary

We used all 121 publicly available *Chandra* ACIS observations of M31 to complete a study of star clusters and H II regions. Specifically, we analyzed 83 star clusters in the bulge of M31 from the PHAT survey and found 15 unique matches (18%) to 17 X-ray point sources within 1″ (3.8 pc). When correcting our percentage of matches to completeness limits of past surveys we found similar results. The most compact, brightest, and reddest clusters preferentially hosted X-ray sources, on average. Logistic regression showed that the star cluster F475W magnitude was the most important predictor of finding a star cluster X-ray source. This follows from the fact that the most luminous and therefore most massive star clusters are more likely to host XRBs. A less significant predictor was $R_{\rm eff}$, which associated smaller star clusters (probes

compactness to some extent) with X-ray sources. The link between these two properties and XRBs stems from the high densities and larger number of stars that create dynamical conditions most favorable for the formation of XRBs. The F475W−F814W color, an indicator of metallicity in old stellar populations, was not a significant predictor for star clusters hosting X-ray point sources. The majority of clusters in our sample are metal-rich and thus we do not have an evenly distributed sample of blue and red clusters. A more complete survey with a larger spread in metallicity is required to confirm this result. A stacking analysis resulted in non-detections across all energy bands and average upper limits of $\approx 10^{32}$ erg s^{-1}. This is consistent with quiescent XRB luminosities in the Milky Way.

From 1566 H II regions in the field of view of the *Chandra* data only 10 matched to 9 unique X-ray point sources within 3″ (11 pc). On average, the matches corresponded to the most compact H II regions. However, a logistic regression analysis showed that neither the radius nor Hα luminosity was a significant predictor of an H II region hosting an X-ray source. From previous optical emission-line classifications most of these sources were supernova remnant candidates. Four sources that have no previous optical identifications are HMXB candidates. A stacking analysis resulted in upper limits of $\approx 10^{32}$ erg s^{-1} for all energy bands. To advance our understanding of the XRB population in M31, specifically the disk, and probe the faintest extragalactic XRBs, a complete *Chandra* survey of the PHAT region is necessary.

Bibliography

Agar, J. R. R., & Barmby, P. 2013, AJ, 146, 135

Antoniou, V., Zezas, A., Hatzidimitriou, D., & McDowell, J. C. 2009, ApJ, 697, 1695

Arnaud, K. A. 1996, in Astronomical Data Analysis Software and Systems V, ed. G. H. Jacoby & J. Barnes, Vol. 101 (ASP Conference Series), 17

Azimlu, M., Marciniak, R., & Barmby, P. 2011, AJ, 142, 139

Bahramian, A., Heinke, C. O., Sivakoff, G. R., et al. 2014, ApJ, 780, 127

Barnard, R., Galache, J. L., Garcia, M. R., et al. 2012a, ApJ, 756, 32

Barnard, R., Garcia, M., & Murray, S. S. 2012b, ApJ, 757, 40

Barnard, R., Garcia, M. R., & Murray, S. S. 2013, ApJ, 770, 148

Barnard, R., Garcia, M. R., Primini, F., et al. 2014, ApJ, 780, 83

Belczynski, K., Kalogera, V., Rasio, F. A., et al. 2008, ApJS, 174, 223

Bellazzini, M., Pasquali, A., Federici, L., Ferraro, F. R., & Pecci, F. F. 1995, ApJ, 439, 687

Berghea, C. T., Dudik, R. P., Tincher, J., & Winter, L. M. 2013, ApJ, 776, 100

Bhadkamkar, H., & Ghosh, P. 2012, ApJ, 746, 22

—. 2013, ArXiv e-prints, arXiv:1301.1283

—. 2014, ApJ, 784, 97

Bodaghee, A., Tomsick, J. A., Rodriguez, J., & James, J. B. 2012, ApJ, 744, 108

Bondi, H., & Hoyle, F. 1944, MNRAS, 104, 273

Brandt, W. N., Hornschemeier, A. E., Schneider, D. P., et al. 2001a, ApJ, 558, L5

Brandt, W. N., Alexander, D. M., Hornschemeier, A. E., et al. 2001b, AJ, 122, 2810

Brandt, W. N., Hornschemeier, A. E., Alexander, D. M., et al. 2001c, AJ, 122, 1

Broos, P. S., Townsley, L. K., Feigelson, E. D., et al. 2010, ApJ, 714, 1582

Caldwell, N., Schiavon, R., Morrison, H., Rose, J. A., & Harding, P. 2011, AJ, 141, 61

Clark, G. W. 1975, ApJ, 199, L143

Coleiro, A., & Chaty, S. 2013, ApJ, 764, 185

Dalcanton, J. J., Williams, B. F., Lang, D., et al. 2012, ApJS, 200, 18

Di Stefano, R., Kong, A. K. H., VanDalfsen, M. L., et al. 2003, ApJ, 599, 1067

Dickey, J. M., & Lockman, F. J. 1990, ARA&A, 28, 215

Ducci, L., Sasaki, M., Haberl, F., & Pietsch, W. 2013, A&A, 553, A7

Fabbiano, G. 2006, ARA&A, 44, 323

Fabian, A. C., Pringle, J. E., & Rees, M. J. 1975, MNRAS, 172, 15P

Fruscione, A., McDowell, J. C., Allen, G. E., et al. 2006, in Society of Photo-Optical Instrumentation Engineers (SPIE) Conference Series, Vol. 6270, CIAO: Chandra's data analysis system

Gehrels, N. 1986, ApJ, 303, 336

Gilfanov, M. 2004, MNRAS, 349, 146

Gordon, K. D., Bailin, J., Engelbracht, C. W., et al. 2006, ApJ, 638, L87

Graessle, D. E., Evans, I. N., Glotfelty, K., et al. 2006, in Society of Photo-Optical Instrumentation Engineers (SPIE) Conference Series, Vol. 6270, The Chandra X-ray Observatory calibration database (CalDB): building, planning, and improving

Grimes, J. P., Heckman, T., Strickland, D., & Ptak, A. 2005, ApJ, 628, 187

Grimm, H.-J., Gilfanov, M., & Sunyaev, R. 2002, A&A, 391, 923

—. 2003, MNRAS, 339, 793

Heinke, C. O., Cohn, H. N., & Lugger, P. M. 2009, ApJ, 692, 584

Heinke, C. O., Grindlay, J. E., Edmonds, P. D., et al. 2005, ApJ, 625, 796

Heinke, C. O., Grindlay, J. E., Lugger, P. M., et al. 2003, ApJ, 598, 501

Heinke, C. O., Wijnands, R., Cohn, H. N., et al. 2006, ApJ, 651, 1098

Heinke, C. O., Altamirano, D., Cohn, H. N., et al. 2010, ApJ, 714, 894

Hofmann, F., Pietsch, W., Henze, M., et al. 2013, A&A, 555, A65

Hornschemeier, A. E., Brandt, W. N., Garmire, G. P., et al. 2001, ApJ, 554, 742

Hurley, J. R., Tout, C. A., & Pols, O. R. 2002, MNRAS, 329, 897

Iben, Jr., I., Tutukov, A. V., & Yungelson, L. R. 1995, ApJS, 100, 217

Johnson, L. C., Seth, A. C., Dalcanton, J. J., et al. 2012, ApJ, 752, 95

Kaaret, P. 2002, ApJ, 578, 114

Katz, J. I. 1975, Nature, 253, 698

Kiel, P. D., & Hurley, J. R. 2006, MNRAS, 369, 1152

Kilgard, R. E., Cowan, J. J., Garcia, M. R., et al. 2005, ApJS, 159, 214

Kim, D.-W., & Fabbiano, G. 2004, ApJ, 611, 846

Kim, D.-W., Fabbiano, G., Ivanova, N., et al. 2013, ApJ, 764, 98

Kong, A. K. H., Garcia, M. R., Primini, F. A., et al. 2002, ApJ, 577, 738

Lehmer, B. D., Alexander, D. M., Bauer, F. E., et al. 2010, ApJ, 724, 559

Li, J.-T., & Wang, Q. D. 2013, MNRAS, 428, 2085

Lipunov, V. M., Postnov, K. A., Prokhorov, M. E., & Bogomazov, A. I. 2009, Astronomy Reports, 53, 915

Lutovinov, A. A., Revnivtsev, M. G., Tsygankov, S. S., & Krivonos, R. A. 2013, MNRAS, 431, 327

Marigo, P., Girardi, L., Bressan, A., et al. 2008, A&A, 482, 883

Massey, P., Olsen, K. A. G., Hodge, P. W., et al. 2006, AJ, 131, 2478

Mineo, S., Gilfanov, M., & Sunyaev, R. 2012a, MNRAS, 419, 2095

—. 2012b, MNRAS, 426, 1870

Mineo, S., Fabbiano, G., D'Abrusco, R., et al. 2014, ApJ, 780, 132

Muno, M. P., Bauer, F. E., Baganoff, F. K., et al. 2009, ApJS, 181, 110

Nebot Gómez-Morán, A., Motch, C., Barcons, X., et al. 2013, A&A, 553, A12

Paolillo, M., Puzia, T. H., Goudfrooij, P., et al. 2011, ApJ, 736, 90

Peacock, M. B., Maccarone, T. J., Knigge, C., et al. 2010a, MNRAS, 402, 803

Peacock, M. B., Maccarone, T. J., Kundu, A., & Zepf, S. E. 2010b, MNRAS, 407, 2611

Persic, M., & Rephaeli, Y. 2007, A&A, 463, 481

Pooley, D., Lewin, W. H. G., Anderson, S. F., et al. 2003, ApJ, 591, L131

R Development Core Team. 2008, R: A Language and Environment for Statistical Computing, R Foundation for Statistical Computing, Vienna, Austria, ISBN 3-900051-07-0

Ranalli, P., Comastri, A., & Setti, G. 2003, A&A, 399, 39

Rangelov, B., Chandar, R., Prestwich, A., & Whitmore, B. C. 2012, ApJ, 758, 99

Revnivtsev, M., Lutovinov, A., Churazov, E., et al. 2008, A&A, 491, 209

Sazonov, S., Revnivtsev, M., Gilfanov, M., Churazov, E., & Sunyaev, R. 2006, A&A, 450, 117

Shaw Greening, L., Barnard, R., Kolb, U., Tonkin, C., & Osborne, J. P. 2009, A&A, 495, 733

Shtykovskiy, P. E., & Gilfanov, M. R. 2007, Astronomy Letters, 33, 299

Siess, L., Izzard, R. G., Davis, P. J., & Deschamps, R. 2013, A&A, 550, A100

Sivakoff, G. R., Jordán, A., Sarazin, C. L., et al. 2007, ApJ, 660, 1246

Skrutskie, M. F., Cutri, R. M., Stiening, R., et al. 2006, AJ, 131, 1163

Stiele, H., Pietsch, W., Haberl, F., et al. 2011, A&A, 534, A55

Strickland, D. K., Heckman, T. M., Weaver, K. A., & Dahlem, M. 2000, AJ, 120, 2965

Swartz, D. A., Ghosh, K. K., Tennant, A. F., & Wu, K. 2004, ApJS, 154, 519

Swartz, D. A., Soria, R., Tennant, A. F., & Yukita, M. 2011, ApJ, 741, 49

Taylor, M. B. 2005, in Astronomical Society of the Pacific Conference Series, Vol. 347, Astronomical Data Analysis Software and Systems XIV, ed. P. Shopbell, M. Britton, & R. Ebert, 29

Trudolyubov, S., & Priedhorsky, W. 2004, ApJ, 616, 821

Tüllmann, R., Long, K. S., Pannuti, T. G., et al. 2009, ApJ, 707, 1361

Ubeda, L., & et al. 2012, Advanced Camera for Surveys Instrument Handbook for Cycle 21 v. 12.0 (Baltimore: STScI)

Voss, R., & Gilfanov, M. 2007a, A&A, 468, 49

—. 2007b, MNRAS, 380, 1685

Vulic, N., Barmby, P., & Gallagher, S. C. 2013, ApJ, 763, 96

Walton, D. J., Roberts, T. P., Mateos, S., & Heard, V. 2011, MNRAS, 416, 1844

Williams, B. F., Garcia, M. R., Kong, A. K. H., et al. 2004, ApJ, 609, 735

Zacharias, N., Urban, S. E., Zacharias, M. I., et al. 2004, AJ, 127, 3043

Zezas, A., Fabbiano, G., Rots, A. H., & Murray, S. S. 2002, ApJ, 577, 710

Zhang, Z., Gilfanov, M., Voss, R., et al. 2011, A&A, 533, A33

Chapter 4

Milky Way Globular Cluster Metallicity and Low-Mass X-ray Binaries: The Red Giant Influence

4.1 Executive Summary

Galactic and extragalactic studies have shown that metal-rich globular clusters (GCs) are approximately three times more likely to host bright low-mass X-ray binaries (LMXBs) than metal poor GCs. There is no satisfactory explanation for this metallicity effect. We used the assumption that the number density of red giant branch (RGB) stars is larger in metal-rich GCs, and thus the cause of the metallicity effect. Using *HST* data from the ACS and WFPC2 instruments for 109 unique Milky Way GCs, we investigated whether RGB star density was correlated with GC metallicity. We fit isochrones to calculate the number of RGB stars, and normalized by the GC mass and fraction of observed GC luminosity, and determined density using the volume at the half-light radius (r_h). The RGB star number density correlated with metallicity [Fe/H], giving a Spearman Rank p-value of 0.00016 and coefficient $r_s = 0.35$. This correlation may be biased by a possible dependence of r_h on [Fe/H], although studies

have shown that r_h is correlated with galactocentric distance and independent of [Fe/H]. Tidal stripping from the bulge, which is thought to cause this dependence, can also promote LMXB formation. No correlation between the RGB star number density and metallicity was found when using only the GCs that hosted quiescent LMXBs (qLMXBs). A complete qLMXB census in our Galaxy is needed to further probe the metallicity effect, which will be possible with the upcoming launch of *eROSITA*.

4.2 Introduction

Low-mass X-ray binaries (LMXBs) have companion stars of masses $\lesssim 1.5\ M_\odot$ and are found in the field of a galaxy as well as in globular clusters (GCs). LMXBs form more efficiently in GCs due to increased stellar densities (Katz, 1975; Clark, 1975; Fabian et al., 1975; Pooley et al., 2003), with studies of Milky Way LMXBs finding that their formation rate is 100 times greater in GCs compared to the field (Katz, 1975; Clark, 1975). Similar results have been found in elliptical galaxies (Sarazin et al., 2003; Jordán et al., 2004; Kim et al., 2006; Sivakoff et al., 2007; Kundu et al., 2007; Humphrey & Buote, 2008; Kim et al., 2009). Numerous relationships exist between GC properties and LMXBs. Globular clusters that are brighter/more massive, more compact (smaller core radius r_c), and more metal-rich (redder) favour LMXB formation in both the Milky Way (Grindlay, 1993; Bellazzini et al., 1995) and other nearby galaxies (Kundu et al., 2002; Maccarone et al., 2004; Jordán, 2004; Trudolyubov & Priedhorsky, 2004; Sivakoff et al., 2007; Kundu et al., 2007; Peacock et al., 2010; Paolillo et al., 2011; Kim et al., 2013; Agar & Barmby, 2013; Mineo et al., 2014; Vulic et al., 2014). These studies have confirmed that metal-rich clusters are ~ 3 times more likely to host bright ($L_X > 10^{36}$ erg s^{-1}) LMXBs, with limiting luminosities $> 10^{36}$ erg s^{-1} and $> 10^{37}$ erg s^{-1} for Milky Way and extragalactic observations respectively. Extragalactic studies have probed the dependence down to $> 10^{36}$ erg s^{-1} and found the same relation but at a lower significance (Kim et al., 2013). The dependence on mass and compactness is straightforward to explain because more stars and a higher

density promote stellar interactions that create binaries. However, the metallicity dependence is still a mystery.

Various explanations have been suggested to explain the metallicity dependence, such as magnetic braking in main sequence stars (Ivanova & Kalogera, 2006) or irradiation-induced stellar winds in low-metallicity stars (Maccarone et al., 2004). Ivanova et al. (2012) posited that the difference in number densities and average masses of red giant stars in metal-rich versus metal-poor extragalactic GCs can explain the difference. Depending on their evolutionary state, GC-LMXBs can have either a main sequence, red giant, or white dwarf companion. Red giants promote dynamical formation of LMXBs via binary exchange interactions and physical collisions. A strong argument for red giants being the donor stars in GC-LMXBs arises from the fact that the bright GC-LMXBs have X-ray luminosities $> 10^{37}$ erg s^{-1}, and thus require companions with higher mass loss rates. A full population synthesis study is still needed to confirm the red giant scenario, but here we attempt to address the observational effect.

We will use observations of galactic GCs to compare the number of red giants in clusters with and without LMXBs. In the Milky Way, 13 bright LMXBs are known in 12 GCs. To assess whether the number of red giants in LMXB-hosting clusters is proportionally larger than in GCs without LMXBs, we will use the method devised by Nataf et al. (2013, hereafter N13). N13 used 72 Galactic GCs to study the red giant branch bump brightness and number counts by combining data from the *Hubble Space Telescope* (*HST*) Advanced Camera for Surveys (ACS) and Wide-field Planetary Camera 2 (WFPC2) instruments. They found that the 'bump' brightness and number have a strong dependence on metallicity, foreshadowing a likely dependence of GC-LMXBs on the number of red giants. They reported the total number of red giants in 48 GCs, which we will use in addition to 61 other GCs to investigate the effect of red giants on the metallicity dependence of LMXBs in Galactic GCs.

4.3 Data

We use data from two large *HST* surveys of Milky Way GCs. The first was carried out by Piotto et al. (2002) using the F439W and F555W filters on the WFPC2 instrument. They studied 74 GCs with a wide range of properties by investigating colour-magnitude diagrams (CMDs), which are complete to approximately the main sequence turnoff. The Planetary Camera was centred on the cluster centre in each case. The more recent treasury survey by Sarajedini et al. (2007) and Dotter et al. (2007) used the F606W and F814W filters on the ACS Wide Field Camera instrument. Each cluster was centred in the ACS field. The program studied 71 GCs and obtained photometry with $S/N \gtrsim 10$ for stars down to 0.2 $M_{\odot}$. The benefit of using these treasury surveys is that in studying various aspects of Galactic GCs the authors produced precise photometric catalogues. Both catalogues have carried out artificial star tests that confirm completeness on the RGB. N13 used 72 Galactic GCs by combining the ACS and WFPC2 surveys. Because the authors were studying the RGB bump, they only chose clusters that had well-populated RGBs and RGB bumps ($N_{\rm RGBB} \geq 10$), and were not affected by differential reddening. They called this their 'gold' sample, which consisted of 48 GCs for which they reported RGB numbers. The remaining 24 GCs that made up their 'silver' sample had anomalous RGB bumps. The RGB numbers from the 48 GCs in the gold sample of N13 will be used in our study; we independently determine $N_{\rm RGB}$ for the remaining clusters. Combining the ACS and WFPC2 datasets there are 109 unique Galactic GCs, of which N13 analysed 48. The remaining 61 GCs consist of 34 from the ACS survey and 27 from the WFPC2 survey. To be consistent in our analysis we followed the methods of N13 to obtain RGB numbers for these GCs. First, we summarize some issues regarding the data that have been addressed by N13. The photometric filters used in each survey were different, and thus a standard calibration needed to be adopted. Photometric values were transformed from the F439W/F555W and F606W/F814W filters for WFPC2 and ACS, respectively, into the Johnson $(V, B-V)$ and $(I, V-I)$ planes in the original catalogue papers. A comparison between 13 GCs that were common to both surveys found that the difference in the derived V magnitudes was

negligible. The magnitudes from both catalogues are not reddening-corrected.

4.4 Isochrone Fitting

Before we determined the number of RGB stars, we plotted isochrones for each of the 61 GCs to guide our analysis. We plotted isochrones only to identify the different regions of the CMD, such as the subgiant, red giant, asymptotic giant, and horizontal branches. We do not aim to determine the age, distance, or metallicity of a GC using this method but only to better approximate the RGB. We used the isochrones provided by the Dartmouth Stellar Evolution Database[1], which provides isochrone grids based on the original 2008 version photometric systems (Dotter et al., 2008). We used the ACS Galactic Globular Cluster Survey isochrones that include the BVI/F606W/F814W empirical colours for our ACS dataset. These isochrones were created by Dotter et al. (2007) specifically for the ACS catalogue we use here. We used the empirical BVI colour isochrones from VandenBerg & Clem (2003) for our WFPC2 dataset. All isochrone grids have age intervals of 250 Myr between ages of $1 - 5$ Gyr, and 500 Myr intervals between ages of $5 - 15$ Gyr. Metallicities for [Fe/H] range from -2.5 to $+0.5$, with steps of 0.5 in the range of interest for our work (0.0 to -2.5). The α-enhancement [α/Fe] is another probe of the metallicity, and in the models it refers to enhancements in the following α-capture elements: O, Ne, Mg, Si, S, Ca, Ti. [α/Fe] ranges from -2 to 8 in steps of 2. The models assume an initial He mass fraction Y = 0.245 + 1.54Z, with additional grids using Y_{init} of 0.33 and 0.40 for [α/Fe] of 0.0 and 0.4 (see Table 2 of Dotter et al. (2007) for more details).

To determine the best-fit isochrones for each of our GCs, we first assumed the metallicity [Fe/H] given by Harris (1996, 2010 edition) and found the nearest value of [Fe/H] from the isochrone grid. We then plotted isochrones with ages ranging from $1 - 15$ Gyr for each of the 10 different combinations of [α/Fe] and initial He mass fraction values on our CMDs. The isochrone BVI magnitudes were adjusted for each cluster using its distance from the Sun

[1] http://stellar.dartmouth.edu/models

(Harris, 1996, 2010 edition). Because we used the raw Johnson BVI magnitudes that were not corrected for reddening, we shifted our isochrones based on the $E(B-V)$ values given in Harris (1996, 2010 edition). For the ACS survey, since we were working in the $(I, V-I)$ plane, we converted the reddening using $E(V-I) = 1.26 \times E(B-V)$ (Cardelli et al., 1989; Barmby et al., 2000). We obtain A_V and A_I using the standard Galactic extinction law (Cardelli et al., 1989). A number of GCs had all their isochrones shifted away from the main sequence and RGB, with no overlap. This arose from the uncertainty in the distance to a GC and also the conversion factor for reddening, which caused inaccurate $E(V-I)$ values. For these isochrones we shifted the $E(V-I)$ values to account for this effect. We chose the best fitting CMD that most accurately represented the main sequence subgiant, and red giant branches. We cross-checked the ages determined from isochrone fitting with results from Dotter et al. (2010), who used the *HST* magnitude plane for isochrone fitting, to ensure our results were consistent. We report the results of our isochrone fitting in Table 4.1, where the parameters do not reflect precise values for each cluster but instead the values for a specific isochrone.

Table 4.1: Isochrone Fitting Parameters

Globular Cluster	Age (Gyr)	[Fe/H]	[α/H]	E(B−V)	E(V−I)	Instrument
Arp 2	13.0	-2.0	2	0.15	0.19	ACS
E 3	13.0	-1.0	2	0.33	0.42	ACS
IC 4499	12.0	-1.5	2	0.25	0.32	ACS
NGC 288	12.5	-1.5	4	0.03	0.04	ACS
NGC 2298	13.0	-2.0	2	0.27	0.33	ACS
NGC 4147	13.0	-2.0	2	0.06	0.08	ACS
NGC 4590	13.0	-2.0	2	0.08	0.09	ACS
NGC 4833	13.0	-2.0	4	0.38	0.48	ACS
NGC 5053	13.5	-2.5	2	0.04	0.05	ACS
NGC 5139	12.0	-1.5	2	0.17	0.21	ACS
NGC 5466	13.0	-2.0	2	0.04	0.04	ACS
NGC 6101	13.0	-2.0	2	0.15	0.19	ACS
NGC 6121	12.5	-1.0	4	0.41	0.52	ACS
NGC 6144	13.5	-2.0	2	0.49	0.62	ACS
NGC 6366	12.0	-0.5	2	0.71	0.89	ACS
NGC 6397	13.5	-2.0	2	0.21	0.27	ACS
NGC 6426	12.0	-2.0	2	0.45	0.56	ACS
NGC 6496	12.0	-0.5	2	0.21	0.26	ACS

Globular Cluster	Age (Gyr)	[Fe/H]	[α/H]	E(B−V)	E(V−I)	Instrument
NGC 6535	13.0	-2.0	2	0.48	0.60	ACS
NGC 6656	12.5	-1.5	2	0.40	0.50	ACS
NGC 6715	12.0	-1.5	2	0.17	0.21	ACS
NGC 6717	13.0	-1.5	2	0.27	0.34	ACS
NGC 6779	13.5	-2.0	2	0.28	0.35	ACS
NGC 6809	13.5	-2.0	2	0.14	0.18	ACS
NGC 6838	12.5	-1.0	2	0.27	0.34	ACS
NGC 7099	13.0	-2.5	2	0.09	0.11	ACS
Palomar 1	7.0	-0.5	2	0.16	0.20	ACS
Palomar 12	9.5	-1.0	0	0.06	0.08	ACS
Palomar 15	13.0	-2.0	2	0.47	0.59	ACS
Palomar 2	12.0	-1.5	2	1.19	1.50	ACS
Ruprecht 106	12.0	-1.0	2	0.28	0.35	ACS
Terzan 7	10.0	-1.5	2	0.23	0.28	ACS
Terzan 8	8.0	-0.5	0	0.08	0.10	ACS
IC 1257	13.0	-2.0	4	0.16	0.20	ACS
NGC 1904	12.0	-1.5	0	0.73	-	WFPC2
NGC 2419	12.0	-1.5	6	0.01	-	WFPC2
NGC 4372	12.5	-2.0	4	0.08	-	WFPC2
NGC 5694	13.5	-2.0	8	0.39	-	WFPC2
NGC 5946	13.5	-2.0	8	0.09	-	WFPC2
NGC 6235	13.5	-1.5	8	0.54	-	WFPC2
NGC 6256	12.0	-1.5	6	0.31	-	WFPC2
NGC 6266	10.0	-1.0	0	1.09	-	WFPC2
NGC 6273	12.0	-1.0	0	0.47	-	WFPC2
NGC 6287	12.0	-1.5	2	0.38	-	WFPC2
NGC 6293	13.5	-2.0	8	0.60	-	WFPC2
NGC 6316	13.5	-2.0	4	0.36	-	WFPC2
NGC 6325	13.5	-0.5	0	0.54	-	WFPC2
NGC 6342	13.5	-1.5	6	0.91	-	WFPC2
NGC 6355	13.5	-0.5	0	0.46	-	WFPC2
NGC 6380	13.5	-1.5	2	0.77	-	WFPC2
NGC 6401	5.0	-1.0	8	1.17	-	WFPC2
NGC 6440	12.5	-1.0	6	0.72	-	WFPC2
NGC 6453	11.0	-0.5	0	1.07	-	WFPC2
NGC 6517	13.5	-1.5	0	0.64	-	WFPC2
NGC 6522	9.0	-1.0	0	1.08	-	WFPC2
NGC 6539	13.0	-1.5	8	0.48	-	WFPC2
NGC 6540	7.0	-0.5	0	1.02	-	WFPC2
NGC 6544	12.0	-1.5	0	0.66	-	WFPC2
NGC 6642	13.0	-1.5	2	0.76	-	WFPC2
NGC 6712	13.5	-1.5	8	0.40	-	WFPC2
Lynga 7	12.5	-1.0	2	0.45	-	WFPC2

Isochrone fitting parameters for the 61 GCs that did not report RGB numbers in N13. The age, metallicity ([Fe/H]), and helium enhancement ([α/Fe]) are the values used for the best fitting isochrones and do not reflect precise values for each cluster. The $E(B-V)$ values are taken from Harris (1996, 2010 edition), while the $E(V-I)$ values were derived using $E(V-I) = 1.26 \times E(B-V)$ (Cardelli et al., 1989; Barmby et al., 2000). This conversion was not accurate for all clusters and therefore an offset was introduced to properly align the isochrone. The last column indicates which survey the photometric data was taken from.

4.5 Red Giant Branch Star Numbers

In order to determine the number of RGB stars in each GC, $N_{\rm RGB}$, we inspected the CMDs of each cluster individually to create a bounded area that represented the RGB. Following the technique of N13 (D. M. Nataf, priv. comm.), we required the bounding region for the RGB to be as long and wide as possible. We selected the lower bound to be approximately 0.5 magnitudes above the mean brightness of the subgiant branch. This attempts to eliminate any foreground stars that may be contaminating the region. Specifically, some clusters had abrupt subgiant branches where the main sequence and RGB are not well-separated, introducing more contamination from foreground stars near the subgiant branch region of the CMD. The upper bound was selected based on the decreasing density of stars towards the tip of the RGB, and the beginning of the curve in the distribution of stars that represents the start of the asymptotic giant branch. In some cases the horizontal branch could be used as a reference point for the end of the RGB. We limited how wide the parallelogram that results from the lower and upper bounds can be for two reasons. First, moving too far blueward of the RGB can result in horizontal branch stars being included in our estimate of $N_{\rm RGB}$. Second, the wider our parallelogram, the higher incidence of foreground stars we can expect to contaminate our sample, further biasing our approximation. In Figure 4.1 we show the CMD of NGC 7099, a metal-poor GC with minimal extinction and large concentration parameter. The blue parallelogram reflects the criteria just summarized, and includes 332 RGB stars.

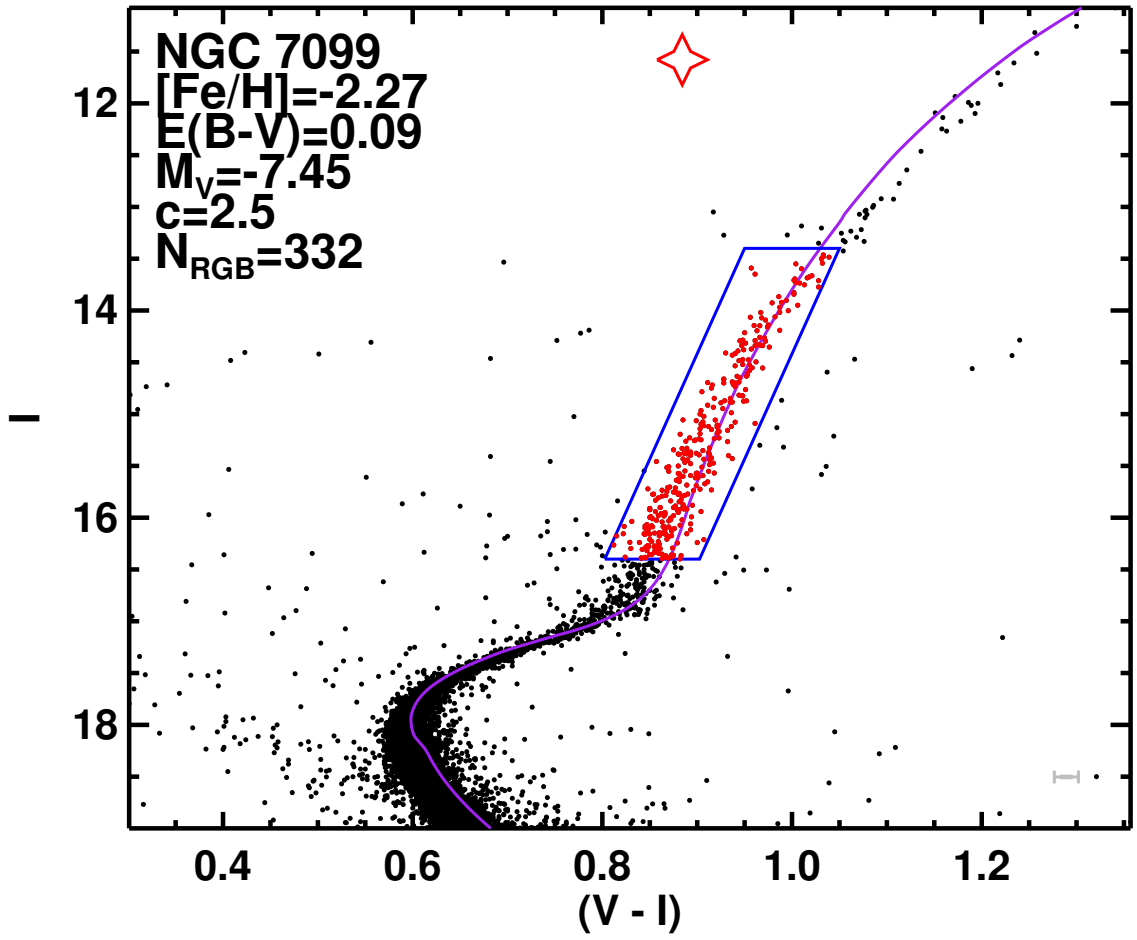

Figure 4.1: Colour-magnitude diagram of NGC 7099 in the Johnson $(I, V-I)$ plane without reddening correction. The overplotted best fitting isochrone has parameters given in Table 4.1. The blue parallelogram corresponds to the conservative estimate of the region where red giant branch stars exist, giving the number of red giant branch stars in the cluster $N_{\rm RGB}$. The open star at top-centre indicates that the cluster hosts a quiescent LMXB. Various cluster parameters from Harris (1996, 2010 edition), including the absolute magnitude M_V and concentration parameter c are shown at top-left. Average photometric uncertainties are represented by the grey error bar at bottom-right. CMDs for the remaining ACS GCs and all WFPC2 GCs are in Appendices D and E respectively.

4.6 Normalizations

4.6.1 Globular Cluster Luminosity and Foreground Contamination

A number of normalizations were required in order to effectively use the $N_{\rm RGB}$ parameter in our analysis. The first and most obvious is for the instrument field of view. For the 109 unique GCs that we have determined $N_{\rm RGB}$ for, 71 come from the ACS survey and 38 from the WFPC2 survey. The ACS instrument has a slight parallelogram shape and is comprised of the Wide Field Camera 1 and 2, with a total field of view of 202″ by 202″. Conversely, the WFPC2 is made up of 4 CCDs, 3 wide field cameras (WF2, WF3, WF4), each with field of view 75″ by 75″, and the Planetary Camera (PC1), having a 32″ by 32″ field of view. Therefore the WFPC2 is essentially a square of area 150″ a side with a piece missing due to the size of PC1. We needed to account for the difference in observed area of each cluster given the different fields of view of ACS and WFPC2. All GCs in the ACS survey were observed twice in each filter, with the fields overlapping each other close to the 100% level. The WFPC2 survey was a snapshot program where the numerous exposures overlapped similar to the ACS survey. We determined the total area observed for each cluster (in pc^2) by counting the nonzero pixels in the merged images for both the ACS and WFPC2 surveys.

However, the issue was exacerbated because the fraction of each GC observed (physical size) depends on the instrument field of view and the cluster's distance. Therefore the appropriate correction involved determining the fraction of cluster luminosity observed, $L_{\rm frac}$= $L_{\rm obs}/L_{\rm total}$, where $L_{\rm obs}$ is observed cluster luminosity and $L_{\rm total}$ is the total luminosity of the cluster. $L_{\rm total}$ was calculated by using GC absolute magnitudes M_V[2] from Harris (1996, 2010 edition). No uncertainties are reported for any of the M_V values and so we adopt a conservative universal uncertainty of 0.2 magnitudes, consistent with the uncertainty of the globular cluster luminosity function peak (Kavelaars & Hanes, 1997). For this calculation and others, we used the reference values from Mamajek (2012) for the Sun[3] of $L_{\odot,\rm bol} = 3.8270 \pm 0.0014 \times 10^{33}$ erg

[2]These absolute magnitudes are corrected for foreground Galactic extinction.

[3]https://sites.google.com/site/mamajeksstarnotes/basic-astronomical-data-for-the-sun

s^{-1}, $M_{\odot,\mathrm{bol}} = 4.7554 \pm 0.0004$, $m_{\odot,\mathrm{bol}} = -26.8167 \pm 0.0004$. The observed cluster luminosities L_{obs} were calculated by summing the photometry from each cluster field. Because each star in a field of view has an apparent magnitude m_V associated with it, we converted to flux and determined L_{obs}. By working in the $V-$band for all clusters and using M_V to get L_{total} we remain consistent within one passband. However, by summing the flux from all stars in a given field of view we were also including the contribution from foreground stars, which biases our calculations. This has the opposite effect of extinction in that it would raise our total observed luminosity. To account for this effect we estimated the contamination from Galactic foreground stars using the Besançon models[4] (Robin et al., 2003). Using the (Galactic) coordinates from the centres of the ACS and WFPC2 images (not always the cluster centres), along with the solid angle in deg^2, we obtained a detailed list of foreground stars parameters for each cluster. For the solid angle, we used the area for each cluster field of view as described above. The models produce reliable predictions for the luminosity and colour distributions in the optical/near-infrared for the stars expected to be in the field of view. We used the apparent magnitudes m_V and given visual extinctions A_V from the model to determine the total absolute V magnitude from foreground stars, $M_V{}^{fgstars}$. Subtracting this foreground flux from the total observed flux allowed us to calculate accurate observed cluster luminosities.

For some of the clusters we were not able to accurately determine a value for L_{frac}, likely due to the uncertainty associated with distance, extinction, and the foreground star modelling/photometry. For 3 GCs, namely Lynga 7, Palomar 12, Terzan 7, we had to remove the brightest star from the photometric catalogue. These stars were $2-3$ magnitudes brighter than the next brightest star, which was part of the smooth distribution of cluster stars. For NGC 6453 and Palomar 2, we used updated extinction values $E(B-V)$ from Schlafly & Finkbeiner (2011) obtained using the NASA/IPAC database[5]. Our L_{frac} values vary from $5\% - 97\%$, where the lower limit corresponds to NGC 4372, a large, nearby (5.8 kpc) GC that was observed with the small field of view of WFPC2. The upper limit of 97% is for Palomar 1, a very dense GC with small

[4] http://model.obs-besancon.fr/
[5] http://irsa.ipac.caltech.edu/applications/DUST/

core and half-light radii observed with ACS. In Figure 4.2 we show the number of RGB stars normalized by the observed GC luminosity vs. metallicity. LMXBs are indicated by filled red circles and qLMXBs by open blue circles. The cluster NGC 6440 has an LMXB and qLMXB and is shown as a red plus. NGC 7078 (M15) also has 2 LMXBs. We used results compiled by Verbunt & Lewin (2006) for LMXBs and qLMXBs in Galactic GCs. The uncertainties on [Fe/H] were taken from Carretta et al. (2009). For the five GCs in our sample that didn't have uncertainties on [Fe/H], IC 1257, Lynga 7, NGC 6426, NGC 6540, and Terzan 8, we set them to the mean uncertainty value of the remaining GCs. The $N_{\rm RGB}$ distribution still needs to be normalized in order to appropriately assess its impact on LMXB formation.

4.6.2 Globular Cluster Mass

Normalizing $N_{\rm RGB}$ by the fraction of observed luminosity accounts for RGB stars that otherwise would have been observed had the field of view been larger. However, even if each GC had $L_{\rm frac}$= 1, our result would still be biased towards clusters that are more massive, which by extension have a larger number of RGB stars. Therefore we need to normalize $N_{\rm RGB}$ by the mass of each GC. We calculated cluster masses using our value for the total cluster luminosity $L_{\rm total}$ and the mass-to-light ratio M/L of the cluster. McLaughlin & van der Marel (2005) tabulated $V-$band M/L (Table 8, column 8 of their paper) for 148 Galactic GCs, which includes the 109 GCs in our work. The M/L ratios were derived using the code from Bruzual & Charlot (2003) and the disk initial mass function of Chabrier (2003). We used our cluster luminosities to determine the mass of each GC in our sample. In Figure 4.3 we show the relationship between $N_{\rm RGB}/L_{\rm frac}$ and the GC mass.

As expected, a strong correlation exists where the number of RGB stars increases with GC mass. The datapoint with a large uncertainty in $N_{\rm RGB}$ is NGC 4372, which happens to be the cluster for which $L_{\rm frac}$ was 5%, having a large uncertainty of 15% (300% relative). A weighted

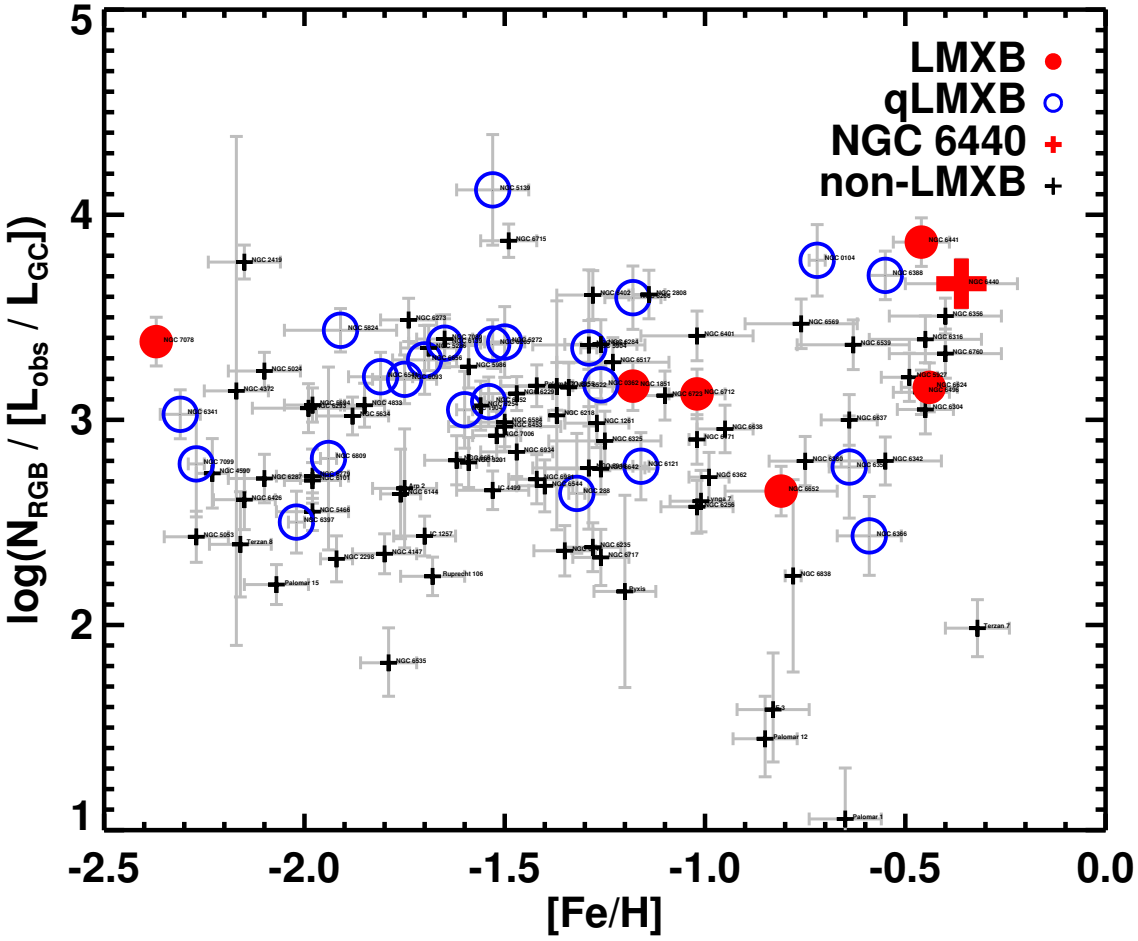

Figure 4.2: RGB star number vs. metallicity [Fe/H]. Black plusses represent normal GCs, open blue circles are GCs hosting quiescent LMXBs and filled red circles are GCs hosting bright LMXBs. NGC 6440, which has an LMXB and qLMXB, is shown with a red plus. GC names are indicated near each datapoint. The $N_{\rm RGB}$ parameter is expected to scale linearly with mass and thus needs to be normalized in order to assess any relationship between RGB stars and LMXBs.

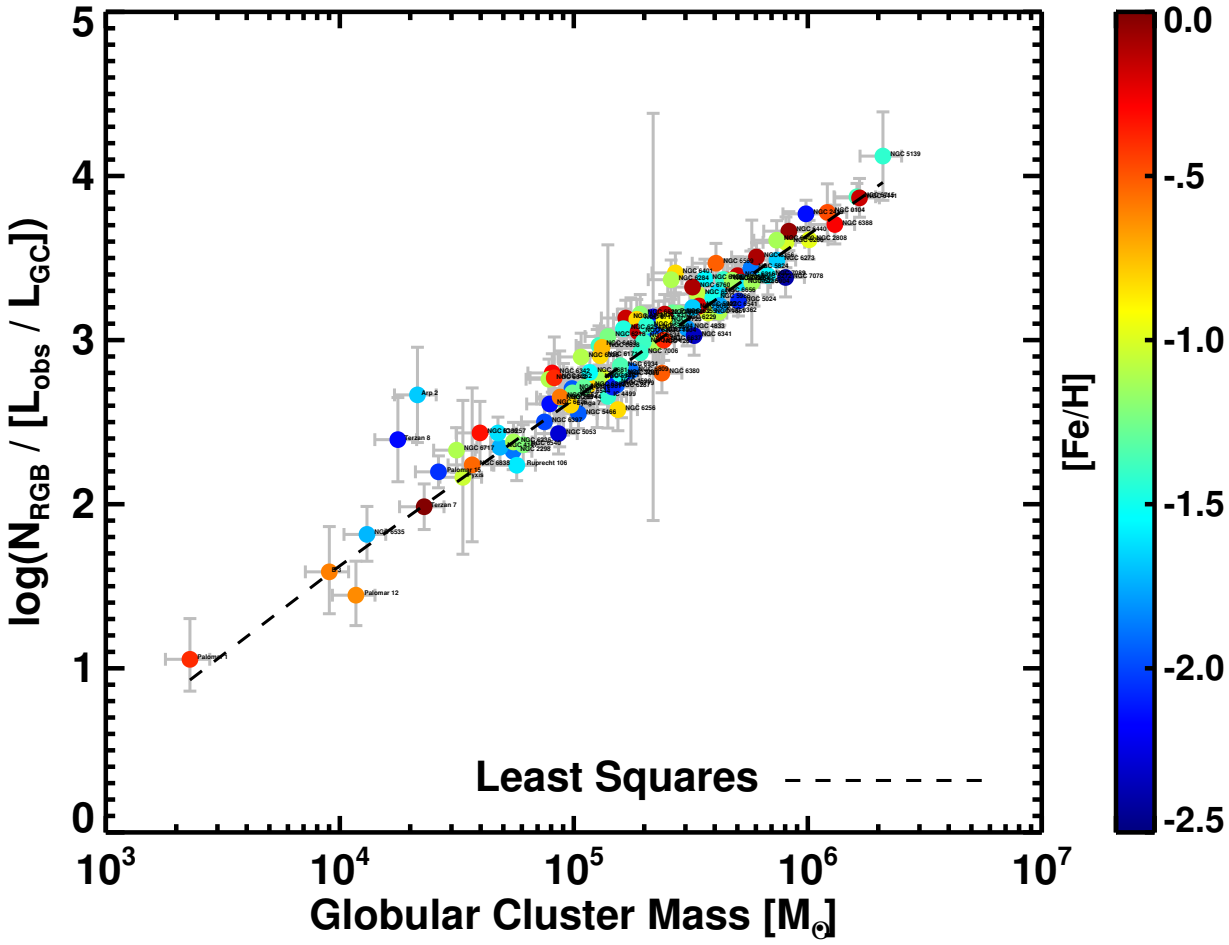

Figure 4.3: The number of RGB stars $N_{\rm RGB}$ normalized by the fraction of observed cluster luminosity $L_{\rm frac}$ vs. the cluster mass. GC metallicity [Fe/H] is indicated by the colourbar to the right. The strong correlation between the total number of RGB stars in a GC and its mass is evident, as expected. The dashed line shows the weighted least squares fit to the data, which is given in equation 4.1.

least-squares fit to the data produced the relationship in equation 4.1.

$$\frac{N_{\rm RGB}}{L_{\rm frac}} = (0.00436 \pm 0.00013) \times \frac{\rm M_{GC}}{M_\odot} - (1.51 \pm 4.99) \tag{4.1}$$

In addition, GC mass has a strong influence on the presence of an LMXB (e.g. Sivakoff et al., 2007; Vulic et al., 2014). Therefore not only are we removing the intrinsic dependence of RGB number on mass but also a parameter (mass, via $N_{\rm RGB}$) that is known to promote the production of LMXBs. When normalizing by GC mass we obtain the number of RGB stars per unit mass, $N_{\rm RGB}\ {M_\odot}^{-1}$, which we call $RGB_{\rm frac}$. In Figure 4.4 we plot $RGB_{\rm frac}$ vs. metallicity using the same format as Figure 4.2.

Figure 4.4 shows that $RGB_{\rm frac}$ varies very little with metallicity, where only a slightly positive correlation may exist. The introduction of much larger uncertainties in the $RGB_{\rm frac}$ parameter are a result of the uncertainty in calculating GC masses, which propagate from our values for total cluster luminosity $L_{\rm total}$. A weighted least squares fit to the data is shown by the solid line and reproduced in equation 4.2, where $\rm M_{GC_6}$ is the GC mass in terms of $10^6\ M_\odot$.

$$RGB_{\rm frac} = \frac{N_{\rm RGB}}{L_{\rm frac}\rm M_{GC_6}} = (462.93 \pm 291.70) \times [\rm Fe/H] + (5019.84 \pm 452.36) \tag{4.2}$$

We have effectively removed the bias that would exist in this relationship due to mass and thus have a quantity $RGB_{\rm frac}$ that can be independently compared to the metallicity. This is important because a mass-metallicity relationship could also affect our results. In early-type galaxies, the brighter metal-poor GCs show a relationship between mass and metallicity, dubbed the 'blue tilt', thought to arise from self-enrichment in GCs (Peng et al., 2006; Harris et al., 2006; Strader et al., 2006; Strader & Smith, 2008). In the Milky Way, a mass-metallicity relationship has not been detected for several reasons (e.g. cluster to cluster scatter in mean [Fe/H], sample size, mass limit), although its existence has not been ruled out (Strader & Smith, 2008). Therefore it is beneficial to remove the dependence on mass to avoid any intrinsic dependence of massive metal-poor Galactic GCs on metallicity. To test whether a statistically significant relationship

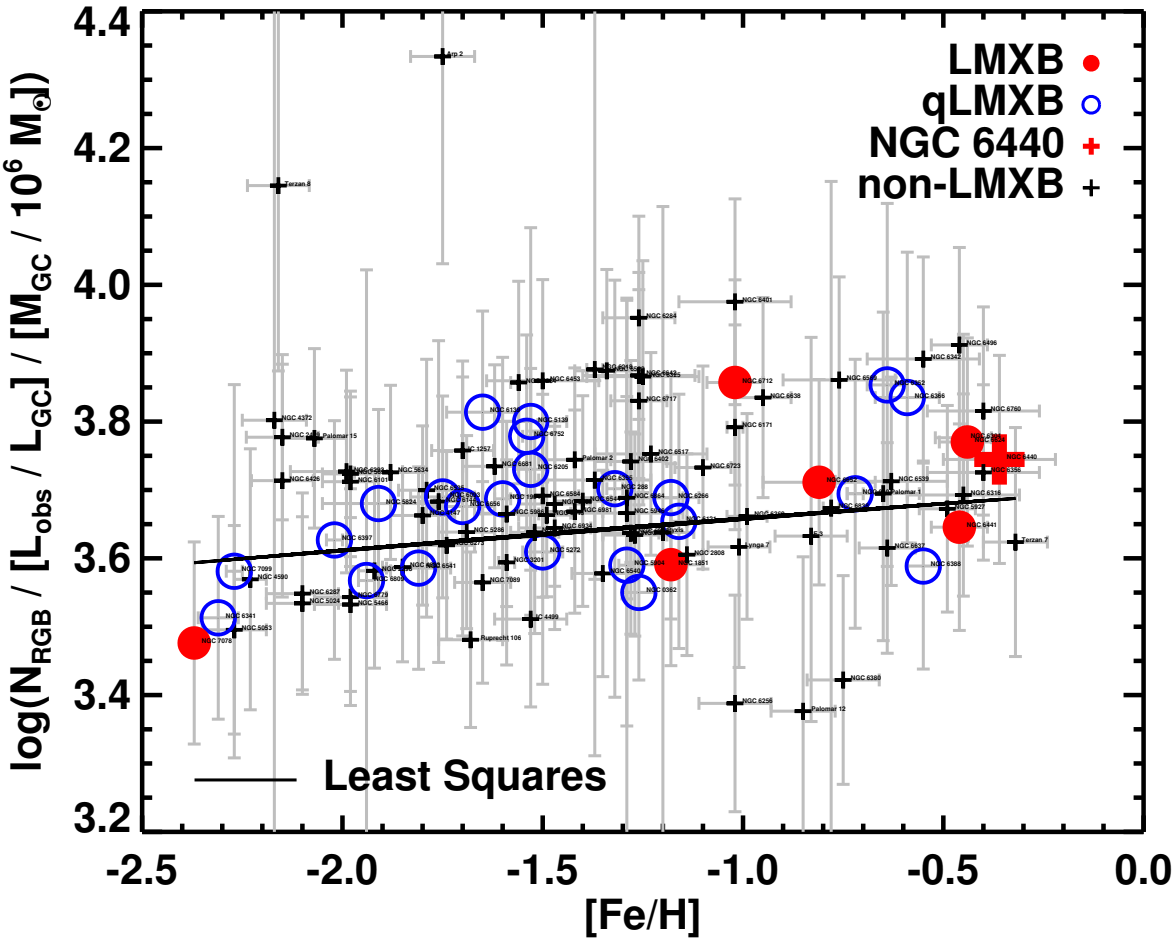

Figure 4.4: $RGB_{\rm frac}$ parameter (RGB star number normalized by GC mass) vs. metallicity [Fe/H]. Black plusses represent normal GCs, open blue circles are GCs hosting quiescent LMXBs and filled red circles are GCs hosting bright LMXBs. NGC 6440, which has an LMXB and qLMXB, is shown with a red plus. GC names are indicated near each datapoint. The weighted least squares fit (equation 4.2) is shown, which is consistent with a flat distribution. This result indicates no relationship with the number of RGB stars per $M_{\odot}$ and metallicity of a GC.

existed between $RGB_{\rm frac}$ and [Fe/H], we split our data into separate groups that represented all GCs, those with LMXB, qLMXBs, and both. Performing Spearman's rank test on each of these groups for the $RGB_{\rm frac}$ and metallicity parameters all returned p-values > 0.1, indicating we cannot reject the null hypothesis that the data were drawn from a random distribution.

4.6.3 Globular Cluster Volume

While there is no correlation between $RGB_{\rm frac}$ and metallicity, the predictions of Ivanova et al. (2012) assumed that the number densities of RGB stars influence the formation rate of LMXBs. Therefore we must normalize this value by some volumetric quantity, given that GCs are well-approximated as self-gravitating spheres. We used the half-light radius r_h (in pc) to determine the volume of a cluster. Uncertainties on r_h were taken from McLaughlin & van der Marel (2005) and were on average $< 10\%$, where this mean value was used for GCs without uncertainties. One would expect the majority of RGB stars to be located near the centre of a GC due to mass segregation, as they are among the most massive members of the cluster that appear on the CMD. There are a number of caveats with using r_h to determine the volume within which RGB stars are located. Firstly, not all RGB stars will be located within r_h. Because we only have projected distances of stars and not a 3D distribution, we can't account for the distance of stars from the GC core along the line of sight. Therefore we cannot determine what fraction of the RGB stars that we have identified will be within r_h. This would affect the number density of RGB stars since the volume within which a percentage of RGB stars resides would be different for each GC. However, while the projected and 3D distributions are not the same, this effect will average out for all clusters. Secondly, r_h is another parameter, like mass, that influences the formation of LMXBs, where GCs with smaller r_h (more compact) have been shown to preferentially host LMXBs in the Milky Way (Bregman et al., 2006) and other galaxies (Sivakoff et al., 2007; Jordán, 2004; Peacock et al., 2010; Vulic et al., 2014). The stellar encounter rate Γ, which influences LMXB production, shows a stronger effect when calculated using the core radius r_c as opposed to r_h (Peacock et al., 2010; Bahramian et al., 2013; Agar &

Barmby, 2013, e.g.). Even so, by using r_h we would introduce an additional undesired effect in attempting to find a relationship between the RGB star density and [Fe/H]. This is a difficult degeneracy to remove since any measurement of the RGB density requires an estimation of the volume. In addition, r_h has been shown to be weakly negatively correlated with [Fe/H] in M31 (Barmby et al., 2007), although both r_h and [Fe/H] are both dependent on galactocentric distance, further confounding this relation. Nevertheless, we calculated the RGB density and show its relationship with [Fe/H] in Figure 4.5.

A stronger relationship between the RGB star number density and metallicity exists compared to $N_{\rm RGB}$. A weighted least-squares fit to the data produced the relationship in equation 4.3.

$$\text{RGB Density} = \log_{10}\left[\frac{\mathrm{N_{RGB}}}{\mathrm{L_{frac}M_{GC_6}} \times \frac{4}{3}\pi \mathrm{r_h^3}}\right] = (0.673 \pm 0.028) \times [\mathrm{Fe/H}] + (2.46 \pm 0.04) \quad (4.3)$$

Using Spearman's rank test we found a p-value of 0.00016 and coefficient $r_s = 0.35$. Our p-value means we can reject the null hypothesis that the data is drawn from a random distribution, and the coefficient indicates a moderate linear relation (a value of 1 means a perfect correlation while 0 indicates no correlation). We also used the Kendall rank test and found a p-value of 0.00021 and coefficient $\tau = 0.24$. Kendall's rank test is not as sensitive to uncertainty as Spearman's rank test but is more accurate for nonlinear correlations. The GCs with LMXBs preferentially have larger RGB star number densities as we expected based on their relation with r_h. They are all located above the line of best fit in Figure 4.5. The qLMXBs are more prevalent in the metal-poor population and have larger mean RGB star number densities than the rest of the metal-poor population. However, GC 47 Tucanae (NGC 104), for example, has 5 qLMXBs, and so the qLMXB distribution in our Figures does not accurately represent number statistics for individual qLMXBs but instead of the clusters within which they reside. A detailed analysis of this population is beyond the scope of this work.

In Figure 4.6 we plot the unnormalized RGB star density (i.e. RGB stars not divided by

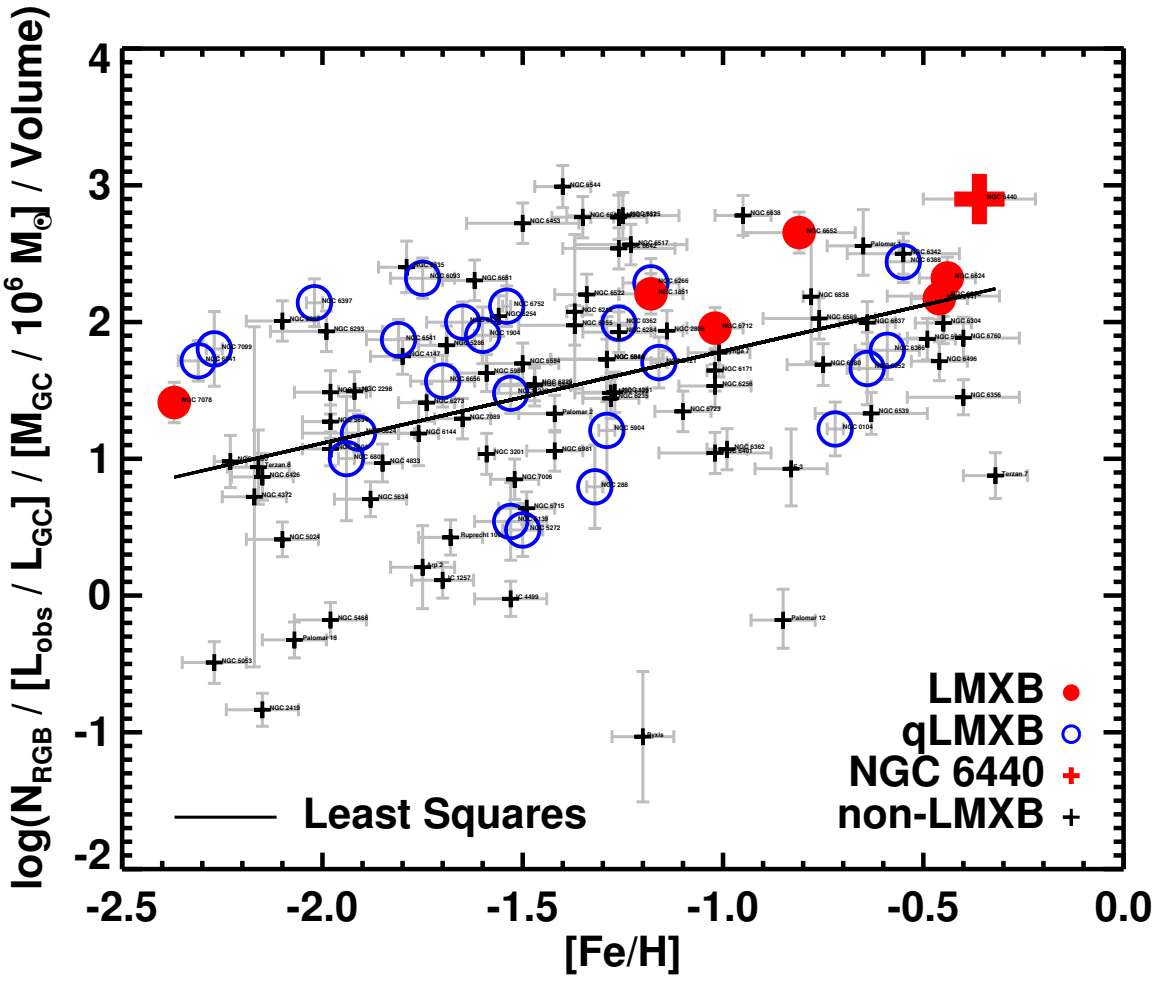

Figure 4.5: RGB star density vs. metallicity [Fe/H]. The volume was calculated using the cluster half-light radius r_h and a spherical distribution for the GC. Black plusses represent normal GCs, open blue circles are GCs hosting quiescent LMXBs and filled red circles are GCs hosting bright LMXBs. NGC 6440, which has an LMXB and qLMXB, is shown with a red plus. GC names are indicated near each datapoint. The solid line shows the weighted least squares fit (equation 4.3), which has a steeper slope than the $RGB_{\rm frac}$ best fit. This stems from the fact that GCs with smaller r_h are more massive. The link between r_h and LMXBs is evident as the metal-rich LMXB-hosting GCs (red circles) are among the GCs with the highest RGB star number density. The correlation is biased by the intrinsic dependence of RGB star density on r_h (compactness), however this degeneracy is difficult to remove.

GC mass) against metallicity. This quantity best represents the number density of RGB stars as defined in Ivanova et al. (2012). Because there is no evidence of a mass-metallicity relation for Galactic GCs, the fact that RGB stars are highly-correlated with mass shouldn't cause a metallicity effect. However, the intrinsic dependence of volume on r_h, which in turn affects LMXB formation and can influence metallicity, remains. In equation 4.4 we present the weighted least squares fit from Figure 4.6. A Spearman Rank test gave a p-value of 0.0035 and coefficient $r_s = 0.28$, indicating a slightly less significant correlation compared to the mass-normalized case.

$$\text{RGB Number Density} = \log_{10}\left[\frac{\mathrm{N_{RGB}}}{\mathrm{L_{frac}}\frac{4}{3}\pi\mathrm{r_h^3}}\right] = (0.819 \pm 0.022) \times [\mathrm{Fe/H}] + (1.95 \pm 0.03) \quad (4.4)$$

In Table 4.2 we present the properties for each GC in our study. This includes cluster parameters from Harris (1996, 2010 edition): M_V, [Fe/H], concentration parameter, r_c, and R_{Sun}. We report our values and uncertainties for N_{RGB}, L_{frac}, $M_V^{fgstars}$, M/L, GC mass, RGB fraction RGB_{frac}, whether the GC hosts an X-ray source, and the instrument used. Where upper and lower limits (UL and LL) are indicated, Poisson statistics (Gehrels, 1986) are used for values < 50 while $\sqrt{N}$ is used for values ≥ 50.

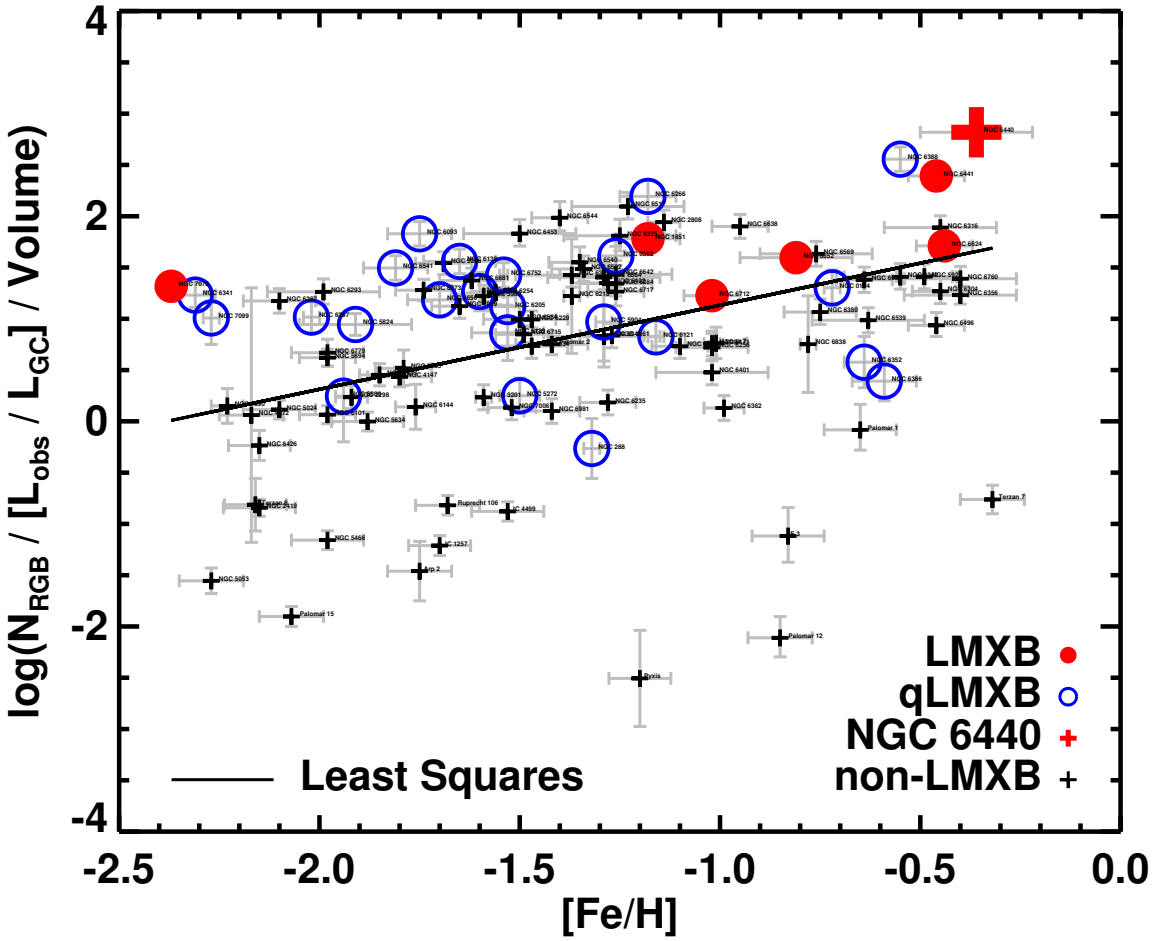

Figure 4.6: RGB star density (not normalized by GC mass) vs. metallicity [Fe/H]. The volume was calculated using the cluster half-light radius r_h and a spherical distribution for the GC. Black plusses represent normal GCs, open blue circles are GCs hosting quiescent LMXBs and filled red circles are GCs hosting bright LMXBs. NGC 6440, which has an LMXB and qLMXB, is shown with a red plus. GC names are indicated near each datapoint. The solid line shows the weighted least squares fit (equation 4.4), which has a steeper slope than the RGB number density normalized by GC mass. As stated for Figure 4.5, r_h affects LMXB formation and GC metallicity.

Table 4.2: Milky Way Globular Cluster Parameters and RGB Values

Globular Cluster	M_V mag	[Fe/H]	Concentration	r_c pc	R_{Sun} pc	N_{RGB}	ΔN_{RGB}(UL)	ΔN_{RGB}(LL)	L_{frac}	ΔL_{frac}	$M_V^{fgstars}$ mag	M/L $M_\odot/L_\odot$	$\Delta M/L$ $M_\odot/L_\odot$	Mass $M_\odot$	ΔMass $M_\odot$	RGB_{frac}	ΔRGB_{frac}(UL)	ΔRGB_{frac}(LL)	X-ray Source	HST
Arp 2	-5.29	-1.75	0.88	9.900	28600	125	11.180	11.180	0.270	0.179	12.56659	1.867	0.156	2.15E+04	4.34E+03	4.334	0.303	0.303	-	ACS
E 3	-4.12	-0.83	0.75	4.400	8100	18	6.754	5.177	0.465	0.239	16.66471	2.303	0.230	9.02E+03	1.89E+03	3.633	0.291	0.271	-	ACS
IC 1257	-6.15	-1.70	1.50	1.800	25000	107	10.344	10.344	0.394	0.079	9.50870	1.867	0.155	4.74E+04	9.58E+03	3.758	0.131	0.131	-	WFPC2
IC 4499	-7.32	-1.53	1.20	4.500	18800	260	16.125	16.125	0.573	0.119	14.02200	1.874	0.154	1.40E+05	2.82E+04	3.511	0.129	0.129	-	ACS
Lynga 7	-6.60	-1.01	0.95	2.000	7300	329	18.138	18.138	0.819	0.279	15.64936	2.524	0.276	9.70E+04	2.08E+04	3.617	0.176	0.176	-	ACS
NGC 0104	-9.42	-0.72	2.00	0.470	4500	2416	49.153	49.153	0.403	0.161	14.01694	2.348	0.239	1.21E+06	2.55E+05	3.694	0.197	0.197	qLMXB	ACS
NGC 1261	-7.80	-1.27	1.10	1.600	16300	808	28.425	28.425	0.838	0.228	10.10437	1.928	0.158	2.24E+05	4.51E+04	3.634	0.148	0.148	-	ACS
NGC 1851	-8.33	-1.18	1.80	0.310	12100	1241	35.228	35.228	0.850	0.231	13.02692	1.981	0.166	3.75E+05	7.58E+04	3.591	0.148	0.148	LMXB	ACS
NGC 1904	-7.86	-1.60	1.70	0.600	12900	446	21.119	21.119	0.398	0.171	10.74033	1.877	0.154	2.30E+05	4.64E+04	3.687	0.207	0.207	qLMXB	WFPC2
NGC 2298	-6.31	-1.92	1.30	0.970	10800	184	13.565	13.565	0.876	0.217	13.16012	1.870	0.157	5.50E+04	1.11E+04	3.582	0.142	0.142	-	ACS
NGC 2419	-9.42	-2.15	1.30	7.600	82600	1229	35.057	35.057	0.209	0.039	10.13530	1.903	0.161	9.82E+05	1.99E+05	3.777	0.121	0.121	-	WFPC2
NGC 2808	-9.39	-1.14	1.50	0.690	9600	3308	57.515	57.515	0.810	0.220	12.33190	2.018	0.172	1.01E+06	2.06E+05	3.605	0.148	0.148	-	ACS
NGC 288	-6.75	-1.32	0.99	3.400	8900	190	13.784	13.784	0.434	0.290	11.59449	1.972	0.165	8.70E+04	1.76E+04	3.702	0.305	0.305	qLMXB	ACS
NGC 3201	-7.45	-1.59	1.20	1.800	4900	214	14.629	14.629	0.345	0.094	11.97579	1.876	0.154	1.58E+05	3.18E+04	3.594	0.150	0.150	-	ACS
NGC 0362	-8.43	-1.26	1.70	0.450	8600	1060	32.558	32.558	0.715	0.152	8.28431	2.013	0.171	4.17E+05	8.47E+04	3.550	0.128	0.128	qLMXB	ACS
NGC 4147	-6.17	-1.80	1.80	0.500	19300	209	14.457	14.457	0.940	0.200	10.37009	1.869	0.157	4.84E+04	9.79E+03	3.663	0.131	0.131	-	ACS
NGC 4372	-7.79	-2.17	1.30	2.900	5800	76	8.718	8.718	0.055	0.157	11.04971	1.898	0.161	2.18E+05	4.43E+04	3.802	1.244	1.244	-	WFPC2
NGC 4590	-7.37	-2.23	1.40	1.700	10300	253	15.906	15.906	0.461	0.177	12.41205	1.893	0.160	1.48E+05	3.00E+04	3.569	0.191	0.191	-	ACS
NGC 4833	-8.17	-1.85	1.20	1.900	6600	483	21.977	21.977	0.410	0.099	9.50870	1.868	0.156	3.05E+05	6.17E+04	3.587	0.139	0.139	-	ACS
NGC 5024	-8.71	-2.10	1.70	1.800	17900	1155	33.985	33.985	0.668	0.139	10.08142	1.884	0.159	5.06E+05	1.02E+05	3.534	0.127	0.127	-	ACS
NGC 5053	-6.76	-2.27	0.74	10.000	17400	70	8.367	8.367	0.260	0.068	10.74033	1.931	0.164	8.60E+04	1.74E+04	3.496	0.153	0.153	-	ACS
NGC 5139	-10.26	-1.53	1.30	3.500	5200	2598	50.971	50.971	0.197	0.122	10.13530	1.872	0.154	2.09E+06	4.23E+05	3.800	0.283	0.283	qLMXB	ACS
NGC 5272	-8.88	-1.50	1.80	1.000	10200	1325	36.401	36.401	0.553	0.219	11.86501	1.877	0.154	5.89E+05	1.19E+05	3.609	0.194	0.194	qLMXB	ACS
NGC 5286	-8.74	-1.69	1.40	0.950	11700	1951	44.170	44.170	0.870	0.221	10.15669	1.868	0.155	5.15E+05	1.04E+05	3.638	0.141	0.141	-	ACS
NGC 5466	-6.98	-1.98	1.00	6.600	16000	128	11.314	11.314	0.359	0.069	11.04971	1.919	0.163	1.05E+05	2.12E+04	3.532	0.127	0.127	-	ACS
NGC 5634	-7.69	-1.88	2.00	0.660	25200	434	20.833	20.833	0.415	0.086	12.76173	1.873	0.157	1.96E+05	3.98E+04	3.726	0.127	0.127	-	WFPC2
NGC 5694	-7.83	-1.98	1.80	0.610	35000	634	25.179	25.179	0.537	0.101	10.42474	1.871	0.157	2.23E+05	4.52E+04	3.724	0.121	0.121	-	WFPC2
NGC 5824	-8.85	-1.91	1.90	0.560	32100	1383	37.189	37.189	0.506	0.122	15.46308	1.870	0.157	5.71E+05	1.16E+05	3.680	0.138	0.138	qLMXB	WFPC2
NGC 5904	-8.81	-1.29	1.70	0.960	7500	968	31.113	31.113	0.432	0.378	10.40342	1.958	0.163	5.76E+05	1.16E+05	3.590	0.391	0.391	qLMXB	ACS
NGC 5927	-7.81	-0.49	1.60	0.940	7700	1103	33.211	33.211	0.684	0.184	15.77700	2.926	0.345	3.43E+05	7.50E+04	3.673	0.151	0.151	-	ACS
NGC 5946	-7.18	-1.29	2.50	0.240	10600	344	18.547	18.547	0.590	0.404	9.61522	1.918	0.157	1.26E+05	2.54E+04	3.666	0.311	0.311	-	WFPC2
NGC 5986	-8.44	-1.59	1.20	1.400	10400	1229	35.057	35.057	0.677	0.160	10.13912	1.876	0.154	3.93E+05	7.92E+04	3.665	0.136	0.136	-	ACS
NGC 6093	-8.23	-1.75	1.60	0.430	10000	1286	35.861	35.861	0.816	0.222	10.33998	1.867	0.155	3.22E+05	6.51E+04	3.690	0.148	0.148	qLMXB	ACS
NGC 6101	-6.94	-1.98	0.80	4.300	15400	278	16.673	16.673	0.549	0.106	10.42474	1.869	0.157	9.83E+04	1.99E+04	3.712	0.124	0.124	-	ACS
NGC 6121	-7.19	-1.16	1.60	0.740	2200	140	11.832	11.832	0.236	0.087	9.61522	1.991	0.168	1.32E+05	2.67E+04	3.654	0.186	0.186	qLMXB	ACS
NGC 6139	-8.36	-1.65	1.80	0.440	10100	904	30.067	30.067	0.382	0.104	8.13620	1.868	0.155	3.63E+05	7.34E+04	3.814	0.148	0.148	qLMXB	WFPC2
NGC 6144	-6.85	-1.76	1.50	2.400	8900	232	15.232	15.232	0.533	0.265	9.92719	1.867	0.155	9.04E+04	1.83E+04	3.683	0.235	0.235	-	ACS
NGC 6171	-7.12	-1.02	1.50	1.000	6400	323	17.972	17.972	0.402	0.109	13.52426	2.089	0.186	1.30E+05	2.65E+04	3.792	0.150	0.150	-	ACS
NGC 6205	-8.55	-1.53	1.50	1.200	7100	1252	35.384	35.384	0.535	0.145	9.16737	1.881	0.154	4.36E+05	8.78E+04	3.730	0.148	0.148	qLMXB	ACS
NGC 6218	-7.31	-1.37	1.30	1.100	4800	380	19.494	19.494	0.361	0.464	11.91284	1.892	0.155	1.40E+05	2.82E+04	3.876	0.565	0.565	-	ACS
NGC 6229	-8.06	-1.47	1.50	1.000	30500	734	27.092	27.092	0.547	0.102	10.87180	1.904	0.156	2.81E+05	5.66E+04	3.680	0.120	0.120	-	WFPC2
NGC 6235	-6.29	-1.28	1.50	1.100	11500	137	11.705	11.705	0.572	0.149	9.92719	1.912	0.157	5.52E+04	1.11E+04	3.637	0.148	0.148	-	WFPC2
NGC 6254	-7.48	-1.56	1.30	0.980	4400	574	23.958	23.958	0.489	0.133	8.89801	1.885	0.154	1.63E+05	3.28E+04	3.857	0.148	0.148	-	ACS
NGC 6256	-7.15	-1.02	2.50	0.059	10300	246	15.684	15.684	0.653	0.189	10.60710	2.419	0.254	1.54E+05	3.27E+04	3.388	0.158	0.158	-	WFPC2
NGC 6266	-9.18	-1.18	1.70	0.430	6800	1210	34.785	34.785	0.307	0.109	9.58422	1.950	0.161	8.07E+05	1.63E+05	3.689	0.178	0.178	qLMXB	WFPC2
NGC 6273	-9.13	-1.74	1.50	1.100	8800	985	31.385	31.385	0.321	0.077	9.22696	1.868	0.155	7.38E+05	1.49E+05	3.619	0.137	0.137	-	WFPC2
NGC 6284	-7.96	-1.26	2.50	0.310	15300	644	25.377	25.377	0.276	0.075	10.89594	1.938	0.160	2.61E+05	5.26E+04	3.952	0.149	0.149	-	WFPC2
NGC 6287	-7.36	-2.10	1.30	0.790	9400	205	14.318	14.318	0.396	0.104	8.75438	1.892	0.160	1.46E+05	2.97E+04	3.548	0.147	0.147	-	WFPC2
NGC 6293	-7.78	-1.99	2.50	0.130	9500	427	20.664	20.664	0.374	0.101	8.91537	1.876	0.158	2.14E+05	4.33E+04	3.727	0.148	0.148	-	WFPC2
NGC 6304	-7.30	-0.45	1.80	0.360	5900	824	28.705	28.705	0.733	0.200	8.39241	2.567	0.284	1.88E+05	4.04E+04	3.776	0.151	0.151	-	ACS
NGC 6316	-8.34	-0.45	1.60	0.510	10400	513	22.650	22.650	0.208	0.054	8.89052	2.625	0.295	5.01E+05	1.08E+05	3.693	0.148	0.148	-	WFPC2
NGC 6325	-6.96	-1.25	2.50	0.068	7800	198	14.071	14.071	0.251	0.082	9.82771	2.007	0.170	1.07E+05	2.18E+04	3.866	0.170	0.170	-	WFPC2
NGC 6341	-8.21	-2.31	1.60	0.620	8300	730	27.019	27.019	0.686	0.186	9.95255	1.929	0.164	3.27E+05	6.63E+04	3.513	0.148	0.148	qLMXB	ACS
NGC 6342	-6.42	-0.55	2.50	0.120	8500	216	14.697	14.697	0.343	0.089	8.63129	2.484	0.267	8.09E+04	1.73E+04	3.892	0.149	0.149	-	WFPC2
NGC 6352	-6.47	-0.64	1.10	1.300	5600	280	16.733	16.733	0.475	0.271	9.07131	2.419	0.254	8.25E+04	1.75E+04	3.854	0.265	0.265	qLMXB	ACS
NGC 6355	-8.07	-1.37	2.50	0.130	9200	321	17.916	17.916	0.220	0.058	9.85393	1.888	0.155	2.81E+05	5.67E+04	3.715	0.145	0.145	-	WFPC2
NGC 6356	-8.51	-0.40	1.50	1.000	15100	1253	35.398	35.398	0.391	0.078	10.68691	2.703	0.309	6.03E+05	1.31E+05	3.726	0.128	0.128	-	WFPC2
NGC 6362	-6.95	-0.99	1.00	2.400	7600	287	16.941	16.941	0.546	0.149	8.73967	2.160	0.200	1.15E+05	2.36E+04	3.661	0.150	0.150	-	ACS
NGC 6366	-5.74	-0.59	0.74	2.200	3500	97	9.849	9.849	0.357	0.154	10.60710	2.282	0.225	3.97E+04	8.30E+03	3.835	0.213	0.213	qLMXB	ACS

Globular Cluster	M_V	[Fe/H]	Concentration	r_c	R_{Sun}	N_{RGB}	ΔN_{RGB}(UL)	ΔN_{RGB}(LL)	L_{frac}	ΔL_{frac}	$M_V^{fgstars}$	M/L	$\Delta M/L$	Mass	ΔMass	RGB_{frac}	ΔRGB_{frac}(UL)	ΔRGB_{frac}(LL)	X-ray Source	HST
NGC 6380	-7.50	-0.75	1.50	1.000	10900	450	21.213	21.213	0.715	0.195	8.52676	2.703	0.309	2.38E+05	5.16E+04	3.422	0.153	0.153	-	WFPC2
NGC 6388	-9.41	-0.55	1.70	0.340	9900	4003	63.269	63.269	0.791	0.215	9.88980	2.552	0.281	1.31E+06	2.80E+05	3.589	0.151	0.151	qLMXB	ACS
NGC 6397	-6.64	-2.02	2.50	0.033	2300	111	10.536	10.536	0.350	0.117	9.58422	1.879	0.159	7.49E+04	1.52E+04	3.627	0.175	0.175	qLMXB	ACS
NGC 6401	-7.90	-1.02	1.60	0.770	10600	447	21.142	21.142	0.174	0.048	8.65301	2.135	0.195	2.72E+05	5.59E+04	3.975	0.150	0.150	-	WFPC2
NGC 6402	-9.10	-1.28	0.99	2.100	9300	942	30.692	30.692	0.232	0.063	9.66426	1.915	0.157	7.36E+05	1.48E+05	3.742	0.148	0.148	-	WFPC2
NGC 6426	-6.67	-2.15	1.70	1.500	20600	215	14.663	14.663	0.527	0.173	9.22696	1.925	0.164	7.89E+04	1.60E+04	3.714	0.170	0.170	-	ACS
NGC 6440	-8.75	-0.36	1.60	0.340	8500	1399	37.403	37.403	0.303	0.083	9.87176	2.981	0.354	8.30E+05	1.82E+05	3.745	0.152	0.152	LMXB/qLMXB	WFPC2
NGC 6441	-9.63	-0.46	1.70	0.430	11600	5777	76.007	76.007	0.785	0.214	10.09970	2.656	0.301	1.66E+06	3.60E+05	3.646	0.151	0.151	LMXB	ACS
NGC 6453	-7.22	-1.50	2.50	0.160	11600	719	26.814	26.814	0.775	0.211	10.00285	1.883	0.154	1.28E+05	2.58E+04	3.860	0.148	0.148	-	WFPC2
NGC 6496	-7.20	-0.46	0.70	3.100	11300	223	14.933	14.933	0.164	0.039	8.75438	2.497	0.270	1.67E+05	3.56E+04	3.912	0.142	0.142	-	ACS
NGC 6517	-8.25	-1.23	1.80	0.180	10600	590	24.290	24.290	0.309	0.084	8.06636	1.921	0.158	3.38E+05	6.81E+04	3.753	0.148	0.148	-	WFPC2
NGC 6522	-7.65	-1.34	2.50	0.110	7700	569	23.854	23.854	0.395	0.108	12.37469	1.901	0.156	1.92E+05	3.88E+04	3.874	0.148	0.148	-	WFPC2
NGC 6535	-4.75	-1.79	1.30	0.710	6800	50	10.340	8.822	0.764	0.254	8.91537	1.868	0.156	1.31E+04	2.64E+03	3.700	0.191	0.186	-	ACS
NGC 6539	-8.29	-0.63	1.70	0.860	7800	296	17.205	17.205	0.127	0.035	16.01500	2.470	0.265	4.50E+05	9.60E+04	3.713	0.152	0.152	-	WFPC2
NGC 6540	-6.35	-1.35	2.50	0.046	5300	176	13.266	13.266	0.765	0.208	13.30663	1.991	0.168	6.08E+04	1.23E+04	3.578	0.151	0.151	-	WFPC2
NGC 6541	-8.52	-1.81	1.80	0.390	7500	832	28.844	28.844	0.513	0.139	10.25138	1.869	0.157	4.21E+05	8.53E+04	3.586	0.148	0.148	qLMXB	ACS
NGC 6544	-6.94	-1.40	1.60	0.043	3000	90	9.487	9.487	0.189	0.051	10.29180	1.878	0.154	9.87E+04	1.99E+04	3.684	0.154	0.154	-	WFPC2
NGC 6569	-8.28	-0.76	1.30	1.100	10900	664	25.768	25.768	0.226	0.062	10.18867	2.242	0.217	4.05E+05	8.43E+04	3.861	0.151	0.151	-	WFPC2
NGC 6584	-7.69	-1.50	1.40	1.000	13500	486	22.045	22.045	0.499	0.136	11.44562	1.890	0.155	1.98E+05	4.00E+04	3.692	0.148	0.148	-	ACS
NGC 6624	-7.49	-0.44	2.50	0.130	7900	892	29.866	29.866	0.619	0.169	9.60132	2.802	0.326	2.44E+05	5.33E+04	3.770	0.152	0.152	LMXB	ACS
NGC 6637	-7.64	-0.64	1.30	0.840	8800	793	28.160	28.160	0.794	0.224	11.84030	2.419	0.254	2.42E+05	5.14E+04	3.615	0.154	0.154	-	ACS
NGC 6638	-7.12	-0.95	1.30	0.600	9400	450	21.213	21.213	0.498	0.131	10.56374	2.127	0.193	1.32E+05	2.71E+04	3.835	0.146	0.146	-	WFPC2
NGC 6642	-6.66	-1.26	1.90	0.230	8100	184	13.565	13.565	0.319	0.087	10.53964	1.928	0.158	7.83E+04	1.58E+04	3.867	0.151	0.151	-	WFPC2
NGC 6652	-6.66	-0.81	1.80	0.290	10000	316	17.776	17.776	0.703	0.191	12.95863	2.151	0.198	8.74E+04	1.80E+04	3.711	0.150	0.150	LMXB	ACS
NGC 6656	-8.50	-1.70	1.30	1.200	3200	671	25.904	25.904	0.342	0.132	8.89052	1.870	0.154	4.14E+05	8.35E+04	3.676	0.189	0.189	qLMXB	ACS
NGC 6681	-7.12	-1.62	2.50	0.079	9000	448	21.166	21.166	0.705	0.192	12.15687	1.886	0.154	1.17E+05	2.36E+04	3.735	0.148	0.148	-	ACS
NGC 6712	-7.50	-1.02	1.00	1.500	6900	296	17.205	17.205	0.221	0.060	12.46119	2.111	0.190	1.86E+05	3.81E+04	3.857	0.150	0.150	LMXB	WFPC2
NGC 6715	-9.98	-1.49	2.00	0.690	26500	5578	74.686	74.686	0.747	0.139	9.82771	1.876	0.154	1.62E+06	3.27E+05	3.663	0.119	0.119	-	ACS
NGC 6717	-5.66	-1.26	2.00	0.160	7100	108	10.392	10.392	0.506	0.152	8.63129	1.950	0.161	3.15E+04	6.37E+03	3.830	0.163	0.163	-	ACS
NGC 6723	-7.83	-1.10	1.10	2.100	8700	686	26.192	26.192	0.522	0.142	11.10416	2.036	0.176	2.43E+05	4.94E+04	3.733	0.148	0.148	-	ACS
NGC 6752	-7.73	-1.54	2.50	0.190	4000	526	22.935	22.935	0.429	0.117	11.63855	1.878	0.154	2.04E+05	4.12E+04	3.779	0.148	0.148	qLMXB	ACS
NGC 6760	-7.84	-0.40	1.60	0.730	7400	558	23.622	23.622	0.265	0.072	11.63855	2.671	0.304	3.22E+05	6.97E+04	3.816	0.152	0.152	-	WFPC2
NGC 6779	-7.41	-1.98	1.30	1.200	9400	422	20.543	20.543	0.794	0.238	9.85393	1.878	0.158	1.52E+05	3.08E+04	3.543	0.158	0.158	-	ACS
NGC 6809	-7.57	-1.94	0.93	2.800	5400	216	14.697	14.697	0.333	0.341	8.52676	1.868	0.156	1.75E+05	3.55E+04	3.568	0.454	0.454	qLMXB	ACS
NGC 6838	-5.61	-0.78	1.10	0.730	4000	135	11.619	11.619	0.778	0.837	8.65301	2.383	0.247	3.68E+04	7.78E+03	3.674	0.478	0.478	-	ACS
NGC 6864	-8.57	-1.29	1.80	0.540	20900	1051	32.419	32.419	0.453	0.123	11.63855	2.013	0.171	4.75E+05	9.63E+04	3.689	0.148	0.148	-	WFPC2
NGC 6934	-7.45	-1.47	1.50	0.990	15600	539	23.216	23.216	0.772	0.211	11.63855	1.881	0.154	1.58E+05	3.19E+04	3.645	0.149	0.149	-	ACS
NGC 6981	-7.04	-1.42	1.20	2.200	17000	405	20.125	20.125	0.789	0.214	11.63855	1.912	0.157	1.10E+05	2.22E+04	3.668	0.149	0.149	-	ACS
NGC 7006	-7.67	-1.52	1.40	2.000	41200	761	27.586	27.586	0.909	0.248	11.63855	1.871	0.154	1.93E+05	3.89E+04	3.638	0.148	0.148	-	ACS
NGC 7078	-9.19	-2.37	2.20	0.420	10400	1403	37.457	37.457	0.583	0.159	11.63855	1.925	0.164	8.04E+05	1.63E+05	3.476	0.148	0.148	LMXB	ACS
NGC 7089	-9.03	-1.65	1.50	1.000	11500	1855	43.070	43.070	0.749	0.204	11.63855	1.872	0.154	6.75E+05	1.36E+05	3.565	0.147	0.147	-	ACS
NGC 7099	-7.45	-2.27	2.50	0.140	8100	332	18.221	18.221	0.544	0.322	9.87176	1.903	0.161	1.60E+05	3.24E+04	3.581	0.273	0.273	qLMXB	ACS
Palomar 1	-2.52	-0.65	2.50	0.032	11100	11	5.594	3.978	0.970	0.254	10.00285	2.552	0.281	2.29E+03	4.91E+02	3.695	0.265	0.215	-	ACS
Palomar 12	-4.47	-0.85	2.90	0.110	19000	21	7.183	5.617	0.753	0.250	12.56659	2.168	0.201	1.17E+04	2.42E+03	3.377	0.226	0.206	-	ACS
Palomar 15	-5.51	-2.07	0.60	15.000	45100	128	11.314	11.314	0.813	0.168	16.66471	1.874	0.158	2.64E+04	5.35E+03	3.776	0.131	0.131	-	ACS
Palomar 2	-7.97	-1.42	1.50	1.300	27200	975	31.225	31.225	0.665	0.154	14.02200	1.946	0.161	2.64E+05	5.34E+04	3.744	0.134	0.134	-	ACS
Pyxis	-5.73	-1.20	1.60	14.000	39400	83	9.110	9.110	0.569	0.611	11.59449	1.946	0.161	3.36E+04	6.78E+03	3.638	0.477	0.477	-	ACS
Ruprecht 106	-6.35	-1.68	0.70	6.100	21200	126	11.225	11.225	0.730	0.143	13.16012	1.868	0.155	5.70E+04	1.15E+04	3.481	0.128	0.128	-	ACS
Terzan 7	-5.01	-0.32	0.93	3.200	22800	80	8.944	8.944	0.829	0.249	10.37009	2.581	0.287	2.29E+04	4.94E+03	3.624	0.167	0.167	-	ACS
Terzan 8	-5.07	-2.16	0.60	7.600	26300	147	12.124	12.124	0.594	0.347	12.41205	1.885	0.159	1.77E+04	3.59E+03	4.145	0.271	0.271	-	ACS

Absolute magnitude M_V, metallciity [Fe/H], concentration, core radius r_c, and distance R_{Sun} are all taken from Harris (1996, 2010 edition). N_{RGB} is the number of RGB stars along with corresponding upper and lower limits (UL and LL), which are derived using $\sqrt{N}$ for values ≥ 50 and Poisson statistics (Gehrels, 1986) for values < 50. L_{frac} is the fraction of the total cluster luminosity that was observed in the field of view of the given *HST* instrument. $M_V^{fgstars}$ is the absolute V magnitude from foreground stars in the cluster field of view obtained from the Besançon models (Robin et al., 2003). Mass-to-light ratios are taken from Table 8 (column 6) of McLaughlin & van der Marel (2005). Masses were derived by multiplying the M/L by total cluster luminosity derived from M_V. $RGB_{frac} = N_{RGB}/\text{Mass}/L_{frac}$.

4.7 Impact of RGB Stars on Globular Cluster LMXBs

To assess the impact of RGB star density on LMXBs we need to identify their properties, such as confirmed optical counterparts and L_X. Our sample contains 8 LMXBs in 7 different GCs and 24 GCs with at least one qLMXB. While qLMXBs have $L_X \lesssim 10^{35}$ erg s^{-1}, XRB duty cycles in general are not well-known and thus qLMXBs could be in a transient state. Based on the low X-ray luminosities and hence low mass transfer rates, they should have main sequence or white dwarf companions. Searches for optical counterparts to qLMXBs have generally only proposed candidates (e.g. Heinke et al., 2005, 2009; Maxwell et al., 2012). This does not rule out the possibility some have RGB star companions, although this scenario would require a large orbital separation and/or reduced mass loss rates. However, no relationship between qLMXBs and mass nor metallicity in the Galaxy (extragalactic observations are not sensitive enough to detect qLMXBs) has been found (Heinke et al., 2003). Therefore a relationship between qLMXBs and RGB star density is not expected to exist, and as Figures 4.4 and 4.5 show the distribution of qLMXB clusters are not metallicity dependent. A KS test of the $RGB_{\rm frac}$ parameter for qLMXBs and non-LMXBs yielded a p-value of 0.66 and for the RGB star density parameter a p-value of 0.42, meaning we cannot reject the null hypothesis that the sample is drawn from a random distribution for either case. The qLMXBs with the largest RGB star numbers (NGC 5139, NGC 6139, NGC 6352, NGC 6366) and densities (NGC 6093, NGC 6266, NGC 6388) in Figures 4.4 and 4.5 are possible transient sources that have previously been in outburst, and thus good candidates for monitoring.

While qLMXBs are not known to be dependent on GC metalliticity, LMXB formation is. However, metallicity is known to be related to many other GC parameters, such as mass and density. Despite this, the metallicity effect has been shown to be independent of other factors. Kim et al. (2013) showed that for a sample of 408 extragalactic GC-LMXBs, the mass-metallicity relation was negligible (15%) compared to the factor of 3 difference in LMXB production between metal-rich and metal-poor GCs. In any case, there is no known mass-metallicity relationship for Milky Way GCs. In addition, Kim et al. (2013) found that for

extragalactic LMXBs, the metallicity dependence not only holds for all bright LMXBs, but that the effect is independent of X-ray luminosity ($> 10^{36}$ erg s^{-1}), stellar age, dynamical properties (e.g. stellar encounter rate), and selection effects. This makes the prediction that RGB star density causes the LMXB-metallicity dependence more intriguing, since the remaining GC parameters have been separated from the metallicity dependence. The significance of our study is only accurate if our initial conjecture is true: that LMXB companions should be RGB stars. Therefore we need to identify what fraction, if any, of the LMXBs in our sample are actually known to have RGB star counterparts.

An issue with work of this nature is that it is incredibly difficult to definitively determine the companions of LMXBs in GCs because the stellar density is so high. Verbunt & Lewin (2006) summarized potential candidates for a number of GC-LMXBs in the literature, with most being classified as a 'faint star' or having no clear counterpart. NGC 6624 could be a white dwarf or stripped core of an evolved main sequence star. NGC 7078 (M15) has 2 LMXBs, where X-1 is thought to have a red giant companion and X-2 a blue star as its companion. The orbital period of an LMXB was often used as an indicator of the type of companion, with orbital periods < 1 hr meaning degenerate stars, 3 hr $\leq P_{orb} \leq$ 10 hr indicating main sequence stars, and > 10 hr for giants. While these studies have suggested a number of LMXB companions are main sequence stars, this is based on the identification of a blue optical counterpart near/at the position of the X-ray source. The accretion disk of an LMXB is known to emit in the UV, which further complicates optical counterpart identification. With no confirmation of counterparts for any LMXBs, we cannot say with any certainty that RGB stars are companions. Population synthesis models (Ivanova et al., 2008, e.g.) have predicted that the LMXB formation rate is highest for neutron stars with main sequence donors. However, the mass transfer rates and thus X-ray luminosities of these systems are low ($< 10^{37}$ erg s^{-1}). Therefore red giant companions are thought to compose the brightest LMXBs because they provide the necessary mass transfer rates to drive higher L_X (Fragos et al., 2008, 2009). Only three of the bright GC-LMXBs in the Milky Way have X-ray luminosities $\gtrsim 10^{37}$ erg s^{-1}, NGC 6441, NGC 6624, and Liller 1 (Liu

et al., 2007), where Liller 1 is not part of our sample. From the candidates and L_X values we can infer that 3 of the 8 LMXBs in different clusters are likely to have RGB star companions.

Our study attempted to address why metal-rich GCs produce more LMXBs than metal-poor GCs by investigating the relationship between the number density of RGB stars in a GC and GC metallicity. Even if our sample of GC-LMXBs does not have RGB star donors, we are still probing the relationship between the number density of RGB stars and metallicity of all GCs and not just those with an LMXB. If all metal-rich GCs had much higher RGB star densities than metal-poor ones, it would be evidence to support the impact of GC metallicity on LMXB formation. In Figure 4.5, the RGB star number density does appear larger for metal-rich LMXBs compared to the best fit relation, and the overall distribution is correlated with [Fe/H] based on a Spearman Rank test. However, we caution that the intrinsic dependence of volume on r_h, which is correlated with both LMXB formation and metallicity, biases this result. When investigating the effect of RGB star density on on GC metallicity, it is difficult to remove the correlation that density (through r_h) has on metallicity.

To exclude the intrinsic dependence of density on metallicity, we can use the $RGB_{\rm frac}$ parameter. While $RGB_{\rm frac}$ only represents the number of RGB stars per $M_\odot$ and not a volume density, it is independent of mass and density, which both influence LMXB formation. Therefore $RGB_{\rm frac}$ can be used as an independent probe of whether the number of RGB stars in a GC varies with metallicity, explaining the enhanced production of LMXBs in metal-rich GCs. From Figure 4.4, we found no dependence between the $RGB_{\rm frac}$ parameter and metallicity. Although we cannot reject the null hypothesis that the parameters are uncorrelated based on a Spearman's Rank test, this does not mean that $RGB_{\rm frac}$ and [Fe/H] are not correlated. The shallow slope from the least squares fit and large uncertainties on $RGB_{\rm frac}$ are an indication that further analysis with improved measurements would lead to a more robust result. While we cannot claim there is an independent relationship between RGB star number density and metallicity, qLMXBs appear more prevalent in the metal-poor GC population. When we split the qLMXBs into populations based on metallicity at [Fe/H] = -1.0 (the approximate separation of

the bimodal [Fe/H] distribution; Bellazzini et al. 1995), we found the fraction of GC-qLMXBs was only 4% larger (as a fraction of the total GCs in that population) in the metal-poor (31%) vs. the metal-rich (27%) population. The number of qLMXBs within a GC can vary (see Section 4.6.3), and so this result is only based on the number of GCs that host at least one qLMXB. In addition, selection effects are a large source of uncertainty because many GCs have not been observed at the L_X limits for detecting qLMXBs. More work into the nature of qLMXBs and GC metallicity is needed. As (Ivanova et al., 2008) states, a independent correlation (or lack thereof) between qLMXB number and metallicity can help us better understand the metallicity dependence on LMXB formation.

We still have not addressed the impact that the accretor in the LMXB has on our interpretation. If the compact object in a GC-LMXB is a black hole, those with luminosities $> 10^{37}$ erg s^{-1} don't require RGB star companions. Conveniently, the compact objects in bright Milky Way GC-LMXBs are all neutron stars. Only 4 black hole candidates have been identified to date, with two detected in radio and not X-ray (Strader et al., 2012), and two with X-ray luminosities $< 10^{33}$ erg s^{-1} (Chomiuk et al., 2013; Miller-Jones et al., 2015). Nonetheless, Ivanova et al. (2010) found that RGB stars have a similar effect on the production of black hole LMXBs indirectly by increasing the formation rates of the seeds (LMXBs with red giant donors) of black hole-white dwarf binaries.

4.8 Improvements and Future Work

To improve our analysis a number of developments need to take place. Firstly, the uncertainties on measurements of GC distances and luminosities need to be improved. The imminent first data release from *GAIA* will improve distance measurements for GCs, which is currently one of the dominant sources of uncertainty in all GC studies. Higher spatial resolution data using *Hubble* that covers the entire GC population will improve both number statistics and consistency between GCs. Specifically, observing the complete extent of each GC will reduce the

large uncertainties associated with luminosity correction. By using the ACS camera (resolution of 0.05″ pixel^{-1}) and WFPC2 (WF2/WF3WF4 each have resolution 0.1″ pixel^{-1}, PC1 has resolution of 0.046″ pixel^{-1}) its possible that crowding could have been an issue. However, because PC1 was centred on the core of each GC, this effect will be minimal given the similar resolution and concentration of RGB stars in cluster cores. The M/L ratios we used can be inaccurate but are internally consistent, only resulting in a systematic error in GC mass. However, our largest source of uncertainty in $RGB_{\rm frac}$ comes from the modelled M/L ratios used to determine masses, which limits the both the interpretation and significance of our results. Follow-up work to localize LMXBs with *Chandra* and analyze the optical counterparts in *HST* images in the X-ray error ellipse can yield further insight in companions.

Future endeavours will need to reduce the uncertainty on GC parameters in order to obtain more robust results. The GCs in M31 might appear to be ideal targets for many reasons. First, each GC is at the same distance and data is available for the entire cluster, eliminating two of the largest uncertainties in our work. The recently completed Panchromatic *Hubble* Andromeda Treasury survey obtained 6-filter photometry in the UV to NIR for one-third of M31's disk, and is complete for the bright-end of the RGB in the field. However, the central stellar density in M31's $\approx$ 500 GCs is too high to count RGB stars. Therefore our analysis remains restricted to our Galaxy and improving measurements such as M/L. As Ivanova et al. (2012) stated, a population synthesis study that includes red giants will also advance our understanding of their effect while controlling for GC parameters such as the affect r_h has on RGB star density. This could be accomplished using models with the same r_h over a wide range of metallicity at fixed mass and galactocentric distance.

4.9 Summary

One of the unanswered questions in GC-LMXB studies is the origin of the metallicity effect. Why are there $\sim$ 3 times more LMXBs in metal-rich GCs compared to metal-poor ones? In

this work we investigated this relationship by assuming that the RGB star number density is correlated with metallicity, and thus is the underlying physical cause of the correlation. We used *HST* data from the ACS and WFPC2 instruments for 109 unique Milky Way GCs to calculate the number of RGB stars $N_{\rm RGB}$. We made corrections for the fraction of cluster light observed and foreground star contamination. Normalizing by GC mass we found no correlation between $RGB_{\rm frac}$ (number of RGB stars per $M_{\odot}$) and metallicity. Because RGB stars are likely mass-segregated, many will be located within the half-light radius of a GC. We normalized $RGB_{\rm frac}$ by the GC volume at the half-light radius to find the number density of RGB stars. The RGB star number density was correlated with metallicity [Fe/H], indicating the underlying cause of the LMXB preference for metal-rich GCs. Spearman and Kendall Rank tests gave p-values of 0.00016 and 0.00021 and coefficients $r_s = 0.35$ and $\tau = 0.24$ respectively. However, we caution that this result is inherently biased by the half-light radius r_h, which affects LMXB formation rate and is negatively correlated with GC metallicity. In addition, not all LMXBs have RGB star companions, but this does not preclude a relationship between RGB star density and [Fe/H]. No correlation between the number of qLMXBs or RGB star parameters for qLMXBs and GC metallicity was found. Follow-up observations of Milky Way GCs with *HST* that cover the entire cluster extent will reduce uncertainties, as will updated distance measurements with *GAIA*. Even next generation space-based optical telescopes will not have the capability to study promising extragalactic GCs in e.g. M31, where a more consistent, relevant, and robust analysis would be possible.

Bibliography

Agar, J. R. R., & Barmby, P. 2013, AJ, 146, 135

Bahramian, A., Heinke, C. O., Sivakoff, G. R., & Gladstone, J. C. 2013, ApJ, 766, 136

Barmby, P., Huchra, J. P., Brodie, J. P., et al. 2000, AJ, 119, 727

Barmby, P., McLaughlin, D. E., Harris, W. E., Harris, G. L. H., & Forbes, D. A. 2007, AJ, 133, 2764

Bellazzini, M., Pasquali, A., Federici, L., Ferraro, F. R., & Pecci, F. F. 1995, ApJ, 439, 687

Bregman, J. N., Irwin, J. A., Seitzer, P., & Flores, M. 2006, ApJ, 640, 282

Bruzual, G., & Charlot, S. 2003, MNRAS, 344, 1000

Cardelli, J. A., Clayton, G. C., & Mathis, J. S. 1989, ApJ, 345, 245

Carretta, E., Bragaglia, A., Gratton, R., D'Orazi, V., & Lucatello, S. 2009, A&A, 508, 695

Chabrier, G. 2003, PASP, 115, 763

Chomiuk, L., Strader, J., Maccarone, T. J., et al. 2013, ApJ, 777, 69

Clark, G. W. 1975, ApJ, 199, L143

Dotter, A., Chaboyer, B., Jevremović, D., et al. 2007, AJ, 134, 376

—. 2008, ApJS, 178, 89

Dotter, A., Sarajedini, A., Anderson, J., et al. 2010, ApJ, 708, 698

Fabian, A. C., Pringle, J. E., & Rees, M. J. 1975, MNRAS, 172, 15P

Fragos, T., Kalogera, V., Belczynski, K., et al. 2008, ApJ, 683, 346

Fragos, T., Kalogera, V., Willems, B., et al. 2009, ApJ, 702, L143

Gehrels, N. 1986, ApJ, 303, 336

Grindlay, J. E. 1993, in Astronomical Society of the Pacific Conference Series, Vol. 48, The Globular Cluster-Galaxy Connection, ed. G. H. Smith & J. P. Brodie, 156

Harris, W. E. 1996, AJ, 112, 1487

Harris, W. E., Whitmore, B. C., Karakla, D., et al. 2006, ApJ, 636, 90

Heinke, C. O., Cohn, H. N., & Lugger, P. M. 2009, ApJ, 692, 584

Heinke, C. O., Grindlay, J. E., Edmonds, P. D., et al. 2005, ApJ, 625, 796

Heinke, C. O., Grindlay, J. E., Lugger, P. M., et al. 2003, ApJ, 598, 501

Humphrey, P. J., & Buote, D. A. 2008, ApJ, 689, 983

Ivanova, N., Chaichenets, S., Fregeau, J., et al. 2010, ApJ, 717, 948

Ivanova, N., Heinke, C. O., Rasio, F. A., Belczynski, K., & Fregeau, J. M. 2008, MNRAS, 386, 553

Ivanova, N., & Kalogera, V. 2006, ApJ, 636, 985

Ivanova, N., Fragos, T., Kim, D.-W., et al. 2012, ApJ, 760, L24

Jordán, A. 2004, ApJ, 613, L117

Jordán, A., Côté, P., Ferrarese, L., et al. 2004, ApJ, 613, 279

Katz, J. I. 1975, Nature, 253, 698

Kavelaars, J. J., & Hanes, D. A. 1997, MNRAS, 285, L31

Kim, D.-W., Fabbiano, G., Ivanova, N., et al. 2013, ApJ, 764, 98

Kim, D.-W., Fabbiano, G., Brassington, N. J., et al. 2009, ApJ, 703, 829

Kim, E., Kim, D.-W., Fabbiano, G., et al. 2006, ApJ, 647, 276

Kundu, A., Maccarone, T. J., & Zepf, S. E. 2002, ApJ, 574, L5

—. 2007, ApJ, 662, 525

Liu, Q. Z., van Paradijs, J., & van den Heuvel, E. P. J. 2007, VizieR Online Data Catalog, 346, 90807

Maccarone, T. J., Kundu, A., & Zepf, S. E. 2004, ApJ, 606, 430

Mamajek, E. E. 2012, ApJ, 754, L20

Maxwell, J. E., Lugger, P. M., Cohn, H. N., et al. 2012, ApJ, 756, 147

McLaughlin, D. E., & van der Marel, R. P. 2005, ApJS, 161, 304

Miller-Jones, J. C. A., Strader, J., Heinke, C. O., et al. 2015, MNRAS, 453, 3919

Mineo, S., Fabbiano, G., D'Abrusco, R., et al. 2014, ApJ, 780, 132

Nataf, D. M., Gould, A. P., Pinsonneault, M. H., & Udalski, A. 2013, ApJ, 766, 77

Paolillo, M., Puzia, T. H., Goudfrooij, P., et al. 2011, ApJ, 736, 90

Peacock, M. B., Maccarone, T. J., Kundu, A., & Zepf, S. E. 2010, MNRAS, 407, 2611

Peng, E. W., Jordán, A., Côté, P., et al. 2006, ApJ, 639, 95

Piotto, G., King, I. R., Djorgovski, S. G., et al. 2002, A&A, 391, 945

Pooley, D., Lewin, W. H. G., Anderson, S. F., et al. 2003, ApJ, 591, L131

Robin, A. C., Reylé, C., Derrière, S., & Picaud, S. 2003, A&A, 409, 523

Sarajedini, A., Bedin, L. R., Chaboyer, B., et al. 2007, AJ, 133, 1658

Sarazin, C. L., Kundu, A., Irwin, J. A., et al. 2003, ApJ, 595, 743

Schlafly, E. F., & Finkbeiner, D. P. 2011, ApJ, 737, 103

Sivakoff, G. R., Jordán, A., Sarazin, C. L., et al. 2007, ApJ, 660, 1246

Strader, J., Brodie, J. P., Spitler, L., & Beasley, M. A. 2006, AJ, 132, 2333

Strader, J., Chomiuk, L., Maccarone, T. J., Miller-Jones, J. C. A., & Seth, A. C. 2012, Nature, 490, 71

Strader, J., & Smith, G. H. 2008, AJ, 136, 1828

Trudolyubov, S., & Priedhorsky, W. 2004, ApJ, 616, 821

VandenBerg, D. A., & Clem, J. L. 2003, AJ, 126, 778

Verbunt, F., & Lewin, W. H. G. 2006, Globular cluster X-ray sources, ed. Lewin, W. H. G. & van der Klis, M., 341–379

Vulic, N., Gallagher, S. C., & Barmby, P. 2014, ApJ, 790, 136

Chapter 5

Conclusions & Future Work

Since the discovery of the first extrasolar X-ray source, Sco X-1, our understanding of these enigmatic sources known as XRBs has moved at a rapid pace. *Chandra* observations, due to their superior angular resolution, have been invaluable to studies of the dense environments in which XRBs are found. We have learned that HMXBs are associated with star-forming regions and LMXBs with GCs. These connections have been well established in spiral and elliptical galaxies, respectively. HMXBs have young stellar companions and therefore are expected to be found near star-forming regions and young star clusters. Conversely, LMXBs have low-mass companions and are found in large numbers in GCs, specifically those that are massive, compact, and metal-rich. The link between mass and compactness is a consequence of the larger number and number densities of stars that create dynamical conditions most favourable for LMXB formation. However, there are still many unanswered questions concerning XRBs and their environments. For instance, do these trends extend down to the faintest X-ray luminosities? The difficulty in detecting faint sources outside our Galaxy has hindered progress on this front. In addition, we still do not understand the underlying physical cause for the dependence of LMXB formation on GC metallicity. These questions are important to address to better understand the nature of the compact object population in the Universe. This thesis has presented an investigation of X-ray sources in M31 and the Milky Way that has attempted to

explain these issues.

In Chapter 2, to probe connections between XRBs and their environments, we studied M31 X-ray sources associated with star clusters and H II regions using 121 publicly available *Chandra* ACIS observations. From a sample of 83 star clusters, we found that on average, those that had the smallest effective radii (most compact), were brightest (most massive), and had the reddest colours (metal-rich) preferentially hosted X-ray sources. A statistical analysis found that brightness was the most important predictor followed by compactness; the colour was not statistically significant. These findings confirmed previous results in M31, albeit using deeper optical and X-ray data with *HST* and *Chandra*, that GC mass and size have a stronger effect on LMXB formation than metallicity. The lack of a strong metallicity effect could stem from our sample size not only being small, but concentrated in the nucleus of M31, resulting in mostly metal-rich GCs. In addition, the X-ray luminosities of our LMXB-hosting star clusters probed 2 orders of magnitude fainter than previous work, suggesting that the metallicity relationship may not hold for quiescent LMXBs. However, our work does imply that the dependence of GC mass and compactness on the presence of an LMXB extends into the quiescent regime (qLMXBs). A larger sample is required in order to properly address the significance of such a relation.

To probe potential HMXBs in star-forming regions we studied a sample of 1566 H II regions and found on average those with smaller radii were more likely to be associated with an X-ray source. A statistical analysis found that neither the radius nor Hα luminosity of an H II region was a significant predictor of it hosting an X-ray source. This was the first attempt to compare the parameters of an H II region in relation to the presence of an X-ray source. HMXBs are generally found near star-forming regions, such as H II regions, but their distribution is not well constrained. Our results indicated that most of the matched X-ray sources are SNRs. This is expected considering our matching analysis used the average radii of all H II regions, therefore identifying only sources within H II regions. The probability of finding an HMXB within an H II region is low because H II regions only survive for a few Myr. Instead, HMXBs have

been found at larger separations from these and other star-forming regions, thought to be the result of compact object natal kicks. Increasing our matching radius was not productive as crowding became an issue, complicating further analysis. A study of the HMXB distribution in M31 is needed, although this is hampered by the lack of any confirmed HMXBs in M31. To confirm an HMXB, high resolution optical and X-ray data (i.e. *Chandra* and *HST*) would be needed to identify only one optical counterpart (high-mass OB star determined through optical photometry and spectroscopy) in the X-ray uncertainty ellipse. A radial velocity measurement along with the period of the binary system can constrain the mass of the compact object.

To investigate the quiescent XRB population, a stacking analysis of both the star clusters and H II regions in M31 was completed. We obtained non-detections across all X-ray energy bands and average upper limits of $\approx 10^{32}$ erg s^{-1}. These limits reach below the known values for qLMXBs and other faint X-ray sources in Milky Way GCs. This result was somewhat surprising for the star cluster population considering that GCs in our Galaxy have a preponderance of faint X-ray sources. Our star cluster sample came from the bulge of M31 and thus consisted of mostly GCs with ages $\gtrsim$ 1 Gyr. We divided our stacked samples into various groups that reflected environments favourable for XRB formation (i.e. bright, compact). These stacked samples showed some improvement in signal but no detection. While there are numerous caveats in the analysis (e.g. PSF, background), the largest obstacle when using this methodology is the sample itself. Specifically, not every star cluster is expected to have a quiescent X-ray source, be it a qLMXB or CV. As such, the average signal from a sample of stacked clusters is reduced based on the percentage of clusters that don't host an X-ray source. Future work to expand the sample in M31, as well as studies of larger samples in 'cleaner' galaxy environments (e.g. elliptical galaxies), may shed more light on the faint X-ray population.

In Chapter 3, we studied the properties of the faint X-ray source population in M31. Being the closest large galaxy and also a Milky Way analogue we can learn much about our own Galaxy's population, where studies are limited by obscuration in the disk. From 133 publicly available *Chandra* ACIS observations totalling $\sim$ 1 Ms we created the deepest X-ray point

source catalogue of M31. Within a field of view of 0.6 deg^2 we detected 795 sources to a limiting unabsorbed 0.5 − 8.0 keV luminosity of $\sim 10^{34}$ erg s^{-1}. Our catalogue is different from previous work in M31 because it has combined all astrometrically-corrected observations to reach the most sensitive X-ray luminosities. In addition, stringent requirements for source detection and processing through *ACIS Extract* produced the most detailed set of source characteristics available. For these reasons the usefulness of our catalogue compared with others is clear. Cross-correlation with all previously-identified X-ray sources yielded 259 new sources. These new sources are all fainter and have lower significance than the rest of the catalogue. XLFs created in the hard energy band indicated that the observational catalogues of AGN are incomplete. Combined with the XLFs in the soft energy band, we found that the bulge XLFs are flatter than the disk. This is consistent with previous studies in M31, but not with other galaxies. It indicates a lack of bright HMXBs in the disk and an aging LMXB population in the bulge. With multi-epoch data of each source we can use source characteristics to study variability over a 15-year time period, which is unparalleled for galaxies observed with *Chandra*.

Chapter 4 focused on exploring the relationship between GC metallicity and LMXB formation. A difference in the number densities of RGB stars has been proposed as an explanation for why metal-rich GCs are ~ 3 times likely to host LMXBs than metal-poor GCs. Using *HST* data for 109 Galactic GCs we determined the number of RGB stars. Correcting for observational effects and individual cluster properties, we found the density of RGB stars in each GC. Spearman and Kendall Rank tests confirmed the correlation of RGB star density with metallicity [Fe/H]. We caution that this result is biased because we calculated volume using the GC half-light radius, r_h. The half-light radius is known to be independently correlated with LMXB formation, as it is an indication of the density of the cluster stars. This inherent connection between r_h and our value of RGB star density is difficult to remove. Any measurement of the density of stars requires that we use a probe of the cluster density, which is tied to its compactness via r_h. Not all LMXBs are expected to have RGB star companions, although this does not

rule out a connection between RGB star density and metallicity. However, there has been indication of a negative correlation between r_h and GC metallicity in M31, which would bias the relationship between RGB star density and metallicity. An in-depth study of this relationship in the Milky Way and other galaxies is required to determine the connection between r_h and metallicity. We found no relationship between the number of qLMXBs and GC metallicity, as expected. The sample of qLMXBs in our Galaxy in not complete and thus an X-ray survey to catalogue their population and provide completeness across the entire GC population is required. In addition, follow-up observations in the optical that probe the entire extent of all GCs will reduce uncertainties.

The progress made in this thesis has set forth a path to understanding the entire range of XRB X-ray luminosities. Future endeavours will require either orders of magnitude more observing time or significant developments in X-ray instrumentation to detect fainter sources outside our Galaxy. While improvements to current measurements can be made, other methods can prove more useful. The next step for advancing XRB research is both survey science and higher energy observations. The *eROSITA* mission, due to launch in 2017, is an all-sky survey in the $2-10$ keV range that will detect all XRBs in our Galaxy down to 10^{33} erg s^{-1} as well as many sources in the nearby Universe. Variability studies will greatly benefit from this survey, especially because XRBs are highly transient systems. A precursor to these studies would come from my M31 catalogue, which has detailed multi-epoch source characteristics over a 15-year period. Results from my catalogue can constrain the evolution of individual sources over a long period of time, with observations that are not periodic.

In terms of higher energy surveys, the recent launch of *NuSTAR* has revolutionized our understanding of the > 10 keV extragalactic XRB population. This energy regime, combined with < 10 keV data, is crucial for classifying XRBs based on their accretion state and compact object type. The recent completion of the *Chandra*-PHAT survey in M31 has expanded the field of view of high angular resolution X-ray observations. This multiwavelength data will result in the first confirmation of HMXBs in M31, and allow us to study their distribution, age,

physical parameters of the donor star, and connections between optical and X-ray properties. Complementary *NuSTAR* data in this same field will result in the most exquisite $0.3 - 30$ keV extragalactic data with *HST* coverage. The *NuSTAR* program intends to start a monitoring campaign which, when combined with the all-sky survey from *eROSITA* in the coming years, will be the most powerful galaxy-wide dataset to study XRBs.

Appendix A

Complete M31 Source List

Table A.1: M31 Source List

Source No.	CXOU J	R.A. (J2000) (°)	Decl. (J2000) (°)	Distance (′)	PosErr (″)	θ (′)	No. of Obs	Detector	Region	Tot Exp (ks)	Tot Exp. Map Value (s cm^2)	R_{src} (sky pixel)	SNR	$E_{\rm median}$ (keV)	Match
(1)	(2)	(3)	(4)	(5)	(6)	(7)	(8)	(9)	(10)	(11)	(12)	(13)	(14)	(15)	(16)
1	004542.90+414312.6	11.428779	41.720189	43.03	0.2	4.1	2	ACIS-S	NE	49	1.14E+07	4.5	6.5	2.1	
2	004551.05+414452.4	11.462750	41.747912	45.26	0.3	3.5	2	ACIS-S	NE	49	1.64E+07	3.5	2.7	2.7	
3	004551.30+414220.7	11.463769	41.705754	43.74	0.2	2.8	3	ACIS-S	NE	64	2.20E+07	2.8	2.4	2.3	AGN
4	004552.93+414441.8	11.470551	41.744965	45.42	0.2	3.1	2	ACIS-S	NE	49	1.68E+07	3.0	2.8	2.0	
5	004555.72+414551.8	11.482172	41.764389	46.56	0.3	3.7	2	ACIS-S	NE	49	1.67E+07	4.0	2.5	2.5	
6	004556.82+414440.8	11.486787	41.744673	45.98	0.2	2.6	2	ACIS-S	NE	49	1.72E+07	2.5	2.5	2.7	
7	004556.99+414831.7	11.487497	41.808829	48.48	0.2	6.2	2	ACIS-S	NE	49	1.60E+07	9.3	9.6	2.4	AGN
8	004559.07+414113.0	11.496132	41.686945	44.27	0.2	2.6	5	ACIS-S	NE	91	3.38E+07	3.0	5.3	2.9	
9	004602.43+414515.7	11.510137	41.754377	47.16	0.2	3.1	3	ACIS-S	NE	63	1.84E+07	3.3	5.7	2.1	
10	004602.70+413856.7	11.511251	41.649095	43.61	0.3	3.4	3	ACIS-S	NE	41	1.62E+07	4.1	3.6	1.4	
11	004604.66+414123.3	11.519431	41.689806	45.23	0.1	2.0	5	ACIS-S	NE	91	3.44E+07	2.4	5.9	0.9	
12	004605.10+414236.5	11.521263	41.710142	45.99	0.2	1.6	5	ACIS-S	NE	91	3.43E+07	2.6	3.6	2.4	
13	004605.79+414303.2	11.524126	41.717559	46.35	0.1	1.8	5	ACIS-S	NE	91	3.42E+07	2.8	7.1	1.0	
14	004606.74+414603.4	11.528114	41.767632	48.29	0.8	4.4	3	ACIS-S	NE	63	2.17E+07	5.6	2.2	2.8	
15	004609.33+414247.1	11.538877	41.713099	46.74	0.2	1.7	5	ACIS-S	NE	91	3.36E+07	2.5	2.8	3.7	
16	004611.46+413940.1	11.547781	41.661161	45.39	0.1	2.2	3	ACIS-S	NE	41	1.69E+07	2.6	5.5	1.6	
17	004612.21+414535.0	11.550908	41.759740	48.81	0.4	4.4	4	ACIS-S	NE	77	2.67E+07	5.6	3.4	2.2	
18	004613.87+414457.6	11.557794	41.749354	48.69	0.4	3.8	5	ACIS-S	NE	91	3.03E+07	4.4	2.1	1.1	
19	004614.58+414013.1	11.560780	41.670310	46.17	0.2	2.1	3	ACIS-S	NE	41	1.64E+07	2.3	3.3	1.8	
20	004614.67+414317.6	11.561131	41.721574	47.85	0.2	2.4	5	ACIS-S	NE	91	3.40E+07	2.8	4.1	1.5	
21	004615.36+414128.1	11.564025	41.691153	46.95	0.1	2.2	5	ACIS-S	NE	91	3.28E+07	2.2	9.8	2.8	
22	004615.86+414026.0	11.566099	41.673892	46.49	0.3	2.4	5	ACIS-S	NE	91	2.39E+07	2.4	1.3	5.5	
23	004616.82+414300.4	11.570103	41.716791	48.02	0.0	2.5	5	ACIS-S	NE	91	3.39E+07	2.7	17.4	1.5	
24	004616.85+413656.6	11.570216	41.615746	44.94	0.2	4.3	3	ACIS-S	NE	41	1.58E+07	5.4	7.0	0.9	
25	004620.54+414336.2	11.585609	41.726736	48.93	0.4	3.3	5	ACIS-S	NE	91	3.31E+07	3.4	1.7	1.0	AGN
26	004620.96+414240.6	11.587361	41.711283	48.49	0.1	2.9	5	ACIS-S	NE	91	3.32E+07	2.9	6.4	1.7	
27	004621.14+414309.2	11.588087	41.719223	48.77	0.3	3.1	5	ACIS-S	NE	91	3.31E+07	3.2	2.1	1.1	
28	004621.82+414116.7	11.590952	41.687983	47.88	0.1	2.9	5	ACIS-S	NE	91	3.19E+07	3.0	7.5	2.6	
29	004622.17+414436.7	11.592416	41.743542	49.75	0.4	4.1	5	ACIS-S	NE	91	3.22E+07	4.8	3.3	2.3	
30	004622.21+413953.4	11.592552	41.664849	47.23	0.2	2.4	3	ACIS-S	NE	41	1.70E+07	2.6	3.6	1.6	
31	004622.33+414419.0	11.593062	41.738623	49.61	0.2	3.9	5	ACIS-S	NE	91	3.24E+07	4.3	5.1	2.3	
32	004622.38+414426.5	11.593285	41.740718	49.69	0.2	4.0	5	ACIS-S	NE	91	3.23E+07	4.6	8.2	2.1	
33	004622.90+414733.2	11.595428	41.792558	51.58	0.6	6.1	2	ACIS-S	NE	49	1.59E+07	9.1	3.4	1.2	
34	004623.43+413546.9	11.597647	41.596363	45.53	0.4	4.3	1	ACIS-S	NE	13	3.61E+06	4.8	2.7	1.4	
35	004623.79+413751.4	11.599140	41.630955	46.51	0.5	3.7	3	ACIS-S	NE	41	1.64E+07	4.5	2.6	1.1	
36	004624.36+414553.1	11.601523	41.764758	50.81	0.3	5.3	3	ACIS-S	NE	63	1.94E+07	7.3	5.6	2.1	
37	004624.44+414124.8	11.601862	41.690225	48.37	0.2	3.2	5	ACIS-S	NE	91	3.09E+07	3.4	4.7	2.0	
38	004625.43+414226.1	11.605971	41.707259	49.06	0.3	3.5	5	ACIS-S	NE	91	3.14E+07	3.7	3.4	1.2	
39	004627.55+413902.5	11.614824	41.650711	47.69	0.2	3.1	3	ACIS-S	NE	41	1.66E+07	3.8	6.2	1.8	
40	004627.69+414510.9	11.615407	41.753029	50.92	0.3	5.1	4	ACIS-S	NE	78	2.48E+07	6.8	6.4	1.9	
41	004629.20+414313.1	11.621683	41.720329	50.07	0.2	3.9	3	ACIS-S	NE	41	1.62E+07	4.5	5.6	1.1	

Source No.	CXOU J	R.A. (J2000) (°)	Decl. (J2000) (°)	Distance (′)	PosErr (″)	θ (′)	No. of Obs	Detector	Region	Tot Exp (ks)	Tot Exp. Map Value (s cm^2)	R_{src} (sky pixel)	SNR	$E_{\rm median}$ (keV)	Match
42	004639.00+413906.4	11.662526	41.651802	49.61	0.7	6.4	1	ACIS-S	NE	14	4.93E+06	9.6	2.8	1.6	
43	003813.88+401521.9	9.557837	40.256086	79.46	0.8	6.4	1	ACIS-S	SW	14	4.31E+06	9.9	2.2	2.0	
44	003815.94+401615.4	9.566454	40.270967	78.52	0.2	4.3	2	ACIS-S	SW	29	1.14E+07	5.6	7.3	1.9	
45	003816.61+401800.4	9.569234	40.300117	77.11	0.8	4.5	3	ACIS-S	SW	43	1.60E+07	5.6	1.7	0.3	
46	003818.90+401532.6	9.578781	40.259082	78.71	0.4	4.0	3	ACIS-S	SW	43	1.44E+07	5.0	3.6	1.6	
47	003821.50+401819.6	9.589616	40.305454	76.26	0.1	3.8	3	ACIS-S	SW	43	1.69E+07	4.2	10.4	1.8	
48	003821.80+401545.0	9.590841	40.262509	78.20	0.4	3.6	3	ACIS-S	SW	43	1.66E+07	4.4	2.1	1.6	
49	003822.01+401747.4	9.591745	40.296523	76.60	0.3	3.6	3	ACIS-S	SW	43	1.70E+07	4.0	4.1	2.6	
50	003823.84+401250.0	9.599338	40.213890	80.25	0.2	7.3	1	ACIS-S	SW	13	2.75E+06	12.6	15.5	1.2	
51	003825.63+401324.3	9.606818	40.223435	79.59	0.8	6.7	1	ACIS-S	SW	13	4.62E+06	10.9	2.8	2.8	
52	003825.65+401739.0	9.606894	40.294185	76.27	0.3	3.0	3	ACIS-S	SW	43	1.73E+07	3.2	2.2	1.2	
53	003827.27+401735.3	9.613640	40.293157	76.12	0.3	2.8	3	ACIS-S	SW	43	1.74E+07	2.9	1.9	1.4	
54	003827.37+401247.3	9.614054	40.213151	79.88	0.5	7.2	1	ACIS-S	SW	13	4.63E+06	12.5	5.7	2.3	AGN
55	003827.61+401832.6	9.615075	40.309082	75.34	0.2	3.0	3	ACIS-S	SW	43	1.73E+07	3.2	3.5	2.7	
56	003831.18+401711.7	9.629953	40.286609	75.95	0.1	2.4	3	ACIS-S	SW	43	1.75E+07	2.4	4.6	0.8	
57	003836.99+401401.0	9.654145	40.233636	77.79	0.3	3.6	3	ACIS-S	SW	43	1.70E+07	4.4	4.0	1.9	
58	003838.66+401510.8	9.661108	40.253007	76.67	0.4	2.7	3	ACIS-S	SW	43	1.74E+07	3.1	2.0	0.8	
59	003838.97+401856.5	9.662394	40.315717	73.66	0.1	2.7	3	ACIS-S	SW	43	1.75E+07	2.8	8.5	1.5	
60	003844.30+401803.6	9.684594	40.301004	73.73	0.3	2.6	3	ACIS-S	SW	43	1.68E+07	2.7	2.2	2.6	
61	003844.34+401659.7	9.684772	40.283262	74.57	0.3	2.4	3	ACIS-S	SW	43	1.75E+07	2.7	2.2	1.4	
62	003850.99+401805.5	9.712489	40.301541	72.93	0.2	3.4	3	ACIS-S	SW	43	1.71E+07	3.7	4.2	1.6	
63	003851.33+401950.1	9.713878	40.330601	71.50	0.5	4.2	3	ACIS-S	SW	43	1.64E+07	5.1	2.5	2.9	
64	003854.74+402009.0	9.728086	40.335850	70.86	0.2	4.9	3	ACIS-S	SW	43	1.55E+07	6.5	6.8	2.0	
65	003855.34+401644.9	9.730604	40.279160	73.52	0.2	3.8	3	ACIS-S	SW	43	1.66E+07	4.7	7.8	1.1	AGN
66	003856.59+401830.4	9.735808	40.308445	71.96	0.5	4.3	3	ACIS-S	SW	43	1.62E+07	5.4	2.4	1.6	
67	003900.36+401603.5	9.751528	40.267662	73.52	0.8	6.3	1	ACIS-S	SW	13	4.75E+06	9.5	2.3	1.4	
68	004111.89+405422.5	10.299570	40.906270	27.86	0.5	8.3	2	ACIS-I		9	1.77E+06	13.9	6.4	2.3	
69	004115.38+410102.5	10.314120	41.017379	22.54	0.6	9.3	4	ACIS-I		18	3.33E+06	16.9	6.2	1.9	
70	004115.84+405744.3	10.316041	40.962310	24.81	0.6	6.9	3	Both	B3	63	1.73E+07	10.9	3.2	2.4	
71	004116.64+405703.2	10.319334	40.950913	25.23	0.7	6.7	3	Both	B3	63	1.87E+07	10.5	1.4	3.0	
72	004117.97+405617.2	10.324903	40.938138	25.65	0.6	6.4	3	Both	B3	63	1.82E+07	9.9	2.7	2.4	
73	004118.65+405158.6	10.327722	40.866293	29.05	0.6	8.1	1	ACIS-I		4	9.43E+05	12.8	4.7	1.0	
74	004119.90+410012.4	10.332943	41.003454	22.50	1.1	8.3	4	ACIS-I		18	3.53E+06	13.8	2.5	1.4	
75	004121.19+410341.7	10.338303	41.061597	19.98	1.0	8.5	2	ACIS-I		8	1.67E+06	14.3	2.7	1.9	
76	004122.34+405750.0	10.343104	40.963916	23.94	0.4	5.9	4	Both	B3	68	2.06E+07	8.3	4.7	1.4	
77	004123.87+405508.9	10.349461	40.919156	25.88	0.3	5.4	3	Both	B3	63	1.84E+07	7.1	5.9	2.1	
78	004125.89+405845.9	10.357895	40.979433	22.79	0.1	5.8	6	Both	B3	85	2.30E+07	8.0	41.2	2.0	
79	004126.25+405326.0	10.359410	40.890572	27.04	0.3	6.2	2	ACIS-I		9	1.98E+06	7.8	6.1	2.0	AGN
80	004127.50+405056.6	10.364593	40.849073	29.05	1.6	7.7	2	ACIS-I		9	1.43E+06	11.9	1.2	2.7	
81	004128.40+405605.7	10.368337	40.934924	24.61	0.3	4.6	4	Both	B3	68	2.03E+07	5.4	4.0	1.7	
82	004128.46+405722.4	10.368602	40.956228	23.58	0.3	4.7	4	Both	B3	68	2.12E+07	5.4	4.2	2.7	
83	004128.74+405448.7	10.369782	40.913532	25.63	0.2	4.8	4	Both	B3	68	1.95E+07	5.7	9.5	2.2	
84	004128.99+410212.2	10.370827	41.036740	19.87	0.2	6.9	6	Both	B3	86	1.88E+07	11.3	17.1	1.9	
85	004129.23+405422.2	10.371797	40.906175	25.95	0.6	4.9	4	Both	B3	68	1.88E+07	5.9	1.4	6.5	
86	004131.53+405958.7	10.381376	40.999655	21.18	0.3	5.2	7	Both	B3	100	3.22E+07	6.9	4.5	3.2	

Source No.	CXOU J	R.A. (J2000) (°)	Decl. (J2000) (°)	Distance (′)	PosErr (″)	θ (′)	No. of Obs	Detector	Region	Tot Exp (ks)	Tot Exp. Map Value (s cm^2)	R_{src} (sky pixel)	SNR	$E_{\rm median}$ (keV)	Match
87	004133.06+405608.4	10.387761	40.935678	24.08	0.4	3.7	4	Both	B3	68	2.04E+07	3.8	1.7	1.7	
88	004133.17+405431.6	10.388242	40.908792	25.42	0.4	4.1	4	Both	B3	68	2.00E+07	4.5	1.6	2.6	
89	004133.73+405747.5	10.390558	40.963196	22.65	0.4	4.0	5	Both	B3	72	2.21E+07	4.4	3.0	3.5	
90	004134.30+410105.3	10.392939	41.018161	20.00	0.4	5.2	8	Both	B3	113	3.61E+07	7.0	4.0	1.4	AGN
91	004134.51+405647.9	10.393797	40.946664	23.38	0.7	3.4	4	Both	B3	68	2.15E+07	3.5	0.9	1.9	
92	004136.49+410135.0	10.402042	41.026403	19.35	0.4	5.2	8	Both	B3	113	3.61E+07	7.0	3.7	2.1	
93	004136.65+410017.0	10.402709	41.004731	20.33	0.3	4.5	8	Both	B3	113	3.75E+07	5.5	4.6	1.1	
94	004137.18+405608.1	10.404953	40.935603	23.65	0.4	3.0	4	Both	B3	68	1.72E+07	2.9	1.2	4.4	
95	004137.74+410029.4	10.407287	41.008187	20.04	0.4	4.5	8	Both	B3	113	3.70E+07	5.4	2.0	3.0	
96	004137.85+410108.2	10.407718	41.018960	19.53	0.1	3.3	8	Both	B3	33	1.21E+07	1.8	8.8	1.8	AGN
97	004137.95+410108.6	10.408163	41.019080	19.51	0.1	3.3	8	Both	B3	33	1.21E+07	1.8	8.8	1.8	AGN
98	004139.38+405412.8	10.414122	40.903559	25.10	0.4	3.3	4	Both	B3	68	2.03E+07	3.2	1.5	2.4	
99	004139.94+410425.3	10.416446	41.073699	16.85	0.6	4.8	5	Both	B3	40	1.30E+07	7.1	2.8	1.1	
100	004139.97+405513.1	10.416543	40.920315	24.17	0.4	2.7	4	Both	B3	68	2.17E+07	2.5	1.4	0.9	
101	004140.04+405945.1	10.416868	40.995862	20.36	0.2	3.9	8	Both	B3	113	3.82E+07	4.4	4.7	1.8	
102	004140.12+410247.0	10.417190	41.046396	18.00	0.3	4.4	7	Both	B3	59	1.88E+07	5.6	4.4	1.8	
103	004140.60+404941.0	10.419178	40.828079	29.04	1.3	7.7	3	ACIS-I		14	2.71E+06	11.9	1.6	3.8	
104	004140.62+410057.5	10.419273	41.015989	19.34	0.3	4.4	8	Both	B3	113	3.73E+07	5.3	3.1	1.8	
105	004141.27+410333.3	10.421981	41.059261	17.29	0.1	4.4	6	Both	B3	54	1.86E+07	5.7	14.8	1.9	
106	004141.28+410402.8	10.422017	41.067454	16.93	0.4	4.6	6	Both	B3	54	1.82E+07	6.4	4.8	1.5	AGN
107	004141.79+405650.8	10.424161	40.947465	22.59	0.9	2.9	5	Both	B3	82	2.66E+07	3.7	1.6	4.5	
108	004142.12+410014.4	10.425530	41.004021	19.73	0.1	3.9	8	Both	B3	113	3.81E+07	4.3	13.0	2.2	
109	004142.29+405303.5	10.426249	40.884317	25.86	0.2	3.9	4	Both	B3	68	1.96E+07	4.0	3.8	1.7	
110	004143.44+410504.7	10.431028	41.084643	15.91	0.2	6.3	6	Both	B3	55	1.02E+07	9.9	10.7	1.0	
111	004144.32+405702.0	10.434705	40.950569	22.19	0.1	1.7	8	Both	B3	68	2.21E+07	1.8	4.7	1.9	
112	004144.34+405703.4	10.434760	40.950966	22.16	0.2	1.7	8	Both	B3	68	2.21E+07	1.4	1.0	3.6	
113	004144.69+411112.4	10.436221	41.186782	12.24	0.3	8.7	2	ACIS-I		8	1.22E+06	15.6	10.5	1.6	
114	004145.24+410229.6	10.438527	41.041566	17.59	0.8	4.0	8	Both	B3	64	2.11E+07	5.0	1.7	1.9	
115	004146.47+411652.8	10.443642	41.281358	10.90	1.1	10.8	15	ACIS-I		61	8.67E+06	22.2	2.8	3.4	
116	004147.04+405412.6	10.446035	40.903525	24.43	1.0	2.7	5	Both	B3	73	2.27E+07	2.9	1.5	3.9	
117	004147.91+410109.9	10.449628	41.019443	18.35	0.8	4.1	10	Both	B3	123	3.78E+07	5.1	1.7	4.5	
118	004149.17+405644.1	10.454899	40.945602	22.00	0.4	2.4	9	Both	B3	118	3.73E+07	3.8	2.6	-0.2	
119	004149.59+410333.6	10.456648	41.059359	16.25	0.4	4.0	8	Both	B3	64	2.09E+07	5.7	2.8	1.9	
120	004149.69+410105.7	10.457058	41.018252	18.21	0.2	3.0	10	Both	B3	59	1.99E+07	1.7	1.5	1.1	
121	004149.87+410106.1	10.457817	41.018370	18.19	0.1	2.9	10	Both	B3	59	1.99E+07	2.3	10.8	2.0	
122	004150.28+411336.6	10.459531	41.226848	10.46	0.5	10.2	18	ACIS-I		72	1.03E+07	20.0	9.7	2.1	
123	004150.47+411212.5	10.460297	41.203492	10.86	0.8	10.4	13	ACIS-I		52	7.17E+06	20.6	5.1	2.4	LMXB
124	004150.60+412113.2	10.460856	41.353678	11.30	0.7	11.2	15	ACIS-I		68	9.65E+06	23.2	5.6	2.3	
125	004151.59+411439.2	10.464964	41.244244	10.02	0.2	9.9	25	ACIS-I		101	1.56E+07	14.4	16.0	2.0	
126	004151.67+411517.2	10.465297	41.254798	9.93	0.8	9.8	28	ACIS-I		112	1.68E+07	18.7	3.5	1.4	
127	004151.96+405428.9	10.466531	40.908043	23.79	0.1	2.0	6	Both	B3	68	2.16E+07	1.7	5.9	2.5	
128	004151.97+405430.5	10.466559	40.908493	23.76	0.2	2.0	6	Both	B3	68	2.16E+07	0.9	2.3	3.0	
129	004152.83+404709.9	10.470154	40.786093	30.54	1.3	9.6	2	ACIS-I		9	1.73E+06	17.8	2.4	1.6	LMXB
130	004153.20+405327.0	10.471675	40.890851	24.64	1.4	3.8	6	Both	B3	78	1.31E+07	4.4	1.2	3.3	
131	004153.27+405302.5	10.471999	40.884047	25.01	0.8	5.6	5	ACIS-I		23	4.97E+06	7.6	2.6	2.2	

Source No.	CXOU J	R.A. (J2000) (°)	Decl. (J2000) (°)	Distance (′)	PosErr (″)	θ (′)	No. of Obs	Detector	Region	Tot Exp (ks)	Tot Exp. Map Value (s cm^2)	R_{src} (sky pixel)	SNR	$E_{\rm median}$ (keV)	Match
132	004153.35+410124.8	10.472299	41.023561	17.56	0.6	3.5	9	Both	B3	69	2.16E+07	4.1	3.6	2.4	
133	004154.55+405958.4	10.477322	40.999579	18.67	0.2	3.4	10	Both	B3	123	3.95E+07	3.8	4.5	2.2	
134	004154.57+405829.6	10.477411	40.974916	19.97	0.9	2.8	10	Both	B3	123	4.07E+07	3.3	1.8	4.2	
135	004154.66+405648.2	10.477781	40.946745	21.47	0.0	2.2	10	Both	B3	123	3.78E+07	3.3	23.9	1.6	
136	004154.94+405713.1	10.478947	40.953657	21.07	0.5	2.6	10	Both	B3	123	4.10E+07	3.7	3.1	3.3	
137	004155.08+412302.6	10.479510	41.384067	11.55	0.7	11.4	9	ACIS-I		43	6.57E+06	23.8	4.8	3.1	
138	004157.79+411439.2	10.490820	41.244244	8.87	0.7	8.7	61	ACIS-I		177	2.94E+07	6.9	2.1	1.4	
139	004159.12+410541.2	10.496352	41.094805	13.46	0.0	4.0	4	Both	B3	27	8.06E+06	5.8	19.1	2.2	
140	004159.93+410116.2	10.499713	41.021176	17.04	0.7	3.5	9	Both	B3	69	2.20E+07	3.9	2.6	2.3	
141	004200.22+405314.2	10.500941	40.887298	24.35	1.2	5.3	6	ACIS-I		28	5.68E+06	6.7	0.6	-1.0	
142	004200.32+405559.3	10.501355	40.933147	21.78	0.6	2.9	9	Both	B3	110	2.84E+07	3.3	1.6	3.0	
143	004200.38+410037.3	10.501624	41.010368	17.57	0.8	3.3	9	Both	B3	69	2.26E+07	3.8	1.4	3.8	
144	004200.45+405942.7	10.501907	40.995220	18.37	0.6	3.4	10	Both	B3	123	3.88E+07	3.8	1.4	5.6	
145	004200.59+411409.7	10.502477	41.236034	8.45	0.4	8.4	68	ACIS-I		300	4.95E+07	13.9	4.8	3.8	
146	004200.65+411632.3	10.502715	41.275639	8.22	0.4	8.2	76	ACIS-I		333	5.68E+07	13.3	3.0	0.9	
147	004200.95+405751.0	10.503962	40.964173	20.02	0.6	3.1	10	Both	B3	123	4.08E+07	3.6	2.0	3.4	
148	004202.46+405631.2	10.510265	40.942009	21.13	0.3	3.1	9	Both	B3	109	2.42E+07	3.5	3.9	2.1	
149	004202.73+412311.2	10.511409	41.386466	10.53	0.6	10.5	22	ACIS-I		115	1.77E+07	21.3	4.6	2.7	
150	004203.66+410926.9	10.515257	41.157484	10.15	0.6	9.8	27	ACIS-I		134	2.04E+07	7.8	3.9	2.1	
151	004204.16+411531.6	10.517356	41.258802	7.57	0.1	7.5	85	ACIS-I		373	6.44E+07	11.4	17.8	2.3	
152	004204.30+410902.5	10.517955	41.150697	10.34	0.5	9.9	23	ACIS-I		122	1.87E+07	18.7	5.7	2.5	
153	004204.40+410930.6	10.518372	41.158509	10.01	0.4	9.6	30	ACIS-I		146	2.30E+07	8.5	6.3	2.5	
154	004204.70+411341.2	10.519586	41.228116	7.84	0.4	7.8	85	ACIS-I		372	6.31E+07	12.1	4.4	1.2	
155	004205.62+405713.4	10.523419	40.953738	20.26	0.4	3.4	8	Both	B3	55	1.68E+07	3.9	3.2	1.8	
156	004205.76+411329.6	10.524035	41.224912	7.71	0.1	7.7	85	ACIS-I		372	6.36E+07	11.7	22.1	2.4	
157	004205.88+411134.1	10.524506	41.192807	8.55	0.3	8.5	67	ACIS-I		299	5.07E+07	14.2	10.5	2.1	
158	004205.96+405011.6	10.524854	40.836571	26.92	0.7	7.6	6	ACIS-I		28	5.63E+06	11.6	3.4	2.6	
159	004206.12+410247.7	10.525512	41.046591	15.15	0.1	4.4	8	Both	B3	64	2.10E+07	5.1	21.6	1.5	AGN
160	004206.36+412138.3	10.526534	41.360658	9.01	0.7	8.9	69	ACIS-I		254	3.92E+07	15.5	1.7	5.4	
161	004207.06+411720.1	10.529447	41.288930	7.10	0.2	7.1	87	ACIS-I		383	7.13E+07	10.3	13.8	2.4	
162	004207.15+410016.3	10.529823	41.004539	17.33	0.1	3.6	9	Both	B3	69	2.19E+07	4.3	18.4	2.0	AGN
163	004207.34+410055.4	10.530587	41.015407	16.72	0.2	3.9	9	Both	B3	69	2.24E+07	4.5	6.4	1.9	
164	004207.57+411027.4	10.531549	41.174288	8.94	0.2	8.8	68	ACIS-I		304	4.85E+07	15.4	16.3	2.0	
165	004207.73+411814.9	10.532222	41.304166	7.20	0.0	7.3	88	ACIS-I		388	7.03E+07	10.7	108.3	2.2	
166	004207.90+410436.2	10.532943	41.076732	13.41	0.1	5.4	6	Both	B3	36	8.89E+06	7.5	16.6	1.8	
167	004208.20+411249.3	10.534189	41.213722	7.55	0.2	7.5	87	ACIS-I		382	6.80E+07	11.4	10.1	2.6	
168	004208.27+405514.0	10.534471	40.920576	21.97	0.4	3.9	6	ACIS-I		28	5.78E+06	4.3	2.4	1.6	
169	004208.44+410339.7	10.535192	41.061031	14.18	0.3	5.1	8	Both	B3	64	2.00E+07	6.8	5.4	1.8	
170	004208.95+412330.7	10.537299	41.391882	9.93	0.6	9.8	35	ACIS-I		171	2.64E+07	18.7	3.0	1.0	
171	004209.06+412048.4	10.537772	41.346786	8.11	0.1	7.7	81	ACIS-I		79	1.36E+07	3.5	8.7	2.1	
172	004209.27+411106.8	10.538633	41.185236	8.28	0.5	8.2	73	ACIS-I		324	5.62E+07	13.4	2.6	0.0	
173	004209.48+411745.5	10.539538	41.295979	6.75	0.0	6.8	88	ACIS-I		388	7.32E+07	9.4	55.0	2.2	LMXB
174	004209.56+412009.6	10.539842	41.336002	7.68	0.3	7.7	86	ACIS-I		378	6.87E+07	11.7	5.4	2.1	
175	004209.99+405035.9	10.541655	40.843331	26.33	0.4	7.1	6	ACIS-I		28	5.80E+06	10.2	6.5	2.7	
176	004210.24+405341.8	10.542668	40.894947	23.33	0.5	4.6	6	ACIS-I		28	5.83E+06	4.8	1.9	2.1	

Source No.	CXOU J	R.A. (J2000) (°)	Decl. (J2000) (°)	Distance (′)	PosErr (″)	θ (′)	No. of Obs	Detector	Region	Tot Exp (ks)	Tot Exp. Map Value (s cm^2)	R_{src} (sky pixel)	SNR	$E_{\rm median}$ (keV)	Match
177	004210.27+411509.8	10.542833	41.252749	6.47	0.1	6.5	88	ACIS-I		388	7.02E+07	8.6	31.9	2.1	
178	004210.36+405149.2	10.543200	40.863682	25.13	1.2	6.1	6	ACIS-I		28	6.04E+06	7.7	0.8	0.1	
179	004210.84+410647.8	10.545183	41.113279	11.26	0.5	10.3	15	ACIS-I		69	1.05E+07	20.7	8.2	2.5	
180	004210.95+411247.9	10.545634	41.213319	7.10	0.1	7.1	88	ACIS-I		387	7.04E+07	10.2	23.4	1.8	
181	004211.29+410428.8	10.547062	41.074671	13.20	0.1	6.2	6	Both	B3	36	6.94E+06	9.0	4.9	1.8	
182	004211.75+411048.8	10.548977	41.180223	8.11	0.1	8.1	82	ACIS-I		360	5.85E+07	12.9	43.4	2.4	
183	004211.93+411648.7	10.549709	41.280198	6.13	0.1	6.2	88	ACIS-I		388	7.36E+07	7.8	31.7	2.3	
184	004212.02+405336.8	10.550090	40.893558	23.32	0.2	4.7	6	ACIS-I		28	6.30E+06	4.9	6.6	2.1	
185	004212.16+411758.6	10.550687	41.299613	6.32	0.0	6.4	89	Both	B2	392	7.56E+07	8.4	66.2	2.4	LMXB
186	004212.75+411244.1	10.553133	41.212256	6.84	0.2	6.8	88	ACIS-I		387	7.11E+07	9.5	10.4	3.3	
187	004213.00+411628.0	10.554176	41.274450	5.90	0.2	6.0	88	ACIS-I		388	7.56E+07	7.3	9.9	2.3	
188	004213.13+411836.4	10.554726	41.310115	6.36	0.0	6.4	89	Both	B2	392	7.61E+07	8.5	135.1	1.9	
189	004213.28+405538.4	10.555347	40.927356	21.30	0.6	4.2	7	ACIS-I		32	6.65E+06	4.6	2.5	4.7	
190	004214.68+412213.6	10.561201	41.370464	8.26	0.4	8.2	76	ACIS-I		339	5.91E+07	12.9	4.0	3.0	
191	004214.80+405200.8	10.561694	40.866904	24.74	0.7	5.9	6	ACIS-I		28	6.11E+06	7.1	1.6	0.6	
192	004214.99+412121.3	10.562487	41.355925	7.60	0.3	7.6	87	ACIS-I		383	6.96E+07	11.6	9.1	2.5	
193	004215.13+411234.3	10.563057	41.209538	6.54	0.0	6.5	88	ACIS-I		387	7.33E+07	8.7	70.9	1.9	
194	004215.23+411801.3	10.563459	41.300377	5.79	0.1	5.5	90	ACIS-I		95	1.73E+07	1.9	6.7	2.0	
195	004215.32+411341.6	10.563864	41.228243	5.97	0.3	6.0	87	ACIS-I		383	7.25E+07	7.3	2.4	1.4	
196	004215.48+412031.5	10.564500	41.342111	6.98	0.1	7.0	89	ACIS-I		392	7.33E+07	10.0	35.0	2.1	
197	004215.64+410113.1	10.565196	41.020326	15.85	0.1	4.3	9	Both	B3	41	1.12E+07	2.4	6.3	2.6	
198	004215.67+411720.7	10.565303	41.289109	5.52	0.0	5.6	90	Both	B2	397	7.81E+07	6.6	54.2	2.1	
199	004215.79+405527.6	10.565794	40.924350	21.35	1.1	4.1	7	ACIS-I		32	6.89E+06	4.4	1.6	2.6	
200	004215.80+411135.9	10.565845	41.193333	7.02	0.3	7.0	88	ACIS-I		387	7.01E+07	9.9	3.6	2.9	
201	004215.87+410114.3	10.566144	41.020651	15.82	0.0	4.8	9	Both	B3	55	1.67E+07	4.1	78.3	2.5	LMXB
202	004216.04+411553.1	10.566873	41.264771	5.32	0.2	5.4	89	Both	B2	392	7.78E+07	6.0	4.5	2.8	
203	004216.05+411926.4	10.566912	41.324009	6.26	0.1	6.4	91	Both	B2	402	7.85E+07	8.3	23.5	2.4	
204	004216.11+412215.5	10.567164	41.370983	8.10	0.4	8.1	81	ACIS-I		360	6.21E+07	12.6	5.2	2.7	
205	004216.48+411430.6	10.568694	41.241854	5.48	0.3	5.5	88	ACIS-I		388	7.58E+07	6.3	3.9	2.0	
206	004216.54+405552.3	10.568931	40.931217	20.92	0.1	4.1	7	ACIS-I		32	7.13E+06	4.7	18.9	1.8	
207	004216.56+411610.3	10.569011	41.269540	5.22	0.3	5.3	89	Both	B2	392	7.84E+07	5.8	5.7	2.3	
208	004216.98+411856.1	10.570773	41.315610	5.86	0.3	6.0	92	Both	B2	407	8.05E+07	7.4	6.1	2.6	
209	004217.03+411508.2	10.570982	41.252303	5.22	0.1	5.3	89	Both	B2	392	7.59E+07	5.8	24.2	2.2	
210	004217.29+411536.9	10.572063	41.260258	5.11	0.0	5.2	90	Both	B2	397	7.55E+07	5.7	31.2	1.3	
211	004217.83+411110.2	10.574327	41.186194	7.02	0.4	7.0	88	ACIS-I		387	7.13E+07	9.9	3.5	3.1	
212	004217.95+410859.1	10.574818	41.149770	8.69	0.4	8.5	69	ACIS-I		307	5.13E+07	14.3	4.4	1.8	
213	004218.33+411223.5	10.576408	41.206546	6.15	0.0	6.2	89	ACIS-I		392	7.55E+07	7.8	114.1	1.6	
214	004218.33+410210.6	10.576415	41.036282	14.78	0.4	5.6	8	Both	B3	55	1.59E+07	7.8	5.6	2.3	
215	004218.40+405850.6	10.576690	40.980745	17.96	0.6	5.7	7	Both	B3	41	1.06E+07	8.0	3.1	4.1	
216	004218.63+411401.7	10.577639	41.233825	5.26	0.0	5.4	89	ACIS-I		392	7.52E+07	6.0	113.6	2.3	LMXB
217	004218.98+412004.4	10.579101	41.334574	6.19	0.2	6.3	93	Both	B2	411	8.05E+07	8.2	8.9	2.4	
218	004219.60+411333.9	10.581674	41.226092	5.31	0.2	5.4	89	ACIS-I		392	7.69E+07	6.0	7.7	2.2	
219	004219.71+412154.3	10.582137	41.365110	7.40	0.2	7.5	91	ACIS-I		402	7.36E+07	11.3	12.0	3.5	LMXB
220	004220.11+410824.2	10.583831	41.140073	8.96	0.4	8.7	63	ACIS-I		284	4.55E+07	15.0	6.1	2.4	
221	004220.35+411313.5	10.584830	41.220421	5.36	0.3	5.2	89	ACIS-I		141	2.68E+07	1.8	1.4	1.0	

Source No.	CXOU J	R.A. (J2000) (°)	Decl. (J2000) (°)	Distance (′)	PosErr (″)	θ (′)	No. of Obs	Detector	Region	Tot Exp (ks)	Tot Exp. Map Value (s cm^2)	R_{src} (sky pixel)	SNR	$E_{\rm median}$ (keV)	Match
222	004220.41+411850.9	10.585069	41.314145	5.25	0.3	5.4	92	Both	B2	407	8.24E+07	6.3	3.9	4.3	
223	004220.45+412639.8	10.585210	41.444391	11.45	0.9	11.4	5	ACIS-I		20	2.56E+06	23.6	5.9	2.4	
224	004220.64+405712.3	10.586015	40.953417	19.44	0.4	4.3	7	ACIS-I		32	6.06E+06	4.9	1.3	1.5	
225	004220.70+411608.2	10.586273	41.268972	4.44	0.2	4.6	93	Both	B2	447	8.60E+07	4.5	3.3	0.8	
226	004220.80+411344.0	10.586676	41.228911	5.03	0.2	5.1	91	Both	B2	437	7.93E+07	5.5	6.0	2.0	
227	004220.85+412256.8	10.586908	41.382462	8.12	0.5	8.1	80	ACIS-I		356	6.14E+07	13.0	2.2	0.5	
228	004220.91+405403.1	10.587133	40.900871	22.51	0.2	4.2	8	Both	B3	38	9.04E+06	4.3	4.7	2.1	
229	004220.93+411520.1	10.587243	41.255601	4.47	0.2	4.6	90	Both	B2	397	7.66E+07	4.6	4.2	2.4	
230	004221.08+411807.7	10.587863	41.302160	4.80	0.2	5.0	92	Both	B2	407	8.28E+07	5.4	6.7	1.5	
231	004221.15+410717.4	10.588154	41.121508	9.85	0.6	9.4	38	ACIS-I		179	2.90E+07	7.8	3.4	1.8	
232	004221.28+411552.4	10.588672	41.264563	4.34	0.1	4.4	95	Both	B2	519	8.70E+07	3.5	16.0	1.5	
233	004221.29+411548.9	10.588735	41.263604	4.34	0.2	4.4	95	Both	B2	519	8.67E+07	3.7	4.3	2.5	
234	004221.48+411601.2	10.589510	41.267000	4.29	0.0	4.4	96	Both	B2	565	9.63E+07	4.5	111.4	2.1	
235	004221.56+411419.6	10.589864	41.238790	4.64	0.0	4.7	93	Both	B2	479	8.41E+07	4.9	30.1	1.8	
236	004221.79+411502.1	10.590800	41.250586	4.37	0.1	4.3	93	Both	B2	280	5.77E+07	1.5	4.5	3.0	
237	004221.83+411206.0	10.590994	41.201687	5.84	0.4	5.8	91	ACIS-I		382	7.30E+07	6.9	1.8	3.2	
238	004222.24+405925.1	10.592697	40.990331	17.21	0.1	5.0	6	ACIS-I		28	6.07E+06	5.7	23.3	2.0	
239	004222.30+411345.3	10.592934	41.229250	4.77	0.2	4.8	93	Both	B2	479	9.31E+07	5.2	5.4	1.3	
240	004222.30+411222.5	10.592942	41.206272	5.59	0.4	5.7	93	Both	B2	478	8.86E+07	6.8	2.4	4.1	
241	004222.36+411335.1	10.593185	41.226441	4.85	0.0	4.7	93	ACIS-I		199	3.83E+07	1.6	3.4	1.9	
242	004222.42+411333.9	10.593422	41.226094	4.85	0.0	4.7	93	Both	B2	267	5.33E+07	1.7	37.0	1.9	
243	004222.48+405743.2	10.593675	40.962021	18.86	0.7	4.4	6	ACIS-I		28	6.03E+06	5.2	2.2	3.1	
244	004222.61+412234.3	10.594249	41.376207	7.63	0.4	7.7	91	ACIS-I		402	7.17E+07	11.9	4.2	1.4	
245	004222.94+411535.2	10.595600	41.259787	4.05	0.0	4.1	97	Both	B2	570	1.15E+08	4.2	230.2	2.2	
246	004223.03+410738.7	10.595985	41.127424	9.38	0.2	9.1	52	ACIS-I		234	3.71E+07	16.0	16.9	1.7	
247	004223.09+411409.0	10.596231	41.235860	4.45	0.1	4.3	96	Both	B2	303	5.59E+07	2.3	2.8	2.2	
248	004223.17+411406.8	10.596562	41.235225	4.46	0.2	3.7	96	ACIS-S	B2	4	1.73E+06	1.5	2.7	1.4	
249	004224.10+411536.9	10.600453	41.260276	3.83	0.4	4.0	98	Both	B2	449	9.17E+07	3.8	2.2	0.8	
250	004224.12+404849.2	10.600529	40.813671	27.57	1.3	8.2	4	ACIS-I		18	3.54E+06	13.5	1.1	5.2	
251	004224.17+411732.8	10.600718	41.292445	4.05	0.2	4.2	95	Both	B2	484	9.98E+07	3.3	4.7	1.1	
252	004224.34+411730.1	10.601428	41.291698	4.00	0.1	4.1	96	Both	B2	525	1.02E+08	3.4	5.5	1.1	
253	004224.52+412401.5	10.602195	41.400444	8.73	0.2	8.6	65	ACIS-I		277	4.55E+07	14.6	22.6	2.2	
254	004224.59+411908.7	10.602485	41.319090	4.78	0.5	5.0	93	Both	B2	391	8.02E+07	5.3	1.6	3.4	
255	004225.04+405719.3	10.604363	40.955378	19.15	0.3	4.1	7	ACIS-I		32	6.60E+06	5.2	6.9	2.0	
256	004225.08+411341.7	10.604524	41.228273	4.36	0.1	4.3	100	Both	B2	341	6.18E+07	1.4	2.7	2.5	
257	004225.12+411340.4	10.604692	41.227903	4.36	0.0	4.2	100	Both	B2	469	8.31E+07	1.8	30.7	1.8	
258	004225.94+411914.6	10.608113	41.320730	4.65	0.0	4.3	93	ACIS-I		151	3.08E+07	1.4	2.4	1.2	LMXB
259	004226.04+411914.8	10.608538	41.320786	4.64	0.0	4.3	93	ACIS-I		206	4.18E+07	1.4	32.3	2.2	LMXB
260	004226.11+411915.7	10.608816	41.321037	4.64	0.0	4.4	93	ACIS-I		234	4.74E+07	1.5	2.7	2.8	
261	004226.14+412551.9	10.608927	41.431108	10.32	0.2	10.2	24	ACIS-I		97	1.37E+07	19.9	24.1	2.3	
262	004226.18+405457.8	10.609123	40.916080	21.43	0.2	3.5	9	Both	B3	29	7.70E+06	1.5	2.5	2.0	
263	004226.25+405458.8	10.609390	40.916352	21.42	0.1	3.4	9	Both	B3	29	7.73E+06	1.6	3.5	2.5	
264	004226.50+411346.5	10.610448	41.229591	4.09	0.2	4.1	100	Both	B2	681	1.45E+08	4.2	3.6	1.8	
265	004226.52+412351.3	10.610540	41.397596	8.42	0.4	8.4	73	ACIS-I		330	5.31E+07	13.8	4.9	3.2	
266	004227.01+410105.1	10.612583	41.018090	15.39	0.9	6.1	6	ACIS-I		28	5.86E+06	8.1	1.4	2.8	

Source No.	CXOU J	R.A. (J2000) (°)	Decl. (J2000) (°)	Distance (′)	PosErr (″)	θ (′)	No. of Obs	Detector	Region	Tot Exp (ks)	Tot Exp. Map Value (s cm^2)	R_{src} (sky pixel)	SNR	$E_{\rm median}$ (keV)	Match
267	004227.22+405658.3	10.613436	40.949545	19.42	0.8	4.4	8	Both	B3	37	8.76E+06	6.0	1.8	2.5	
268	004227.35+405527.1	10.613978	40.924211	20.92	0.2	4.2	9	Both	B3	42	1.05E+07	5.1	6.7	3.1	
269	004227.41+405936.1	10.614227	40.993381	16.83	0.4	5.3	6	ACIS-I		28	5.92E+06	6.7	4.8	2.0	LMXB
270	004227.47+411452.4	10.614482	41.247899	3.41	0.1	3.5	102	Both	B2	656	1.38E+08	3.3	6.4	2.2	
271	004227.62+412048.3	10.615115	41.346763	5.63	0.1	5.8	93	Both	B2	411	8.21E+07	7.0	11.3	2.2	
272	004227.92+411817.6	10.616373	41.304897	3.77	0.2	4.0	96	Both	B2	464	9.66E+07	3.8	5.8	2.8	
273	004228.03+411807.6	10.616824	41.302129	3.66	0.2	3.9	96	Both	B2	464	9.60E+07	3.7	5.1	1.6	
274	004228.11+411001.7	10.617151	41.167140	6.82	0.1	6.5	92	ACIS-I		151	3.00E+07	2.6	2.9	2.8	
275	004228.21+411000.1	10.617555	41.166719	6.83	0.0	6.5	92	ACIS-I		187	3.67E+07	2.6	39.4	2.2	
276	004228.28+411223.1	10.617865	41.206418	4.80	0.0	4.9	98	Both	B2	574	1.23E+08	5.5	159.2	2.1	
277	004228.35+411449.1	10.618128	41.246980	3.27	0.3	3.4	102	Both	B2	656	1.44E+08	3.3	3.3	1.3	
278	004228.42+410854.5	10.618431	41.148473	7.81	0.3	7.8	86	ACIS-I		378	6.58E+07	12.0	5.2	3.0	
279	004228.47+411938.5	10.618655	41.327374	4.61	0.2	4.8	94	Both	B2	416	8.52E+07	5.0	3.3	2.6	
280	004228.82+411741.3	10.620094	41.294807	3.31	0.2	3.5	98	Both	B2	541	1.14E+08	3.4	4.1	3.4	
281	004228.94+410436.1	10.620596	41.076701	11.88	0.2	9.7	9	ACIS-I		38	5.43E+06	18.3	27.2	1.9	
282	004229.02+411432.8	10.620952	41.242465	3.28	0.2	3.4	102	Both	B2	691	1.56E+08	3.2	5.2	1.6	
283	004229.09+411547.8	10.621229	41.263284	2.88	0.2	3.0	101	Both	B2	619	1.35E+08	2.9	4.0	1.7	
284	004229.09+411348.7	10.621247	41.230211	3.68	0.1	3.8	102	Both	B2	691	1.55E+08	3.8	12.1	1.9	
285	004229.24+404907.7	10.621858	40.818821	27.15	0.9	6.5	5	Both	B3	24	5.77E+06	9.8	3.1	1.5	
286	004229.35+405750.1	10.622331	40.963926	18.51	1.1	5.6	7	Both	B3	33	6.45E+06	8.1	1.4	-0.2	
287	004229.72+405247.8	10.623850	40.879968	23.49	0.9	3.4	9	Both	B3	44	1.23E+07	4.2	1.1	0.1	
288	004230.10+411841.8	10.625444	41.311614	3.71	0.2	3.9	96	Both	B2	464	9.65E+07	3.8	3.1	1.1	
289	004230.26+411653.1	10.626104	41.281424	2.75	0.1	2.9	100	Both	B2	623	1.40E+08	2.8	17.1	2.3	
290	004230.55+410909.9	10.627295	41.152753	7.43	0.4	7.4	90	Both	B2	433	7.80E+07	11.2	3.7	2.7	
291	004230.72+405641.8	10.628010	40.944968	19.60	0.9	4.0	7	Both	B3	33	8.26E+06	5.3	1.6	4.4	
292	004230.96+411910.2	10.629002	41.319509	3.95	0.1	4.1	96	Both	B2	497	1.02E+08	4.0	17.6	2.4	
293	004231.13+411621.5	10.629732	41.272662	2.49	0.0	2.6	101	Both	B2	660	1.45E+08	2.6	183.4	2.1	
294	004231.24+411938.8	10.630170	41.327467	4.30	0.0	4.4	95	Both	B2	454	9.30E+07	4.4	85.9	2.1	LMXB
295	004231.29+410437.1	10.630409	41.076996	11.76	0.6	9.7	10	ACIS-I		42	6.54E+06	18.5	7.8	1.8	
296	004231.30+412007.7	10.630454	41.335494	4.69	0.1	4.8	95	Both	B2	454	9.21E+07	5.1	14.4	2.1	
297	004231.61+411259.7	10.631737	41.216592	3.94	0.2	4.0	103	Both	B2	729	1.63E+08	4.1	2.8	0.8	
298	004231.88+412306.4	10.632851	41.385133	7.36	0.3	7.1	92	ACIS-I		225	4.10E+07	3.7	2.6	2.4	
299	004232.07+411314.4	10.633630	41.220674	3.69	0.0	3.8	103	Both	B2	729	1.70E+08	3.8	190.0	2.3	
300	004232.08+411912.9	10.633683	41.320269	3.85	0.1	3.9	96	Both	B2	497	1.10E+08	3.8	8.4	2.4	
301	004232.14+412305.3	10.633952	41.384813	7.33	0.3	7.0	92	ACIS-I		225	4.12E+07	3.9	3.7	1.6	
302	004232.17+411944.6	10.634044	41.329067	4.28	0.3	4.3	96	Both	B2	497	9.96E+07	4.3	2.1	1.0	
303	004232.52+411545.3	10.635520	41.262599	2.25	0.1	2.3	104	Both	B2	734	1.74E+08	2.4	11.3	3.6	
304	004232.74+411310.8	10.636457	41.219675	3.66	0.0	3.8	103	Both	B2	729	1.72E+08	3.6	63.1	2.1	
305	004232.78+411303.9	10.636620	41.217750	3.75	0.1	3.9	103	Both	B2	729	1.71E+08	3.8	10.6	1.7	
306	004232.90+411142.6	10.637104	41.195179	4.91	0.2	4.9	98	Both	B2	433	9.76E+07	2.1	2.4	2.4	
307	004232.95+411143.9	10.637315	41.195543	4.89	0.3	4.9	98	Both	B2	428	9.66E+07	2.0	1.6	2.8	
308	004233.13+410328.8	10.638070	41.058001	12.82	0.3	10.1	7	ACIS-I		84	1.26E+07	20.2	15.5	2.1	LMXB
309	004233.25+411742.2	10.638557	41.295061	2.61	0.0	2.7	100	Both	B2	583	1.35E+08	2.6	32.4	2.0	
310	004233.27+410647.7	10.638646	41.113255	9.56	0.5	9.3	43	ACIS-I		175	2.79E+07	17.0	5.8	2.3	
311	004233.41+411703.4	10.639215	41.284293	2.25	0.0	2.3	101	Both	B2	660	1.57E+08	2.3	13.7	2.2	

Source No.	CXOU J	R.A. (J2000) (°)	Decl. (J2000) (°)	Distance (′)	PosErr (″)	θ (′)	No. of Obs	Detector	Region	Tot Exp (ks)	Tot Exp. Map Value (s cm^2)	R_{src} (sky pixel)	SNR	$E_{\rm median}$ (keV)	Match
312	004233.51+412138.4	10.639626	41.360679	5.88	0.2	6.0	94	Both	B2	416	7.91E+07	7.5	10.4	1.0	
313	004233.80+405454.1	10.640860	40.915044	21.31	0.5	3.6	9	Both	B3	44	1.27E+07	4.2	2.8	3.1	
314	004233.80+412039.9	10.640875	41.344441	4.95	0.2	5.0	95	Both	B2	454	9.53E+07	5.5	4.3	2.1	
315	004233.87+412331.3	10.641137	41.392031	7.65	0.1	7.7	91	ACIS-I		402	7.28E+07	11.8	29.4	1.8	
316	004233.88+411619.7	10.641204	41.272148	1.97	0.0	2.0	105	Both	B2	777	1.78E+08	2.2	77.5	2.0	
317	004234.04+412249.0	10.641868	41.380305	6.97	0.3	7.0	92	ACIS-I		407	7.73E+07	10.0	4.4	2.9	
318	004234.15+412149.8	10.642301	41.363852	6.02	0.1	6.1	94	Both	B2	416	8.10E+07	7.8	30.1	2.6	
319	004234.38+405709.1	10.643263	40.952531	19.07	0.3	4.2	7	Both	B3	33	8.23E+06	6.1	5.9	2.0	LMXB
320	004234.43+411809.3	10.643491	41.302601	2.75	0.1	2.8	97	Both	B2	502	1.16E+08	2.7	4.9	1.8	LMXB
321	004234.71+404904.0	10.644629	40.817799	27.12	1.2	5.1	5	Both	B3	25	6.08E+06	7.1	2.0	1.9	
322	004234.76+411523.1	10.644869	41.256437	1.94	0.1	2.0	104	Both	B2	734	1.80E+08	2.2	9.6	1.5	
323	004234.93+405720.8	10.645566	40.955779	18.86	0.0	4.3	7	Both	B3	33	8.19E+06	6.2	12.0	2.1	
324	004234.98+404838.8	10.645751	40.810778	27.53	0.2	5.7	4	Both	B3	20	4.66E+06	8.4	15.8	1.7	
325	004235.18+405249.9	10.646612	40.880534	23.36	0.6	2.7	8	Both	B3	39	1.18E+07	3.6	1.9	3.2	
326	004235.20+412005.6	10.646681	41.334889	4.32	0.0	4.4	96	Both	B2	497	1.01E+08	4.4	67.3	2.3	
327	004235.47+411607.0	10.647829	41.268615	1.66	0.2	1.7	105	Both	B2	777	1.93E+08	2.1	5.1	4.4	
328	004235.88+411007.4	10.649507	41.168747	6.21	0.2	6.3	96	Both	B2	564	1.19E+08	8.6	7.4	2.3	
329	004236.07+412021.3	10.650325	41.339277	4.51	0.3	4.7	96	Both	B2	303	5.50E+07	1.6	1.5	2.4	
330	004236.13+411046.4	10.650549	41.179561	5.57	0.3	5.7	97	Both	B2	569	1.24E+08	7.2	4.3	1.3	
331	004236.38+405848.8	10.651607	40.980230	17.38	0.5	5.2	4	ACIS-I		19	3.40E+06	7.4	4.4	2.7	
332	004236.58+411554.3	10.652437	41.265100	1.47	0.2	1.5	105	Both	B2	543	1.30E+08	2.0	1.7	1.0	
333	004236.60+411350.3	10.652541	41.230651	2.71	0.0	2.8	104	Both	B2	734	1.80E+08	2.7	25.6	1.2	
334	004236.66+405605.0	10.652780	40.934749	20.09	0.2	3.7	8	Both	B3	40	1.17E+07	4.6	3.3	1.1	
335	004237.04+411427.9	10.654360	41.241094	2.15	0.2	2.3	104	Both	B2	734	1.82E+08	2.3	2.9	1.2	
336	004237.54+405505.0	10.656423	40.918081	21.08	1.4	3.3	8	Both	B3	40	1.19E+07	3.9	1.0	2.9	
337	004237.84+412133.7	10.657700	41.359387	5.57	0.2	5.7	95	Both	B2	421	8.41E+07	6.7	5.3	2.0	
338	004237.93+410526.4	10.658055	41.090683	10.75	0.3	9.7	20	ACIS-I		136	2.09E+07	18.2	12.8	2.4	
339	004238.38+412010.6	10.659923	41.336301	4.20	0.3	4.2	96	Both	B2	471	1.02E+08	4.2	1.2	-0.3	
340	004238.58+411603.6	10.660768	41.267680	1.08	0.0	1.2	105	Both	B2	777	1.91E+08	1.9	317.8	2.8	LMXB
341	004238.66+411723.7	10.661096	41.289935	1.66	0.1	1.7	106	Both	B2	781	1.80E+08	2.0	7.2	2.7	
342	004238.76+411526.7	10.661517	41.257443	1.25	0.1	1.4	105	Both	B2	777	1.90E+08	2.0	5.5	1.3	
343	004239.02+411325.5	10.662589	41.223775	2.88	0.3	3.0	104	Both	B2	734	1.77E+08	2.9	2.5	1.2	
344	004239.22+411424.7	10.663430	41.240217	1.96	0.0	2.1	104	Both	B2	734	1.81E+08	2.1	13.8	1.7	
345	004239.40+405425.0	10.664190	40.906964	21.73	1.2	3.2	8	Both	B3	40	1.18E+07	3.6	1.0	0.3	
346	004239.53+411428.4	10.664736	41.241248	1.88	0.0	2.1	105	Both	B2	777	1.82E+08	2.1	70.7	1.6	
347	004239.57+411614.0	10.664877	41.270569	0.90	0.0	1.0	106	Both	B2	781	1.85E+08	1.9	51.6	1.8	
348	004239.64+411700.7	10.665204	41.283536	1.25	0.1	1.3	106	Both	B2	781	1.87E+08	1.9	11.2	1.6	
349	004239.80+411453.9	10.665862	41.248317	1.49	0.2	1.7	105	Both	B2	777	1.91E+08	2.0	3.5	2.5	
350	004239.96+411522.1	10.666502	41.256147	1.12	0.2	1.3	105	Both	B2	777	1.85E+08	2.0	2.4	1.8	
351	004239.98+411547.4	10.666621	41.263194	0.88	0.0	1.0	105	Both	B2	777	1.87E+08	1.9	134.3	1.8	
352	004240.11+411628.3	10.667143	41.274551	0.87	0.2	0.9	106	Both	B2	731	1.68E+08	1.9	1.7	1.0	
353	004240.20+411845.0	10.667528	41.312520	2.74	0.0	2.8	97	Both	B2	501	1.10E+08	2.6	71.3	2.2	
354	004240.45+411545.9	10.668570	41.262760	0.81	0.1	1.0	105	Both	B2	777	1.84E+08	1.8	3.8	2.4	
355	004240.53+411355.3	10.668894	41.232036	2.32	0.2	2.5	104	Both	B2	734	1.80E+08	2.5	2.4	1.4	
356	004240.56+411034.4	10.669040	41.176236	5.60	0.1	5.3	99	ACIS-I		267	5.07E+07	1.9	1.9	2.1	

Source No.	CXOU J	R.A. (J2000) (°)	Decl. (J2000) (°)	Distance (′)	PosErr (″)	θ (′)	No. of Obs	Detector	Region	Tot Exp (ks)	Tot Exp. Map Value (s cm^2)	R_{src} (sky pixel)	SNR	$E_{\rm median}$ (keV)	Match
357	004240.65+411327.4	10.669392	41.224291	2.76	0.0	2.9	104	Both	B2	734	1.79E+08	2.8	111.3	2.0	
358	004240.66+411033.2	10.669456	41.175889	5.61	0.1	5.4	99	ACIS-I		267	5.09E+07	2.1	10.8	2.0	LMXB
359	004240.71+405116.5	10.669660	40.854597	24.86	0.0	2.8	7	Both	B3	35	1.03E+07	3.9	28.6	1.0	
360	004240.72+411833.2	10.669679	41.309248	2.52	0.3	2.6	98	Both	B2	506	1.12E+08	2.4	1.5	2.0	
361	004240.73+411004.3	10.669735	41.167874	6.09	0.3	6.2	97	Both	B2	343	7.81E+07	3.2	3.1	1.3	
362	004240.85+411005.5	10.670241	41.168198	6.07	0.3	6.2	97	Both	B2	351	7.97E+07	3.2	2.3	0.7	
363	004240.89+412216.2	10.670401	41.371184	6.18	0.2	6.2	95	Both	B2	421	8.09E+07	8.0	6.9	1.0	
364	004241.02+405711.4	10.670955	40.953167	18.95	1.3	5.0	6	Both	B3	29	7.80E+06	7.0	1.0	6.3	
365	004241.05+410701.3	10.671060	41.117054	9.12	0.3	8.8	59	ACIS-I		312	4.67E+07	15.2	9.5	2.4	
366	004241.08+411101.7	10.671195	41.183832	5.13	0.2	4.9	99	ACIS-I		271	5.37E+07	1.8	3.7	1.8	
367	004241.14+411821.2	10.671433	41.305902	2.31	0.0	2.4	101	Both	B2	589	1.22E+08	2.3	10.0	1.4	
368	004241.17+411545.2	10.671558	41.262570	0.70	0.2	0.9	106	Both	B2	647	1.41E+08	1.9	1.5	-0.3	
369	004241.38+411528.4	10.672419	41.257911	0.85	0.1	1.1	106	Both	B2	781	1.82E+08	1.8	3.0	1.7	
370	004241.43+411523.8	10.672646	41.256612	0.91	0.0	1.1	106	Both	B2	781	1.82E+08	1.9	50.5	1.9	LMXB
371	004241.46+411617.8	10.672779	41.271631	0.57	0.0	0.7	107	Both	B2	785	1.80E+08	1.8	24.6	2.1	
372	004241.61+411436.9	10.673411	41.243591	1.59	0.0	1.8	105	Both	B2	777	1.95E+08	2.0	24.3	2.4	
373	004241.64+412105.4	10.673511	41.351504	4.99	0.0	5.1	96	Both	B2	464	9.08E+07	5.6	38.0	2.3	
374	004241.78+411635.8	10.674119	41.276628	0.67	0.0	0.8	107	Both	B2	785	1.80E+08	1.8	23.0	1.8	LMXB
375	004241.80+405154.6	10.674181	40.865167	24.22	0.2	2.7	7	Both	B3	35	1.09E+07	3.7	7.3	1.6	AGN
376	004242.07+411531.9	10.675323	41.258881	0.73	0.0	1.0	106	Both	B2	781	1.82E+08	1.9	44.0	1.6	
377	004242.17+411608.0	10.675719	41.268898	0.41	0.0	0.6	107	Both	B2	785	1.94E+08	1.8	62.5	2.1	LMXB
378	004242.20+411913.8	10.675864	41.320505	3.13	0.1	3.2	97	Both	B2	501	1.14E+08	2.9	7.7	3.6	
379	004242.32+411445.4	10.676359	41.245953	1.42	0.0	1.6	106	Both	B2	781	1.92E+08	2.0	94.5	1.8	
380	004242.36+411544.9	10.676525	41.262477	0.53	0.1	0.8	107	Both	B2	785	1.87E+08	1.8	3.5	1.7	
381	004242.47+411553.6	10.676966	41.264899	0.42	0.0	0.7	107	Both	B2	785	1.95E+08	1.8	115.4	2.2	
382	004242.50+405152.0	10.677096	40.864461	24.26	0.0	1.1	7	ACIS-S	B3	16	6.83E+06	1.1	32.5	1.8	
383	004242.52+411659.3	10.677175	41.283148	0.93	0.0	1.0	107	Both	B2	785	1.91E+08	1.8	39.8	2.0	
384	004242.52+411558.3	10.677185	41.266203	0.37	0.1	0.7	107	Both	B2	605	1.42E+08	1.8	2.0	1.4	
385	004242.63+411405.0	10.677661	41.234732	2.07	0.1	2.3	106	Both	B2	781	1.90E+08	2.3	7.1	1.2	
386	004242.64+411645.5	10.677676	41.279316	0.71	0.1	0.9	107	Both	B2	785	1.83E+08	1.9	5.1	3.6	
387	004242.68+405112.7	10.677838	40.853544	24.91	0.9	3.2	7	Both	B3	35	1.07E+07	4.3	1.6	2.2	
388	004242.71+411446.5	10.677988	41.246268	1.38	0.1	1.6	106	Both	B2	781	1.91E+08	1.9	5.5	1.5	
389	004242.72+411455.4	10.678005	41.248732	1.24	0.1	1.5	106	Both	B2	781	1.90E+08	2.0	5.1	1.3	
390	004242.75+411614.2	10.678147	41.270615	0.32	0.1	0.5	107	Both	B2	675	1.66E+08	1.8	1.6	0.2	
391	004242.80+411940.0	10.678357	41.327783	3.55	0.2	3.6	97	Both	B2	501	1.13E+08	3.3	3.6	4.1	
392	004242.99+411543.1	10.679136	41.261973	0.48	0.0	0.7	107	Both	B2	785	1.92E+08	1.8	103.4	2.0	
393	004243.09+411603.9	10.679549	41.267765	0.24	0.1	0.5	107	Both	B2	664	1.70E+08	1.7	1.8	2.9	
394	004243.13+411627.3	10.679737	41.274271	0.40	0.1	0.6	107	Both	B2	685	1.69E+08	1.8	1.9	1.8	
395	004243.18+411640.0	10.679946	41.277799	0.58	0.0	0.8	107	Both	B2	785	1.84E+08	1.8	23.4	1.9	
396	004243.23+411559.2	10.680157	41.266468	0.25	0.1	0.6	107	Both	B2	785	2.06E+08	1.7	2.2	0.5	
397	004243.27+405350.7	10.680310	40.897444	22.28	0.1	2.9	7	Both	B3	35	1.10E+07	3.1	4.9	2.0	
398	004243.30+411319.4	10.680455	41.222062	2.81	0.0	3.0	104	Both	B2	733	1.80E+08	2.8	31.1	1.1	
399	004243.66+411241.8	10.681923	41.211638	3.43	0.2	3.6	104	Both	B2	697	1.67E+08	3.5	1.9	1.7	
400	004243.66+405514.8	10.681945	40.920778	20.88	0.4	4.1	7	Both	B3	35	1.04E+07	4.7	4.1	2.0	
401	004243.70+412519.2	10.682091	41.422027	9.20	0.1	9.0	62	ACIS-I		268	4.09E+07	15.6	67.6	2.0	

Source No.	CXOU J	R.A. (J2000) (°)	Decl. (J2000) (°)	Distance (′)	PosErr (″)	θ (′)	No. of Obs	Detector	Region	Tot Exp (ks)	Tot Exp. Map Value (s cm^2)	R_{src} (sky pixel)	SNR	$E_{\rm median}$ (keV)	Match
402	004243.74+411632.3	10.682263	41.275658	0.43	0.0	0.7	107	Both	B2	785	1.96E+08	1.7	120.4	1.9	
403	004243.78+411514.1	10.682430	41.253917	0.90	0.0	1.1	106	Both	B2	781	1.90E+08	1.9	34.6	1.8	
404	004243.80+411612.4	10.682506	41.270133	0.13	0.0	0.5	107	Both	B2	785	2.05E+08	1.7	10.7	1.6	
405	004243.85+411603.8	10.682744	41.267730	0.11	0.0	0.5	107	Both	B2	785	2.06E+08	1.7	71.8	2.0	
406	004243.88+411629.6	10.682856	41.274912	0.38	0.0	0.6	107	Both	B2	785	2.00E+08	1.7	74.6	2.2	
407	004243.91+411755.0	10.683000	41.298618	1.79	0.1	1.9	107	Both	B2	785	1.62E+08	2.0	1.6	0.8	
408	004243.93+411610.6	10.683060	41.269634	0.09	0.0	0.5	107	Both	B2	785	2.05E+08	1.7	57.9	2.1	
409	004243.98+411636.9	10.683258	41.276926	0.49	0.1	0.7	107	Both	B2	785	1.90E+08	1.8	6.8	1.4	
410	004244.02+411645.0	10.683434	41.279188	0.63	0.1	0.9	107	Both	B2	785	1.84E+08	1.8	2.7	1.4	
411	004244.12+411603.9	10.683840	41.267770	0.07	0.1	0.6	107	Both	B2	744	1.94E+08	1.7	4.0	1.6	
412	004244.28+411613.9	10.684519	41.270535	0.11	0.0	0.5	107	Both	B2	785	2.05E+08	1.7	33.5	1.7	
413	004244.35+411608.6	10.684799	41.269076	0.02	0.0	0.5	107	Both	B2	776	2.03E+08	1.4	83.1	1.8	AGN
414	004244.36+405629.7	10.684836	40.941587	19.63	0.6	4.9	7	Both	B3	35	9.99E+06	6.4	2.8	3.5	
415	004244.36+411605.3	10.684843	41.268165	0.04	0.0	0.5	107	Both	B2	785	2.06E+08	1.7	69.7	1.9	
416	004244.36+411607.3	10.684863	41.268714	0.01	0.0	0.5	107	Both	B2	776	2.03E+08	1.5	94.3	1.2	AGN
417	004244.37+411158.4	10.684905	41.199565	4.15	0.0	4.3	102	Both	B2	691	1.60E+08	4.5	59.6	1.7	
418	004244.40+410000.2	10.685017	41.000056	16.12	0.7	6.7	3	ACIS-I		14	2.93E+06	10.7	3.8	2.7	
419	004244.45+410939.7	10.685219	41.161028	6.46	0.3	6.7	98	Both	B2	656	1.29E+08	9.6	4.6	1.3	
420	004244.49+411404.0	10.685391	41.234466	2.06	0.1	2.2	106	Both	B2	781	1.95E+08	2.2	4.6	3.6	
421	004244.60+411802.6	10.685865	41.300724	1.92	0.1	2.1	103	Both	B2	628	1.52E+08	2.1	4.4	2.0	
422	004244.66+411618.0	10.686111	41.271693	0.19	0.0	0.6	107	Both	B2	785	2.05E+08	1.7	61.1	1.6	
423	004244.73+411614.6	10.686410	41.270741	0.14	0.1	0.5	107	Both	B2	634	1.58E+08	1.7	2.1	1.8	
424	004244.82+411138.1	10.686791	41.193920	4.49	0.0	4.7	103	Both	B2	749	1.61E+08	5.2	152.2	1.8	
425	004244.89+411739.6	10.687046	41.294347	1.54	0.0	1.6	107	Both	B2	785	1.97E+08	1.9	60.8	2.0	
426	004244.94+411509.8	10.687256	41.252727	0.97	0.2	1.2	107	Both	B2	785	1.93E+08	1.9	2.8	1.8	
427	004244.94+411518.7	10.687271	41.255220	0.82	0.1	1.1	107	Both	B2	614	1.45E+08	1.8	1.3	3.3	
428	004245.05+411521.0	10.687728	41.255842	0.79	0.1	1.1	107	Both	B2	541	1.21E+08	1.8	1.9	1.0	
429	004245.08+411523.1	10.687858	41.256426	0.75	0.0	1.0	107	Both	B2	785	1.89E+08	1.8	37.8	1.7	
430	004245.09+411407.0	10.687878	41.235294	2.01	0.0	2.2	106	Both	B2	781	1.94E+08	2.2	35.0	1.8	
431	004245.10+411645.6	10.687946	41.279346	0.65	0.1	0.9	107	Both	B2	785	1.85E+08	1.8	2.5	1.1	
432	004245.11+411621.6	10.687963	41.272685	0.28	0.0	0.6	107	Both	B2	785	2.05E+08	1.8	126.3	2.0	
433	004245.11+411542.5	10.687972	41.261806	0.44	0.0	0.8	107	Both	B2	785	1.95E+08	1.8	35.6	2.0	
434	004245.11+411536.9	10.687976	41.260261	0.53	0.1	0.9	107	Both	B2	785	1.90E+08	1.8	2.6	4.3	
435	004245.21+411722.2	10.688385	41.289521	1.26	0.0	1.4	107	Both	B2	785	1.93E+08	1.9	53.0	2.0	
436	004245.22+411611.0	10.688449	41.269744	0.18	0.0	0.6	107	Both	B2	785	2.05E+08	1.7	46.4	1.7	
437	004245.52+411652.3	10.689701	41.281212	0.78	0.1	1.0	107	Both	B2	785	1.86E+08	1.8	6.8	3.2	
438	004245.58+411608.5	10.689948	41.269051	0.24	0.0	0.7	107	Both	B2	785	2.05E+08	1.7	62.0	1.8	
439	004245.59+411606.4	10.689964	41.268459	0.24	0.1	0.6	107	Both	B2	487	1.22E+08	1.7	1.5	0.6	
440	004245.80+412432.8	10.690859	41.409124	8.43	0.2	8.2	77	ACIS-I		328	5.59E+07	13.5	11.4	2.3	
441	004245.92+411651.5	10.691347	41.280990	0.79	0.1	1.1	107	Both	B2	507	1.05E+08	1.9	1.6	0.3	
442	004245.93+411036.3	10.691398	41.176774	5.53	0.0	5.8	102	Both	B2	708	1.50E+08	7.6	63.4	1.8	
443	004245.99+411619.5	10.691639	41.272097	0.37	0.0	0.7	107	Both	B2	785	2.01E+08	1.8	44.3	1.8	
444	004246.08+411736.1	10.692008	41.293385	1.51	0.0	1.6	107	Both	B2	785	1.96E+08	1.9	28.9	2.1	
445	004246.12+411728.7	10.692168	41.291308	1.39	0.1	1.5	107	Both	B2	785	1.94E+08	1.9	7.0	3.4	
446	004246.15+411543.1	10.692298	41.261986	0.53	0.0	0.9	107	Both	B2	785	1.91E+08	1.8	40.6	1.9	

Source No.	CXOU J	R.A. (J2000) (°)	Decl. (J2000) (°)	Distance (′)	PosErr (″)	θ (′)	No. of Obs	Detector	Region	Tot Exp (ks)	Tot Exp. Map Value (s cm^2)	R_{src} (sky pixel)	SNR	$E_{\rm median}$ (keV)	Match
447	004246.27+412723.7	10.692815	41.456601	11.28	1.2	10.3	10	ACIS-I		43	7.15E+06	20.4	2.7	2.0	
448	004246.41+411609.9	10.693414	41.269425	0.39	0.0	0.8	107	Both	B2	785	2.00E+08	1.8	15.7	1.4	
449	004246.70+410735.4	10.694619	41.126517	8.55	0.3	8.2	64	ACIS-I		333	5.58E+07	13.4	8.3	2.2	
450	004246.72+411359.5	10.694694	41.233222	2.18	0.1	2.4	106	Both	B2	781	1.93E+08	2.3	4.0	1.8	
451	004246.85+411605.6	10.695219	41.268241	0.47	0.1	0.8	107	Both	B2	785	1.95E+08	1.8	3.6	2.0	
452	004246.90+412119.3	10.695418	41.355387	5.22	0.1	5.3	96	Both	B2	464	9.38E+07	6.0	25.1	2.4	
453	004246.95+411615.5	10.695664	41.270991	0.51	0.0	0.9	107	Both	B2	785	1.93E+08	1.8	148.0	2.0	
454	004247.03+411731.0	10.695962	41.291963	1.48	0.1	1.6	107	Both	B2	785	1.96E+08	1.9	2.0	1.9	
455	004247.07+411910.7	10.696132	41.319666	3.10	0.2	3.2	99	Both	B2	579	1.35E+08	2.9	3.2	1.8	
456	004247.15+411619.6	10.696489	41.272119	0.57	0.0	0.9	107	Both	B2	785	1.90E+08	1.8	16.4	0.6	
457	004247.16+411628.4	10.696516	41.274558	0.64	0.0	1.0	107	Both	B2	785	1.89E+08	1.8	198.0	2.1	
458	004247.16+411407.0	10.696532	41.235289	2.08	0.0	2.3	106	Both	B2	781	1.95E+08	2.2	60.7	1.2	
459	004247.16+411413.0	10.696541	41.236948	1.98	0.2	2.2	106	Both	B2	781	1.95E+08	2.2	2.9	0.8	
460	004247.22+411157.8	10.696763	41.199407	4.20	0.0	4.5	103	Both	B2	749	1.70E+08	5.1	31.2	1.8	
461	004247.37+410832.3	10.697403	41.142316	7.61	0.4	7.6	90	ACIS-I		445	7.87E+07	11.4	2.8	3.9	
462	004247.46+411619.2	10.697769	41.272009	0.62	0.1	0.9	107	Both	B2	706	1.61E+08	1.7	2.1	1.0	
463	004247.47+411526.7	10.697794	41.257422	0.90	0.1	1.3	107	Both	B2	625	1.43E+08	1.9	1.8	0.5	
464	004247.69+405837.3	10.698746	40.977028	17.51	0.5	6.8	4	ACIS-I		19	2.95E+06	11.1	6.0	2.6	
465	004247.78+405021.8	10.699119	40.839413	25.77	0.8	4.3	7	Both	B3	35	1.03E+07	5.7	2.0	2.2	
466	004247.79+411113.7	10.699153	41.187163	4.94	0.0	5.1	104	Both	B2	753	1.61E+08	6.2	50.2	2.0	LMXB
467	004247.85+411622.9	10.699413	41.273032	0.71	0.0	1.0	107	Both	B2	785	1.88E+08	1.8	30.8	2.1	
468	004247.87+411549.6	10.699470	41.263797	0.73	0.0	1.1	107	Both	B2	785	1.88E+08	1.8	32.1	1.1	
469	004247.88+411532.8	10.699524	41.259127	0.88	0.0	1.2	107	Both	B2	785	1.90E+08	1.8	130.1	1.8	
470	004247.91+411052.6	10.699655	41.181304	5.29	0.1	5.5	103	Both	B2	748	1.63E+08	7.0	17.6	2.0	
471	004247.92+411602.2	10.699675	41.267302	0.68	0.1	1.0	107	Both	B2	785	1.88E+08	1.8	3.2	2.5	
472	004247.94+412404.6	10.699781	41.401285	7.98	0.5	7.9	91	ACIS-I		367	6.33E+07	9.2	2.2	3.2	
473	004248.11+411729.5	10.700481	41.291535	1.54	0.1	1.7	107	Both	B2	785	1.97E+08	1.9	2.2	1.6	
474	004248.26+412032.8	10.701111	41.342445	4.48	0.2	4.5	98	Both	B2	541	1.11E+08	4.6	5.8	2.3	
475	004248.46+412522.3	10.701924	41.422863	9.28	0.1	9.0	57	ACIS-I		247	4.06E+07	15.9	75.3	2.4	
476	004248.52+411521.1	10.702178	41.255877	1.10	0.0	1.4	107	Both	B2	785	1.91E+08	1.9	229.5	2.1	
477	004248.60+411612.9	10.702539	41.270254	0.81	0.1	1.1	107	Both	B2	785	1.90E+08	1.8	4.1	1.5	
478	004248.70+411624.4	10.702951	41.273446	0.87	0.0	1.2	107	Both	B2	785	1.92E+08	1.8	44.7	1.8	
479	004248.83+411745.7	10.703472	41.296055	1.84	0.1	2.0	107	Both	B2	785	1.85E+08	2.0	4.7	1.5	
480	004248.83+411512.9	10.703484	41.253587	1.24	0.1	1.5	107	Both	B2	785	1.93E+08	1.9	2.6	0.5	
481	004248.89+412406.9	10.703739	41.401930	8.04	0.3	7.9	90	ACIS-I		381	6.52E+07	11.8	10.0	1.1	
482	004249.02+411945.8	10.704257	41.329397	3.74	0.1	3.8	99	Both	B2	579	1.28E+08	3.6	8.3	1.7	AGN
483	004249.11+411456.6	10.704652	41.249058	1.48	0.1	1.7	107	Both	B2	785	1.97E+08	2.0	3.0	1.6	
484	004249.12+411233.7	10.704695	41.209388	3.67	0.3	4.1	106	Both	B2	834	1.86E+08	4.4	4.6	2.7	
485	004249.13+411742.0	10.704713	41.295002	1.82	0.0	2.0	107	Both	B2	785	1.93E+08	2.0	24.4	1.4	
486	004249.16+411623.4	10.704848	41.273172	0.95	0.1	1.2	107	Both	B2	785	1.94E+08	1.8	4.2	1.4	
487	004249.22+411815.8	10.705093	41.304405	2.33	0.0	2.5	104	Both	B2	668	1.52E+08	2.3	76.0	2.0	
488	004249.22+411601.1	10.705104	41.266984	0.93	0.0	1.2	107	Both	B2	785	1.94E+08	1.8	79.1	2.0	
489	004249.42+412235.1	10.705934	41.376442	6.53	0.2	6.5	95	Both	B2	459	8.16E+07	8.7	6.4	2.8	
490	004249.47+410635.3	10.706160	41.109819	9.58	0.4	8.6	37	ACIS-I		205	3.33E+07	14.8	8.4	2.2	
491	004249.76+405327.8	10.707338	40.891071	22.68	0.5	3.8	6	Both	B3	30	9.71E+06	4.3	2.0	1.2	

Source No.	CXOU J	R.A. (J2000) (°)	Decl. (J2000) (°)	Distance (′)	PosErr (″)	θ (′)	No. of Obs	Detector	Region	Tot Exp (ks)	Tot Exp. Map Value (s cm^2)	R_{src} (sky pixel)	SNR	$E_{\rm median}$ (keV)	Match
492	004249.92+411718.2	10.708013	41.288390	1.58	0.0	1.8	107	Both	B2	785	1.96E+08	1.9	16.4	1.7	
493	004249.96+412205.8	10.708193	41.368302	6.07	0.3	6.1	96	Both	B2	464	9.05E+07	7.7	4.7	3.0	
494	004250.14+404749.5	10.708933	40.797107	28.32	0.8	6.2	2	Both	B3	10	3.09E+06	8.9	2.6	2.3	
495	004250.21+404955.1	10.709236	40.831993	26.23	0.6	3.6	4	Both	B3	21	7.59E+06	3.8	1.1	3.1	
496	004250.23+411812.9	10.709295	41.303607	2.37	0.1	2.5	104	Both	B2	668	1.56E+08	2.3	7.1	2.0	
497	004250.41+411556.5	10.710063	41.265713	1.16	0.1	1.4	107	Both	B2	776	1.92E+08	1.3	4.7	0.9	
498	004250.50+411555.9	10.710426	41.265535	1.18	0.1	1.4	107	Both	B2	776	1.92E+08	1.2	3.8	1.3	
499	004250.59+411033.4	10.710832	41.175956	5.69	0.2	5.3	103	ACIS-I		215	4.18E+07	2.0	2.5	2.9	
500	004250.76+411033.5	10.711521	41.175997	5.70	0.1	5.3	103	ACIS-I		211	4.10E+07	2.3	6.4	2.9	LMXB
501	004250.80+411551.5	10.711686	41.264318	1.25	0.1	1.5	107	Both	B2	785	1.94E+08	1.9	5.3	3.3	
502	004250.81+411707.3	10.711741	41.285387	1.58	0.1	1.8	107	Both	B2	785	1.94E+08	1.9	5.9	2.0	
503	004251.17+411917.8	10.713225	41.321613	3.42	0.0	3.5	101	Both	B2	617	1.42E+08	3.2	18.1	2.2	
504	004251.23+405650.3	10.713493	40.947312	19.33	0.8	5.9	6	Both	B3	29	7.76E+06	8.6	2.4	1.5	
505	004251.24+411607.4	10.713527	41.268743	1.30	0.1	1.6	107	Both	B2	785	1.97E+08	1.9	4.6	1.4	
506	004251.29+410448.0	10.713744	41.080018	11.40	0.6	8.1	8	ACIS-I		86	1.51E+07	13.2	3.9	1.4	
507	004251.34+411639.7	10.713947	41.277715	1.42	0.1	1.7	107	Both	B2	785	1.97E+08	1.9	2.3	1.1	
508	004251.60+411701.3	10.715037	41.283701	1.64	0.0	1.8	107	Both	B2	785	1.94E+08	1.9	16.9	1.7	
509	004251.62+411512.1	10.715111	41.253383	1.65	0.1	1.9	107	Both	B2	785	1.97E+08	2.0	6.8	2.1	
510	004251.63+411922.6	10.715152	41.322948	3.53	0.2	3.6	101	Both	B2	617	1.42E+08	3.4	3.7	3.1	
511	004251.63+411302.8	10.715164	41.217459	3.37	0.0	3.8	106	Both	B2	834	1.99E+08	4.0	39.6	2.2	
512	004251.65+412634.4	10.715247	41.442900	10.54	0.5	9.9	20	ACIS-I		84	1.34E+07	18.8	8.5	2.6	
513	004251.79+411727.2	10.715809	41.290911	1.93	0.0	2.1	107	Both	B2	785	1.97E+08	2.1	14.5	1.7	
514	004251.86+405240.1	10.716110	40.877828	23.50	0.6	4.1	6	Both	B3	30	9.61E+06	5.0	2.5	1.1	
515	004252.29+411734.7	10.717887	41.292989	2.09	0.0	2.2	107	Both	B2	785	1.95E+08	2.1	22.9	1.8	
516	004252.30+405616.1	10.717956	40.937815	19.91	0.6	5.3	6	Both	B3	30	7.61E+06	6.7	1.6	3.8	
517	004252.33+412142.4	10.718055	41.361792	5.78	0.2	5.8	95	Both	B2	459	9.26E+07	7.0	5.9	2.9	
518	004252.41+411648.7	10.718407	41.280197	1.67	0.0	1.9	107	Both	B2	785	1.96E+08	1.9	56.6	1.7	
519	004252.50+412204.0	10.718756	41.367785	6.14	0.1	6.1	95	Both	B2	459	9.07E+07	7.8	14.0	2.5	
520	004252.51+411854.3	10.718800	41.315092	3.18	0.0	3.2	102	Both	B2	623	1.43E+08	3.0	211.9	2.1	
521	004252.51+411834.8	10.718818	41.309673	2.90	0.1	3.0	102	Both	B2	623	1.46E+08	2.7	12.0	2.5	
522	004252.51+411539.9	10.718833	41.261084	1.61	0.0	1.8	107	Both	B2	785	1.98E+08	2.0	91.0	0.6	
523	004252.62+411328.4	10.719281	41.224572	3.08	0.1	3.5	106	Both	B2	834	2.00E+08	3.6	14.4	2.3	
524	004252.72+410911.6	10.719694	41.153227	7.11	0.5	6.9	94	Both	B2	374	6.97E+07	9.7	1.7	2.2	
525	004252.99+405019.9	10.720796	40.838883	25.84	1.7	4.3	5	Both	B3	25	7.98E+06	5.4	0.8	-0.5	
526	004253.04+410709.5	10.721005	41.119313	9.11	0.6	8.2	53	ACIS-I		288	4.54E+07	13.6	2.9	3.0	
527	004253.16+411422.7	10.721516	41.239641	2.41	0.0	2.9	108	Both	B2	843	2.02E+08	3.1	30.0	2.2	
528	004253.39+411115.6	10.722467	41.187691	5.15	0.3	5.4	104	Both	B2	754	1.69E+08	6.6	4.1	2.4	
529	004253.58+411639.0	10.723280	41.277502	1.82	0.1	2.0	107	Both	B2	785	1.94E+08	2.0	2.4	0.6	
530	004253.63+405318.0	10.723484	40.888337	22.89	0.2	4.4	6	Both	B3	30	9.58E+06	5.3	5.5	2.2	
531	004253.64+412551.0	10.723526	41.430844	9.88	0.2	9.4	38	ACIS-I		166	2.49E+07	16.9	15.6	0.9	
532	004253.66+405243.6	10.723585	40.878802	23.46	0.9	4.4	6	Both	B3	30	9.55E+06	5.4	1.6	0.4	
533	004253.95+405546.5	10.724803	40.929602	20.43	0.5	5.1	6	Both	B3	30	9.26E+06	6.5	2.4	1.6	
534	004254.15+412037.2	10.725665	41.343689	4.86	0.2	4.8	96	Both	B2	496	1.08E+08	5.1	3.4	1.8	
535	004254.47+410401.3	10.726972	41.067030	12.25	0.4	7.2	3	ACIS-I		66	1.18E+07	10.1	5.0	3.0	
536	004254.68+411053.9	10.727835	41.181661	5.58	0.3	5.7	102	Both	B2	716	1.57E+08	7.3	2.1	4.4	

Source No.	CXOU J	R.A. (J2000) (°)	Decl. (J2000) (°)	Distance (′)	PosErr (″)	θ (′)	No. of Obs	Detector	Region	Tot Exp (ks)	Tot Exp. Map Value (s cm^2)	R_{src} (sky pixel)	SNR	$E_{\rm median}$ (keV)	Match
537	004254.81+412011.5	10.728407	41.336542	4.52	0.2	4.5	99	Both	B2	540	1.12E+08	4.6	4.1	2.1	
538	004254.90+411617.7	10.728761	41.271600	1.99	0.2	2.4	108	Both	B2	844	2.02E+08	2.3	3.4	4.0	
539	004254.92+411603.1	10.728856	41.267551	1.99	0.0	2.5	108	Both	B2	843	2.06E+08	2.6	194.7	2.0	
540	004255.17+411836.0	10.729879	41.310007	3.21	0.0	3.3	103	Both	B2	662	1.49E+08	3.0	45.8	1.9	
541	004255.33+404829.0	10.730576	40.808073	27.72	0.9	5.1	2	ACIS-S	B3	11	3.05E+06	6.6	1.3	3.0	
542	004255.36+412557.4	10.730690	41.432632	10.05	0.1	9.6	36	ACIS-I		158	2.32E+07	17.5	46.9	2.3	
543	004255.43+405946.3	10.730986	40.996195	16.49	0.6	5.0	1	ACIS-I		4	1.12E+06	5.3	1.7	1.2	
544	004255.60+411835.0	10.731686	41.309739	3.25	0.0	3.3	103	Both	B2	662	1.51E+08	3.0	43.2	1.9	
545	004256.01+411218.3	10.733381	41.205096	4.41	0.0	4.7	105	Both	B2	797	1.78E+08	5.3	19.6	1.6	
546	004256.37+411914.8	10.734890	41.320780	3.86	0.2	3.9	102	Both	B2	585	1.32E+08	3.7	2.0	2.6	
547	004256.76+410432.8	10.736532	41.075798	11.81	0.4	7.1	5	ACIS-I		75	1.32E+07	10.1	5.8	2.0	
548	004256.92+411843.8	10.737170	41.312190	3.52	0.0	3.6	103	Both	B2	662	1.48E+08	3.4	31.9	2.0	
549	004256.98+412005.0	10.737440	41.334749	4.62	0.1	4.6	96	Both	B2	496	1.10E+08	4.5	10.3	2.0	
550	004257.15+411959.2	10.738148	41.333124	4.55	0.2	4.5	96	Both	B2	496	1.09E+08	4.4	3.1	2.7	
551	004257.28+405359.0	10.738681	40.899744	22.27	0.7	5.1	6	Both	B3	30	9.43E+06	6.5	2.3	1.4	
552	004257.38+411209.4	10.739124	41.202631	4.67	0.2	4.9	104	Both	B2	754	1.74E+08	5.6	5.6	3.6	
553	004257.63+412137.6	10.740153	41.360466	6.04	0.3	6.0	95	Both	B2	459	9.32E+07	7.5	2.8	4.1	
554	004257.70+405059.4	10.740444	40.849837	25.26	0.6	5.3	6	Both	B3	30	8.80E+06	7.4	2.2	1.6	
555	004257.90+411104.6	10.741271	41.184626	5.66	0.0	5.8	104	Both	B2	754	1.69E+08	7.5	169.5	2.0	
556	004258.04+411319.2	10.741846	41.222005	3.81	0.1	4.2	107	Both	B2	839	1.99E+08	4.0	8.6	3.0	
557	004258.10+411337.5	10.742116	41.227104	3.60	0.1	4.0	107	Both	B2	839	2.00E+08	4.2	12.5	2.3	
558	004258.30+411802.9	10.742928	41.300828	3.25	0.6	3.6	107	Both	B2	804	1.70E+08	3.9	2.6	1.1	
559	004258.31+411529.2	10.742964	41.258113	2.70	0.0	3.2	108	Both	B2	843	2.02E+08	2.8	72.9	2.0	
560	004258.60+411159.1	10.744187	41.199769	4.93	0.1	5.1	104	Both	B2	658	1.45E+08	3.3	8.2	2.9	
561	004258.66+411527.0	10.744421	41.257500	2.78	0.0	3.3	108	Both	B2	843	2.01E+08	2.8	30.7	1.7	
562	004258.77+405901.6	10.744893	40.983782	17.31	0.7	5.2	2	ACIS-I		9	2.14E+06	5.9	1.6	0.9	
563	004258.82+411157.7	10.745113	41.199386	4.97	0.2	5.2	104	Both	B2	744	1.68E+08	2.7	3.2	3.1	
564	004259.08+411611.7	10.746194	41.269939	2.77	0.1	3.3	108	Both	B2	843	1.99E+08	2.9	6.1	1.2	
565	004259.09+411159.1	10.746209	41.199759	4.98	0.2	5.2	104	Both	B2	754	1.71E+08	3.6	5.7	3.1	
566	004259.44+412946.0	10.747669	41.496114	13.93	1.5	10.6	1	ACIS-I		4	9.16E+05	22.0	2.8	2.2	
567	004259.50+411242.2	10.747924	41.211748	4.45	0.1	4.8	106	Both	B2	796	1.85E+08	5.4	29.4	2.0	
568	004259.58+411918.4	10.748287	41.321789	4.28	0.0	4.2	100	Both	B2	379	6.96E+07	1.6	13.8	2.2	LMXB
569	004259.65+411919.3	10.748554	41.322045	4.30	0.0	4.2	97	Both	B2	300	6.61E+07	1.6	71.3	2.0	LMXB
570	004259.85+411142.7	10.749382	41.195203	5.29	0.3	5.5	104	Both	B2	754	1.70E+08	6.8	2.4	0.3	
571	004259.86+411605.7	10.749443	41.268268	2.92	0.0	3.4	108	Both	B2	843	1.98E+08	3.4	177.4	2.2	LMXB
572	004300.82+411349.2	10.753451	41.230348	3.86	0.1	4.2	107	Both	B2	839	1.96E+08	3.2	9.2	1.9	
573	004300.88+411504.2	10.753690	41.251186	3.28	0.2	3.4	108	Both	B2	743	1.79E+08	3.3	1.5	5.0	
574	004301.09+411351.6	10.754567	41.231019	3.88	0.0	4.2	107	Both	B2	839	1.96E+08	3.6	24.0	2.0	
575	004301.13+411317.2	10.754738	41.221457	4.25	0.1	4.6	107	Both	B2	839	1.92E+08	5.0	15.5	2.0	
576	004301.42+413017.3	10.755946	41.504831	14.52	0.6	11.1	1	ACIS-I		4	8.71E+05	23.9	10.0	2.7	LMXB
577	004301.62+411052.7	10.756775	41.181313	6.17	0.1	6.2	103	Both	B2	749	1.63E+08	8.5	13.4	0.9	
578	004301.65+411757.2	10.756907	41.299235	3.73	0.5	4.1	106	Both	B2	799	1.75E+08	4.5	2.8	3.7	
579	004301.70+411814.6	10.757112	41.304058	3.89	0.2	4.3	105	Both	B2	762	1.60E+08	4.2	2.6	1.6	
580	004301.77+411726.4	10.757403	41.290676	3.53	0.1	3.9	108	Both	B2	843	1.89E+08	4.0	10.9	1.2	
581	004301.96+405620.3	10.758208	40.938977	20.06	0.6	6.3	4	Both	B3	19	5.96E+06	9.1	2.9	1.8	

Source No.	CXOU J	R.A. (J2000) (°)	Decl. (J2000) (°)	Distance (′)	PosErr (″)	θ (′)	No. of Obs	Detector	Region	Tot Exp (ks)	Tot Exp. Map Value (s cm^2)	R_{src} (sky pixel)	SNR	$E_{\rm median}$ (keV)	Match
582	004301.98+411649.2	10.758291	41.280344	3.39	0.5	3.8	108	Both	B2	843	1.93E+08	4.1	2.8	2.6	
583	004302.45+411202.9	10.760245	41.200821	5.31	0.2	4.9	104	ACIS-I		109	2.14E+07	1.6	2.5	3.3	
584	004302.54+411202.3	10.760619	41.200666	5.33	0.2	4.9	104	ACIS-I		101	1.98E+07	1.6	1.4	1.9	
585	004302.92+411522.5	10.762206	41.256274	3.57	0.0	4.0	108	Both	B2	843	1.96E+08	3.6	148.1	2.0	LMXB
586	004302.95+411015.9	10.762300	41.171111	6.83	0.1	6.4	102	ACIS-I		312	5.42E+07	2.6	2.2	2.3	
587	004303.00+412041.7	10.762519	41.344936	5.76	0.1	5.7	96	Both	B2	496	1.05E+08	7.0	28.0	2.5	
588	004303.14+411015.3	10.763093	41.170926	6.85	0.0	6.4	102	ACIS-I		308	5.35E+07	2.8	22.3	2.3	
589	004303.21+411527.7	10.763406	41.257707	3.61	0.0	4.0	108	Both	B2	843	1.96E+08	3.9	154.0	1.8	
590	004303.30+412121.6	10.763754	41.356024	6.33	0.0	5.8	95	ACIS-I		211	4.25E+07	2.5	32.9	1.8	LMXB
591	004303.86+411804.8	10.766093	41.301354	4.16	0.0	4.5	106	Both	B2	799	1.61E+08	5.4	151.8	2.1	LMXB
592	004304.23+411601.3	10.767651	41.267038	3.74	0.0	4.1	108	Both	B2	843	1.92E+08	4.5	59.8	1.9	
593	004304.39+411643.0	10.768312	41.278618	3.82	0.4	4.2	107	Both	B2	839	1.89E+08	4.7	3.9	3.0	
594	004304.74+411113.8	10.769780	41.187167	6.22	0.2	6.2	104	Both	B2	754	1.62E+08	8.6	10.1	1.8	
595	004305.20+411132.3	10.771695	41.192314	6.04	0.2	6.1	104	Both	B2	754	1.61E+08	8.2	5.7	2.5	
596	004305.67+411702.7	10.773642	41.284086	4.11	0.0	4.5	107	Both	B2	839	1.79E+08	5.1	141.3	1.5	
597	004306.43+411314.1	10.776819	41.220584	5.06	0.2	5.3	106	Both	B2	796	1.70E+08	6.3	4.7	3.8	
598	004306.55+411916.2	10.777298	41.321172	5.23	0.1	5.1	96	Both	B2	472	1.04E+08	2.5	5.3	1.4	
599	004306.60+412244.4	10.777539	41.379002	7.83	0.2	3.7	91	ACIS-I		14	3.38E+06	1.5	1.6	1.9	
600	004306.72+411917.6	10.778017	41.321557	5.27	0.2	5.1	96	Both	B2	481	1.06E+08	2.7	5.2	1.6	
601	004306.73+412244.3	10.778043	41.378985	7.84	0.2	3.7	91	ACIS-I		14	3.38E+06	1.3	1.6	1.2	
602	004306.74+410435.9	10.778107	41.076656	12.27	1.8	5.7	4	ACIS-I		71	1.31E+07	7.1	1.4	5.8	
603	004306.79+411912.0	10.778317	41.320024	5.22	0.1	5.1	96	Both	B2	496	1.08E+08	5.2	9.9	1.4	
604	004307.11+411810.0	10.779647	41.302805	4.74	0.1	5.1	100	Both	B2	637	1.26E+08	5.4	10.2	2.0	
605	004307.49+412019.6	10.781216	41.338786	6.05	0.1	5.9	96	Both	B2	496	1.05E+08	7.6	39.5	2.0	LMXB
606	004307.62+404816.5	10.781755	40.804600	28.19	1.1	7.1	1	ACIS-S	B3	5	9.27E+05	12.1	2.5	2.3	
607	004307.73+412416.0	10.782233	41.404451	9.25	0.4	8.7	66	ACIS-I		285	4.64E+07	14.1	5.6	2.7	
608	004308.63+411248.3	10.785999	41.213419	5.65	0.0	5.8	103	Both	B2	714	1.54E+08	7.4	67.8	2.7	LMXB
609	004308.91+410731.5	10.787157	41.125434	9.76	0.3	7.2	30	ACIS-I		195	3.23E+07	11.9	11.5	1.4	
610	004309.65+405922.9	10.790241	40.989711	17.41	0.4	7.3	2	ACIS-I		9	1.94E+06	11.1	6.2	2.0	
611	004309.84+411900.7	10.791013	41.316881	5.60	0.0	5.4	96	Both	B2	496	1.07E+08	6.7	49.6	2.1	
612	004309.95+412332.4	10.791494	41.392359	8.84	0.3	8.5	71	ACIS-I		324	5.53E+07	14.2	10.5	2.1	LMXB
613	004309.96+412718.5	10.791541	41.455148	12.17	1.3	9.3	6	ACIS-I		27	4.61E+06	17.0	2.5	1.1	
614	004310.17+411719.7	10.792406	41.288825	5.00	0.4	5.4	99	Both	B2	632	1.35E+08	6.7	3.3	4.2	AGN
615	004310.61+411451.2	10.794250	41.247571	5.10	0.0	5.4	102	Both	B2	676	1.45E+08	6.5	244.2	2.2	LMXB
616	004310.96+411255.7	10.795672	41.215496	5.94	0.4	6.0	102	Both	B2	522	1.13E+08	7.9	1.9	3.9	
617	004311.35+411809.5	10.797296	41.302656	5.47	0.1	5.7	97	Both	B2	555	1.16E+08	7.6	28.6	2.9	
618	004311.64+410605.7	10.798521	41.101596	11.27	1.2	4.8	6	ACIS-I		78	1.47E+07	6.6	1.8	3.3	
619	004312.42+405856.0	10.801785	40.982229	17.99	0.6	9.0	3	ACIS-I		29	4.90E+06	16.4	6.5	2.3	
620	004312.99+410034.8	10.804152	41.009677	16.45	0.4	7.7	2	ACIS-I		63	7.56E+06	11.8	6.8	2.3	
621	004313.21+411813.1	10.805080	41.303663	5.82	0.1	6.1	97	Both	B2	555	1.13E+08	8.1	30.2	1.9	
622	004313.84+411711.2	10.807687	41.286457	5.65	0.2	5.9	98	Both	B2	627	1.27E+08	7.9	11.4	2.6	
623	004314.10+411302.6	10.808759	41.217408	6.39	0.2	5.6	100	ACIS-I		136	2.69E+07	2.1	3.6	3.2	
624	004314.36+410721.1	10.809847	41.122535	10.43	0.0	6.4	19	ACIS-I		151	2.56E+07	11.2	81.3	3.1	LMXB
625	004314.36+411650.1	10.809848	41.280593	5.69	0.1	5.9	98	Both	B2	627	1.32E+08	7.9	18.0	1.6	
626	004314.59+412513.9	10.810831	41.420531	10.73	0.6	9.8	25	ACIS-I		117	1.68E+07	18.3	4.3	1.8	LMXB

Source No.	CXOU J	R.A. (J2000) (°)	Decl. (J2000) (°)	Distance (′)	PosErr (″)	θ (′)	No. of Obs	Detector	Region	Tot Exp (ks)	Tot Exp. Map Value (s cm^2)	R_{src} (sky pixel)	SNR	$E_{\rm median}$ (keV)	Match
627	004315.03+411326.2	10.812627	41.223952	6.37	0.2	6.4	99	Both	B2	623	1.34E+08	8.8	8.1	2.5	
628	004315.41+411124.6	10.814224	41.190189	7.51	0.1	7.0	94	Both	B2	504	9.11E+07	10.3	20.8	1.7	LMXB
629	004315.66+411556.0	10.815280	41.265559	5.89	0.3	6.1	100	Both	B2	666	1.28E+08	8.2	2.1	5.0	
630	004316.10+411841.3	10.817085	41.311476	6.50	0.1	5.9	95	ACIS-I		203	3.83E+07	2.6	12.6	1.9	
631	004316.11+405415.7	10.817145	40.904362	22.67	0.8	7.8	2	Both	B3	10	2.93E+06	13.4	3.7	2.4	
632	004316.36+411630.0	10.818202	41.275024	6.03	0.3	6.2	98	Both	B2	627	1.20E+08	8.4	3.4	-0.4	
633	004316.39+410348.8	10.818315	41.063574	13.71	0.0	4.4	1	ACIS-I		58	1.13E+07	4.2	22.7	2.0	
634	004317.90+411112.7	10.824603	41.186867	8.00	0.3	7.3	86	ACIS-I		436	7.78E+07	11.0	5.5	1.0	
635	004318.45+411142.2	10.826903	41.195073	7.79	0.3	7.2	93	ACIS-I		464	8.42E+07	10.7	8.1	2.9	
636	004318.87+412016.9	10.828628	41.338052	7.71	0.3	7.4	91	ACIS-I		403	7.10E+07	11.3	8.6	0.7	
637	004319.16+411000.5	10.829859	41.166815	8.96	0.5	7.6	66	ACIS-I		354	6.15E+07	12.6	3.7	3.7	
638	004319.92+411318.5	10.833040	41.221827	7.26	0.5	6.9	96	Both	B2	429	8.10E+07	9.8	2.0	2.9	
639	004320.00+411249.3	10.833346	41.213703	7.48	0.3	7.1	94	ACIS-I		469	8.61E+07	10.3	6.1	3.1	
640	004320.73+411531.2	10.836414	41.258668	6.87	0.1	6.9	96	Both	B2	546	1.06E+08	10.0	40.7	1.6	
641	004320.94+411315.7	10.837269	41.221043	7.45	0.5	7.4	96	Both	B2	411	7.42E+07	7.4	1.5	2.5	
642	004321.06+411750.5	10.837783	41.297370	7.11	0.1	7.1	95	Both	B2	512	9.11E+07	10.8	47.0	1.9	
643	004321.52+411557.3	10.839692	41.265932	6.99	0.3	7.0	96	Both	B2	546	9.97E+07	10.3	6.7	2.8	
644	004321.97+405754.7	10.841580	40.965198	19.54	0.7	8.3	1	ACIS-I		19	3.45E+06	13.5	4.2	1.2	
645	004322.11+410924.0	10.842132	41.156682	9.78	0.6	7.1	35	ACIS-I		222	3.86E+07	12.7	4.3	3.2	
646	004322.33+411255.8	10.843043	41.215508	7.83	0.3	7.3	92	ACIS-I		460	8.31E+07	11.0	7.4	2.4	
647	004322.96+411143.9	10.845675	41.195546	8.49	0.6	7.4	73	ACIS-I		335	5.79E+07	11.4	2.0	3.1	
648	004323.14+410601.0	10.846456	41.100279	12.47	0.1	1.9	1	ACIS-I		58	6.72E+06	1.9	3.8	3.4	
649	004323.57+411347.0	10.848236	41.229743	7.74	0.5	7.6	95	Both	B2	382	6.75E+07	11.6	2.0	2.2	
650	004324.83+411726.6	10.853461	41.290744	7.72	0.1	7.8	94	Both	B2	508	8.56E+07	12.3	26.3	2.4	
651	004325.00+405747.0	10.854178	40.963057	19.88	0.8	7.9	1	ACIS-I		19	3.53E+06	12.1	3.1	2.7	
652	004325.64+411537.4	10.856839	41.260392	7.78	0.3	7.6	93	Both	B2	498	8.21E+07	11.7	4.9	2.5	
653	004326.02+411411.7	10.858446	41.236606	8.07	0.5	7.6	85	ACIS-I		385	6.42E+07	11.4	1.9	3.6	
654	004326.30+411453.2	10.859614	41.248112	7.99	0.5	7.8	90	ACIS-I		376	6.33E+07	11.4	2.2	4.9	
655	004326.30+411911.7	10.859623	41.319940	8.46	0.2	8.0	64	ACIS-I		286	4.66E+07	12.9	16.7	3.5	AGN
656	004326.62+410756.3	10.860919	41.132324	11.41	0.6	6.8	15	ACIS-I		115	1.31E+07	14.6	6.8	2.7	
657	004327.53+410643.7	10.864734	41.112159	12.42	0.7	2.5	3	ACIS-I		82	1.46E+07	4.5	3.6	2.7	
658	004327.72+410504.4	10.865524	41.084570	13.74	0.2	3.9	2	ACIS-I		77	1.52E+07	4.7	5.9	2.4	
659	004327.97+411828.3	10.866542	41.307874	8.53	0.1	8.0	67	ACIS-I		279	4.61E+07	13.2	24.3	1.0	
660	004328.16+411454.7	10.867366	41.248555	8.33	0.5	7.9	76	ACIS-I		354	6.20E+07	12.4	1.8	2.0	
661	004329.11+410748.0	10.871304	41.130002	11.84	0.0	2.9	10	ACIS-I		91	1.58E+07	3.8	47.0	3.0	
662	004329.16+411514.7	10.871509	41.254088	8.47	0.5	8.1	73	ACIS-I		300	5.06E+07	13.3	2.3	2.3	
663	004329.16+411736.7	10.871541	41.293530	8.55	0.8	8.1	63	ACIS-I		263	4.43E+07	7.4	1.6	4.7	
664	004329.53+410905.1	10.873068	41.151434	11.04	0.8	5.9	16	ACIS-I		125	1.82E+07	11.1	3.7	3.7	
665	004330.14+410521.2	10.875598	41.089232	13.80	0.2	2.6	2	ACIS-I		58	1.20E+07	1.4	1.3	2.0	
666	004330.15+410522.6	10.875637	41.089615	13.78	0.2	2.5	2	ACIS-I		58	1.20E+07	1.4	1.4	2.3	
667	004330.18+411718.5	10.875765	41.288487	8.70	0.7	8.4	60	ACIS-I		305	4.63E+07	10.9	2.2	3.7	
668	004330.26+411648.0	10.876110	41.280026	8.66	0.6	8.4	63	ACIS-I		317	5.11E+07	11.5	2.6	3.8	
669	004330.30+411626.8	10.876280	41.274125	8.65	0.7	8.3	67	ACIS-I		330	5.30E+07	7.4	1.3	5.2	
670	004331.09+410833.6	10.879571	41.142668	11.60	0.9	3.6	7	ACIS-I		102	1.65E+07	6.6	3.4	2.2	
671	004331.10+405705.8	10.879617	40.951619	20.97	0.9	7.1	1	ACIS-I		19	3.58E+06	10.0	2.0	3.0	

Source No.	CXOU J	R.A. (J2000) (°)	Decl. (J2000) (°)	Distance (′)	PosErr (″)	θ (′)	No. of Obs	Detector	Region	Tot Exp (ks)	Tot Exp. Map Value (s cm^2)	R_{src} (sky pixel)	SNR	$E_{\rm median}$ (keV)	Match
672	004332.17+411702.6	10.884070	41.284065	9.04	0.6	8.6	57	ACIS-I		294	4.57E+07	14.9	2.9	2.9	
673	004332.21+410648.4	10.884232	41.113451	12.96	0.3	3.0	2	ACIS-I		77	1.57E+07	4.5	5.2	2.3	
674	004332.37+411040.8	10.884898	41.178020	10.55	0.1	8.0	25	ACIS-I		169	2.48E+07	14.7	54.8	3.4	
675	004332.96+411629.4	10.887350	41.274836	9.15	0.7	8.7	57	ACIS-I		294	4.41E+07	11.8	2.0	5.1	
676	004333.59+412139.2	10.889975	41.360891	10.78	0.5	9.1	22	ACIS-I		101	1.49E+07	16.3	6.5	1.9	
677	004333.77+410821.8	10.890723	41.139415	12.11	0.6	3.2	2	ACIS-I		77	1.55E+07	5.0	3.3	3.1	
678	004333.80+411407.0	10.890863	41.235292	9.51	0.4	8.3	44	ACIS-I		241	4.07E+07	14.0	7.1	3.1	
679	004334.16+410207.8	10.892362	41.035505	16.85	0.3	5.8	2	ACIS-I		77	1.50E+07	6.8	4.9	2.1	
680	004334.31+411323.5	10.892964	41.223215	9.78	0.0	8.2	40	ACIS-I		220	3.77E+07	13.9	76.7	2.0	
681	004335.84+411433.6	10.899342	41.242673	9.81	0.3	6.9	36	ACIS-I		81	1.50E+07	3.4	2.2	3.3	
682	004336.05+411433.9	10.900236	41.242767	9.85	0.3	6.9	35	ACIS-I		77	1.48E+07	3.3	2.2	3.7	
683	004336.63+410811.8	10.902645	41.136624	12.63	1.2	3.5	2	ACIS-I		77	1.57E+07	4.9	1.7	1.4	LMXB
684	004337.27+411443.6	10.905315	41.245469	10.05	0.0	8.5	31	ACIS-I		184	3.07E+07	14.3	81.2	2.2	LMXB
685	004339.32+410937.1	10.913850	41.160317	12.22	1.2	5.0	4	ACIS-I		87	1.67E+07	7.1	1.6	2.9	
686	004340.16+410045.4	10.917339	41.012637	18.62	0.2	6.7	2	ACIS-I		77	1.45E+07	9.0	11.8	2.2	
687	004341.26+405446.3	10.921957	40.912884	23.90	0.2	7.3	1	ACIS-I		19	3.24E+06	11.0	12.1	2.9	AGN
688	004341.45+405427.0	10.922740	40.907515	24.20	0.4	7.5	1	ACIS-I		19	3.10E+06	11.7	6.7	2.2	
689	004341.61+410015.3	10.923409	41.004262	19.19	0.4	7.0	2	ACIS-I		77	1.42E+07	10.1	5.9	2.3	
690	004342.68+412606.8	10.927846	41.435228	14.82	0.5	5.7	1	ACIS-I		8	1.52E+06	7.0	2.7	3.8	
691	004343.01+412849.6	10.929239	41.480447	16.81	0.3	6.1	1	ACIS-I		8	1.53E+06	7.7	5.2	2.5	AGN
692	004343.23+405631.2	10.930160	40.942004	22.53	0.3	5.7	1	ACIS-I		19	3.72E+06	6.7	4.4	2.7	
693	004343.30+410103.7	10.930439	41.017711	18.71	0.6	6.5	2	ACIS-I		77	1.47E+07	8.8	2.9	2.6	
694	004343.75+410339.7	10.932312	41.061028	16.75	0.3	5.2	2	ACIS-I		77	1.55E+07	5.5	4.1	2.7	
695	004343.99+411231.5	10.933321	41.208754	11.78	0.3	6.7	7	ACIS-I		84	1.53E+07	9.1	9.8	1.1	
696	004344.08+405639.0	10.933678	40.944168	22.49	0.6	5.5	1	ACIS-I		19	3.75E+06	6.3	1.7	2.1	
697	004344.34+411155.5	10.934783	41.198768	12.04	0.8	6.9	5	ACIS-I		92	1.65E+07	9.8	3.0	3.1	
698	004344.47+410752.7	10.935318	41.131323	14.00	1.1	4.5	2	ACIS-I		77	1.59E+07	5.3	1.4	4.6	
699	004344.61+412409.9	10.935904	41.402759	13.88	0.1	7.6	3	ACIS-I		17	3.39E+06	12.1	12.0	2.0	
700	004344.67+412841.5	10.936155	41.478204	16.91	0.7	5.8	1	ACIS-I		8	1.55E+06	6.7	1.6	1.8	
701	004345.65+412706.4	10.940211	41.451787	15.91	0.7	5.2	1	ACIS-I		8	1.58E+06	5.6	1.4	1.6	
702	004345.75+410803.0	10.940660	41.134173	14.10	0.7	4.7	2	ACIS-I		77	1.58E+07	5.5	1.9	2.5	
703	004345.89+411202.6	10.941239	41.200727	12.27	0.3	6.8	5	ACIS-I		92	1.55E+07	8.6	6.8	2.3	
704	004345.90+411025.9	10.941264	41.173880	12.90	0.6	6.0	3	ACIS-I		82	1.61E+07	6.9	3.2	3.4	
705	004346.13+410955.2	10.942237	41.165341	13.18	0.5	5.8	3	ACIS-I		82	1.56E+07	8.2	5.8	2.7	
706	004346.14+410118.0	10.942283	41.021686	18.85	0.7	6.3	2	ACIS-I		77	1.48E+07	8.7	2.0	1.0	
707	004347.19+410654.0	10.946661	41.115001	15.00	0.2	4.9	2	ACIS-I		77	1.21E+07	5.5	5.4	2.4	
708	004347.29+410404.4	10.947075	41.067913	16.90	0.4	5.2	2	ACIS-I		77	1.55E+07	5.6	2.8	2.0	
709	004348.81+410521.1	10.953396	41.089202	16.23	0.6	5.0	2	ACIS-I		77	1.57E+07	5.3	1.4	0.9	
710	004349.30+411053.3	10.955420	41.181481	13.29	1.0	6.5	3	ACIS-I		82	1.52E+07	9.0	2.3	3.9	AGN
711	004349.80+410634.0	10.957536	41.109458	15.59	0.5	5.0	2	ACIS-I		77	1.58E+07	5.4	2.1	2.4	
712	004350.75+412117.5	10.961462	41.354878	13.50	0.5	8.1	3	ACIS-I		17	3.45E+06	13.2	6.4	2.3	
713	004353.58+411202.0	10.973255	41.200567	13.65	0.5	6.7	1	ACIS-I		58	1.14E+07	9.0	3.4	1.6	
714	004353.65+411655.0	10.973571	41.281949	13.05	0.3	8.7	2	ACIS-I		9	1.84E+06	14.8	13.4	1.5	
715	004353.70+412041.9	10.973785	41.344990	13.81	2.4	7.6	2	ACIS-I		13	2.59E+06	11.4	0.6	-1.1	
716	004353.70+410024.5	10.973786	41.006815	20.44	0.5	6.9	2	ACIS-I		77	1.41E+07	11.7	5.9	2.5	

Source No.	CXOU J	R.A. (J2000) (°)	Decl. (J2000) (°)	Distance (′)	PosErr (″)	θ (′)	No. of Obs	Detector	Region	Tot Exp (ks)	Tot Exp. Map Value (s cm^2)	R_{src} (sky pixel)	SNR	$E_{\rm median}$ (keV)	Match
717	004354.40+410612.8	10.976674	41.103580	16.49	0.1	5.6	2	ACIS-I		77	1.55E+07	6.6	14.4	2.4	AGN
718	004356.31+412316.1	10.984663	41.387828	15.29	2.1	6.4	2	ACIS-I		13	2.55E+06	9.2	0.9	0.5	
719	004356.33+405505.1	10.984742	40.918099	25.03	1.0	5.8	1	ACIS-I		19	3.64E+06	7.1	1.0	1.9	
720	004356.41+412202.2	10.985044	41.367281	14.77	0.4	7.0	2	ACIS-I		13	2.60E+06	10.2	8.1	1.9	LMXB
721	004356.55+410416.6	10.985630	41.071291	18.03	0.5	5.9	2	ACIS-I		77	1.51E+07	7.6	2.8	1.4	
722	004356.59+410644.3	10.985825	41.112333	16.52	0.5	5.9	2	ACIS-I		77	1.52E+07	7.2	2.5	3.4	
723	004357.01+410045.4	10.987565	41.012617	20.58	0.9	6.7	2	ACIS-I		77	1.38E+07	11.7	2.7	2.2	
724	004357.57+413054.5	10.989897	41.515145	20.18	0.3	5.4	1	ACIS-I		8	1.61E+06	5.5	3.3	2.4	
725	004358.04+405341.9	10.991870	40.894999	26.38	1.0	7.1	1	ACIS-I		19	3.32E+06	10.2	1.6	4.0	
726	004358.47+411330.6	10.993641	41.225170	14.18	0.7	8.6	3	ACIS-I		67	1.19E+07	14.2	3.8	1.4	
727	004359.82+412435.4	10.999275	41.409840	16.51	0.4	3.1	1	ACIS-I		8	1.69E+06	2.5	1.0	2.6	
728	004401.04+412808.2	11.004338	41.468952	18.75	0.4	2.9	1	ACIS-I		8	1.70E+06	2.4	1.0	2.0	
729	004403.11+410404.4	11.012977	41.067910	19.11	0.5	6.6	2	ACIS-I		77	1.41E+07	9.7	4.4	3.7	
730	004403.16+410800.9	11.013192	41.133596	16.90	0.2	7.0	2	ACIS-I		77	1.49E+07	10.0	10.1	2.1	AGN
731	004403.30+411229.1	11.013791	41.208097	15.29	0.7	8.4	1	ACIS-I		58	1.08E+07	13.9	3.5	2.7	
732	004404.75+412126.2	11.019803	41.357302	16.01	0.8	7.2	2	ACIS-I		13	2.56E+06	11.8	3.7	2.5	
733	004404.77+405901.6	11.019880	40.983804	22.84	0.2	1.7	1	ACIS-I		19	4.15E+06	1.8	1.7	2.1	
734	004405.52+410235.9	11.023011	41.043327	20.41	0.2	1.9	1	ACIS-I		19	4.19E+06	2.0	2.2	4.2	
735	004405.65+410638.6	11.023551	41.110728	18.00	0.5	7.1	2	ACIS-I		77	1.44E+07	10.5	4.9	2.0	
736	004405.69+405336.5	11.023721	40.893480	27.24	0.9	7.1	1	ACIS-I		19	3.47E+06	9.9	1.8	1.7	
737	004405.70+410310.4	11.023778	41.052892	20.06	0.3	2.5	1	ACIS-I		19	4.17E+06	2.3	1.6	3.0	
738	004407.80+413107.8	11.032518	41.518845	21.69	0.4	4.8	1	ACIS-I		8	1.65E+06	4.8	2.2	1.7	
739	004408.65+405803.7	11.036044	40.967721	24.05	0.3	2.8	1	ACIS-I		19	4.10E+06	2.3	1.2	2.0	
740	004409.38+410939.8	11.039102	41.161059	17.25	0.8	8.5	2	ACIS-I		77	1.35E+07	14.2	2.7	2.3	
741	004409.44+410406.0	11.039356	41.068346	20.03	0.5	3.6	1	ACIS-I		19	2.81E+06	3.4	1.0	2.5	
742	004409.84+412813.9	11.041027	41.470541	20.10	0.3	1.9	1	ACIS-I		8	1.74E+06	2.0	1.0	1.0	
743	004410.16+411830.4	11.042375	41.308452	16.30	1.3	7.9	1	ACIS-I		8	1.45E+06	12.7	1.7	2.6	
744	004411.08+405646.6	11.046173	40.946279	25.33	0.3	4.2	1	ACIS-I		19	3.98E+06	3.6	2.0	1.9	
745	004411.41+405433.2	11.047578	40.909234	27.10	0.4	6.3	1	ACIS-I		19	3.74E+06	7.8	4.5	2.1	
746	004411.81+410208.6	11.049249	41.035748	21.60	0.3	2.1	1	ACIS-I		19	4.23E+06	2.0	1.2	2.5	
747	004412.01+405421.6	11.050060	40.906012	27.33	0.5	6.5	1	ACIS-I		19	3.71E+06	8.4	3.2	1.9	AGN
748	004412.20+413148.2	11.050855	41.530057	22.75	0.5	5.4	1	ACIS-I		8	1.63E+06	6.0	2.4	1.8	
749	004412.89+412555.5	11.053723	41.432098	19.30	0.0	0.5	1	ACIS-I		8	1.75E+06	1.6	9.1	1.1	
750	004413.22+412910.2	11.055086	41.486185	21.17	0.4	2.8	1	ACIS-I		8	1.73E+06	2.4	1.0	3.7	
751	004413.46+410004.9	11.056111	41.001368	23.22	0.2	1.9	1	ACIS-I		19	4.22E+06	1.9	1.8	2.4	
752	004413.80+410536.0	11.057521	41.093355	19.85	0.5	5.3	1	ACIS-I		19	1.66E+06	5.9	2.3	2.1	
753	004413.84+405451.1	11.057695	40.914202	27.15	0.5	6.2	1	ACIS-I		19	3.79E+06	7.4	2.6	3.8	AGN
754	004416.02+405722.0	11.066765	40.956129	25.50	0.3	4.1	1	ACIS-I		19	4.04E+06	3.5	2.6	3.5	
755	004416.03+413057.2	11.066831	41.515893	22.71	0.2	4.6	1	ACIS-I		8	1.67E+06	4.8	5.5	2.9	LMXB
756	004416.85+411114.9	11.070213	41.187498	18.07	0.7	10.1	1	ACIS-I		58	9.69E+06	20.0	6.0	2.7	
757	004416.97+410343.5	11.070717	41.062093	21.39	0.3	3.9	1	ACIS-I		19	4.12E+06	3.6	3.0	1.9	
758	004417.20+405612.0	11.071683	40.936680	26.52	0.6	5.2	1	ACIS-I		19	3.93E+06	5.1	1.4	2.9	
759	004419.21+410306.7	11.080053	41.051886	22.10	0.2	3.8	1	ACIS-I		19	3.77E+06	3.4	3.1	2.1	
760	004420.42+411302.1	11.085088	41.217260	18.33	1.2	11.5	1	ACIS-I		58	8.86E+06	25.3	2.4	4.6	
761	004420.81+412206.7	11.086724	41.368549	19.08	0.7	4.0	2	Both	B1	13	3.43E+06	4.0	0.9	4.1	

Source No.	CXOU J	R.A. (J2000) (°)	Decl. (J2000) (°)	Distance (′)	PosErr (″)	θ (′)	No. of Obs	Detector	Region	Tot Exp (ks)	Tot Exp. Map Value (s cm^2)	R_{src} (sky pixel)	SNR	$E_{\rm median}$ (keV)	Match
762	004421.09+410457.7	11.087903	41.082705	21.36	0.4	5.4	1	ACIS-I		19	3.96E+06	5.9	3.2	2.8	
763	004421.97+405501.7	11.091563	40.917157	27.99	1.3	6.6	1	ACIS-I		19	3.77E+06	8.6	0.9	4.3	
764	004423.31+405753.7	11.097139	40.964943	26.07	0.7	4.6	1	ACIS-I		19	4.03E+06	4.3	0.9	1.3	
765	004424.84+413200.5	11.103537	41.533482	24.65	0.4	6.0	1	ACIS-I		8	1.59E+06	7.3	4.6	2.0	
766	004424.86+410333.7	11.103592	41.059384	22.71	0.5	4.9	1	ACIS-I		19	3.81E+06	4.8	1.6	1.7	
767	004425.73+412241.7	11.107221	41.378275	20.14	0.2	3.6	2	Both	B1	13	3.56E+06	3.4	4.4	2.7	
768	004426.48+410250.0	11.110371	41.047230	23.38	0.4	4.8	1	ACIS-I		19	4.09E+06	4.6	2.4	2.0	
769	004426.51+410042.0	11.110486	41.011690	24.66	0.4	4.3	1	ACIS-I		19	4.12E+06	4.0	2.1	2.1	
770	004426.91+410100.6	11.112132	41.016856	24.52	0.3	4.4	1	ACIS-I		19	4.12E+06	4.1	2.6	1.8	
771	004429.55+412135.3	11.123142	41.359826	20.50	0.0	3.6	2	Both	B1	13	3.47E+06	4.1	32.1	2.2	LMXB
772	004429.70+412257.5	11.123765	41.382641	20.93	0.3	3.4	2	Both	B1	13	3.49E+06	3.2	2.1	2.8	
773	004429.75+410030.7	11.123974	41.008534	25.25	0.4	4.9	1	ACIS-I		19	4.07E+06	5.0	2.7	2.0	
774	004430.47+412310.2	11.126980	41.386190	21.14	0.2	3.3	2	Both	B1	13	3.44E+06	3.2	3.5	2.7	
775	004431.98+412519.5	11.133284	41.422103	22.20	0.5	3.9	2	Both	B1	13	3.56E+06	3.9	1.2	1.7	
776	004432.46+410533.7	11.135263	41.092719	22.92	1.0	7.3	1	ACIS-I		19	3.80E+06	10.7	1.7	0.0	
777	004435.49+405911.9	11.147901	40.986641	26.92	0.6	6.2	1	ACIS-I		19	3.43E+06	8.1	2.5	2.9	
778	004435.71+410706.5	11.148813	41.118499	22.81	1.2	8.8	1	ACIS-I		19	3.36E+06	15.1	2.0	2.6	
779	004437.07+411951.3	11.154499	41.330942	21.50	1.0	5.4	2	Both	B1	13	2.67E+06	8.1	1.5	3.9	AGN
780	004437.84+405713.9	11.157674	40.953877	28.53	0.6	7.3	1	ACIS-I		19	3.59E+06	11.1	3.6	2.2	
781	004438.33+412530.3	11.159720	41.425098	23.36	0.8	4.4	2	Both	B1	13	3.53E+06	4.6	0.9	3.9	
782	004438.47+413412.1	11.160303	41.570041	28.01	1.6	9.1	1	ACIS-I		8	1.39E+06	16.2	1.7	2.5	
783	004440.01+410232.7	11.166727	41.042433	25.66	0.9	7.1	1	ACIS-I		19	3.78E+06	10.1	1.8	1.7	
784	004440.48+410138.9	11.168705	41.027492	26.22	0.9	7.0	1	ACIS-I		19	3.84E+06	9.9	1.9	2.3	AGN
785	004441.54+405913.1	11.173115	40.986977	27.80	0.9	7.3	1	ACIS-I		19	3.64E+06	10.8	2.4	2.1	AGN
786	004446.02+412147.9	11.191775	41.363320	23.54	0.7	4.2	2	Both	B1	13	3.49E+06	6.3	1.5	0.5	
787	004448.15+412247.1	11.200641	41.379767	24.18	0.3	4.5	2	Both	B1	13	3.47E+06	6.3	4.7	2.0	
788	004449.27+405949.4	11.205302	40.997062	28.62	0.9	8.6	1	ACIS-I		19	2.25E+06	15.1	3.3	1.7	
789	004451.08+412904.9	11.212866	41.484721	27.08	1.1	7.6	1	ACIS-I		8	1.53E+06	11.4	1.8	0.7	
790	004452.35+412717.0	11.218135	41.454727	26.49	0.3	6.8	2	Both	B1	13	3.28E+06	10.2	10.0	1.8	
791	004457.39+412247.3	11.239152	41.379811	25.86	0.3	6.0	2	Both	B1	13	3.15E+06	9.1	9.8	2.2	
792	004457.96+412342.5	11.241513	41.395165	26.21	0.6	6.2	2	Both	B1	13	3.13E+06	9.4	3.8	1.7	
793	004458.51+412120.1	11.243808	41.355610	25.73	1.2	6.4	2	Both	B1	13	3.04E+06	4.6	0.9	5.2	
794	004500.17+412100.1	11.250713	41.350048	25.97	1.0	6.6	2	Both	B1	13	2.78E+06	10.9	2.5	1.5	
795	004500.94+412652.4	11.253953	41.447916	27.80	1.0	7.7	2	Both	B1	13	2.93E+06	13.2	2.7	3.2	

Column 2: source ID, which contains the source coordinates (J2000.0). Column 5: distance in arcminutes of the source from the centre of M31 (J004244.33+411607.50). Column 6: positional uncertainty $\sqrt{\sigma_x^2 + \sigma_y^2}$, where the single-axis position errors σ_x and σ_y are estimated from the standard deviations of the PSF in the extraction region and the number of counts extracted. Column 7: average off-axis angle for merged observations. Column 8: number of observations extracted. Column 9: source detected in ACIS-I, ACIS-S, or Both. Column 10: for a source detected in ACIS-S or Both, indicates which region from Figure 1 it belongs to. Columns 11 & 12: total values for merged observations. Column 13: average radius of the source extraction region (1 sky pixel = 0.492″). Column 14: photometric significance (net counts / upper error on net counts) (0.3 − 8.0 keV). Column 15: background-corrected median photon energy (0.3 − 8.0 keV). Column 16: cross-match results from Section 3.4: active galactic nuclei (AGN) or low-mass X-ray binary (LMXB).

Appendix B

Complete Additional M31 Source Properties

Table B.1: Additional M31 Source Properties

Source No. (1)	*pns* (0.5 − 8.0 keV) (2)	*pns* (0.5 − 2.0 keV) (3)	*pns* (2.0 − 8.0 keV) (4)	*net_cts* (0.5 − 8.0 keV) (5)	*net_cts* (0.5 − 2.0 keV) (6)	*net_cts* (2.0 − 8.0 keV) (7)	*luminosity* (0.5 − 8.0 keV) (8)	*luminosity* (0.5 − 2.0 keV) (9)	*luminosity* (2.0 − 8.0 keV) (10)
1	0.00E+00	1.40E-45	1.37E-23	$55.65^{+8.60}_{-7.53}$	$33.52^{+6.90}_{-5.80}$	$22.13^{+5.87}_{-4.76}$	2.22E+36	2.86E+35	6.36E+35
2	7.48E-12	6.96E-09	6.96E-05	$13.01^{+4.84}_{-3.69}$	$7.65^{+3.96}_{-2.76}$	$5.35^{+3.60}_{-2.38}$	3.87E+35	4.56E+34	1.19E+35
3	2.17E-09	1.18E-08	5.55E-03	$10.96^{+4.57}_{-3.41}$	$7.63^{+3.96}_{-2.76}$	$3.33^{+3.18}_{-1.91}$	2.45E+35	3.43E+34	5.55E+34
4	4.98E-14	1.50E-10	1.19E-05	$13.32^{+4.84}_{-3.69}$	$7.79^{+3.96}_{-2.76}$	$5.53^{+3.60}_{-2.38}$	3.93E+35	4.57E+34	1.22E+35
5	2.19E-09	1.08E-06	2.45E-04	$11.71^{+4.71}_{-3.56}$	$6.53^{+3.78}_{-2.58}$	$5.18^{+3.60}_{-2.38}$	3.50E+35	3.85E+34	1.17E+35
6	1.04E-13	2.88E-08	5.85E-07	$11.56^{+4.57}_{-3.41}$	$5.84^{+3.60}_{-2.37}$	$5.72^{+3.60}_{-2.37}$	3.36E+35	3.36E+34	1.25E+35
7	0.00E+00	2.01E-41	0.00E+00	$117.40^{+12.23}_{-11.18}$	$50.47^{+8.34}_{-7.26}$	$66.93^{+9.55}_{-8.48}$	3.68E+36	3.12E+35	1.58E+36
8	1.88E-39	1.19E-12	2.21E-28	$40.21^{+7.54}_{-6.45}$	$12.37^{+4.71}_{-3.56}$	$27.84^{+6.46}_{-5.35}$	6.21E+35	3.74E+34	3.25E+35
9	0.00E+00	6.44E-38	1.24E-16	$44.71^{+7.84}_{-6.76}$	$28.51^{+6.45}_{-5.35}$	$16.20^{+5.21}_{-4.08}$	1.22E+36	1.52E+35	3.34E+35
10	3.91E-18	8.90E-20	5.38E-03	$21.35^{+5.88}_{-4.76}$	$17.42^{+5.33}_{-4.20}$	$3.93^{+3.40}_{-2.16}$	7.29E+35	1.14E+35	1.03E+35
11	0.00E+00	0.00E+00	1.46E-01	$47.07^{+7.98}_{-6.90}$	$45.74^{+7.84}_{-6.76}$	$1.34^{+2.66}_{-1.29}$	7.16E+35	1.37E+35	1.54E+34
12	4.27E-19	7.05E-14	8.71E-08	$20.70^{+5.77}_{-4.65}$	$11.62^{+4.57}_{-3.41}$	$9.08^{+4.28}_{-3.11}$	3.16E+35	3.48E+34	1.04E+35
13	0.00E+00	0.00E+00	8.75E-02	$65.45^{+9.23}_{-8.16}$	$63.47^{+9.05}_{-7.98}$	$1.98^{+2.94}_{-1.63}$	1.00E+36	1.91E+35	2.29E+34
14	2.34E-05	3.22E-01	9.69E-06	$10.57^{+4.85}_{-3.70}$	$0.87^{+2.67}_{-1.30}$	$9.71^{+4.58}_{-3.42}$	2.50E+35	4.02E+33	1.74E+35
15	3.27E-13	4.93E-02	3.71E-13	$14.04^{+4.97}_{-3.83}$	$1.66^{+2.66}_{-1.29}$	$12.39^{+4.71}_{-3.56}$	2.19E+35	5.07E+33	1.46E+35
16	0.00E+00	0.00E+00	7.16E-08	$41.32^{+7.54}_{-6.45}$	$33.81^{+6.90}_{-5.80}$	$7.51^{+3.96}_{-2.76}$	1.37E+36	2.12E+35	1.93E+35
17	3.61E-11	1.49E-10	1.39E-03	$20.70^{+6.09}_{-4.98}$	$13.67^{+4.97}_{-3.83}$	$7.03^{+4.29}_{-3.12}$	3.98E+35	5.17E+34	1.02E+35
18	4.81E-05	3.54E-07	3.81E-01	$9.74^{+4.71}_{-3.56}$	$8.94^{+4.28}_{-3.11}$	$0.80^{+2.94}_{-1.64}$	1.69E+35	3.02E+34	1.05E+34
19	1.70E-22	3.89E-20	1.46E-05	$17.55^{+5.33}_{-4.20}$	$12.84^{+4.71}_{-3.55}$	$4.71^{+3.40}_{-2.15}$	5.99E+35	8.26E+34	1.24E+35
20	7.78E-25	3.53E-25	2.81E-04	$25.67^{+6.27}_{-5.16}$	$20.51^{+5.66}_{-4.54}$	$5.17^{+3.60}_{-2.38}$	3.95E+35	6.18E+34	6.01E+34
21	0.00E+00	0.00E+00	0.00E+00	$115.40^{+11.81}_{-10.75}$	$44.80^{+7.76}_{-6.68}$	$70.61^{+9.47}_{-8.40}$	1.82E+36	1.39E+35	8.41E+35
22	5.81E-04	1.84E-01	1.22E-03	$4.35^{+3.40}_{-2.15}$	$0.80^{+2.32}_{-0.83}$	$3.56^{+3.18}_{-1.91}$	9.91E+34	3.49E+33	6.18E+34
23	0.00E+00	0.00E+00	0.00E+00	$337.54^{+19.43}_{-18.40}$	$280.38^{+17.79}_{-16.75}$	$57.16^{+8.67}_{-7.59}$	5.19E+36	8.47E+35	6.64E+35
24	0.00E+00	0.00E+00	7.20E-01	$65.88^{+9.42}_{-8.35}$	$66.41^{+9.30}_{-8.23}$	$-0.53^{+2.68}_{-1.32}$	2.28E+36	4.40E+35	-9.99E+00
25	3.04E-04	4.25E-07	7.61E-01	$6.98^{+4.13}_{-2.94}$	$7.40^{+3.96}_{-2.76}$	$-0.43^{+2.33}_{-0.84}$	1.09E+35	2.29E+34	-9.99E+00
26	0.00E+00	0.00E+00	1.38E-10	$54.43^{+8.53}_{-7.46}$	$42.42^{+7.61}_{-6.53}$	$12.01^{+4.71}_{-3.56}$	8.54E+35	1.31E+35	1.42E+35
27	2.71E-06	1.50E-08	3.32E-01	$9.29^{+4.43}_{-3.26}$	$8.46^{+4.12}_{-2.94}$	$0.83^{+2.66}_{-1.29}$	1.45E+35	2.61E+34	9.72E+33
28	0.00E+00	9.21E-40	0.00E+00	$71.72^{+9.59}_{-8.52}$	$27.66^{+6.36}_{-5.26}$	$44.06^{+7.76}_{-6.68}$	1.15E+36	8.82E+34	5.29E+35
29	9.29E-11	2.53E-10	2.11E-03	$19.18^{+5.88}_{-4.77}$	$12.82^{+4.85}_{-3.70}$	$6.36^{+4.13}_{-2.95}$	3.07E+35	4.05E+34	7.65E+34
30	5.83E-23	2.88E-22	1.37E-04	$20.27^{+5.66}_{-4.54}$	$15.73^{+5.09}_{-3.95}$	$4.54^{+3.40}_{-2.15}$	6.74E+35	9.87E+34	1.16E+35
31	4.34E-30	3.31E-24	7.06E-10	$38.81^{+7.54}_{-6.46}$	$24.02^{+6.08}_{-4.97}$	$14.79^{+5.22}_{-4.08}$	6.25E+35	7.64E+34	1.79E+35
32	0.00E+00	0.00E+00	5.04E-20	$87.21^{+10.58}_{-9.53}$	$59.85^{+8.86}_{-7.79}$	$27.35^{+6.55}_{-5.45}$	1.39E+36	1.89E+35	3.28E+35
33	4.51E-10	3.93E-12	1.04E-01	$20.75^{+6.19}_{-5.08}$	$17.86^{+5.57}_{-4.44}$	$2.89^{+3.62}_{-2.40}$	6.41E+35	1.11E+35	6.66E+34
34	2.83E-16	2.45E-18	2.61E-02	$12.66^{+4.71}_{-3.55}$	$10.90^{+4.43}_{-3.26}$	$1.76^{+2.66}_{-1.29}$	1.83E+36	3.14E+35	1.90E+35
35	4.29E-08	6.33E-09	3.79E-02	$13.32^{+5.10}_{-3.96}$	$10.11^{+4.43}_{-3.26}$	$3.20^{+3.40}_{-2.16}$	4.51E+35	6.52E+34	8.33E+34
36	2.41E-28	2.84E-21	1.68E-11	$46.88^{+8.35}_{-7.27}$	$24.67^{+6.18}_{-5.07}$	$22.21^{+6.29}_{-5.18}$	1.22E+36	1.29E+35	4.33E+35
37	4.62E-30	9.37E-28	6.71E-08	$33.07^{+6.98}_{-5.89}$	$22.49^{+5.87}_{-4.76}$	$10.58^{+4.57}_{-3.41}$	5.37E+35	7.37E+34	1.28E+35
38	3.38E-14	2.71E-15	5.82E-03	$19.72^{+5.77}_{-4.66}$	$15.26^{+5.09}_{-3.96}$	$4.46^{+3.60}_{-2.38}$	3.15E+35	4.91E+34	5.29E+34
39	0.00E+00	0.00E+00	1.09E-11	$51.26^{+8.33}_{-7.26}$	$37.46^{+7.23}_{-6.14}$	$13.80^{+4.97}_{-3.83}$	1.73E+36	2.40E+35	3.58E+35

Source No.	*pns* (0.5 − 8.0 keV)	*pns* (0.5 − 2.0 keV)	*pns* (2.0 − 8.0 keV)	*net_cts* (0.5 − 8.0 keV)	*net_cts* (0.5 − 2.0 keV)	*net_cts* (2.0 − 8.0 keV)	*luminosity* (0.5 − 8.0 keV)	*luminosity* (0.5 − 2.0 keV)	*luminosity* (2.0 − 8.0 keV)
40	7.94E-36	3.35E-33	5.23E-08	$58.98^{+9.19}_{-8.12}$	$42.41^{+7.78}_{-6.69}$	$16.56^{+5.69}_{-4.57}$	1.15E+36	1.68E+35	2.39E+35
41	4.50E-43	0.00E+00	4.59E-04	$43.18^{+7.77}_{-6.68}$	$37.46^{+7.23}_{-6.14}$	$5.72^{+3.79}_{-2.58}$	1.47E+36	2.44E+35	1.49E+35
42	3.51E-09	5.17E-11	5.49E-02	$15.20^{+5.34}_{-4.21}$	$12.18^{+4.71}_{-3.56}$	$3.03^{+3.41}_{-2.17}$	1.64E+36	2.54E+35	2.49E+35
43	1.16E-06	6.40E-08	1.36E-01	$10.15^{+4.58}_{-3.42}$	$8.39^{+4.12}_{-2.94}$	$1.76^{+2.94}_{-1.64}$	1.08E+36	1.77E+35	1.41E+35
44	0.00E+00	0.00E+00	4.69E-21	$69.43^{+9.47}_{-8.41}$	$48.44^{+8.05}_{-6.97}$	$20.99^{+5.77}_{-4.65}$	3.38E+36	4.46E+35	7.87E+35
45	5.42E-04	1.68E-06	7.71E-01	$6.82^{+4.13}_{-2.94}$	$7.29^{+3.96}_{-2.77}$	$-0.47^{+2.33}_{-0.84}$	2.30E+35	4.73E+34	-9.99E+00
46	5.07E-18	8.79E-20	5.84E-03	$21.33^{+5.88}_{-4.76}$	$17.42^{+5.33}_{-4.20}$	$3.91^{+3.40}_{-2.16}$	8.09E+35	1.27E+35	1.13E+35
47	0.00E+00	0.00E+00	0.00E+00	$130.48^{+12.52}_{-11.47}$	$90.44^{+10.58}_{-9.52}$	$40.04^{+7.46}_{-6.38}$	4.32E+36	5.69E+35	1.02E+36
48	1.08E-06	2.49E-08	2.58E-01	$9.45^{+4.43}_{-3.26}$	$8.42^{+4.12}_{-2.94}$	$1.03^{+2.66}_{-1.29}$	3.13E+35	5.36E+34	2.60E+34
49	6.19E-25	2.27E-17	4.67E-10	$25.67^{+6.27}_{-5.16}$	$14.56^{+4.97}_{-3.83}$	$11.11^{+4.57}_{-3.41}$	8.38E+35	9.05E+34	2.79E+35
50	0.00E+00	0.00E+00	9.30E-23	$271.52^{+17.55}_{-16.51}$	$251.19^{+16.90}_{-15.86}$	$20.34^{+5.66}_{-4.54}$	5.31E+37	9.95E+36	2.96E+36
51	6.01E-11	5.25E-04	8.90E-09	$14.39^{+5.10}_{-3.96}$	$5.07^{+3.60}_{-2.38}$	$9.32^{+4.28}_{-3.11}$	1.60E+36	1.11E+35	7.78E+35
52	9.70E-09	6.55E-12	4.09E-01	$9.26^{+4.28}_{-3.10}$	$8.78^{+4.12}_{-2.94}$	$0.48^{+2.32}_{-0.83}$	3.01E+35	5.40E+34	1.20E+34
53	3.23E-07	2.67E-09	3.42E-01	$7.40^{+3.96}_{-2.76}$	$6.81^{+3.78}_{-2.58}$	$0.59^{+2.32}_{-0.83}$	2.40E+35	4.18E+34	1.47E+34
54	1.24E-38	4.38E-20	3.82E-20	$45.52^{+7.99}_{-6.91}$	$21.94^{+5.88}_{-4.76}$	$23.58^{+6.08}_{-4.97}$	5.10E+36	4.82E+35	2.00E+36
55	1.62E-22	2.44E-14	6.25E-10	$19.35^{+5.56}_{-4.43}$	$10.74^{+4.43}_{-3.26}$	$8.62^{+4.12}_{-2.94}$	6.35E+35	6.62E+34	2.18E+35
56	4.62E-44	0.00E+00	1.00E+00	$30.55^{+6.63}_{-5.53}$	$30.85^{+6.63}_{-5.53}$	$-0.30^{+1.87}_{-99.99}$	9.93E+35	1.88E+35	-9.99E+00
57	2.27E-23	1.43E-20	1.09E-06	$24.63^{+6.17}_{-5.06}$	$16.57^{+5.21}_{-4.08}$	$8.05^{+4.12}_{-2.94}$	8.02E+35	1.03E+35	2.01E+35
58	8.65E-08	4.55E-10	3.75E-01	$8.29^{+4.12}_{-2.94}$	$7.76^{+3.96}_{-2.76}$	$0.53^{+2.32}_{-0.83}$	2.70E+35	4.78E+34	1.34E+34
59	0.00E+00	0.00E+00	1.59E-20	$90.28^{+10.58}_{-9.52}$	$73.74^{+9.65}_{-8.58}$	$16.54^{+5.21}_{-4.08}$	2.91E+36	4.49E+35	4.12E+35
60	1.99E-09	1.44E-07	9.81E-04	$9.38^{+4.28}_{-3.10}$	$5.79^{+3.60}_{-2.37}$	$3.58^{+3.18}_{-1.91}$	3.16E+35	3.67E+34	9.33E+34
61	1.42E-10	1.35E-11	4.24E-02	$9.53^{+4.28}_{-3.10}$	$7.85^{+3.96}_{-2.76}$	$1.68^{+2.66}_{-1.29}$	3.07E+35	4.78E+34	4.18E+34
62	8.79E-26	5.80E-24	2.44E-05	$26.64^{+6.36}_{-5.26}$	$20.42^{+5.66}_{-4.54}$	$6.22^{+3.79}_{-2.58}$	8.74E+35	1.27E+35	1.57E+35
63	4.50E-07	2.69E-05	2.34E-03	$12.25^{+4.98}_{-3.83}$	$6.94^{+3.96}_{-2.77}$	$5.30^{+3.79}_{-2.58}$	4.08E+35	4.44E+34	1.35E+35
64	0.00E+00	4.13E-38	3.49E-15	$62.93^{+9.24}_{-8.17}$	$41.28^{+7.62}_{-6.53}$	$21.65^{+5.98}_{-4.87}$	2.14E+36	2.75E+35	5.58E+35
65	0.00E+00	0.00E+00	7.44E-06	$77.98^{+9.99}_{-8.93}$	$70.18^{+9.47}_{-8.40}$	$7.80^{+4.13}_{-2.94}$	2.59E+36	4.47E+35	1.98E+35
66	1.06E-06	4.64E-08	2.04E-01	$11.42^{+4.85}_{-3.70}$	$9.95^{+4.43}_{-3.26}$	$1.47^{+2.94}_{-1.64}$	3.84E+35	6.44E+34	3.79E+34
67	5.95E-08	1.35E-08	6.32E-02	$10.62^{+4.57}_{-3.41}$	$8.50^{+4.12}_{-2.94}$	$2.13^{+2.94}_{-1.63}$	1.21E+36	1.85E+35	1.85E+35
68	0.00E+00	5.48E-42	2.41E-20	$54.84^{+8.54}_{-7.46}$	$33.70^{+6.90}_{-5.80}$	$21.13^{+5.77}_{-4.65}$	1.14E+37	1.72E+36	2.99E+36
69	1.52E-37	1.99E-32	1.34E-09	$53.25^{+8.62}_{-7.54}$	$36.85^{+7.23}_{-6.14}$	$16.40^{+5.47}_{-4.34}$	5.86E+36	9.92E+35	1.23E+36
70	1.00E-06	4.30E-04	3.67E-04	$24.28^{+7.49}_{-6.40}$	$10.14^{+5.02}_{-3.88}$	$14.15^{+6.17}_{-5.06}$	6.62E+35	5.44E+34	2.91E+35
71	2.90E-02	4.30E-03	3.75E-01	$8.59^{+6.00}_{-4.89}$	$7.10^{+4.48}_{-3.31}$	$1.49^{+4.69}_{-3.54}$	2.24E+35	3.69E+34	2.90E+34
72	3.24E-05	9.64E-05	1.66E-02	$17.28^{+6.52}_{-5.42}$	$9.72^{+4.74}_{-3.58}$	$7.56^{+5.15}_{-4.02}$	4.46E+35	5.12E+34	1.45E+35
73	2.54E-42	0.00E+00	1.97E-01	$31.70^{+6.72}_{-5.62}$	$30.90^{+6.64}_{-5.53}$	$0.80^{+2.32}_{-0.83}$	1.29E+37	3.00E+36	2.26E+35
74	8.98E-07	4.82E-08	2.31E-01	$12.24^{+4.99}_{-3.84}$	$10.84^{+4.58}_{-3.42}$	$1.40^{+2.95}_{-1.65}$	1.30E+36	2.78E+35	1.02E+35
75	6.28E-10	2.48E-07	6.82E-04	$13.58^{+4.98}_{-3.83}$	$9.15^{+4.29}_{-3.11}$	$4.43^{+3.40}_{-2.16}$	3.00E+36	4.96E+35	6.69E+35
76	5.61E-15	7.15E-18	1.72E-02	$38.89^{+8.26}_{-7.18}$	$31.58^{+7.09}_{-6.00}$	$7.30^{+5.04}_{-3.90}$	9.16E+35	1.51E+35	1.28E+35
77	1.57E-32	3.35E-23	3.17E-12	$51.03^{+8.61}_{-7.54}$	$29.78^{+6.73}_{-5.63}$	$21.26^{+6.09}_{-4.98}$	1.27E+36	1.56E+35	3.88E+35
78	0.00E+00	0.00E+00	0.00E+00	$1798.20^{+43.69}_{-42.67}$	$1229.91^{+36.23}_{-35.21}$	$568.29^{+25.13}_{-24.10}$	3.80E+37	5.33E+36	8.88E+36
79	0.00E+00	0.00E+00	5.73E-18	$49.50^{+8.12}_{-7.05}$	$35.78^{+7.06}_{-5.97}$	$13.72^{+4.84}_{-3.69}$	9.64E+36	1.66E+36	1.84E+36
80	1.80E-03	6.01E-03	8.97E-02	$4.22^{+3.40}_{-2.16}$	$2.69^{+2.94}_{-1.63}$	$1.53^{+2.66}_{-1.29}$	1.12E+36	1.73E+35	2.78E+35
81	5.00E-16	2.09E-18	7.55E-03	$25.98^{+6.55}_{-5.45}$	$20.69^{+5.77}_{-4.65}$	$5.30^{+3.97}_{-2.77}$	6.12E+35	9.91E+34	9.24E+34

Source No.	*pns* (0.5 – 8.0 keV)	*pns* (0.5 – 2.0 keV)	*pns* (2.0 – 8.0 keV)	*net_cts* (0.5 – 8.0 keV)	*net_cts* (0.5 – 2.0 keV)	*net_cts* (2.0 – 8.0 keV)	*luminosity* (0.5 – 8.0 keV)	*luminosity* (0.5 – 2.0 keV)	*luminosity* (2.0 – 8.0 keV)
82	4.66E-17	6.16E-13	5.79E-07	$28.41^{+6.82}_{-5.72}$	$15.66^{+5.22}_{-4.08}$	$12.75^{+5.10}_{-3.96}$	6.49E+35	7.30E+34	2.16E+35
83	0.00E+00	0.00E+00	2.98E-37	$113.59^{+11.90}_{-10.85}$	$68.47^{+9.41}_{-8.35}$	$45.12^{+7.99}_{-6.91}$	2.66E+36	3.35E+35	7.75E+35
84	0.00E+00	0.00E+00	0.00E+00	$342.94^{+20.06}_{-19.02}$	$239.12^{+16.73}_{-15.69}$	$103.82^{+11.80}_{-10.74}$	8.73E+36	1.28E+36	1.93E+36
85	7.66E-03	8.01E-01	7.60E-04	$6.10^{+4.29}_{-3.11}$	$-0.61^{+2.33}_{-0.84}$	$6.71^{+4.13}_{-2.95}$	1.45E+35	-9.99E+00	1.16E+35
86	1.32E-14	3.83E-05	5.40E-11	$36.21^{+8.01}_{-6.93}$	$10.96^{+4.99}_{-3.84}$	$25.26^{+6.83}_{-5.74}$	5.60E+35	3.41E+34	2.91E+35
87	4.92E-04	1.14E-04	1.88E-01	$6.83^{+4.13}_{-2.94}$	$5.31^{+3.60}_{-2.38}$	$1.53^{+2.94}_{-1.63}$	1.61E+35	2.53E+34	2.68E+34
88	1.66E-03	2.74E-03	9.56E-02	$6.41^{+4.13}_{-2.95}$	$4.10^{+3.40}_{-2.16}$	$2.31^{+3.18}_{-1.92}$	1.49E+35	1.97E+34	3.93E+34
89	3.11E-10	9.14E-03	3.73E-09	$16.85^{+5.56}_{-4.43}$	$3.78^{+3.40}_{-2.16}$	$13.07^{+4.97}_{-3.83}$	3.59E+35	1.66E+34	2.05E+35
90	2.56E-10	7.40E-13	7.18E-02	$31.25^{+7.88}_{-6.80}$	$26.07^{+6.75}_{-5.65}$	$5.18^{+4.89}_{-3.75}$	4.33E+35	7.28E+34	5.33E+34
91	6.12E-02	4.67E-03	7.62E-01	$2.94^{+3.40}_{-2.16}$	$3.37^{+3.18}_{-1.91}$	$-0.43^{+2.33}_{-0.84}$	6.55E+34	1.53E+34	-9.99E+00
92	3.77E-09	1.12E-07	1.25E-03	$28.69^{+7.68}_{-6.59}$	$17.47^{+5.91}_{-4.79}$	$11.22^{+5.61}_{-4.49}$	3.92E+35	4.85E+34	1.14E+35
93	2.61E-15	5.31E-20	3.92E-01	$36.33^{+7.94}_{-6.86}$	$35.34^{+7.48}_{-6.39}$	$0.99^{+3.63}_{-2.42}$	4.87E+35	9.53E+34	9.90E+33
94	3.08E-03	2.18E-01	6.23E-03	$4.05^{+3.40}_{-2.16}$	$0.76^{+2.32}_{-0.83}$	$3.30^{+3.18}_{-1.91}$	1.15E+35	4.37E+33	6.93E+34
95	8.69E-04	3.29E-02	7.41E-03	$11.24^{+5.57}_{-4.45}$	$4.39^{+3.97}_{-2.77}$	$6.85^{+4.58}_{-3.42}$	1.53E+35	1.20E+34	6.97E+34
96	0.00E+00	0.00E+00	6.76E-20	$99.25^{+11.25}_{-10.19}$	$72.94^{+9.77}_{-8.71}$	$26.31^{+6.38}_{-5.27}$	7.33E+36	1.01E+36	1.51E+36
97	0.00E+00	0.00E+00	2.01E-30	$96.48^{+10.99}_{-9.93}$	$70.23^{+9.53}_{-8.46}$	$26.25^{+6.27}_{-5.16}$	6.55E+36	8.92E+35	1.38E+36
98	9.00E-04	7.86E-02	4.22E-03	$5.53^{+3.79}_{-2.58}$	$1.55^{+2.66}_{-1.29}$	$3.98^{+3.40}_{-2.16}$	1.28E+35	7.43E+33	6.77E+34
99	2.61E-08	7.20E-11	5.02E-01	$14.76^{+5.34}_{-4.21}$	$14.43^{+5.10}_{-3.96}$	$0.33^{+2.67}_{-1.30}$	5.67E+35	1.13E+35	9.44E+33
100	5.36E-04	5.32E-05	4.49E-01	$5.04^{+3.60}_{-2.38}$	$4.63^{+3.40}_{-2.15}$	$0.41^{+2.32}_{-0.83}$	1.10E+35	2.08E+34	6.58E+33
101	9.17E-22	5.27E-21	6.30E-05	$34.28^{+7.31}_{-6.22}$	$25.15^{+6.27}_{-5.16}$	$9.14^{+4.58}_{-3.42}$	4.51E+35	6.65E+34	8.96E+34
102	4.78E-23	5.19E-23	1.18E-04	$30.16^{+6.81}_{-5.72}$	$22.92^{+5.98}_{-4.86}$	$7.23^{+4.13}_{-2.94}$	8.07E+35	1.24E+35	1.44E+35
103	3.75E-04	2.73E-02	4.79E-03	$6.42^{+3.97}_{-2.77}$	$2.41^{+2.94}_{-1.63}$	$4.01^{+3.40}_{-2.16}$	8.78E+35	8.05E+34	3.75E+35
104	7.55E-08	4.95E-07	6.88E-03	$20.33^{+6.47}_{-5.37}$	$13.40^{+5.22}_{-4.09}$	$6.93^{+4.58}_{-3.43}$	2.71E+35	3.62E+34	6.86E+34
105	0.00E+00	0.00E+00	0.00E+00	$253.00^{+17.06}_{-16.02}$	$178.28^{+14.45}_{-13.40}$	$74.72^{+9.82}_{-8.76}$	7.05E+36	9.93E+35	1.56E+36
106	1.11E-24	5.37E-26	1.62E-03	$35.17^{+7.31}_{-6.22}$	$29.24^{+6.64}_{-5.54}$	$5.94^{+3.96}_{-2.77}$	9.88E+35	1.65E+35	1.24E+35
107	6.55E-04	2.63E-01	4.43E-04	$6.76^{+4.13}_{-2.95}$	$1.02^{+2.66}_{-1.30}$	$5.74^{+3.79}_{-2.58}$	1.24E+35	3.82E+33	7.82E+34
108	0.00E+00	0.00E+00	0.00E+00	$200.16^{+15.34}_{-14.31}$	$126.18^{+12.35}_{-11.30}$	$73.98^{+9.82}_{-8.75}$	2.64E+36	3.36E+35	7.27E+35
109	9.26E-19	3.22E-16	1.13E-05	$23.04^{+6.08}_{-4.97}$	$15.32^{+5.09}_{-3.95}$	$7.71^{+4.12}_{-2.94}$	5.26E+35	7.48E+34	1.27E+35
110	0.00E+00	0.00E+00	4.06E-03	$140.40^{+13.08}_{-12.03}$	$134.82^{+12.74}_{-11.69}$	$5.58^{+3.97}_{-2.77}$	6.94E+36	1.37E+36	2.04E+35
111	1.98E-41	2.48E-38	2.30E-09	$31.35^{+6.72}_{-5.62}$	$22.81^{+5.87}_{-4.76}$	$8.54^{+4.12}_{-2.94}$	7.13E+35	1.06E+35	1.44E+35
112	7.75E-03	2.81E-02	9.20E-02	$3.24^{+3.18}_{-1.91}$	$1.74^{+2.66}_{-1.29}$	$1.50^{+2.66}_{-1.29}$	8.01E+34	8.68E+33	2.75E+34
113	0.00E+00	0.00E+00	9.76E-15	$133.63^{+12.71}_{-11.66}$	$111.95^{+11.67}_{-10.62}$	$21.68^{+5.90}_{-4.77}$	3.68E+37	8.39E+36	3.92E+36
114	6.25E-04	8.76E-05	3.05E-01	$7.75^{+4.43}_{-3.27}$	$6.67^{+3.96}_{-2.77}$	$1.08^{+2.94}_{-1.63}$	1.85E+35	3.23E+34	1.91E+34
115	4.45E-05	2.37E-03	3.23E-03	$20.55^{+7.36}_{-6.28}$	$8.72^{+4.91}_{-3.76}$	$11.83^{+6.10}_{-4.99}$	8.24E+35	9.16E+34	3.16E+35
116	1.06E-03	5.40E-01	1.39E-04	$5.49^{+3.79}_{-2.58}$	$0.23^{+2.33}_{-0.83}$	$5.26^{+3.60}_{-2.38}$	1.13E+35	9.89E+32	7.92E+34
117	7.14E-03	7.39E-01	6.95E-04	$9.36^{+5.52}_{-4.39}$	$-0.85^{+2.99}_{-1.71}$	$10.20^{+5.14}_{-4.01}$	1.17E+35	-9.99E+00	9.36E+34
118	1.55E-07	7.95E-15	1.00E+00	$13.57^{+5.21}_{-4.08}$	$15.89^{+5.21}_{-4.08}$	$-2.32^{+1.87}_{-99.99}$	1.79E+35	4.28E+34	-9.99E+00
119	3.45E-08	7.73E-08	8.23E-03	$15.86^{+5.56}_{-4.44}$	$10.60^{+4.57}_{-3.42}$	$5.26^{+3.97}_{-2.77}$	3.87E+35	5.25E+34	9.55E+34
120	8.59E-03	4.04E-03	5.54E-01	$7.45^{+4.86}_{-3.72}$	$7.30^{+4.59}_{-3.43}$	$0.16^{+2.67}_{-1.31}$	2.82E+35	5.17E+34	4.59E+33
121	0.00E+00	0.00E+00	0.00E+00	$138.49^{+12.87}_{-11.82}$	$99.03^{+11.04}_{-9.98}$	$39.46^{+7.38}_{-6.30}$	4.22E+36	5.80E+35	9.20E+35
122	0.00E+00	0.00E+00	2.06E-17	$128.48^{+13.31}_{-12.26}$	$84.15^{+10.67}_{-9.60}$	$44.33^{+8.67}_{-7.60}$	4.31E+36	7.52E+35	9.85E+35
123	1.74E-16	4.34E-10	1.37E-08	$45.59^{+8.94}_{-7.86}$	$20.51^{+6.11}_{-5.00}$	$25.09^{+7.14}_{-6.04}$	2.28E+36	2.70E+35	8.36E+35

Source No.	*pns* (0.5 − 8.0 keV)	*pns* (0.5 − 2.0 keV)	*pns* (2.0 − 8.0 keV)	*net_cts* (0.5 − 8.0 keV)	*net_cts* (0.5 − 2.0 keV)	*net_cts* (2.0 − 8.0 keV)	*luminosity* (0.5 − 8.0 keV)	*luminosity* (0.5 − 2.0 keV)	*luminosity* (2.0 − 8.0 keV)
124	5.01E-15	1.79E-11	9.67E-07	$65.44^{+11.66}_{-10.60}$	$32.52^{+7.79}_{-6.70}$	$32.92^{+9.26}_{-8.19}$	2.57E+36	3.22E+35	8.72E+35
125	0.00E+00	0.00E+00	0.00E+00	$302.89^{+18.99}_{-17.95}$	$196.09^{+15.26}_{-14.22}$	$106.80^{+12.00}_{-10.94}$	8.28E+36	1.36E+36	1.97E+36
126	4.66E-07	1.24E-09	1.23E-01	$30.27^{+8.60}_{-7.53}$	$24.72^{+6.87}_{-5.77}$	$5.55^{+5.91}_{-4.80}$	6.38E+35	1.36E+35	7.81E+34
127	0.00E+00	9.81E-44	2.10E-29	$46.43^{+7.91}_{-6.83}$	$25.79^{+6.17}_{-5.06}$	$20.64^{+5.66}_{-4.54}$	1.14E+36	1.28E+35	3.76E+35
128	3.79E-13	4.71E-08	1.19E-06	$9.74^{+4.28}_{-3.10}$	$4.91^{+3.40}_{-2.15}$	$4.83^{+3.40}_{-2.15}$	4.32E+35	4.38E+34	1.60E+35
129	7.94E-07	9.80E-07	2.93E-02	$11.75^{+4.86}_{-3.71}$	$8.31^{+4.13}_{-2.95}$	$3.44^{+3.42}_{-2.18}$	2.51E+36	4.32E+35	5.03E+35
130	8.81E-03	1.99E-01	1.48E-02	$4.33^{+3.61}_{-2.38}$	$1.21^{+2.66}_{-1.30}$	$3.12^{+3.18}_{-1.91}$	1.48E+35	8.80E+33	7.75E+34
131	3.84E-09	3.34E-05	2.52E-05	$12.50^{+4.85}_{-3.70}$	$5.53^{+3.60}_{-2.38}$	$6.97^{+3.96}_{-2.77}$	9.62E+35	1.02E+35	3.70E+35
132	2.36E-18	5.22E-09	8.06E-11	$21.31^{+5.87}_{-4.76}$	$9.30^{+4.28}_{-3.10}$	$12.01^{+4.71}_{-3.56}$	4.93E+35	4.36E+34	2.06E+35
133	3.64E-21	3.65E-19	6.67E-06	$31.83^{+7.07}_{-5.97}$	$21.52^{+5.87}_{-4.76}$	$10.31^{+4.71}_{-3.56}$	3.90E+35	5.44E+34	9.30E+34
134	2.80E-04	1.43E-02	5.48E-03	$8.07^{+4.43}_{-3.27}$	$3.11^{+3.18}_{-1.91}$	$4.96^{+3.79}_{-2.58}$	9.76E+34	7.67E+33	4.45E+34
135	0.00E+00	0.00E+00	0.00E+00	$619.12^{+25.96}_{-24.93}$	$509.95^{+23.62}_{-22.60}$	$109.17^{+11.57}_{-10.52}$	7.98E+36	1.35E+36	1.04E+36
136	7.60E-11	7.08E-02	1.04E-10	$17.77^{+5.67}_{-4.55}$	$2.07^{+2.94}_{-1.63}$	$15.70^{+5.33}_{-4.20}$	2.13E+35	5.07E+33	1.39E+35
137	6.24E-11	3.29E-06	1.19E-06	$52.81^{+11.01}_{-9.95}$	$19.85^{+6.67}_{-5.56}$	$32.96^{+9.30}_{-8.23}$	2.84E+36	2.72E+35	1.19E+36
138	6.12E-04	6.82E-04	7.05E-02	$11.54^{+5.57}_{-4.45}$	$7.28^{+4.29}_{-3.11}$	$4.26^{+4.30}_{-3.12}$	2.55E+35	3.90E+34	6.45E+34
139	0.00E+00	0.00E+00	0.00E+00	$405.35^{+21.19}_{-20.17}$	$240.39^{+16.55}_{-15.51}$	$164.96^{+13.91}_{-12.87}$	2.38E+37	2.96E+36	7.07E+36
140	2.28E-09	4.16E-06	8.69E-05	$12.42^{+4.84}_{-3.69}$	$6.40^{+3.78}_{-2.58}$	$6.02^{+3.78}_{-2.58}$	2.87E+35	2.98E+34	1.03E+35
141	1.62E-01	8.86E-03	1.00E+00	$1.64^{+2.94}_{-1.63}$	$2.62^{+2.94}_{-1.63}$	$-0.98^{+1.87}_{-99.99}$	1.12E+35	4.27E+34	-9.99E+00
142	5.71E-04	2.04E-02	8.73E-03	$6.22^{+3.96}_{-2.77}$	$2.44^{+2.94}_{-1.63}$	$3.78^{+3.40}_{-2.16}$	1.05E+35	8.53E+33	4.68E+34
143	1.46E-03	4.19E-01	9.05E-04	$5.39^{+3.78}_{-2.58}$	$0.46^{+2.32}_{-0.83}$	$4.93^{+3.60}_{-2.38}$	1.20E+35	2.08E+33	8.15E+34
144	4.39E-03	7.11E-02	2.16E-02	$5.98^{+4.13}_{-2.95}$	$2.07^{+2.94}_{-1.63}$	$3.91^{+3.60}_{-2.38}$	7.38E+34	5.33E+33	3.53E+34
145	1.07E-10	1.28E-03	1.17E-08	$57.95^{+12.00}_{-10.95}$	$15.78^{+7.09}_{-6.00}$	$42.17^{+10.20}_{-9.14}$	4.20E+35	2.93E+34	2.05E+35
146	7.94E-05	3.96E-09	4.73E-01	$32.54^{+10.72}_{-9.66}$	$31.73^{+8.21}_{-7.13}$	$0.81^{+7.27}_{-6.50}$	2.03E+35	5.06E+34	3.41E+33
147	6.47E-05	4.20E-02	4.15E-04	$9.63^{+4.71}_{-3.56}$	$2.74^{+3.18}_{-1.91}$	$6.89^{+4.13}_{-2.94}$	1.16E+35	6.77E+33	6.16E+34
148	1.75E-20	5.69E-21	3.54E-04	$24.21^{+6.17}_{-5.07}$	$18.43^{+5.45}_{-4.32}$	$5.78^{+3.79}_{-2.58}$	4.83E+35	7.64E+34	8.46E+34
149	9.55E-10	8.57E-04	1.96E-07	$51.78^{+11.36}_{-10.31}$	$14.67^{+6.57}_{-5.47}$	$37.11^{+9.78}_{-8.72}$	1.03E+36	7.48E+34	4.99E+35
150	3.63E-10	1.01E-08	8.37E-04	$30.17^{+7.74}_{-6.65}$	$18.72^{+6.00}_{-4.89}$	$11.45^{+5.60}_{-4.47}$	1.04E+36	1.60E+35	2.69E+35
151	0.00E+00	0.00E+00	0.00E+00	$392.36^{+22.05}_{-21.03}$	$222.77^{+16.48}_{-15.44}$	$169.59^{+15.30}_{-14.26}$	2.18E+36	3.15E+35	6.33E+35
152	8.78E-15	7.60E-13	3.01E-05	$68.89^{+12.14}_{-11.08}$	$41.28^{+8.81}_{-7.73}$	$27.61^{+8.99}_{-7.92}$	1.35E+36	2.03E+35	3.66E+35
153	6.35E-25	4.90E-16	2.83E-11	$64.05^{+10.21}_{-9.15}$	$33.00^{+7.42}_{-6.33}$	$31.05^{+7.67}_{-6.58}$	1.83E+36	2.32E+35	6.06E+35
154	5.42E-09	2.76E-14	2.08E-01	$50.02^{+11.45}_{-10.40}$	$44.51^{+9.12}_{-8.05}$	$5.51^{+7.63}_{-6.55}$	2.79E+35	6.38E+34	2.07E+34
155	1.66E-15	4.45E-15	4.75E-04	$17.64^{+5.45}_{-4.32}$	$12.58^{+4.71}_{-3.55}$	$5.06^{+3.60}_{-2.38}$	4.94E+35	7.46E+34	1.03E+35
156	0.00E+00	0.00E+00	0.00E+00	$581.21^{+26.25}_{-25.22}$	$327.26^{+19.62}_{-18.59}$	$253.95^{+18.07}_{-17.04}$	3.23E+36	4.66E+35	9.48E+35
157	0.00E+00	0.00E+00	3.37E-14	$178.48^{+17.03}_{-15.98}$	$112.93^{+12.83}_{-11.77}$	$65.55^{+11.85}_{-10.80}$	1.25E+36	2.02E+35	3.08E+35
158	7.18E-13	5.92E-06	2.46E-08	$19.45^{+5.78}_{-4.66}$	$7.21^{+3.96}_{-2.77}$	$12.23^{+4.85}_{-3.70}$	1.30E+36	1.16E+35	5.63E+35
159	0.00E+00	0.00E+00	0.00E+00	$510.80^{+23.69}_{-22.66}$	$424.47^{+21.66}_{-20.63}$	$86.33^{+10.42}_{-9.36}$	1.23E+37	2.07E+36	1.54E+36
160	1.74E-02	5.07E-01	7.95E-03	$14.22^{+8.28}_{-7.21}$	$0.31^{+4.32}_{-3.37}$	$13.90^{+7.43}_{-6.34}$	1.27E+35	7.29E+32	8.30E+34
161	0.00E+00	0.00E+00	2.17E-43	$257.68^{+18.69}_{-17.65}$	$142.64^{+13.78}_{-12.73}$	$115.04^{+13.26}_{-12.21}$	1.30E+36	1.81E+35	3.94E+35
162	0.00E+00	0.00E+00	0.00E+00	$375.11^{+20.44}_{-19.41}$	$248.25^{+16.80}_{-15.77}$	$126.86^{+12.35}_{-11.30}$	8.61E+36	1.16E+36	2.16E+36
163	0.00E+00	5.61E-45	3.53E-15	$55.70^{+8.67}_{-7.59}$	$38.06^{+7.31}_{-6.22}$	$17.64^{+5.45}_{-4.32}$	1.24E+36	1.73E+35	2.91E+35
164	0.00E+00	0.00E+00	1.50E-33	$361.65^{+22.19}_{-21.15}$	$242.29^{+17.54}_{-16.49}$	$119.36^{+14.28}_{-13.23}$	2.61E+36	4.53E+35	5.78E+35
165	0.00E+00	0.00E+00	0.00E+00	$12046.18^{+111.25}_{-110.24}$	$7250.37^{+86.46}_{-85.45}$	$4795.81^{+70.66}_{-69.65}$	6.21E+37	9.38E+36	1.67E+37

Source No.	*pns* (0.5 – 8.0 keV)	*pns* (0.5 – 2.0 keV)	*pns* (2.0 – 8.0 keV)	*net_cts* (0.5 – 8.0 keV)	*net_cts* (0.5 – 2.0 keV)	*net_cts* (2.0 – 8.0 keV)	*luminosity* (0.5 – 8.0 keV)	*luminosity* (0.5 – 2.0 keV)	*luminosity* (2.0 – 8.0 keV)
166	0.00E+00	0.00E+00	0.00E+00	$311.45^{+18.74}_{-17.71}$	$228.93^{+16.19}_{-15.15}$	$82.52^{+10.21}_{-9.15}$	1.54E+37	2.48E+36	2.93E+36
167	0.00E+00	8.93E-29	5.59E-26	$162.46^{+16.03}_{-14.99}$	$76.90^{+11.09}_{-10.03}$	$85.57^{+12.17}_{-11.12}$	8.47E+35	1.02E+35	3.00E+35
168	1.01E-11	9.12E-10	4.18E-04	$10.51^{+4.43}_{-3.26}$	$6.84^{+3.78}_{-2.58}$	$3.67^{+3.18}_{-1.91}$	7.08E+35	1.09E+35	1.71E+35
169	2.62E-30	1.52E-29	2.37E-06	$42.67^{+7.92}_{-6.84}$	$31.45^{+6.81}_{-5.72}$	$11.22^{+4.85}_{-3.70}$	1.04E+36	1.58E+35	2.02E+35
170	6.52E-05	8.15E-08	2.28E-01	$31.31^{+10.29}_{-9.24}$	$26.20^{+7.54}_{-6.46}$	$5.10^{+7.65}_{-6.57}$	4.19E+35	8.99E+34	4.59E+34
171	4.58E-31	7.11E-22	4.92E-11	$125.80^{+14.46}_{-13.33}$	$79.46^{+11.42}_{-10.27}$	$46.34^{+9.62}_{-8.48}$	7.85E+36	1.18E+36	2.00E+36
172	9.59E-04	9.77E-09	8.82E-01	$29.24^{+11.26}_{-10.21}$	$36.64^{+9.14}_{-8.07}$	$-7.40^{+7.30}_{-6.23}$	1.85E+35	5.91E+34	-9.99E+00
173	0.00E+00	0.00E+00	0.00E+00	$3194.75^{+58.06}_{-57.05}$	$2017.26^{+46.21}_{-45.19}$	$1177.49^{+35.83}_{-34.81}$	1.59E+37	2.50E+36	3.97E+36
174	1.09E-13	7.84E-11	1.63E-05	$64.89^{+12.01}_{-10.96}$	$36.73^{+8.62}_{-7.55}$	$28.15^{+9.00}_{-7.93}$	3.39E+35	4.84E+34	9.92E+34
175	0.00E+00	2.98E-28	1.23E-30	$56.95^{+8.73}_{-7.66}$	$26.20^{+6.27}_{-5.16}$	$30.75^{+6.73}_{-5.63}$	3.75E+36	4.12E+35	1.40E+36
176	3.94E-07	5.88E-06	7.80E-03	$7.38^{+3.96}_{-2.76}$	$4.77^{+3.40}_{-2.15}$	$2.61^{+2.94}_{-1.63}$	4.96E+35	7.59E+34	1.21E+35
177	0.00E+00	0.00E+00	0.00E+00	$1109.67^{+34.80}_{-33.79}$	$702.12^{+27.74}_{-26.72}$	$407.55^{+21.70}_{-20.67}$	5.75E+36	9.10E+35	1.43E+36
178	4.60E-02	2.64E-03	1.00E+00	$2.70^{+3.18}_{-1.91}$	$3.47^{+3.18}_{-1.91}$	$-0.77^{+1.87}_{-99.99}$	1.72E+35	5.25E+34	-9.99E+00
179	6.82E-34	2.42E-20	9.41E-17	$113.03^{+13.73}_{-12.68}$	$50.84^{+9.09}_{-8.01}$	$62.19^{+10.88}_{-9.81}$	3.97E+36	4.47E+35	1.48E+36
180	0.00E+00	0.00E+00	0.00E+00	$636.51^{+27.26}_{-26.23}$	$468.91^{+23.14}_{-22.11}$	$167.60^{+15.14}_{-14.10}$	3.25E+36	6.04E+35	5.78E+35
181	4.90E-30	3.74E-23	1.05E-09	$35.49^{+7.23}_{-6.14}$	$22.92^{+5.98}_{-4.86}$	$12.57^{+4.84}_{-3.70}$	2.14E+36	3.13E+35	5.35E+35
182	0.00E+00	0.00E+00	0.00E+00	$2038.85^{+47.02}_{-46.01}$	$1113.31^{+34.82}_{-33.80}$	$925.54^{+32.23}_{-31.21}$	1.25E+37	1.73E+36	3.80E+36
183	0.00E+00	0.00E+00	0.00E+00	$1094.49^{+34.56}_{-33.54}$	$638.68^{+26.52}_{-25.50}$	$455.81^{+22.81}_{-21.78}$	5.46E+36	7.91E+35	1.54E+36
184	0.00E+00	0.00E+00	3.71E-25	$56.41^{+8.60}_{-7.53}$	$37.78^{+7.23}_{-6.13}$	$18.63^{+5.44}_{-4.32}$	3.50E+36	5.55E+35	8.00E+35
185	0.00E+00	0.00E+00	0.00E+00	$4562.41^{+68.95}_{-67.94}$	$2570.22^{+51.93}_{-50.91}$	$1992.19^{+46.00}_{-44.99}$	2.22E+37	3.09E+36	6.61E+36
186	0.00E+00	1.06E-12	0.00E+00	$160.54^{+15.43}_{-14.39}$	$39.10^{+8.65}_{-7.58}$	$121.43^{+13.26}_{-12.21}$	8.17E+35	4.99E+34	4.18E+35
187	0.00E+00	0.00E+00	5.25E-23	$136.55^{+13.84}_{-12.80}$	$78.84^{+10.44}_{-9.38}$	$57.71^{+9.75}_{-8.68}$	6.64E+35	9.50E+34	1.91E+35
188	0.00E+00	0.00E+00	0.00E+00	$18617.71^{+137.84}_{-136.84}$	$12863.19^{+114.70}_{-113.69}$	$5754.52^{+77.15}_{-76.14}$	8.98E+37	1.54E+37	1.89E+37
189	1.45E-09	4.66E-01	8.76E-12	$11.79^{+4.71}_{-3.56}$	$0.38^{+2.33}_{-0.83}$	$11.41^{+4.57}_{-3.41}$	6.92E+35	5.38E+33	4.62E+35
190	1.10E-07	2.17E-02	6.97E-07	$44.44^{+11.11}_{-10.06}$	$9.78^{+6.37}_{-5.27}$	$34.66^{+9.61}_{-8.55}$	2.74E+35	1.52E+34	1.44E+35
191	2.13E-04	9.60E-08	1.00E+00	$5.87^{+3.79}_{-2.58}$	$6.69^{+3.78}_{-2.58}$	$-0.82^{+1.87}_{-99.99}$	3.71E+35	1.00E+35	-9.99E+00
192	3.12E-43	3.66E-32	1.36E-16	$133.16^{+14.67}_{-13.63}$	$71.48^{+10.42}_{-9.36}$	$61.68^{+10.95}_{-9.89}$	6.86E+35	9.30E+34	2.15E+35
193	0.00E+00	0.00E+00	0.00E+00	$5215.20^{+73.56}_{-72.55}$	$3667.97^{+61.75}_{-60.74}$	$1547.22^{+40.68}_{-39.66}$	2.59E+37	4.54E+36	5.21E+36
194	0.00E+00	0.00E+00	1.02E-15	$59.03^{+8.86}_{-7.79}$	$42.92^{+7.69}_{-6.61}$	$16.11^{+5.21}_{-4.08}$	3.06E+36	5.05E+35	5.89E+35
195	5.48E-04	6.57E-06	4.17E-01	$19.28^{+7.89}_{-6.81}$	$18.08^{+6.48}_{-5.38}$	$1.20^{+5.26}_{-4.14}$	9.80E+34	2.28E+34	4.16E+33
196	0.00E+00	0.00E+00	0.00E+00	$1340.32^{+38.30}_{-37.28}$	$864.55^{+30.70}_{-29.68}$	$475.77^{+23.58}_{-22.55}$	6.65E+36	1.07E+36	1.60E+36
197	4.25E-12	6.42E-07	1.01E-06	$131.78^{+20.76}_{-19.31}$	$63.87^{+14.58}_{-13.10}$	$67.91^{+15.64}_{-14.16}$	7.92E+36	7.82E+35	3.03E+36
198	0.00E+00	0.00E+00	0.00E+00	$3078.67^{+56.75}_{-55.74}$	$1988.02^{+45.74}_{-44.72}$	$1090.66^{+34.28}_{-33.26}$	1.47E+37	2.33E+36	3.55E+36
199	2.20E-04	1.35E-02	4.83E-03	$6.50^{+3.96}_{-2.77}$	$3.13^{+3.18}_{-1.91}$	$3.37^{+3.18}_{-1.91}$	3.69E+35	4.25E+34	1.32E+35
200	1.48E-06	1.41E-03	1.99E-04	$36.18^{+10.15}_{-9.09}$	$14.65^{+6.79}_{-5.70}$	$21.53^{+8.14}_{-7.06}$	1.87E+35	1.90E+34	7.51E+34
201	0.00E+00	0.00E+00	0.00E+00	$6343.62^{+81.01}_{-79.98}$	$3131.97^{+57.22}_{-56.19}$	$3211.65^{+57.95}_{-56.92}$	2.25E+38	2.27E+37	8.43E+37
202	7.47E-13	1.60E-05	6.89E-09	$39.70^{+8.76}_{-7.68}$	$14.99^{+5.89}_{-4.78}$	$24.71^{+7.08}_{-5.99}$	1.90E+35	1.76E+34	8.04E+34
203	0.00E+00	0.00E+00	0.00E+00	$634.17^{+26.94}_{-25.91}$	$340.70^{+19.88}_{-18.85}$	$293.47^{+18.80}_{-17.77}$	2.99E+36	3.96E+35	9.42E+35
204	5.98E-13	2.59E-11	4.47E-05	$61.12^{+11.76}_{-10.71}$	$34.14^{+8.17}_{-7.09}$	$26.98^{+9.07}_{-8.00}$	3.59E+35	5.07E+34	1.07E+35
205	9.13E-09	7.65E-09	1.45E-02	$34.15^{+8.78}_{-7.71}$	$24.78^{+7.09}_{-6.00}$	$9.37^{+5.92}_{-4.81}$	1.66E+35	2.98E+34	3.10E+34
206	0.00E+00	0.00E+00	0.00E+00	$395.97^{+20.97}_{-19.94}$	$293.30^{+18.17}_{-17.14}$	$102.67^{+11.24}_{-10.18}$	2.14E+37	3.79E+36	3.82E+36
207	2.21E-21	1.38E-16	1.00E-07	$54.71^{+9.61}_{-8.54}$	$32.70^{+7.39}_{-6.31}$	$22.00^{+6.83}_{-5.73}$	2.59E+35	3.81E+34	7.11E+34

Source No.	*pns* (0.5 − 8.0 keV)	*pns* (0.5 − 2.0 keV)	*pns* (2.0 − 8.0 keV)	*net_cts* (0.5 − 8.0 keV)	*net_cts* (0.5 − 2.0 keV)	*net_cts* (2.0 − 8.0 keV)	*luminosity* (0.5 − 8.0 keV)	*luminosity* (0.5 − 2.0 keV)	*luminosity* (2.0 − 8.0 keV)
208	5.72E-21	1.97E-16	1.03E-07	$65.56^{+10.79}_{-9.74}$	$38.30^{+8.08}_{-7.01}$	$27.26^{+7.82}_{-6.74}$	3.03E+35	4.36E+34	8.58E+34
209	0.00E+00	0.00E+00	0.00E+00	$653.91^{+26.98}_{-25.96}$	$390.99^{+21.02}_{-19.99}$	$262.92^{+17.58}_{-16.55}$	3.20E+36	4.72E+35	8.76E+35
210	0.00E+00	0.00E+00	0.00E+00	$1055.85^{+33.80}_{-32.79}$	$957.87^{+32.11}_{-31.09}$	$97.98^{+11.44}_{-10.38}$	5.22E+36	1.16E+36	3.30E+35
211	3.16E-06	8.12E-03	7.17E-05	$35.26^{+10.16}_{-9.11}$	$11.88^{+6.62}_{-5.53}$	$23.38^{+8.29}_{-7.21}$	1.79E+35	1.51E+34	8.02E+34
212	7.70E-09	5.93E-09	5.18E-03	$51.76^{+11.85}_{-10.81}$	$33.63^{+8.61}_{-7.53}$	$18.13^{+8.79}_{-7.72}$	3.55E+35	5.94E+34	8.33E+34
213	0.00E+00	0.00E+00	0.00E+00	$13292.12^{+116.53}_{-115.53}$	$10808.72^{+105.11}_{-104.11}$	$2483.40^{+51.09}_{-50.08}$	6.46E+37	1.31E+37	8.19E+36
214	8.14E-34	9.57E-23	1.28E-13	$44.98^{+8.06}_{-6.98}$	$25.44^{+6.27}_{-5.16}$	$19.55^{+5.77}_{-4.66}$	1.35E+36	1.61E+35	4.29E+35
215	2.55E-10	7.41E-01	4.17E-13	$17.62^{+5.67}_{-4.55}$	$-0.35^{+2.33}_{-0.84}$	$17.96^{+5.56}_{-4.44}$	7.22E+35	-9.99E+00	5.26E+35
216	0.00E+00	0.00E+00	0.00E+00	$13165.06^{+115.93}_{-114.93}$	$7519.94^{+87.84}_{-86.83}$	$5645.12^{+76.29}_{-75.29}$	6.49E+37	9.15E+36	1.90E+37
217	0.00E+00	4.32E-37	2.62E-16	$117.74^{+13.29}_{-12.24}$	$70.16^{+10.12}_{-9.06}$	$47.58^{+9.28}_{-8.21}$	5.43E+35	7.97E+34	1.49E+35
218	1.45E-39	7.36E-29	1.66E-13	$90.48^{+11.73}_{-10.68}$	$56.48^{+9.30}_{-8.24}$	$34.01^{+7.85}_{-6.77}$	4.37E+35	6.72E+34	1.12E+35
219	0.00E+00	2.13E-12	0.00E+00	$205.87^{+17.12}_{-16.08}$	$37.10^{+8.39}_{-7.32}$	$168.77^{+15.35}_{-14.31}$	1.01E+36	4.58E+34	5.61E+35
220	1.22E-16	1.20E-14	5.58E-06	$82.29^{+13.48}_{-12.44}$	$47.64^{+9.49}_{-8.42}$	$34.65^{+10.19}_{-9.13}$	6.45E+35	9.61E+34	1.82E+35
221	4.81E-04	1.59E-04	3.74E-01	$5.04^{+3.60}_{-2.37}$	$4.51^{+3.40}_{-2.15}$	$0.53^{+2.32}_{-0.83}$	1.67E+35	3.38E+34	1.24E+34
222	1.88E-09	7.65E-01	2.42E-13	$32.30^{+8.29}_{-7.21}$	$-1.56^{+3.62}_{-2.41}$	$33.86^{+7.85}_{-6.77}$	1.46E+35	-9.99E+00	1.04E+35
223	2.80E-27	2.32E-19	6.46E-11	$50.73^{+8.65}_{-7.57}$	$28.12^{+6.57}_{-5.46}$	$22.60^{+6.32}_{-5.21}$	6.91E+36	1.05E+36	2.02E+36
224	1.94E-03	1.14E-03	9.24E-02	$4.76^{+3.60}_{-2.38}$	$2.81^{+2.94}_{-1.63}$	$1.95^{+2.94}_{-1.63}$	3.04E+35	4.29E+34	8.59E+34
225	1.53E-06	1.36E-08	3.54E-01	$28.43^{+8.52}_{-7.45}$	$26.72^{+7.49}_{-6.41}$	$1.71^{+4.88}_{-3.74}$	1.25E+35	2.89E+34	5.12E+33
226	7.36E-22	5.63E-17	2.85E-07	$61.14^{+10.24}_{-9.18}$	$39.55^{+8.22}_{-7.14}$	$21.60^{+6.84}_{-5.74}$	2.87E+35	4.58E+34	6.91E+34
227	3.58E-03	3.32E-04	2.41E-01	$21.86^{+9.89}_{-8.83}$	$17.09^{+7.04}_{-5.95}$	$4.77^{+7.58}_{-6.50}$	1.28E+35	2.53E+34	1.88E+34
228	5.86E-42	7.21E-27	4.49E-18	$31.39^{+6.72}_{-5.62}$	$16.82^{+5.21}_{-4.08}$	$14.57^{+4.97}_{-3.83}$	1.48E+36	1.78E+35	4.87E+35
229	1.68E-10	2.01E-06	1.35E-05	$36.81^{+8.80}_{-7.73}$	$20.18^{+6.82}_{-5.72}$	$16.63^{+6.27}_{-5.17}$	1.79E+35	2.41E+34	5.52E+34
230	2.93E-31	2.55E-37	6.77E-04	$68.97^{+10.33}_{-9.27}$	$56.46^{+8.99}_{-7.92}$	$12.51^{+5.89}_{-4.78}$	3.10E+35	6.24E+34	3.84E+34
231	3.41E-07	7.54E-10	1.38E-01	$26.73^{+7.89}_{-6.81}$	$22.24^{+6.48}_{-5.37}$	$4.49^{+5.27}_{-4.14}$	6.29E+35	1.27E+35	7.24E+34
232	0.00E+00	0.00E+00	1.56E-26	$303.34^{+19.01}_{-17.98}$	$252.90^{+17.25}_{-16.21}$	$50.44^{+8.81}_{-7.74}$	1.48E+36	3.00E+35	1.68E+35
233	1.83E-11	2.74E-07	1.07E-05	$37.14^{+8.63}_{-7.55}$	$21.07^{+6.74}_{-5.65}$	$16.07^{+6.09}_{-4.98}$	1.77E+35	2.45E+34	5.25E+34
234	0.00E+00	0.00E+00	0.00E+00	$12665.85^{+113.73}_{-112.73}$	$7960.85^{+90.36}_{-89.35}$	$4705.00^{+69.73}_{-68.72}$	4.90E+37	7.63E+36	1.24E+37
235	0.00E+00	0.00E+00	0.00E+00	$984.72^{+32.74}_{-31.72}$	$720.12^{+28.06}_{-27.04}$	$264.60^{+17.62}_{-16.58}$	4.38E+36	7.88E+35	8.03E+35
236	8.00E-26	2.06E-13	5.98E-14	$30.64^{+6.81}_{-5.71}$	$14.88^{+5.09}_{-3.95}$	$15.77^{+5.21}_{-4.08}$	4.58E+35	4.92E+34	1.68E+35
237	7.36E-03	9.92E-02	2.06E-02	$12.99^{+7.03}_{-5.94}$	$4.80^{+5.00}_{-3.87}$	$8.18^{+5.59}_{-4.47}$	6.54E+34	6.00E+33	2.80E+34
238	0.00E+00	0.00E+00	0.00E+00	$589.72^{+25.33}_{-24.30}$	$398.40^{+20.99}_{-19.97}$	$191.32^{+14.88}_{-13.84}$	3.71E+37	6.01E+36	8.30E+36
239	7.39E-16	1.12E-19	1.37E-01	$56.87^{+10.53}_{-9.47}$	$52.11^{+9.45}_{-8.38}$	$4.76^{+5.49}_{-4.37}$	2.27E+35	5.13E+34	1.30E+34
240	6.00E-04	1.05E-01	8.65E-04	$19.38^{+7.96}_{-6.88}$	$5.17^{+5.37}_{-4.24}$	$14.20^{+6.49}_{-5.39}$	8.09E+34	5.34E+33	4.04E+34
241	7.57E-05	2.57E-04	5.24E-02	$63.11^{+18.46}_{-17.38}$	$46.64^{+15.16}_{-14.07}$	$16.47^{+11.28}_{-10.19}$	1.49E+36	2.46E+35	2.75E+35
242	0.00E+00	0.00E+00	0.00E+00	$1457.22^{+39.39}_{-38.37}$	$1034.59^{+33.31}_{-32.30}$	$422.63^{+21.74}_{-20.71}$	2.34E+37	3.68E+36	4.83E+36
243	1.16E-07	4.32E-04	5.96E-05	$9.83^{+4.43}_{-3.26}$	$3.71^{+3.18}_{-1.91}$	$6.12^{+3.79}_{-2.58}$	6.30E+35	5.70E+34	2.70E+35
244	2.67E-08	1.46E-10	4.18E-02	$46.60^{+11.17}_{-10.12}$	$35.12^{+8.42}_{-7.34}$	$11.47^{+8.01}_{-6.94}$	2.34E+35	4.45E+34	3.89E+34
245	0.00E+00	0.00E+00	0.00E+00	$53560.60^{+232.64}_{-231.64}$	$31861.08^{+179.65}_{-178.65}$	$21699.52^{+148.45}_{-147.45}$	1.72E+38	2.53E+37	4.75E+37
246	0.00E+00	0.00E+00	6.05E-24	$371.00^{+21.96}_{-20.93}$	$285.67^{+18.59}_{-17.55}$	$85.33^{+12.43}_{-11.38}$	3.57E+36	7.06E+35	5.52E+35
247	1.76E-03	8.10E-03	5.43E-02	$64.08^{+23.27}_{-22.03}$	$41.95^{+18.65}_{-17.41}$	$22.13^{+14.74}_{-13.48}$	6.36E+35	9.68E+34	1.53E+35
248	8.02E-27	2.12E-26	1.75E-02	$12.95^{+4.71}_{-3.55}$	$11.96^{+4.57}_{-3.41}$	$0.98^{+2.32}_{-0.83}$	9.62E+36	1.63E+36	5.74E+35
249	2.88E-03	3.40E-04	4.59E-01	$18.63^{+8.55}_{-7.48}$	$17.85^{+7.28}_{-6.19}$	$0.78^{+5.27}_{-4.15}$	7.68E+34	1.79E+34	2.20E+33

Source No.	*pns* (0.5 – 8.0 keV)	*pns* (0.5 – 2.0 keV)	*pns* (2.0 – 8.0 keV)	*net_cts* (0.5 – 8.0 keV)	*net_cts* (0.5 – 2.0 keV)	*net_cts* (2.0 – 8.0 keV)	*luminosity* (0.5 – 8.0 keV)	*luminosity* (0.5 – 2.0 keV)	*luminosity* (2.0 – 8.0 keV)
250	1.55E-02	1.00E+00	1.62E-03	$4.14^{+3.61}_{-2.39}$	$-0.77^{+1.88}_{-99.99}$	$4.90^{+3.61}_{-2.38}$	4.29E+35	-9.99E+00	3.48E+35
251	2.78E-16	1.25E-19	3.06E-01	$38.81^{+8.21}_{-7.13}$	$37.34^{+7.77}_{-6.69}$	$1.47^{+3.61}_{-2.39}$	1.62E+35	3.79E+34	4.22E+33
252	3.25E-24	5.75E-32	5.16E-01	$48.25^{+8.74}_{-7.66}$	$48.00^{+8.40}_{-7.33}$	$0.25^{+3.40}_{-2.16}$	1.94E+35	4.69E+34	6.78E+32
253	0.00E+00	0.00E+00	0.00E+00	$599.10^{+26.48}_{-25.46}$	$375.96^{+20.81}_{-19.78}$	$223.14^{+17.04}_{-16.01}$	4.68E+36	7.49E+35	1.17E+36
254	1.47E-02	3.47E-01	8.70E-03	$10.43^{+6.41}_{-5.31}$	$1.47^{+4.15}_{-2.98}$	$8.95^{+5.48}_{-4.35}$	4.81E+34	1.68E+33	2.82E+34
255	0.00E+00	0.00E+00	3.18E-23	$61.78^{+8.99}_{-7.92}$	$38.71^{+7.31}_{-6.22}$	$23.06^{+5.98}_{-4.86}$	3.56E+36	5.36E+35	9.14E+35
256	1.10E-03	3.41E-02	3.30E-03	$33.99^{+12.82}_{-11.77}$	$17.06^{+10.65}_{-9.59}$	$16.93^{+7.89}_{-6.80}$	5.07E+35	5.64E+34	1.80E+35
257	0.00E+00	0.00E+00	0.00E+00	$1016.32^{+33.10}_{-32.08}$	$759.08^{+28.71}_{-27.69}$	$257.24^{+17.21}_{-16.18}$	8.82E+36	1.50E+36	1.57E+36
258	4.69E-03	5.56E-03	1.76E-01	$41.70^{+17.55}_{-16.49}$	$31.98^{+14.08}_{-13.02}$	$9.72^{+11.19}_{-10.11}$	1.27E+36	2.13E+35	2.11E+35
259	0.00E+00	0.00E+00	0.00E+00	$1134.66^{+35.09}_{-34.07}$	$711.71^{+28.01}_{-26.98}$	$422.96^{+21.82}_{-20.79}$	2.51E+37	3.48E+36	6.67E+36
260	2.03E-03	5.53E-02	5.93E-03	$77.73^{+28.29}_{-27.00}$	$33.50^{+21.90}_{-20.62}$	$44.23^{+18.75}_{-17.43}$	1.52E+36	1.45E+35	6.16E+35
261	0.00E+00	0.00E+00	0.00E+00	$660.82^{+27.37}_{-26.33}$	$388.73^{+21.08}_{-20.04}$	$272.09^{+18.12}_{-17.07}$	1.72E+37	2.64E+36	4.72E+36
262	2.23E-10	3.14E-07	1.73E-04	$12.01^{+4.71}_{-3.56}$	$7.46^{+3.96}_{-2.77}$	$4.55^{+3.40}_{-2.16}$	1.51E+36	1.85E+35	4.29E+35
263	1.69E-15	4.80E-09	7.88E-08	$20.22^{+5.78}_{-4.66}$	$11.85^{+4.72}_{-3.56}$	$8.37^{+4.12}_{-2.94}$	1.96E+36	2.43E+35	5.92E+35
264	2.01E-07	8.05E-07	1.88E-02	$30.85^{+8.64}_{-7.57}$	$22.57^{+7.17}_{-6.08}$	$8.29^{+5.59}_{-4.47}$	8.07E+34	1.43E+34	1.49E+34
265	4.36E-11	4.72E-03	8.86E-10	$56.48^{+11.63}_{-10.59}$	$12.73^{+6.64}_{-5.54}$	$43.75^{+10.06}_{-9.00}$	3.84E+35	2.20E+34	2.00E+35
266	1.91E-03	3.01E-03	1.06E-01	$5.35^{+3.79}_{-2.58}$	$3.46^{+3.18}_{-1.91}$	$1.89^{+2.94}_{-1.63}$	3.49E+35	5.42E+34	8.50E+34
267	9.56E-05	9.82E-03	2.90E-03	$7.86^{+4.28}_{-3.11}$	$3.20^{+3.18}_{-1.91}$	$4.66^{+3.60}_{-2.38}$	3.57E+35	3.39E+34	1.47E+35
268	0.00E+00	3.20E-26	6.10E-42	$59.62^{+8.86}_{-7.79}$	$22.54^{+5.88}_{-4.76}$	$37.09^{+7.23}_{-6.14}$	2.45E+36	2.08E+35	1.08E+36
269	8.46E-35	6.73E-24	9.66E-14	$32.81^{+6.90}_{-5.80}$	$18.64^{+5.44}_{-4.32}$	$14.17^{+4.97}_{-3.83}$	2.12E+36	2.90E+35	6.29E+35
270	1.04E-26	1.88E-18	6.74E-10	$67.10^{+10.45}_{-9.39}$	$44.98^{+8.75}_{-7.68}$	$22.13^{+6.47}_{-5.37}$	1.90E+35	3.04E+34	4.32E+34
271	0.00E+00	0.00E+00	2.00E-36	$169.15^{+14.90}_{-13.86}$	$96.58^{+11.29}_{-10.24}$	$72.57^{+10.39}_{-9.33}$	7.66E+35	1.08E+35	2.24E+35
272	1.69E-24	6.10E-11	3.17E-15	$54.75^{+9.37}_{-8.30}$	$23.39^{+6.56}_{-5.46}$	$31.36^{+7.32}_{-6.23}$	2.13E+35	2.22E+34	8.35E+34
273	1.42E-19	6.26E-20	1.60E-03	$42.15^{+8.34}_{-7.27}$	$33.55^{+7.31}_{-6.22}$	$8.60^{+4.85}_{-3.70}$	1.66E+35	3.21E+34	2.31E+34
274	5.03E-04	1.30E-02	1.02E-02	$58.00^{+19.94}_{-18.92}$	$31.44^{+15.65}_{-14.62}$	$26.56^{+13.03}_{-11.99}$	1.75E+36	2.13E+35	5.67E+35
275	0.00E+00	0.00E+00	0.00E+00	$1658.20^{+42.07}_{-41.05}$	$1029.93^{+33.34}_{-32.32}$	$628.26^{+26.34}_{-25.31}$	4.06E+37	5.68E+36	1.09E+37
276	0.00E+00	0.00E+00	0.00E+00	$25732.42^{+161.68}_{-160.68}$	$16430.84^{+129.37}_{-128.37}$	$9301.58^{+97.65}_{-96.64}$	8.05E+37	1.24E+37	2.00E+37
277	1.12E-06	3.57E-07	1.95E-01	$26.65^{+8.09}_{-7.01}$	$23.84^{+7.33}_{-6.24}$	$2.80^{+4.30}_{-3.13}$	7.17E+34	1.53E+34	5.21E+33
278	2.43E-12	9.59E-09	1.04E-05	$65.42^{+12.47}_{-11.42}$	$34.43^{+8.75}_{-7.67}$	$31.00^{+9.50}_{-8.44}$	3.54E+35	4.75E+34	1.13E+35
279	7.93E-08	3.94E-04	3.94E-05	$23.74^{+7.15}_{-6.06}$	$10.19^{+5.10}_{-3.96}$	$13.56^{+5.67}_{-4.55}$	1.04E+35	1.10E+34	4.05E+34
280	9.83E-12	1.90E-03	8.39E-11	$31.25^{+7.70}_{-6.62}$	$9.22^{+5.10}_{-3.96}$	$22.03^{+6.37}_{-5.26}$	1.05E+35	7.45E+33	5.08E+34
281	0.00E+00	0.00E+00	0.00E+00	$802.34^{+29.50}_{-28.48}$	$576.33^{+25.13}_{-24.10}$	$226.00^{+16.20}_{-15.16}$	5.33E+37	9.76E+36	1.01E+37
282	2.90E-16	4.89E-15	1.48E-03	$49.66^{+9.56}_{-8.50}$	$39.10^{+8.36}_{-7.28}$	$10.56^{+5.47}_{-4.34}$	1.25E+35	2.32E+34	1.84E+34
283	1.30E-09	1.72E-09	3.52E-02	$34.14^{+8.56}_{-7.49}$	$28.11^{+7.56}_{-6.47}$	$6.03^{+4.86}_{-3.71}$	9.85E+34	1.93E+34	1.20E+34
284	0.00E+00	0.00E+00	1.94E-23	$189.31^{+15.65}_{-14.61}$	$142.17^{+13.54}_{-12.49}$	$47.14^{+8.62}_{-7.55}$	4.74E+35	8.47E+34	8.16E+34
285	2.41E-11	7.96E-14	1.91E-01	$17.46^{+5.56}_{-4.44}$	$15.93^{+5.22}_{-4.08}$	$1.53^{+2.95}_{-1.64}$	1.26E+36	2.62E+35	7.81E+34
286	4.99E-03	4.27E-07	1.00E+00	$5.49^{+3.97}_{-2.77}$	$7.41^{+3.96}_{-2.76}$	$-1.91^{+1.88}_{-99.99}$	3.48E+35	1.08E+35	-9.99E+00
287	1.50E-02	2.69E-04	1.00E+00	$3.59^{+3.40}_{-2.16}$	$4.47^{+3.40}_{-2.16}$	$-0.87^{+1.87}_{-99.99}$	1.36E+35	3.62E+34	-9.99E+00
288	2.52E-07	3.24E-09	2.40E-01	$21.46^{+6.82}_{-5.73}$	$19.32^{+6.08}_{-4.97}$	$2.14^{+3.97}_{-2.78}$	8.28E+34	1.83E+34	5.64E+33
289	0.00E+00	0.00E+00	0.00E+00	$343.73^{+20.06}_{-19.03}$	$193.40^{+15.35}_{-14.31}$	$150.33^{+13.56}_{-12.52}$	9.70E+35	1.29E+35	2.94E+35
290	1.34E-06	2.71E-07	3.33E-02	$42.49^{+11.42}_{-10.37}$	$29.68^{+8.39}_{-7.31}$	$12.81^{+8.40}_{-7.33}$	1.99E+35	3.48E+34	4.07E+34
291	1.32E-04	7.19E-02	5.43E-04	$5.95^{+3.79}_{-2.58}$	$1.57^{+2.66}_{-1.29}$	$4.38^{+3.40}_{-2.16}$	2.97E+35	1.80E+34	1.53E+35

Source No.	*pns* (0.5 − 8.0 keV)	*pns* (0.5 − 2.0 keV)	*pns* (2.0 − 8.0 keV)	*net_cts* (0.5 − 8.0 keV)	*net_cts* (0.5 − 2.0 keV)	*net_cts* (2.0 − 8.0 keV)	*luminosity* (0.5 − 8.0 keV)	*luminosity* (0.5 − 2.0 keV)	*luminosity* (2.0 − 8.0 keV)
292	0.00E+00	0.00E+00	0.00E+00	$356.99^{+20.29}_{-19.26}$	$203.02^{+15.52}_{-14.48}$	$153.97^{+13.72}_{-12.68}$	1.33E+36	1.85E+35	3.93E+35
293	0.00E+00	0.00E+00	0.00E+00	$34058.19^{+185.70}_{-184.70}$	$21917.28^{+149.16}_{-148.16}$	$12140.91^{+111.28}_{-110.27}$	9.28E+37	1.40E+37	2.29E+37
294	0.00E+00	0.00E+00	0.00E+00	$7576.50^{+88.16}_{-87.15}$	$4899.79^{+71.07}_{-70.06}$	$2676.71^{+52.84}_{-51.82}$	3.13E+37	4.89E+36	7.59E+36
295	8.55E-44	6.18E-43	6.22E-08	$87.79^{+11.19}_{-10.13}$	$66.63^{+9.61}_{-8.55}$	$21.15^{+6.53}_{-5.42}$	4.92E+36	9.43E+35	8.01E+35
296	0.00E+00	0.00E+00	0.00E+00	$248.89^{+17.31}_{-16.28}$	$162.47^{+14.03}_{-12.99}$	$86.42^{+10.85}_{-9.79}$	1.04E+36	1.63E+35	2.47E+35
297	9.79E-05	1.25E-07	8.50E-01	$25.11^{+8.87}_{-7.80}$	$28.55^{+8.10}_{-7.03}$	$-3.45^{+4.49}_{-3.33}$	6.08E+34	1.63E+34	-9.99E+00
298	3.20E-06	2.08E-03	3.70E-04	$14.83^{+5.68}_{-4.56}$	$6.35^{+4.13}_{-2.95}$	$8.48^{+4.58}_{-3.42}$	2.77E+35	2.76E+34	1.10E+35
299	0.00E+00	0.00E+00	0.00E+00	$36665.96^{+193.02}_{-192.01}$	$21465.85^{+147.86}_{-146.85}$	$15200.12^{+124.72}_{-123.71}$	8.60E+37	1.18E+37	2.48E+37
300	0.00E+00	2.34E-42	1.52E-18	$96.99^{+11.58}_{-10.53}$	$61.44^{+9.30}_{-8.23}$	$35.55^{+7.62}_{-6.54}$	3.42E+35	5.19E+34	8.63E+34
301	2.59E-13	1.49E-14	6.47E-03	$24.08^{+6.46}_{-5.36}$	$18.30^{+5.56}_{-4.43}$	$5.78^{+4.13}_{-2.95}$	4.24E+35	7.50E+34	7.08E+34
302	1.83E-03	2.74E-03	1.14E-01	$13.87^{+6.66}_{-5.56}$	$9.67^{+5.35}_{-4.22}$	$4.19^{+4.73}_{-3.58}$	5.45E+34	9.10E+33	1.14E+34
303	0.00E+00	2.23E-14	0.00E+00	$165.76^{+14.72}_{-13.68}$	$39.41^{+8.49}_{-7.41}$	$126.35^{+12.53}_{-11.48}$	3.88E+35	2.13E+34	2.07E+35
304	0.00E+00	0.00E+00	0.00E+00	$4157.08^{+65.87}_{-64.86}$	$2673.66^{+52.98}_{-51.97}$	$1483.42^{+39.82}_{-38.81}$	9.75E+36	1.46E+36	2.42E+36
305	0.00E+00	0.00E+00	1.83E-08	$165.05^{+15.63}_{-14.59}$	$134.15^{+13.70}_{-12.66}$	$30.90^{+8.30}_{-7.22}$	3.88E+35	7.37E+34	5.06E+34
306	1.60E-05	3.36E-03	1.12E-03	$12.67^{+5.34}_{-4.21}$	$6.11^{+4.13}_{-2.95}$	$6.56^{+4.13}_{-2.94}$	1.22E+35	1.28E+34	4.55E+34
307	3.91E-03	5.37E-02	2.18E-02	$7.27^{+4.58}_{-3.42}$	$3.37^{+3.60}_{-2.38}$	$3.90^{+3.60}_{-2.38}$	7.08E+34	7.13E+33	2.73E+34
308	0.00E+00	0.00E+00	0.00E+00	$296.48^{+19.11}_{-18.07}$	$184.73^{+14.93}_{-13.88}$	$111.76^{+12.60}_{-11.55}$	8.15E+36	1.33E+36	2.04E+36
309	0.00E+00	0.00E+00	0.00E+00	$1122.84^{+34.69}_{-33.67}$	$735.74^{+28.27}_{-27.25}$	$387.09^{+20.79}_{-19.77}$	3.32E+36	5.10E+35	7.95E+35
310	6.63E-17	4.01E-15	6.10E-06	$66.06^{+11.34}_{-10.28}$	$38.58^{+8.14}_{-7.06}$	$27.48^{+8.52}_{-7.45}$	8.33E+35	1.25E+35	2.32E+35
311	0.00E+00	0.00E+00	0.00E+00	$226.57^{+16.59}_{-15.55}$	$137.09^{+13.20}_{-12.15}$	$89.48^{+10.74}_{-9.68}$	5.86E+35	8.21E+34	1.62E+35
312	0.00E+00	0.00E+00	2.71E-01	$148.09^{+14.25}_{-13.21}$	$145.13^{+13.45}_{-12.41}$	$2.96^{+5.60}_{-4.49}$	6.93E+35	1.68E+35	9.45E+33
313	1.63E-13	4.76E-07	4.92E-08	$14.08^{+4.97}_{-3.83}$	$5.74^{+3.60}_{-2.38}$	$8.34^{+4.12}_{-2.94}$	5.08E+35	4.45E+34	2.17E+35
314	1.24E-11	2.26E-10	4.15E-04	$35.99^{+8.42}_{-7.35}$	$22.42^{+6.47}_{-5.36}$	$13.56^{+6.09}_{-4.99}$	1.45E+35	2.17E+34	3.76E+34
315	0.00E+00	0.00E+00	0.00E+00	$972.80^{+33.10}_{-32.08}$	$712.43^{+28.07}_{-27.05}$	$260.37^{+18.27}_{-17.24}$	4.81E+36	8.89E+35	8.69E+35
316	0.00E+00	0.00E+00	0.00E+00	$6190.88^{+79.84}_{-78.84}$	$4220.60^{+66.11}_{-65.10}$	$1970.28^{+45.47}_{-44.46}$	1.43E+37	2.24E+36	3.19E+36
317	8.50E-10	3.68E-06	1.92E-05	$44.48^{+10.22}_{-9.16}$	$20.08^{+6.85}_{-5.75}$	$24.41^{+8.18}_{-7.11}$	2.09E+35	2.36E+34	7.79E+34
318	0.00E+00	0.00E+00	0.00E+00	$987.81^{+32.85}_{-31.83}$	$454.10^{+22.54}_{-21.51}$	$533.71^{+24.48}_{-23.45}$	4.50E+36	5.11E+35	1.66E+36
319	0.00E+00	2.80E-45	5.16E-14	$47.55^{+8.05}_{-6.97}$	$32.55^{+6.81}_{-5.71}$	$15.01^{+5.09}_{-3.96}$	2.39E+36	3.76E+35	5.30E+35
320	9.39E-19	7.13E-15	1.15E-05	$39.19^{+8.06}_{-6.98}$	$27.95^{+6.90}_{-5.80}$	$11.25^{+4.97}_{-3.83}$	1.33E+35	2.25E+34	2.63E+34
321	4.87E-05	5.46E-04	2.42E-02	$8.70^{+4.44}_{-3.27}$	$5.72^{+3.79}_{-2.58}$	$2.98^{+3.19}_{-1.92}$	6.87E+35	9.56E+34	1.71E+35
322	0.00E+00	0.00E+00	9.60E-07	$128.54^{+13.34}_{-12.29}$	$113.21^{+12.45}_{-11.40}$	$15.33^{+5.68}_{-4.56}$	2.94E+35	5.95E+34	2.46E+34
323	0.00E+00	0.00E+00	0.00E+00	$168.26^{+14.07}_{-13.03}$	$109.24^{+11.52}_{-10.47}$	$59.02^{+8.80}_{-7.72}$	8.49E+36	1.27E+36	2.09E+36
324	0.00E+00	0.00E+00	0.00E+00	$284.24^{+17.97}_{-16.94}$	$215.91^{+15.76}_{-14.72}$	$68.33^{+9.42}_{-8.35}$	2.78E+37	4.54E+36	4.83E+36
325	1.90E-06	7.47E-02	4.14E-06	$7.95^{+4.12}_{-2.94}$	$1.56^{+2.66}_{-1.29}$	$6.40^{+3.78}_{-2.58}$	3.16E+35	1.32E+34	1.85E+35
326	0.00E+00	0.00E+00	0.00E+00	$4677.22^{+69.52}_{-68.51}$	$2782.94^{+53.84}_{-52.83}$	$1894.28^{+44.63}_{-43.62}$	1.79E+37	2.57E+36	5.00E+36
327	9.30E-15	9.17E-02	4.74E-27	$50.74^{+9.96}_{-8.90}$	$6.94^{+6.49}_{-5.39}$	$43.80^{+8.13}_{-7.05}$	1.09E+35	3.40E+33	6.60E+34
328	7.74E-27	6.69E-19	1.05E-10	$102.15^{+13.79}_{-12.75}$	$57.34^{+10.14}_{-9.08}$	$44.82^{+9.99}_{-8.93}$	3.34E+35	4.44E+34	1.01E+35
329	2.70E-04	2.61E-03	2.91E-02	$5.79^{+3.78}_{-2.58}$	$3.44^{+3.18}_{-1.91}$	$2.35^{+2.94}_{-1.63}$	9.82E+34	1.29E+34	2.83E+34
330	3.17E-09	3.89E-14	3.67E-01	$44.65^{+10.48}_{-9.42}$	$42.60^{+8.95}_{-7.88}$	$2.05^{+6.22}_{-5.12}$	1.42E+35	3.20E+34	4.52E+33
331	8.28E-35	1.26E-12	1.31E-23	$28.36^{+6.46}_{-5.35}$	$9.77^{+4.28}_{-3.10}$	$18.59^{+5.44}_{-4.32}$	3.35E+36	2.76E+35	1.52E+36
332	1.36E-02	4.58E-03	6.90E-01	$11.30^{+6.76}_{-5.66}$	$11.99^{+6.39}_{-5.29}$	$-0.70^{+3.20}_{-1.93}$	3.54E+34	8.74E+33	-9.99E+00
333	0.00E+00	0.00E+00	8.97E-42	$727.92^{+28.39}_{-27.37}$	$665.03^{+27.08}_{-26.06}$	$62.89^{+9.42}_{-8.35}$	1.65E+36	3.46E+35	9.98E+34

Source No.	*pns* (0.5 – 8.0 keV)	*pns* (0.5 – 2.0 keV)	*pns* (2.0 – 8.0 keV)	*net_cts* (0.5 – 8.0 keV)	*net_cts* (0.5 – 2.0 keV)	*net_cts* (2.0 – 8.0 keV)	*luminosity* (0.5 – 8.0 keV)	*luminosity* (0.5 – 2.0 keV)	*luminosity* (2.0 – 8.0 keV)
334	3.62E-16	4.30E-20	1.79E-01	$17.76^{+5.44}_{-4.32}$	$16.52^{+5.21}_{-4.08}$	$1.24^{+2.66}_{-1.29}$	7.03E+35	1.40E+35	3.56E+34
335	1.73E-05	1.44E-05	2.10E-01	$21.57^{+7.49}_{-6.41}$	$19.35^{+6.92}_{-5.83}$	$2.23^{+3.80}_{-2.60}$	4.85E+34	9.99E+33	3.51E+33
336	6.57E-03	2.64E-01	9.22E-03	$3.28^{+3.18}_{-1.91}$	$0.70^{+2.32}_{-0.83}$	$2.58^{+2.94}_{-1.63}$	1.31E+35	5.90E+33	7.52E+34
337	1.79E-17	3.40E-18	2.48E-04	$51.56^{+9.66}_{-8.60}$	$35.96^{+7.70}_{-6.61}$	$15.60^{+6.56}_{-5.46}$	2.28E+35	3.91E+34	4.70E+34
338	0.00E+00	0.00E+00	2.98E-37	$217.39^{+16.97}_{-15.94}$	$125.77^{+12.77}_{-11.72}$	$91.62^{+11.83}_{-10.78}$	3.67E+36	5.48E+35	1.04E+36
339	4.73E-02	5.80E-03	7.37E-01	$6.91^{+5.58}_{-4.46}$	$8.08^{+4.98}_{-3.84}$	$-1.17^{+3.42}_{-2.18}$	2.59E+34	7.33E+33	-9.99E+00
340	0.00E+00	0.00E+00	0.00E+00	$102169.22^{+321.51}_{-320.51}$	$44387.89^{+212.49}_{-211.48}$	$57781.32^{+241.85}_{-240.84}$	2.22E+38	2.20E+37	8.84E+37
341	1.87E-38	1.06E-13	3.00E-33	$77.44^{+10.74}_{-9.69}$	$35.05^{+7.99}_{-6.91}$	$42.39^{+7.84}_{-6.76}$	1.78E+35	1.84E+34	6.84E+34
342	2.62E-16	8.09E-14	5.30E-04	$58.27^{+10.66}_{-9.60}$	$47.79^{+9.73}_{-8.67}$	$10.47^{+5.23}_{-4.09}$	1.27E+35	2.38E+34	1.61E+34
343	2.66E-04	7.84E-05	3.43E-01	$18.90^{+7.51}_{-6.43}$	$17.41^{+6.76}_{-5.67}$	$1.49^{+4.15}_{-2.97}$	4.36E+34	9.20E+33	2.42E+33
344	0.00E+00	0.00E+00	1.10E-36	$235.95^{+17.04}_{-16.00}$	$186.38^{+15.25}_{-14.21}$	$49.57^{+8.41}_{-7.33}$	5.49E+35	9.90E+34	8.10E+34
345	8.62E-03	3.44E-05	1.00E+00	$3.22^{+3.18}_{-1.91}$	$3.83^{+3.18}_{-1.91}$	$-0.61^{+1.87}_{-99.99}$	1.32E+35	3.31E+34	-9.99E+00
346	0.00E+00	0.00E+00	0.00E+00	$5170.28^{+73.09}_{-72.08}$	$4157.01^{+65.63}_{-64.62}$	$1013.27^{+32.94}_{-31.92}$	1.19E+37	2.18E+36	1.63E+36
347	0.00E+00	0.00E+00	0.00E+00	$2813.10^{+54.47}_{-53.46}$	$2056.85^{+46.74}_{-45.73}$	$756.25^{+28.71}_{-27.69}$	6.37E+36	1.06E+36	1.21E+36
348	0.00E+00	0.00E+00	9.35E-27	$163.55^{+14.63}_{-13.59}$	$127.29^{+13.08}_{-12.03}$	$36.26^{+7.39}_{-6.30}$	3.65E+35	6.45E+34	5.70E+34
349	1.85E-07	4.56E-04	9.61E-06	$29.44^{+8.36}_{-7.29}$	$16.53^{+7.01}_{-5.91}$	$12.90^{+5.34}_{-4.21}$	6.39E+34	8.17E+33	1.97E+34
350	9.25E-04	2.44E-03	1.11E-01	$19.76^{+8.30}_{-7.22}$	$16.09^{+7.57}_{-6.48}$	$3.67^{+4.29}_{-3.12}$	4.44E+34	8.21E+33	5.80E+33
351	0.00E+00	0.00E+00	0.00E+00	$18366.61^{+136.79}_{-135.78}$	$13325.37^{+116.68}_{-115.68}$	$5041.24^{+72.11}_{-71.10}$	4.11E+37	6.77E+36	7.94E+36
352	1.90E-02	8.03E-03	7.39E-01	$12.94^{+7.81}_{-6.73}$	$13.97^{+7.50}_{-6.42}$	$-1.03^{+3.20}_{-1.94}$	3.23E+34	7.91E+33	-9.99E+00
353	0.00E+00	0.00E+00	0.00E+00	$5238.73^{+73.45}_{-72.44}$	$3239.56^{+57.97}_{-56.96}$	$1999.17^{+45.76}_{-44.75}$	1.87E+37	2.74E+36	4.93E+36
354	1.60E-07	8.43E-04	8.46E-07	$37.50^{+9.92}_{-8.86}$	$20.17^{+8.37}_{-7.30}$	$17.33^{+6.09}_{-4.98}$	8.60E+34	1.05E+34	2.80E+34
355	3.77E-04	5.83E-04	1.51E-01	$17.50^{+7.24}_{-6.15}$	$14.46^{+6.47}_{-5.37}$	$3.04^{+4.13}_{-2.95}$	4.00E+34	7.56E+33	4.88E+33
356	4.65E-03	1.74E-01	3.11E-03	$13.57^{+6.97}_{-5.88}$	$3.87^{+5.15}_{-4.02}$	$9.70^{+5.37}_{-4.24}$	2.40E+35	1.53E+34	1.21E+35
357	0.00E+00	0.00E+00	0.00E+00	$12645.00^{+113.59}_{-112.58}$	$8422.66^{+92.89}_{-91.88}$	$4222.34^{+66.07}_{-65.06}$	2.90E+37	4.42E+36	6.81E+36
358	0.00E+00	0.00E+00	8.13E-44	$141.76^{+13.16}_{-12.11}$	$93.45^{+10.84}_{-9.78}$	$48.32^{+8.20}_{-7.12}$	2.31E+36	3.43E+35	5.57E+35
359	0.00E+00	0.00E+00	1.63E-42	$876.88^{+30.66}_{-29.64}$	$838.91^{+30.00}_{-28.98}$	$37.96^{+7.31}_{-6.22}$	4.16E+37	8.28E+36	1.32E+36
360	1.35E-02	7.98E-03	4.01E-01	$7.56^{+5.10}_{-3.96}$	$6.77^{+4.58}_{-3.42}$	$0.79^{+3.18}_{-1.92}$	2.67E+34	5.68E+33	1.94E+33
361	5.96E-07	1.84E-08	4.20E-01	$20.37^{+6.67}_{-5.57}$	$19.59^{+6.20}_{-5.09}$	$0.77^{+3.42}_{-2.18}$	2.49E+35	5.21E+34	6.78E+33
362	3.12E-04	1.68E-05	5.15E-01	$13.56^{+6.01}_{-4.90}$	$13.29^{+5.47}_{-4.34}$	$0.27^{+3.42}_{-2.19}$	1.62E+35	3.45E+34	2.27E+33
363	1.65E-28	7.01E-45	1.79E-01	$79.21^{+11.46}_{-10.41}$	$74.72^{+10.27}_{-9.21}$	$4.49^{+5.91}_{-4.80}$	3.63E+35	8.45E+34	1.40E+34
364	2.03E-02	1.00E+00	3.27E-03	$3.49^{+3.40}_{-2.16}$	$-0.56^{+1.87}_{-99.99}$	$4.05^{+3.40}_{-2.16}$	1.97E+35	-9.99E+00	1.64E+35
365	0.00E+00	8.23E-38	1.60E-17	$140.55^{+14.78}_{-13.74}$	$78.71^{+10.74}_{-9.68}$	$61.85^{+10.80}_{-9.74}$	1.06E+36	1.54E+35	3.12E+35
366	1.04E-19	2.56E-18	5.70E-05	$21.54^{+5.87}_{-4.76}$	$15.47^{+5.09}_{-3.95}$	$6.07^{+3.78}_{-2.58}$	3.29E+35	5.30E+34	6.56E+34
367	0.00E+00	0.00E+00	8.58E-10	$127.35^{+12.70}_{-11.65}$	$111.37^{+11.85}_{-10.80}$	$15.98^{+5.45}_{-4.32}$	4.18E+35	8.58E+34	3.65E+34
368	2.78E-02	2.03E-03	9.86E-01	$11.38^{+7.47}_{-6.39}$	$15.60^{+7.32}_{-6.23}$	$-4.22^{+2.66}_{-1.30}$	3.37E+34	1.05E+34	-9.99E+00
369	1.76E-05	1.45E-04	2.74E-02	$26.30^{+8.63}_{-7.56}$	$21.11^{+7.94}_{-6.86}$	$5.18^{+4.29}_{-3.12}$	6.10E+34	1.11E+34	8.47E+33
370	0.00E+00	0.00E+00	0.00E+00	$2673.89^{+52.99}_{-51.98}$	$1875.50^{+44.59}_{-43.58}$	$798.40^{+29.35}_{-28.33}$	6.18E+36	9.84E+35	1.30E+36
371	0.00E+00	0.00E+00	0.00E+00	$684.74^{+27.87}_{-26.85}$	$437.93^{+22.66}_{-21.63}$	$246.81^{+16.93}_{-15.90}$	1.60E+36	2.32E+35	4.08E+35
372	0.00E+00	0.00E+00	0.00E+00	$659.15^{+27.12}_{-26.10}$	$363.99^{+20.52}_{-19.49}$	$295.16^{+18.37}_{-17.34}$	1.40E+36	1.76E+35	4.40E+35
373	0.00E+00	0.00E+00	0.00E+00	$1535.10^{+40.43}_{-39.42}$	$900.12^{+31.15}_{-30.13}$	$634.98^{+26.43}_{-25.41}$	6.31E+36	9.09E+35	1.78E+36
374	0.00E+00	0.00E+00	0.00E+00	$606.56^{+26.34}_{-25.32}$	$429.24^{+22.45}_{-21.42}$	$177.32^{+14.52}_{-13.48}$	1.42E+36	2.27E+35	2.93E+35
375	2.44E-27	3.14E-25	8.82E-05	$91.84^{+12.62}_{-11.57}$	$74.77^{+11.20}_{-10.14}$	$17.07^{+6.64}_{-5.54}$	4.08E+36	6.94E+35	5.55E+35

Source No.	*pns* (0.5 − 8.0 keV)	*pns* (0.5 − 2.0 keV)	*pns* (2.0 − 8.0 keV)	*net_cts* (0.5 − 8.0 keV)	*net_cts* (0.5 − 2.0 keV)	*net_cts* (2.0 − 8.0 keV)	*luminosity* (0.5 − 8.0 keV)	*luminosity* (0.5 − 2.0 keV)	*luminosity* (2.0 − 8.0 keV)
376	0.00E+00	0.00E+00	0.00E+00	$2061.33^{+46.81}_{-45.80}$	$1636.23^{+41.84}_{-40.82}$	$425.10^{+21.78}_{-20.76}$	4.75E+36	8.54E+35	6.91E+35
377	0.00E+00	0.00E+00	0.00E+00	$4067.62^{+65.12}_{-64.11}$	$2542.88^{+51.78}_{-50.77}$	$1524.73^{+40.15}_{-39.14}$	8.72E+36	1.24E+36	2.30E+36
378	0.00E+00	2.49E-06	0.00E+00	$81.97^{+10.58}_{-9.52}$	$13.84^{+5.45}_{-4.32}$	$68.13^{+9.53}_{-8.46}$	2.80E+35	1.13E+34	1.61E+35
379	0.00E+00	0.00E+00	0.00E+00	$9152.46^{+96.86}_{-95.85}$	$6800.55^{+83.64}_{-82.63}$	$2351.91^{+49.58}_{-48.57}$	1.98E+37	3.35E+36	3.57E+36
380	1.70E-06	7.53E-05	3.35E-03	$33.82^{+9.73}_{-8.67}$	$24.68^{+8.69}_{-7.62}$	$9.14^{+5.22}_{-4.09}$	7.56E+34	1.25E+34	1.44E+34
381	0.00E+00	0.00E+00	0.00E+00	$13608.33^{+117.88}_{-116.87}$	$8488.29^{+93.36}_{-92.35}$	$5120.04^{+72.63}_{-71.62}$	2.90E+37	4.12E+36	7.67E+36
382	0.00E+00	0.00E+00	0.00E+00	$1129.11^{+34.71}_{-33.69}$	$823.07^{+29.80}_{-28.77}$	$306.04^{+18.56}_{-17.52}$	1.17E+38	1.56E+37	2.48E+37
383	0.00E+00	0.00E+00	0.00E+00	$1687.04^{+42.38}_{-41.36}$	$1102.39^{+34.51}_{-33.49}$	$584.66^{+25.29}_{-24.26}$	3.70E+36	5.49E+35	9.04E+35
384	5.68E-03	6.93E-03	2.72E-01	$16.71^{+8.33}_{-7.26}$	$14.68^{+7.67}_{-6.59}$	$2.03^{+4.15}_{-2.97}$	4.73E+34	9.77E+33	3.99E+33
385	5.16E-35	2.00E-37	2.26E-02	$75.80^{+10.75}_{-9.69}$	$70.15^{+10.16}_{-9.10}$	$5.65^{+4.44}_{-3.27}$	1.65E+35	3.48E+34	8.66E+33
386	3.29E-14	3.97E-02	5.34E-29	$52.21^{+10.27}_{-9.22}$	$10.14^{+7.24}_{-6.15}$	$42.07^{+7.91}_{-6.83}$	1.20E+35	5.26E+33	6.81E+34
387	7.35E-04	1.17E-03	1.03E-01	$6.17^{+3.96}_{-2.77}$	$4.26^{+3.40}_{-2.16}$	$1.91^{+2.94}_{-1.63}$	2.77E+35	4.01E+34	6.27E+34
388	7.46E-18	5.12E-14	2.07E-05	$54.76^{+10.00}_{-8.94}$	$42.69^{+9.00}_{-7.93}$	$12.07^{+5.22}_{-4.09}$	1.20E+35	2.13E+34	1.87E+34
389	3.58E-15	3.92E-14	1.39E-02	$49.44^{+9.72}_{-8.66}$	$43.75^{+9.13}_{-8.06}$	$5.69^{+4.29}_{-3.11}$	1.08E+35	2.17E+34	8.72E+33
390	2.17E-02	2.78E-03	9.92E-01	$13.00^{+7.98}_{-6.90}$	$16.85^{+7.90}_{-6.82}$	$-3.85^{+2.36}_{-0.91}$	3.14E+34	9.52E+33	-9.99E+00
391	1.10E-09	2.95E-02	2.53E-10	$25.31^{+7.07}_{-5.97}$	$5.38^{+4.43}_{-3.27}$	$19.94^{+6.08}_{-4.97}$	8.77E+34	4.43E+33	4.77E+34
392	0.00E+00	0.00E+00	0.00E+00	$10941.00^{+105.80}_{-104.80}$	$7189.23^{+86.00}_{-84.99}$	$3751.77^{+62.32}_{-61.31}$	2.38E+37	3.56E+36	5.75E+36
393	1.35E-02	2.55E-01	1.68E-04	$15.02^{+8.40}_{-7.33}$	$4.26^{+7.22}_{-6.13}$	$10.76^{+5.11}_{-3.97}$	3.61E+34	2.37E+33	1.81E+34
394	9.28E-03	2.25E-02	1.18E-01	$16.08^{+8.51}_{-7.44}$	$12.69^{+7.88}_{-6.80}$	$3.40^{+4.14}_{-2.96}$	3.92E+34	7.11E+33	5.79E+33
395	0.00E+00	0.00E+00	0.00E+00	$625.40^{+26.77}_{-25.75}$	$440.86^{+22.77}_{-21.75}$	$184.54^{+14.81}_{-13.77}$	1.43E+36	2.28E+35	2.97E+35
396	2.84E-03	9.65E-04	7.02E-01	$21.07^{+9.43}_{-8.36}$	$22.09^{+9.05}_{-7.99}$	$-1.02^{+3.63}_{-2.42}$	4.26E+34	1.02E+34	-9.99E+00
397	0.00E+00	0.00E+00	1.19E-11	$34.52^{+6.98}_{-5.88}$	$24.88^{+6.07}_{-4.96}$	$9.64^{+4.28}_{-3.10}$	1.52E+36	2.28E+35	3.12E+35
398	0.00E+00	0.00E+00	0.00E+00	$1046.92^{+33.67}_{-32.65}$	$979.43^{+32.51}_{-31.49}$	$67.48^{+9.65}_{-8.59}$	2.38E+36	5.11E+35	1.08E+35
399	4.89E-03	4.03E-03	2.47E-01	$13.46^{+6.99}_{-5.90}$	$11.04^{+5.99}_{-4.87}$	$2.42^{+4.44}_{-3.27}$	3.26E+34	6.18E+33	4.10E+33
400	1.33E-27	3.52E-24	3.58E-09	$25.93^{+6.27}_{-5.16}$	$15.79^{+5.09}_{-3.95}$	$10.14^{+4.43}_{-3.26}$	1.21E+36	1.54E+35	3.48E+35
401	0.00E+00	0.00E+00	0.00E+00	$4767.17^{+70.55}_{-69.54}$	$3227.43^{+58.05}_{-57.04}$	$1539.74^{+40.80}_{-39.78}$	4.27E+37	7.39E+36	9.28E+36
402	0.00E+00	0.00E+00	0.00E+00	$14819.06^{+123.09}_{-122.09}$	$10201.84^{+102.34}_{-101.33}$	$4617.21^{+69.10}_{-68.09}$	3.17E+37	4.97E+36	6.95E+36
403	0.00E+00	0.00E+00	0.00E+00	$1294.26^{+37.43}_{-36.41}$	$951.26^{+32.29}_{-31.27}$	$343.00^{+19.68}_{-18.65}$	2.85E+36	4.76E+35	5.33E+35
404	0.00E+00	4.34E-44	9.69E-13	$191.43^{+17.86}_{-16.83}$	$150.81^{+15.94}_{-14.91}$	$40.62^{+8.86}_{-7.79}$	3.90E+35	7.05E+34	5.81E+34
405	0.00E+00	0.00E+00	0.00E+00	$5372.38^{+74.83}_{-73.82}$	$3662.75^{+62.05}_{-61.04}$	$1709.63^{+42.52}_{-41.51}$	1.09E+37	1.70E+36	2.42E+36
406	0.00E+00	0.00E+00	0.00E+00	$5811.42^{+77.89}_{-76.88}$	$3583.00^{+61.50}_{-60.48}$	$2228.42^{+48.48}_{-47.46}$	1.21E+37	1.71E+36	3.26E+36
407	9.41E-03	8.84E-03	3.34E-01	$8.74^{+5.45}_{-4.32}$	$7.65^{+4.97}_{-3.83}$	$1.09^{+3.18}_{-1.91}$	2.22E+34	4.47E+33	1.94E+33
408	0.00E+00	0.00E+00	0.00E+00	$3532.16^{+60.99}_{-59.98}$	$2311.22^{+49.65}_{-48.64}$	$1220.94^{+36.12}_{-35.10}$	7.19E+36	1.08E+36	1.74E+36
409	7.91E-24	6.81E-22	1.39E-03	$84.18^{+12.44}_{-11.39}$	$74.30^{+11.66}_{-10.61}$	$9.88^{+5.23}_{-4.10}$	1.85E+35	3.71E+34	1.53E+34
410	1.69E-04	1.53E-03	2.01E-02	$22.35^{+8.35}_{-7.27}$	$16.95^{+7.63}_{-6.55}$	$5.41^{+4.28}_{-3.11}$	5.11E+34	8.76E+33	8.73E+33
411	6.00E-07	1.06E-06	8.98E-02	$54.55^{+13.69}_{-12.65}$	$47.28^{+12.39}_{-11.35}$	$7.26^{+6.65}_{-5.55}$	1.18E+35	2.35E+34	1.10E+34
412	0.00E+00	0.00E+00	0.00E+00	$1274.29^{+38.02}_{-36.99}$	$987.97^{+33.67}_{-32.65}$	$286.32^{+18.43}_{-17.39}$	2.57E+36	4.58E+35	4.06E+35
413	0.00E+00	0.00E+00	0.00E+00	$7531.62^{+90.62}_{-89.56}$	$5484.46^{+77.98}_{-76.92}$	$2047.17^{+46.93}_{-45.89}$	1.67E+37	2.76E+36	3.21E+36
414	2.01E-11	9.12E-03	5.04E-10	$14.47^{+5.09}_{-3.96}$	$2.59^{+2.94}_{-1.63}$	$11.88^{+4.71}_{-3.56}$	6.79E+35	2.59E+34	4.04E+35
415	0.00E+00	0.00E+00	0.00E+00	$5251.45^{+75.38}_{-74.34}$	$3783.85^{+64.51}_{-63.47}$	$1467.59^{+39.76}_{-38.73}$	1.07E+37	1.76E+36	2.09E+36
416	0.00E+00	0.00E+00	0.00E+00	$10063.08^{+106.72}_{-105.66}$	$9469.00^{+102.40}_{-101.35}$	$594.08^{+30.96}_{-29.87}$	2.17E+37	4.64E+36	9.05E+35
417	0.00E+00	0.00E+00	0.00E+00	$3699.21^{+62.09}_{-61.08}$	$2807.78^{+54.16}_{-53.15}$	$891.43^{+31.10}_{-30.08}$	9.28E+36	1.64E+36	1.56E+36

Source No.	*pns* (0.5 – 8.0 keV)	*pns* (0.5 – 2.0 keV)	*pns* (2.0 – 8.0 keV)	*net_cts* (0.5 – 8.0 keV)	*net_cts* (0.5 – 2.0 keV)	*net_cts* (2.0 – 8.0 keV)	*luminosity* (0.5 – 8.0 keV)	*luminosity* (0.5 – 2.0 keV)	*luminosity* (2.0 – 8.0 keV)
418	8.72E-20	3.87E-17	7.44E-07	$22.62^{+5.98}_{-4.87}$	$13.70^{+4.84}_{-3.69}$	$8.92^{+4.28}_{-3.11}$	2.91E+36	4.27E+35	7.88E+35
419	1.94E-09	3.67E-11	1.93E-02	$57.66^{+12.59}_{-11.55}$	$42.33^{+9.47}_{-8.40}$	$15.33^{+8.96}_{-7.89}$	1.74E+35	3.03E+34	3.19E+34
420	7.31E-14	1.71E-01	2.68E-23	$39.24^{+8.55}_{-7.47}$	$3.83^{+5.11}_{-3.98}$	$35.41^{+7.39}_{-6.30}$	8.38E+34	1.86E+33	5.33E+34
421	4.92E-15	9.67E-08	1.56E-09	$33.30^{+7.62}_{-6.53}$	$18.09^{+6.08}_{-4.97}$	$15.21^{+5.33}_{-4.20}$	8.94E+34	1.12E+34	2.85E+34
422	0.00E+00	0.00E+00	0.00E+00	$3911.49^{+64.06}_{-63.05}$	$3093.56^{+57.12}_{-56.11}$	$817.93^{+29.78}_{-28.76}$	7.91E+36	1.43E+36	1.16E+36
423	5.68E-03	2.42E-02	4.73E-02	$19.35^{+9.35}_{-8.29}$	$13.84^{+8.51}_{-7.45}$	$5.52^{+4.75}_{-3.60}$	4.91E+34	8.25E+33	9.72E+33
424	0.00E+00	0.00E+00	0.00E+00	$23533.23^{+154.64}_{-153.63}$	$17433.49^{+133.20}_{-132.19}$	$6099.73^{+79.28}_{-78.28}$	5.88E+37	1.02E+37	1.06E+37
425	0.00E+00	0.00E+00	0.00E+00	$3830.70^{+63.02}_{-62.01}$	$2516.83^{+51.29}_{-50.28}$	$1313.87^{+37.31}_{-36.30}$	8.08E+36	1.21E+36	1.95E+36
426	6.69E-05	1.50E-03	5.56E-03	$24.11^{+8.47}_{-7.40}$	$16.98^{+7.60}_{-6.52}$	$7.13^{+4.59}_{-3.44}$	5.21E+34	8.34E+33	1.09E+34
427	4.82E-02	3.53E-01	2.14E-03	$8.25^{+6.39}_{-5.29}$	$1.94^{+5.47}_{-4.35}$	$6.31^{+4.13}_{-2.95}$	2.34E+34	1.27E+33	1.26E+34
428	7.66E-03	1.25E-02	2.14E-01	$13.60^{+7.30}_{-6.21}$	$11.37^{+6.70}_{-5.61}$	$2.23^{+3.81}_{-2.61}$	4.60E+34	8.97E+33	5.25E+33
429	0.00E+00	0.00E+00	0.00E+00	$1530.68^{+40.53}_{-39.52}$	$1148.00^{+35.29}_{-34.27}$	$382.68^{+20.70}_{-19.67}$	3.44E+36	5.84E+35	6.06E+35
430	0.00E+00	0.00E+00	0.00E+00	$1308.88^{+37.43}_{-36.41}$	$973.63^{+32.41}_{-31.40}$	$335.25^{+19.46}_{-18.43}$	2.80E+36	4.72E+35	5.05E+35
431	4.91E-04	2.67E-04	4.92E-01	$20.60^{+8.27}_{-7.20}$	$20.22^{+7.92}_{-6.84}$	$0.38^{+3.40}_{-2.16}$	4.69E+34	1.04E+34	6.03E+32
432	0.00E+00	0.00E+00	0.00E+00	$16272.56^{+128.83}_{-127.83}$	$11239.99^{+107.29}_{-106.28}$	$5032.56^{+72.02}_{-71.01}$	3.29E+37	5.20E+36	7.13E+36
433	0.00E+00	0.00E+00	0.00E+00	$1369.39^{+38.50}_{-37.48}$	$914.84^{+31.74}_{-30.72}$	$454.56^{+22.49}_{-21.46}$	2.92E+36	4.45E+35	6.83E+35
434	2.33E-04	3.50E-01	1.27E-10	$21.96^{+8.36}_{-7.28}$	$2.37^{+6.48}_{-5.38}$	$19.59^{+5.98}_{-4.87}$	4.83E+34	1.18E+33	3.04E+34
435	0.00E+00	0.00E+00	0.00E+00	$2934.95^{+55.33}_{-54.32}$	$2017.45^{+46.06}_{-45.05}$	$917.50^{+31.36}_{-30.34}$	6.31E+36	9.84E+35	1.39E+36
436	0.00E+00	0.00E+00	0.00E+00	$2303.18^{+49.67}_{-48.66}$	$1766.72^{+43.70}_{-42.69}$	$536.46^{+24.37}_{-23.34}$	4.64E+36	8.17E+35	7.59E+35
437	6.29E-28	1.01E-06	1.23E-37	$78.41^{+11.45}_{-10.40}$	$27.96^{+8.36}_{-7.28}$	$50.45^{+8.47}_{-7.40}$	1.77E+35	1.43E+34	8.03E+34
438	0.00E+00	0.00E+00	0.00E+00	$4019.25^{+64.81}_{-63.80}$	$2988.00^{+56.07}_{-55.05}$	$1031.25^{+33.25}_{-32.23}$	8.15E+36	1.39E+36	1.47E+36
439	3.73E-02	6.67E-03	8.64E-01	$11.77^{+8.03}_{-6.95}$	$14.50^{+7.56}_{-6.48}$	$-2.73^{+3.67}_{-2.46}$	3.95E+34	1.14E+34	-9.99E+00
440	0.00E+00	0.00E+00	9.27E-23	$193.18^{+16.91}_{-15.88}$	$115.14^{+12.66}_{-11.61}$	$78.04^{+11.86}_{-10.81}$	1.24E+36	1.88E+35	3.39E+35
441	1.93E-02	5.71E-03	9.24E-01	$10.13^{+6.49}_{-5.39}$	$11.71^{+6.39}_{-5.29}$	$-1.58^{+2.34}_{-0.86}$	3.91E+34	1.06E+34	-9.99E+00
442	0.00E+00	0.00E+00	0.00E+00	$4216.02^{+66.50}_{-65.49}$	$3076.64^{+56.75}_{-55.74}$	$1139.38^{+35.40}_{-34.39}$	1.10E+37	1.90E+36	2.06E+36
443	0.00E+00	0.00E+00	0.00E+00	$2102.49^{+47.45}_{-46.44}$	$1532.62^{+40.76}_{-39.74}$	$569.87^{+25.04}_{-24.02}$	4.32E+36	7.20E+35	8.22E+35
444	0.00E+00	0.00E+00	0.00E+00	$904.25^{+31.33}_{-30.31}$	$606.95^{+25.88}_{-24.85}$	$297.30^{+18.37}_{-17.34}$	1.93E+36	2.93E+35	4.46E+35
445	9.96E-37	3.79E-04	0.00E+00	$73.99^{+10.53}_{-9.47}$	$13.89^{+6.18}_{-5.07}$	$60.09^{+9.05}_{-7.98}$	1.58E+35	6.73E+33	9.05E+34
446	0.00E+00	0.00E+00	0.00E+00	$1755.71^{+43.30}_{-42.28}$	$1215.32^{+36.27}_{-35.25}$	$540.39^{+24.36}_{-23.34}$	3.84E+36	6.02E+35	8.32E+35
447	2.50E-05	1.83E-05	3.86E-02	$17.77^{+6.55}_{-5.45}$	$11.59^{+5.01}_{-3.87}$	$6.18^{+4.94}_{-3.79}$	9.03E+35	1.49E+35	2.12E+35
448	0.00E+00	0.00E+00	2.05E-19	$315.08^{+20.04}_{-19.01}$	$279.11^{+18.87}_{-17.84}$	$35.97^{+7.62}_{-6.54}$	6.55E+35	1.33E+35	5.26E+34
449	1.18E-35	3.78E-34	8.80E-10	$116.02^{+13.91}_{-12.86}$	$73.30^{+10.43}_{-9.37}$	$42.72^{+9.86}_{-8.79}$	7.34E+35	1.19E+35	1.82E+35
450	4.50E-10	1.48E-08	5.26E-03	$32.25^{+8.14}_{-7.06}$	$25.16^{+7.24}_{-6.15}$	$7.08^{+4.58}_{-3.42}$	6.95E+34	1.23E+34	1.08E+34
451	4.35E-07	1.95E-05	2.79E-03	$35.47^{+9.74}_{-8.68}$	$27.22^{+8.89}_{-7.82}$	$8.25^{+4.85}_{-3.71}$	7.60E+34	1.33E+34	1.25E+34
452	0.00E+00	0.00E+00	0.00E+00	$698.12^{+27.85}_{-26.83}$	$378.62^{+20.72}_{-19.69}$	$319.50^{+19.24}_{-18.21}$	2.79E+36	3.70E+35	8.72E+35
453	0.00E+00	0.00E+00	0.00E+00	$22259.86^{+150.37}_{-149.36}$	$14970.30^{+123.52}_{-122.51}$	$7289.56^{+86.44}_{-85.43}$	4.81E+37	7.34E+36	1.11E+37
454	2.42E-03	3.38E-03	2.14E-01	$12.72^{+6.38}_{-5.28}$	$10.70^{+5.79}_{-4.67}$	$2.03^{+3.61}_{-2.39}$	2.71E+34	5.17E+33	3.05E+33
455	3.23E-07	1.13E-05	5.46E-03	$22.20^{+7.00}_{-5.90}$	$15.14^{+5.89}_{-4.77}$	$7.07^{+4.58}_{-3.42}$	6.55E+34	1.05E+34	1.45E+34
456	0.00E+00	0.00E+00	5.06E-02	$341.60^{+20.84}_{-19.81}$	$335.19^{+20.38}_{-19.35}$	$6.41^{+5.35}_{-4.22}$	7.57E+35	1.68E+35	1.00E+34
457	0.00E+00	0.00E+00	0.00E+00	$39645.06^{+200.24}_{-199.24}$	$24769.55^{+158.51}_{-157.50}$	$14875.51^{+123.01}_{-122.01}$	8.82E+37	1.25E+37	2.34E+37
458	0.00E+00	0.00E+00	0.00E+00	$3821.59^{+62.96}_{-61.95}$	$3535.75^{+60.57}_{-59.56}$	$285.84^{+18.05}_{-17.02}$	8.20E+36	1.72E+36	4.33E+35
459	8.73E-06	3.18E-06	3.08E-01	$21.41^{+7.32}_{-6.23}$	$19.96^{+6.82}_{-5.73}$	$1.45^{+3.61}_{-2.39}$	4.57E+34	9.65E+33	2.19E+33

Source No.	*pns* (0.5 − 8.0 keV)	*pns* (0.5 − 2.0 keV)	*pns* (2.0 − 8.0 keV)	*net_cts* (0.5 − 8.0 keV)	*net_cts* (0.5 − 2.0 keV)	*net_cts* (2.0 − 8.0 keV)	*luminosity* (0.5 − 8.0 keV)	*luminosity* (0.5 − 2.0 keV)	*luminosity* (2.0 − 8.0 keV)
460	0.00E+00	0.00E+00	0.00E+00	$1073.15^{+34.39}_{-33.38}$	$794.49^{+29.56}_{-28.54}$	$278.65^{+18.33}_{-17.30}$	2.52E+36	4.36E+35	4.56E+35
461	2.02E-04	2.96E-01	6.19E-05	$28.87^{+10.23}_{-9.17}$	$2.73^{+5.71}_{-4.60}$	$26.15^{+8.98}_{-7.92}$	1.31E+35	3.15E+33	8.00E+34
462	3.44E-03	5.35E-03	1.98E-01	$16.76^{+8.01}_{-6.94}$	$14.01^{+7.25}_{-6.16}$	$2.76^{+4.29}_{-3.12}$	4.30E+34	8.25E+33	4.97E+33
463	1.40E-02	7.80E-03	6.08E-01	$13.97^{+7.97}_{-6.89}$	$14.25^{+7.59}_{-6.51}$	$-0.28^{+3.42}_{-2.18}$	4.01E+34	9.41E+33	-9.99E+00
464	1.40E-45	3.40E-24	2.52E-23	$49.35^{+8.20}_{-7.12}$	$23.44^{+5.98}_{-4.86}$	$25.91^{+6.27}_{-5.17}$	6.38E+36	7.26E+35	2.31E+36
465	3.33E-05	3.83E-05	5.99E-02	$8.72^{+4.43}_{-3.27}$	$6.16^{+3.79}_{-2.58}$	$2.57^{+3.18}_{-1.91}$	4.02E+35	6.01E+34	8.61E+34
466	0.00E+00	0.00E+00	0.00E+00	$2669.31^{+53.15}_{-52.14}$	$1753.29^{+43.15}_{-42.14}$	$916.03^{+31.73}_{-30.71}$	6.65E+36	1.02E+36	1.59E+36
467	0.00E+00	0.00E+00	0.00E+00	$1041.90^{+33.82}_{-32.80}$	$672.86^{+27.48}_{-26.46}$	$369.04^{+20.41}_{-19.38}$	2.34E+36	3.41E+35	5.84E+35
468	0.00E+00	0.00E+00	1.03E-32	$1121.07^{+34.90}_{-33.88}$	$1078.78^{+34.21}_{-33.19}$	$42.29^{+7.84}_{-6.76}$	2.50E+36	5.44E+35	6.66E+34
469	0.00E+00	0.00E+00	0.00E+00	$17222.79^{+132.39}_{-131.39}$	$12630.87^{+113.54}_{-112.53}$	$4591.91^{+68.82}_{-67.81}$	3.78E+37	6.29E+36	7.11E+36
470	0.00E+00	0.00E+00	0.00E+00	$393.44^{+22.39}_{-21.36}$	$271.20^{+18.32}_{-17.28}$	$122.24^{+13.58}_{-12.54}$	9.48E+35	1.54E+35	2.04E+35
471	3.79E-06	1.32E-02	6.54E-08	$27.91^{+8.63}_{-7.55}$	$12.28^{+7.17}_{-6.08}$	$15.63^{+5.56}_{-4.44}$	6.22E+34	6.19E+33	2.46E+34
472	2.76E-03	4.78E-02	1.57E-02	$18.43^{+8.44}_{-7.37}$	$7.00^{+5.62}_{-4.50}$	$11.43^{+6.89}_{-5.80}$	1.29E+35	1.21E+34	5.45E+34
473	8.96E-04	3.60E-03	7.26E-02	$13.72^{+6.37}_{-5.27}$	$10.30^{+5.67}_{-4.55}$	$3.42^{+3.79}_{-2.58}$	2.90E+34	4.94E+33	5.10E+33
474	4.36E-22	7.67E-13	6.10E-11	$56.63^{+9.73}_{-8.67}$	$29.34^{+7.24}_{-6.16}$	$27.29^{+7.17}_{-6.08}$	1.98E+35	2.44E+34	6.58E+34
475	0.00E+00	0.00E+00	0.00E+00	$5904.49^{+78.43}_{-77.42}$	$3281.71^{+58.60}_{-57.59}$	$2622.78^{+52.75}_{-51.74}$	5.22E+37	7.38E+36	1.56E+37
476	0.00E+00	0.00E+00	0.00E+00	$53197.45^{+231.75}_{-230.75}$	$33365.90^{+183.77}_{-182.77}$	$19831.55^{+141.87}_{-140.87}$	1.16E+38	1.65E+37	3.06E+37
477	1.38E-09	1.17E-07	1.90E-03	$37.45^{+9.13}_{-8.07}$	$29.75^{+8.35}_{-7.28}$	$7.70^{+4.58}_{-3.42}$	8.24E+34	1.48E+34	1.19E+34
478	0.00E+00	0.00E+00	0.00E+00	$2108.27^{+47.22}_{-46.20}$	$1567.93^{+40.89}_{-39.87}$	$540.34^{+24.36}_{-23.34}$	4.57E+36	7.71E+35	8.25E+35
479	5.65E-16	6.71E-13	1.28E-04	$38.96^{+8.27}_{-7.19}$	$29.61^{+7.31}_{-6.22}$	$9.35^{+4.71}_{-3.56}$	8.76E+34	1.51E+34	1.48E+34
480	2.23E-04	6.36E-06	8.85E-01	$22.50^{+8.49}_{-7.42}$	$25.26^{+8.15}_{-7.07}$	$-2.76^{+3.41}_{-2.18}$	4.86E+34	1.24E+34	-9.99E+00
481	0.00E+00	0.00E+00	2.62E-01	$154.86^{+15.42}_{-14.38}$	$150.74^{+14.06}_{-13.02}$	$4.12^{+7.17}_{-6.09}$	8.87E+35	2.17E+35	1.60E+34
482	0.00E+00	0.00E+00	1.25E-07	$96.62^{+11.58}_{-10.52}$	$79.11^{+10.37}_{-9.31}$	$17.51^{+5.98}_{-4.87}$	2.98E+35	5.74E+34	3.76E+34
483	6.81E-06	5.27E-05	3.22E-02	$23.65^{+7.79}_{-6.71}$	$18.92^{+7.08}_{-5.99}$	$4.73^{+4.13}_{-2.95}$	5.00E+34	9.07E+33	7.05E+33
484	8.35E-11	5.40E-07	2.20E-05	$46.70^{+10.26}_{-9.20}$	$25.90^{+7.80}_{-6.72}$	$20.81^{+7.34}_{-6.26}$	1.01E+35	1.30E+34	3.16E+34
485	0.00E+00	0.00E+00	0.00E+00	$653.74^{+26.84}_{-25.82}$	$587.18^{+25.45}_{-24.43}$	$66.56^{+9.41}_{-8.35}$	1.41E+36	2.87E+35	1.01E+35
486	6.21E-10	8.37E-09	1.62E-02	$38.43^{+9.20}_{-8.13}$	$32.84^{+8.56}_{-7.49}$	$5.60^{+4.29}_{-3.12}$	8.24E+34	1.60E+34	8.46E+33
487	0.00E+00	0.00E+00	0.00E+00	$5944.35^{+78.19}_{-77.18}$	$4058.95^{+64.79}_{-63.78}$	$1885.39^{+44.47}_{-43.46}$	1.59E+37	2.50E+36	3.53E+36
488	0.00E+00	0.00E+00	0.00E+00	$6444.36^{+81.46}_{-80.45}$	$4281.28^{+66.61}_{-65.60}$	$2163.08^{+47.57}_{-46.56}$	1.39E+37	2.09E+36	3.27E+36
489	1.49E-21	1.74E-11	7.75E-12	$74.15^{+11.67}_{-10.62}$	$33.76^{+8.09}_{-7.01}$	$40.40^{+9.03}_{-7.96}$	3.34E+35	3.78E+34	1.24E+35
490	4.01E-43	1.08E-38	2.55E-12	$109.16^{+12.92}_{-11.88}$	$68.30^{+9.90}_{-8.84}$	$40.87^{+8.98}_{-7.91}$	1.16E+36	1.85E+35	2.91E+35
491	6.13E-08	9.33E-10	3.41E-01	$8.32^{+4.12}_{-2.94}$	$7.73^{+3.96}_{-2.76}$	$0.59^{+2.32}_{-0.83}$	4.31E+35	8.15E+34	2.26E+34
492	0.00E+00	0.00E+00	0.00E+00	$316.55^{+19.24}_{-18.21}$	$233.95^{+16.71}_{-15.68}$	$82.60^{+10.32}_{-9.26}$	6.72E+35	1.13E+35	1.24E+35
493	1.11E-11	2.35E-03	1.92E-10	$47.93^{+10.20}_{-9.15}$	$12.85^{+6.40}_{-5.30}$	$35.08^{+8.50}_{-7.43}$	1.96E+35	1.30E+34	9.75E+34
494	4.40E-10	4.05E-05	4.48E-06	$12.24^{+4.72}_{-3.56}$	$5.58^{+3.61}_{-2.38}$	$6.66^{+3.79}_{-2.58}$	1.84E+36	1.79E+35	7.28E+35
495	1.75E-03	1.31E-02	4.38E-02	$3.51^{+3.18}_{-1.91}$	$1.83^{+2.66}_{-1.29}$	$1.67^{+2.66}_{-1.29}$	2.45E+35	2.53E+34	8.81E+34
496	5.68E-39	2.36E-24	1.10E-16	$73.86^{+10.43}_{-9.37}$	$47.75^{+8.67}_{-7.60}$	$26.11^{+6.55}_{-5.45}$	1.93E+35	2.87E+34	4.77E+34
497	2.79E-14	8.13E-15	3.31E-01	$40.08^{+8.61}_{-7.54}$	$39.10^{+8.41}_{-7.33}$	$0.98^{+2.94}_{-1.63}$	1.05E+35	2.28E+34	1.84E+33
498	4.15E-09	1.52E-08	7.19E-02	$30.14^{+8.00}_{-6.92}$	$27.31^{+7.63}_{-6.55}$	$2.84^{+3.40}_{-2.16}$	8.48E+34	1.70E+34	5.68E+33
499	4.72E-05	1.35E-04	3.10E-02	$15.69^{+6.21}_{-5.10}$	$9.97^{+4.86}_{-3.71}$	$5.71^{+4.60}_{-3.45}$	3.13E+35	4.49E+34	8.04E+34
500	0.00E+00	9.32E-19	3.48E-33	$56.60^{+8.80}_{-7.72}$	$22.30^{+5.98}_{-4.86}$	$34.30^{+7.06}_{-5.97}$	1.03E+36	9.24E+34	4.38E+35
501	2.51E-17	1.25E-03	2.56E-28	$52.11^{+9.77}_{-8.70}$	$15.51^{+7.07}_{-5.98}$	$36.60^{+7.38}_{-6.30}$	1.12E+35	7.55E+33	5.53E+34

Source No.	*pns* (0.5 – 8.0 keV)	*pns* (0.5 – 2.0 keV)	*pns* (2.0 – 8.0 keV)	*net_cts* (0.5 – 8.0 keV)	*net_cts* (0.5 – 2.0 keV)	*net_cts* (2.0 – 8.0 keV)	*luminosity* (0.5 – 8.0 keV)	*luminosity* (0.5 – 2.0 keV)	*luminosity* (2.0 – 8.0 keV)
502	1.55E-23	9.82E-15	2.49E-11	$58.37^{+9.83}_{-8.77}$	$39.06^{+8.41}_{-7.34}$	$19.31^{+5.88}_{-4.76}$	1.25E+35	1.90E+34	2.90E+34
503	0.00E+00	0.00E+00	0.00E+00	$377.00^{+20.87}_{-19.84}$	$232.20^{+16.58}_{-15.55}$	$144.80^{+13.36}_{-12.32}$	1.05E+36	1.51E+35	2.80E+35
504	5.78E-07	1.52E-11	3.88E-01	$12.16^{+4.98}_{-3.83}$	$11.38^{+4.57}_{-3.41}$	$0.78^{+2.95}_{-1.64}$	7.29E+35	1.46E+35	3.37E+34
505	9.86E-13	4.48E-11	4.26E-03	$42.51^{+9.19}_{-8.12}$	$35.67^{+8.49}_{-7.41}$	$6.83^{+4.44}_{-3.27}$	8.94E+34	1.71E+34	1.01E+34
506	4.38E-10	1.02E-14	2.45E-01	$30.00^{+7.69}_{-6.60}$	$27.46^{+6.76}_{-5.65}$	$2.55^{+4.51}_{-3.35}$	7.12E+35	1.65E+35	4.08E+34
507	9.37E-04	7.18E-04	3.76E-01	$16.70^{+7.33}_{-6.24}$	$15.71^{+6.91}_{-5.82}$	$0.99^{+3.41}_{-2.17}$	3.52E+34	7.53E+33	1.47E+33
508	0.00E+00	0.00E+00	0.00E+00	$335.60^{+19.84}_{-18.81}$	$254.08^{+17.43}_{-16.40}$	$81.52^{+10.26}_{-9.20}$	7.19E+35	1.24E+35	1.23E+35
509	8.11E-33	8.64E-16	1.20E-22	$72.36^{+10.59}_{-9.53}$	$40.89^{+8.54}_{-7.47}$	$31.48^{+6.98}_{-5.89}$	1.53E+35	1.96E+34	4.68E+34
510	4.07E-09	1.09E-02	4.73E-09	$29.67^{+7.92}_{-6.84}$	$8.35^{+5.34}_{-4.21}$	$21.32^{+6.46}_{-5.36}$	8.25E+34	5.44E+33	4.12E+34
511	0.00E+00	0.00E+00	0.00E+00	$1680.11^{+42.45}_{-41.43}$	$1016.52^{+33.19}_{-32.17}$	$663.59^{+27.12}_{-26.10}$	3.43E+36	4.77E+35	9.51E+35
512	2.28E-43	2.29E-32	1.16E-15	$105.02^{+12.42}_{-11.36}$	$59.99^{+9.29}_{-8.21}$	$45.03^{+8.91}_{-7.83}$	2.74E+36	4.05E+35	7.86E+35
513	0.00E+00	0.00E+00	0.00E+00	$251.96^{+17.40}_{-16.37}$	$193.72^{+15.38}_{-14.35}$	$58.24^{+8.92}_{-7.85}$	5.30E+35	9.26E+34	8.63E+34
514	6.53E-09	3.99E-13	6.19E-01	$11.57^{+4.71}_{-3.56}$	$11.53^{+4.57}_{-3.41}$	$0.04^{+2.32}_{-0.83}$	6.02E+35	1.22E+35	1.53E+33
515	0.00E+00	0.00E+00	0.00E+00	$582.87^{+25.49}_{-24.47}$	$443.80^{+22.37}_{-21.35}$	$139.07^{+12.99}_{-11.94}$	1.23E+36	2.13E+35	2.06E+35
516	1.80E-04	1.80E-02	3.26E-03	$6.51^{+3.96}_{-2.77}$	$2.47^{+2.94}_{-1.63}$	$4.05^{+3.40}_{-2.16}$	4.15E+35	3.30E+34	1.88E+35
517	6.43E-20	8.22E-06	1.82E-16	$63.64^{+10.76}_{-9.70}$	$19.37^{+6.83}_{-5.73}$	$44.27^{+8.88}_{-7.81}$	2.56E+35	1.91E+34	1.22E+35
518	0.00E+00	0.00E+00	0.00E+00	$3331.05^{+58.89}_{-57.88}$	$2509.55^{+51.26}_{-50.25}$	$821.50^{+29.74}_{-28.72}$	7.05E+36	1.21E+36	1.22E+36
519	0.00E+00	0.00E+00	0.00E+00	$253.89^{+18.07}_{-17.04}$	$128.46^{+13.04}_{-12.00}$	$125.43^{+13.13}_{-12.08}$	1.04E+36	1.29E+35	3.49E+35
520	0.00E+00	0.00E+00	0.00E+00	$45354.20^{+214.06}_{-213.05}$	$28973.73^{+171.29}_{-170.29}$	$16380.46^{+129.05}_{-128.04}$	1.26E+38	1.88E+37	3.17E+37
521	0.00E+00	0.00E+00	0.00E+00	$181.80^{+15.14}_{-14.10}$	$94.00^{+11.29}_{-10.24}$	$87.81^{+10.74}_{-9.68}$	4.96E+35	5.97E+34	1.67E+35
522	0.00E+00	0.00E+00	9.73E-01	$8483.33^{+93.23}_{-92.22}$	$8485.96^{+93.22}_{-92.22}$	$-2.63^{+2.33}_{-0.85}$	1.78E+37	4.04E+36	-9.99E+00
523	0.00E+00	0.00E+00	0.00E+00	$264.16^{+18.37}_{-17.34}$	$145.55^{+13.97}_{-12.93}$	$118.62^{+12.58}_{-11.53}$	5.39E+35	6.79E+34	1.70E+35
524	1.62E-02	3.82E-03	2.99E-01	$13.56^{+7.92}_{-6.84}$	$10.69^{+5.81}_{-4.69}$	$2.87^{+6.04}_{-4.94}$	7.07E+34	1.39E+34	1.01E+34
525	8.27E-02	5.05E-04	1.00E+00	$2.39^{+3.18}_{-1.91}$	$3.66^{+3.18}_{-1.91}$	$-1.27^{+1.87}_{-99.99}$	1.54E+35	4.79E+34	-9.99E+00
526	1.09E-04	2.28E-04	2.51E-02	$26.17^{+9.15}_{-8.08}$	$14.79^{+6.25}_{-5.14}$	$11.38^{+7.29}_{-6.21}$	2.06E+35	2.99E+34	6.02E+34
527	0.00E+00	0.00E+00	0.00E+00	$1004.80^{+33.44}_{-32.42}$	$633.59^{+26.81}_{-25.79}$	$371.21^{+20.67}_{-19.64}$	2.03E+36	2.94E+35	5.28E+35
528	2.51E-08	1.96E-06	1.04E-03	$44.24^{+10.82}_{-9.76}$	$26.02^{+8.07}_{-6.99}$	$18.22^{+7.86}_{-6.78}$	1.05E+35	1.44E+34	3.02E+34
529	3.27E-04	9.29E-05	5.63E-01	$17.11^{+7.08}_{-5.99}$	$17.08^{+6.74}_{-5.64}$	$0.02^{+3.19}_{-1.92}$	3.66E+34	8.32E+33	3.53E+31
530	0.00E+00	1.18E-34	5.84E-16	$41.66^{+7.62}_{-6.53}$	$25.55^{+6.17}_{-5.06}$	$16.11^{+5.21}_{-4.08}$	2.17E+36	2.71E+35	6.22E+35
531	0.00E+00	0.00E+00	7.35E-01	$321.37^{+20.36}_{-19.53}$	$324.87^{+19.61}_{-18.58}$	$-3.50^{+7.07}_{-5.99}$	4.78E+36	1.23E+36	-9.99E+00
532	4.54E-04	2.60E-06	6.89E-01	$6.31^{+3.96}_{-2.77}$	$6.47^{+3.79}_{-2.58}$	$-0.16^{+2.33}_{-0.84}$	3.30E+35	6.90E+34	-9.99E+00
533	1.21E-07	2.37E-09	7.78E-02	$11.82^{+4.84}_{-3.70}$	$9.39^{+4.28}_{-3.11}$	$2.43^{+3.18}_{-1.91}$	6.24E+35	1.02E+35	9.43E+34
534	3.41E-07	3.09E-05	1.76E-03	$26.75^{+7.93}_{-6.85}$	$15.76^{+6.18}_{-5.08}$	$10.99^{+5.68}_{-4.56}$	9.55E+34	1.34E+34	2.71E+34
535	2.48E-25	1.30E-12	2.28E-14	$37.59^{+7.35}_{-6.46}$	$16.35^{+5.33}_{-4.20}$	$21.23^{+5.98}_{-4.87}$	1.16E+36	1.26E+35	4.44E+35
536	6.39E-03	3.09E-01	3.03E-03	$20.04^{+9.76}_{-8.70}$	$2.81^{+6.21}_{-5.11}$	$17.23^{+8.10}_{-7.02}$	5.15E+34	1.68E+33	3.09E+34
537	1.70E-10	1.67E-08	9.24E-04	$34.69^{+8.43}_{-7.36}$	$23.44^{+6.92}_{-5.82}$	$11.26^{+5.58}_{-4.46}$	1.21E+35	1.94E+34	2.72E+34
538	7.02E-06	1.86E-01	1.92E-08	$34.65^{+10.34}_{-9.28}$	$5.58^{+7.25}_{-6.16}$	$29.07^{+7.99}_{-6.91}$	7.24E+34	2.65E+33	4.28E+34
539	0.00E+00	0.00E+00	0.00E+00	$38384.65^{+197.16}_{-196.15}$	$24994.04^{+159.28}_{-158.27}$	$13390.61^{+116.88}_{-115.87}$	7.68E+37	1.14E+37	1.88E+37
540	0.00E+00	0.00E+00	0.00E+00	$2209.77^{+48.21}_{-47.20}$	$1571.43^{+40.80}_{-39.78}$	$638.34^{+26.41}_{-25.39}$	5.93E+36	9.84E+35	1.19E+36
541	7.60E-04	2.85E-03	6.77E-02	$4.33^{+3.40}_{-2.16}$	$2.74^{+2.94}_{-1.63}$	$1.59^{+2.66}_{-1.29}$	7.88E+35	9.53E+34	2.22E+35
542	0.00E+00	0.00E+00	0.00E+00	$2343.41^{+49.93}_{-48.91}$	$1348.51^{+37.98}_{-36.96}$	$994.89^{+33.05}_{-32.03}$	3.75E+37	5.52E+36	1.07E+37
543	2.22E-10	2.02E-13	1.00E+00	$5.94^{+3.60}_{-2.37}$	$5.99^{+3.60}_{-2.37}$	$-0.05^{+1.87}_{-99.99}$	2.05E+36	4.90E+35	-9.99E+00

Source No.	*pns* (0.5 − 8.0 keV)	*pns* (0.5 − 2.0 keV)	*pns* (2.0 − 8.0 keV)	*net_cts* (0.5 − 8.0 keV)	*net_cts* (0.5 − 2.0 keV)	*net_cts* (2.0 − 8.0 keV)	*luminosity* (0.5 − 8.0 keV)	*luminosity* (0.5 − 2.0 keV)	*luminosity* (2.0 − 8.0 keV)
544	0.00E+00	0.00E+00	0.00E+00	$1971.97^{+45.62}_{-44.61}$	$1383.48^{+38.36}_{-37.35}$	$588.49^{+25.41}_{-24.39}$	5.23E+36	8.56E+35	1.09E+36
545	0.00E+00	0.00E+00	3.31E-37	$455.74^{+23.20}_{-22.18}$	$375.37^{+20.82}_{-19.79}$	$80.36^{+11.05}_{-9.99}$	1.03E+36	1.96E+35	1.26E+35
546	3.59E-03	3.58E-01	4.59E-04	$13.25^{+6.74}_{-5.65}$	$1.55^{+4.59}_{-3.43}$	$11.70^{+5.57}_{-4.44}$	3.94E+34	1.09E+33	2.41E+34
547	5.20E-31	3.63E-24	5.11E-11	$48.44^{+8.41}_{-7.34}$	$28.37^{+6.55}_{-5.45}$	$20.07^{+5.99}_{-4.88}$	1.36E+36	1.99E+35	3.83E+35
548	0.00E+00	0.00E+00	0.00E+00	$1099.79^{+34.45}_{-33.43}$	$724.16^{+28.13}_{-27.11}$	$375.62^{+20.59}_{-19.56}$	2.95E+36	4.56E+35	7.01E+35
549	0.00E+00	0.00E+00	3.75E-21	$140.49^{+13.70}_{-12.65}$	$98.48^{+11.49}_{-10.43}$	$42.01^{+8.21}_{-7.13}$	5.14E+35	8.54E+34	1.06E+35
550	3.81E-06	5.55E-03	9.31E-05	$23.17^{+7.56}_{-6.48}$	$9.64^{+5.57}_{-4.45}$	$13.53^{+5.78}_{-4.67}$	8.48E+34	8.36E+33	3.43E+34
551	7.11E-07	2.47E-09	3.99E-01	$10.84^{+4.71}_{-3.56}$	$10.20^{+4.43}_{-3.26}$	$0.64^{+2.66}_{-1.29}$	5.71E+35	1.10E+35	2.48E+34
552	1.88E-16	6.37E-03	4.42E-17	$61.35^{+11.02}_{-9.97}$	$11.56^{+6.39}_{-5.28}$	$49.79^{+9.49}_{-8.43}$	1.42E+35	6.20E+33	8.05E+34
553	1.06E-04	3.10E-02	6.63E-04	$24.56^{+8.77}_{-7.70}$	$8.17^{+5.90}_{-4.79}$	$16.39^{+7.09}_{-6.00}$	9.86E+34	8.00E+33	4.50E+34
554	4.75E-06	6.61E-08	1.34E-01	$10.42^{+4.71}_{-3.56}$	$8.35^{+4.12}_{-2.94}$	$2.07^{+3.19}_{-1.92}$	5.87E+35	9.73E+34	8.60E+34
555	0.00E+00	0.00E+00	0.00E+00	$29174.13^{+172.14}_{-171.13}$	$19864.01^{+142.14}_{-141.13}$	$9310.13^{+97.80}_{-96.79}$	6.87E+37	1.09E+37	1.53E+37
556	0.00E+00	6.20E-13	7.12E-41	$109.29^{+12.75}_{-11.71}$	$36.41^{+8.28}_{-7.20}$	$72.89^{+10.27}_{-9.21}$	2.32E+35	1.77E+34	1.09E+35
557	0.00E+00	0.00E+00	1.40E-45	$207.62^{+16.65}_{-15.62}$	$123.84^{+13.08}_{-12.03}$	$83.78^{+10.99}_{-9.94}$	4.22E+35	5.78E+34	1.19E+35
558	4.96E-04	9.61E-05	2.90E-01	$24.88^{+9.54}_{-8.48}$	$21.95^{+8.03}_{-6.95}$	$2.93^{+5.93}_{-4.83}$	5.89E+34	1.21E+34	4.84E+33
559	0.00E+00	0.00E+00	0.00E+00	$5481.35^{+75.22}_{-74.21}$	$3737.12^{+62.29}_{-61.28}$	$1744.23^{+42.87}_{-41.85}$	1.15E+37	1.78E+36	2.56E+36
560	0.00E+00	2.06E-17	1.35E-39	$93.99^{+11.44}_{-10.39}$	$30.51^{+7.07}_{-5.98}$	$63.48^{+9.54}_{-8.47}$	3.79E+35	2.81E+34	1.80E+35
561	0.00E+00	0.00E+00	0.00E+00	$1055.68^{+34.34}_{-33.32}$	$824.30^{+30.33}_{-29.31}$	$231.38^{+16.88}_{-15.84}$	2.23E+36	3.96E+35	3.44E+35
562	1.77E-06	2.35E-08	1.00E+00	$5.68^{+3.60}_{-2.38}$	$5.86^{+3.60}_{-2.37}$	$-0.18^{+1.87}_{-99.99}$	1.03E+36	2.52E+35	-9.99E+00
563	1.67E-06	3.01E-02	9.67E-06	$25.37^{+7.88}_{-6.80}$	$5.98^{+4.73}_{-3.58}$	$19.39^{+6.84}_{-5.75}$	1.11E+35	5.89E+33	6.03E+34
564	3.52E-18	1.47E-21	6.16E-02	$75.52^{+12.40}_{-11.35}$	$67.47^{+10.97}_{-9.92}$	$8.05^{+6.59}_{-5.49}$	1.60E+35	3.26E+34	1.20E+34
565	2.92E-20	1.91E-04	4.31E-18	$56.14^{+9.85}_{-8.79}$	$12.36^{+5.58}_{-4.46}$	$43.78^{+8.63}_{-7.55}$	1.90E+35	9.52E+33	1.05E+35
566	8.45E-09	3.82E-08	7.55E-03	$14.39^{+5.22}_{-4.09}$	$10.00^{+4.43}_{-3.27}$	$4.39^{+3.61}_{-2.38}$	5.95E+36	9.76E+35	1.26E+36
567	0.00E+00	0.00E+00	0.00E+00	$960.08^{+32.64}_{-31.62}$	$647.92^{+26.84}_{-25.82}$	$312.16^{+19.27}_{-18.24}$	2.10E+36	3.26E+35	4.79E+35
568	0.00E+00	0.00E+00	0.00E+00	$551.58^{+39.87}_{-38.86}$	$336.56^{+32.26}_{-31.25}$	$215.02^{+24.11}_{-23.09}$	7.11E+36	9.53E+35	1.98E+36
569	0.00E+00	0.00E+00	0.00E+00	$5274.98^{+73.96}_{-72.95}$	$3620.69^{+61.42}_{-60.41}$	$1654.29^{+41.92}_{-40.90}$	6.64E+37	1.00E+37	1.49E+37
570	1.86E-03	8.57E-06	5.56E-01	$22.89^{+9.74}_{-8.68}$	$23.33^{+7.74}_{-6.66}$	$-0.44^{+6.63}_{-5.54}$	5.39E+34	1.28E+34	-9.99E+00
571	0.00E+00	0.00E+00	0.00E+00	$31897.04^{+179.81}_{-178.81}$	$19123.91^{+139.45}_{-138.44}$	$12773.13^{+114.17}_{-113.16}$	6.59E+37	9.06E+36	1.85E+37
572	0.00E+00	8.97E-36	2.62E-19	$126.84^{+13.72}_{-12.68}$	$81.65^{+11.17}_{-10.11}$	$45.19^{+8.69}_{-7.62}$	3.17E+35	4.65E+34	7.92E+34
573	2.53E-02	3.50E-01	5.35E-03	$10.70^{+7.01}_{-5.92}$	$1.93^{+5.36}_{-4.23}$	$8.77^{+5.23}_{-4.09}$	2.45E+34	1.01E+33	1.41E+34
574	0.00E+00	0.00E+00	0.00E+00	$651.86^{+27.22}_{-26.19}$	$421.58^{+22.04}_{-21.01}$	$230.27^{+16.67}_{-15.63}$	1.52E+36	2.24E+35	3.77E+35
575	0.00E+00	0.00E+00	0.00E+00	$303.67^{+19.55}_{-18.52}$	$209.54^{+16.20}_{-15.16}$	$94.13^{+11.68}_{-10.62}$	6.40E+35	1.02E+35	1.39E+35
576	0.00E+00	2.52E-44	0.00E+00	$121.93^{+12.23}_{-11.17}$	$48.70^{+8.13}_{-7.05}$	$73.22^{+9.71}_{-8.65}$	5.13E+37	4.88E+36	2.13E+37
577	0.00E+00	0.00E+00	9.31E-01	$262.02^{+19.51}_{-18.48}$	$271.62^{+18.42}_{-17.39}$	$-9.60^{+7.31}_{-6.23}$	6.38E+35	1.54E+35	-9.99E+00
578	1.88E-04	3.38E-02	5.66E-04	$29.45^{+10.37}_{-9.31}$	$11.58^{+7.81}_{-6.73}$	$17.87^{+7.49}_{-6.41}$	6.68E+34	6.15E+33	2.82E+34
579	3.53E-04	1.00E-03	6.58E-02	$21.47^{+8.37}_{-7.30}$	$15.12^{+6.84}_{-5.75}$	$6.35^{+5.58}_{-4.46}$	5.43E+34	9.01E+33	1.12E+34
580	0.00E+00	0.00E+00	7.52E-03	$172.04^{+15.73}_{-14.69}$	$159.97^{+14.62}_{-13.58}$	$12.07^{+6.68}_{-5.58}$	3.70E+35	7.95E+34	1.81E+34
581	1.95E-11	4.17E-09	2.19E-04	$15.28^{+5.22}_{-4.08}$	$9.39^{+4.28}_{-3.11}$	$5.89^{+3.79}_{-2.58}$	1.27E+36	1.60E+35	3.61E+35
582	2.06E-04	1.29E-02	3.01E-03	$28.85^{+10.25}_{-9.19}$	$13.72^{+7.80}_{-6.72}$	$15.13^{+7.34}_{-6.25}$	6.00E+34	6.61E+33	2.20E+34
583	7.42E-09	1.00E+00	8.16E-12	$12.31^{+4.84}_{-3.70}$	$-0.74^{+1.87}_{-99.99}$	$13.05^{+4.84}_{-3.69}$	5.33E+35	-9.99E+00	4.03E+35
584	4.28E-03	1.54E-03	1.46E-01	$5.56^{+3.97}_{-2.77}$	$3.54^{+3.18}_{-1.91}$	$2.02^{+3.19}_{-1.92}$	2.58E+35	3.63E+34	6.67E+34
585	0.00E+00	0.00E+00	0.00E+00	$22381.81^{+151.08}_{-150.08}$	$15391.10^{+125.47}_{-124.46}$	$6990.71^{+84.87}_{-83.86}$	4.81E+37	7.61E+36	1.05E+37

Source No.	*pns* (0.5 – 8.0 keV)	*pns* (0.5 – 2.0 keV)	*pns* (2.0 – 8.0 keV)	*net_cts* (0.5 – 8.0 keV)	*net_cts* (0.5 – 2.0 keV)	*net_cts* (2.0 – 8.0 keV)	*luminosity* (0.5 – 8.0 keV)	*luminosity* (0.5 – 2.0 keV)	*luminosity* (2.0 – 8.0 keV)
586	5.21E-03	2.95E-02	4.71E-02	$27.72^{+12.43}_{-11.39}$	$15.32^{+9.50}_{-8.43}$	$12.40^{+8.70}_{-7.63}$	4.54E+35	5.69E+34	1.43E+35
587	0.00E+00	0.00E+00	0.00E+00	$869.44^{+31.09}_{-30.07}$	$436.30^{+22.28}_{-21.26}$	$433.15^{+22.28}_{-21.26}$	3.22E+36	3.85E+35	1.11E+36
588	0.00E+00	0.00E+00	0.00E+00	$551.73^{+24.75}_{-23.73}$	$317.75^{+19.00}_{-17.97}$	$233.98^{+16.52}_{-15.49}$	8.41E+36	1.10E+36	2.51E+36
589	0.00E+00	0.00E+00	0.00E+00	$24166.08^{+156.94}_{-155.94}$	$17585.79^{+133.99}_{-132.99}$	$6580.29^{+82.43}_{-81.42}$	5.07E+37	8.49E+36	9.66E+36
590	0.00E+00	0.00E+00	0.00E+00	$1155.57^{+35.13}_{-34.12}$	$858.19^{+30.39}_{-29.37}$	$297.37^{+18.37}_{-17.34}$	2.07E+37	3.53E+36	3.74E+36
591	0.00E+00	0.00E+00	0.00E+00	$23420.68^{+154.29}_{-153.29}$	$15396.76^{+125.25}_{-124.25}$	$8023.92^{+90.79}_{-89.78}$	5.68E+37	8.86E+36	1.34E+37
592	0.00E+00	0.00E+00	0.00E+00	$3748.57^{+62.72}_{-61.71}$	$2604.89^{+52.41}_{-51.40}$	$1143.68^{+35.15}_{-34.14}$	7.79E+36	1.26E+36	1.66E+36
593	1.66E-07	4.51E-03	1.68E-06	$43.40^{+11.09}_{-10.03}$	$16.49^{+8.09}_{-7.01}$	$26.91^{+8.23}_{-7.15}$	9.10E+34	8.09E+33	3.92E+34
594	0.00E+00	0.00E+00	4.14E-11	$168.90^{+16.71}_{-15.67}$	$116.26^{+13.06}_{-12.02}$	$52.64^{+11.10}_{-10.05}$	4.09E+35	6.62E+34	8.86E+34
595	1.69E-14	2.04E-12	1.93E-05	$74.34^{+13.12}_{-12.08}$	$42.87^{+9.28}_{-8.21}$	$31.47^{+9.90}_{-8.84}$	1.82E+35	2.47E+34	5.34E+34
596	0.00E+00	0.00E+00	0.00E+00	$20314.74^{+143.81}_{-142.80}$	$16730.01^{+130.53}_{-129.53}$	$3584.73^{+61.13}_{-60.12}$	4.45E+37	8.66E+36	5.45E+36
597	7.95E-11	3.27E-02	7.59E-12	$52.34^{+11.17}_{-10.12}$	$9.83^{+6.83}_{-5.74}$	$42.51^{+9.37}_{-8.31}$	1.24E+35	5.41E+33	6.99E+34
598	2.34E-18	1.80E-16	7.39E-04	$48.70^{+9.20}_{-8.13}$	$39.20^{+8.22}_{-7.14}$	$9.50^{+4.98}_{-3.84}$	3.42E+35	6.14E+34	4.75E+34
599	5.26E-07	9.87E-04	1.29E-04	$5.75^{+3.60}_{-2.38}$	$2.83^{+2.94}_{-1.63}$	$2.92^{+2.94}_{-1.63}$	1.21E+36	1.31E+35	4.38E+35
600	1.70E-16	7.64E-14	3.52E-04	$50.15^{+9.58}_{-8.51}$	$39.79^{+8.58}_{-7.51}$	$10.36^{+5.11}_{-3.97}$	3.30E+35	5.89E+34	4.83E+34
601	7.81E-07	2.33E-08	1.00E+00	$5.74^{+3.60}_{-2.38}$	$5.87^{+3.60}_{-2.38}$	$-0.13^{+1.87}_{-99.99}$	1.38E+36	3.07E+35	-9.99E+00
602	1.51E-02	1.00E+00	3.72E-03	$6.03^{+4.45}_{-3.28}$	$-0.94^{+1.88}_{-99.99}$	$6.97^{+4.45}_{-3.28}$	1.69E+35	-9.99E+00	1.32E+35
603	0.00E+00	0.00E+00	2.31E-08	$148.66^{+15.01}_{-13.97}$	$120.23^{+13.26}_{-12.22}$	$28.43^{+7.83}_{-6.75}$	5.79E+35	1.10E+35	7.70E+34
604	0.00E+00	0.00E+00	6.06E-19	$146.12^{+14.39}_{-13.35}$	$99.33^{+11.82}_{-10.77}$	$46.79^{+8.94}_{-7.87}$	4.74E+35	7.63E+34	1.05E+35
605	0.00E+00	0.00E+00	0.00E+00	$1674.97^{+42.45}_{-41.44}$	$1113.40^{+34.69}_{-33.67}$	$561.57^{+25.17}_{-24.14}$	6.21E+36	9.83E+35	1.44E+36
606	6.00E-11	4.40E-06	3.59E-06	$11.30^{+4.57}_{-3.41}$	$5.64^{+3.60}_{-2.38}$	$5.65^{+3.60}_{-2.38}$	7.00E+36	6.45E+35	2.74E+36
607	2.57E-15	2.17E-06	1.60E-10	$66.50^{+11.83}_{-10.78}$	$22.59^{+7.29}_{-6.20}$	$43.91^{+9.86}_{-8.80}$	5.37E+35	4.65E+34	2.38E+35
608	0.00E+00	0.00E+00	0.00E+00	$4788.55^{+70.65}_{-69.64}$	$2270.20^{+48.92}_{-47.91}$	$2518.35^{+51.55}_{-50.54}$	1.24E+37	1.37E+36	4.52E+36
609	0.00E+00	0.00E+00	7.49E-06	$177.39^{+15.41}_{-14.37}$	$153.92^{+13.78}_{-12.73}$	$23.47^{+7.71}_{-6.62}$	1.97E+36	4.35E+35	1.76E+35
610	0.00E+00	0.00E+00	1.03E-20	$50.42^{+8.19}_{-7.12}$	$33.76^{+6.90}_{-5.80}$	$16.65^{+5.21}_{-4.08}$	9.70E+36	1.58E+36	2.20E+36
611	0.00E+00	0.00E+00	0.00E+00	$2594.98^{+52.33}_{-51.32}$	$1651.50^{+41.89}_{-40.88}$	$943.48^{+32.05}_{-31.03}$	9.50E+36	1.43E+36	2.39E+36
612	0.00E+00	0.00E+00	2.14E-09	$176.45^{+16.84}_{-15.80}$	$128.49^{+13.37}_{-12.33}$	$47.96^{+10.92}_{-9.87}$	1.14E+36	2.12E+35	2.09E+35
613	9.99E-06	4.85E-07	9.07E-02	$13.33^{+5.38}_{-4.25}$	$9.95^{+4.45}_{-3.27}$	$3.38^{+3.84}_{-2.63}$	1.08E+36	1.98E+35	1.87E+35
614	1.38E-05	1.38E-01	1.58E-06	$36.57^{+11.01}_{-9.96}$	$6.70^{+7.28}_{-6.20}$	$29.87^{+8.84}_{-7.77}$	1.06E+35	4.61E+33	6.00E+34
615	0.00E+00	0.00E+00	0.00E+00	$60252.81^{+246.70}_{-245.70}$	$36282.84^{+191.64}_{-190.63}$	$23969.97^{+156.01}_{-155.01}$	1.65E+38	2.33E+37	4.56E+37
616	8.68E-03	2.61E-02	8.00E-02	$17.68^{+9.11}_{-8.04}$	$9.62^{+6.49}_{-5.39}$	$8.06^{+7.03}_{-5.94}$	6.18E+34	7.90E+33	1.96E+34
617	0.00E+00	0.00E+00	0.00E+00	$934.56^{+32.70}_{-31.68}$	$356.84^{+20.80}_{-19.77}$	$577.72^{+25.78}_{-24.75}$	3.12E+36	2.85E+35	1.33E+36
618	1.23E-03	4.52E-03	3.67E-02	$9.20^{+4.98}_{-3.84}$	$4.55^{+3.60}_{-2.38}$	$4.65^{+4.14}_{-2.96}$	2.21E+35	2.78E+34	7.51E+34
619	4.37E-38	6.13E-30	1.83E-12	$59.73^{+9.19}_{-8.12}$	$36.86^{+7.31}_{-6.22}$	$22.87^{+6.29}_{-5.18}$	4.20E+36	6.65E+35	1.08E+36
620	0.00E+00	2.48E-36	4.96E-16	$63.63^{+9.36}_{-8.29}$	$37.55^{+7.31}_{-6.22}$	$26.09^{+6.55}_{-5.45}$	2.70E+36	4.40E+35	7.25E+35
621	0.00E+00	0.00E+00	0.00E+00	$1036.11^{+34.27}_{-33.25}$	$735.65^{+28.76}_{-27.74}$	$300.47^{+19.35}_{-18.32}$	3.55E+36	6.04E+35	7.09E+35
622	0.00E+00	3.22E-36	9.12E-36	$198.90^{+17.49}_{-16.46}$	$99.63^{+12.68}_{-11.63}$	$99.27^{+12.68}_{-11.63}$	6.06E+35	7.28E+34	2.08E+35
623	2.92E-18	6.21E-09	7.59E-11	$20.59^{+5.77}_{-4.65}$	$8.52^{+4.12}_{-2.94}$	$12.07^{+4.71}_{-3.56}$	6.76E+35	6.28E+34	2.81E+35
624	0.00E+00	0.00E+00	0.00E+00	$6832.73^{+84.05}_{-83.03}$	$2299.08^{+49.11}_{-48.09}$	$4533.65^{+68.70}_{-67.69}$	9.63E+37	8.29E+36	4.29E+37
625	0.00E+00	0.00E+00	7.91E-30	$415.22^{+23.05}_{-22.02}$	$327.92^{+20.06}_{-19.03}$	$87.30^{+12.11}_{-11.06}$	1.21E+36	2.29E+35	1.76E+35
626	8.26E-09	5.37E-11	2.04E-02	$48.28^{+11.20}_{-10.15}$	$34.43^{+8.21}_{-7.13}$	$13.85^{+8.26}_{-7.19}$	1.11E+36	1.96E+35	2.16E+35
627	0.00E+00	2.58E-18	7.29E-15	$119.81^{+14.87}_{-13.83}$	$61.06^{+10.67}_{-9.61}$	$58.75^{+10.98}_{-9.93}$	3.51E+35	4.19E+34	1.20E+35

Source No.	*pns* (0.5 − 8.0 keV)	*pns* (0.5 − 2.0 keV)	*pns* (2.0 − 8.0 keV)	*net_cts* (0.5 − 8.0 keV)	*net_cts* (0.5 − 2.0 keV)	*net_cts* (2.0 − 8.0 keV)	*luminosity* (0.5 − 8.0 keV)	*luminosity* (0.5 − 2.0 keV)	*luminosity* (2.0 − 8.0 keV)
628	0.00E+00	0.00E+00	1.16E-42	$525.17^{+25.21}_{-24.19}$	$407.36^{+21.71}_{-20.68}$	$117.81^{+13.57}_{-12.52}$	2.09E+36	4.07E+35	3.17E+35
629	5.87E-03	9.21E-01	5.95E-06	$21.90^{+10.42}_{-9.36}$	$-7.25^{+6.02}_{-4.91}$	$29.15^{+9.02}_{-7.95}$	6.57E+34	-9.99E+00	6.01E+34
630	0.00E+00	0.00E+00	0.00E+00	$188.47^{+15.00}_{-13.96}$	$132.53^{+12.70}_{-11.65}$	$55.95^{+8.73}_{-7.66}$	3.78E+36	6.17E+35	7.82E+35
631	7.08E-16	6.88E-12	6.25E-06	$22.66^{+6.08}_{-4.97}$	$14.04^{+4.97}_{-3.83}$	$8.62^{+4.29}_{-3.11}$	3.71E+36	4.67E+35	1.05E+36
632	1.48E-05	3.60E-13	9.64E-01	$38.79^{+11.53}_{-10.49}$	$49.24^{+10.01}_{-8.95}$	$-10.45^{+6.52}_{-5.44}$	1.21E+35	3.74E+34	-9.99E+00
633	0.00E+00	0.00E+00	0.00E+00	$562.07^{+24.74}_{-23.72}$	$382.72^{+20.59}_{-19.56}$	$179.35^{+14.44}_{-13.40}$	1.81E+37	3.06E+36	3.92E+36
634	2.09E-14	1.47E-25	3.14E-01	$67.09^{+12.15}_{-11.10}$	$63.72^{+10.15}_{-9.08}$	$3.37^{+7.43}_{-6.36}$	3.10E+35	7.44E+34	1.05E+34
635	1.72E-32	1.18E-13	1.35E-20	$115.36^{+14.25}_{-13.21}$	$43.07^{+9.05}_{-7.98}$	$72.29^{+11.56}_{-10.51}$	4.90E+35	4.63E+34	2.07E+35
636	7.86E-38	0.00E+00	4.35E-01	$126.81^{+14.73}_{-13.69}$	$125.48^{+13.31}_{-12.26}$	$1.33^{+7.14}_{-6.05}$	6.34E+35	1.60E+35	4.48E+33
637	1.33E-06	2.57E-01	2.12E-07	$43.15^{+11.56}_{-10.51}$	$3.46^{+6.02}_{-4.91}$	$39.69^{+10.33}_{-9.27}$	2.51E+35	5.10E+33	1.56E+35
638	6.63E-03	3.40E-03	1.92E-01	$17.11^{+8.59}_{-7.53}$	$12.31^{+6.34}_{-5.23}$	$4.81^{+6.47}_{-5.37}$	7.68E+34	1.37E+34	1.47E+34
639	7.23E-18	1.99E-05	2.19E-14	$76.59^{+12.52}_{-11.47}$	$22.48^{+7.70}_{-6.62}$	$54.10^{+10.41}_{-9.35}$	3.20E+35	2.37E+34	1.53E+35
640	0.00E+00	0.00E+00	0.00E+00	$1815.69^{+44.59}_{-43.58}$	$1508.97^{+40.30}_{-39.29}$	$306.72^{+19.88}_{-18.85}$	6.30E+36	1.28E+36	7.27E+35
641	2.32E-02	8.14E-03	3.31E-01	$10.73^{+6.93}_{-5.84}$	$8.70^{+5.35}_{-4.22}$	$2.03^{+5.13}_{-3.99}$	6.91E+34	1.36E+34	8.96E+33
642	0.00E+00	0.00E+00	0.00E+00	$2373.56^{+50.55}_{-49.54}$	$1642.41^{+41.96}_{-40.95}$	$731.15^{+28.90}_{-27.88}$	9.50E+36	1.65E+36	1.98E+36
643	0.00E+00	3.75E-12	9.59E-10	$94.89^{+14.27}_{-13.23}$	$47.58^{+10.06}_{-9.00}$	$47.31^{+10.73}_{-9.68}$	3.50E+35	4.34E+34	1.19E+35
644	5.07E-20	7.18E-29	3.55E-01	$28.21^{+6.64}_{-5.54}$	$27.29^{+6.36}_{-5.26}$	$0.92^{+2.95}_{-1.65}$	2.91E+36	7.07E+35	6.40E+34
645	1.87E-09	1.28E-03	2.65E-07	$43.06^{+10.03}_{-8.97}$	$12.32^{+5.96}_{-4.85}$	$30.74^{+8.60}_{-7.52}$	4.00E+35	2.90E+34	1.92E+35
646	3.28E-26	1.40E-16	3.38E-12	$104.55^{+14.07}_{-13.03}$	$51.93^{+9.77}_{-8.70}$	$52.62^{+10.73}_{-9.67}$	4.50E+35	5.66E+34	1.53E+35
647	6.51E-03	1.50E-02	7.72E-02	$16.26^{+8.26}_{-7.19}$	$8.58^{+5.59}_{-4.47}$	$7.68^{+6.69}_{-5.60}$	1.00E+35	1.34E+34	3.18E+34
648	4.02E-43	5.91E-11	1.43E-33	$21.90^{+5.77}_{-4.65}$	$4.98^{+3.40}_{-2.15}$	$16.92^{+5.21}_{-4.08}$	1.17E+36	6.69E+34	6.12E+35
649	8.29E-03	6.04E-03	1.62E-01	$19.53^{+9.78}_{-8.73}$	$13.08^{+6.91}_{-5.82}$	$6.45^{+7.55}_{-6.47}$	1.04E+35	1.76E+34	2.32E+34
650	0.00E+00	0.00E+00	0.00E+00	$822.28^{+31.25}_{-30.23}$	$469.04^{+23.52}_{-22.49}$	$353.24^{+21.23}_{-20.20}$	3.30E+36	4.87E+35	9.50E+35
651	2.65E-12	6.39E-07	5.63E-07	$17.07^{+5.45}_{-4.32}$	$7.43^{+3.96}_{-2.77}$	$9.64^{+4.43}_{-3.27}$	1.73E+36	1.88E+35	6.60E+35
652	7.06E-11	5.13E-10	1.05E-03	$61.42^{+12.49}_{-11.44}$	$39.47^{+9.27}_{-8.21}$	$21.95^{+9.01}_{-7.95}$	2.70E+35	4.40E+34	6.49E+34
653	9.16E-03	6.61E-02	3.97E-02	$16.48^{+8.64}_{-7.57}$	$6.76^{+5.83}_{-4.72}$	$9.72^{+6.97}_{-5.89}$	9.35E+34	9.70E+33	3.72E+34
654	4.27E-03	7.66E-01	1.40E-04	$20.51^{+9.54}_{-8.48}$	$-2.75^{+5.19}_{-4.06}$	$23.26^{+8.49}_{-7.42}$	1.21E+35	-9.99E+00	9.26E+34
655	0.00E+00	2.03E-24	0.00E+00	$350.32^{+20.99}_{-19.96}$	$61.87^{+10.08}_{-9.02}$	$288.45^{+18.83}_{-17.79}$	2.66E+36	1.21E+35	1.47E+36
656	1.96E-27	8.33E-16	6.95E-14	$75.86^{+11.16}_{-10.10}$	$35.25^{+7.73}_{-6.64}$	$40.61^{+8.66}_{-7.59}$	2.03E+36	2.44E+35	7.25E+35
657	3.57E-14	9.60E-06	7.19E-10	$21.88^{+6.08}_{-4.97}$	$7.79^{+4.13}_{-2.94}$	$14.08^{+5.10}_{-3.96}$	5.39E+35	4.91E+34	2.33E+35
658	1.26E-44	9.73E-31	8.77E-18	$47.71^{+8.13}_{-7.05}$	$26.35^{+6.27}_{-5.16}$	$21.36^{+5.88}_{-4.76}$	1.10E+36	1.55E+35	3.31E+35
659	0.00E+00	0.00E+00	3.13E-01	$692.14^{+28.52}_{-27.50}$	$688.91^{+27.85}_{-26.83}$	$3.23^{+7.08}_{-6.00}$	5.27E+36	1.36E+36	1.65E+34
660	1.55E-02	3.12E-03	3.65E-01	$16.74^{+9.29}_{-8.23}$	$14.43^{+7.03}_{-5.94}$	$2.31^{+6.74}_{-5.66}$	9.59E+34	2.11E+34	8.90E+33
661	0.00E+00	0.00E+00	0.00E+00	$2304.56^{+49.07}_{-48.06}$	$830.28^{+29.86}_{-28.84}$	$1474.28^{+39.46}_{-38.44}$	5.87E+37	5.34E+36	2.54E+37
662	2.10E-03	6.04E-03	5.55E-02	$21.59^{+9.36}_{-8.30}$	$12.06^{+6.53}_{-5.43}$	$9.53^{+7.33}_{-6.25}$	1.51E+35	2.17E+34	4.49E+34
663	1.44E-02	4.27E-01	8.11E-03	$8.82^{+5.68}_{-4.57}$	$0.73^{+3.41}_{-2.17}$	$8.09^{+5.11}_{-3.97}$	1.06E+35	2.16E+33	6.64E+34
664	1.79E-08	1.58E-01	6.90E-09	$29.77^{+8.01}_{-6.93}$	$2.94^{+4.03}_{-2.84}$	$26.84^{+7.38}_{-6.29}$	5.98E+35	1.50E+34	3.63E+35
665	4.03E-04	1.13E-03	6.80E-02	$4.51^{+3.40}_{-2.16}$	$2.88^{+2.94}_{-1.63}$	$1.63^{+2.66}_{-1.29}$	1.72E+35	2.67E+34	4.24E+34
666	1.44E-06	1.87E-03	2.95E-04	$4.85^{+3.40}_{-2.15}$	$1.95^{+2.66}_{-1.29}$	$2.89^{+2.94}_{-1.63}$	1.83E+35	1.80E+34	7.48E+34
667	1.61E-03	2.17E-02	1.81E-02	$17.02^{+7.63}_{-6.55}$	$7.22^{+5.15}_{-4.01}$	$9.80^{+6.25}_{-5.15}$	1.55E+35	1.67E+34	6.04E+34
668	4.65E-04	8.33E-02	1.05E-03	$21.99^{+8.60}_{-7.53}$	$6.06^{+5.65}_{-4.53}$	$15.94^{+7.08}_{-5.99}$	1.74E+35	1.23E+34	8.49E+34
669	3.76E-02	8.46E-01	2.87E-03	$7.69^{+5.80}_{-4.69}$	$-1.98^{+3.21}_{-1.95}$	$9.67^{+5.35}_{-4.22}$	8.13E+34	-9.99E+00	6.97E+34

Source No.	*pns* (0.5 – 8.0 keV)	*pns* (0.5 – 2.0 keV)	*pns* (2.0 – 8.0 keV)	*net_cts* (0.5 – 8.0 keV)	*net_cts* (0.5 – 2.0 keV)	*net_cts* (2.0 – 8.0 keV)	*luminosity* (0.5 – 8.0 keV)	*luminosity* (0.5 – 2.0 keV)	*luminosity* (2.0 – 8.0 keV)
670	6.85E-09	4.02E-09	2.74E-03	$23.05^{+6.76}_{-5.66}$	$13.91^{+5.10}_{-3.96}$	$9.14^{+5.13}_{-3.99}$	5.23E+35	8.06E+34	1.39E+35
671	2.33E-06	1.37E-04	1.28E-03	$8.69^{+4.28}_{-3.11}$	$3.80^{+3.18}_{-1.91}$	$4.90^{+3.60}_{-2.38}$	8.65E+35	9.48E+34	3.30E+35
672	1.00E-04	2.54E-02	8.97E-04	$28.56^{+9.76}_{-8.70}$	$9.12^{+6.17}_{-5.07}$	$19.44^{+8.12}_{-7.05}$	2.20E+35	1.84E+34	9.97E+34
673	5.59E-32	2.69E-28	1.47E-08	$39.93^{+7.62}_{-6.53}$	$27.03^{+6.36}_{-5.26}$	$12.90^{+4.97}_{-3.83}$	8.93E+35	1.55E+35	1.94E+35
674	0.00E+00	0.00E+00	0.00E+00	$3203.65^{+58.42}_{-57.40}$	$794.64^{+29.70}_{-28.66}$	$2409.01^{+50.75}_{-49.73}$	4.62E+37	2.89E+36	2.35E+37
675	5.72E-03	2.09E-01	6.45E-03	$15.14^{+7.71}_{-6.63}$	$3.20^{+4.90}_{-3.76}$	$11.94^{+6.52}_{-5.42}$	1.44E+35	7.76E+33	7.62E+34
676	7.99E-25	1.67E-26	5.85E-05	$69.46^{+10.72}_{-9.66}$	$51.06^{+8.77}_{-7.70}$	$18.40^{+6.90}_{-5.81}$	1.69E+36	3.21E+35	3.01E+35
677	2.24E-11	1.41E-07	5.75E-06	$20.00^{+5.98}_{-4.87}$	$9.05^{+4.28}_{-3.11}$	$10.95^{+4.85}_{-3.70}$	4.60E+35	5.32E+34	1.69E+35
678	5.89E-25	2.05E-09	3.28E-17	$93.21^{+13.04}_{-11.99}$	$32.11^{+8.16}_{-7.08}$	$61.10^{+10.72}_{-9.66}$	8.19E+35	7.19E+34	3.61E+35
679	2.38E-27	4.30E-23	1.44E-08	$35.15^{+7.23}_{-6.14}$	$22.21^{+5.88}_{-4.76}$	$12.95^{+4.97}_{-3.83}$	8.40E+35	1.33E+35	2.09E+35
680	0.00E+00	0.00E+00	0.00E+00	$6096.70^{+79.50}_{-78.49}$	$4110.09^{+65.30}_{-64.29}$	$1986.62^{+46.04}_{-45.02}$	5.81E+37	9.97E+36	1.27E+37
681	2.57E-05	7.33E-03	9.79E-04	$10.67^{+4.86}_{-3.71}$	$4.46^{+3.61}_{-2.39}$	$6.21^{+3.97}_{-2.78}$	6.05E+35	5.89E+34	2.46E+35
682	3.91E-05	1.30E-02	8.20E-04	$11.05^{+4.99}_{-3.85}$	$4.23^{+3.61}_{-2.39}$	$6.82^{+4.14}_{-2.96}$	6.30E+35	5.58E+34	2.72E+35
683	1.59E-03	7.98E-06	3.55E-01	$7.36^{+4.44}_{-3.27}$	$6.35^{+3.79}_{-2.58}$	$1.01^{+3.19}_{-1.92}$	1.68E+35	3.68E+34	1.54E+34
684	0.00E+00	0.00E+00	0.00E+00	$6862.97^{+84.47}_{-83.45}$	$4048.24^{+65.00}_{-63.98}$	$2814.73^{+54.60}_{-53.57}$	8.19E+37	1.22E+37	2.27E+37
685	7.11E-03	1.10E-01	2.19E-02	$8.33^{+5.13}_{-4.00}$	$2.25^{+3.19}_{-1.93}$	$6.08^{+4.61}_{-3.45}$	1.81E+35	1.23E+34	8.93E+34
686	0.00E+00	0.00E+00	0.00E+00	$168.42^{+14.23}_{-13.18}$	$106.69^{+11.43}_{-10.38}$	$61.73^{+9.18}_{-8.11}$	4.16E+36	6.64E+35	1.03E+36
687	0.00E+00	0.00E+00	0.00E+00	$173.06^{+14.26}_{-13.22}$	$62.12^{+8.99}_{-7.91}$	$110.94^{+11.62}_{-10.57}$	1.78E+37	1.71E+36	7.56E+36
688	0.00E+00	0.00E+00	2.46E-18	$59.76^{+8.92}_{-7.85}$	$39.20^{+7.38}_{-6.30}$	$20.56^{+5.77}_{-4.65}$	6.30E+36	1.13E+36	1.42E+36
689	5.40E-30	3.00E-24	3.45E-11	$51.93^{+8.75}_{-7.68}$	$28.59^{+6.55}_{-5.45}$	$23.34^{+6.48}_{-5.38}$	1.29E+36	1.80E+35	3.92E+35
690	2.21E-15	1.73E-04	3.89E-12	$12.63^{+4.71}_{-3.56}$	$2.92^{+2.94}_{-1.63}$	$9.72^{+4.28}_{-3.10}$	2.97E+36	1.72E+35	1.55E+36
691	0.00E+00	3.84E-29	1.23E-24	$37.51^{+7.23}_{-6.13}$	$19.78^{+5.56}_{-4.43}$	$17.73^{+5.33}_{-4.20}$	8.82E+36	1.16E+36	2.83E+36
692	1.29E-34	2.82E-20	9.84E-17	$28.30^{+6.45}_{-5.35}$	$13.81^{+4.84}_{-3.69}$	$14.49^{+4.97}_{-3.83}$	2.70E+36	3.31E+35	9.34E+35
693	6.11E-08	3.25E-05	1.26E-04	$16.82^{+5.78}_{-4.66}$	$6.91^{+3.96}_{-2.77}$	$9.92^{+4.85}_{-3.70}$	4.09E+35	4.23E+34	1.63E+35
694	6.27E-21	2.00E-10	2.96E-12	$25.90^{+6.37}_{-5.26}$	$10.41^{+4.43}_{-3.26}$	$15.49^{+5.22}_{-4.08}$	5.97E+35	6.05E+34	2.41E+35
695	0.00E+00	0.00E+00	9.24E-02	$121.11^{+12.36}_{-11.31}$	$117.60^{+11.99}_{-10.94}$	$3.51^{+3.98}_{-2.79}$	2.98E+36	7.18E+35	5.87E+34
696	3.96E-06	7.38E-05	8.25E-03	$6.40^{+3.78}_{-2.58}$	$3.80^{+3.18}_{-1.91}$	$2.60^{+2.94}_{-1.63}$	6.07E+35	9.05E+34	1.67E+35
697	1.93E-06	4.08E-04	5.40E-04	$20.41^{+6.79}_{-5.69}$	$8.10^{+4.45}_{-3.28}$	$12.31^{+5.73}_{-4.61}$	4.52E+35	4.49E+34	1.85E+35
698	7.28E-03	4.92E-01	6.10E-03	$5.74^{+4.13}_{-2.95}$	$0.34^{+2.33}_{-0.84}$	$5.40^{+3.97}_{-2.77}$	1.28E+35	1.90E+33	8.16E+34
699	0.00E+00	0.00E+00	0.00E+00	$171.14^{+14.22}_{-13.18}$	$108.96^{+11.53}_{-10.47}$	$62.18^{+9.05}_{-7.98}$	1.84E+37	2.89E+36	4.57E+36
700	7.01E-07	2.17E-07	1.58E-01	$5.72^{+3.60}_{-2.37}$	$4.89^{+3.40}_{-2.15}$	$0.83^{+2.32}_{-0.83}$	1.35E+36	2.86E+35	1.34E+35
701	1.66E-06	5.92E-05	6.57E-03	$4.83^{+3.40}_{-2.15}$	$2.94^{+2.94}_{-1.63}$	$1.89^{+2.66}_{-1.29}$	1.13E+36	1.71E+35	3.02E+35
702	2.94E-04	1.86E-04	5.78E-02	$8.58^{+4.58}_{-3.42}$	$5.25^{+3.60}_{-2.38}$	$3.33^{+3.61}_{-2.38}$	1.92E+35	2.98E+34	5.03E+34
703	0.00E+00	1.86E-28	1.14E-20	$62.93^{+9.30}_{-8.23}$	$33.08^{+6.98}_{-5.89}$	$29.85^{+6.82}_{-5.72}$	1.58E+36	2.06E+35	5.08E+35
704	1.40E-09	1.09E-02	1.84E-08	$19.25^{+5.99}_{-4.88}$	$4.29^{+3.61}_{-2.39}$	$14.96^{+5.34}_{-4.21}$	4.59E+35	2.54E+34	2.42E+35
705	5.60E-28	2.20E-17	1.12E-12	$50.75^{+8.70}_{-7.62}$	$26.41^{+6.47}_{-5.37}$	$24.35^{+6.48}_{-5.38}$	1.17E+36	1.53E+35	3.80E+35
706	8.86E-04	2.22E-05	2.58E-01	$10.28^{+5.25}_{-4.11}$	$8.36^{+4.29}_{-3.12}$	$1.92^{+3.82}_{-2.62}$	2.48E+35	5.10E+34	3.13E+34
707	1.79E-40	1.67E-31	2.23E-15	$41.13^{+7.62}_{-6.53}$	$22.68^{+5.87}_{-4.76}$	$18.45^{+5.56}_{-4.43}$	1.25E+36	1.72E+35	3.79E+35
708	1.43E-10	7.63E-11	3.01E-03	$14.25^{+5.09}_{-3.96}$	$9.60^{+4.28}_{-3.10}$	$4.65^{+3.60}_{-2.38}$	3.27E+35	5.55E+34	7.21E+34
709	2.73E-03	8.17E-06	7.46E-01	$5.20^{+3.79}_{-2.58}$	$5.57^{+3.60}_{-2.38}$	$-0.37^{+2.32}_{-0.83}$	1.18E+35	3.19E+34	-9.99E+00
710	1.06E-04	1.21E-01	2.45E-04	$12.36^{+5.47}_{-4.35}$	$2.18^{+3.19}_{-1.92}$	$10.19^{+4.99}_{-3.85}$	2.93E+35	1.31E+34	1.63E+35
711	6.87E-06	1.22E-03	9.66E-04	$9.09^{+4.43}_{-3.26}$	$3.57^{+3.18}_{-1.91}$	$5.52^{+3.79}_{-2.58}$	2.10E+35	2.07E+34	8.62E+34

Source No.	*pns* (0.5 − 8.0 keV)	*pns* (0.5 − 2.0 keV)	*pns* (2.0 − 8.0 keV)	*net_cts* (0.5 − 8.0 keV)	*net_cts* (0.5 − 2.0 keV)	*net_cts* (2.0 − 8.0 keV)	*luminosity* (0.5 − 8.0 keV)	*luminosity* (0.5 − 2.0 keV)	*luminosity* (2.0 − 8.0 keV)
712	0.00E+00	2.21E-31	2.76E-17	$55.75^{+8.68}_{-7.60}$	$33.20^{+6.90}_{-5.80}$	$22.55^{+5.99}_{-4.87}$	5.99E+36	8.68E+35	1.66E+36
713	2.29E-11	3.63E-13	9.09E-02	$20.81^{+6.09}_{-4.98}$	$18.11^{+5.56}_{-4.44}$	$2.70^{+3.41}_{-2.17}$	6.54E+35	1.43E+35	5.75E+34
714	0.00E+00	0.00E+00	8.12E-35	$206.56^{+15.45}_{-14.41}$	$176.16^{+14.33}_{-13.29}$	$30.39^{+6.64}_{-5.54}$	4.24E+37	8.64E+36	4.30E+36
715	1.46E-01	7.06E-03	1.00E+00	$1.73^{+2.95}_{-1.64}$	$2.66^{+2.94}_{-1.63}$	$-0.94^{+1.88}_{-99.99}$	2.49E+35	9.32E+34	-9.99E+00
716	1.77E-27	1.32E-19	3.01E-11	$52.77^{+8.95}_{-7.88}$	$28.27^{+6.65}_{-5.55}$	$24.50^{+6.66}_{-5.56}$	1.31E+36	1.81E+35	4.08E+35
717	0.00E+00	0.00E+00	0.00E+00	$237.18^{+16.52}_{-15.48}$	$133.25^{+12.61}_{-11.56}$	$103.93^{+11.33}_{-10.28}$	5.46E+36	7.75E+35	1.62E+36
718	3.40E-02	4.12E-03	5.92E-01	$2.85^{+3.19}_{-1.92}$	$2.73^{+2.94}_{-1.63}$	$0.12^{+2.33}_{-0.84}$	4.11E+35	9.73E+34	1.18E+34
719	9.00E-03	1.69E-01	2.49E-02	$3.22^{+3.18}_{-1.91}$	$0.82^{+2.32}_{-0.83}$	$2.40^{+2.94}_{-1.63}$	3.10E+35	2.02E+34	1.55E+35
720	0.00E+00	0.00E+00	9.36E-23	$82.86^{+10.21}_{-9.15}$	$59.62^{+8.80}_{-7.72}$	$23.24^{+5.98}_{-4.86}$	1.19E+37	2.08E+36	2.28E+36
721	1.16E-08	4.16E-10	2.05E-02	$15.49^{+5.45}_{-4.32}$	$11.15^{+4.57}_{-3.41}$	$4.34^{+3.79}_{-2.58}$	3.63E+35	6.66E+34	6.85E+34
722	1.87E-07	1.22E-02	3.88E-06	$12.42^{+4.97}_{-3.83}$	$3.17^{+3.18}_{-1.91}$	$9.26^{+4.43}_{-3.27}$	2.90E+35	1.86E+34	1.46E+35
723	1.49E-05	2.84E-05	1.65E-02	$17.35^{+6.41}_{-5.31}$	$10.10^{+4.73}_{-3.58}$	$7.25^{+5.02}_{-3.88}$	4.34E+35	6.59E+34	1.21E+35
724	7.28E-28	7.01E-19	1.09E-10	$17.82^{+5.33}_{-4.20}$	$10.92^{+4.43}_{-3.26}$	$6.89^{+3.78}_{-2.58}$	4.15E+36	6.22E+35	1.10E+36
725	3.39E-04	7.28E-02	1.74E-03	$6.41^{+3.96}_{-2.77}$	$1.59^{+2.66}_{-1.29}$	$4.83^{+3.60}_{-2.38}$	6.50E+35	4.27E+34	3.24E+35
726	4.06E-10	5.65E-14	1.13E-01	$28.44^{+7.44}_{-6.35}$	$24.30^{+6.38}_{-5.28}$	$4.14^{+4.63}_{-3.48}$	8.68E+35	1.88E+35	8.53E+34
727	8.99E-06	8.26E-05	2.55E-02	$2.96^{+2.94}_{-1.63}$	$1.99^{+2.66}_{-1.29}$	$0.98^{+2.32}_{-0.83}$	6.37E+35	1.07E+35	1.42E+35
728	1.53E-05	5.15E-05	3.54E-02	$2.96^{+2.94}_{-1.63}$	$1.99^{+2.66}_{-1.29}$	$0.97^{+2.32}_{-0.83}$	6.34E+35	1.06E+35	1.41E+35
729	3.33E-16	3.38E-02	2.12E-16	$32.69^{+7.40}_{-6.31}$	$3.70^{+3.61}_{-2.39}$	$28.99^{+6.91}_{-5.81}$	7.98E+35	2.36E+34	4.72E+35
730	0.00E+00	0.00E+00	1.16E-28	$126.71^{+12.58}_{-11.53}$	$83.27^{+10.27}_{-9.20}$	$43.44^{+8.00}_{-6.92}$	3.03E+36	5.04E+35	6.99E+35
731	1.30E-09	1.21E-07	3.71E-04	$23.67^{+6.75}_{-5.65}$	$13.28^{+5.11}_{-3.97}$	$10.39^{+5.12}_{-3.98}$	7.80E+35	1.10E+35	2.32E+35
732	1.03E-17	5.39E-10	5.20E-09	$21.57^{+5.88}_{-4.76}$	$10.55^{+4.43}_{-3.26}$	$11.03^{+4.58}_{-3.42}$	3.07E+36	3.70E+35	1.07E+36
733	4.38E-11	1.95E-09	8.68E-04	$5.95^{+3.60}_{-2.37}$	$3.99^{+3.18}_{-1.91}$	$1.96^{+2.66}_{-1.29}$	5.11E+35	8.74E+34	1.13E+35
734	2.84E-17	1.00E+00	7.43E-19	$8.94^{+4.12}_{-2.94}$	$-0.02^{+1.87}_{-99.99}$	$8.96^{+4.12}_{-2.94}$	7.60E+35	-9.99E+00	5.13E+35
735	7.74E-20	2.15E-22	3.38E-04	$38.70^{+7.86}_{-6.78}$	$28.20^{+6.55}_{-5.45}$	$10.50^{+5.13}_{-3.99}$	9.35E+35	1.76E+35	1.70E+35
736	5.76E-05	1.77E-04	3.03E-02	$7.43^{+4.13}_{-2.94}$	$4.55^{+3.40}_{-2.16}$	$2.88^{+3.18}_{-1.91}$	7.43E+35	1.18E+35	1.93E+35
737	5.29E-10	1.82E-06	4.26E-05	$5.92^{+3.60}_{-2.37}$	$2.98^{+2.94}_{-1.63}$	$2.94^{+2.94}_{-1.63}$	5.01E+35	6.42E+34	1.68E+35
738	6.73E-14	1.62E-13	4.32E-03	$8.88^{+4.12}_{-2.94}$	$6.97^{+3.78}_{-2.58}$	$1.91^{+2.66}_{-1.29}$	1.99E+36	3.85E+35	2.92E+35
739	1.74E-06	1.85E-06	5.81E-02	$3.92^{+3.18}_{-1.91}$	$2.98^{+2.94}_{-1.63}$	$0.94^{+2.32}_{-0.83}$	3.43E+35	6.60E+34	5.55E+34
740	1.97E-05	2.69E-03	1.20E-03	$17.78^{+6.53}_{-5.43}$	$6.43^{+4.16}_{-2.97}$	$11.35^{+5.63}_{-4.51}$	4.70E+35	4.39E+34	2.01E+35
741	3.82E-04	3.28E-04	1.06E-01	$2.87^{+2.94}_{-1.63}$	$1.98^{+2.66}_{-1.29}$	$0.89^{+2.32}_{-0.83}$	3.66E+35	6.35E+34	7.68E+34
742	1.14E-06	2.80E-08	1.00E+00	$2.98^{+2.94}_{-1.63}$	$3.00^{+2.94}_{-1.63}$	$-0.01^{+1.87}_{-99.99}$	6.22E+35	1.57E+35	-9.99E+00
743	4.66E-06	2.67E-02	6.07E-05	$6.49^{+3.79}_{-2.58}$	$1.80^{+2.66}_{-1.29}$	$4.69^{+3.40}_{-2.16}$	1.54E+36	1.11E+35	7.45E+35
744	1.50E-11	6.66E-12	7.76E-03	$7.84^{+3.96}_{-2.76}$	$5.97^{+3.60}_{-2.37}$	$1.87^{+2.66}_{-1.29}$	7.09E+35	1.35E+35	1.15E+35
745	1.42E-33	3.51E-28	3.51E-09	$30.01^{+6.64}_{-5.54}$	$20.65^{+5.66}_{-4.54}$	$9.36^{+4.28}_{-3.10}$	2.87E+36	4.97E+35	6.05E+35
746	1.04E-06	1.77E-02	2.56E-05	$3.93^{+3.18}_{-1.91}$	$0.98^{+2.32}_{-0.83}$	$2.95^{+2.94}_{-1.63}$	3.32E+35	2.11E+34	1.68E+35
747	1.53E-16	5.75E-15	3.64E-04	$17.02^{+5.33}_{-4.20}$	$12.59^{+4.71}_{-3.55}$	$4.43^{+3.40}_{-2.16}$	1.63E+36	3.05E+35	2.88E+35
748	2.80E-15	1.70E-13	4.54E-04	$10.80^{+4.43}_{-3.26}$	$7.93^{+3.96}_{-2.76}$	$2.87^{+2.94}_{-1.63}$	2.45E+36	4.44E+35	4.44E+35
749	0.00E+00	0.00E+00	3.64E-07	$100.98^{+11.09}_{-10.03}$	$97.99^{+10.94}_{-9.88}$	$2.99^{+2.94}_{-1.63}$	2.10E+37	5.13E+36	4.21E+35
750	5.64E-06	6.02E-03	3.63E-04	$2.97^{+2.94}_{-1.63}$	$1.00^{+2.32}_{-0.83}$	$1.97^{+2.66}_{-1.29}$	6.22E+35	5.20E+34	2.81E+35
751	5.48E-13	7.24E-07	1.55E-07	$6.94^{+3.78}_{-2.58}$	$2.99^{+2.94}_{-1.63}$	$3.96^{+3.18}_{-1.91}$	5.92E+35	6.46E+34	2.28E+35
752	5.82E-14	2.34E-06	6.89E-09	$9.80^{+4.28}_{-3.10}$	$3.92^{+3.18}_{-1.91}$	$5.88^{+3.60}_{-2.37}$	2.04E+36	2.01E+35	8.35E+35
753	3.85E-11	5.85E-02	3.31E-11	$12.08^{+4.71}_{-3.56}$	$1.62^{+2.66}_{-1.29}$	$10.46^{+4.43}_{-3.26}$	1.14E+36	3.85E+34	6.67E+35

Source No.	*pns* (0.5 – 8.0 keV)	*pns* (0.5 – 2.0 keV)	*pns* (2.0 – 8.0 keV)	*net_cts* (0.5 – 8.0 keV)	*net_cts* (0.5 – 2.0 keV)	*net_cts* (2.0 – 8.0 keV)	*luminosity* (0.5 – 8.0 keV)	*luminosity* (0.5 – 2.0 keV)	*luminosity* (2.0 – 8.0 keV)
754	2.78E-18	1.26E-05	6.17E-14	$11.83^{+4.57}_{-3.41}$	$2.96^{+2.94}_{-1.63}$	$8.87^{+4.12}_{-2.94}$	1.05E+36	6.63E+34	5.32E+35
755	0.00E+00	3.78E-19	0.00E+00	$40.80^{+7.46}_{-6.37}$	$10.93^{+4.43}_{-3.26}$	$29.87^{+6.55}_{-5.44}$	8.95E+36	5.93E+35	4.46E+36
756	4.18E-23	3.39E-16	1.69E-10	$57.15^{+9.60}_{-8.54}$	$27.54^{+6.66}_{-5.56}$	$29.62^{+7.54}_{-6.45}$	2.02E+36	2.53E+35	6.99E+35
757	8.86E-24	1.66E-19	2.74E-07	$14.83^{+4.97}_{-3.83}$	$9.95^{+4.28}_{-3.10}$	$4.88^{+3.40}_{-2.15}$	1.29E+36	2.18E+35	2.87E+35
758	7.65E-05	4.25E-04	3.27E-02	$4.60^{+3.40}_{-2.15}$	$2.87^{+2.94}_{-1.63}$	$1.73^{+2.66}_{-1.29}$	4.28E+35	6.68E+34	1.09E+35
759	8.98E-26	7.59E-20	6.62E-09	$15.83^{+5.09}_{-3.95}$	$9.96^{+4.28}_{-3.10}$	$5.88^{+3.60}_{-2.37}$	1.49E+36	2.36E+35	3.74E+35
760	8.00E-04	5.15E-01	2.30E-04	$19.47^{+8.01}_{-6.93}$	$0.32^{+3.94}_{-2.74}$	$19.15^{+7.43}_{-6.34}$	7.25E+35	3.17E+33	4.71E+35
761	2.07E-03	7.19E-02	1.34E-02	$2.76^{+2.94}_{-1.63}$	$0.93^{+2.32}_{-0.83}$	$1.83^{+2.66}_{-1.29}$	3.38E+35	2.57E+34	1.58E+35
762	4.57E-19	6.46E-11	7.36E-10	$16.44^{+5.21}_{-4.08}$	$7.83^{+3.96}_{-2.76}$	$8.62^{+4.12}_{-2.94}$	1.53E+36	1.80E+35	5.44E+35
763	2.11E-02	1.00E+00	6.70E-03	$3.00^{+3.18}_{-1.91}$	$-0.30^{+1.87}_{-99.99}$	$3.30^{+3.18}_{-1.91}$	2.84E+35	-9.99E+00	2.12E+35
764	3.74E-03	4.40E-03	1.89E-01	$2.70^{+2.94}_{-1.63}$	$1.91^{+2.66}_{-1.29}$	$0.79^{+2.32}_{-0.83}$	2.45E+35	4.34E+34	4.88E+34
765	0.00E+00	3.07E-39	2.23E-12	$29.79^{+6.55}_{-5.44}$	$20.96^{+5.66}_{-4.54}$	$8.83^{+4.12}_{-2.94}$	6.90E+36	1.20E+36	1.39E+36
766	7.91E-07	4.34E-06	1.75E-02	$5.71^{+3.60}_{-2.38}$	$3.91^{+3.18}_{-1.91}$	$1.81^{+2.66}_{-1.29}$	5.46E+35	9.37E+34	1.17E+35
767	0.00E+00	6.79E-25	2.76E-26	$27.83^{+6.36}_{-5.26}$	$12.94^{+4.71}_{-3.55}$	$14.89^{+4.97}_{-3.83}$	3.35E+36	3.48E+35	1.27E+36
768	1.50E-13	1.86E-15	2.65E-02	$10.68^{+4.43}_{-3.26}$	$8.92^{+4.12}_{-2.94}$	$1.76^{+2.66}_{-1.29}$	9.55E+35	2.00E+35	1.06E+35
769	1.16E-11	3.51E-10	8.53E-04	$8.75^{+4.12}_{-2.94}$	$5.93^{+3.60}_{-2.37}$	$2.82^{+2.94}_{-1.63}$	7.72E+35	1.31E+35	1.68E+35
770	3.94E-17	2.60E-17	7.52E-04	$11.79^{+4.57}_{-3.41}$	$8.95^{+4.12}_{-2.94}$	$2.83^{+2.94}_{-1.63}$	1.04E+36	1.98E+35	1.69E+35
771	0.00E+00	0.00E+00	0.00E+00	$1093.50^{+34.09}_{-33.07}$	$670.72^{+26.92}_{-25.90}$	$422.78^{+21.59}_{-20.56}$	1.37E+38	1.86E+37	3.78E+37
772	4.54E-13	1.39E-03	9.32E-11	$8.83^{+4.12}_{-2.94}$	$1.95^{+2.66}_{-1.29}$	$6.88^{+3.78}_{-2.58}$	1.11E+36	5.40E+34	6.14E+35
773	1.85E-16	2.97E-16	2.09E-04	$12.68^{+4.71}_{-3.55}$	$8.95^{+4.12}_{-2.94}$	$3.73^{+3.18}_{-1.91}$	1.14E+36	2.01E+35	2.26E+35
774	3.76E-33	3.66E-21	9.67E-15	$18.86^{+5.44}_{-4.32}$	$9.97^{+4.28}_{-3.10}$	$8.89^{+4.12}_{-2.94}$	2.40E+36	2.80E+35	8.06E+35
775	1.64E-04	1.43E-04	1.55E-01	$3.74^{+3.18}_{-1.91}$	$2.91^{+2.94}_{-1.63}$	$0.83^{+2.32}_{-0.83}$	4.59E+35	7.89E+34	7.29E+34
776	2.33E-04	3.73E-08	1.00E+00	$7.10^{+4.13}_{-2.95}$	$8.45^{+4.12}_{-2.94}$	$-1.35^{+1.88}_{-99.99}$	6.62E+35	1.98E+35	-9.99E+00
777	1.64E-11	4.63E-06	7.65E-07	$11.38^{+4.57}_{-3.41}$	$4.81^{+3.40}_{-2.16}$	$6.57^{+3.79}_{-2.58}$	1.13E+36	1.22E+35	4.40E+35
778	1.39E-04	8.87E-03	4.31E-03	$9.51^{+4.73}_{-3.58}$	$3.87^{+3.41}_{-2.17}$	$5.64^{+3.98}_{-2.78}$	9.72E+35	1.04E+35	3.84E+35
779	7.97E-05	1.42E-02	1.91E-03	$5.35^{+3.60}_{-2.38}$	$1.84^{+2.66}_{-1.29}$	$3.51^{+3.18}_{-1.91}$	8.33E+35	6.52E+34	3.85E+35
780	2.46E-16	4.15E-15	1.24E-04	$21.11^{+5.88}_{-4.76}$	$14.44^{+4.97}_{-3.83}$	$6.66^{+3.96}_{-2.77}$	2.01E+36	3.59E+35	4.23E+35
781	6.12E-03	1.64E-01	1.55E-02	$2.64^{+2.94}_{-1.63}$	$0.83^{+2.32}_{-0.83}$	$1.82^{+2.66}_{-1.29}$	3.30E+35	2.27E+34	1.62E+35
782	1.51E-04	6.45E-03	8.25E-03	$6.73^{+3.97}_{-2.78}$	$3.39^{+3.19}_{-1.92}$	$3.34^{+3.19}_{-1.92}$	1.71E+36	2.21E+35	5.72E+35
783	2.23E-05	6.41E-06	3.55E-02	$7.63^{+4.13}_{-2.94}$	$4.81^{+3.40}_{-2.16}$	$2.82^{+3.18}_{-1.92}$	7.05E+35	1.12E+35	1.76E+35
784	1.95E-05	3.27E-02	2.08E-04	$7.66^{+4.13}_{-2.94}$	$1.75^{+2.66}_{-1.29}$	$5.91^{+3.79}_{-2.58}$	7.07E+35	4.08E+34	3.68E+35
785	1.27E-07	3.49E-09	2.26E-02	$11.23^{+4.71}_{-3.56}$	$7.76^{+3.96}_{-2.76}$	$3.47^{+3.40}_{-2.16}$	1.08E+36	1.93E+35	2.23E+35
786	1.15E-04	2.49E-07	1.00E+00	$5.30^{+3.60}_{-2.38}$	$5.79^{+3.60}_{-2.38}$	$-0.48^{+1.87}_{-99.99}$	6.57E+35	1.59E+35	-9.99E+00
787	1.44E-35	3.50E-35	2.14E-07	$31.99^{+6.81}_{-5.71}$	$23.75^{+5.98}_{-4.86}$	$8.24^{+4.12}_{-2.94}$	3.99E+36	6.56E+35	7.32E+35
788	9.02E-14	7.41E-15	3.56E-03	$18.30^{+5.56}_{-4.44}$	$13.63^{+4.84}_{-3.69}$	$4.67^{+3.61}_{-2.38}$	2.95E+36	6.02E+35	4.94E+35
789	1.68E-05	2.08E-07	4.98E-01	$7.03^{+3.96}_{-2.77}$	$6.70^{+3.79}_{-2.58}$	$0.33^{+2.33}_{-0.84}$	1.68E+36	3.97E+35	5.31E+34
790	0.00E+00	0.00E+00	2.21E-37	$120.62^{+12.08}_{-11.03}$	$87.50^{+10.42}_{-9.36}$	$33.12^{+6.90}_{-5.80}$	1.60E+37	2.58E+36	3.14E+36
791	0.00E+00	0.00E+00	0.00E+00	$116.78^{+11.90}_{-10.85}$	$70.65^{+9.47}_{-8.40}$	$46.13^{+7.91}_{-6.83}$	1.56E+37	2.14E+36	4.32E+36
792	1.06E-22	6.92E-22	2.37E-05	$22.95^{+5.98}_{-4.86}$	$16.70^{+5.21}_{-4.08}$	$6.25^{+3.79}_{-2.58}$	3.06E+36	5.09E+35	5.85E+35
793	5.53E-03	1.00E+00	1.56E-03	$2.66^{+2.94}_{-1.63}$	$-0.13^{+1.87}_{-99.99}$	$2.79^{+2.94}_{-1.63}$	5.88E+35	-9.99E+00	4.45E+35
794	1.94E-07	2.82E-08	2.83E-02	$12.03^{+4.86}_{-3.71}$	$8.57^{+4.13}_{-2.94}$	$3.46^{+3.42}_{-2.18}$	1.65E+36	2.78E+35	3.29E+35
795	5.98E-09	2.17E-04	4.77E-06	$13.89^{+5.10}_{-3.96}$	$4.56^{+3.40}_{-2.16}$	$9.33^{+4.44}_{-3.27}$	1.93E+36	1.47E+35	9.04E+35

Columns (2)-(4) represent the *pns* values discussed in Section 2.4. Columns (5)-(7) are net counts with 90% uncertainty limits. Blank values correspond to undetermined uncertainties. Columns (8)-(10) give luminosities (derived from the *flux2* parameter in *AE*) in units of erg s^{-1}. Conversion factors were 3.94, 1.34, and 2.43 in units of $10^{41} \left(\frac{d}{776\,\mathrm{kpc}}\right)^2$ erg cm^2 $photons^{-1}$ for the full, soft, and hard bands (to convert from photon flux in photons cm^{-2} s^{-1}). For some sources the soft or hard band had < 0 counts, and so uncertainties could not be determined and are represented as -99.99. By extension, some fluxes in the soft or hard band were < 0 and so luminosities appear as -9.99. Each source has a *pns* value $< 1 \times 10^{-2}$ in at least one energy band.

Appendix C

Complete Catalogue Cross-Matches

Table C.1: Catalogue Cross-Matches

Source	CXOU J	*XMM-Newton* Match		*Chandra* Match		LMXB Match			AGN Match			
No.		ID	Classification	Catalogue	ID	Peacock et al.; GC	Stiele et al.; Field	Stiele et al.; GC	PHAT	SDSS DR12	NED	SIMBAD
(1)	(2)	(3)	(4)	(5)	(6)	(7)	(8)	(9)	(10)	(11)	(12)	(13)
1	004542.90+414312.6	1685	<hard>	-	-	-	-	-	-	-	-	-
2	004551.05+414452.4	-	-	-	-	-	-	-	-	-	-	-
3	004551.30+414220.7	-	-	-	-	-	-	-	3900	-	-	-
4	004552.93+414441.8	-	-	-	-	-	-	-	-	-	-	-
5	004555.72+414551.8	-	-	-	-	-	-	-	-	-	-	-
6	004556.82+414440.8	-	-	-	-	-	-	-	-	-	-	-
7	004556.99+414831.7	1716	<hard>	-	-	-	-	-	1938	-	-	-
8	004559.07+414113.0	-	-	-	-	-	-	-	-	-	-	-
9	004602.43+414515.7	1732	<SNR>	-	-	-	-	-	-	-	-	-
10	004602.70+413856.7	-	-	-	-	-	-	-	-	-	-	-
11	004604.66+414123.3	1742	<fgStar>	DS04	n1-15	-	-	-	-	-	-	-
12	004605.10+414236.5	-	-	-	-	-	-	-	-	-	-	-
13	004605.79+414303.2	1747	<fgStar>	-	-	-	-	-	-	-	-	-
14	004606.74+414603.4	-	-	-	-	-	-	-	-	-	-	-
15	004609.33+414247.1	-	-	-	-	-	-	-	-	-	-	-
16	004611.46+413940.1	1761	<hard>	-	-	-	-	-	-	-	-	-
17	004612.21+414535.0	-	-	-	-	-	-	-	-	-	-	-
18	004613.87+414457.6	-	-	-	-	-	-	-	-	-	-	-
19	004614.58+414013.1	-	-	-	-	-	-	-	-	-	-	-
20	004614.67+414317.6	-	-	-	-	-	-	-	-	-	-	-
21	004615.36+414128.1	-	-	-	-	-	-	-	-	-	-	-
22	004615.86+414026.0	-	-	-	-	-	-	-	-	-	-	-
23	004616.82+414300.4	1772	<hard>	-	-	-	-	-	-	-	-	-
24	004616.85+413656.6	1773	<fgStar>	-	-	-	-	-	-	-	-	-
25	004620.54+414336.2	-	-	-	-	-	-	-	21	-	NED	-
26	004620.96+414240.6	-	-	-	-	-	-	-	-	-	-	-
27	004621.14+414309.2	-	-	-	-	-	-	-	-	-	-	-
28	004621.82+414116.7	1783	<hard>	-	-	-	-	-	-	-	-	-
29	004622.17+414436.7	-	-	-	-	-	-	-	-	-	-	-
30	004622.21+413953.4	-	-	-	-	-	-	-	-	-	-	-
31	004622.33+414419.0	-	-	-	-	-	-	-	-	-	-	-
32	004622.38+414426.5	1784	<AGN>	-	-	-	-	-	-	-	-	-
33	004622.90+414733.2	-	-	-	-	-	-	-	-	-	-	-
34	004623.43+413546.9	1788	<hard>	-	-	-	-	-	-	-	-	-
35	004623.79+413751.4	-	-	-	-	-	-	-	-	-	-	-
36	004624.36+414553.1	1791	<hard>	-	-	-	-	-	-	-	-	-
37	004624.44+414124.8	-	-	-	-	-	-	-	-	-	-	-
38	004625.43+414226.1	-	-	-	-	-	-	-	-	-	-	-
39	004627.55+413902.5	1804	<hard>	-	-	-	-	-	-	-	-	-
40	004627.69+414510.9	-	-	-	-	-	-	-	-	-	-	-
41	004629.20+414313.1	1806	<fgStar>	-	-	-	-	-	-	-	-	-

Source	CXOU J	*XMM-Newton* Match		*Chandra* Match		LMXB Match			AGN Match			
No.		ID	Classification	Catalogue	ID	Peacock et al.; GC	Stiele et al.; Field	Stiele et al.; GC	PHAT	SDSS DR12	NED	SIMBAD
42	004639.00+413906.4	-	-	-	-	-	-	-	-	-	-	-
43	003813.88+401521.9	23	<fgStar>	-	-	-	-	-	-	-	-	-
44	003815.94+401615.4	27	none	-	-	-	-	-	-	-	-	-
45	003816.61+401800.4	-	-	-	-	-	-	-	-	-	-	-
46	003818.90+401532.6	32	none	DS04	s2-28	-	-	-	-	-	-	-
47	003821.50+401819.6	37	<hard>	-	-	-	-	-	-	-	-	-
48	003821.80+401545.0	-	-	-	-	-	-	-	-	-	-	-
49	003822.01+401747.4	-	-	-	-	-	-	-	-	-	-	-
50	003823.84+401250.0	42	<fgStar>	-	-	-	-	-	-	-	-	-
51	003825.63+401324.3	44	<hard>	-	-	-	-	-	-	-	-	-
52	003825.65+401739.0	-	-	DS04	s2-10	-	-	-	-	-	-	-
53	003827.27+401735.3	-	-	-	-	-	-	-	-	-	-	-
54	003827.37+401247.3	50	<hard>	-	-	-	-	-	-	SDSS DR12	-	-
55	003827.61+401832.6	-	-	-	-	-	-	-	-	-	-	-
56	003831.18+401711.7	52	<fgStar>	DS04	s2-7	-	-	-	-	-	-	-
57	003836.99+401401.0	63	<hard>	-	-	-	-	-	-	-	-	-
58	003838.66+401510.8	-	-	DS04	s2-62	-	-	-	-	-	-	-
59	003838.97+401856.5	66	<hard>	-	-	-	-	-	-	-	-	-
60	003844.30+401803.6	-	-	-	-	-	-	-	-	-	-	-
61	003844.34+401659.7	77	<hard>	-	-	-	-	-	-	-	-	-
62	003850.99+401805.5	95	<hard>	-	-	-	-	-	-	-	-	-
63	003851.33+401950.1	-	-	-	-	-	-	-	-	-	-	-
64	003854.74+402009.0	98	<hard>	-	-	-	-	-	-	-	-	-
65	003855.34+401644.9	102	<hard>	-	-	-	-	-	-	-	-	-
66	003856.59+401830.4	106	none	-	-	-	-	-	-	-	-	-
67	003900.36+401603.5	119	<hard>	-	-	-	-	-	-	-	-	-
68	004111.89+405422.5	576	<hard>	-	-	-	-	-	-	-	-	-
69	004115.38+410102.5	588	<hard>	-	-	-	-	-	-	-	-	-
70	004115.84+405744.3	590	<hard>	-	-	-	-	-	-	-	-	-
71	004116.64+405703.2	-	-	-	-	-	-	-	-	-	-	-
72	004117.97+405617.2	-	-	-	-	-	-	-	-	-	-	-
73	004118.65+405158.6	603	fgStar	-	-	-	-	-	-	-	-	-
74	004119.90+410012.4	608	<hard>	-	-	-	-	-	-	-	-	-
75	004121.19+410341.7	611	<hard>	-	-	-	-	-	-	-	-	-
76	004122.34+405750.0	-	-	-	-	-	-	-	-	-	-	-
77	004123.87+405508.9	-	-	-	-	-	-	-	-	-	-	-
78	004125.89+405845.9	633	<hard>	-	-	-	-	-	-	-	-	-
79	004126.25+405326.0	636	AGN	-	-	-	-	-	-	-	-	-
80	004127.50+405056.6	640	<hard>	-	-	-	-	-	-	-	-	-
81	004128.40+405605.7	-	-	-	-	-	-	-	-	-	-	-
82	004128.46+405722.4	-	-	-	-	-	-	-	-	-	-	-
83	004128.74+405448.7	643	<hard>	-	-	-	-	-	-	-	-	-
84	004128.99+410212.2	644	<hard>	-	-	-	-	-	-	-	-	-
85	004129.23+405422.2	-	-	-	-	-	-	-	-	-	-	-
86	004131.53+405958.7	653	<hard>	-	-	-	-	-	-	-	-	-

Source	CXOU J	*XMM-Newton* Match		*Chandra* Match		LMXB Match			AGN Match			
No.		ID	Classification	Catalogue	ID	Peacock et al.; GC	Stiele et al.; Field	Stiele et al.; GC	PHAT	SDSS DR12	NED	SIMBAD
87	004133.06+405608.4	-	-	-	-	-	-	-	-	-	-	-
88	004133.17+405431.6	-	-	-	-	-	-	-	-	-	-	-
89	004133.73+405747.5	-	-	-	-	-	-	-	-	-	-	-
90	004134.30+410105.3	-	-	-	-	-	-	-	-	-	-	SIMBAD
91	004134.51+405647.9	-	-	-	-	-	-	-	-	-	-	-
92	004136.49+410135.0	-	-	-	-	-	-	-	-	-	-	-
93	004136.65+410017.0	673	<Gal>	-	-	-	-	-	-	-	-	-
94	004137.18+405608.1	-	-	-	-	-	-	-	-	-	-	-
95	004137.74+410029.4	-	-	-	-	-	-	-	-	-	-	-
96	004137.85+410108.2	675	AGN	-	-	-	-	-	-	-	NED	SIMBAD
97	004137.95+410108.6	675	AGN	-	-	-	-	-	-	-	NED	SIMBAD
98	004139.38+405412.8	-	-	-	-	-	-	-	-	-	-	-
99	004139.94+410425.3	-	-	DS04	s1-27	-	-	-	-	-	-	-
100	004139.97+405513.1	-	-	-	-	-	-	-	-	-	-	-
101	004140.04+405945.1	682	<SNR>	-	-	-	-	-	-	-	-	-
102	004140.12+410247.0	-	-	BA	37	-	-	-	-	-	-	-
103	004140.60+404941.0	683	<hard>	-	-	-	-	-	-	-	-	-
104	004140.62+410057.5	-	-	-	-	-	-	-	-	-	-	-
105	004141.27+410333.3	685	<AGN>	BA	38	-	-	-	-	-	-	-
106	004141.28+410402.8	684	<GlC>	-	-	-	-	-	-	-	NED	-
107	004141.79+405650.8	-	-	-	-	-	-	-	-	-	-	-
108	004142.12+410014.4	690	<hard>	-	-	-	-	-	-	-	-	-
109	004142.29+405303.5	-	-	-	-	-	-	-	-	-	-	-
110	004143.44+410504.7	696	fgStar	BA	41	-	-	-	-	-	-	-
111	004144.32+405702.0	-	-	-	-	-	-	-	-	-	-	-
112	004144.34+405703.4	-	-	-	-	-	-	-	-	-	-	-
113	004144.69+411112.4	705	<XRB>	-	-	-	-	-	-	-	-	-
114	004145.24+410229.6	-	-	-	-	-	-	-	-	-	-	-
115	004146.47+411652.8	715	<AGN>	-	-	-	-	-	-	-	-	-
116	004147.04+405412.6	-	-	-	-	-	-	-	-	-	-	-
117	004147.91+410109.9	-	-	-	-	-	-	-	-	-	-	-
118	004149.17+405644.1	-	-	DS04	s1-18	-	-	-	-	-	-	-
119	004149.59+410333.6	-	-	BA	49	-	-	-	-	-	-	-
120	004149.69+410105.7	726	<hard>	-	-	-	-	-	-	-	-	-
121	004149.87+410106.1	726	<hard>	WI	s1-16	-	-	-	-	-	-	-
122	004150.28+411336.6	730	<AGN>	KO	r3-110	-	-	-	-	-	-	-
123	004150.47+411212.5	732	GlC	-	-	-	-	732	-	-	-	-
124	004150.60+412113.2	733	<hard>	-	-	-	-	-	-	-	-	-
125	004151.59+411439.2	738	<AGN>	BA	55	-	-	-	-	-	-	-
126	004151.67+411517.2	740	<fgStar>	-	-	-	-	-	-	-	-	-
127	004151.96+405428.9	741	<hard>	-	-	-	-	-	-	-	-	-
128	004151.97+405430.5	741	<hard>	-	-	-	-	-	-	-	-	-
129	004152.83+404709.9	743	GlC	DS02	22	-	-	743	-	-	-	-
130	004153.20+405327.0	-	-	-	-	-	-	-	-	-	-	-
131	004153.27+405302.5	744	<hard>	-	-	-	-	-	-	-	-	-

Source	CXOU J	*XMM-Newton* Match		*Chandra* Match		LMXB Match			AGN Match			
No.		ID	Classification	Catalogue	ID	Peacock et al.; GC	Stiele et al.; Field	Stiele et al.; GC	PHAT	SDSS DR12	NED	SIMBAD
132	004153.35+410124.8	-	-	-	-	-	-	-	-	-	-	-
133	004154.55+405958.4	-	-	-	-	-	-	-	-	-	-	-
134	004154.57+405829.6	-	-	-	-	-	-	-	-	-	-	-
135	004154.66+405648.2	-	-	WI	s1-80	-	-	-	-	-	-	-
136	004154.94+405713.1	-	-	-	-	-	-	-	-	-	-	-
137	004155.08+412302.6	753	<hard>	VO	260	-	-	-	-	-	-	-
138	004157.79+411439.2	-	-	-	-	-	-	-	-	-	-	-
139	004159.12+410541.2	-	-	HO	12	-	-	-	-	-	-	-
140	004159.93+410116.2	-	-	-	-	-	-	-	-	-	-	-
141	004200.22+405314.2	-	-	-	-	-	-	-	-	-	-	-
142	004200.32+405559.3	-	-	-	-	-	-	-	-	-	-	-
143	004200.38+410037.3	-	-	-	-	-	-	-	-	-	-	-
144	004200.45+405942.7	-	-	-	-	-	-	-	-	-	-	-
145	004200.59+411409.7	-	-	-	-	-	-	-	-	-	-	-
146	004200.65+411632.3	-	-	-	-	-	-	-	-	-	-	-
147	004200.95+405751.0	-	-	-	-	-	-	-	-	-	-	-
148	004202.46+405631.2	772	<fgStar>	-	-	-	-	-	-	-	-	-
149	004202.73+412311.2	775	<hard>	-	-	-	-	-	-	-	-	-
150	004203.66+410926.9	782	<hard>	-	-	-	-	-	-	-	-	-
151	004204.16+411531.6	783	<hard>	BA	68	-	-	-	-	-	-	-
152	004204.30+410902.5	-	-	-	-	-	-	-	-	-	-	-
153	004204.40+410930.6	-	-	KO	r3-107	-	-	-	-	-	-	-
154	004204.70+411341.2	-	-	-	-	-	-	-	-	-	-	-
155	004205.62+405713.4	792	none	-	-	-	-	-	-	-	-	-
156	004205.76+411329.6	788	<XRB>	VO	216	-	-	-	-	-	-	-
157	004205.88+411134.1	791	<hard>	VO	232	-	-	-	-	-	-	-
158	004205.96+405011.6	790	<hard>	-	-	-	-	-	-	-	-	-
159	004206.12+410247.7	793	<Gal>	WI	s1-12	-	-	-	-	-	NED	SIMBAD
160	004206.36+412138.3	-	-	-	-	-	-	-	-	-	-	-
161	004207.06+411720.1	795	<hard>	BA	74	-	-	-	-	-	-	-
162	004207.15+410016.3	796	<Gal>	DS02	15	-	-	-	-	-	NED	SIMBAD
163	004207.34+410055.4	-	-	BA	76	-	-	-	-	-	-	-
164	004207.57+411027.4	797	<hard>	VO	235	-	-	-	-	-	-	-
165	004207.73+411814.9	798	<hard>	WI	r3-61	-	-	-	-	-	-	-
166	004207.90+410436.2	799	<hard>	BA	79	-	-	-	-	-	-	-
167	004208.20+411249.3	800	<hard>	VO	209	-	-	-	-	-	-	-
168	004208.27+405514.0	801	<hard>	-	-	-	-	-	-	-	-	-
169	004208.44+410339.7	-	-	-	-	-	-	-	-	-	-	-
170	004208.95+412330.7	803	fgStar	BA	82	-	-	-	-	-	-	-
171	004209.06+412048.4	804	<hard>	KO	r3-60	-	-	-	-	-	-	-
172	004209.27+411106.8	-	-	-	-	-	-	-	-	-	-	-
173	004209.48+411745.5	807	<GlC>	VO	190	MITA140	-	-	-	-	-	-
174	004209.56+412009.6	-	-	VO	213	-	-	-	-	-	-	-
175	004209.99+405035.9	809	<hard>	-	-	-	-	-	-	-	-	-
176	004210.24+405341.8	-	-	-	-	-	-	-	-	-	-	-

Source	CXOU J	*XMM-Newton* Match		*Chandra* Match		LMXB Match			AGN Match			
No.		ID	Classification	Catalogue	ID	Peacock et al.; GC	Stiele et al.; Field	Stiele et al.; GC	PHAT	SDSS DR12	NED	SIMBAD
177	004210.27+411509.8	810	<hard>	VO	184	-	-	-	-	-	-	-
178	004210.36+405149.2	811	<hard>	-	-	-	-	-	-	-	-	-
179	004210.84+410647.8	814	<XRB>	VO	258	-	-	-	-	-	-	-
180	004210.95+411247.9	816	<hard>	BA	89	-	-	-	-	-	-	-
181	004211.29+410428.8	-	-	-	-	-	-	-	-	-	-	-
182	004211.75+411048.8	819	<hard>	KA	10	-	-	-	-	-	-	-
183	004211.93+411648.7	820	<hard>	WI	r3-55	-	-	-	-	-	-	-
184	004212.02+405336.8	822	<hard>	-	-	-	-	-	-	-	-	-
185	004212.16+411758.6	823	<GlC>	VO	179	B078-G140	-	-	-	-	-	-
186	004212.75+411244.1	-	-	BA	97	-	-	-	-	-	-	-
187	004213.00+411628.0	-	-	BA	99	-	-	-	-	-	-	-
188	004213.13+411836.4	829	<hard>	WI	r3-52	-	-	-	-	-	-	-
189	004213.28+405538.4	-	-	-	-	-	-	-	-	-	-	-
190	004214.68+412213.6	-	-	BA	101	-	-	-	-	-	-	-
191	004214.80+405200.8	833	none	-	-	-	-	-	-	-	-	-
192	004214.99+412121.3	-	-	BA	102	-	-	-	-	-	-	-
193	004215.13+411234.3	835	<hard>	WI	r3-50	-	-	-	-	-	-	-
194	004215.23+411801.3	836	<hard>	VO	165	-	-	-	-	-	-	-
195	004215.32+411341.6	-	-	-	-	-	-	-	-	-	-	-
196	004215.48+412031.5	838	<GlC>	VO	196	-	-	-	-	-	-	-
197	004215.64+410113.1	841	GlC	-	-	-	-	-	-	-	-	-
198	004215.67+411720.7	840	<hard>	VO	154	-	-	-	-	-	-	-
199	004215.79+405527.6	-	-	-	-	-	-	-	-	-	-	-
200	004215.80+411135.9	-	-	-	-	-	-	-	-	-	-	-
201	004215.87+410114.3	841	GlC	WI	s1-7	B082-G144	-	841	-	-	-	-
202	004216.04+411553.1	-	-	KO	r3-76	-	-	-	-	-	-	-
203	004216.05+411926.4	-	-	BA	111	-	-	-	-	-	-	-
204	004216.11+412215.5	-	-	-	-	-	-	-	-	-	-	-
205	004216.48+411430.6	-	-	BA	113	-	-	-	-	-	-	-
206	004216.54+405552.3	843	<hard>	WI	s1-6	-	-	-	-	-	-	-
207	004216.56+411610.3	-	-	KO	r3-75	-	-	-	-	-	-	-
208	004216.98+411856.1	-	-	VO	167	-	-	-	-	-	-	-
209	004217.03+411508.2	-	-	VO	146	-	-	-	-	-	-	-
210	004217.29+411536.9	-	-	HO	41	-	-	-	-	-	-	-
211	004217.83+411110.2	-	-	-	-	-	-	-	-	-	-	-
212	004217.95+410859.1	-	-	-	-	-	-	-	-	-	-	-
213	004218.33+411223.5	853	<hard>	KO	r3-45	-	-	-	-	-	-	-
214	004218.33+410210.6	-	-	BA	119	-	-	-	-	-	-	-
215	004218.40+405850.6	-	-	-	-	-	-	-	-	-	-	-
216	004218.63+411401.7	855	GlC	WI	r3-44	B086-G148	-	-	-	-	-	-
217	004218.98+412004.4	859	<hard>	VO	176	-	-	-	-	-	-	-
218	004219.60+411333.9	-	-	BA	127	-	-	-	-	-	-	-
219	004219.71+412154.3	862	GlC	BA	128	-	-	-	-	-	-	-
220	004220.11+410824.2	-	-	BA	129	-	-	-	-	-	-	-
221	004220.35+411313.5	-	-	KO	r3-89	-	-	-	-	-	-	-

Source	CXOU J	*XMM-Newton* Match		*Chandra* Match		LMXB Match			AGN Match			
No.		ID	Classification	Catalogue	ID	Peacock et al.; GC	Stiele et al.; Field	Stiele et al.; GC	PHAT	SDSS DR12	NED	SIMBAD
222	004220.41+411850.9	-	-	-	-	-	-	-	-	-	-	-
223	004220.45+412639.8	864	<AGN>	-	-	-	-	-	-	-	-	-
224	004220.64+405712.3	-	-	-	-	-	-	-	-	-	-	-
225	004220.70+411608.2	-	-	BA	134	-	-	-	-	-	-	-
226	004220.80+411344.0	-	-	BA	135	-	-	-	-	-	-	-
227	004220.85+412256.8	868	<hard>	-	-	-	-	-	-	-	-	-
228	004220.91+405403.1	-	-	-	-	-	-	-	-	-	-	-
229	004220.93+411520.1	-	-	BA	137	-	-	-	-	-	-	-
230	004221.08+411807.7	-	-	KO	r3-43	-	-	-	-	-	-	-
231	004221.15+410717.4	-	-	-	-	-	-	-	-	-	-	-
232	004221.28+411552.4	-	-	HO	47	-	-	-	-	-	-	-
233	004221.29+411548.9	-	-	VO	115	-	-	-	-	-	-	-
234	004221.48+411601.2	870	<hard>	VO	112	-	-	-	-	-	-	-
235	004221.56+411419.6	872	<GlC>	VO	126	-	-	-	-	-	-	-
236	004221.79+411502.1	-	-	BA	145	-	-	-	-	-	-	-
237	004221.83+411206.0	-	-	-	-	-	-	-	-	-	-	-
238	004222.24+405925.1	875	<hard>	WI	s1-5	-	-	-	-	-	-	-
239	004222.30+411345.3	-	-	BA	147	-	-	-	-	-	-	-
240	004222.30+411222.5	-	-	-	-	-	-	-	-	-	-	-
241	004222.36+411335.1	876	<hard>	-	-	-	-	-	-	-	-	-
242	004222.42+411333.9	876	<hard>	VO	132	-	-	-	-	-	-	-
243	004222.48+405743.2	-	-	BA	149	-	-	-	-	-	-	-
244	004222.61+412234.3	-	-	KO	r3-88	-	-	-	-	-	-	-
245	004222.94+411535.2	877	<hard>	WI	r3-39	-	-	-	-	-	-	-
246	004223.03+410738.7	878	<hard>	BA	152	-	-	-	-	-	-	-
247	004223.09+411409.0	879	<hard>	-	-	-	-	-	-	-	-	-
248	004223.17+411406.8	879	<hard>	WI	r3-38	-	-	-	-	-	-	-
249	004224.10+411536.9	-	-	VO	96	-	-	-	-	-	-	-
250	004224.12+404849.2	-	-	-	-	-	-	-	-	-	-	-
251	004224.17+411732.8	883	SNR	KO	r2-57	-	-	-	-	-	-	-
252	004224.34+411730.1	883	SNR	BA	154	-	-	-	-	-	-	-
253	004224.52+412401.5	884	<XRB>	VO	233	-	-	-	-	-	-	-
254	004224.59+411908.7	-	-	-	-	-	-	-	-	-	-	-
255	004225.04+405719.3	885	GlC	DS02	21	-	-	-	-	-	-	-
256	004225.08+411341.7	888	<fgStar>	-	-	-	-	-	-	-	-	-
257	004225.12+411340.4	888	<fgStar>	KO	r2-45	-	-	-	-	-	-	-
258	004225.94+411914.6	895	GlC	DS02	14	-	-	-	-	-	-	-
259	004226.04+411914.8	895	GlC	VO	125	B096-G158	-	895	-	-	-	-
260	004226.11+411915.7	895	GlC	-	-	-	-	-	-	-	-	-
261	004226.14+412551.9	896	<hard>	KO	r3-87	-	-	-	-	-	-	-
262	004226.18+405457.8	897	<hard>	-	-	-	-	-	-	-	-	-
263	004226.25+405458.8	897	<hard>	-	-	-	-	-	-	-	-	-
264	004226.50+411346.5	-	-	BA	161	-	-	-	-	-	-	-
265	004226.52+412351.3	-	-	BA	162	-	-	-	-	-	-	-
266	004227.01+410105.1	-	-	-	-	-	-	-	-	-	-	-

Source	CXOU J	*XMM-Newton* Match		*Chandra* Match		LMXB Match			AGN Match			
No.		ID	Classification	Catalogue	ID	Peacock et al.; GC	Stiele et al.; Field	Stiele et al.; GC	PHAT	SDSS DR12	NED	SIMBAD
267	004227.22+405658.3	-	-	-	-	-	-	-	-	-	-	-
268	004227.35+405527.1	904	<hard>	-	-	-	-	-	-	-	-	-
269	004227.41+405936.1	906	GlC	DS02	25	B098	-	906	-	-	-	-
270	004227.47+411452.4	-	-	BA	164	-	-	-	-	-	-	-
271	004227.62+412048.3	907	<hard>	KO	r3-37	-	-	-	-	-	-	-
272	004227.92+411817.6	-	-	BA	166	-	-	-	-	-	-	-
273	004228.03+411807.6	-	-	-	-	-	-	-	-	-	-	-
274	004228.11+411001.7	910	<XRB>	-	-	-	-	-	-	-	-	-
275	004228.21+411000.1	910	<XRB>	VO	192	-	-	-	-	-	-	-
276	004228.28+411223.1	911	<hard>	WI	r2-35	-	-	-	-	-	-	-
277	004228.35+411449.1	-	-	BA	169	-	-	-	-	-	-	-
278	004228.42+410854.5	-	-	-	-	-	-	-	-	-	-	-
279	004228.47+411938.5	-	-	-	-	-	-	-	-	-	-	-
280	004228.82+411741.3	-	-	BA	170	-	-	-	-	-	-	-
281	004228.94+410436.1	912	<hard>	WI	r3-111	-	-	-	-	-	-	-
282	004229.02+411432.8	-	-	-	-	-	-	-	-	-	-	-
283	004229.09+411547.8	-	-	HO	65	-	-	-	-	-	-	-
284	004229.09+411348.7	-	-	HO	67	-	-	-	-	-	-	-
285	004229.24+404907.7	916	<hard>	-	-	-	-	-	-	-	-	-
286	004229.35+405750.1	-	-	-	-	-	-	-	-	-	-	-
287	004229.72+405247.8	-	-	-	-	-	-	-	-	-	-	-
288	004230.10+411841.8	-	-	-	-	-	-	-	-	-	-	-
289	004230.26+411653.1	-	-	VO	70	-	-	-	-	-	-	-
290	004230.55+410909.9	-	-	-	-	-	-	-	-	-	-	-
291	004230.72+405641.8	-	-	-	-	-	-	-	-	-	-	-
292	004230.96+411910.2	921	<hard>	VO	101	-	-	-	-	-	-	-
293	004231.13+411621.5	922	<hard>	VO	64	-	-	-	-	-	-	-
294	004231.24+411938.8	923	GlC	KA	37	B107-G169	-	923	-	-	-	-
295	004231.29+410437.1	925	<hard>	-	-	-	-	-	-	-	-	-
296	004231.30+412007.7	924	<GlC>	VO	127	-	-	-	-	-	-	-
297	004231.61+411259.7	-	-	-	-	-	-	-	-	-	-	-
298	004231.88+412306.4	929	<hard>	-	-	-	-	-	-	-	-	-
299	004232.07+411314.4	930	<hard>	WI	r2-32	-	-	-	-	-	-	-
300	004232.08+411912.9	-	-	VO	97	-	-	-	-	-	-	-
301	004232.14+412305.3	929	<hard>	BA	183	-	-	-	-	-	-	-
302	004232.17+411944.6	-	-	-	-	-	-	-	-	-	-	-
303	004232.52+411545.3	-	-	KO	r2-55	-	-	-	-	-	-	-
304	004232.74+411310.8	-	-	VO	92	-	-	-	-	-	-	-
305	004232.78+411303.9	-	-	-	-	-	-	-	-	-	-	-
306	004232.90+411142.6	-	-	-	-	-	-	-	-	-	-	-
307	004232.95+411143.9	-	-	-	-	-	-	-	-	-	-	-
308	004233.13+410328.8	933	GlC	BA	189	B110-G172	-	933	-	-	-	-
309	004233.25+411742.2	-	-	HO	82	-	-	-	-	-	-	-
310	004233.27+410647.7	935	<hard>	BA	190	-	-	-	-	-	-	-
311	004233.41+411703.4	-	-	VO	59	-	-	-	-	-	-	-

Source	CXOU J	*XMM-Newton* Match		*Chandra* Match		LMXB Match			AGN Match			
No.		ID	Classification	Catalogue	ID	Peacock et al.; GC	Stiele et al.; Field	Stiele et al.; GC	PHAT	SDSS DR12	NED	SIMBAD
312	004233.51+412138.4	936	fgStar	BA	192	-	-	-	-	-	-	-
313	004233.80+405454.1	937	<hard>	-	-	-	-	-	-	-	-	-
314	004233.80+412039.9	-	-	VO	133	-	-	-	-	-	-	-
315	004233.87+412331.3	939	<XRB>	VO	212	-	-	-	-	-	-	-
316	004233.88+411619.7	940	<hard>	VO	52	-	-	-	-	-	-	-
317	004234.04+412249.0	-	-	-	-	-	-	-	-	-	-	-
318	004234.15+412149.8	942	<hard>	VO	170	-	-	-	-	-	-	-
319	004234.38+405709.1	946	GlC	-	-	B117-G176	-	-	-	-	-	-
320	004234.43+411809.3	944	XRB	KO	r2-29	-	944	-	-	-	-	-
321	004234.71+404904.0	-	-	-	-	-	-	-	-	-	-	-
322	004234.76+411523.1	-	-	KO	r2-28	-	-	-	-	-	-	-
323	004234.93+405720.8	949	<XRB>	WI	s1-1	-	-	-	-	-	-	-
324	004234.98+404838.8	948	AGN	WI	s1-83	-	-	-	-	-	-	-
325	004235.18+405249.9	-	-	-	-	-	-	-	-	-	-	-
326	004235.20+412005.6	952	<hard>	VO	113	-	-	-	-	-	-	-
327	004235.47+411607.0	-	-	-	-	-	-	-	-	-	-	-
328	004235.88+411007.4	957	<hard>	BA	202	-	-	-	-	-	-	-
329	004236.07+412021.3	-	-	BA	203	-	-	-	-	-	-	-
330	004236.13+411046.4	-	-	-	-	-	-	-	-	-	-	-
331	004236.38+405848.8	959	<hard>	-	-	-	-	-	-	-	-	-
332	004236.58+411554.3	-	-	HO	98	-	-	-	-	-	-	-
333	004236.60+411350.3	960	<fgStar>	VO	69	-	-	-	-	-	-	-
334	004236.66+405605.0	961	<fgStar>	-	-	-	-	-	-	-	-	-
335	004237.04+411427.9	-	-	BA	206	-	-	-	-	-	-	-
336	004237.54+405505.0	-	-	-	-	-	-	-	-	-	-	-
337	004237.84+412133.7	-	-	BA	207	-	-	-	-	-	-	-
338	004237.93+410526.4	965	<hard>	KO	r3-100	-	-	-	-	-	-	-
339	004238.38+412010.6	-	-	-	-	-	-	-	-	-	-	-
340	004238.58+411603.6	966	XRB	VO	34	-	966	-	-	-	-	-
341	004238.66+411723.7	-	-	BA	210	-	-	-	-	-	-	-
342	004238.76+411526.7	-	-	BA	211	-	-	-	-	-	-	-
343	004239.02+411325.5	-	-	HO	108	-	-	-	-	-	-	-
344	004239.22+411424.7	-	-	BA	212	-	-	-	-	-	-	-
345	004239.40+405425.0	-	-	-	-	-	-	-	-	-	-	-
346	004239.53+411428.4	968	<hard>	VO	50	-	-	-	-	-	-	-
347	004239.57+411614.0	-	-	VO	29	-	-	-	-	-	-	-
348	004239.64+411700.7	-	-	KA	47	-	-	-	-	-	-	-
349	004239.80+411453.9	-	-	BA	216	-	-	-	-	-	-	-
350	004239.96+411522.1	-	-	-	-	-	-	-	-	-	-	-
351	004239.98+411547.4	971	<hard>	VO	28	-	-	-	-	-	-	-
352	004240.11+411628.3	-	-	-	-	-	-	-	-	-	-	-
353	004240.20+411845.0	972	<hard>	VO	66	-	-	-	-	-	-	-
354	004240.45+411545.9	971	<hard>	BA	220	-	-	-	-	-	-	-
355	004240.53+411355.3	-	-	KO	r2-23	-	-	-	-	-	-	-
356	004240.56+411034.4	975	GlC	KA	50	-	-	-	-	-	-	-

Source	CXOU J	*XMM-Newton* Match		*Chandra* Match		LMXB Match			AGN Match			
No.		ID	Classification	Catalogue	ID	Peacock et al.; GC	Stiele et al.; Field	Stiele et al.; GC	PHAT	SDSS DR12	NED	SIMBAD
357	004240.65+411327.4	974	<hard>	WI	r2-22	-	-	-	-	-	-	-
358	004240.66+411033.2	975	GlC	VO	157	B123-G182	-	-	-	-	-	-
359	004240.71+405116.5	-	-	-	-	-	-	-	-	-	-	-
360	004240.72+411833.2	-	-	-	-	-	-	-	-	-	-	-
361	004240.73+411004.3	-	-	BA	224	-	-	-	-	-	-	-
362	004240.85+411005.5	-	-	-	-	-	-	-	-	-	-	-
363	004240.89+412216.2	976	<fgStar>	VO	175	-	-	-	-	-	-	-
364	004241.02+405711.4	-	-	-	-	-	-	-	-	-	-	-
365	004241.05+410701.3	979	<hard>	KO	r3-85	-	-	-	-	-	-	-
366	004241.08+411101.7	-	-	BA	226	-	-	-	-	-	-	-
367	004241.14+411821.2	-	-	-	-	-	-	-	-	-	-	-
368	004241.17+411545.2	-	-	-	-	-	-	-	-	-	-	-
369	004241.38+411528.4	981	GlC	-	-	-	-	-	-	-	-	-
370	004241.43+411523.8	981	GlC	KO	r1-32	B124-NB10	-	981	-	-	-	-
371	004241.46+411617.8	-	-	HO	127	-	-	-	-	-	-	-
372	004241.61+411436.9	-	-	HO	128	-	-	-	-	-	-	-
373	004241.64+412105.4	984	<hard>	VO	135	-	-	-	-	-	-	-
374	004241.78+411635.8	985	XRB	-	-	-	985	-	-	-	-	-
375	004241.80+405154.6	-	-	-	-	-	-	-	-	-	NED	-
376	004242.07+411531.9	-	-	VO	24	-	-	-	-	-	-	-
377	004242.17+411608.0	990	XRB	VO	14	-	990	-	-	-	-	-
378	004242.20+411913.8	-	-	VO	76	-	-	-	-	-	-	-
379	004242.32+411445.4	992	<hard>	KO	r2-21	-	-	-	-	-	-	-
380	004242.36+411544.9	-	-	HO	135	-	-	-	-	-	-	-
381	004242.47+411553.6	994	<hard>	VO	15	-	-	-	-	-	-	-
382	004242.50+405152.0	995	Gal	-	-	-	-	-	-	-	-	-
383	004242.52+411659.3	-	-	KA	58	-	-	-	-	-	-	-
384	004242.52+411558.3	-	-	-	-	-	-	-	-	-	-	-
385	004242.63+411405.0	-	-	BA	243	-	-	-	-	-	-	-
386	004242.64+411645.5	-	-	BA	244	-	-	-	-	-	-	-
387	004242.68+405112.7	-	-	-	-	-	-	-	-	-	-	-
388	004242.71+411446.5	992	<hard>	HO	139	-	-	-	-	-	-	-
389	004242.72+411455.4	-	-	BA	245	-	-	-	-	-	-	-
390	004242.75+411614.2	-	-	HO	143	-	-	-	-	-	-	-
391	004242.80+411940.0	-	-	BA	246	-	-	-	-	-	-	-
392	004242.99+411543.1	997	<hard>	VO	16	-	-	-	-	-	-	-
393	004243.09+411603.9	-	-	KA	61	-	-	-	-	-	-	-
394	004243.13+411627.3	-	-	-	-	-	-	-	-	-	-	-
395	004243.18+411640.0	-	-	KO	r1-24	-	-	-	-	-	-	-
396	004243.23+411559.2	-	-	-	-	-	-	-	-	-	-	-
397	004243.27+405350.7	1001	<hard>	-	-	-	-	-	-	-	-	-
398	004243.30+411319.4	1000	none	KO	r2-19	-	-	-	-	-	-	-
399	004243.66+411241.8	-	-	-	-	-	-	-	-	-	-	-
400	004243.66+405514.8	1003	<hard>	-	-	-	-	-	-	-	-	-
401	004243.70+412519.2	-	-	HO	149	-	-	-	-	-	-	-

Source	CXOU J	*XMM-Newton* Match		*Chandra* Match		LMXB Match			AGN Match			
No.		ID	Classification	Catalogue	ID	Peacock et al.; GC	Stiele et al.; Field	Stiele et al.; GC	PHAT	SDSS DR12	NED	SIMBAD
402	004243.74+411632.3	1005	<XRB>	VO	13	-	-	-	-	-	-	-
403	004243.78+411514.1	-	-	VO	32	-	-	-	-	-	-	-
404	004243.80+411612.4	-	-	HO	154	-	-	-	-	-	-	-
405	004243.85+411603.8	-	-	VO	6	-	-	-	-	-	-	-
406	004243.88+411629.6	1005	<XRB>	VO	11	-	-	-	-	-	-	-
407	004243.91+411755.0	1006	<SSS>	DS04	r2-60	-	-	-	-	-	-	-
408	004243.93+411610.6	-	-	HO	159	-	-	-	-	-	-	-
409	004243.98+411636.9	-	-	HO	161	-	-	-	-	-	-	-
410	004244.02+411645.0	-	-	-	-	-	-	-	-	-	-	-
411	004244.12+411603.9	-	-	KO	r1-33	-	-	-	-	-	-	-
412	004244.28+411613.9	-	-	VO	4	-	-	-	-	-	-	-
413	004244.35+411608.6	1010	<XRB>	VO	1	-	-	-	-	-	NED	SIMBAD
414	004244.36+405629.7	-	-	-	-	-	-	-	-	-	-	-
415	004244.36+411605.3	1010	<XRB>	KA	70	-	-	-	-	-	-	-
416	004244.36+411607.3	1010	<XRB>	VO	2	-	-	-	-	-	-	SIMBAD
417	004244.37+411158.4	1011	<hard>	VO	107	-	-	-	-	-	-	-
418	004244.40+410000.2	1009	<hard>	-	-	-	-	-	-	-	-	-
419	004244.45+410939.7	-	-	-	-	-	-	-	-	-	-	-
420	004244.49+411404.0	-	-	-	-	-	-	-	-	-	-	-
421	004244.60+411802.6	-	-	VO	49	-	-	-	-	-	-	-
422	004244.66+411618.0	1015	<hard>	VO	7	-	-	-	-	-	-	-
423	004244.73+411614.6	-	-	-	-	-	-	-	-	-	-	-
424	004244.82+411138.1	1013	<hard>	WI	r3-29	-	-	-	-	-	-	-
425	004244.89+411739.6	1012	<hard>	KO	r2-18	-	-	-	-	-	-	-
426	004244.94+411509.8	-	-	-	-	-	-	-	-	-	-	-
427	004244.94+411518.7	-	-	-	-	-	-	-	-	-	-	-
428	004245.05+411521.0	-	-	HO	176	-	-	-	-	-	-	-
429	004245.08+411523.1	-	-	VO	26	-	-	-	-	-	-	-
430	004245.09+411407.0	1016	<XRB>	KO	r2-17	-	-	-	-	-	-	-
431	004245.10+411645.6	-	-	-	-	-	-	-	-	-	-	-
432	004245.11+411621.6	1015	<hard>	VO	10	-	-	-	-	-	-	-
433	004245.11+411542.5	-	-	HO	180	-	-	-	-	-	-	-
434	004245.11+411536.9	-	-	-	-	-	-	-	-	-	-	-
435	004245.21+411722.2	1017	<XRB>	VO	38	-	-	-	-	-	-	-
436	004245.22+411611.0	-	-	VO	8	-	-	-	-	-	-	-
437	004245.52+411652.3	-	-	VO	25	-	-	-	-	-	-	-
438	004245.58+411608.5	-	-	WI	r1-7	-	-	-	-	-	-	-
439	004245.59+411606.4	-	-	-	-	-	-	-	-	-	-	-
440	004245.80+412432.8	1018	<hard>	VO	229	-	-	-	-	-	-	-
441	004245.92+411651.5	-	-	-	-	-	-	-	-	-	-	-
442	004245.93+411036.3	-	-	HO	185	-	-	-	-	-	-	-
443	004245.99+411619.5	-	-	KA	81	-	-	-	-	-	-	-
444	004246.08+411736.1	-	-	VO	44	-	-	-	-	-	-	-
445	004246.12+411728.7	-	-	BA	279	-	-	-	-	-	-	-
446	004246.15+411543.1	-	-	VO	19	-	-	-	-	-	-	-

Source	CXOU J	*XMM-Newton* Match		*Chandra* Match		LMXB Match			AGN Match			
No.		ID	Classification	Catalogue	ID	Peacock et al.; GC	Stiele et al.; Field	Stiele et al.; GC	PHAT	SDSS DR12	NED	SIMBAD
447	004246.27+412723.7	1021	<hard>	BA	282	-	-	-	-	-	-	-
448	004246.41+411609.9	-	-	HO	189	-	-	-	-	-	-	-
449	004246.70+410735.4	-	-	-	-	-	-	-	-	-	-	-
450	004246.72+411359.5	-	-	-	-	-	-	-	-	-	-	-
451	004246.85+411605.6	-	-	-	-	-	-	-	-	-	-	-
452	004246.90+412119.3	1022	<hard>	KO	r3-28	-	-	-	-	-	-	-
453	004246.95+411615.5	1023	<AGN>	VO	17	-	-	-	-	-	-	-
454	004247.03+411731.0	-	-	-	-	-	-	-	-	-	-	-
455	004247.07+411910.7	-	-	-	-	-	-	-	-	-	-	-
456	004247.15+411619.6	-	-	-	-	-	-	-	-	-	-	-
457	004247.16+411628.4	1024	<XRB>	VO	20	-	-	-	-	-	-	-
458	004247.16+411407.0	-	-	BA	287	-	-	-	-	-	-	-
459	004247.16+411413.0	1025	<SSS>	BA	288	-	-	-	-	-	-	-
460	004247.22+411157.8	1028	<hard>	KO	r3-27	-	-	-	-	-	-	-
461	004247.37+410832.3	-	-	-	-	-	-	-	-	-	-	-
462	004247.46+411619.2	-	-	-	-	-	-	-	-	-	-	-
463	004247.47+411526.7	-	-	-	-	-	-	-	-	-	-	-
464	004247.69+405837.3	1031	<hard>	-	-	-	-	-	-	-	-	-
465	004247.78+405021.8	-	-	-	-	-	-	-	-	-	-	-
466	004247.79+411113.7	1032	<GlC>	VO	136	B128-G187	-	-	-	-	-	-
467	004247.85+411622.9	-	-	VO	22	-	-	-	-	-	-	-
468	004247.87+411549.6	1034	<XRB>	VO	23	-	-	-	-	-	-	-
469	004247.88+411532.8	1033	<hard>	VO	31	-	-	-	-	-	-	-
470	004247.91+411052.6	-	-	BA	295	-	-	-	-	-	-	-
471	004247.92+411602.2	-	-	-	-	-	-	-	-	-	-	-
472	004247.94+412404.6	-	-	-	-	-	-	-	-	-	-	-
473	004248.11+411729.5	-	-	-	-	-	-	-	-	-	-	-
474	004248.26+412032.8	-	-	VO	119	-	-	-	-	-	-	-
475	004248.46+412522.3	1035	<XRB>	KA	91	-	-	-	-	-	-	-
476	004248.52+411521.1	1036	<hard>	VO	35	-	-	-	-	-	-	-
477	004248.60+411612.9	-	-	-	-	-	-	-	-	-	-	-
478	004248.70+411624.4	-	-	VO	27	-	-	-	-	-	-	-
479	004248.83+411745.7	-	-	BA	302	-	-	-	-	-	-	-
480	004248.83+411512.9	-	-	-	-	-	-	-	-	-	-	-
481	004248.89+412406.9	1040	SNR	VO	223	-	-	-	-	-	-	-
482	004249.02+411945.8	-	-	VO	94	-	-	-	2180	-	-	-
483	004249.11+411456.6	-	-	-	-	-	-	-	-	-	-	-
484	004249.12+411233.7	-	-	-	-	-	-	-	-	-	-	-
485	004249.13+411742.0	-	-	VO	48	-	-	-	-	-	-	-
486	004249.16+411623.4	-	-	HO	209	-	-	-	-	-	-	-
487	004249.22+411815.8	1041	<hard>	VO	61	-	-	-	-	-	-	-
488	004249.22+411601.1	-	-	HO	210	-	-	-	-	-	-	-
489	004249.42+412235.1	1043	<hard>	BA	309	-	-	-	-	-	-	-
490	004249.47+410635.3	1045	<hard>	-	-	-	-	-	-	-	-	-
491	004249.76+405327.8	-	-	-	-	-	-	-	-	-	-	-

Source	CXOU J	*XMM-Newton* Match		*Chandra* Match		LMXB Match			AGN Match			
No.		ID	Classification	Catalogue	ID	Peacock et al.; GC	Stiele et al.; Field	Stiele et al.; GC	PHAT	SDSS DR12	NED	SIMBAD
492	004249.92+411718.2	-	-	-	-	-	-	-	-	-	-	-
493	004249.96+412205.8	-	-	-	-	-	-	-	-	-	-	-
494	004250.14+404749.5	1047	<hard>	-	-	-	-	-	-	-	-	-
495	004250.21+404955.1	-	-	-	-	-	-	-	-	-	-	-
496	004250.23+411812.9	-	-	KO	r2-40	-	-	-	-	-	-	-
497	004250.41+411556.5	1050	SNR	DS04	r2-56	-	-	-	-	-	-	-
498	004250.50+411555.9	1050	SNR	KO	r2-56	-	-	-	-	-	-	-
499	004250.59+411033.4	-	-	-	-	-	-	-	-	-	-	-
500	004250.76+411033.5	-	-	BA	316	BH18	-	-	-	-	-	-
501	004250.80+411551.5	-	-	BA	318	-	-	-	-	-	-	-
502	004250.81+411707.3	-	-	BA	317	-	-	-	-	-	-	-
503	004251.17+411917.8	-	-	-	-	-	-	-	-	-	-	-
504	004251.23+405650.3	1052	<hard>	-	-	-	-	-	-	-	-	-
505	004251.24+411607.4	-	-	-	-	-	-	-	-	-	-	-
506	004251.29+410448.0	1053	<fgStar>	-	-	-	-	-	-	-	-	-
507	004251.34+411639.7	-	-	BA	320	-	-	-	-	-	-	-
508	004251.60+411701.3	-	-	-	-	-	-	-	-	-	-	-
509	004251.62+411512.1	-	-	BA	323	-	-	-	-	-	-	-
510	004251.63+411922.6	-	-	-	-	-	-	-	-	-	-	-
511	004251.63+411302.8	1056	<hard>	KO	r2-39	-	-	-	-	-	-	-
512	004251.65+412634.4	1055	<AGN>	VO	251	-	-	-	-	-	-	-
513	004251.79+411727.2	-	-	HO	222	-	-	-	-	-	-	-
514	004251.86+405240.1	-	-	-	-	-	-	-	-	-	-	-
515	004252.29+411734.7	-	-	KA	99	-	-	-	-	-	-	-
516	004252.30+405616.1	-	-	-	-	-	-	-	-	-	-	-
517	004252.33+412142.4	-	-	VO	164	-	-	-	-	-	-	-
518	004252.41+411648.7	1059	<XRB>	VO	47	-	-	-	-	-	-	-
519	004252.50+412204.0	-	-	BA	332	-	-	-	-	-	-	-
520	004252.51+411854.3	1060	<XRB>	KA	101	-	-	-	-	-	-	-
521	004252.51+411834.8	-	-	VO	73	-	-	-	-	-	-	-
522	004252.51+411539.9	1061	<SSS>	VO	46	-	-	-	-	-	-	-
523	004252.62+411328.4	-	-	BA	336	-	-	-	-	-	-	-
524	004252.72+410911.6	-	-	-	-	-	-	-	-	-	-	-
525	004252.99+405019.9	-	-	-	-	-	-	-	-	-	-	-
526	004253.04+410709.5	-	-	-	-	-	-	-	-	-	-	-
527	004253.16+411422.7	-	-	HO	234	-	-	-	-	-	-	-
528	004253.39+411115.6	-	-	-	-	-	-	-	-	-	-	-
529	004253.58+411639.0	-	-	-	-	-	-	-	-	-	-	-
530	004253.63+405318.0	1071	<hard>	-	-	-	-	-	-	-	-	-
531	004253.64+412551.0	1066	SNR	BA	341	-	-	-	-	-	-	-
532	004253.66+405243.6	1070	<hard>	-	-	-	-	-	-	-	-	-
533	004253.95+405546.5	-	-	-	-	-	-	-	-	-	-	-
534	004254.15+412037.2	-	-	-	-	-	-	-	-	-	-	-
535	004254.47+410401.3	-	-	-	-	-	-	-	-	-	-	-
536	004254.68+411053.9	-	-	-	-	-	-	-	-	-	-	-

Source	CXOU J	*XMM-Newton* Match		*Chandra* Match		LMXB Match			AGN Match			
No.		ID	Classification	Catalogue	ID	Peacock et al.; GC	Stiele et al.; Field	Stiele et al.; GC	PHAT	SDSS DR12	NED	SIMBAD
537	004254.81+412011.5	-	-	VO	122	-	-	-	-	-	-	-
538	004254.90+411617.7	-	-	-	-	-	-	-	-	-	-	-
539	004254.92+411603.1	1075	<hard>	VO	54	-	-	-	-	-	-	-
540	004255.17+411836.0	1078	<hard>	VO	79	-	-	-	-	-	-	-
541	004255.33+404829.0	-	-	-	-	-	-	-	-	-	-	-
542	004255.36+412557.4	1077	<hard>	KA	107	-	-	-	-	-	-	-
543	004255.43+405946.3	1079	<SNR>	-	-	-	-	-	-	-	-	-
544	004255.60+411835.0	1078	<hard>	VO	81	-	-	-	-	-	-	-
545	004256.01+411218.3	-	-	VO	118	-	-	-	-	-	-	-
546	004256.37+411914.8	-	-	-	-	-	-	-	-	-	-	-
547	004256.76+410432.8	1086	<hard>	BA	352	-	-	-	-	-	-	-
548	004256.92+411843.8	1084	<XRB>	VO	85	-	-	-	-	-	-	-
549	004256.98+412005.0	-	-	BA	355	-	-	-	-	-	-	-
550	004257.15+411959.2	-	-	VO	124	-	-	-	-	-	-	-
551	004257.28+405359.0	-	-	-	-	-	-	-	-	-	-	-
552	004257.38+411209.4	-	-	BA	357	-	-	-	-	-	-	-
553	004257.63+412137.6	-	-	-	-	-	-	-	-	-	-	-
554	004257.70+405059.4	1089	<hard>	-	-	-	-	-	-	-	-	-
555	004257.90+411104.6	1091	<hard>	VO	160	-	-	-	-	-	-	-
556	004258.04+411319.2	-	-	BA	359	-	-	-	-	-	-	-
557	004258.10+411337.5	-	-	VO	91	-	-	-	-	-	-	-
558	004258.30+411802.9	-	-	-	-	-	-	-	-	-	-	-
559	004258.31+411529.2	1093	<hard>	VO	67	-	-	-	-	-	-	-
560	004258.60+411159.1	1096	<hard>	BA	364	-	-	-	-	-	-	-
561	004258.66+411527.0	1093	<hard>	-	-	-	-	-	-	-	-	-
562	004258.77+405901.6	1095	<fgStar>	-	-	-	-	-	-	-	-	-
563	004258.82+411157.7	1096	<hard>	-	-	-	-	-	-	-	-	-
564	004259.08+411611.7	-	-	-	-	-	-	-	-	-	-	-
565	004259.09+411159.1	1096	<hard>	KO	r2-58	-	-	-	-	-	-	-
566	004259.44+412946.0	1099	<hard>	-	-	-	-	-	-	-	-	-
567	004259.50+411242.2	1101	<hard>	VO	121	-	-	-	-	-	-	-
568	004259.58+411918.4	1102	GlC	DS02	5	-	-	-	-	-	-	-
569	004259.65+411919.3	1102	GlC	VO	111	B143-G198	-	1102	-	-	-	-
570	004259.85+411142.7	-	-	-	-	-	-	-	-	-	-	-
571	004259.86+411605.7	1103	GlC	VO	74	B144	-	1103	-	-	-	-
572	004300.82+411349.2	1108	<hard>	BA	375	-	-	-	-	-	-	-
573	004300.88+411504.2	-	-	-	-	-	-	-	-	-	-	-
574	004301.09+411351.6	1108	<hard>	KA	115	-	-	-	-	-	-	-
575	004301.13+411317.2	-	-	BA	377	-	-	-	-	-	-	-
576	004301.42+413017.3	1109	GlC	BA	378	B091D-D058	-	1109	-	-	-	-
577	004301.62+411052.7	1110	<fgStar>	BA	379	-	-	-	-	-	-	-
578	004301.65+411757.2	-	-	-	-	-	-	-	-	-	-	-
579	004301.70+411814.6	-	-	VO	99	-	-	-	-	-	-	-
580	004301.77+411726.4	-	-	VO	86	-	-	-	-	-	-	-
581	004301.96+405620.3	1112	<hard>	-	-	-	-	-	-	-	-	-

Source	CXOU J	*XMM-Newton* Match		*Chandra* Match		LMXB Match			AGN Match			
No.		ID	Classification	Catalogue	ID	Peacock et al.; GC	Stiele et al.; Field	Stiele et al.; GC	PHAT	SDSS DR12	NED	SIMBAD
582	004301.98+411649.2	-	-	-	-	-	-	-	-	-	-	-
583	004302.45+411202.9	1114	<hard>	VO	151	-	-	-	-	-	-	-
584	004302.54+411202.3	1114	<hard>	-	-	-	-	-	-	-	-	-
585	004302.92+411522.5	1116	GlC	VO	88	B146	-	-	-	-	-	-
586	004302.95+411015.9	1117	<GlC>	-	-	-	-	-	-	-	-	-
587	004303.00+412041.7	1115	<hard>	KA	118	-	-	-	-	-	-	-
588	004303.14+411015.3	1117	<GlC>	BA	388	-	-	-	-	-	-	-
589	004303.21+411527.7	1116	GlC	VO	90	-	-	-	-	-	-	-
590	004303.30+412121.6	1118	GlC	VO	180	B147-G199	-	1118	-	-	-	-
591	004303.86+411804.8	1122	GlC	VO	106	B148-G200	-	1122	-	-	-	-
592	004304.23+411601.3	1124	<GlC>	VO	95	-	-	-	-	-	-	-
593	004304.39+411643.0	-	-	-	-	-	-	-	-	-	-	-
594	004304.74+411113.8	-	-	BA	394	-	-	-	-	-	-	-
595	004305.20+411132.3	-	-	BA	395	-	-	-	-	-	-	-
596	004305.67+411702.7	1131	<XRB>	VO	105	-	-	-	-	-	-	-
597	004306.43+411314.1	-	-	BA	397	-	-	-	-	-	-	-
598	004306.55+411916.2	1134	none	-	-	-	-	-	-	-	-	-
599	004306.60+412244.4	1132	<hard>	VO	218	-	-	-	-	-	-	-
600	004306.72+411917.6	1134	none	-	-	-	-	-	-	-	-	-
601	004306.73+412244.3	1132	<hard>	BA	399	-	-	-	-	-	-	-
602	004306.74+410435.9	-	-	-	-	-	-	-	-	-	-	-
603	004306.79+411912.0	1134	none	KO	r3-67	-	-	-	-	-	-	-
604	004307.11+411810.0	1136	<XRB>	VO	128	-	-	-	-	-	-	-
605	004307.49+412019.6	1137	<GlC>	VO	172	B150-G203	-	-	-	-	-	-
606	004307.62+404816.5	1140	<hard>	-	-	-	-	-	-	-	-	-
607	004307.73+412416.0	1138	<hard>	-	-	-	-	-	-	-	-	-
608	004308.63+411248.3	1146	XRB	VO	159	-	-	-	-	-	-	-
609	004308.91+410731.5	1149	<fgStar>	-	-	-	-	-	-	-	-	-
610	004309.65+405922.9	1151	<hard>	-	-	-	-	-	-	-	-	-
611	004309.84+411900.7	1152	<XRB>	VO	155	-	-	-	-	-	-	-
612	004309.95+412332.4	1153	XRB	BA	412	-	1153	-	-	-	-	-
613	004309.96+412718.5	1154	<hard>	-	-	-	-	-	-	-	-	-
614	004310.17+411719.7	-	-	BA	414	-	-	-	2958	-	-	-
615	004310.61+411451.2	1157	GlC	VO	139	B153	-	1157	-	-	-	-
616	004310.96+411255.7	-	-	-	-	-	-	-	-	-	-	-
617	004311.35+411809.5	1160	<hard>	BA	418	-	-	-	-	-	-	-
618	004311.64+410605.7	-	-	-	-	-	-	-	-	-	-	-
619	004312.42+405856.0	1162	<hard>	BA	421	-	-	-	-	-	-	-
620	004312.99+410034.8	1165	<hard>	-	-	-	-	-	-	-	-	-
621	004313.21+411813.1	1167	<hard>	BA	424	-	-	-	-	-	-	-
622	004313.84+411711.2	-	-	-	-	-	-	-	-	-	-	-
623	004314.10+411302.6	-	-	BA	426	-	-	-	-	-	-	-
624	004314.36+410721.1	1171	GlC	BA	427	B158-G213	-	-	-	-	-	-
625	004314.36+411650.1	1172	<hard>	BA	428	-	-	-	-	-	-	-
626	004314.59+412513.9	1173	GlC	KO	r3-105	B159	-	1173	-	-	-	-

Source	CXOU J	*XMM-Newton* Match		*Chandra* Match		LMXB Match			AGN Match			
No.		ID	Classification	Catalogue	ID	Peacock et al.; GC	Stiele et al.; Field	Stiele et al.; GC	PHAT	SDSS DR12	NED	SIMBAD
627	004315.03+411326.2	-	-	BA	431	-	-	-	-	-	-	-
628	004315.41+411124.6	1176	GlC	VO	208	B161-G215	-	1176	-	-	-	-
629	004315.66+411556.0	-	-	-	-	-	-	-	-	-	-	-
630	004316.10+411841.3	1180	<XRB>	VO	185	-	-	-	-	-	-	-
631	004316.11+405415.7	1181	<hard>	-	-	-	-	-	-	-	-	-
632	004316.36+411630.0	-	-	BA	435	-	-	-	-	-	-	-
633	004316.39+410348.8	1183	<hard>	-	-	-	-	-	-	-	-	-
634	004317.90+411112.7	1189	none	BA	439	-	-	-	-	-	-	-
635	004318.45+411142.2	-	-	VO	219	-	-	-	-	-	-	-
636	004318.87+412016.9	1194	<SSS>	VO	214	-	-	-	-	-	-	-
637	004319.16+411000.5	-	-	-	-	-	-	-	-	-	-	-
638	004319.92+411318.5	-	-	-	-	-	-	-	-	-	-	-
639	004320.00+411249.3	1199	<fgStar>	BA	446	-	-	-	-	-	-	-
640	004320.73+411531.2	-	-	HO	296	-	-	-	-	-	-	-
641	004320.94+411315.7	-	-	-	-	-	-	-	-	-	-	-
642	004321.06+411750.5	1203	<hard>	VO	200	-	-	-	-	-	-	-
643	004321.52+411557.3	-	-	VO	197	-	-	-	-	-	-	-
644	004321.97+405754.7	1207	<fgStar>	-	-	-	-	-	-	-	-	-
645	004322.11+410924.0	-	-	BA	453	-	-	-	-	-	-	-
646	004322.33+411255.8	-	-	BA	454	-	-	-	-	-	-	-
647	004322.96+411143.9	-	-	-	-	-	-	-	-	-	-	-
648	004323.14+410601.0	1210	<hard>	BA	456	-	-	-	-	-	-	-
649	004323.57+411347.0	-	-	-	-	-	-	-	-	-	-	-
650	004324.83+411726.6	1216	<hard>	BA	461	-	-	-	-	-	-	-
651	004325.00+405747.0	1218	<hard>	-	-	-	-	-	-	-	-	-
652	004325.64+411537.4	-	-	HO	302	-	-	-	-	-	-	-
653	004326.02+411411.7	-	-	-	-	-	-	-	-	-	-	-
654	004326.30+411453.2	-	-	-	-	-	-	-	-	-	-	-
655	004326.30+411911.7	1224	<AGN>	VO	230	-	-	-	-	-	-	-
656	004326.62+410756.3	1226	<hard>	BA	463	-	-	-	-	-	-	-
657	004327.53+410643.7	1231	<hard>	-	-	-	-	-	-	-	-	-
658	004327.72+410504.4	1233	<hard>	-	-	-	-	-	-	-	-	-
659	004327.97+411828.3	1234	SNR	-	-	-	-	-	-	-	-	-
660	004328.16+411454.7	-	-	-	-	-	-	-	-	-	-	-
661	004329.11+410748.0	1238	<hard>	KA	139	-	-	-	-	-	-	-
662	004329.16+411514.7	-	-	-	-	-	-	-	-	-	-	-
663	004329.16+411736.7	-	-	-	-	-	-	-	-	-	-	-
664	004329.53+410905.1	1240	<hard>	BA	472	-	-	-	-	-	-	-
665	004330.14+410521.2	-	-	-	-	-	-	-	-	-	-	-
666	004330.15+410522.6	-	-	-	-	-	-	-	-	-	-	-
667	004330.18+411718.5	-	-	-	-	-	-	-	-	-	-	-
668	004330.26+411648.0	-	-	-	-	-	-	-	-	-	-	-
669	004330.30+411626.8	-	-	-	-	-	-	-	-	-	-	-
670	004331.09+410833.6	-	-	-	-	-	-	-	-	-	-	-
671	004331.10+405705.8	1246	<hard>	-	-	-	-	-	-	-	-	-

Source	CXOU J	*XMM-Newton* Match		*Chandra* Match		LMXB Match			AGN Match			
No.		ID	Classification	Catalogue	ID	Peacock et al.; GC	Stiele et al.; Field	Stiele et al.; GC	PHAT	SDSS DR12	NED	SIMBAD
672	004332.17+411702.6	-	-	-	-	-	-	-	-	-	-	-
673	004332.21+410648.4	1252	<hard>	-	-	-	-	-	-	-	-	-
674	004332.37+411040.8	1253	<hard>	VO	252	-	-	-	-	-	-	-
675	004332.96+411629.4	-	-	-	-	-	-	-	-	-	-	-
676	004333.59+412139.2	1256	<hard>	VO	254	-	-	-	-	-	-	-
677	004333.77+410821.8	-	-	-	-	-	-	-	-	-	-	-
678	004333.80+411407.0	1257	<hard>	VO	239	-	-	-	-	-	-	-
679	004334.16+410207.8	1260	<hard>	-	-	-	-	-	-	-	-	-
680	004334.31+411323.5	1261	<hard>	VO	242	-	-	-	-	-	-	-
681	004335.84+411433.6	1262	none	-	-	-	-	-	-	-	-	-
682	004336.05+411433.9	1262	none	-	-	-	-	-	-	-	-	-
683	004336.63+410811.8	1266	GlC	-	-	B182-G233	-	1266	-	-	-	-
684	004337.27+411443.6	1267	GlC	WI	r3-1	B185-G235	-	1267	-	-	-	-
685	004339.32+410937.1	-	-	-	-	-	-	-	-	-	-	-
686	004340.16+410045.4	1276	<hard>	-	-	-	-	-	-	-	-	-
687	004341.26+405446.3	1279	<Gal>	-	-	-	-	-	-	-	NED	SIMBAD
688	004341.45+405427.0	1280	<AGN>	-	-	-	-	-	-	-	-	-
689	004341.61+410015.3	1284	<hard>	-	-	-	-	-	-	-	-	-
690	004342.68+412606.8	-	-	BA	493	-	-	-	-	-	-	-
691	004343.01+412849.6	1289	<GlC>	BA	494	-	-	-	2259	-	-	-
692	004343.23+405631.2	1290	<hard>	-	-	-	-	-	-	-	-	-
693	004343.30+410103.7	-	-	-	-	-	-	-	-	-	-	-
694	004343.75+410339.7	-	-	-	-	-	-	-	-	-	-	-
695	004343.99+411231.5	1291	SNR	VO	261	-	-	-	-	-	-	-
696	004344.08+405639.0	1292	none	-	-	-	-	-	-	-	-	-
697	004344.34+411155.5	-	-	-	-	-	-	-	-	-	-	-
698	004344.47+410752.7	-	-	-	-	-	-	-	-	-	-	-
699	004344.61+412409.9	-	-	BA	497	-	-	-	-	-	-	-
700	004344.67+412841.5	1293	<AGN>	-	-	-	-	-	-	-	-	-
701	004345.65+412706.4	1297	<hard>	-	-	-	-	-	-	-	-	-
702	004345.75+410803.0	-	-	-	-	-	-	-	-	-	-	-
703	004345.89+411202.6	1298	<hard>	-	-	-	-	-	-	-	-	-
704	004345.90+411025.9	-	-	-	-	-	-	-	-	-	-	-
705	004346.13+410955.2	1299	<hard>	-	-	-	-	-	-	-	-	-
706	004346.14+410118.0	1301	<hard>	-	-	-	-	-	-	-	-	-
707	004347.19+410654.0	1303	<hard>	-	-	-	-	-	-	-	-	-
708	004347.29+410404.4	-	-	-	-	-	-	-	-	-	-	-
709	004348.81+410521.1	-	-	-	-	-	-	-	-	-	-	-
710	004349.30+411053.3	-	-	-	-	-	-	-	1194	-	-	-
711	004349.80+410634.0	-	-	-	-	-	-	-	-	-	-	-
712	004350.75+412117.5	1319	<hard>	-	-	-	-	-	-	-	-	-
713	004353.58+411202.0	1328	SNR	-	-	-	-	-	-	-	-	-
714	004353.65+411655.0	1327	<GlC>	-	-	-	-	-	-	-	-	-
715	004353.70+412041.9	-	-	-	-	-	-	-	-	-	-	-
716	004353.70+410024.5	1329	<hard>	-	-	-	-	-	-	-	-	-

Source	CXOU J	*XMM-Newton* Match		*Chandra* Match		LMXB Match			AGN Match			
No.		ID	Classification	Catalogue	ID	Peacock et al.; GC	Stiele et al.; Field	Stiele et al.; GC	PHAT	SDSS DR12	NED	SIMBAD
717	004354.40+410612.8	1333	<hard>	-	-	-	-	-	467	-	-	-
718	004356.31+412316.1	-	-	-	-	-	-	-	-	-	-	-
719	004356.33+405505.1	-	-	-	-	-	-	-	-	-	-	-
720	004356.41+412202.2	1340	GlC	BA	512	B204-G254	-	-	-	-	-	-
721	004356.55+410416.6	-	-	-	-	-	-	-	-	-	-	-
722	004356.59+410644.3	1342	<hard>	BA	513	-	-	-	-	-	-	-
723	004357.01+410045.4	1346	<hard>	-	-	-	-	-	-	-	-	-
724	004357.57+413054.5	1348	<hard>	-	-	-	-	-	-	-	-	-
725	004358.04+405341.9	1350	<hard>	-	-	-	-	-	-	-	-	-
726	004358.47+411330.6	1351	SNR	-	-	-	-	-	-	-	-	-
727	004359.82+412435.4	-	-	-	-	-	-	-	-	-	-	-
728	004401.04+412808.2	1357	<hard>	BA	516	-	-	-	-	-	-	-
729	004403.11+410404.4	1366	<hard>	-	-	-	-	-	-	-	-	-
730	004403.16+410800.9	1363	<hard>	-	-	-	-	-	3908	-	-	-
731	004403.30+411229.1	1367	<hard>	-	-	-	-	-	-	-	-	-
732	004404.75+412126.2	1373	<AGN>	-	-	-	-	-	-	-	-	-
733	004404.77+405901.6	1374	<hard>	-	-	-	-	-	-	-	-	-
734	004405.52+410235.9	-	-	-	-	-	-	-	-	-	-	-
735	004405.65+410638.6	1376	none	-	-	-	-	-	-	-	-	-
736	004405.69+405336.5	1377	<hard>	-	-	-	-	-	-	-	-	-
737	004405.70+410310.4	-	-	-	-	-	-	-	-	-	-	-
738	004407.80+413107.8	-	-	-	-	-	-	-	-	-	-	-
739	004408.65+405803.7	-	-	-	-	-	-	-	-	-	-	-
740	004409.38+410939.8	1385	<hard>	BA	520	-	-	-	-	-	-	-
741	004409.44+410406.0	-	-	-	-	-	-	-	-	-	-	-
742	004409.84+412813.9	1389	<fgStar>	-	-	-	-	-	-	-	-	-
743	004410.16+411830.4	-	-	-	-	-	-	-	-	-	-	-
744	004411.08+405646.6	1394	<hard>	-	-	-	-	-	-	-	-	-
745	004411.41+405433.2	1397	<hard>	-	-	-	-	-	-	-	-	-
746	004411.81+410208.6	-	-	-	-	-	-	-	-	-	-	-
747	004412.01+405421.6	1398	<hard>	-	-	-	-	-	-	SDSS DR12	-	-
748	004412.20+413148.2	1399	<hard>	-	-	-	-	-	-	-	-	-
749	004412.89+412555.5	-	-	-	-	-	-	-	-	-	-	-
750	004413.22+412910.2	1406	<hard>	-	-	-	-	-	-	-	-	-
751	004413.46+410004.9	-	-	-	-	-	-	-	-	-	-	-
752	004413.80+410536.0	1412	<hard>	-	-	-	-	-	-	-	-	-
753	004413.84+405451.1	-	-	-	-	-	-	-	-	SDSS DR12	-	-
754	004416.02+405722.0	-	-	-	-	-	-	-	-	-	-	-
755	004416.03+413057.2	1420	XRB	-	-	-	1420	-	-	-	-	-
756	004416.85+411114.9	1423	<hard>	-	-	-	-	-	-	-	-	-
757	004416.97+410343.5	1422	<hard>	-	-	-	-	-	-	-	-	-
758	004417.20+405612.0	1424	none	-	-	-	-	-	-	-	-	-
759	004419.21+410306.7	1431	<hard>	-	-	-	-	-	-	-	-	-
760	004420.42+411302.1	-	-	-	-	-	-	-	-	-	-	-
761	004420.81+412206.7	-	-	-	-	-	-	-	-	-	-	-

Source	CXOU J	*XMM-Newton* Match		*Chandra* Match		LMXB Match			AGN Match			
No.		ID	Classification	Catalogue	ID	Peacock et al.; GC	Stiele et al.; Field	Stiele et al.; GC	PHAT	SDSS DR12	NED	SIMBAD
762	004421.09+410457.7	1438	none	-	-	-	-	-	-	-	-	-
763	004421.97+405501.7	-	-	-	-	-	-	-	-	-	-	-
764	004423.31+405753.7	-	-	-	-	-	-	-	-	-	-	-
765	004424.84+413200.5	1446	<hard>	-	-	-	-	-	-	-	-	-
766	004424.86+410333.7	-	-	-	-	-	-	-	-	-	-	-
767	004425.73+412241.7	1450	<hard>	-	-	-	-	-	-	-	-	-
768	004426.48+410250.0	1456	<hard>	-	-	-	-	-	-	-	-	-
769	004426.51+410042.0	1454	<hard>	-	-	-	-	-	-	-	-	-
770	004426.91+410100.6	1459	<fgStar>	-	-	-	-	-	-	-	-	-
771	004429.55+412135.3	1463	GlC	-	-	B225-G280	-	1463	-	-	-	-
772	004429.70+412257.5	-	-	-	-	-	-	-	-	-	-	-
773	004429.75+410030.7	-	-	-	-	-	-	-	-	-	-	-
774	004430.47+412310.2	1468	<hard>	-	-	-	-	-	-	-	-	-
775	004431.98+412519.5	1473	fgStar	-	-	-	-	-	-	-	-	-
776	004432.46+410533.7	1476	<fgStar>	-	-	-	-	-	-	-	-	-
777	004435.49+405911.9	1483	<hard>	-	-	-	-	-	-	-	-	-
778	004435.71+410706.5	1484	<hard>	-	-	-	-	-	-	-	-	-
779	004437.07+411951.3	1488	<hard>	-	-	-	-	-	586	-	-	-
780	004437.84+405713.9	1490	none	-	-	-	-	-	-	-	-	-
781	004438.33+412530.3	-	-	-	-	-	-	-	-	-	-	-
782	004438.47+413412.1	1494	<hard>	-	-	-	-	-	-	-	-	-
783	004440.01+410232.7	-	-	-	-	-	-	-	-	-	-	-
784	004440.48+410138.9	-	-	-	-	-	-	-	-	SDSS DR12	-	-
785	004441.54+405913.1	-	-	-	-	-	-	-	-	SDSS DR12	-	-
786	004446.02+412147.9	1517	<fgStar>	-	-	-	-	-	-	-	-	-
787	004448.15+412247.1	1525	<hard>	-	-	-	-	-	-	-	-	-
788	004449.27+405949.4	1531	none	-	-	-	-	-	-	-	-	-
789	004451.08+412904.9	1535	SNR	-	-	-	-	-	-	-	-	-
790	004452.35+412717.0	1537	<hard>	-	-	-	-	-	-	-	-	-
791	004457.39+412247.3	1553	<XRB>	-	-	-	-	-	-	-	-	-
792	004457.96+412342.5	1559	AGN	-	-	-	-	-	-	-	-	-
793	004458.51+412120.1	-	-	-	-	-	-	-	-	-	-	-
794	004500.17+412100.1	1563	<hard>	-	-	-	-	-	-	-	-	-
795	004500.94+412652.4	-	-	-	-	-	-	-	-	-	-	-

This table summarizes the details of the cross-match between our catalogue and various others. Columns (1) and (2) represent our catalogue. Columns (3) and (4) are the *XMM-Newton* catalogue identification number and classification. Column (5) is the *Chandra* catalogue matched to: BA (Barnard et al., 2014), DS02 (Di Stefano et al., 2002), DS04 (Di Stefano et al., 2004), HO (Hofmann et al., 2013), KA (Kaaret, 2002), KO (Kong et al., 2002), VO (Voss & Gilfanov, 2007), WI (Williams et al., 2004). Column (6) is the catalogue source identification value taken from each respective paper. Columns (7)-(9) represent matches to LMXBs from Peacock et al. (2010) globular clusters (GC), and Stiele et al. (2011) field and globular clusters (GC), with the corresponding names or identification number. Columns (10)-(13) show the results of AGN matching to various catalogues. For PHAT, we used the Andromeda project identification number from Johnson et al. (2015). See Section 3.4 for more details on matching.

Bibliography

Barnard, R., Garcia, M. R., Primini, F., et al. 2014, ApJ, 780, 83

Di Stefano, R., Kong, A. K. H., Garcia, M. R., et al. 2002, ApJ, 570, 618

Di Stefano, R., Kong, A. K. H., Greiner, J., et al. 2004, ApJ, 610, 247

Hofmann, F., Pietsch, W., Henze, M., et al. 2013, A&A, 555, A65

Johnson, L. C., Seth, A. C., Dalcanton, J. J., et al. 2015, ApJ, 802, 127

Kaaret, P. 2002, ApJ, 578, 114

Kong, A. K. H., Garcia, M. R., Primini, F. A., et al. 2002, ApJ, 577, 738

Peacock, M. B., Maccarone, T. J., Kundu, A., & Zepf, S. E. 2010, MNRAS, 407, 2611

Stiele, H., Pietsch, W., Haberl, F., et al. 2011, A&A, 534, A55

Voss, R., & Gilfanov, M. 2007, A&A, 468, 49

Williams, B. F., Garcia, M. R., Kong, A. K. H., et al. 2004, ApJ, 609, 735

Appendix D

Colour-Magnitude Diagrams For ACS Globular Clusters

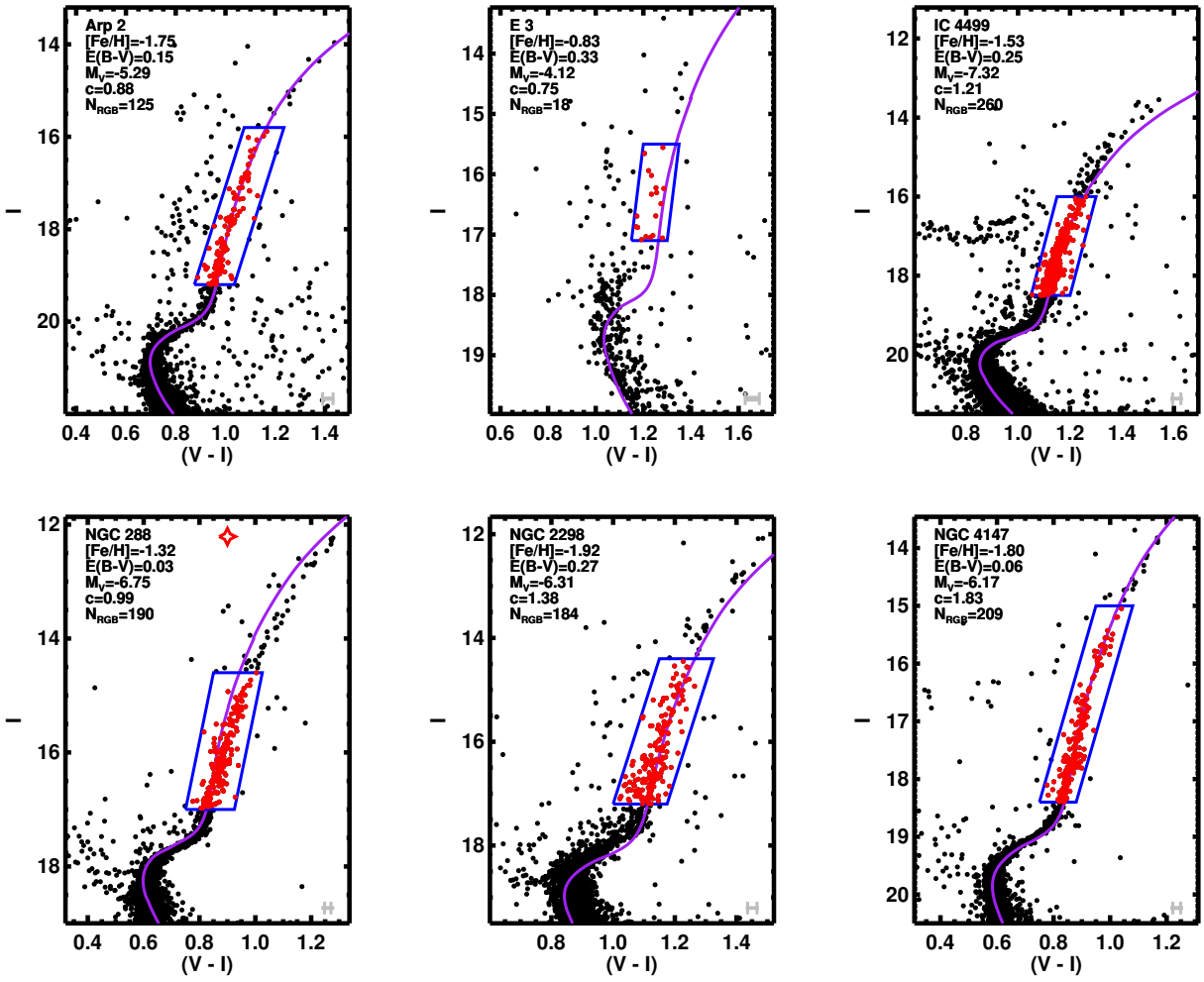

Figure D.1: Colour-magnitude diagrams in the Johnson $(I, V - I)$ plane without reddening correction as in Figure 4.1 for the ACS survey GCs. The overplotted best fitting isochrone has parameters given in Table 4.1. The blue parallelogram corresponds to the conservative estimate of the region where red giant branch stars exist, giving the number of red giant branch stars in the cluster $N_{\rm RGB}$. The open star at top-centre indicates that the cluster hosts a quiescent LMXB. Various cluster parameters from Harris (1996, 2010 edition), including the absolute magnitude M_V and concentration parameter c are shown at top-left. Average photometric uncertainties are represented by the grey error bar at bottom-right.

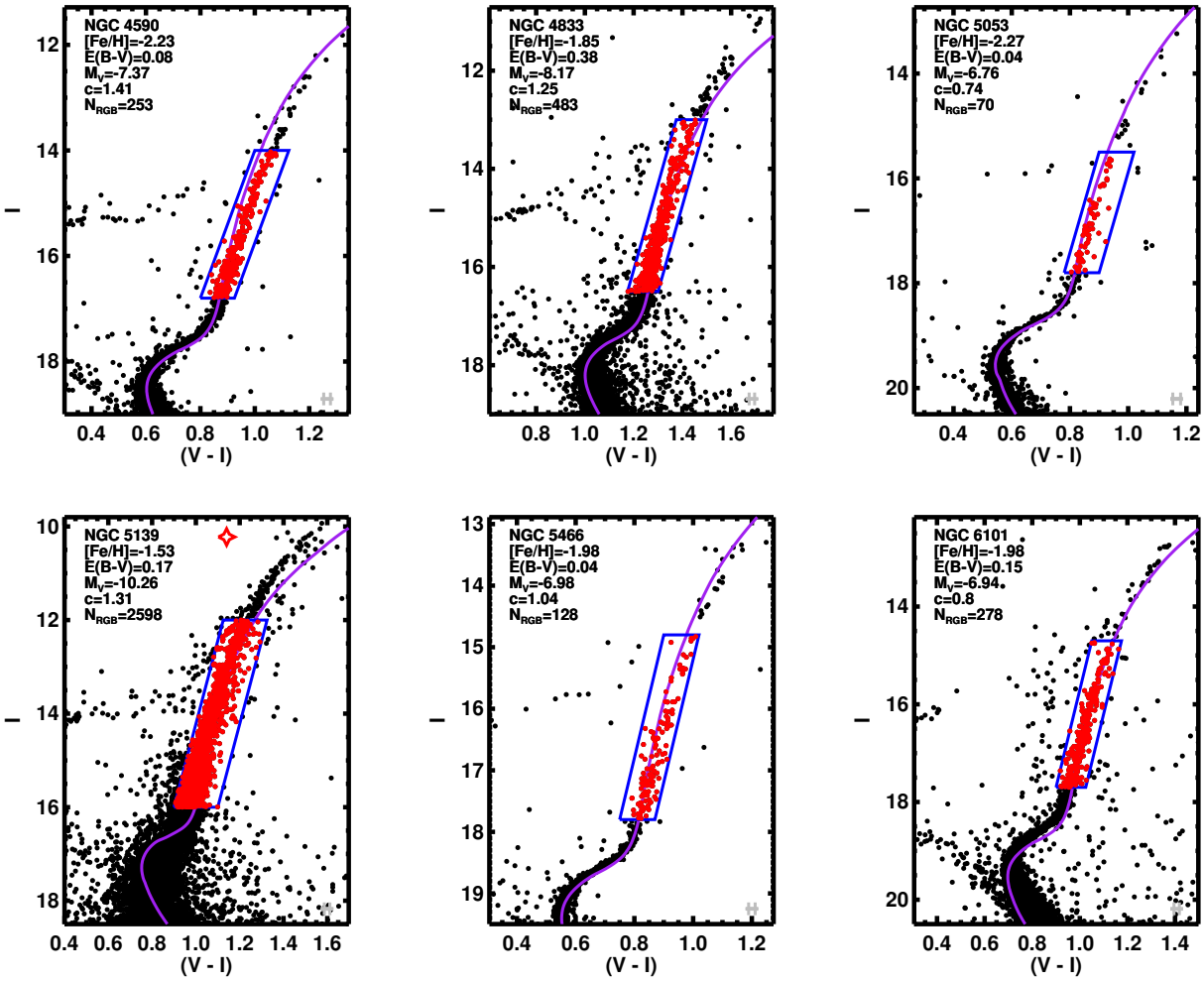
NGC 4590
[Fe/H]=-2.23
E(B-V)=0.08
M_V=-7.37
c=1.41
N_RGB=253
NGC 4833
[Fe/H]=-1.85
E(B-V)=0.38
M_V=-8.17
c=1.25
N_RGB=483
NGC 5053
[Fe/H]=-2.27
E(B-V)=0.04
M_V=-6.76
c=0.74
N_RGB=70
NGC 5139
[Fe/H]=-1.53
E(B-V)=0.17
M_V=-10.26
c=1.31
N_RGB=2598
NGC 5466
[Fe/H]=-1.98
E(B-V)=0.04
M_V=-6.98
c=1.04
N_RGB=128
NGC 6101
[Fe/H]=-1.98
E(B-V)=0.15
M_V=-6.94
c=0.8
N_RGB=278
(V - I)

Figure D.2

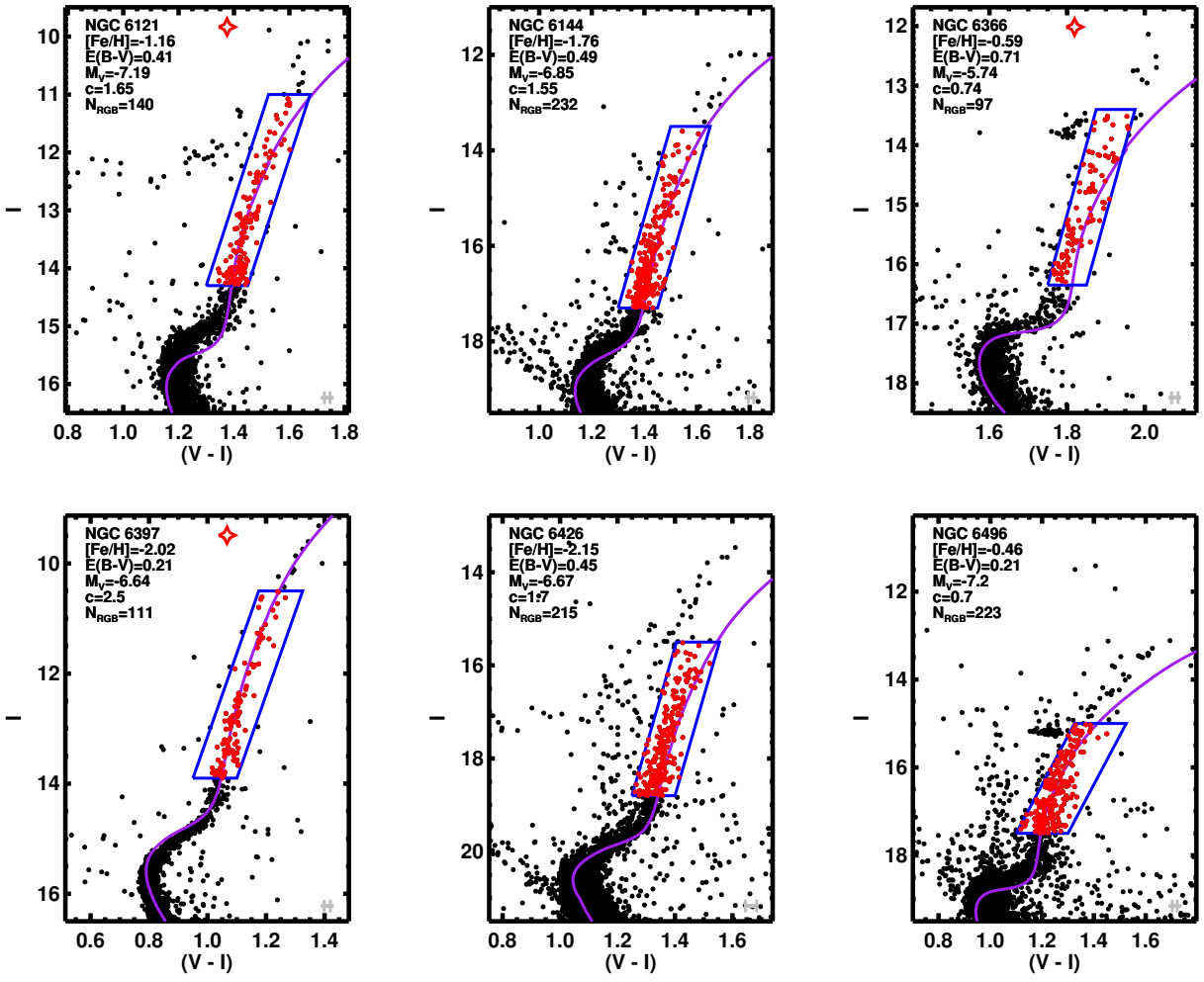
NGC 6121
[Fe/H]=-1.16
E(B-V)=0.41
M_V=-7.19
c=1.65
N_RGB=140
NGC 6144
[Fe/H]=-1.76
E(B-V)=0.49
M_V=-6.85
c=1.55
N_RGB=232
NGC 6366
[Fe/H]=-0.59
E(B-V)=0.71
M_V=-5.74
c=0.74
N_RGB=97
NGC 6397
[Fe/H]=-2.02
E(B-V)=0.21
M_V=-6.64
c=2.5
N_RGB=111
NGC 6426
[Fe/H]=-2.15
E(B-V)=0.45
M_V=-6.67
c=1.7
N_RGB=215
NGC 6496
[Fe/H]=-0.46
E(B-V)=0.21
M_V=-7.2
c=0.7
N_RGB=223
(V - I)

Figure D.3

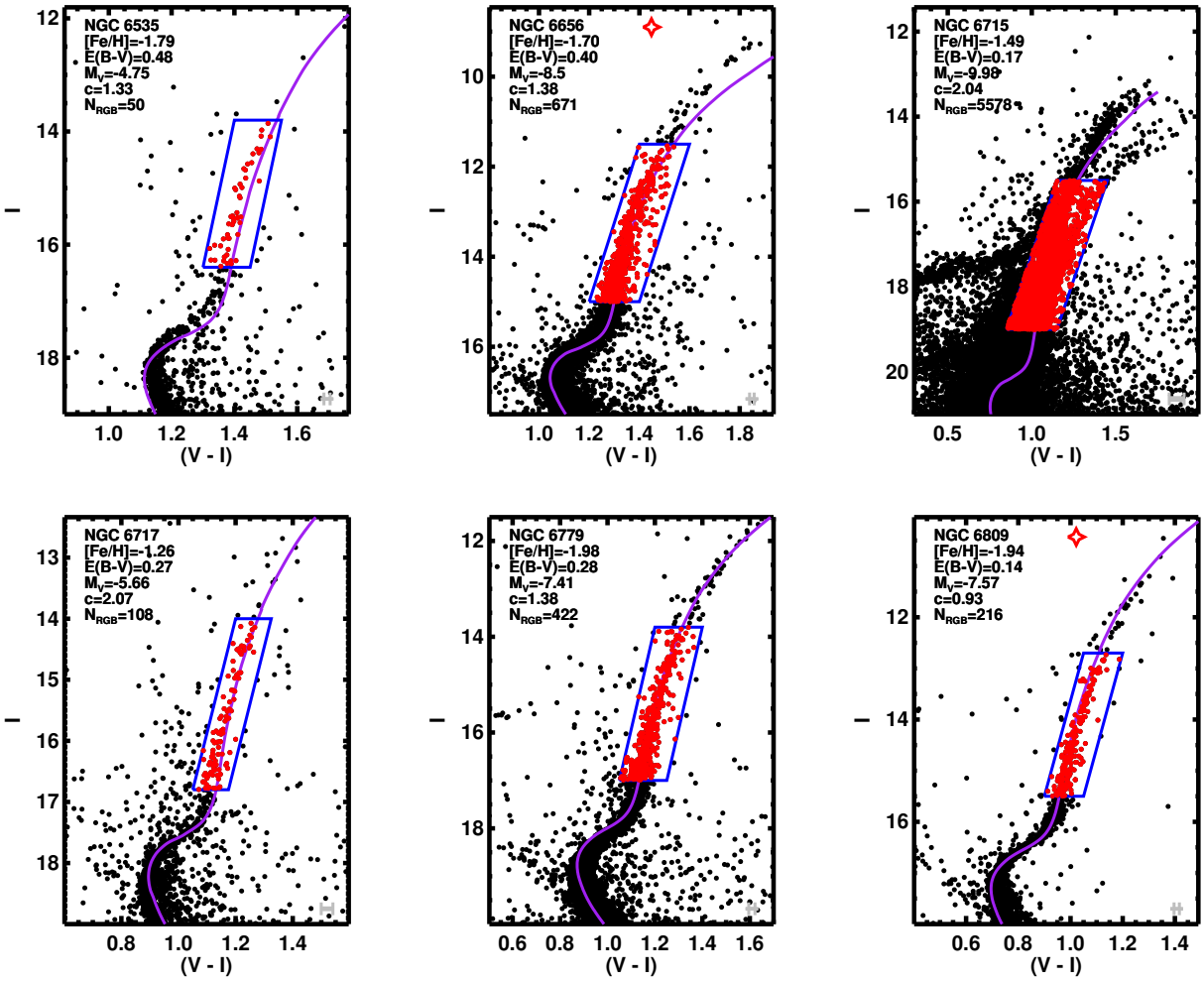
NGC 6535
[Fe/H]=-1.79
E(B-V)=0.48
M_V=-4.75
c=1.33
N_RGB=50
NGC 6656
[Fe/H]=-1.70
E(B-V)=0.40
M_V=-8.5
c=1.38
N_RGB=671
NGC 6715
[Fe/H]=-1.49
E(B-V)=0.17
M_V=-9.98
c=2.04
N_RGB=5578
NGC 6717
[Fe/H]=-1.26
E(B-V)=0.27
M_V=-5.66
c=2.07
N_RGB=108
NGC 6779
[Fe/H]=-1.98
E(B-V)=0.28
M_V=-7.41
c=1.38
N_RGB=422
NGC 6809
[Fe/H]=-1.94
E(B-V)=0.14
M_V=-7.57
c=0.93
N_RGB=216
(V - I)
I

Figure D.4

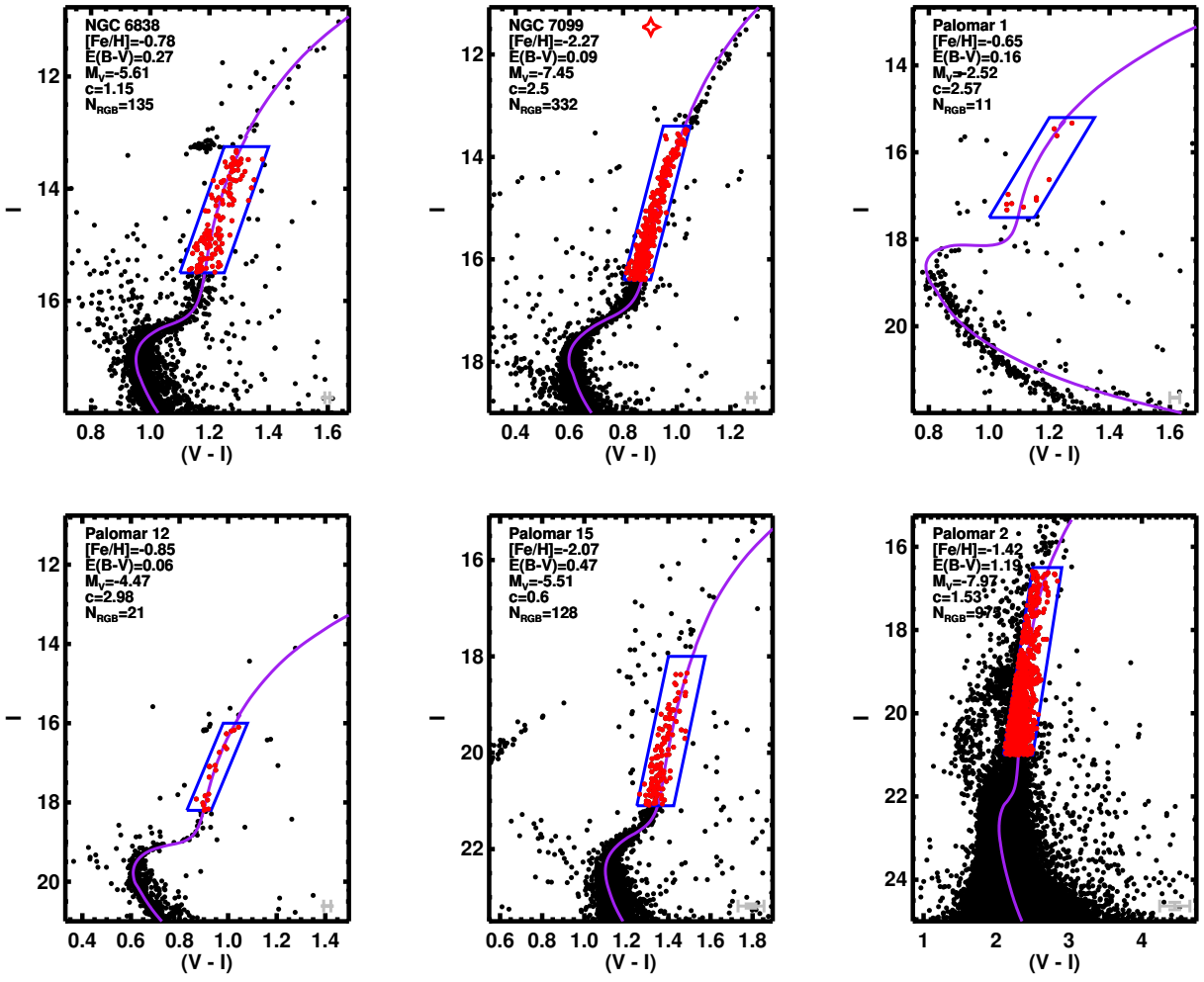
NGC 6838
[Fe/H]=-0.78
E(B-V)=0.27
M_V=-5.61
c=1.15
N_RGB=135
NGC 7099
[Fe/H]=-2.27
E(B-V)=0.09
M_V=-7.45
c=2.5
N_RGB=332
Palomar 1
[Fe/H]=-0.65
E(B-V)=0.16
M_V=-2.52
c=2.57
N_RGB=11
Palomar 12
[Fe/H]=-0.85
E(B-V)=0.06
M_V=-4.47
c=2.98
N_RGB=21
Palomar 15
[Fe/H]=-2.07
E(B-V)=0.47
M_V=-5.51
c=0.6
N_RGB=128
Palomar 2
[Fe/H]=-1.42
E(B-V)=1.19
M_V=-7.97
c=1.53
N_RGB=973
(V - I)

Figure D.5

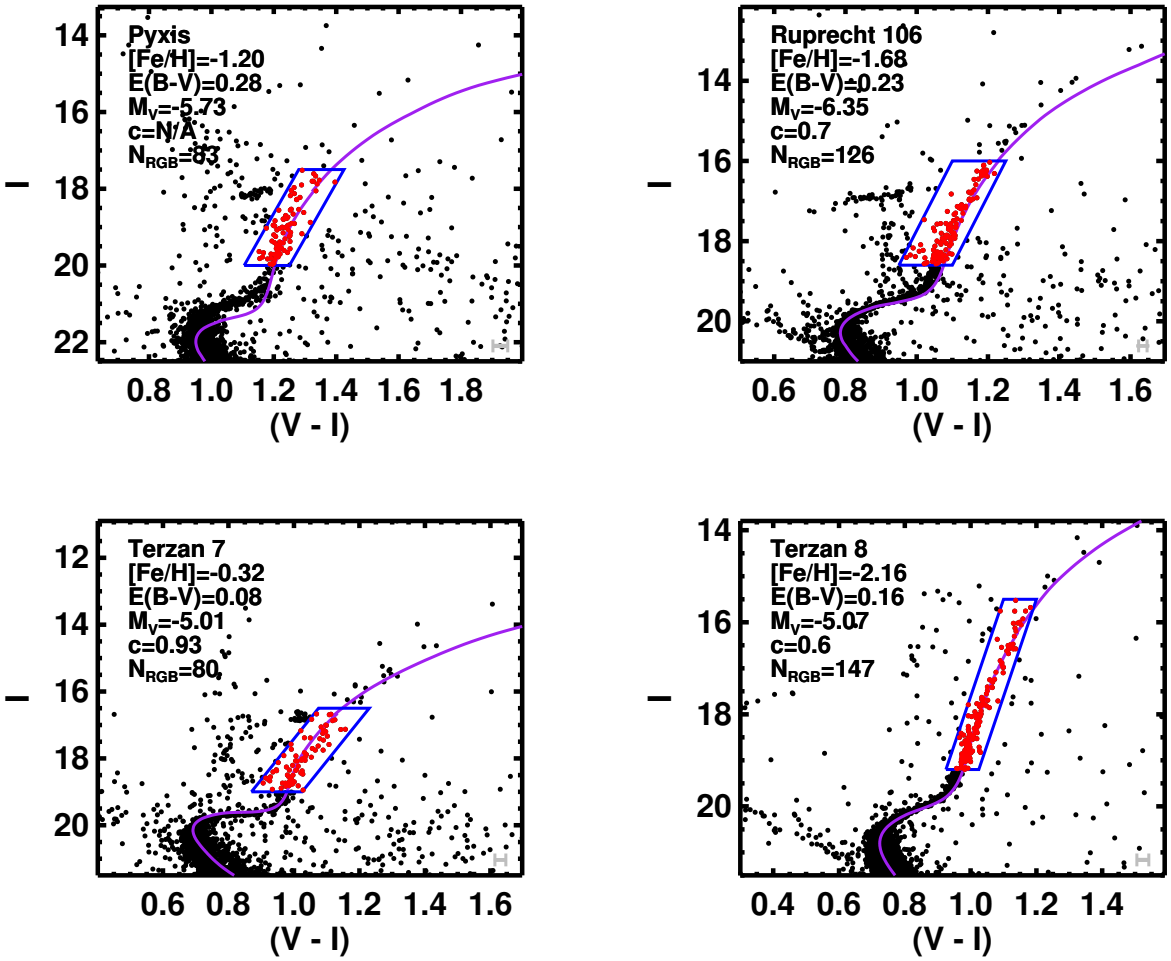
Pyxis
[Fe/H]=-1.20
E(B-V)=0.28
M_V=-5.73
c=N/A
N_RGB=83
Ruprecht 106
[Fe/H]=-1.68
E(B-V)=0.23
M_V=-6.35
c=0.7
N_RGB=126
Terzan 7
[Fe/H]=-0.32
E(B-V)=0.08
M_V=-5.01
c=0.93
N_RGB=80
Terzan 8
[Fe/H]=-2.16
E(B-V)=0.16
M_V=-5.07
c=0.6
N_RGB=147
(V - I)

Figure D.6

Bibliography

Harris, W. E. 1996, AJ, 112, 1487

Appendix E

Colour-Magnitude Diagrams For WFPC2 Globular Clusters

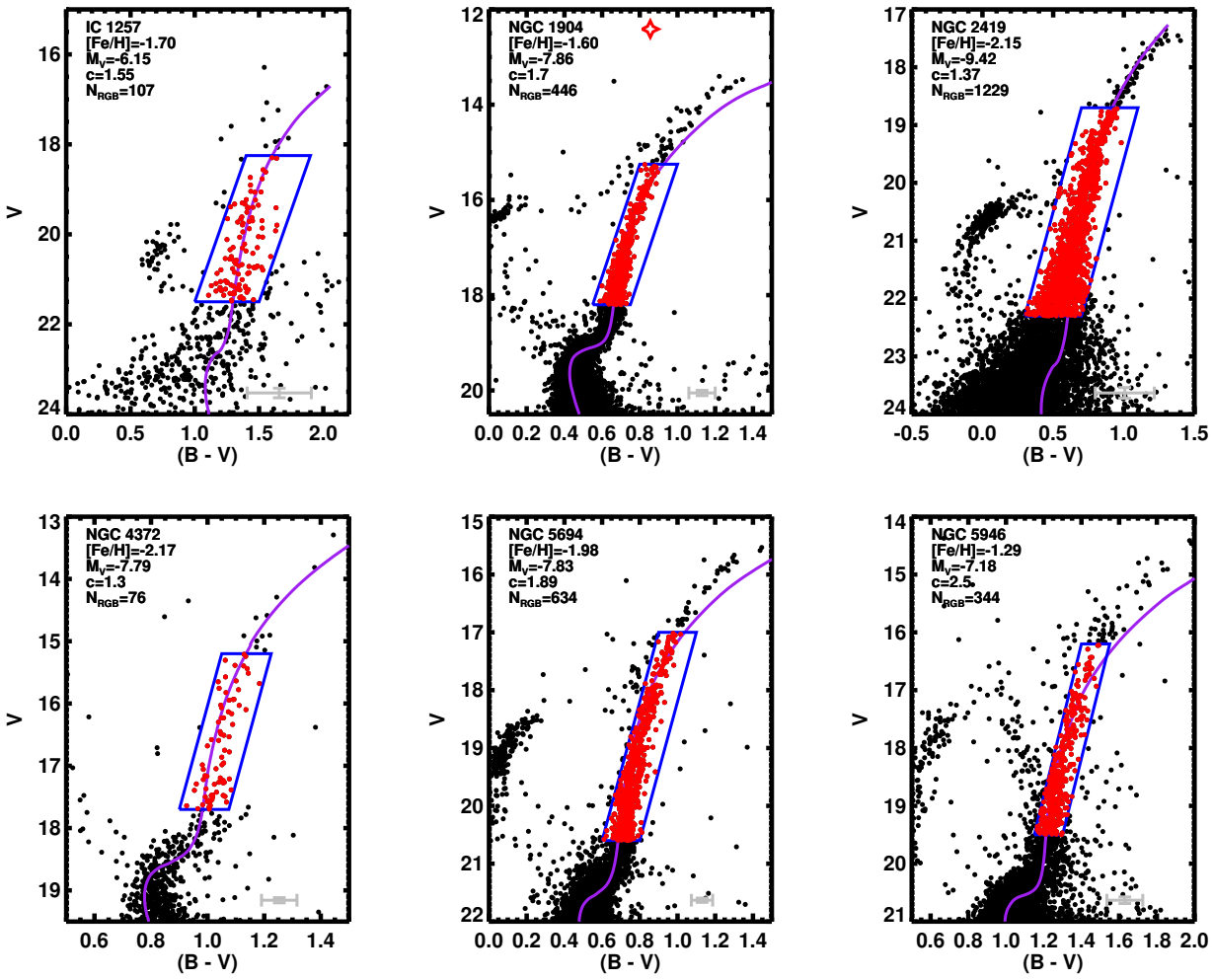

Figure E.1: Colour-magnitude diagrams in the Johnson $(V, B-V)$ plane without reddening correction as in Figure 4.1 except for the WFPC2 survey GCs. The overplotted best fitting isochrone has parameters given in Table 4.1. The blue parallelogram corresponds to the conservative estimate of the region where red giant branch stars exist, giving the number of red giant branch stars in the cluster $N_{\rm RGB}$. The open star at top-centre indicates that the cluster hosts a quiescent LMXB. Various cluster parameters from Harris (1996, 2010 edition), including the absolute magnitude M_V and concentration parameter c are shown at top-left. Average photometric uncertainties are represented by the grey error bar at bottom-right.

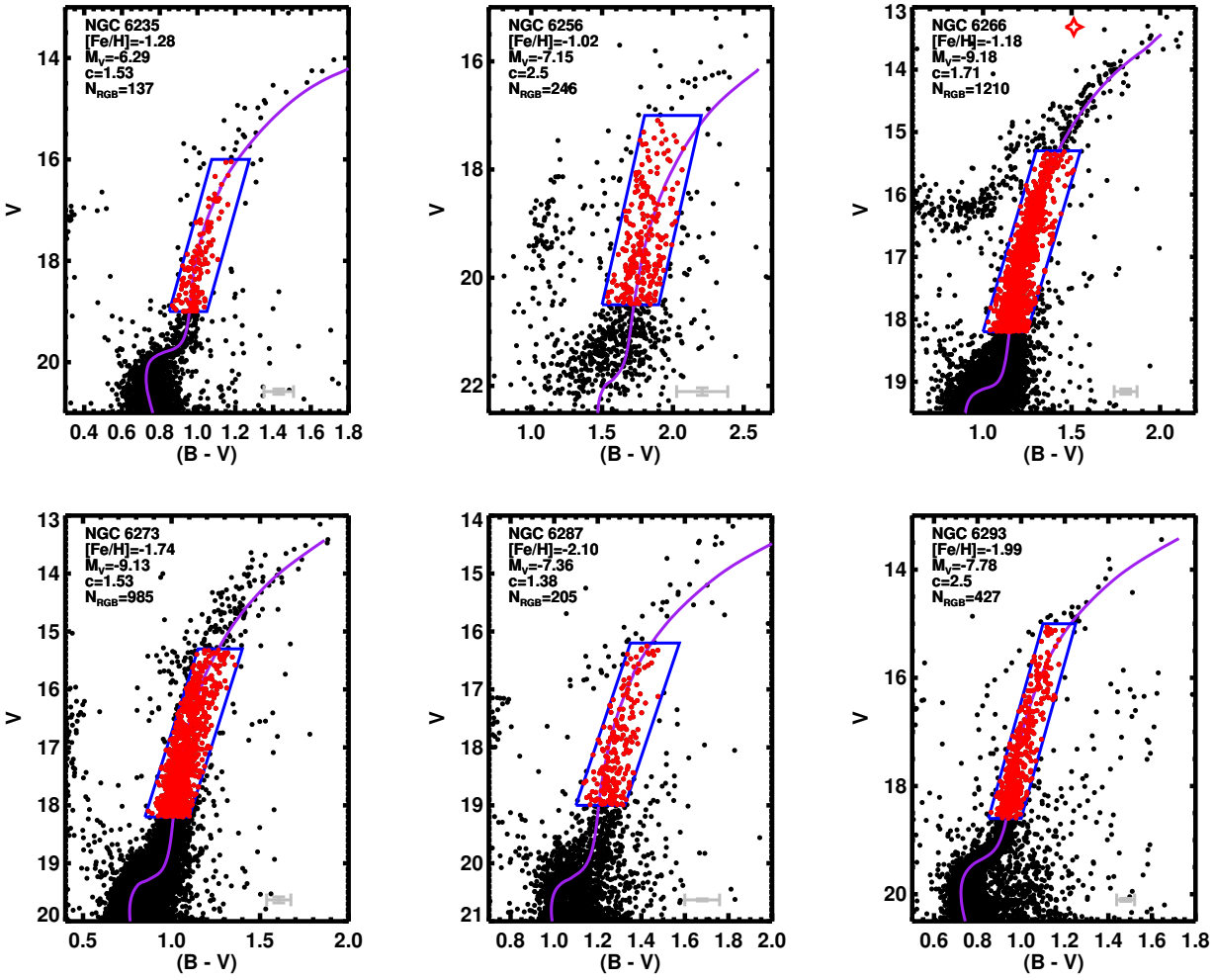
NGC 6235
[Fe/H]=-1.28
M_V=-6.29
c=1.53
N_RGB=137
NGC 6256
[Fe/H]=-1.02
M_V=-7.15
c=2.5
N_RGB=246
NGC 6266
[Fe/H]=-1.18
M_V=-9.18
c=1.71
N_RGB=1210
NGC 6273
[Fe/H]=-1.74
M_V=-9.13
c=1.53
N_RGB=985
NGC 6287
[Fe/H]=-2.10
M_V=-7.36
c=1.38
N_RGB=205
NGC 6293
[Fe/H]=-1.99
M_V=-7.78
c=2.5
N_RGB=427
V
(B - V)

Figure E.2

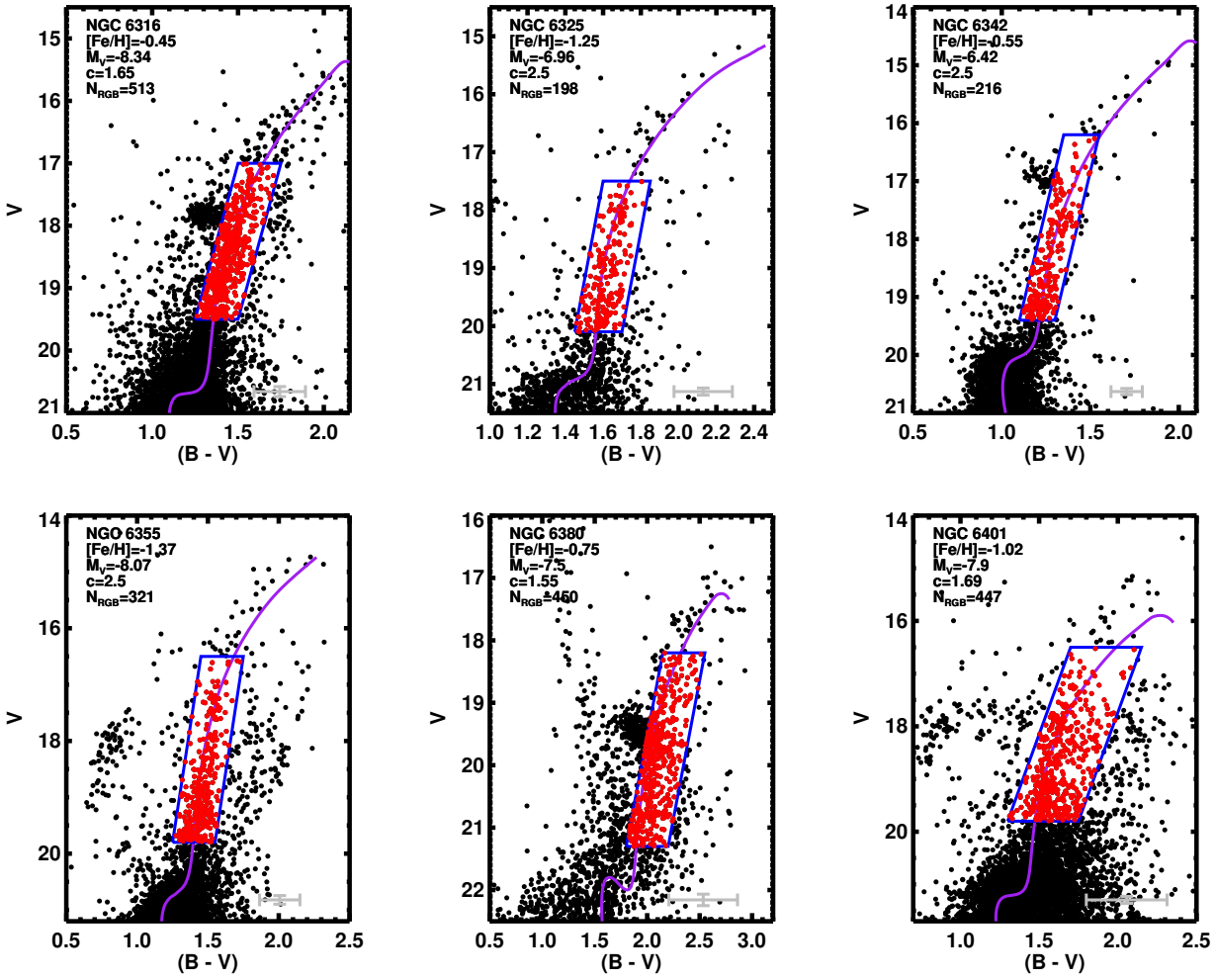
NGC 6316
[Fe/H]=-0.45
M_V=-8.34
c=1.65
N_RGB=513
NGC 6325
[Fe/H]=-1.25
M_V=-6.96
c=2.5
N_RGB=198
NGC 6342
[Fe/H]=-0.55
M_V=-6.42
c=2.5
N_RGB=216
NGC 6355
[Fe/H]=-1.37
M_V=-8.07
c=2.5
N_RGB=321
NGC 6380
[Fe/H]=-0.75
M_V=-7.5
c=1.55
N_RGB=460
NGC 6401
[Fe/H]=-1.02
M_V=-7.9
c=1.69
N_RGB=447
V
(B - V)

Figure E.3

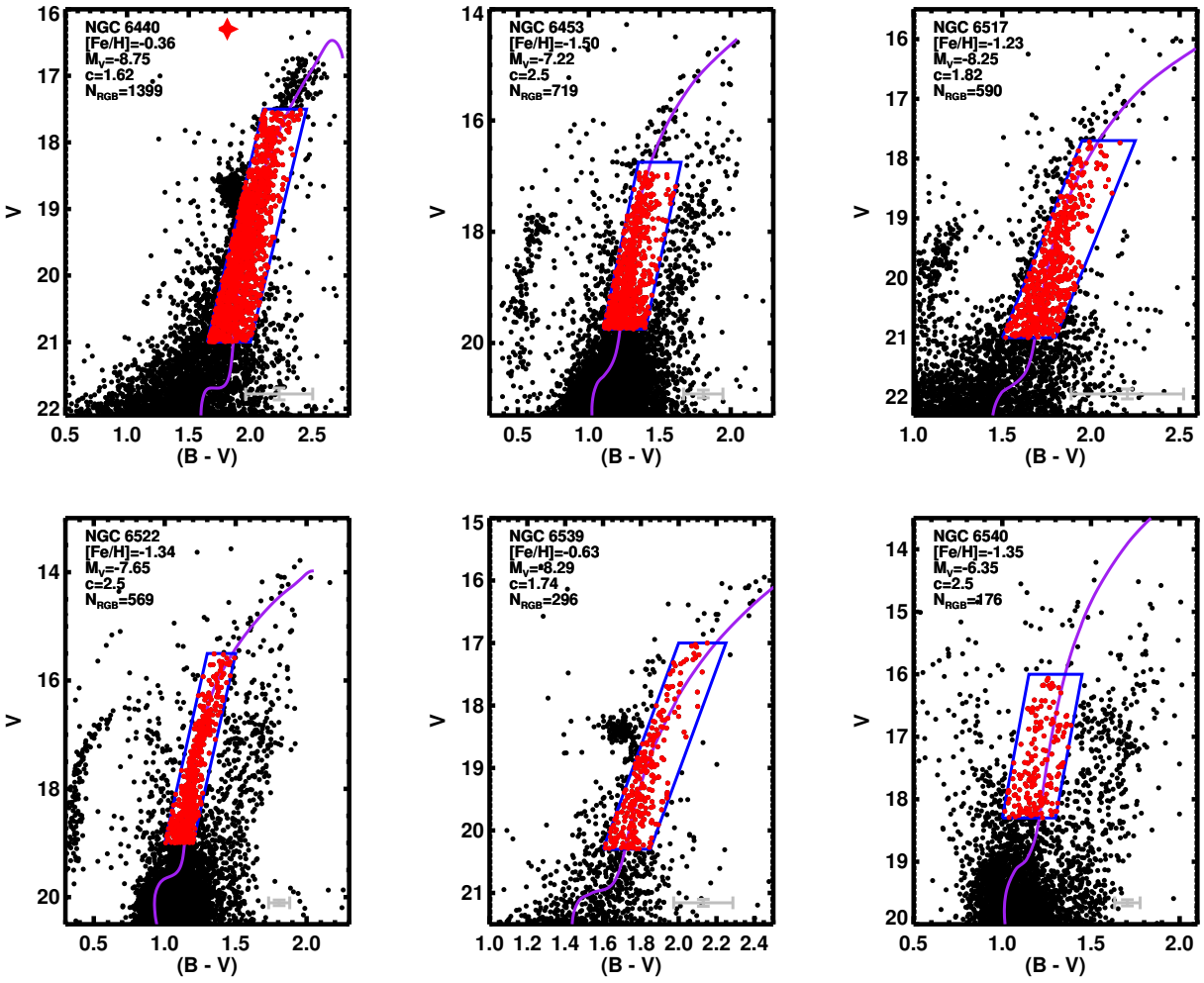
NGC 6440
[Fe/H]=-0.36
M_V=-8.75
c=1.62
N_RGB=1399
NGC 6453
[Fe/H]=-1.50
M_V=-7.22
c=2.5
N_RGB=719
NGC 6517
[Fe/H]=-1.23
M_V=-8.25
c=1.82
N_RGB=590
NGC 6522
[Fe/H]=-1.34
M_V=-7.65
c=2.5
N_RGB=569
NGC 6539
[Fe/H]=-0.63
M_V=-8.29
c=1.74
N_RGB=296
NGC 6540
[Fe/H]=-1.35
M_V=-6.35
c=2.5
N_RGB=176
V
(B - V)

Figure E.4

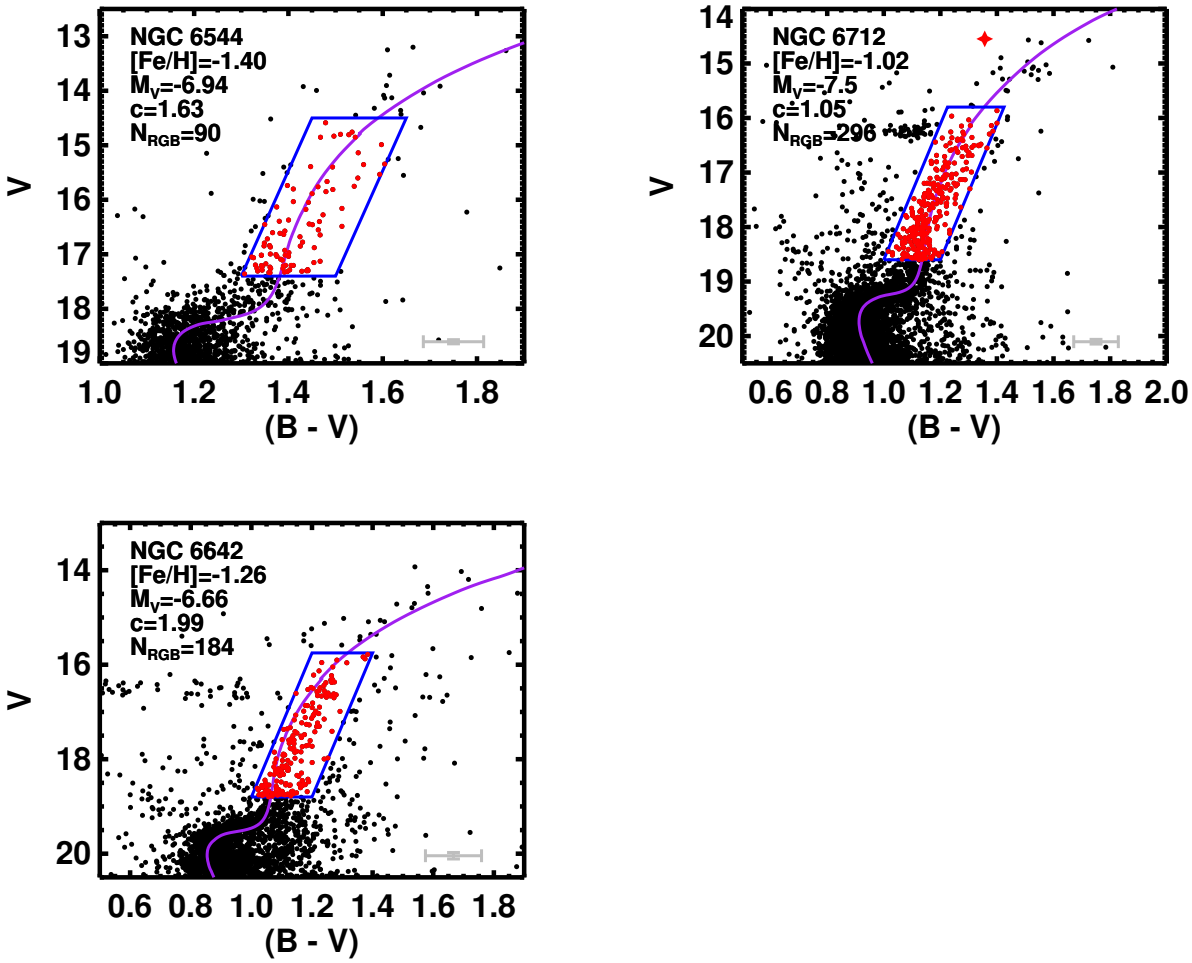
NGC 6544
[Fe/H]=-1.40
M_V=-6.94
c=1.63
N_RGB=90
V
(B - V)
NGC 6712
[Fe/H]=-1.02
M_V=-7.5
c=1.05
N_RGB=296
V
(B - V)
NGC 6642
[Fe/H]=-1.26
M_V=-6.66
c=1.99
N_RGB=184
V
(B - V)

Figure E.5

Bibliography

Harris, W. E. 1996, AJ, 112, 1487

Neven Vulic

Education

Degree	Institution	Completed
Ph.D. in Astronomy	University of Western Ontario	June 2016
M.Sc. in Astronomy	University of Western Ontario	May 2012
B.Ed. in Math & Physics	OISE, University of Toronto	June 2009
H.B.Sc. in Physics & Astronomy	University of Toronto	May 2008

Awards

Award	Value	Date
Ontario Graduate Scholarship, University of Western Ontario	$15,000	May 2015-2016
UWO Physics & Astronomy Award of Excellence in Teaching	$100	2014-2015

Grants

Grant	Value	Date
Society of Graduate Students Travel Grant	$200	Sept 2015
Canadian Astronomical Society Annual General Meeting	$50	June 2015
Society of Graduate Students Travel Grant	$350	Sept 2014
Canadian Astronomical Society Annual General Meeting	$400	June 2013
Society of Graduate Students Travel Grant	$300	Sept 2012
Astronomy's Discoveries & Physics Education Gordon Conference	$800	June 2012
Canadian Astronomical Society Annual General Meeting	$400	June 2012

Accepted Co-I Observing Proposals

Chandra, 350 ks ($141,235), *A Chandra Legacy Survey of the Disk of M31*, PI: Ben Williams, 2015A

Research Contributions

Articles Published in Refereed Journals

1. **Vulic, N.**, Gallagher, S. C., and Barmby, P., (2016) *X-Rays Beware: The Deepest Chandra Catalogue of Point Sources in M31*, *MNRAS*, DOI: 10.1093/mnras/stw1523.

2. **Vulic, N.**, Gallagher, S. C., and Barmby, P., (2014) *Faint X-ray Binaries and Their Optical Counterparts in M31*, *ApJ*, vol. 790 pp. 136-153 (arXiv:astro-ph/1406.4121).

3. **Vulic, N.**, Barmby, P., and Gallagher, S. C. (2013) *Stacking Star Clusters in M51: Searching for Faint X-Ray Binaries*, *ApJ*, vol. 763 pp. 96-108 (arXiv:astro-ph/1212.0859).

Contributed Conference Presentations

1. **Vulic, N.**, Barmby, P., and Gallagher, S. C. (2015) *Over '1001011000' Chandra X-ray Point Sources in M31: Into the Faint Abyss*, Canadian Astronomical Society Annual General Meeting held in Hamilton, Ontario, May 24 - 27, 2015; **talk**.

2. **Vulic, N.**, Gallagher, S. C., and Barmby, P. (2014) *Faint X-ray Binaries and Their Optical Counterparts in M31*, High Energy Astrophysics Division of the AAS held in Chicago, Illinois, August 17 - 21, 2014; **poster**.

3. **Vulic, N.**, Gallagher, S. C., and Barmby, P. (2013) *Searching for Faint X-ray Binaries in M31*, Canadian Astronomical Society Annual General Meeting held in Vancouver, British Columbia, May 27 - 30, 2013; **talk**.

4. **Vulic, N.**, Barmby, P., and Gallagher, S. C. (2012) *A Stacking Analysis of Star Clusters in M51: The Search for X-ray Binaries*, X-ray Binaries: Celebrating 50 Years Since the Discovery of Sco X-1 conference held in Boston, MA, July 10 - 12, 2012; **poster**.

5. **Vulic, N.**, Barmby, P., and Gallagher, S. C. (2012) *A Stacking Analysis of Star Clusters in M51: The Search for X-ray Binaries*, Canadian Astronomical Society Annual General Meeting held in Calgary, Alberta, June 3 - 7, 2012; **talk**.

6. **Vulic, N.**, Barmby, P., and Gallagher, S. C. (2011) *Optical Vs. X-rays in M51: Searching for X-ray Binaries in Star Clusters*, Canadian Astronomical Society Annual General Meeting held in London, Ontario, May 30 - June 2, 2011; **poster**.

Teaching Assistant Experience

Teaching Assistant, *The University of Western Ontario* 2010–Present
Courses: Introductory Graduate and Undergraduate Astronomy,
1st and 2nd Year Physics Labs and Tutorials, Origin of the Universe
Undergraduate Research Supervision:
Ljubisa Sehovac Summer 2015
Gabe Keenleyside 2013–2014

Leadership Experience

Physics & Astronomy Outreach Committee Fall 2012–Summer 2013
Physics & Astronomy Graduate Student Council 2012–Present
Society of Graduate Students Physics & Astronomy Councillor Fall 2011–Summer 2015

Professional Societies

Canadian Astronomical Society (CASCA)
American Astronomical Society (AAS); High-Energy Astrophysics Division

Outreach and Broader Impact

Presenter, Cronyn Observatory Open Houses, *University of Western Ontario* 2010–Present
Extragalactic Astronomy Journal Club Member, *University of Western Ontario* 2010–Present
London Science Olympics Volunteer May 2014
Organized 1st Annual Astronomy Seminar Jamboree, *University of Western Ontario* Sept 2012
Astronomy Educational Journal Club Member, *University of Western Ontario* 2012
Centre for Planetary Science/Exploration Volunteer, *University of Western Ontario* 2011–2012
Judge for University of Toronto Schools Science Fair, *University of Toronto* 2009